IEA GHG Weyburn CO_2 Monitoring & Storage Project Summary Report 2000-2004

An International Collaborative Research Program
Led by the PTRC Based in
Regina, Saskatchewan, Canada

Editors:
M. Wilson
M. Monea

Theme Leaders:
S.Whittaker, S I R
D.White, GSC
D.Law, ARC
R.Chalaturnyk, U of A

ptrc
Petroleum Technology Research Centre

Canada

IEA Greenhouse Gas R&D Programme

University of Regina

Table of Contents

IEA GHG Weyburn CO_2 Monitoring & Storage Project Summary Report 2000-2004

From the proceedings of the 7th International Conference on Greenhouse Gas Control Technologies

September 5-9, 2004, Vancouver, Canada

Volume III

Table of Contents

PTRC Internet Homepage

http://www.ptrc.ca

Consult the PTRC Internet Homepage for full catalogue information on all books, journals, and electronic products and services.

PTRC publications of Related Interest

IEA GHG Weyburn CO_2 Monitoring and Storage Project: Phase 2 Proposal
Available on request

For Publication Inquiries, contact:

PTRC

Mike Monea

Executive Director,
Petroleum Technology
Research Centre
6 Research Drive
Regina, Saskatchewan,
S4S 7J7 Canada

Tel: +306-787-8290
Fax: +306-787-8811
Email: monea.ptrc@src.sk.ca

Malcolm Wilson
Director,
Energy and Environment
University of Regina
and Petroleum Technology
Research Centre
6 Research Drive
Regina, Saskatchewan,
S4S 7J7 Canada

Tel: +306-337-2287
Fax: +306-787-2333
Email: wilsomal@uregina.ca

General Inquiries, including placing orders, should be directed to PTRC.

IEA GHG Weyburn CO_2 Monitoring & Storage Project Summary Report 2000-2004

From the proceedings of the 7th International Conference on Greenhouse Gas Control Technologies

September 5-9, 2004, Vancouver, Canada

Theme Leaders

S. Whittaker
Saskatchewan Industry and Resources,
Regina, Saskatchewan, CA
D. White
Geological Survey of Canada,
Ottawa, Ontario, CA
D. Law
Alberta Research Council,
Edmonton, Alberta, CA
R. Chalaturnyk
University of Alberta,
Edmonton, Alberta, CA

Edited by

M. Wilson
University of Regina,
Regina, Saskatchewan, CA.
M. Monea
PTRC
Regina, Saskatchewan, CA

Volume III

2004

PETROLEUM TECHNOLOGY RESEARCH CENTRE
Regina

Table of Contents

PETROLEUM TECHNOLOGY RESEARCH CENTRE
6 Research Drive
Regina, Saskatchewan
S4S 7J7, CA

First Edition 2004

Cataloguing & Publication Data

Library and Archives Canada / Bibliothèque et Archives Canada
Canadian ISBN Agency / Agence canadienne de l' ISBN

IEA GHG Weyburn CO_2 Monitoring & Storage Project Summary Report 2000-2004

ISBN 0-9736290-0-2

FORWARD

In 1998, when it became clear that the proposed CO_2 Enhanced Oil Recovery project of EnCana (then PanCanadian) was a reality, discussions began within government and with EnCana to initiate a major research project to operate in parallel with the commercial oil recovery project. This phase of the project culminated with a workshop in August of 1999, when the basics of the project and, more importantly, the core of the research team were determined. It was at this time that the new General Manager of the Petroleum Technology Research Centre (PTRC) became responsible for the fledgeling research project.

From the very start of this project, it was clear that a baseline survey was critical to the ultimate success of the larger research project. The timing was short, however, given the schedule for project start-up set by EnCana. To undertake a planned baseline survey would take a substantial amount of money. It is at this point that credit must be given to the politicians who supported this project. While there was considerable technical support for the concept, it was necessary to move this support through the government infrastructure in Saskatchewan and Canada to obtain the necessary funding for the baseline survey. Two senior politicians stepped up to the plate, demonstrating confidence in their technical staff, and supported the release of the necessary funding. While numerous people deserve mention for their role in this project, too many to mention in these notes, these two politicians stand at the front. Minister Ralph Goodale, then the federal Minister responsible for Natural Resources Canada and Minister Eldon Lautermilch, then the provincial Minister responsible for Saskatchewan Energy and Mines took the initiative to support funding.

The original project proponents envisaged a project that would require in the order of $20 million Canadian over four years to complete. Partly as a result of the importance of the project and partly due to the tenacity of Roland Moberg, the General Manager of the PTRC, this goal was more than achieved with cash and in-kind contributions. At least as importantly, this project demonstrated that a truly international research project could be managed in an effective manner, producing excellent results at the culmination of the four years of research. This is due, in no small part, to Project Manager Waleed Jazrawi.

This book provides a public overview of the work of the many excellent researchers who were involved in the research program. This is a very brief overview of the total work and the Editors would like to thank the Theme writers for the effort they put into synthesizing the huge volume of good work into a book of manageable length that captures the essence of this research. These writers include Steve Whittaker (Saskatchewan Industry and Resources), Don White (Geological Survey of Canada), David Law (Alberta Research Council), and Rick Chalaturnyk (University of Alberta).

During the course of the project, the International Energy Agency Greenhouse Gas R&D Programme (IEA GHG) undertook a formal expert review of the work underway. The IEA GHG had always been a strong supporter of the project and helped greatly in maintaining the visibility of the project. The review was a very positive demonstration of this support and highlighted in a very positive way the value of the work and the professionalism of the research team. This was the start of the peer-review process, and the editors would like to recognize the efforts of Paul Freund and John Gale of IEA GHG for their efforts and support. The peer-review process has been completed by three very credible groups. The draft of this book was sent out to three research groups: Researchers at Stanford University in California; Researchers with the CO_2 Cooperative Research Centre (CO_2CRC) in Australia; and Researchers at the University of Saskatchewan in Saskatchewan. The Editors would like to extend their thanks to the individuals with these three groups who provide excellent comments to the Theme writers and allowed us to complete the peer-review in a timely fashion.

The combination of good researchers, good writers, good project management, and good peer-reviewers has made the editors' job easy. We are convinced that this book is a fitting tribute to research that will set the international standard for geological storage of CO_2. Our thanks go out once again to all those involved in this excellent work.

Mike Monea, Executive Director, PTRC
Malcolm Wilson, Director Energy and Environment, University of Regina and PTRC

EDITORS' NOTE

As the IEA Greenhouse Gas R&D Programme has played such a significant role in the Project and in the production of this book, it is only fitting that this group have an opportunity to express their sentiments regarding this great achievement, and so they have capped their participation with the following Note…

From the earliest days, when the idea of injecting CO_2 into the Weyburn oil field was first mooted, the IEA Greenhouse Gas R&D Programme has been deeply interested in, and closely associated with, the Weyburn project. The IEA Greenhouse Gas R&D Programme is an international collaboration that has been working on capture and storage of CO_2 for more than 13 years. When Malcolm Wilson first made us aware of the possibility of an EOR project in Saskatchewan involving captured CO_2, we were keen to do whatever we could to help and assist and, especially, to take advantage of this opportunity to learn about the behaviour of CO_2 underground.

We expect the technique of capture and geological storage of CO_2 will have a significant part to play in tackling climate change this century. In order for this to happen, there is a need for data on the behaviour of CO_2, to validate models and to influence decision-makers about the reliability of this method of managing greenhouse gas emissions. So, over the years we have helped in establishing international collaboration, given publicity to the developments and achievements at Weyburn, and helped to broaden the international research base, which is learning from the Weyburn project, and contributed by organising external reviews of the scientific work being conducted.

We are very pleased to see the collection of papers in this book, which will be an important step towards disseminating the knowledge that has been acquired from this world leading project.

Kelly Thambimuthu, Chairman Executive Committee, IEA Greenhouse Gas R&D Programme
Paul Freund, Project Director, IEA Greenhouse Gas R&D Programme

ACKNOWLEDGEMENTS

To try to identify all of the people involved in the research leading to the successful conclusion of the IEA GHG Weyburn CO_2 Capture and Storage Project would lead to a list of names extending over several pages. These individuals are all key parts of this project and are thanked for their efforts. This book is a testament to those efforts. There are, however, some individuals that should be mentioned in order to effectively recognize their contributions to the success of this project. The first of these are Kyle Worth and Heidi Smithson of the PTRC. These two individuals have worked quietly in the background, but without their dedication, the project would certainly have foundered. Chris Rochelle and Jim Riding from the British Geological Survey also deserve recognition for developing the successful proposal to the European Commission and for guiding the European research program. John Gale of the IEA GHG should be recognized for bringing together the expert-review team and guiding it to a successful conclusion with only a few guiding principles and limited time to work with. His team also deserves credit for the work they did for the project. Similarly, the groups involved in the peer-review exercise must be congratulated for their excellent comments and their timeliness. Two others that provided significant input were Roland Moberg for his persistence in obtaining funding, and Waleed Jazrawi, for his guidance of the project, managing it to success. Finally, no set of acknowledgements would be complete without mention of Bruce Stewart, one of the "Founding Fathers" without whose enthusiastic support over the entire lifetime of the project, it could not have succeeded.

TABLE OF CONTENTS

INTRODUCTION

1 PROJECT OVERVIEW

1.1 Project History

In July, 2000, a major research project to study the geological storage of CO_2 was launched by the Petroleum Technology Research Centre (PTRC) located in Regina, Saskatchewan, in close collaboration with EnCana Resources of Calgary, Alberta. Known as the IEA GHG Weyburn CO_2 Monitoring and Storage Project, the project is funded by fifteen sponsors, including governments and industry, among them Natural Resources Canada, United States Department of Energy, Alberta Energy Research Institute, Saskatchewan Industry and Resources, the European Commission, and ten industrial sponsors in Canada, the US, and Japan. The project employs about 22 research and consulting organizations and about seventy technical and project personnel.

The project has the support of the International Energy Agency Greenhouse Gas R&D Programme (IEA GHG), which focuses on promoting technologies for reducing GHG emissions arising from the use of fossil fuels. Based in Paris, France, the IEA is an energy forum for 25 countries whose objectives include global energy policy development and the integration of environmental and energy policies. The IEA supports a number of Implementing Agreements, including the IEA Greenhouse Gas R&D Programme.

This CO_2 monitoring and storage project was essentially a field-demonstration of carbon storage in the subsurface made possible by adding a research component to EnCana's CO_2 Enhanced Oil Recovery (EOR) project that has been underway since 2000 at its Weyburn Unit. Located in the southeast corner of the province of Saskatchewan in Western Canada, the Weyburn Unit is a 180 square kilometer (70 square mile) oil field discovered in 1954. Production is 25 to 34 degree API medium gravity sour crude from the Midale beds of the Mississippian Charles Formation. The two main reservoir layers in the Midale beds are the Marly zone, a low permeability chalky dolomite overlying the Vuggy zone, a highly fractured and permeable limestone. The Weyburn field is part of the large Williston sedimentary basin, which straddles Canada and the US (Figure A).

Waterflooding was initiated in 1964 and significant field development, including the extensive use of horizontal wells, was begun in 1991. In September 2000, EnCana initiated the first phase (Phase 1A) of a CO_2 enhanced oil recovery scheme in 18 inverted 9-spot patterns (Figure B). The flood is to be expanded in phases to a total of 75 patterns over the next 15 years. The CO_2 is approximately 95% pure, and the initial injection rate is 5000 tonnes/day (equivalent to 95 mmscfd). A total of approximately 20 million tonnes of CO_2 is expected to be injected into the reservoir over the project life. The CO_2 is a purchased byproduct from the Dakota Gasification Company's synthetic fuel plant in Beulah, North Dakota, and is transported through a 320 km pipeline to Weyburn. An operations update for the Weyburn Unit EOR Project operated by EnCana is given in Table A.

TABLE A: operations update for the Weyburn Unit EOR Project operated by EnCanA – Feb. 29, 2004

- CO_2 injection into Phase 1a started September 15, 2000
- 98 BCF CO_2 injected as of Feb 29th, 2004
- Current CO_2 purchase is 105MMscfd (approximately 5.5 thousand tonnes) per day
- 25 mmscfd (approximately 1.3 thousand tones) of associated gas and CO_2 is being recycled daily
- EOR Operations include Phase 1a (start Sept., 2000), Phase 1b (start Oct., 2002), and Phase 1c (start June, 2003)
- Of the 210 producing wells in the EOR area:
  - -71 producers experienced operational response (CO_2 detected in casing gas)
  - -45 producers experienced production response (incremental production)
- Incremental production 9000 bbl/day (almost 1500 m^3)
- Current Unit production 22,400 bbl/day (over 3500 m^3)

The Weyburn Unit has proven to be an exceptional natural laboratory for the study of CO_2 storage, based in part on the extensive historical field and well data available combined with the baseline data collected prior to first CO_2 injection, abundant core material, and accessibility to the site.

1.2 Project Mission and Objectives

The project mission is to assess the technical and economic feasibility of CO_2 storage in geological formations with a focus on oil reservoirs, together with the development of project implementation guidelines. This will contribute significantly to the understanding of Greenhouse Gas Management and enhanced oil recovery.

The overall objective is to predict and verify the ability of an oil reservoir to securely store and economically contain CO_2. This is to be done through a comprehensive analysis of the various process factors as well as monitoring/modeling methods intended to address the migration and fate of CO_2 in a specific EOR environment.

The scope of work focused on understanding mechanisms of CO_2 distribution and containment within the reservoir into which the CO_2 is injected and the degree to which CO_2 can be permanently sequestered. The technology and design and operating know-how thus obtained could then be applied in screening and selecting other CO_2 storage sites, in developing effective monitoring programs, and in designing and implementing successful CO_2 storage projects worldwide.

A secondary objective was the application of economic realities to such an undertaking by predicting the point at which a CO_2 storage project reaches its economic limit. The application of customized economic models to the various storage cases helped in assessing not only cases of CO_2 storage in conjunction with EOR operations, but also of CO_2 storage in non-EOR situations such as saline aquifers. Saline aquifers could provide extensive CO_2 storage potential beyond that of depleting oil pools.

The ultimate deliverable from this project is a credible assessment of the permanent containment of injected CO_2 as determined by formal risk analysis techniques, including long-term predictive reservoir simulations. The results will help answer questions by regulatory bodies as to the security of large volume CO_2 storage and sequestration, not only in the Williston Basin, but also at other sedimentary basins where CO_2 storage is contemplated.

1.3 Project Sponsors and Research Providers

Project Sponsors:

Government:
Alberta Energy Research Institute
European Community
Natural Resources Canada
Petroleum Technology Research Centre
Saskatchewan Industry and Resources
US Department of Energy

Industry:
BP (British Petroleum)
ChevronTexaco
Dakota Gasification Co.
Engineering Advancement Assoc of Japan
EnCana Corporation
Nexen Inc.
SaskPower
Total
TransAlta Utilities

Research Providers:

Canada
Alberta Research Council (ARC)
Canadian Energy Research Institute (CERI)
ECOMatters (ECOM)
EnCana Corporation (ECC)
GEDCO Inc. (GEDCO)
Geological Survey of Canada (GSC)
Hampson Russell (HR)
J.D. Mollard and Associates Ltd. (JDMA)
Rakhit Petroleum Consulting Ltd. (RPCL)
Saskatchewan Industry & Resources (SIR)
Saskatchewan Research Council (SRC)
University of Alberta (U of A)
University of Calgary (U of C)
University of Regina (U of R)
University of Saskatchewan (U of S)

European Community
British Geological Survey, Britain (BGS)
Bureau de Recherches Geologiques et Minieres, France (BRGM)
Geological Survey of Denmark and Greenland (GEUS)
Istituto Nazionale di Geofisica e Vulcanologia (INGV)
Quintessa Ltd.

USA
Colorado School of Mines, Golden, CO (CSM)
Lawrence Berkeley National Laboratories, Berkeley, CA (LBNL)
Monitor Scientific Corporation International, Denver, CO (MSCI)
North Dakota Geological Survey (NDGS)

1.4 Project Organization

The project was organized into eight Principal Tasks, each led by a Principal Task Leader (Figure C). In turn, each Principal Task was subdivided into a number of subtasks (individual projects) being carried out by one or more Research Provider (RP).

There were over 50 subtasks in all. Subtask leaders funneled their work through the Principal Task Leaders who were coordinated by the Project Director. The Project Director was responsible to a Management Committee (MC) made up of representatives of some of the major sponsors. The principal role of the Project Director was to first ensure the development and implementation of yearly technical plans focused on meeting the project objectives outlined above. The resulting multi-faceted project was then put on a project footing through the application of good project management principles (*i.e.* managing to deliverables and milestones) and accounting practices.

A major effort was devoted to forging a team environment to integrate the disparate project entities in an effort to raise productivity, minimize redundancy, and ensure a high degree of information integration. This, and the assignment of a number of Project Integrators to assist the Project Director, proved successful in fulfilling the objective of information integration and other project expectations.

1.5 Project Financials

This project was financed by cash and in-kind contributions. Project cash costs totaling Can$16.38 million are shown in Table B, allocated among each of the four project Themes over the four-year project life. In-kind contributions amounted to another Can$23 million, mostly in field support and European Community-funded work. The European Community work was conducted in collaboration with the North American, but was separately funded.

1.6 Integrated Key Results

At completion, the project will have received a total of 472 deliverables. These deliverables are melded into some 50 Final Reports, one for each subtask. This Thematic Report represents the public summary of the outcomes of the research undertaken over the past four years.

The project was organized into four main “themes,” so chosen as to group all subtasks in a manner corresponding to the main objectives of the project. This project summary is organized following these same themes. The four Themes are:

Theme 1: Geological Characterization of the Geosphere and Biosphere
Theme 2: Prediction, Monitoring and Verification of CO_2 Movements

Theme 3: CO_2 Storage Capacity and Distribution Predictions and the Application of Economic Limits
Theme 4: Long Term Risk Assessments of the Storage Site

The cost allocation among the four Themes over the four-year project life is given in Table B.

TABLE B: TOTAL PROJECT COSTS PER THEME OVER PROJECT LIFE: 2000 – 2004

CAN$Millions

Theme	2000	2001	2002	2003	2004	Total	% of Total
1	$0.08	$0.27	$0.84	$1.64	$0.21	$3.04	19%
2	$2.61	$2.42	$1.92	$1.93	$0.24	$9.11	56%
3	$0.09	$0.43	$0.69	$0.92	$0.14	$2.27	14%
4	$0.08	$0.27	$0.40	$0.93	$0.28	$1.95	12%
Total for 4 Themes Over Project Life =						**$16.38**	

Included in the total effort expended on the four Themes is integration of information and technologies from each Theme, to make up the whole. This Information and Technology Integration effort was quite substantial, estimated to exceed 13.5% of the total cost of $16.38 million for the four Themes, or a net of $2.2 million.

The key results and "learnings" gained over the life of this project are substantial. Considerable progress has been made to meet the objectives originally set out for this project. Further work to adequately conclude and improve the lessons learned from this project is being proposed in a second Phase. The four "theme" summaries that follow this Integrated Project Summary capture the highlights of all the subtasks that fed into each Theme.

The following are highlights extracted from the Theme summaries:

Theme 1: This Theme provides a detailed geological description of the reservoir and a large surrounding region, which outlines the geological framework within which the Weyburn reservoir can be placed. This geological description was developed from both existing and newly-generated geological, geophysical, and hydrogeological information. A robust systems model of the geosphere and the biosphere was constructed to serve as the platform for the long-term risk assessments of the Weyburn CO_2 storage site. This portion of the work included the development of a clear understanding of the nature of the sealing horizons in the area of the geological model as well as the hydrologic regimes of the region. The main conclusion of the work is that the geological setting at the Weyburn field appears to be highly suitable for long-term geological storage of CO_2.

Important areas of further investigations (Phase 2) include the development of a better understanding of natural faults and fractures surrounding the host storage reservoir, understanding the effects of CO_2 injection practices on the integrity of the geosphere, and understanding the controls on salt dissolution below the host reservoir to aid in understanding rock fracturing in the vicinity of the Weyburn field.

Theme 2: The methods used for predicting, monitoring and verifying the movement of CO_2 included reservoir modeling, geochemical modeling, geochemical fluid sampling, tracer surveys, reservoir pressure surveys, and a variety of geophysical surveys. The greatest success was encountered with seismic surveys, which were used in "ground-truthing" reservoir modeling. The seismic surveys clearly demonstrated an ability to detect anomalies in the reservoir induced by CO_2 invasion. The seismic monitoring and interpretation suggests that relatively small volumes of CO_2 can be reliably identified at these depths and reservoir conditions, an important finding when considering the identification of leakage from the storage container in storage projects. Also, successful was the geochemical fluid sampling that gave good insights into the movement of CO_2 within the reservoir and gave strong indication of incipient CO_2 breakthrough at wells. Much less successful were tracer surveys, as a result of a variety of technical and operational problems. On the other hand, geochemical modeling to determine the long-term CO_2 material capture in

various sequestration forms (trapping mechanisms) was reasonably concluded, but it was not possible to do much reactive transport modeling to complete the geochemical picture with the time available for the research work. Similarly, passive seismic monitoring was initiated late in the project with only limited results at the time of the conclusion of analysis prior to reporting. Without a well designed and implemented baseline survey, the value of monitoring work and its interpretation would have been significantly reduced.

Areas of further work (Phase 2) would include verifying predictions through spinner surveys and selective drilling, additional coring and the logging of vertical slim holes to determine CO_2 distribution. Also, there is a need to conduct *in situ* time-lapse geophysical logging to improve understanding of the seismic images. As well, seismic monitoring lends itself well to assessing the success of conformance control tests in the field. The collection and analysis of the passive (micro-) seismic and geochemical data will continue.

Theme 3: Good progress was made in reservoir modeling of the entire 75 patterns slated for CO_2 EOR. Modeling started with fine-grid, individual well patterns and gradually up-scaled to a coarser, 75-pattern grid. Good history matching was achieved with actual production data. Also, predictions of total CO_2 injected matched reasonably well EnCana's internal estimates, although there are some differences in the detail of performance predictions between the oil company and research simulations. Other CO_2 storage cases were also investigated, including the continuation of CO_2 injection past the termination of the commercial EOR project (approximately year 2033), while continuing to produce incremental oil from wells still operating under a predetermined GOR (Gas-Oil Ratio) limit and reinjecting produced water elsewhere to make room for the additional CO_2 injected. Storage gas (CO_2 or emission) credits were assumed to be intiated at the start of this phase of the operation. The Storage Economic Model was then run to determine the economic limit for such an operation. Of the significant amount of additional CO_2 that can be physically stored in this manner, the model predicted various limits of CO_2 volumes that can be economically stored as a function of the value of CO_2 credits received and the desired rate of return for the operation.

Conformance control treatments developed in this project predicted a substantial improvement in volumetric sweep efficiency from the application of specially-formulated gel treatments to the best candidate wells. If successfully applied, conformance control may contribute an additional 10% recovery of oil from the treated wells. This in turn could accommodate 1.83 million tons of additional CO_2 stored, assuming a case that 20% of the EOR patterns have received a gel treatment.

Knowledge gaps identified include implementation of conformance control field trials to establish the level of success, collecting further performance data from the CO_2 flood to history-match the 75-pattern reservoir model (to date there is only three years of EOR production data available for history matching) and looking at a dual-porosity approach to reservoir simulation in recognition of the fractured nature of the carbonates of the Weyburn reservoir.

Theme 4: As anticipated, this has been the most challenging area of the project. The reasons for this include the application of risk assessment to a new area and a dependency on input from all three previous Themes before the final analysis could be undertaken. Also, risk assessment methodologies are very diverse and the challenges of selecting an optimum methodology as well as agreeing on a representative systems model and Base and Alternative risk scenarios matched these diversities.

A comprehensive, deterministic, numerical simulation approach was employed in simulating the potential of CO_2 migration away from the Weyburn Unit and into the geosphere and the biosphere over a period of 5000 years following the conclusion of the commercial EOR project. Augmenting the deterministic assessment was a smaller, stochastic (probabilistic) simulation of the same systems model, but using a compartment model and analytical methods. A benchmarking exercise was also undertaken to ensure that the two PA/RA approaches gave similar results on a simple, idealized test case. The benchmarking proved reasonably successful, illustrating both the challenges and value in comparing deterministic and stochastic simulation approaches and highlighting the limitations inherent in both approaches. Initial numerical simulation results on a single pattern, and using the latest of the geological models developed in the project, estimated that a cumulative 26.8% of the initial CO_2-in-place may migrate out of the 75-patterns over the 5000 years following the end of EOR. Approximately 18.2% of the CO_2-in-place is predicted to move down by gravity flow into the underlying aquifer, 8.6% to migrate laterally beyond the bounds of the EOR

area, and 0.02% to diffuse into the overlying caprock. However, no CO_2 appears to ever reach or penetrate the Watrous Formation, a regionally extensive and thick aquitard above the main anhydrite cap rock. It forms a secondary seal for the Midale reservoir, and certainly never reaches any potable water zones. Simulations undertaken to determine the risk of leakage along wellbores, particularly aging and abandoned wellbores, suggest a maximum of 0.14% of the cumulative CO_2 injected would leak upwards over the 5,000 year period following cessation of EOR. A mean of the estimates arrived at during research would suggest only a cumulative 0.001% of CO_2-in-place leaking over this period of time.

Gaps and areas of future work (Phase 2) include better understanding of the degradation characteristics of abandoned well sealing materials and completion of the comprehensive risk assessment of the long-term fate of stored CO_2.

1.7 Key Conclusions and Recommendations for Future Work

This has been a world class project in terms of organization and accomplishments. A significant range of core competencies was built over the three-and-a-half year life of the project (Phase 1). A great deal of understanding was achieved about the concept of geological storage of CO_2. These results provide a significant step in the development of a Design and Operating Manual aimed at site assessment, project design, and field implementation of commercial CO_2 geological storage projects. Phase 2 is being configured to ensure that such a manual is complete.

Recommendations for future work include:

- Future studies will involve deriving geological models using reduced data sets to reflect the availability of information at other locations and to determine minimum requirements for a credible assessment.
- Geostatistical work to help in the development of methodologies for determining petrophysical property distribution. Additional work is also required on petrophysical characterization of low-permeability clastic aquitards and their effectiveness as barriers to vertical CO_2 migration.
- Integrating fault and hydrogeological data could be used in the estimation of the hydraulic influence of fractures in seals to help in determining long-term monitoring programs and predict potential leakage areas.
- Assessing the potential for reactivation of faults resulting from CO_2 injection.
- Uncertainty exists in understanding the mixing and solution state of fluids within the reservoir, which translates into significant uncertainty in interpreting the time-lapse seismic results. Further work involving detailed seismic modeling and reservoir simulation is required to better quantify these effects.
- It has been concluded in this study that the monitoring results track the spread of CO_2 in the reservoir, and identify zones of enhanced permeability. There is a general need to further verify these assumptions. Spinner, geochemical tracer surveys, and selective drilling, coring, and logging of vertical slimholes could be used to test the seismically determined CO_2 distribution and flow-path details along the lengths of horizontal wells and in the interwell regions. Interpreted prominent fracture zones could also be tested by selective drilling.
- Improved understanding of the seismic images would be achieved by undertaking *in situ* time-lapse geophysical logging and by further modeling of the seismic response.
- A test of conformance control could be conducted and monitored seismically to determine its effectiveness.
- Follow-up work on the use of seismic data to monitor dissolution and the effects of mineral precipitation along high permeability fracture networks would be a possibility.
- Currently, estimates of long-term CO_2 trapping based on geochemical modeling are very preliminary. Improved estimates can be achieved with more detailed assessments of production fluid compositions, from a continued sampling program, and by taking into account the dynamic flow of CO_2. Reservoir simulation and geochemical models can be coupled to allow more accurate estimates. Reactive transport modeling remains a gap.
- Currently, limited post-CO_2 breakthrough field fluid data is available. There is still a question as to how the natural variation of fluid properties across the Weyburn Unit could be accommodated in fluid characterization.

- Currently, single-porosity models have been used in the reservoir simulation. Due to the fractured nature of the carbonate reservoir in the Weyburn Unit, some consideration should be given to the application of dual-porosity models.
- Further evaluation of the total CO_2 storage potential of the Weyburn Unit and surrounding Midale Formation aquifers would be useful. Developing means of monitoring and verifying CO_2 storage outside the Weyburn Unit would equally be useful.
- There remains a need to continue to assess the validity and accuracy of upscaling, especially over the long time frames required for risk assessment.
- More work is required to determine the degradation characteristics of well construction materials (cement and casing), including abandoned well sealing materials. This would include the development of a statistical database on well sealing degradation rates and annulus cement quality.
- There is a need to establish the relationship between caprock topography, a primary control on hydrostratigraphic trapping mechanisms, and CO_2 leakage predictions through wellbores.
- More work is required to fully exploit the power of risk assessment in assessing the ability of the Weyburn reservoir to securely store CO_2 by:
    - refining and auditing the input data for key System Model parameters (*e.g.*, Midale caprock capillary pressure or cement relative permeability curves)
    - including geochemical reactions within the model used for risk analysis.
- Revise and, most importantly, conduct field verification of wellbore transport models using well testing techniques or downhole cement core retrieval.
- Develop a verified probabilistic risk assessment model that contains the relevant physics to evaluate geological storage.
- Assess whether or not CO_2-EOR processes may influence the hydraulic conductivity of faults identified within the System Model.
- Investigate the impact of temperature changes resulting from the injection of CO_2 on wellbore transport properties, reservoir behavior, and the integrity of the bounding seals.
- Experimental evaluation of initial and evolving permeability, degradation mechanisms, and rates, capillary pressure, pH effects, and carbonation processes for oil field cements.

FIGURES

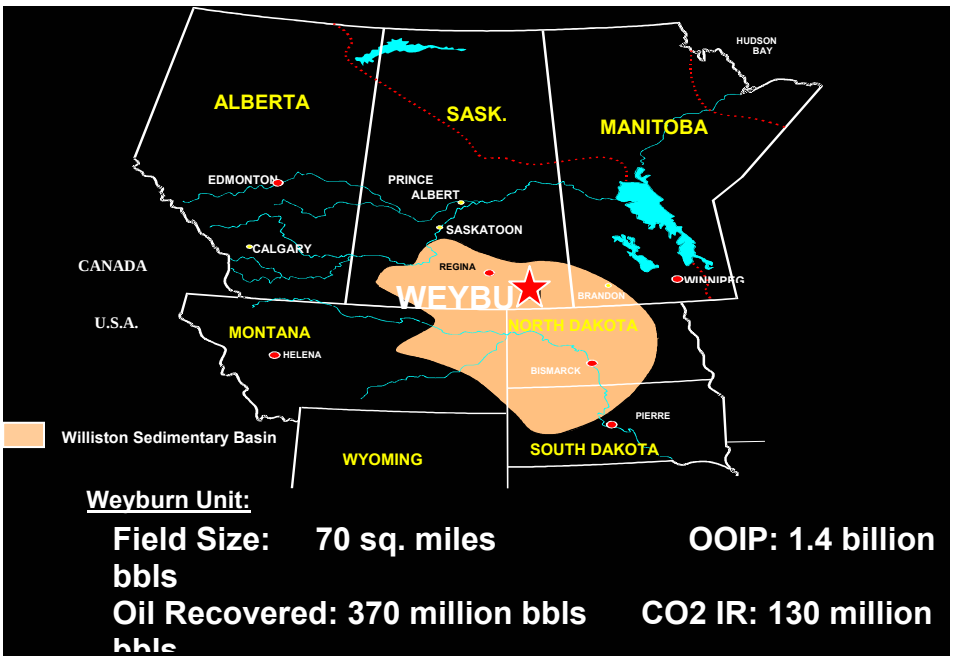

Figure A: Location of the Weyburn Unit

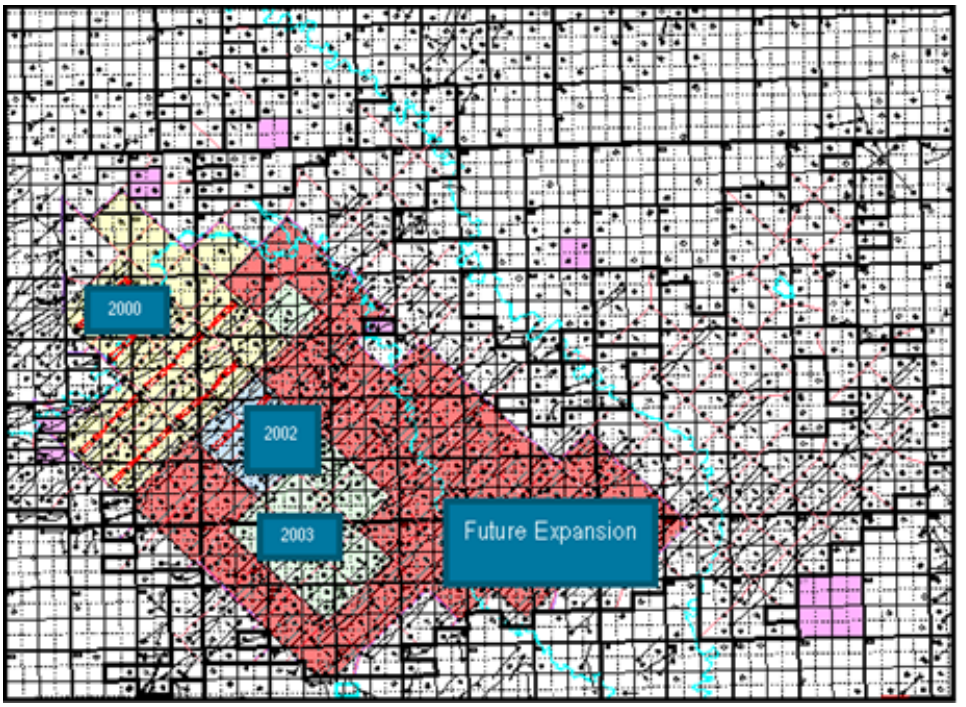

Figure B: CO_2 Flood Expansion Areas (Weyburn Unit)

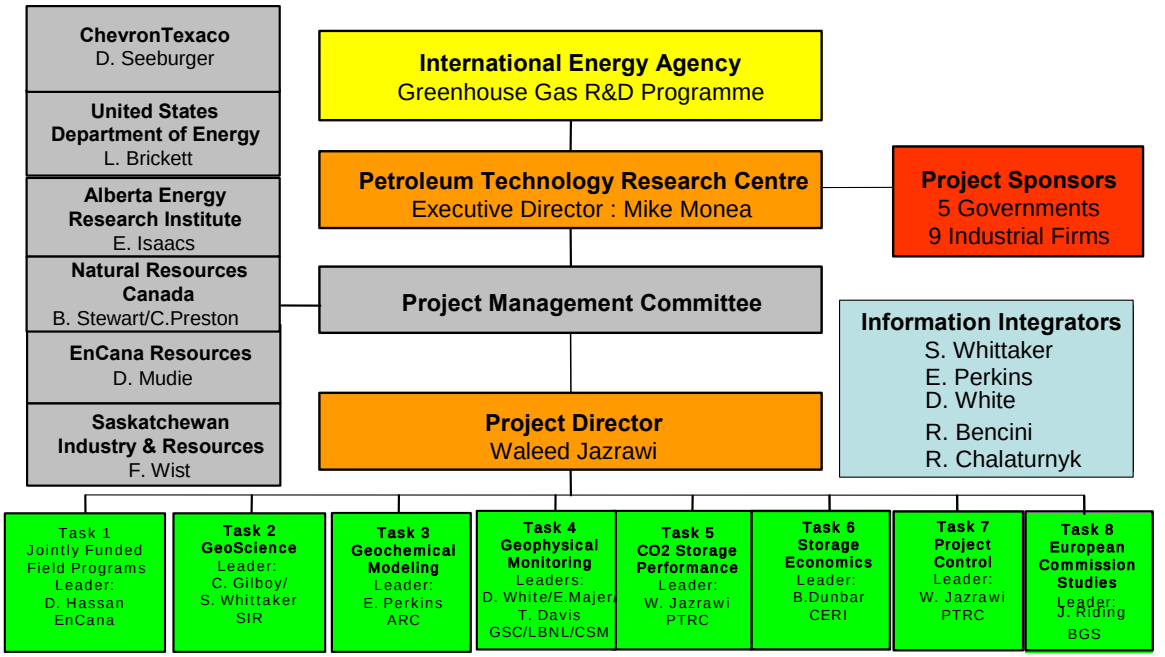

Figure C: Project Organization

2 PROJECT MANAGEMENT: WHAT WORKED AND WHAT DIDN'T

2.1 Purpose

Effective project management was critical to the success of the project. In spite of this, as with any research project, there were successes and failures. The following is a list of what worked well in this project and what did not work quite as well. The objective is to highlight some success indicators for running projects of this type in the future.

The information is organized into technical and non-technical categories. Also given are the contributing factors for assessing performance.

2.2 Technical Performance and Key Success Factors

The vast majority of technical facets of this project achieved success, some more than others, depending on scope, complexity, and the capabilities of the RP and his/her organization.

Examples of project facets that performed above expectations include:

- Geological characterization of the geosphere, including the hydrogeological regime. Success in this work was due to an abundance of readily available data, a homogeneous team, and a strong focus on quality.
- Field fluid sampling (11 sampling trips were made over the project life, including the collection of baseline samples prior to first injection of CO_2) due to the experience and dedication of the geochemistry team.
- Soil gas sampling and monitoring, again due to the experience and commitment of the team responsible for this activity.
- 3D-3C surface seismic integration with reservoir information over a 4 pattern area. Success was due to meticulous planning, creativity within the team, and follow-up with other project activity areas.
- Caprock and wellbore integrity work resulting from a extensive data collection, starting with a detailed examination of EnCana's well files.
- The second attempt at developing a storage economic model and crafting a meaningful demonstration case. Success was due to the detailed preparation of the scope of work and a determination not to fail a second time.

The following facets made significant contributions to the project. Given more time and resources, these activity areas would have delivered greater contributions:

- Geochemical modeling, especially the reactive transport simulations, delivered a good product, but could have provided more information if time and resources had not been constrained.
- The 75-pattern reservoir simulation, while providing informative results, could not be satisfactorily reconciled with EnCana's reservoir performance predictions. The main reason was the lack of resources for effective coordination with EnCana in the history-matching and predictive phases.
- 3D-9C surface seismic interpretation will require more effort. This relatively new technique is complex but is a promising technology. One significant constraint was the availability of people with the appropriate processing and interpretation skills.
- The integration of the seismic results and reservoir simulation information provided less information than expected due to the underestimation of the complexity of the undertaking and to under-resourcing, despite appointing several information integrators in this area alone.
- Deterministic risk assessment due to an initial lack of a detailed work plan within the Weyburn Project and to the lack of resources to adequately apply a complex simulator (Eclipse) to predict CO_2 migration. Some time was effectively spent in evaluating techniques developed for the nuclear waste sector as a model for assessing risks in the geological storage of carbon dioxide (the Features, Events, and Processes technique).

- Probabilistic Risk Assessment in the context of geological storage of CO_2 had a late start and will require more effort to align a new, in-house developed model with the needs of geological storage.
- Conformance control experimental work will require field trials to test the effectiveness of the chemical formulations and placement techniques. During the period of this phase of the Weyburn EOR project, no good candidate wells were identified for field tests.

The only failures experienced in the project were:

- The reservoir fluid tracer survey failed as a result of sampling and other procedural shortfalls.
- The horizontal crosswell seismic survey could not be repeated following start-up of CO_2 injection because of the inability to re-enter one of the horizontal wells to place the seismic recording string.
- The first storage economic model was terminated due to slow progress

2.3 Management Performance and Key Success Factors

- A key success factor was the early appointment of a capable Program Director, trained and experienced in project management, especially in the management of technology projects and having a strong grasp of oil field development and operations. Care was taken to identify this appointment as a separated project task with well defined responsibilities and authority and accountable directly to the Management Committee of the project.
- Sufficient funds were allotted to allow the Program Director the time and resources to fulfill the tasks assigned by the Management Committee and bring the project to a successful conclusion.
- Early introduction by the Program Director of sound project management practices, tools, and procedures to a diverse group of researchers who were only partially familiar with the essentials of managing complex projects. Management tools and processes included:
    - Team building from the initiation of the project to meld diverse groups into a single project team, sharing a common culture and project vocabulary. Extensive coaching and mentoring to RPs was provided by the Program Director, who effectively implemented the clear direction provided by the Management Committee and Steering Committee (meeting of all sponsors) throughout the project.
    - An evergreen Project Control Document was developed, which outlined the full spectrum of project scope and organization.
    - A detailed Project Schedule was constructed, integrating all project activities and displaying important milestones.
    - A Master Budget Sheet was created to track actual expenditures against assigned budgets for each subtask.
    - "Attachment Ds" were appended to the RP and IP agreements to set out the scope of work, deliverables, deadlines and approved budget on a calendar year basis.
    - An AFE-driven accounting system (by chart of accounts) was managed by an oil and gas-trained accountant.
    - Hold-back payments were contingent on receiving all deliverables stated in Attachment Ds.
    - A web-based information management system was established to give all researchers and sponsors access to information delivered by the project team.
- Also contributing to project success was the introduction of a comprehensive integration strategy (for information and technologies), tying together various subtasks to better serve the overall objectives of the project instead of just individual subtask objectives ("Think Project not Subtask"). The integration strategy included:
    - Issuing specific integration process guidelines very early in the project and developing schematics showing inputs and outputs to guide the researchers.
    - Formally appointing project Integrators and Theme Leaders to provide project support and direction within research areas.
    - Holding, at least once a year, formal information integration workshops in various project centres (Calgary, Regina, Saskatoon, Edmonton, Berkley, Golden, Denver, Keyworth (UK), Rome (Italy), Orleans (France), *etc*.).

  - Holding formal Thematic workshops under the direction of the Theme Leaders and key Research Providers, especially in the run up to project completion.
  - Holding regular Project Coordination Committee (PCC) conference calls (approximately monthly), chaired by the Program Director and involving all Principal Task Leaders, Theme Leaders, Project Integrators, and interested members of the MC (typically 15 participants).
  - Holding three-day Project Coordination and Sponsors Meetings (PCSM) twice a year for all RPs and Sponsors (70 to 80 people). This involved both project integration workshops and integrated stewardship reviews to the Sponsors. Integration of information and technology was first organized along six allied Clusters that later evolved into the four main theme areas.
  - Continual follow-up with RPs by the Program Director and Project Integrators through e-mail, conference calls, and face-to-face meetings as necessary to meet the project goals.
- Support and cooperation by EnCana's field personnel from project inception. Similarly, cooperation by the technical and management teams of the Weyburn Business Unit in Calgary, the head office of EnCana.
- The Program Director played a proactive role in influencing the direction and major decisions of the project. Initiatives, such as the introduction of project management principles, insistence on information and technology integration, appointment of Principal Task Leaders and later Theme Leaders and official Integrators, as well as continual follow up with all members of the team, played a key role in the success of the project. Furthermore, initiatives such as the Sponsors' strategic planning workshop in Kananaskis midway through the project to fine-tune direction, as well as the Phase 2 strategic planning sessions in Calgary in December, 2003, helped define direction for the successful development of this technology.
- An Expert Review exercise was undertaken in mid-2003, with leadership provided by the IEA Greenhouse Gas R&D Programme. This initiative provided a benchmark for the project and fine-tuned its direction.
- Management Committee meetings (mostly by conference call) were held twice a month to review project issues and provide direction to the Program Director.

2.4 Continuous Improvement

No project is without short-falls. The successful conclusion of the project is a testament, however, to the expertise and willingness of such a technically and geographically diverse group of researchers to work together. In the spirit of continuous improvement, the following are a few recommendations for improving overall project performance, particularly for higher risk, higher cost tasks such as field surveys:

- Implement standard screening of RP's proposals.
- Prepare execution plans for each discrete task, reviewed and approved by Principal Task Leaders, and with accountability clearly assigned.
- Undertake a risk assessment of project activities and develop mitigation measures.
- Improve project monitoring at the Principal Task Leader and Project Integrator level to maximize compliance with scope and quality of work.

THEME 1: GEOLOGICAL CHARACTERIZATION

THEME LEADER: STEVE WHITTAKER
THEME AUTHORS: STEVE WHITTAKER, BEN ROSTRON, DAN KHAN, ZOLTAN HAJNAL, HAIRUO QING, LYNDEN PENNER, HARM MAATHUIS, AND SERGUEI GOUSSEV

1 SUMMARY

The geosphere encompassing the Mississippian Midale Beds of the Weyburn oil pool was examined by a variety of methods to determine the integrity of the geological system for long-term storage of CO_2. A regional investigation was performed over a 200 x 200 km area of the Williston Basin, centred on the Weyburn field, to map stratigraphic distributions and extents of reservoirs, seals, regional aquifers, and aquitards from the Precambrian basement to the ground surface. These results provided the framework for extensive hydrogeological characterization of the subsurface fluid flow regime, which greatly influences the eventual distribution of injected CO_2. Regional geophysical studies using seismic, high resolution aeromagnetic, and other remotely sensed data delineated tectonic features and basin structures and their possible surface expression to evaluate potential locations of preferential CO_2 migration in the study area. The near-surface hydrogeological environment was also characterized to determine topography, drainage basin demarcation, and the distribution of shallow aquifers. An integrated 3D geological model was constructed for an area extending 10 km beyond the limits of the CO_2 injection area. The geological model, which describes the natural system, serves as the basis for a more comprehensive System Model that includes anthropogenic attributes, such as well bores and production parameters, and that is used for numerical risk and performance assessment modeling.

A suitable geological setting for long-term geological storage must meet certain criteria; these include having effective trapping mechanisms, competent bounding seals, hydraulic isolation from overlying aquifers, an appropriate hydrogeological regime, and minimal potential pathways for fast migration of CO_2 along faults or fractures. The Weyburn reservoir was investigated with the aim determining whether or not it meets these criteria. Carbonate beds of the 1.5 km deep Weyburn reservoir include an upper dolostone layer, the Marly, and a lower limestone layer, the Vuggy, into which the CO_2 is being injected. The upper seals to the reservoir are the Midale Evaporite, a competent anhydrite layer, and a diagenetically altered zone that has very low permeability and occurs at the up-dip portion of the Midale Beds subjacent to the regional Sub-Mesozoic Unconformity. Anhydrite beds of the Frobisher Evaporite occur below the Weyburn reservoir in the northern portion of the field. Above the Sub-Mesozoic Unconformity are relatively impermeable beds of the Triassic Lower Watrous Member that extend across much of southern Saskatchewan. Regional hydrogeological studies demonstrate that the Watrous aquitard is regionally effective, as it separates a deep hydrogeological system, including the Midale aquifer, from intermediate (1000 to 300 m depth) and shallow hydrogeologic systems. The intermediate and shallow aquifer systems are characterized by lower salinities, higher permeability aquifers, and faster flowing formation waters than the deeper regime. Hydrogeological data indicate there is no evidence for regional flow of formation waters from the Midale aquifer across the Watrous aquitard into the upper aquifers within the project area. The Watrous aquitard, therefore, should serve as an excellent regional seal for CO_2 injected into the Midale reservoir at the Weyburn field. In addition, low flow velocities in the Midale aquifer (<1 m/yr) and favourable (horizontal) flow directions will hydrodynamically trap injected CO_2, thereby limiting the effectiveness of formation-water flow acting as a transport agent. Within the Midale aquifer, a steep salinity gradient (TDS <50 to >150 g/L) across the CO_2 injection area must be accounted for in geochemical modeling and risk assessment. The high flow velocities in overlying Mesozoic aquifers (1 to 10 m/yr) are important parameters for scenario analysis of any CO_2 leakage into overlying beds. The Weyburn field is situated within a tectonically quiescent region. Most faults and fracture zones in the greater region are observed as localized disturbances without recognizable offset. Larger scale features are also observed, and one fault identified in this study is included in the geological model used in risk assessment. Although the trace of this fault may be observed in strata overlying the reservoir, it appears to not have compromised reservoir integrity during the past 50 million years. In summary, the geological setting of the Weyburn oil pool is considered highly suitable for secure, long-term storage of CO_2.

2 OBJECTIVES AND ROLE IN CO_2 STORAGE ASSESSMENT

A major objective of the IEA GHG Weyburn CO_2 Monitoring and Storage Project was to assess the integrity of the geosphere encompassing the Weyburn oil pool for effective long-term storage of CO_2. This objective was addressed by defining components of the geological system through mapping of primary trapping components, mapping of aquitards and aquifers, characterization of the subsurface fluid flow system, and the identification of potential pathways for subsurface CO_2 migration. Additional work required to characterize the system involved mapping in the near-surface environment to outline the distribution of shallow aquifers and identify potential surface expressions of deeper structural features. The accumulated information is essential in conducting potable aquifer and soil gas baseline surveys and in developing effective monitoring programs at depth in confining strata and along probable subsurface migration pathways.

Risk and performance assessment of the long-term CO_2 storage potential at Weyburn was a primary goal of the overall project. The role of geological characterization is to develop a comprehensive geological model of the natural system, incorporating geometries and properties of strata in the vicinity of the injection site. This geological model serves as the foundation to the overall System Model used for risk and performance assessment modeling. The System Model includes additional information, such as well degradation and production histories. Geological information regarding features and processes in the subsurface is also very important for developing the base-case scenarios for the expected evolution of the system, as well as credible alternative scenarios. Geological characterization is a fundamental undertaking of any assessment or screening process regarding greenhouse gas storage in the subsurface.

3 SCOPE OF INVESTIGATION

The geosphere was characterized in this project through the coordination of the efforts of about 40 researchers from a variety of geoscience disciplines. The investigations were generally targeted towards a) defining the subsurface flow regime, including the extent, distribution, and character of flow units, barriers to flow, and main traps and b) identifying processes and features that may provide enhanced pathways for subsurface fluid migration. Transport properties associated with flow units, such as permeability, porosity, and fracture distribution, were determined where possible. To effectively understand basin hydrogeological flow characteristics or reveal the underlying tectonic framework that greatly influences sedimentary depositional patterns, erosion, and fracture development, a large area must be considered. Therefore, a regional study was performed on an area extending 100 km outward (40,000 km^2) from the Weyburn pool (Figure 1.1). Additional work and detail focused on the features and properties of strata within a more restricted area, the Risk Assessment (RA) region, extending 10 km beyond the boundaries of the CO_2 EOR flood (Figure 1.2 new). The 3D geological model required for risk assessment was constructed for the area included in the RA region.

The initial phase of any geological characterization involves the definition of the geometry of the system, or the establishment of a regional stratigraphic framework. In this study, the regional stratigraphy was mapped by Saskatchewan Industry and Resources and the North Dakota Geological Survey from the Precambrian basement to the ground surface, primarily through geophysical well log interpretations but also using core samples where possible. Over 140 stratigraphic units were identified and mapped for structure, distribution, and thickness, although not all units were present at each well location. The generalized stratigraphy of the study area is shown in Figure 1.3. Regional seismic investigations at the University of Saskatchewan examined over 2000 km of 2D-seismic data (Figure 1.2) that augmented the stratigraphic mapping and highlighted basement features and basinal tectonic elements within the study area. More detailed geological studies were conducted by the University of Regina on specific units and, in particular, primary seals, to better assess their nature using core examination, petrography, isotope and fluid inclusion analyses, sequence stratigraphic studies, and geophysical log analysis. Hydrogeological investigations were carried out at a wide range of depths and spatial scales. Studies of the regional "deep" hydrogeology (the Upper Cretaceous Bearpaw Formation shale and deeper) were carried out by the University of Alberta (Khan and Rostron, 2004). Regional "shallow" hydrogeology (above the Bearpaw Formation, generally less than 100 m deep in the risk assessment region, but up to 600 m deep in the southwest portion of the regional area) was examined by the Saskatchewan Research Council (Maathuis

and Simpson, 2003a). Local "shallow" hydrogeology was studied by J. D. Mollard and Associates (Mollard and Cosford, 2003) in conjunction with the Saskatchewan Research Council (Maathuis and Simpson, 2003b). The shallow interval includes all potable aquifers and is termed the "biosphere" for the purposes of the geological model. The base of the biosphere is defined as the top of relatively impermeable thick shales of the Upper Cretaceous Bearpaw Formation (Figure 1.2). Additional parallel hydrogeological studies were conducted by the Bureau de recherches géologiques et minières. High resolution aeromagnetic data compiled by GEDCO Corporation were used, in conjunction with the regional seismic results, to develop a 3D network of faults and fractures for identifying parts of the study area that may be susceptible to preferential subsurface fluid migration. Surface lineament identification by J.D. Mollard and Associates, using air photos and satellite imagery, helped to refine this network, as these studies indicated potential surface expressions of deeper structural and stratigraphic features. Surface lineament studies were also used to help identify soil gas monitoring survey locations.

4 REGIONAL SETTING OF THE WEYBURN FIELD

Assessing long-term subsurface storage of CO_2 requires an understanding of not only the host reservoir, but also the regional geological and tectonic framework from basement to surface. This requirement arises because, as with any sedimentary basin, fluid migration pathways may extend for hundreds of kilometres, and tectonic processes that have affected depositional and erosional patterns are, by nature, basin-scale. In addition, through the examination of regional characteristics and processes, the appropriate lateral and vertical extents of the geological model used for risk and performance assessment can be determined.

4.1 Tectonic Framework

The Weyburn pool occurs in Mississippian-aged carbonates about 1.5 km deep within the northeastern Williston Basin (Figure 1.1), an intracratonic sedimentary basin on the western shelf of the North American craton. Intracratonic basins contain some of the most promising sites for CO_2 storage, as they contain thick sequences of sedimentary rocks potentially suitable for greenhouse gas injection (Bachu, 2002) and many, such as the Illinois and Michigan basins, are near heavily industrialized regions. The Williston Basin is an elliptical depression approximately 560 km in diameter and centred in North Dakota. It obtains a maximum thickness of sedimentary rocks of about 4900 m, although below the Weyburn field the thickness ranges from 2800 to 3000 m. Initial phases of basin development began during the Late Cambrian to Early Ordovician periods and continued episodically until the Late Cretaceous, when regional tectonism was dominated by foreland basin development associated with the Laramide orogeny along the western margin of North America (Kent and Christopher, 1994).

The Williston Basin is bordered by tectonic elements including the Punnichy Arch to the north, the Black Hills uplift to the south, the Sweetgrass Arch to the west, and the Transcontinental Arch to the southeast (Figure 1.1). The basement beneath the Williston Basin is a mosaic of Precambrian lithotectonic domains and crustal boundaries (Figure 1.4). Vertical movements of peripheral structural blocks and reactivation of basement faults during the Phanerozoic evolution of the basin influenced depositional patterns that affected the distribution of lithofacies, porosity, and areas of erosion. These processes also very likely affected hydrodynamic patterns, which influenced areas of salt-dissolution within the subsurface of the Williston Basin (Dietrich *et al*., 1999). The investigation into the genetic and spatial associations between the regional Precambrian crustal boundaries, the basement structures, the surface lineament orientations, and the Phanerozoic depositional, structural, and salt dissolution trends may assist in the identification of potential pathways for CO_2 migration.

4.2 Geologic Setting

The entire stratigraphic succession in the study area ranges from Middle Cambrian and Early Ordovician sandstones that directly overlie the Precambrian basement to Quaternary glacial drift at ground surface (Figure 1.3). The regional style of sedimentation reflects the basin configuration at a particular stage of tectonic evolution. Rocks of the Williston Basin can be subdivided into two broad packages: Paleozoic strata dominated by carbonates, evaporates, and minor shales and Mesozoic strata dominated by shales, siltstones, and sandstones. The Mississippian Midale Beds of the Weyburn reservoir occur near the uppermost part of the Paleozoic sequence (Figure 1.3), immediately below a basin-wide angular unconformity that separates the Paleozoic and Mesozoic packages and represents a depositional hiatus of approximately 60 million years (Figure 1.5). The Sub-Mesozoic Unconformity delimits a very important and effective regional flow barrier throughout the northern portion of the basin, as tilted porous Paleozoic carbonates are truncated against relatively impermeable siliclastics of the Triassic-Jurassic Watrous Formation. Immediately subjacent to the unconformity surface, within many of the Paleozoic carbonate layers, diagenesis has produced a highly cemented impermeable zone that forms an effective seal against vertical fluid migration. The overlying Mesozoic succession includes marine and non-marine sandstones and siltstones but is volumetrically dominated by thick transgressive shales that formed within the Cretaceous foreland basin. Above the Weyburn pool, the thickness of the Mesozoic sequence is 1300 to 1400 m, but in the broader study area, it ranges from 675 m in the northeast to 2300 m in the south (Figure 1.6).

The Williston Basin is a prolific hydrocarbon province containing numerous structural and stratigraphic configurations effective for trapping and containing oil and gas. Hydrocarbons are most abundant in Paleozoic rocks and, in particular, in Mississippian carbonates formed within shallow shelf environments. The Midale Beds of the Mississippian Charles Formation constitute the Weyburn reservoir and are a classic example of a shallowing-upward succession of peritidal deposits. Relatively porous and permeable limestone and dolostone layers originally deposited in marine to marginal marine environments are capped by dense anhydrite units formed in extremely shallow to periodically exposed evaporitic environments. Cycles of shallowing-upward successions containing alternating porous and non-porous layers occur below and above the Midale Beds and characterize Late Mississippian sedimentation in the northeast portion of the Williston Basin. The stratigraphic relation among Mississippian carbonate beds and evaporite units is shown in the detailed stratigraphic chart in Figure 1.7.

4.3 Natural Analogue for CO_2 Storage in the Williston Basin

About 400 km west of the Weyburn CO_2 injection site on the western flank of the Williston Basin in southwestern Saskatchewan, natural accumulations of CO_2 occur within Devonian carbonates and Cambrian siliciclastics (Figure 1.1). Some of the carbonate reservoirs in this area contain inert gases with greater than 80 per cent CO_2 and have sustained flow rates of up to 425,000 m^3/day. Previous estimates of this resource suggested nearly two million tonnes of CO_2, or about one billion m^3 of recoverable gas, are present in these rocks (Lane, 1987).

The naturally occurring CO_2 and associated N_2 and He (Lee, 1962) are generally trapped in the Devonian Duperow Formation (Figure 1.8) within a succession of thin cycles of carbonates capped by evaporite units. The cycles resulted from deposition within shallow, periodically restricted waters along a carbonate platform, a geological environment similar to that which produced the Midale Beds of the Weyburn reservoir. The reservoir units are limestones and dolomitized limestones that have porosities generally around six to eight per cent, but which may be as high as 18 per cent. The porous intervals are capped by dense anhydrite layers ranging in thickness from less than 2 m to more than 10 m.

Anomalously high geothermal gradients in the subsurface of southwesternmost Saskatchewan are the result of nearby Tertiary intrusions at the Bearpaw and Little Rocky Mountains in Montana (Figure 1.1). The intrusives have been dated at approximately 50 million years and were related to the Cretaceous Cordilleran orogeny. CO_2 found in Devonian rocks of southwestern Saskatchewan was likely generated during intrusion of hot alkaline magma into Lower Paleozoic carbonates in Montana. The CO_2 migrated north, up-dip, about 100 km to where it became trapped in local structures that had been previously formed

through dissolution of underlying salt layers. Further reduction of porosity up-dip also influenced the containment of CO_2. At present, the CO_2-bearing intervals within the Devonian carbonates occur at depths between 1675 and 2050 m below surface. They are overlain by about 350 m of Devonian and Mississippian carbonates and an approximately 1500 m-thick package of Mesozoic shales, siltstones, and sandstones, lithologically and genetically similar to those encountered at the Weyburn site (Figure 1.8).

It is notable that natural gas produced from shallow wells (penetrating only Mesozoic strata) in the same location as the deeper natural CO_2 contains only trace or non-detectable amounts of CO_2. This suggests that leakage from the underlying natural CO_2 reservoirs into shallower beds in southwestern Saskatchewan has not been significant during the past 50 million years. The natural CO_2 occurrences in Devonian carbonates of southwestern Saskatchewan are considered an analog to the Weyburn injection site because of their geological similarity.

5 GEOLOGICAL COMPONENTS OF THE SYSTEM MODEL

Performance or risk assessment of geological storage of CO_2 in the Weyburn reservoir is based mainly on numerical analysis of a System Model that includes many geological, hydrogeological, and geophysical characteristics of the Weyburn site, but also includes information such as well bore stability, CO_2 transport properties, and fluid phase and pressure distributions. The geological components of the System Model are mainly associated with determining trapping mechanisms, identifying potential transport pathways, and defining transport properties. These geological features are integrated into a 3D geological model (constructed for the RA region 10 km beyond the CO_2 flood limits) that is used as the basis for the overall System Model (Figure 1.9). Many of the geological features incorporated into the System Model are important in constraining the expected evolution of the system (base case scenario) and developing feasible alternative scenarios for the long-term fate of CO_2 in the subsurface. Other aspects of the System Model are described in detail in Theme 4.

The geological layers included in the model are separated, somewhat informally, into the geosphere and biosphere. The geosphere is considered to represent all strata and features below the maximum depth of potable aquifers, which is variable but between about 50 to 100 m in the RA region. The biosphere is made up of all beds in which potable aquifers are present and was mapped as part of the regional and local shallow hydrogeological programs.

Geological, hydrogeological, and geophysical mapping and characterization of the subsurface was performed over a much larger area than the RA region considered in the System Model (Figure 1.2). It was determined that a large initial study area would provide greater confidence in determining the areal and vertical limits suitable for inclusion in risk assessment and allow for adjustments to the System Model extent if needed. A large investigative area also incorporates information regarding regional-scale features, such as hydrogeological flow and basin tectonic element distribution, that are essential for developing credible scenario evaluations.

5.1 Lithostratigraphic Framework

The lithostratigraphic framework of the regional study defined the distribution of the rocks around the Weyburn reservoir. Establishing this framework is essential for any storage project, as it provides the foundation for all other geologically-related components involved in site assessment including: determining the principal seals and trapping mechanisms; delineating the regional distribution of aquifers and aquitards; locating areas having potential discontinuities of fluid flow due to faulting, fracturing, local thinning, or absence of aquitards; and determining the spatial extent of the geological model required in risk assessment.

The regional study encompassed a volume of strata about 100,000 km^3 (200 km by 200 km by 1.5 to 3.5 km) with the Weyburn field at its geographic centre. This included parts of southeastern Saskatchewan, northwestern North Dakota, and northeastern Montana (Figure 1.2). A major focus in developing the regional lithostratigraphic framework was to provide a consistent database for establishing a well-defined

hydrostratigraphic framework. Emphasis was also placed on identifying and characterizing primary and secondary seals and determining whether preferential migration pathways were present, particularly in strata overlying the Mississippian reservoir. To maintain consistency in stratigraphic correlations of lithostratigraphic units, individual researchers focused on specific stratigraphic packages broadly aligned with the three major aquifer groups in the basin, the pre-Mississippian Paleozoic (Cambrian to Devonian), the Mississippian, and the Mesozoic (Figure 1.3). Examples of the importance of mapping each these packages are presented below.

5.1.1 Paleozoic salt dissolution

The Paleozoic succession is about 1350 m thick in the Weyburn area, and many of the deposits exhibit cyclic depositional patterns with relatively porous carbonate intervals capped by non-porous argillaceous carbonates and evaporites. Evaporites are an important lithology within the Paleozoic sequence, as they form both thin and discontinuous bodies and thick and extensive units that may influence regional and local fluid-flow behaviour within the basin. Although evaporite beds are usually effective aquitards within the Williston Basin, they may undergo subsurface dissolution that can lead to the development of collapse structures in overlying beds (De Mille *et al*., 1964).

Because salt dissolution may produce collapse features that can impact the integrity of confining strata (Smith and Pullen, 1967; Nemeth *et al*., 2002), an emphasis was placed on mapping evaporite units in Mississippian and older strata to identify areas where evaporite removal may have occurred. Twenty-nine evaporite units were mapped in the Weyburn area within the Paleozoic to Middle Jurassic succession. The Middle Devonian Prairie Evaporite, which is the best developed evaporite sequence in the Phanerozoic section of the Williston Basin, is particularly notable. The Prairie Evaporite contains thick salts mined for potash elsewhere in the basin and forms aquitards that are among the most competent in the basin. It has undergone post-depositional dissolution in both localized areas and large regions and, in the study area, ranges in thickness from more than 200 m in North Dakota to zero thickness in areas of total dissolution (Figure 1.10). By examining these thickness variations and associated overlying and underlying strata, interpretations regarding the timing of salt dissolution and its impact on stratigraphic continuity can be made (Smith and Pullen, 1967; Nemeth *et al*., 2002). This, in turn, provides the mechanism to assess the risk of collapse and fracturing of overlying strata that may impact seal integrity or possibly result in cross-formational fluid flow, either of which would reduce a considered reservoir's suitability for long-term storage of CO_2 (Haidl *et al*., 2004).

Features of collapse structures related to salt dissolution include brecciation and disruption of normal stratigraphic layering. Recent work using depth-migrated 3D seismic data indicates that the disturbed zone is tightly focused above the dissolution area but may extend vertically hundreds of metres and even potentially to the surface (Prugger *et al*., 2002). The structures are important in that they may provide a conduit for vertical fluid movement across formation boundaries, which is a significant consideration for long-term geological storage of CO_2. When collapse zones are encountered during mining of Prairie Evaporite potash salts, inflow of water from overlying strata through these structures may be sufficient to compromise the mine itself (Gendzwill and Martin, 1996). Figure 1.11 presents a series of schematic diagrams used to assess the timing and vertical disruption of strata related to multi-stage salt dissolution in the southern portion of the study (see Figure 1.10). In Phase I of Figure 1.11, the initial stages of salt dissolution from the Prairie Evaporite are observed in the westernmost and easternmost wells shown on the diagram. The different amounts of salt removed at each location are reflected by a compensating increase in thickness of Manitoba Group sediments deposited over the dissolved areas. The middle wells, only a few kilometres from the westernmost well, are largely unaffected by dissolution, indicating the localized circumstances under which dissolution may occur. The Prairie Evaporite at one location was deposited over a reef (commonly present in the Winnipegosis Formation) so is slightly thinner than the regional average. Phase II indicates that dissolution continued during the Devonian, although, in well 10-28-1-10W2, it had lessened by the time the Three Forks sediments were being deposited. However, approximately 20 km east, in well 15-5-1-8W2, dissolution was more pronounced and continued through deposition of the Three Forks and into the Mississippian, as shown by the thicker Mission Canyon and Lodgepole strata in Phase III. Further dissolution is not observed in these wells, indicating that collapse

features are unlikely to be present in strata of the Charles Formation or higher, which includes the Midale Beds that are laterally equivalent to the reservoir strata of the Weyburn pool.

Similarly the Prairie Evaporite thins by more than 30 m beneath part of the Weyburn reservoir, and there is a suggestion of a NNW trending zone of dissolution (Figure 1.10). Three other Devonian salt beds present elsewhere in the study area are also absent at this location, providing further indication that localized salt dissolution occurred in the Weyburn reservoir area. At this location, however, anomalous thickening of overlying Late Devonian and earliest Mississippian strata indicates compensating deposition occurred contemporaneously with dissolution of the underlying Devonian salts. Therefore, the integrity of seals overlying the reservoir was not compromised by earlier dissolution events. No thickening in overlying strata that would indicate significant evaporite dissolution occurred following the formation of the Midale Beds has been observed in the Weyburn RA region. The spatial distribution of salt dissolution is important for planning future sites of CO_2 storage, and evaluating the potential for present-day and future subsurface salt removal is useful in scenario development for risk assessment in site characterization.

5.1.2 Mississippian strata

Mississippian strata encompass the reservoir beds into which CO_2 is being injected, their laterally equivalent aquifers, and the primary seals for containing the CO_2. As such, they represent the most important stratigraphic interval in the Weyburn site characterization. Geological mapping of the Mississippian succession was focused on a) examining the regional extent and lateral continuity of reservoir equivalent layers, b) determining the distribution and nature of the containment strata, and c) providing sufficient consistency in stratigraphic delineation to permit the resolution of Mississippian hydrostratigraphy into individual aquifers.

The overall Mississippian succession in the study area consists of lithologically similar rocks that form a series of aquifers and thin and variably continuous aquitards. The Mississippian beds were mapped in detail because any natural migration of CO_2 upward or downward out of the Midale Beds will be associated with porous zones in these units (Zhou *et al*., 2004). Although it is difficult to separate the individual Mississippian beds hydrogeologically, an attempt was made to distinguish these units, as discussed later, using the characteristics of formation water defined through detailed geological mapping results. In general, two broad phases of deposition influenced the fabric of the Mississippian sedimentary rocks (Kent *et al*., 2004). The earlier was a progradational phase represented by predominantly basin-fill deposits of the Souris Valley, Tilston, and Alida beds. The Souris Valley Beds, in particular, tend to be more argillaceous and were probably deposited in deeper, poorly oxygenated, basinal environments. The later phase was aggradational, resulting in one or more shallowing-or brining-upward cycles in the Frobisher, Midale, Ratcliffe, and Poplar beds. The geological model used for risk assessment contains Mississippian units down to and including the Tilston Beds.

5.1.3 Mesozoic strata

The Mesozoic units are significant in this region in that they contain both the most important regional barriers to vertical fluid migration above the Mississippian reservoir and aquifers having the greatest transmissivity in the entire stratigraphic section. Shales are the dominant lithology in the Mesozoic succession, in terms of thickness and areal extent. They become increasingly indurated with depth, which, above the Weyburn pool, reaches around 1350 m (Christopher *et al*., 2004). The mainly clastic sequences were subdivided into 38 units used to define four aquifers and five aquitards between the Midale Beds and the biosphere (Figure 1.3). In the Mesozoic sequence of this region, four significant unconformities, the Sub-Mesozoic, the Sub-Cretaceous, the Late Cretaceous Sub-Lea Park (Pierre), and the Mid-Tertiary unconformities, have been identified. They represent major changes in depositional patterns within the basin.

The Mesozoic aquitards are the Watrous Formation, Vanguard Group, Joli Fou Formation, Colorado Group, and the Bearpaw Formation (Figure 1.3). They are regionally extensive and form significant barriers to vertical fluid migration, with the Colorado Group and Bearpaw Formation, in particular, comprising massive shaly packages. The major regional aquifer in the region is the Cretaceous Mannville

Formation. Sandstones of the Newcastle Formation are also relatively extensive but are encased within the massive Colorado Group shales (Ferdous, 2004). Less extensive sandstones (aquifers) are present in the Jurassic Shaunavon and Gravelbourg Formations, mainly east of the Weyburn field. Argillaceous sandstones are also scattered within the Upper Cretaceous Lea Park and Belly River Formations.

5.2 Weyburn Midale Reservoir

Reservoir layers of the Weyburn pool occur within the Midale Beds of the Mississippian Charles Formation (Figures 1.3, 1.5, and 1.7) and represent a carbonate-evaporite cycle of deposition in a shallow peritidal environment. The Midale Beds are informally subdivided into a lower limestone layer (the Vuggy), and an upper dolostone layer (the Marly). Each of these layers, in turn, can be subdivided based on depositional and lithological variations for detailed reservoir characterization and modeling. The Vuggy unit was formed mainly in a marine lagoonal environment, where carbonate shoal development produced high quality reservoir rocks (Figure 1.12; Burrowes, 2001). In the Weyburn pool, the Vuggy ranges from about 10 to 22 m thick, with the shoal facies lithology being predominantly coated-grain wackestone to grainstone having around 15 per cent vuggy and fenestral porosity. Partly as a result of its depositional environment, the Vuggy is relatively heterogeneous and has permeabilities that range from 1 to 500 md, but average around 20 md. Intershoal deposits, also part of the overall Vuggy layer (Figure 1.5), exhibit much poorer reservoir characteristics, having smaller pores and lower permeability. Because shoals are found mainly in the western part of the pool, the planned CO_2-flood rollout is focused on the western portion of the reservoir (Figure 1.13). Although most early oil production from the Weyburn oilfield was from the Midale Vuggy layer, current CO_2 injection is mainly into the overlying Midale Marly layer with the sweep extending down into the Vuggy layer. The Marly is a low-permeability microsucrosic dolostone having porosities that average about 26 per cent. The Marly is more homogeneous than the Vuggy, and deposition of its sediments, prior to dolomitization, took place in relatively quiet waters.

The northern extent of the Midale Beds is sharply defined, as tilted Mississippian layers are truncated by the erosional surface of the Sub-Mesozoic Unconformity (Figure 1.5). The contact between the Midale Beds and the unconformity surface, which is directly overlain by low-permeability siliciclastics of the Triassic Lower Watrous "Red Beds," is the Midale subcrop. This configuration has resulted in the Midale Beds of the northern Williston Basin being among the most hydrocarbon-rich reservoirs of the entire basin, as several other large oilfields found along the Midale subcrop trend east of the Weyburn field (Figure 1.13). West and south of the Weyburn field, however, shoal development is rarer in the Midale Beds and reservoir quality is scattered and generally poorer. In fact, much beyond the vicinity of the Weyburn pool, the terms Vuggy and Marly lose their significance, and these strata were mapped regionally as lower and upper Midale Beds, respectively. Conditions bounding the system relative to potential CO_2 migration in the vicinity of the Weyburn reservoir are the northward truncation of reservoir rocks and the generally poor-quality reservoir to the west and south (Figure 1.13). Regional groundwater flow from the southwest up-dip toward the subcrop also reduces the likelihood of fluid movement southward. Although reservoir quality is poorer in the eastern half of the Weyburn pool, lateral continuity exists throughout the reservoir and likely continues east beyond the Weyburn pool limits.

Within the Weyburn reservoir itself, the trapping mechanism is a combination of stratigraphic, structural, diagenetic, and hydrodynamic components (Wegelin 1984; Burrowes, 2001). In the Midale Beds, grain size becomes markedly finer up-dip toward the subcrop and irreducible water becomes a factor limiting the movement of hydrocarbons (Burrowes, 2001). In addition, diagenesis within the porous carbonate units immediately subjacent to the unconformity has resulted in micritization that, along with carbonate and anhydrite cementation, has effectively occluded most porosity (Figure 1.5). This zone of alteration is common below the unconformity in many of the Mississippian beds mapped in the present study (Rott, 2004). The shallowing-upward nature of deposition along the shallow ramp resulted in formation of a very low-permeability evaporite cap, the Midale Evaporite, that serves as an important seal to porous carbonates of the Weyburn Oil field (Figure 1.7). Moreover, the cap of the underlying Mississippian cycle, the Frobisher Evaporite, forms a bottom seal to the Midale Beds, although this did not develop below the southern portion of the field (Figures 1.5 and 1.14a). Similarly, beds of the Ratcliffe cycle and, in turn, Poplar Cycle, overlie the Midale Beds but are present only above the southern portion of the Weyburn pool, as they are progressively truncated by the Sub-Mesozoic Unconformity (Figures 1.5 and 1.7). The Triassic

Watrous Formation is the most regionally extensive seal that overlies the Mississippian strata throughout the northern portion of the basin.

5.2.1 Mississippian seals

The effectiveness of the storage system is largely dependent on the character, distribution, and extent of bounding seals. The primary Mississippian seals of the Weyburn reservoir include the overlying Midale Evaporite, the underlying Frobisher Evaporite, and an altered zone at the subcrop of the Midale Beds. The relation of these units to the Midale Beds is shown in Figure 1.5. Fractures are present throughout the Midale reservoir but are more common in the Vuggy unit than the Marly. They are observed to have a generally SW-NE orientation (Edmonds and Moroney, 1998). Wegelin (1987) suggested that the inferred regular pattern of fractures in the Midale reservoir may be related to basement features formed during basin development and that some structural irregularities may also be due to the effects of salt dissolution. Therefore, to assess the integrity of the Weyburn system, the impact of fractures and structural features on the seals of the reservoir was addressed.

The Frobisher Evaporite forms a lower seal to the northern portion of the Weyburn reservoir but is not present beneath the southern portion of the Weyburn pool (Figures 1.5 and 1.14a). It has a nodular texture, with the nodules commonly separated by dolomicrite or argillaceous dolostone. This contrasts with a more massive texture observed in the Midale Evaporite. The Frobisher Evaporite is generally not fractured, although its nodular character makes it slightly prone to small-scale (mm to cm) fractures (Kent, 2004). In addition, the presence of dolomicrite between nodules suggests that the unit may be potentially susceptible to fluid migration, as some samples exhibited oil staining.

The Midale Evaporite was formed during the latest phase of the brining-upward cycle of the deposition of the Midale Beds, although current nomenclatural convention, established prior to understanding the genesis of carbonate-evaporite cycles, places it at the base of the Mississippian Ratcliffe Beds (Figure 1.7). It now forms a band of relatively impermeable caprock that stretches across much of southeastern Saskatchewan (Figure 1.14b). The Midale Evaporite sits conformably on the uppermost unit of the Midale Beds, and its top is defined by a sharp transition to the dolostones of the Ratcliffe Beds (Figure 1.13b). Its geophysical log signature is that of a highly dense two to 11 m thick anhydrite. Core samples of the Midale Evaporite indicate that four distinct lithotypes are present within the unit, as shown in the generalized profile in Figure 1.15. In general, the succession is made up of laminated to massive anhydrite at its base, grading upwards into nodular anhydrite with scattered dolostone interbeds occurring throughout (Nickel and Qing, 2004). The transitional Three Fingers zone at the top of the Midale Beds contains argillaceous, mottled carbonates generally having very low permeability. These are typically dolomitic in the Weyburn pool region but become increasingly calcareous in the southern portion of the study area.

Although fractures are present in the Midale Beds, they are rare in the Midale Evaporite and, where present, are mainly interpreted to have developed contemporaneously to, or shortly after, deposition (Nickel and Qing, 2004). No fractures were observed in the Midale Evaporite to suggest any evidence of fluid conductance, such as oil staining or precipitation of cements along fracture surfaces. Sulphur isotope ratios of primary Midale Evaporite anhydrites are similar to contemporaneous Mississippian seawater compositions, which further supports the suggestion that these rocks did not experience significant interaction with post-depositional fluids (Qing, 2004). Moreover, the Midale Evaporite has clearly been a very effective seal to hydrocarbon migration for the past 50 million years.

A diagenetically altered zone occurs along the subcrop region of the Poplar, Ratcliffe, Midale, Frobisher, and Alida beds throughout the Weyburn area and in much of southeastern Saskatchewan (Figure 1.5). This zone, which ranges in thickness from 2 to 10 m and is immediately subjacent to the Sub-Mesozoic Unconformity surface at the Weyburn pool, is a region of almost complete porosity reduction that developed through a complex process of micritization, dolomitization, and anhydritization. Early diagenesis primarily involved micritization (Figure 1.16a) and dolomitization (Figure 1.16b), which destroyed much of the original depositional textures of the Midale Beds. Secondary anhydrite cements are present as nodules (Figure 1.16c) and veinlets (Figures 1.16d and 1.16e) that have effectively reduced porosity. The paragenetically latest diagenetic process was the emplacement of metasomatic anhydrites

(Figure 1.16f). Petrographic and fluid inclusion studies have shown that most diagenetic minerals in the altered zone pre-date migration of oil into the Midale Beds, except for some metasomatic anhydrites that formed contemporaneously with oil migration (Yang, 2004) during the Late Cretaceous or Early Tertiary (Osadetz *et al*., 1998).

5.2.2 Mesozoic seals

The Lower Watrous Member forms the most extensive primary seal to the Weyburn system and is an important trap for many of the Mississippian oil pools of southeastern Saskatchewan. Informally, the Lower Watrous can be locally subdivided into a lower sandstone – siltstone unit and an upper siltstone – mudstone unit, but in general, it has a mixed lithological character (Gerla, 2004). Grains are of granitic origin with micrite lithoclasts in an argillaceous dolomitic matrix wherein clay content rarely exceeds 40 per cent (Le Nindre, 2003). Anhydrite and dolomicrosparite are the most common secondary cements. They effectively reduce porosity through carbonate replacement and void filling. The clays are mainly interlayered smectite and chlorite with abundant illites and other micas. Regionally, the Lower Watrous is an effective aquitard, although restricted fluid migration into this unit has been observed elsewhere within the basin, usually in locations lacking a significant Mississippian caprock. Although the Lower Watrous is most porous in the lowermost section, where measured porosities reach 11 per cent (they are, however, generally lower than this), the effective porosity is considerably less, at around 1 per cent (Le Nindre and Gaus, 2004). Stratigraphically higher in the Lower Watrous, porosity is even further reduced. No significant fractures were observed in the Lower Watrous, although small (1 to 2mm) offset micofractures exist in the muddier units.

The depositional pattern of the Lower Watrous Member west of the field was influenced by the subsurface removal of Devonian salt, as shown in Figure 1.17. Here, Lower Watrous strata are thicker than elsewhere in the project area, indicating that subsurface salt dissolution has occurred subsequent to deposition of the Midale Beds in places outside of the RA region.

6 HYDROGEOLOGY

Secure geological storage of CO_2 in the Weyburn pool depends on the structural and stratigraphic configuration of the reservoir and also the efficiency of solubility, ionic, mineral, and hydrodynamic trapping (Bachu, 2001). Because the effectiveness of these mechanisms is largely determined by the subsurface pressure, temperature, and geochemical regime, hydrogeology is a fundamental component to this and to any investigation assessing the integrity of a geological storage site.

The role of hydrogeological mapping is to characterize the natural hydraulic regime of the sedimentary succession in order to determine the impact of fluid flow on CO_2 storage and to define the necessary boundary conditions for the risk analysis system model. The principal goals were to a) identify the directions and rates of formation-fluid flow through water-transmitting strata (aquifers); b) locate preferential pathways (if any) for cross-formational fluid flow; c) assess the competence of low-permeability confining strata (aquitards); d) characterize the hydrochemistry of each aquifer; and e) provide hydrogeological data (*e.g.*, pressures, temperatures, porosities, and permeabilities) for predictive modeling of CO_2 storage performance. Shallow aquifers of the biosphere were characterized in terms of distribution, groundwater levels, and compositions to establish baseline parameters.

6.1 Deep Regional Hydrogeology

Regionally, the hydrogeology and hydrochemistry of the Williston Basin have been widely studied, with examples from the Canadian (Hannon, 1987; Toop and Toth, 1995; Bachu and Hitchon, 1996) and American (Downey 1982; 1984; Downey *et al*., 1987; Berg *et al*., 1994; Busby, 1995; DeMis, 1995; LeFever, 1998) portions of the basin, as well as on a basin-wide scale (Benn and Rostron, 1998). Formation waters generally flow across the basin from the SSW-NNE. This cross-basin flow arises from a regional hydraulic gradient created by topographic elevation differences, approximately 1000 m on average, between major aquifer outcrop areas at opposite edges of the basin. Meteoric waters enter the basin at elevated aquifer outcrops along the southern, southwestern, and western basin flanks (Figure 1.1) and are driven towards the basin centre, as suggested by very fresh formation waters with meteoric isotopic signatures (Rostron and Holmden, 2003) found in the basal aquifers (Hitchon, 1996; Benn and Rostron, 1998). In the deepest portions of the basin, meteoric waters mix with saline brines (Iampen and Rostron, 2000) and the resulting mixtures are displaced up-dip from the basin centre onto the northeastern basin flank (Downey *et al*., 1987). This cross-basinal flow system is considered to have originated relatively recently, with the current boundary conditions set up in the Eocene in association with the onset of the Laramide orogeny. In some areas of the basin, the effects of hydrodynamic forces have been observed as tilted oil-water contacts in oil pools and as brine inflows that threaten subsurface potash mines (DeMis, 1995; Wittrup and Kyser, 1990).

6.1.1 Database and methods

The regional hydrogeological characterization area (bounded by meridians 102 to 106W and parallels 48.5 to 50.5N) includes an additional 50 km west of the 200 by 200 km block used in geological mapping (Figure 1.2). A hydrogeological and hydrochemical database of over 5300 fluid pressures and formation temperatures and over 8500 formation-water analyses was assembled from public and private data sources. This was supplemented with petrophysical data from core analyses within key aquifers and over 100 privately collected wellhead water samples.

Hydrogeological data were assigned to their respective aquifer units and tested against structural controls provided by the geological mapping. Where aquifer nomenclature was incomplete or vague (*e.g.* "Mississippian" aquifers), data were assigned to individual aquifers through a series of interval tests. Data spanning multiple aquifers were removed from the mapped data. Following these measures, and after examination of preliminary results, a hydrostratigraphic framework consisting of 18 major aquifers and 13 major aquitards was developed (Figure 1.3). Data were dealt with on an individual aquifer basis and later recombined for cross-section construction.

All data were carefully screened using automated and manual techniques to remove inaccurate or non-representative samples. Only quality pressure data with full Horner-type extrapolations were used. Each pressure measurement was screened for production-influenced pressure drawdown using a quantitative index accounting for radial proximity of a drill stem test (DST) to production or injection wells and the duration of production or injection (Toth and Corbet, 1986; Barson, 1993; Alkalali, 2002). Chemical data were screened to remove non-representative data (*e.g.* mixtures, drilling mud filtrates, spent acid-fracture fluids, injection waters) using automated techniques (Hitchon, 1996) supplemented by manual inspection.

Pressure data were used for pressure versus depth (p[d]) profiles and converted into potentiometric surfaces and hydraulic cross-sections. Variable-density flow effects were present in many aquifers, and procedures for identifying and dealing with these effects are discussed in the following section. Hydrochemical data were mapped as individual ions, ion ratios, and total dissolved solids (TDS). In this manner, all geological and hydrogeological data were synthesized into a regional picture of fluid flow in the study area.

6.1.2 Formation-water chemistry

Geochemical mapping revealed large variations in water chemistry (both composition and TDS) within and among aquifers in the study. These variations are evident in TDS patterns shown from typical aquifers in each of the three main aquifer groups: pre-Mississippian Paleozoic (Figure 1.18), Mississippian (Figure 1.19), and Mesozoic (Figure 1.20). Vertical variations in TDS are visible in two typical TDS cross-sections (Figures 1.21 and 1.22).

In pre-Mississippian aquifers, TDS patterns have a similar overall character, with fresh waters (TDS <5 g/L) occurring in the west and north of the map area, Na-Cl brines with intermediate TDS (100 to 300 g/L) occupying the central area, and Ca-Na-Cl brines (TDS >300 g/L) in the south and east areas. In general, there is no clear dependence between salinity and stratigraphic depth in Paleozoic aquifers. For example, the most concentrated brines occur within the Manitoba and Duperow aquifers, not in the deepest aquifers (Figures 1.18 to 1.22). Within each aquifer, however, salinity systematically increases toward the deeper part of the basin in the ESE (Figures 1.21 and 1.22). In addition, the degree of penetration of fresh (originally meteoric) waters that now recharge the basin along its southern and western flanks into the Paleozoic rocks within the study area decreases with depth (Figures 1.21 and 1.22). The fresh waters are of the Ca-SO_4 type. Concentrated brines in the pre-Mississippian aquifers are Ca-Na-Cl type waters, with Ca occurring in equal or greater reactive concentrations than Na, reflecting an origin as seawater concentrated through evaporation (Hanor, 1994). Intermediate TDS waters (10 to 100 g/L) constitute various mixing-type hydrochemical facies and are best characterized as Na-SO_4 type waters. The 25 to 50 g/L contour interval marks the transition between significantly different water chemistries and is interpreted to be a mixing zone between invading fresh waters and more "connate" brines. The width and position of this transition zone varies between aquifers (Figures 1.18 and 1.19). In Mississippian aquifers, TDS values have a similar range and distribution to those in the underlying Paleozoic aquifers (compare Figures 1.18 and 1.19). Of particular interest is the steep salinity gradient from less than 50 to over 150 g/L within the Midale and Frobisher aquifers across the Weyburn pool (Figures 1.19c and 1.19d). Invading fresher waters mix to transition-type Na-SO_4 waters across the pool. Hydrochemical facies (Ca-SO_4, Na-Cl, and Ca-Na-Cl types) and the interpreted origin of waters in Mississippian aquifers are the same as those in the pre-Mississippian aquifers. Although waters in Mississippian aquifers have similar chemical compositions and origins, the spatial distribution of water types is variable between each aquifer (Figures 1.19, 1.21, and 1.22), indicating differences in aquifer hydraulics.

Formation fluids in Mesozoic aquifers (Figure 1.20) are markedly different from those of the underlying aquifers. The TDS values are much lower, with maximum values of up to 85 g/L (Figure 1.20c) and typical values ranging from 10 to 50 g/L (Figures 1.20a and 1.20b). In contrast with observations in Paleozoic aquifers, there is no consistent spatial pattern of TDS in the Mesozoic aquifers, where Na-HCO_3 waters are the dominant water type. These characteristics suggest an active flow regime predominantly made up of meteoric waters. The most relevant difference between the Mesozoic aquifers and the underlying Mississippian aquifers is the absence of brines (TDS >100 g/L) in any Mesozoic aquifer within the study area (compare Figure 1.20 to Figures 1.18 and 1.19).

6.1.3 Driving forces and fluid-flow directions

Directions of formation-water flow in each aquifer of the study were determined using potentiometric surfaces obtained from pressure measurements. Although each aquifer has unique flow characteristics, discussion of fluid-flow results will focus on: (a) a typical pre-Mississippian aquifer, the Devonian Winnipegosis aquifer (Figure 1.23), (b) a representative Mississippian aquifer, the Midale Beds into which CO_2 is being injected (Figure 1.24), and (c) a Mesozoic aquifer, the Mannville aquifer (Figure 1.25). Flow patterns of formation waters are normally interpreted from gradients of equivalent freshwater hydraulic head (EFWH), with flow directed toward lower values of EFWH (Figure 1.23). However, the presence of saline brines, and thus the potential for significant density-related flow effects in the Mississippian and pre-Mississippian aquifers, complicates the process of determining flow directions.

For aquifers with significant variations in formation-water density, a parallel approach of mapping EFWH and calculating point estimates of density-corrected driving forces was used. A detailed description of this process can be found in Alkalali (2002), but, in short, density-related flow effects become significant where

the aquifer slope increases, density (TDS) increases, gradient of EFWH decreases, or any combination of the preceding factors occurs (Davies, 1987; Bachu, 1995; Alkalali and Rostron 2003). A density-corrected water driving force (WDF) was calculated over a regular grid of points in each aquifer. The WDF was calculated by adding a buoyancy correction to the gradient of EFWH. Flow directions are indicated by the direction of the WDF vectors, and an indication of the magnitude of the driving force is given by the length of the WDF vector. For example, density effects are significant in the Winnipegosis and Midale aquifers (Figures 1.23 and 1.24) and insignificant in the Mannville aquifer (Figure 1.25).

Water driving force analyses indicate that the deep brines are dynamic (Figures 1.23 and 1.24), in agreement with Downey, (1986), although the pattern of brine movement has not been previously shown. Patterns of lateral brine migration in the Lower Paleozoic and Mississippian aquifers are not uniform. Local areas of intense density-driven flows correspond, in many cases, to complete reversals of flow and to down structural dip, opposing the local hydraulic gradient. This suggests that the brines within the study area are re-adjusting to transient boundary conditions outside the study area. Erosion and reduction of the topographic gradient, and therefore the hydraulic gradient, across the basin has allowed buoyancy to dominate where the combination of structural dip and hydraulic gradient are unfavourable for continued up-dip migration of the brines. The result is either an effective stagnation of flow or a complete reversal and down-dip sinking of brines (Figure 1.23).

In pre-Mississippian aquifers (Figure 1.23), EFWH values range from over 1000 m in the south to less than 600 m in the northeast. Hydraulic gradients ranging in magnitude from 0.1 to 7 m/km, with an average value of about 1 m/km, drive formation waters across the study area in a generally northeasterly direction. Individual aquifers exhibit similar trends in magnitude and gradient of EFWH, with little dependence on aquifer depth. Formation water densities are generally high in the pre-Mississippian aquifers (Figure 1.18), and large areas of intense density-flow reversals are common. Water driving forces deviate strongly from the driving force predicted by the hydraulic gradient, and down-dip basin-inward flows are common.

Within Mississippian aquifers (*e.g.* Midale aquifer; Figure 1.24), hydraulic head distributions are similar overall to those in the underlying aquifers (Figure 1.23). Hydraulic heads range from high values, over 850 m in the SSW, towards the lowest values, under 600 m in the northeast (Figure 1.24). The average direction of fluid flow in the Midale aquifer is diverted to the ESE in the vicinity of the Weyburn pool. The diverted flow directions are attributed to geological heterogeneity within the aquifer and to the barrier created by the Midale subcrop against the Watrous aquitard. Hydraulic gradients are generally comparable to those of underlying aquifers, except for local areas in the east with gradients of up to 20 m/km (Figure 1.24). Locally, high gradients in EFWH indicate the existence of barriers to lateral flow. Density-corrected driving force vectors within the Midale aquifer indicate that flow directions are correctly represented by EFWH in the west due to low TDS in that portion of the aquifer (Figure 1.24). Water driving forces are deflected down-dip in the southern half of the Weyburn pool as increasingly dense brines and a southward-increasing structural gradient become important controls on flow (Figure 1.19). The steep salinity gradient across the Weyburn pool in the Midale aquifer marks the approximate position of this transition to buoyancy-dominated flows. Other Mississippian aquifers show similar patterns of fluid flow. This divergence of flow down-dip related to increased density will only affect the migration pathway of dissolved or ionically trapped CO_2, although, as discussed later, advective flow in the Midale aquifer is relatively sluggish.

In the Mesozoic aquifers, average water-flow directions are more variable between aquifers. Magnitudes of hydraulic gradients are also lower than those observed in the underlying aquifers. Flow directions in the Jurassic aquifer (not shown) are directed NNE, similarly to those in underlying Mississippian aquifers. Within the Mannville aquifer, hydraulic heads range from over 650 m in the west to less than 500 m in the ENE, driving fluid flow in a generally west to east direction (Figure 1.25). In the Newcastle aquifer (not shown), formation waters flow south to north, following the elongate orientation of the permeable Newcastle sandstone body (a pattern previously observed by Hannon, 1987). The absence of dense brines in the Mesozoic aquifers (Figure 1.20) allows the sole use of potentiometric surface maps to delineate lateral formation-water flow directions.

6.1.4 Vertical pressure gradients

Vertical pressure profiles indicate the presence or absence of a vertical component to the hydraulic gradient, which cannot be quantified from potentiometric surface maps. Two pressure versus depth (p[d]) profiles in the vicinity of the Weyburn field (Figure 1.26) reveal important elements of the hydraulic regime through the entire stratigraphic section. First, there is no significant vertical component to flow in the pre-Mississippian and Mississippian aquifers, as all pressure data fall along the nominal hydrostatic gradient (Figures 1.26a and 1.26b). In this case, a hydrostatic vertical pressure gradient indicates a lack of vertical flow; in other words, formation-water flow is almost entirely horizontal in these units. Second, within the Weyburn field (Figure 1.26a, 1.26 to 1.51 km depth), most of the Mississippian data suggest slight overpressuring. The origin of these overpressures is ambiguous; they could indicate minor isolation of that portion of the aquifer or simply reflect the pressurization effects of water injection. In either case, these data fall along a single hydrostatic gradient, indicating that water flow through the reservoir zone is predominantly horizontal. Third, east of the Weyburn field, p[d] data show a change in slope or an apparent break between the Midale aquifer and the Watrous aquitard. If these were both permeable units, the change in slope would indicate an upward component of flow. However, given the relatively low permeability of the Watrous aquitard, the more likely interpretation of the break in the p[d] profile is a hydraulic discontinuity between the Mississippian (Midale aquifer) and the Mesozoic (Jurassic aquifer). Finally, Mesozoic aquifers are normally pressured to underpressured (Figure 1.26, <1.25 km depth), which, in the area east of the Risk Assessment region (Figure 1.2), results in a superhydrostatic vertical pressure gradient between the Jurassic and Mannville aquifers. Where pressure configurations such as these are present and coincide with zones of relatively high permeability within intervening aquitards, upward flow may occur locally in shallow aquifers overlying the sequestration horizon.

6.1.5 Aquifer permeabilities, flow velocities, and CO_2 migration

Formation-water fluxes and velocities were estimated based on combining mapped WDF with grid node hydraulic conductivities from the permeability field realizations, conditioned to data derived from DSTs, and a constant average porosity from core samples. The grid node hydraulic gradient and hydraulic conductivities were used to calculate a flux, which was divided by an average value for porosity to determine water velocity at a given node. Of most importance was the Midale aquifer, which has an average permeability of approximately 35 md after correction for sample bias due to clustered preferential sampling of reservoir-quality rock. Using an average porosity of 14 per cent, a representative estimate of bulk water flow-velocity through the Midale reservoir in the vicinity of the Weyburn pool is 0.80 m/yr. In contrast, overlying Jurassic, Mannville, and Viking aquifers host connected sandstone bodies with permeabilities exceeding 10 Darcy. Consequently, these aquifers host an active hydrodynamic regime with estimated formation-water velocities of 4, 9, and 2.5 m/yr, respectively, in the Weyburn field area.

Conditional geostatistical simulation (Deutsch and Journel, 1998) of regional aquifer permeability fields was used to supplement univariate statistical summaries of the hydraulic property data discussed above. Stochastic images of aquifer permeability that honoured the permeability data were produced, and these reproduced the spatial covariance between permeability data in four key aquifers from the storage layer (Midale) to the shallowest Mesozoic aquifer mapped (Figures 1.27 to 1.30). Stochastic simulation utilizes variograms to characterize the distribution of data and generate multiple equally-probable images, or realizations, and is an alternative to deterministic mapping. The pattern of the permeability field revealed through stochastic simulation may indicate high-conductivity pathways that, potentially, are conduits for subsurface CO_2 migration. A single realization of permeability distribution was chosen to model the flow velocity within selected aquifers. The selected realization exhibited the smallest difference between observed and model-calculated steady-state hydraulic heads based on one set of specified head boundary conditions. Simulation of the permeability distribution in the Midale aquifer (Figure 1.27) was focused on the near-field area around the injection site and displays a slight N-S anisotropy. This anisotropy may potentially reflect the influence of large-scale fracture or other structural trends. Although high permeabilities of several Darcy are present in local areas, water flow-velocity of the region is more strongly controlled by the mean- and low-permeability regions because high-permeability areas are not interpreted to be regionally connected.

Permeability data from the Jurassic aquifer (Figure 1.28) suggest that the variogram of the Jurassic permeability field is directionally isotropic; thus, the simulated permeability field does not exhibit any preferentially-oriented features. Patches of high-valued permeability of several Darcy are common and are typical of Mesozoic aquifers in general. In the Weyburn field area, permeabilities are quite high (average 470 md); however, a low-permeability zone immediately northeast of the Weyburn field, in the direction of water flow, will likely impede lateral CO_2 migration through the Jurassic aquifer if CO_2 were to reach this level.

A sample realization of the permeability structure of the Mannville aquifer (Figure 1.29) reveals large channel structures interpreted to reflect relatively thick, extremely permeable sandstone, which is consistent with results from geological mapping (Haidl *et al*., 2004). Calculated point velocities in these channels approach 50 m/yr.

Permeability distributions in the Newcastle aquifer (Figure 1.30) are affected by the net distribution of sandstones in a north-south direction. The highest permeabilities, and consequently the highest water flow-velocities, are in the south of the study area. The Newcastle aquifer has, however, comparatively low permeabilities (for Mesozoic aquifers) north of the Weyburn field. This broad, relatively low-permeability area averages less than 2 md and is structurally up-dip and in the direction of CO_2 transport and bulk water flow from the Weyburn pool. Were CO_2 to reach the Newcastle aquifer, the rate of CO_2 migration through the aquifer north of the Weyburn field would be relatively slow, as compared to the other Mesozoic aquifers.

Similar calculations were carried out to predict the directions of lateral migration of separate-phase (supercritical or gaseous) CO_2 in key aquifers. CO_2 densities at aquifer conditions were estimated using a solution to an equation of state for CO_2 (Pruess and Garcia, 2002). The in-situ CO_2 density was then combined with the WDF to calculate the trajectory of stringers of separate-phase CO_2 migrating through each aquifer (Midale and Mannville aquifers; Figures 1.24b and 1.25b, respectively). In general, formation-water flow has little effect on separate-phase CO_2 migration because CO_2 is driven primarily by buoyant forces acting in the direction of the local structural gradient. Driving force magnitudes for CO_2 are increased, compared to those for water, due to the additional buoyant driving force (compare Figures 1.24a and 1.24b).

6.2 Shallow Hydrogeology

Shallow aquifers of the biosphere were characterized in terms of distribution, groundwater levels, and compositions to establish baseline parameters (Maathuis and Simpson, 2003a; Mollard and Cosford, 2003). The geological section was subdivided into hydrostratigraphic units (Figure 1.31), and the major aquifers in the study area were delineated (Figure 1.32).

At the base of the shallow section, sandstones and siltstones of the Late Cretaceous-Tertiary Eastend-to-Ravenscrag succession are difficult to distinguish and are considered together as the Undifferentiated Late Cretaceous-Tertiary Unit (Figure 1.31). This unit is present in the southern portion of the regional study area (Figure 1.32) and is a complex system containing aquifers and aquitards that vary significantly in size, thickness, and hydraulic conductivity (Maathuis and Simpson, 2003a).

The second significant shallow aquifer in the area is the Empress Group. In southern Saskatchewan, sediments of the Empress Group often fill valleys incised into the underlying bedrock to form buried-valley aquifer systems such as the Weyburn and Estevan Valley aquifers. The Estevan Valley aquifer system consists of the interconnection of the Estevan, Missouri, Yellowstone, and North channels (Figure 1.32). This is the most extensive shallow aquifer system in the region. During this project, it was observed that the continuity and location of the North Channel and Weyburn Valley in the vicinity of the Weyburn field were not fully constrained (Mollard and Cosford, 2003); thus, a detailed mapping, geophysics, and drilling program was undertaken to define the limits of this aquifer (Maathuis and Simpson, 2003b). An electrical resistivity tomography survey was conducted, and 12 test holes, including six monitoring wells, were drilled to define the extent and hydraulic continuity of the Weyburn Valley aquifer with the Estevan Valley aquifer. Results indicated the presence of a groundwater divide west of the Weyburn field and a

transmissivity barrier in the southern part of the aquifer (Figure 1.33). Typical water chemistries obtained from the Weyburn Valley aquifer are of the mixed type – Na-SO_4-Cl-HCO_3 (Figure 1.34).

Quaternary drift deposits contain shallow aquifers in isolated pockets of stratified granular sediment within unsorted and unstratified glacial till (Figure 1.32). Other than the buried-valley aquifer type mentioned above, quaternary aquifers in the area are generally of limited extent and occur at varying depths (Figure 1.35). These aquifers are, however, an important supply of water for small communities and farms in the area.

7 STRUCTURAL ELEMENTS

Structural features, including basement structures, faults, and intra-sedimentary fracture zones, are fundamental elements affecting depositional patterns or subsurface processes. Faults and fractures are among the most important of these features for CO_2 storage, as they represent, potentially, the most direct natural pathways between sequestration strata and shallower aquifers. The nature and distribution of these features are best characterized through an overview that includes consideration of the tectonic evolution of the rocks making up the storage site.

The structural network of the Weyburn area was determined through examining the relationship of basement structures to intra-sedimentary features using approximately 2000 km of 2D-seismic data, high resolution aeromagnetics (HRAM), and airphoto and Landsat imagery analysis of surface lineaments. The Weyburn regional assessment area is centred on the basement rocks of the Paleoproterozoic Trans-Hudson Orogen (THO), which is a collision zone between the Archean Superior Craton to the east and the Archean Hearne and Wyoming Cratons to the west (Figure 1.4). The structural and petrophysical properties of these rocks define the tectonic and magnetic fabric of the region. A change in the basement character is observed between the somewhat uniform basement surface of the THO zone, underlying the Weyburn site, and the more irregular surface of the Hearne-Reindeer Zone and Wyoming Craton to the west (Figures 1.36 and 1.37). The east-west section shown in Figure 1.37 spans 157 km and was constructed from four seismic lines that are shown in Figure 1.2. Although gaps of 3 to 13 km exist between the lines, similar seismic signatures among the profiles allow recognizable horizons to be traced along this combined section. Depth to the Precambrian basement increases from east to west by about 200 m (0.10 s), and evidence of structural disturbance is seen near each end.

Structural trends on the Precambrian surface, as defined seismically, exhibit a radial pattern of plunging synclines and anticlines that are up to approximately 50 km long (Figure 1.36). The relation of one basement structural trend with overlying strata is depicted in Figure 1.38; it is intersected by three seismic sections over a length of 11 km. Along this trend, the Precambrian basement is deeper than regional values and becomes even deeper southward. The trend occurs within the zone of salt dissolution west of the RA region and its lateral extent is variable, ranging from more than 15 km wide along the northern seismic profile (CBY-7W) to less than 10 km along the southern profile (NOR-83314). The lateral limits of the structure on all three profiles are distinct but not abrupt, which indicates that the collapse of overlying strata was gradational and proceeded largely from north to south where intervals affected may include Late Cretaceous strata. The regional influence of salt dissolution on overlying sediments in this area is shown in Figure 1.17.

The Hummingbird Trough is a prominent intra-sedimentary subsurface feature (Figure 1.10) that was produced by multistage dissolution of the Middle Devonian Prairie Evaporite at the eastern margin of the Wyoming Craton. Apart from this major feature, most of the sedimentary fill within the study area exhibits a uniform depositional environment having relatively few tectonic disruptions. The northern extension of the western margin of the Hummingbird Trough is marked by a fracture zone (identified as F13 in Figure 1.37). Other structural disturbances (F6 to F12 in Figure 1.37) are observed within the region of salt dissolution and may be associated with the reactivation of the boundary zone of the Wyoming Craton. In general, the central region in the vicinity of the Weyburn field shows the least disturbance from tectonism. Correlation of basement and surface trends with the Hummingbird Trough and areas of salt dissolution suggest a probable genetic connection among deep-seated structural trends, their surface expression, and related intra-sedimentary structural features.

Seismic data indicate that local segments of the subsurface were deformed by anorogenic stresses throughout the Paleozoic and, to a lesser extent, at some more recent times. Local structural anomalies, such as small fault zones, are recognized on many of the 2D-seismic sections. Nearly all are observable within the deeper Paleozoic sequences, whereas Watrous strata overlying the Mississippian reservoirs are relatively undeformed, and Upper Cretaceous strata are even less tectonically disturbed. This suggests that the majority of structural discontinuities are absent above the Midale Beds. This interpretation, however, may be biased, as processing of the seismic data was focused to image strata below and immediately above the storage interval, which reduced the resolution at shallower levels. Reprocessing the seismic information with an emphasis on resolving shallow strata would help establish the vertical limits of tectonic disturbances and the effect of salt dissolution on overlying sediments.

The general lack of distinguishable features and, in most cases, large spatial separation between seismic survey lines hinders correlation of faults and fractures among seismic profiles. High resolution aeromagnetic (HRAM) data were used to help correlate structures among seismic sections to determine fault and fracture orientations more clearly. The HRAM response is related to the content of magnetic mineralization and to the ratio of induced-to-remnant magnetism (Goussev *et al*., 2004). Commonly, it provides additional information regarding the orientation of structural features. In Figure 1.39, fault traces from three seismic sections are linked through the integration of filtered HRAM signatures. Using this integrated seismic - HRAM technique, a network of interpreted intra-sedimentary faults and fractures was developed for the vicinity around the Weyburn RA area (Figure 1.40). One linear magnetic anomaly that trends NNW-SSE through the RA region was interpreted as the magnetic signature of a fault identified seismically (Figure 1.41). This fault is named the Souris River Fault and is included in the geological model for risk assessment.

Correlation of deeper structural features with surface lineaments helped assess their vertical extent. Surface lineaments identified through airphoto and Landsat imagery analysis (Penner *et al*., 2004) were grouped into lineament zones where many relatively closely spaced, similarly trending lineaments were observed. Figure 1.42 is a satellite lineament map covering the regional assessment area, including a rose diagram of lineament trends. The regional assessment area is characterized by systematic NE-SW and NW-SE oriented lineaments and lineament zones and by minor N-S and E-W trends. Surface lineaments in this young glaciated landscape appear as discontinuously aligned linear escarpments, valleys, and smaller surface drainage depressions that vary in length and relief. Clusters of collinear individual lineaments that are aligned in the same direction within narrow tracts define longer lineament zones. Dominant surface lineament trends closely match systematic fractures in glacial drift and bedrock exposures. The NE-SW trend also matches the preferred permeability in the Weyburn pool.

The location and orientation of surficial lineament zones were compared to faults and flexures identified from seismic and HRAM data (Penner *et al*., 2003). In the regional study, several subsurface features were found to be spatially related to surface lineament zones. Examples of correlated features include the Missouri Coteau, a prominent surface topographic feature, and the Ceylon-Tyvan and Regina-Lampman lineament zones associated with regions of subsurface salt dissolution (Figure 1.43). Within the RA area, a close correspondence was noted between a lineament associated with the Souris River and the underlying fault identified through seismic and HRAM data (Figure 1.44). The association of these three independent data sets suggests that the Souris River Fault extends through the sedimentary column to near-surface.

8 GEOLOGICAL MODEL

A 3D geological model of the RA region extending 10 km beyond the limits of the CO_2 injection area of the Weyburn field was constructed by integrating geological, hydrogeological, and geophysical data generated within the larger regional study. The model is intended to describe the natural system and, as such, includes the geometry of the strata and faults in the RA region and many of the properties associated with those rocks, including porosity, permeability, TDS of formation fluids, temperature, hydraulic head, formation pressure, and oil and water saturation. The geological model (Figure 1.45) was made using geological modeling software (Gocad) and can be tailored for use in a variety of risk-assessment techniques or scenario analyses. The geological model serves as the basis for the more complete System Model, which

incorporates data collected under all four Themes and which is used for numerical risk assessment. For example, data from the predictions of storage capacity and distribution of CO_2 resulting from the planned 75 injection patterns as described in Theme 3 are embedded into the geological model as part of the System Model to permit a credible assessment regarding long-term storage of CO_2 in the Weyburn field. Table 4.1 of Theme 4 lists the flow units and many of the parameters of the geological model included in the System Model. The Theme 4 chapter also describes the long-term migration of CO_2 in the Geosphere based on numerical simulations using the geological model.

The lateral extent of the geological model was determined from preliminary scoping calculations to cover an area that would significantly exceed the expected migration of CO_2 over thousands of years. The vertical extent of the model includes the Mississippian Tilston Beds, about 100 m below the base of the reservoir, to the ground surface. The basal limit was determined in part from the slightly argillaceous character of the underlying Souris Valley Beds, but mainly from hydrogeological information that indicated there is little, if any, fluid communication with underlying aquifers.

The horizontal layers included in the model are the major hydrostratigraphic flow units present in the study area. At the level of the reservoir, the resolution of the model is slightly increased by including the Midale Marly and Midale Vuggy layers, the overlying Midale Evaporite seal, and the underlying Frobisher Beds. The Frobisher Evaporite is not included in the model, however, nor is the region of reduced permeability at the top of the Midale Beds represented by the diagenetically altered zone. These units were excluded in order to reduce the processing requirements of the numerical risk assessment. By not including these two components to the sealing framework of the reservoir, the modeling results of long-term migration may be considered as conservative with regards to CO_2 retention in the reservoir. Below the Frobisher Beds, the Alida and Tilston Beds are combined into a single layer, as are the Ratcliffe and Poplar Beds that are present above the Midale Evaporite cap over a portion of the study area. In addition, many of the Mississippian units, including the Poplar, Ratcliffe, and Midale beds, are not present throughout the RA region, as they are truncated at the Sub-Mesozoic Unconformity. The Mesozoic hydrostratigraphic divisions are used to define the upper layers of the model. The Souris Valley Fault was included in the model because it passes through the eastern portion of the RA region. This is the only fault considered in the geological model. Additional geomechanical work will be required to assess the likelihood of reactivation of this fault through increase in pressure resulting from CO_2 injection.

Where available, the model is populated with property data derived from core analyses, laboratory analyses, drill stem tests, and geophysical log analyses. Literature and historical data are also incorporated. In addition, stochastic simulations performed to provide permeability data for several of the regional aquifers are included in the model. Seismic inversion techniques are a potential source of property information but were not available to be included in the present model.

The geological model was successfully integrated with additional information gathered within Themes 2, 3, and 4 and subjected to deterministic numerical analysis for risk and performance assessment. The results of these assessments are presented in the chapter on Theme 4 activities.

9 CONCLUSIONS AND RECOMMENDATIONS FOR FUTURE WORK

9.1 Conclusions

The geological setting at the Weyburn field is suitable for long-term subsurface storage of CO_2. Primary seals enclosing the reservoir (including the overlying Midale Evaporite, a highly anhydritized altered zone, and the underlying Frobisher Evaporite) are observed to be competent and exhibit only rare discontinuities, most of which formed shortly after deposition, and exhibit essentially no detectable evidence of fluid conductance. In addition, as part of the primary sealing package, the Jura-Triassic Watrous Formation forms a regionally extensive and effective aquitard. Overlying the Watrous Formation are predominantly clastic strata that are more than one kilometre in total thickness and contain several thick, regionally extensive additional barriers to upward fluid migration.

There are three main hydraulic regimes in the study area: a deep regime, consisting of the pre-Mississippian and Mississippian aquifer groups, a middle regime made up of the Mesozoic aquifer group, and a shallow regime in Cretaceous to Pleistocene sediments. There is significant variability in water chemistry and pressure distributions between and within the hydraulic regimes and all individual aquifers in the section. In general, however, all aquifer flow is laterally confined within regionally continuous aquifer units. The lack of cross-formational flow in the Weyburn area indicates that formation fluids, and any injected fluids such as CO_2, tend to stay within their respective aquifers.

Hydrochemical characteristics of the Midale aquifer in the Weyburn pool are highly variable, but the aquifer has a fairly uniform flow pattern. Within the Weyburn pool, relatively low hydraulic gradients drive flow sluggishly (<1 m/yr) through the water zone in the Midale aquifer, with flow roughly parallel to the subcrop. South and east of the Weyburn pool, density-driven flows drive formation waters down-dip and inward into the basin. The Midale aquifer is effectively separated from the overlying Jurassic aquifer by the competent Watrous aquitard. Although in direct contact with the Mississippian aquifers, the overlying Mesozoic aquifer system exhibits markedly different chemical characteristics, fluid-flow directions, and rates.

Hydrogeological conditions are favourable for CO_2 storage in the Midale (and other) aquifers. Firstly, vertical pressure profiles indicate negligible vertical flow in the Midale aquifer at Weyburn, which is consistent with the interpretation that formation waters are flowing slowly (<1 m/yr) horizontally along the subcrop through the relatively high-permeability aquifer. Secondly, hydrochemistry of the Mesozoic aquifer group further supports the lack of vertical flow from the underlying Mississippian aquifers. The absence of brines in the Mesozoic section, or anywhere above it, supports the interpretation that there are no major vertically continuous heterogeneities in the Watrous aquitard allowing cross-flow upward from the Mississippian aquifers along the subcrop trend. The Watrous aquitard appears to be regionally intact based on natural fluid-flow patterns. Moreover, formation water flow in Mesozoic aquifers may provide a sensitive parameter in scenario modeling in CO_2 sequestration performance due to predicted flow velocities as high as 10 m/yr. These high flow rates are advantageous to geological storage because the more vigorous the flow rate, the greater an aquifer's capacity to absorb CO_2, although CO_2 will disperse over greater distances with time. Thirdly, within this study area, there are regions where down-dip flows create favourable sites for hydrodynamic trapping of CO_2. Finally, the aquifers used for water supply are generally less than 50 m deep in glacial deposits and are local in extent. The Weyburn Valley aquifer is the only shallow aquifer that covers a significant portion of the study area and is generally located west and south of the EOR injection area. Thus, in the unlikely event that CO_2 migrates to the shallow aquifers, they would not promote widespread migration of CO_2 in the biosphere.

Basement structures and an intra-sedimentary fault and fracture network were mapped within the regional system assessment area. Paleozoic salt dissolution has occurred throughout the system assessment region, and that may have induced fracturing of overlying rocks, including the RA area region, although with no apparent compromise of the reservoir around Weyburn. A deep-rooted fault was identified in the RA area and included in the geological model. No evidence of significant vertical fluid migration along faults or fracture zones in Mississippian or younger strata was observed from geological or hydrogeological data.

In general, the work arising from the geological characterization of the Weyburn site indicates that geological storage of CO_2 in hydrocarbon reservoirs is a viable and promising technique for mitigation of CO_2 emissions to the atmosphere.

9.2 Gaps and Suggestions for Future Work

Procedures and results from this work may help to identify and characterize other sites for CO_2 storage in sedimentary basins worldwide. Geological information in the northern Williston Basin, however, is more abundant and readily available than what is typically encountered in characterizing potential storage sites. Future studies will involve deriving geological models using reduced data sets to reflect the more limited availability of information at other locations and to determine minimum requirements for a credible assessment. Geostatistical work may also be employed to help develop methods for determining petrophysical property distribution for use in geological models. Additional work is required on petrophysical characterization of low-permeability clastic aquitards and their effectiveness as seals to vertical CO_2 migration. This may also entail active monitoring of aquitards using instrumented boreholes. Integrating fault and hydrogeological data could be useful in estimating the hydraulic influence of fractures in seals and aquitards to help in determining long-term monitoring programs and predict potential leakage areas. In addition, assessing the potential for reactivation of faults resulting from CO_2 injection will involve geomechanical studies. Continued assessment of existing hydrogeological data is needed to further understand formational flow in aquifers overlying the Weyburn reservoir. Characterization of shallow faults using enhanced seismic processing would better define potential pathways to the biosphere.

10 REFERENCES

Alkalali, A. I, 2002, *Petroleum Hydrogeology of the Nisku Aquifer*. Unpublished M.Sc. Thesis, University of Alberta, Edmonton, p. 152.

Alkalali, A. I., and B. J. Rostron, 2003, Basin-scale analysis of variable-density groundwater flow: Nisku aquifer, Western Canada Basin, *Journal of Geochemical Exploration*, 78-79, pp. 313-316.

Bachu, S., 1995, Flow of variable-density formation water in deep sloping aquifers: review of methods of representation with case studies, *Journal of Hydrology*, 164, pp. 19-39.

Bachu, S., 2001, Geological sequestration of anthropogenic carbon dioxide: Applicability and current issues; In: *Geological Perspectives in Global Climate Change, AAPG Studies in Geology*, 47*,* Ed. Gerhard, L. C., W. E. Harrison, B. M. Hanson, American Association of Petroleum Geologists, pp. 285-303.

Bachu, S., 2002, Sequestration of CO_2 in geologic media in response to climate change: road map for site selection using the transform of the geological space into the CO_2 phase space, *Energy Conservation and Management*, 43, pp. 277-289.

Bachu, S., and B. Hitchon, 1996, Regional-scale flow of formation waters in the Williston Basin, *AAPG Bulletin* 80, 2, pp. 248-264.

Barson, D., 1993, *The Hydrogeological Characterization of Oil Fields in North-Central Alberta for Exploration Purposes*. Unpublished Ph.D. Thesis, University of Alberta, 301p.

Benn, A. A. and B. J. Rostron, 1998, Regional hydrochemistry and Cambrian to Devonian aquifers in the Williston Basin, Canada – U.S.A., In: Christopher, J. E., C. Gilboy, D. Patterson, S. Bend (Eds.), *Eighth International Williston Basin Symposium*. Regina: Sask. Geol. Soc., pp. 238-246.

Berg, R. R., W. D. DeMis, and A. R. Mitsdarffer, 1994, Hydrodynamic effects on Mission Canyon (Mississippian) oil accumulations, Billings Nose area, North Dakota, *AAPG Bulletin*, 78, pp. 501-518.

Burrowes, O. G., 2001, Investigating CO_2 storage potential of carbonate rocks during tertiary recovery from a billion barrel oil field, Weyburn Saskatchewan: Part 2 – reservoir geology (IEA GHG Weyburn CO_2 Monitoring and Storage Project); In: *Summary of Investigations 2001, Volume 1*, Saskatchewan Geological Survey, Sask. Energy Mines, Misc. Rep. 2001-4.1, pp. 64-71.

Busby, J. F., B. A. Kimball, and J. S. Downey, 1995, *Geochemistry of water in aquifers and confining units of the Northern Great Plains in parts of Montana, North Dakota, South Dakota, and Wyoming*. U.S. Geological Survey Professional Paper, v. 1402-F, U.S. Geological Survey, 146 p.

Christopher, J. E., J. LeFever, A. Marsh, M. Yurkowski, and P. Thomas, 2004, *Report on the Mesozoic Formations of the IEA GHG Weyburn CO2 Monitoring and Storage Project; subtask 2.1.2: Southeastern Saskatchewan and contiguous North Dakota and Montana*. Internal report, IEA GHG Weyburn CO_2 Monitoring and Storage Project, 14p.

Davies, P. B., 1987, Modeling Areal, Variable-Density, Ground-Water Flow Using Equivalent Freshwater Head – Analysis of Potentially Significant Errors, *Proceedings of the NWWA Conference on Solving Ground Water Problems With Models*, February 10-12, 1987, Denver, Colorado, v. II, pp. 888-903..

De Mille, G., J. R. Shouldice, and H. W. Nelson, 1964, Collapse structures related to evaporites of the Prairie Formation, Saskatchewan, *Geological Association of America Bulletin*, 69, pp. 307-316.

DeMis, W. D., 1995, Effect of cross-basinal hydrodynamic flow on oil accumulations and oil migration history of the Bakken-Madison Petroleum System; Williston Basin, North America; In: Hunter, L. D. V. and R. A. Schalla (Eds.), *Seventh International Williston Basin Symposium*, Billings, Montana. Geol. Soc., pp. 291-301.

Deutsch, C. V. and A. G. Journel, 1998, *GSLIB, Geostatistical Software Library and Users Guide*. New York: Oxford.

Dietrich, J. R., J. A. Majorowicz, and M. D. Thomas, 1999, *Williston Basin profile, southeast Saskatchewan and southwest Manitoba: a window on basement—sedimentary cover interaction.* Geological Survey of Canada, Open File 3824.

Downey, J. S., 1982, Hydrodynamics of the Williston Basin in the Northern Great Plains, *C.V. Thesis Conferences on Geohydrology, 1st*, pp. 92-98.

Downey, J. S., 1984, *Geohydrology of the Madison and associated aquifers in parts of Montana, North Dakota, South Dakota, and Wyoming*. U. S. Geological Survey Professional Paper: Reston, VA, United States, United States Geological Survey, G1-G47 p.

Downey, J. S., 1986, *Geohydrology of bedrock aquifers in the Northern Great Plains in parts of Montana, North Dakota, South Dakota, and Wyoming*. United States Geological Survey, v. 1402-E, 87p.

Downey, J. S., J. F. Busby, and G. A. Dinwiddie, 1987, Regional aquifers and petroleum in the Williston Basin region of the United States; *In*: Longman, M. (Ed.), W*illiston Basin: Anatomy of a Cratonic Oil Province: Symposium of the Rocky Mountain Association of Geologists*, Denver: Rocky Mtn. Assoc. Geol., pp. 299-312.

Edmonds, A. C. and A. P. Moroney, 1998, Geology, Development and Optimization of the Weyburn Unit, Southeastern Saskatchewan; *In*: J. R. Hogg (Ed.), *Oil and Gas Pools of the Western Canada Sedimentary Basin*, Canadian Society of Petroleum Geologists, Special Publication S-51, pp. 1-12.

Ferdous, H., 2004, *Subtask 2.4.5: Sedimentology and allostratigraphy of the Newcastle (Viking) Formation: sealing potential of the Lower Colorado Group units in the Weyburn area, Saskatchewan, Canada*. Internal report, IEA GHG Weyburn CO_2 Monitoring and Storage Project, 25p.

Gendzwill, D. J. and N. Martin, 1996, Flooding and loss of the Patience Lake Mine, *CIM Bulletin* 89, pp.62-73.

Gerla, G., 2004, *Geology of the Lower Member of the Watrous Formation*. Internal report, IEA GHG Weyburn CO_2 Monitoring and Storage Project, 14p.

Goussev, S., L. Griffith, J. Peirce, and A. Cordsen, 2004, Using enhanced HRAM anomalies to correlated faults between 2-D seismic lines, *Proceedings and Abstracts*, *Canadian Society of Petroleum Geologists Annual Convention*, Calgary.

Haidl, F. M., M. Yurkowski, S. G. Whittaker, L. K. Kreis, C. F. Gilboy, and R. B. Burke, 2004, The importance of regional geological mapping in CO_2 storage site characterization: examples from the IEA GHG Weyburn CO_2 Monitoring and Storage Project, *Accepted, GHGT-7 Conference Proceedings.*

Hannon, N., 1987, Subsurface water flow patterns in the Canadian sector of the Williston Basin; In: Longman, M. (Ed.), *Williston Basin: Anatomy of a Cratonic Oil Province: Symposium of the Rocky Mountain Association of Geologists*, Denver, Rocky Mtn. Assoc. Geol., pp. 313-321.

Hanor, J. S., 1994, Origin of saline fluids in sedimentary basins, In: Parnell, J. (Ed.), *Geofluids: Origin, Migration and Evolution of Fluids in Sedimentary Basins,*, Geol. Soc. Spec. Pub., pp. 151-174.

Hitchon, B., 1996, Rapid evaluation of the hydrochemistry of a sedimentary basin using only standard formation water analyses: example from the Canadian portion of the Williston Basin, *Applied Geochemistry* 11, pp. 789-795.

Iampen, H. T. and B. J. Rostron, 2000, Hydrogeochemistry of pre-Mississippian brines, Williston Basin, Canada-USA, *Journal of Geochemical Exploration,* 69-70, pp. 29-35.

Kent, D. M. and J. E. Christopher, 1994, Geological history of the Williston Basin and Sweetgrass Arch; *In:* Mossop, G. D. and I. Shetsen, I. (comps.), *Geologic Atlas of the Western Canada Sedimentary Basin. Calgary*, Canadian Society of Petroleum Geologists and Alberta Research Council, pp. 421-430.

Kent, D. M., P. L. Thomas, and T. Heck, 2004, Geological mapping of Mississippian strata in southeastern Saskatchewan, northwestern North Dakota and northeastern Montana (IEA Weyburn CO_2 Monitoring and Storage Project): In*: Summary of Investigations 2004, Volume 1*, Saskatchewan Geological Survey, Sask. Industry Resources, Misc. Rep. 2004-4.1, CD-ROM, (*in press*).

Kent, D. K., 2004, *Characterization of lithologies and fractures in the Frobisher Beds and the Midale and Frobisher evaporites underlying the Weyburn Oil Pool*. Internal report, IEA GHG Weyburn CO_2 Monitoring and Storage Project*,* 15p.

Khan, D. K. and B. J. Rostron, 2004, Regional hydrogeological investigation around the IEA GHG Weyburn CO_2 Monitoring and Storage Project site, *Accepted, GHGT-7 Conference Proceedings*.

Lane, D. M., 1987, *Subsurface carbon dioxide in Saskatchewan: sources and potential use in enhanced oil recovery.* Saskatchewan Energy and Mines, Open File Report 87-2, 40p.

Lee, H., 1962, *The technical and economic aspects of helium production in Saskatchewan, Canada.* Department of Mineral Resources, Saskatchewan, Report 72, 36p.

LeFever, R. D., 1998, Hydrodynamics of formation waters in the North Dakota Williston Basin; In: J. Christopher, C. Gilboy, D. Paterson, S. Bend (Eds.), *Eighth International Williston Basin Symposium*, Regina, Special Publication, Saskatchewan Geological Society, No. 13, pp. 229-237.

Le Nindre, Y. and I. Gaus, 2004, Characterization of the Lower Watrous aquitard as a major seal for CO_2 geological sequestration (Weyburn Unit, Canada), *Submitted to GHGT-7 Conference Proceedings.*

Le Nindre, Y. M., 2003, *Geological characterisation of the Lower Watrous aquitard as major seal for CO_2 geological storage*. IEA GHG Weyburn CO_2 Monitoring and Storage Project Subtask 2.1.6. Report BRGM/RP52826-FR. 47p., 19 Fig., 3 Tables., 6 app.

Maathuis, H. and M. Simpson, 2003a, *Regional hydrogeology of the Weyburn CO_2 Monitoring Project area: Task 2.2.3 – Regional "Shallow" Hydrogeology, Volumes I and II*. Saskatchewan Research Council Publication No. 11410-1E03, 45p.

Maathuis, H. and M. Simpson, 2003b, *Delineation of the Weyburn Valley Aquifer in the "Local" IEA Weyburn CO_2 Monitoring area, Saskatchewan*. *Saskatchewan Research Council Publication No*. 11634-1E03, 8p.

Mollard, J. D. and J. I. Cosford, 2003, *Shallow hydrogeology of the Weyburn Phase 1a EOR area*. Internal report, IEA GHG Weyburn CO_2 Monitoring and Storage Project, 40p, 114 Figs.

Nemeth, B., A. Prugger, S. Halabura, and T. Danyluk, 2002, Benefits of 3D poststack depth migration: Case study from the potash belt of Saskatchewan, *Proceedings of Canadian Society of Exploration Geophysicists meeting*, Calgary, 4p.

Nickel, E. and H. Qing, 2004, Geochemical and petrographic characterization of the unconformity-related seal in the Weyburn Midale Pool, southeastern Saskatchewan; In: *Summary of Investigations 2004, Volume 1*, Saskatchewan Geological Survey, Sask. Industry Resources, Misc. Rep. 2004-4.1, CD-ROM, Paper A-10 10p.

Osadetz, K. G., P. K. Hannigan, L. D. Stasiuk, B. P. Kohn, P. O'Sullivan, S. Feinstein, R. A. Everitt, C. F. Gilboy, and R. K. Bezys, 1998, Williston Basin thermotectonics: variations in heat flow and hydrocarbon generation; In: J. Christopher, C. Gilboy, D. Patterson, S. Bend (Eds.), *Eighth International Williston Basin Symposium*, Regina, Special Publication, Saskatchewan Geological Society, No. 13, p. 147-165.

Penner, L., J. Cosford, J. Mollard, and T. Zimmer, 2003, *Remote sensing studies*. Internal report, IEA GHG Weyburn CO_2 Monitoring and Storage Project. 74p, 113 Figs.

Pruess, K. and J. Garcia, 2002, Multiphase flow dynamics during CO_2 disposal into saline aquifers, *Environmental Geology* 42, pp. 282-295.

Prugger, A., B., Nemeth, and T. Danyluk, 2002, A new model for Saskatchewan collapse structures. Abstract, Saskatoon 2002, *Joint Annual Meeting of Geological Association of Canada/Mineralogical Association of Canada*, Abstracts, 27, p. 93.

Qing, H., 2004, *Isotopic geochemistry of anhydrites from Midale, Frobisher and Watrous strata: implications for communication of Mississippian reservoirs with Watrous Formation*. Internal report, IEA GHG Weyburn CO_2 Monitoring and Storage Project, 5p.

Rostron, B. J., and C. Holmden, 2003, Regional variations in oxygen isotopic compositions in the Yeoman and Duperow aquifers, Williston basin (Canada-USA), *Journal of Geochemical Exploration* 78-79, pp. 337-341.

Rott, C., 2003, *Sealing potential of Mississippian Alida Beds.* Internal report, IEA GHG Weyburn CO_2 Monitoring and Storage Project, 26p.

Smith, D. G. and J. R. Pullen, 1967, Hummingbird Structure of southeast Saskatchewan, *Bulletin of Canadian Petroleum Geology*, 15, pp. 468-482.

Toop, D. C. and J. Toth, 1995, Hydrogeological characterization of formation waters using ionic ratios, south-central Saskatchewan; In: Hunter, L. D. V., R. A. Schalla (Eds.), *Seventh International Williston Basin Symposium*, Billings, Montana. Geol. Soc., pp. 313-319.

Toth, J. and T. F. Corbet, 1986, Post-Paleocene evolution of regional groundwater flow-systems and their relation to petroleum accumulations, Taber area, southern Alberta, Canada, *Bulletin of Canadian Petroleum Geology*, 34, pp. 339-363.

Wegelin, A., 1984, Geology and reservoir properties of the Weyburn Field, southeastern Saskatchewan; In: Lorsong J. A. and Wilson M. A. (Eds.), *Oil and Gas In Saskatchewan*, Saskatchewan Geological Society Special Publication Number 7, pp. 71-82.

Wegelin, A., 1987, Reservoir characteristics of the Weyburn field, southeastern Saskatchewan, *Journal of Canadian Petroleum Technology*, 87-04-05, 60-66.

Wittrup, M. B. and T. K. Kyser, 1990, The petrogenesis of brines in Devonian potash deposits of western Canada, *Chemical Geology*, 82, pp. 103-128.

Yang, C., 2004, *Fluid inclusion study of Mississippian anhydrite cements: Weyburn and adjacent areas, southeastern Saskatchewan*. Internal report, IEA GHG Weyburn CO_2 Monitoring and Storage Project, 14p.

Zhou, W., M. Stenhouse, S. Whittaker, D. Law, R. Chalaturnyk, and W. Jazrawi, 2004, The IEA GHG Weyburn CO_2 Monitoring and Storage Project – Modeling of the long-term migration of CO_2 from Weyburn. *Accepted*, *GHGT-7 Conference Proceedings.*

FIGURES

Figure 1.1: Regional map showing the setting of the study area within the northeastern portion of the Williston Basin. Several tectonic elements bordering the Williston Basin are shown (brown shading), as are highlands (red), to the south and southwest, where meteoric waters enter the basin. Basin waters are discharged in Manitoba along the northeast margin of the basin. The 200 x 200 km area of the regional study centred on the Weyburn field is highlighted and includes portions of Saskatchewan, North Dakota, and Montana. An area of natural CO_2 occurrences along the western margin of the Williston Basin is also shown (green).

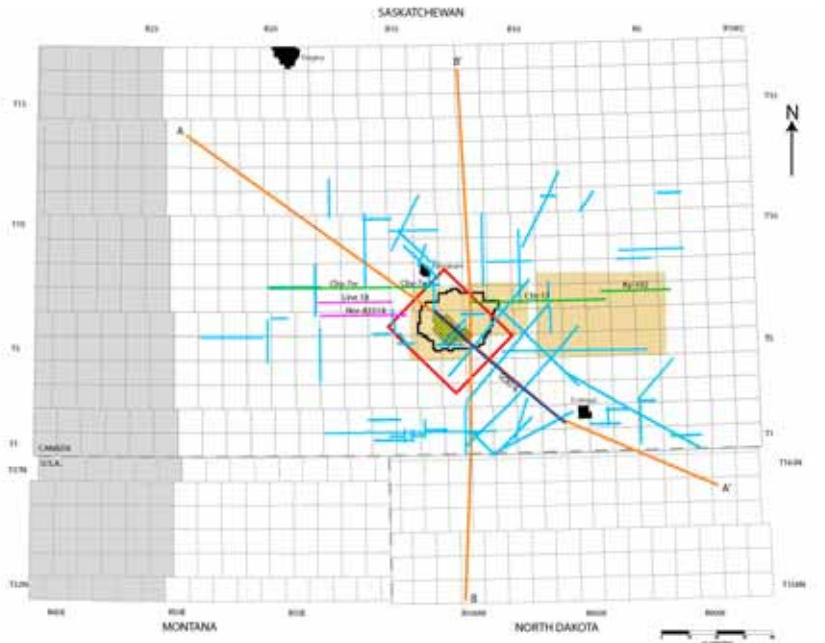

Figure 1.2: Detailed map of the regional study area. The shaded area of the western margin of the map indicates the region included in some of the hydrogeological mapping within the project. The Risk Assessment region is represented by the red rectangle around the Weyburn field (black outline). The area of CO_2 flooding is shown as the gridded region in the western part of the Weyburn field. The location of two hydraulic cross-sections (Figures 1.21 and 1.22) are shown in orange and labeled A-A' and B-B'. The yellow shaded areas are the regions where data for pressure-depth profiles (shown in Figure 1.26) were obtained. The locations of 2D-seismic lines used in this study are shown in blue. Specific lines referred to in the text are highlighted in different colors and labeled (see Figures 1.37, 1.38, and 1.41).

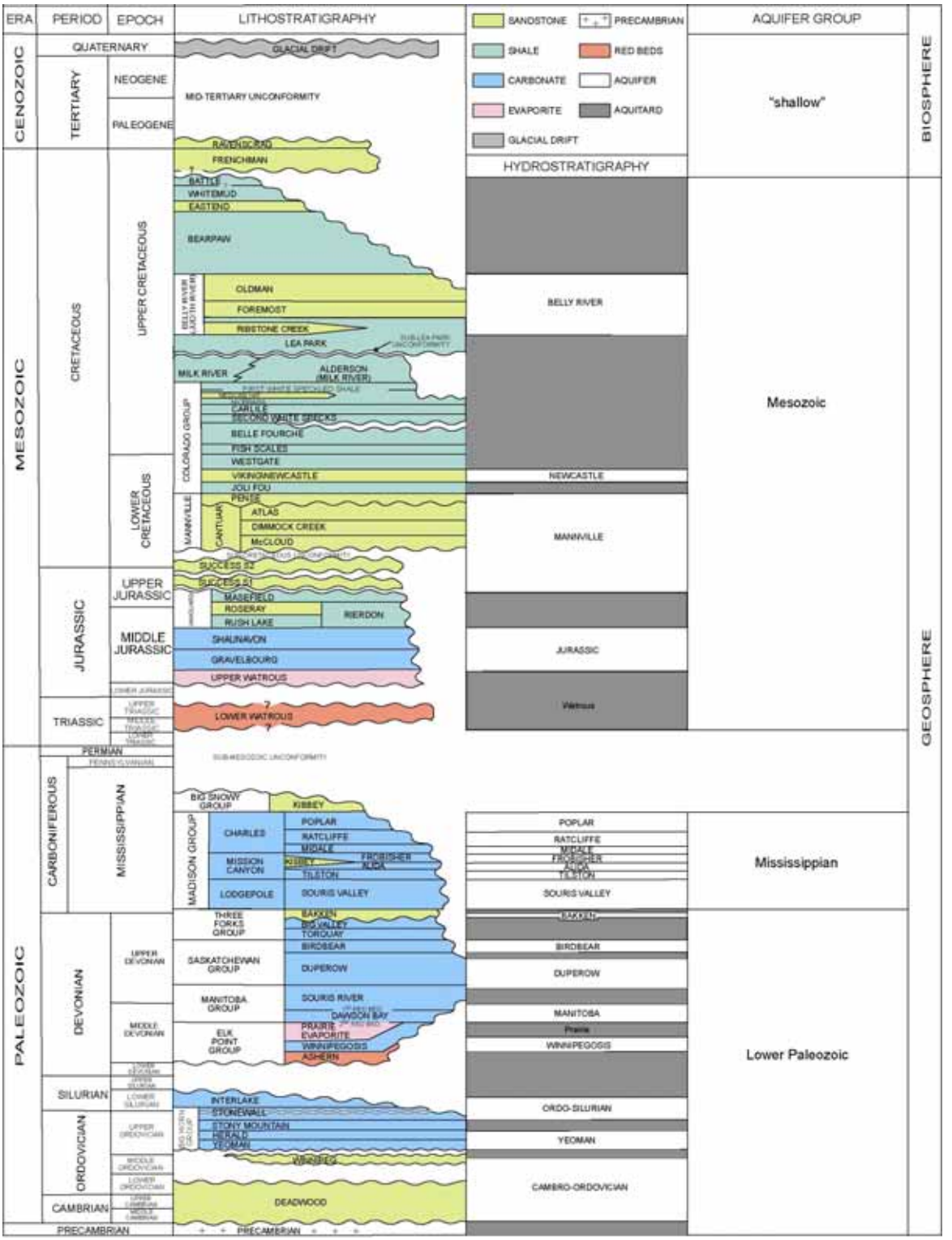

Figure 1.3: Generalized stratigraphy of the study area showing the major lithostratigraphic units and their representative lithology. Numerous minor evaporite beds that occur in Paleozoic strata, and many other detailed stratigraphic units used in the geological characterization of the Weyburn region, cannot be resolved at the scale of this diagram. The relation between major lithostratigraphic units and hydrostratigraphic units in southern Saskatchewan is also shown (Khan and Rostron, 2004).

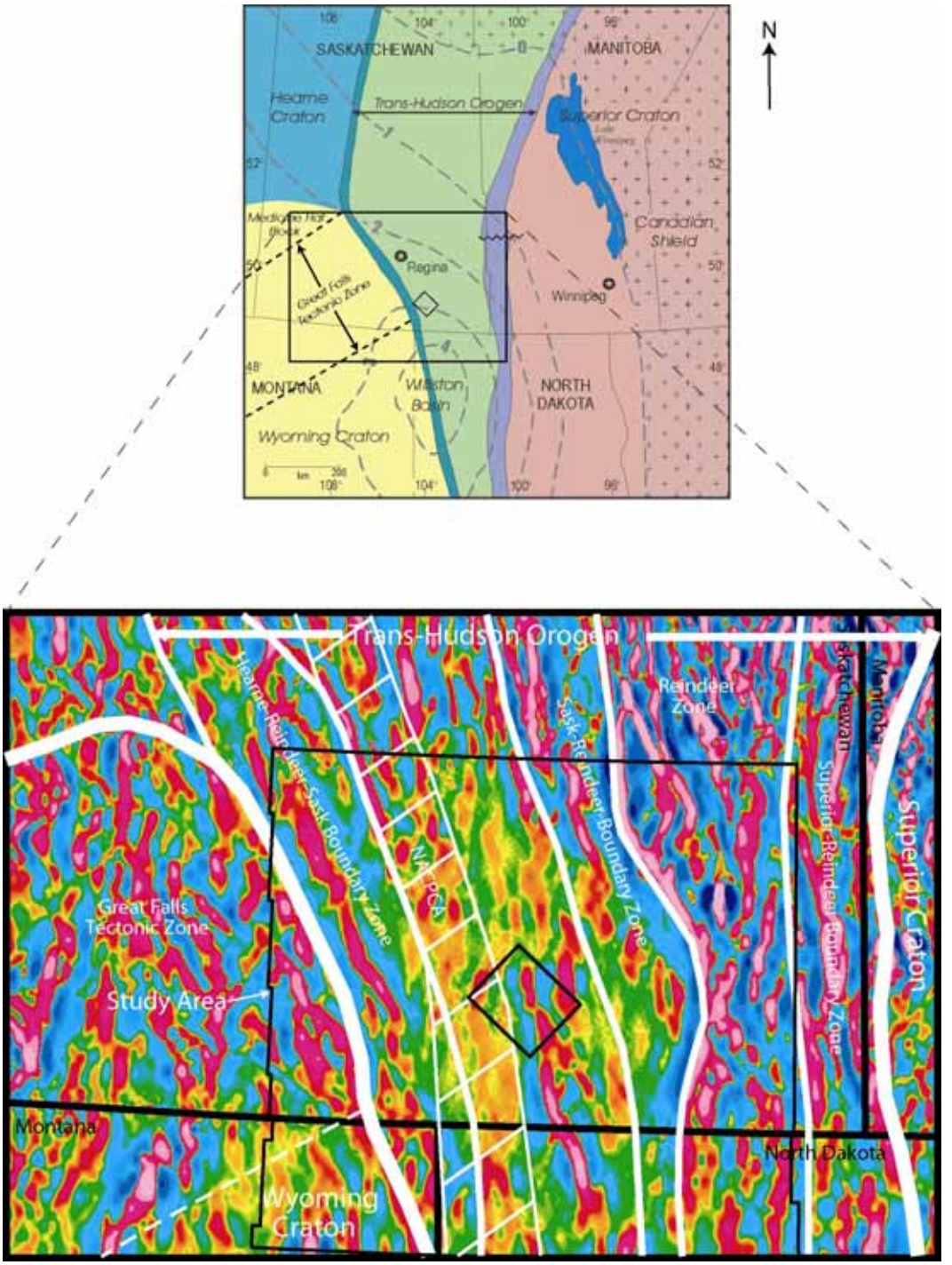

Figure 1.4: The upper map indicates the Precambrian tectonic provinces comprising the basement of the study area. The Risk Assessment region is shown as the small rectangular outline near the centre of the map. The contours reflect the thickness (km) of the Phanerozoic strata in the Williston Basin. (Diagram is modified after Dietrich et al., 1999). The lower map shows the magnetic signature of basement rocks and more detailed tectonic divisions within the basement around the study area. Most of the study area is underpinned by the Trans-Hudson Orogen, a collision zone between the Archean Superior Craton to the east and the Archean Hearne and Wyoming Cratons to the west. NACPCA: North American Central Plains Conductivity Anomaly.

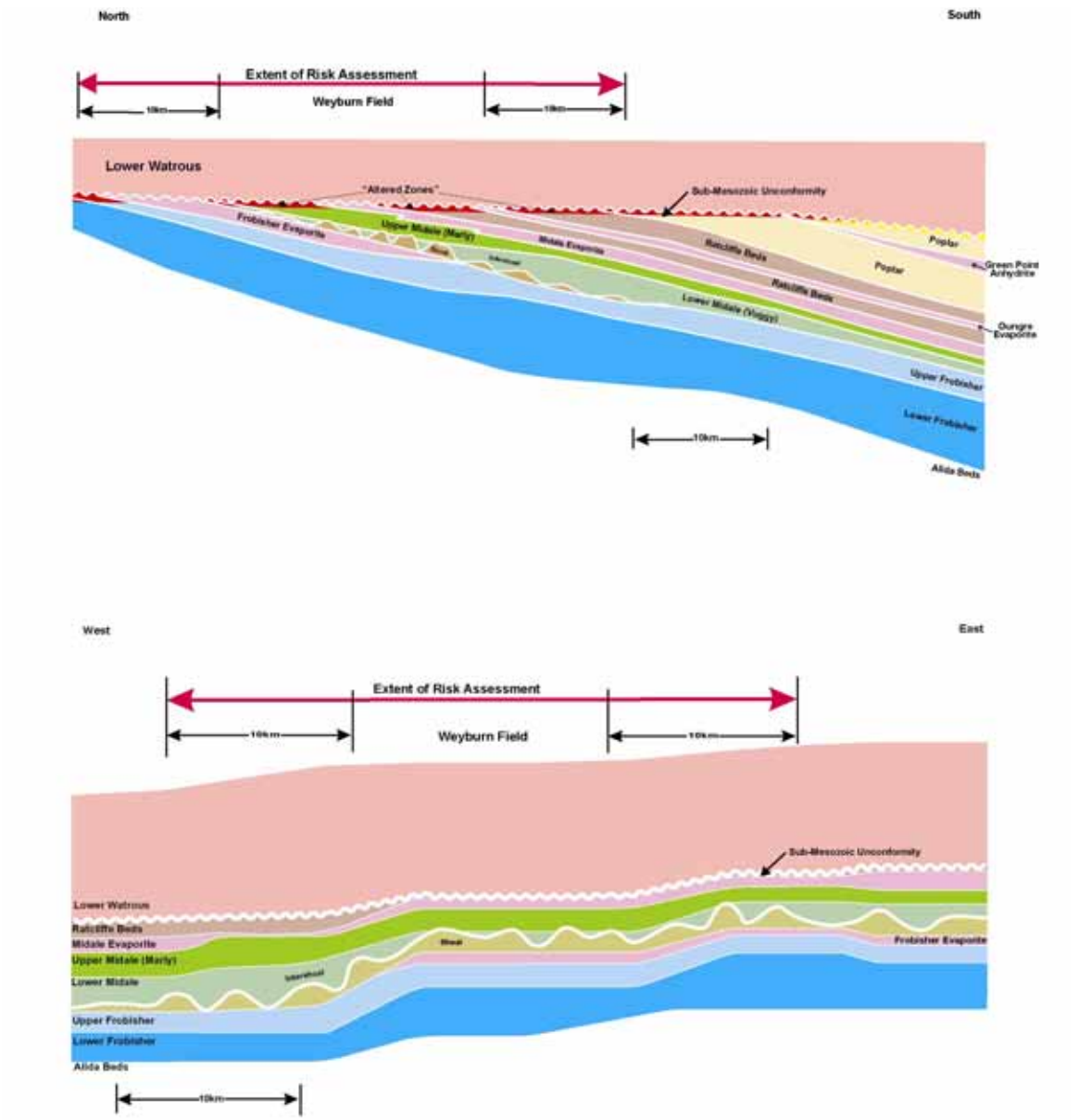

Figure 1.5: The upper diagram is a schematic north-south cross-section (across the regional study area) illustrating truncation of inclined Mississippian strata at the Sub-Mesozoic Unconformity. Evaporite beds act as sealing units for more porous carbonate strata. In addition, porosity has been largely occluded through micritization and anhydrite cementation in the diagenetically altered zone beneath the Sub-Mesozoic Unconformity. The Triassic Lower Watrous Member, which overlies the unconformity, is also an important primary seal for Mississippian reservoirs. The lower diagram is an east-west cross-section through the Weyburn field along the general strike of the Mississippian beds. The lateral continuity of Midale strata beyond the Weyburn pool is strongest to the east where Vuggy shoals are commonly developed. To the west and south of the Weyburn pool, shoal development is less prevalent and lateral continuity is weaker. See Figure 1.13 for location of cross-section lines.

Theme 1: Geological Characterization

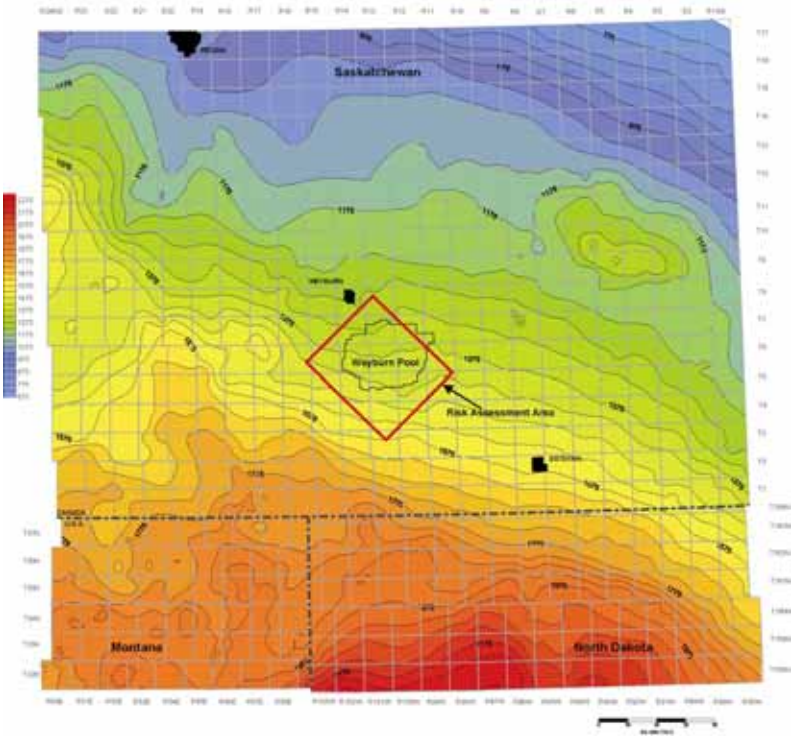

Figure 1.6: Isopach map of the Mesozoic succession in the regional study. This package of predominantly clastic rocks contains the major aquitards and aquifers overlying the Midale Beds of the Weyburn oilfield. The thickness of this sequence ranges from near 600 m to more than 2200 m across the study area and is around 1325 to 1425 m thick above the Weyburn pool.

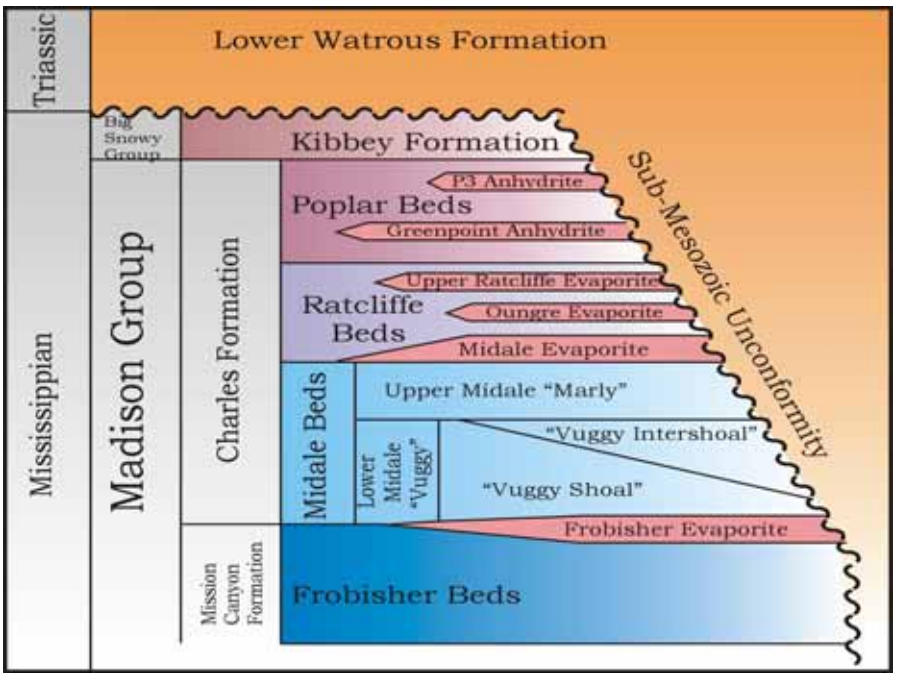

Figure 1.7: Detailed Mississippian stratigraphy of the study area. The Mississippian beds are progressively truncated to the north by the Sub-Mesozoic Unconformity. The Kibbey Formation is present only in the U.S. and southernmost Canadian portion of the study and is not found in the Risk Assessment region. The Poplar and Ratcliffe beds are found only in the southern part of the Weyburn field. The evaporite beds are predominantly anhydrite and form several barriers to upward movement of fluids.

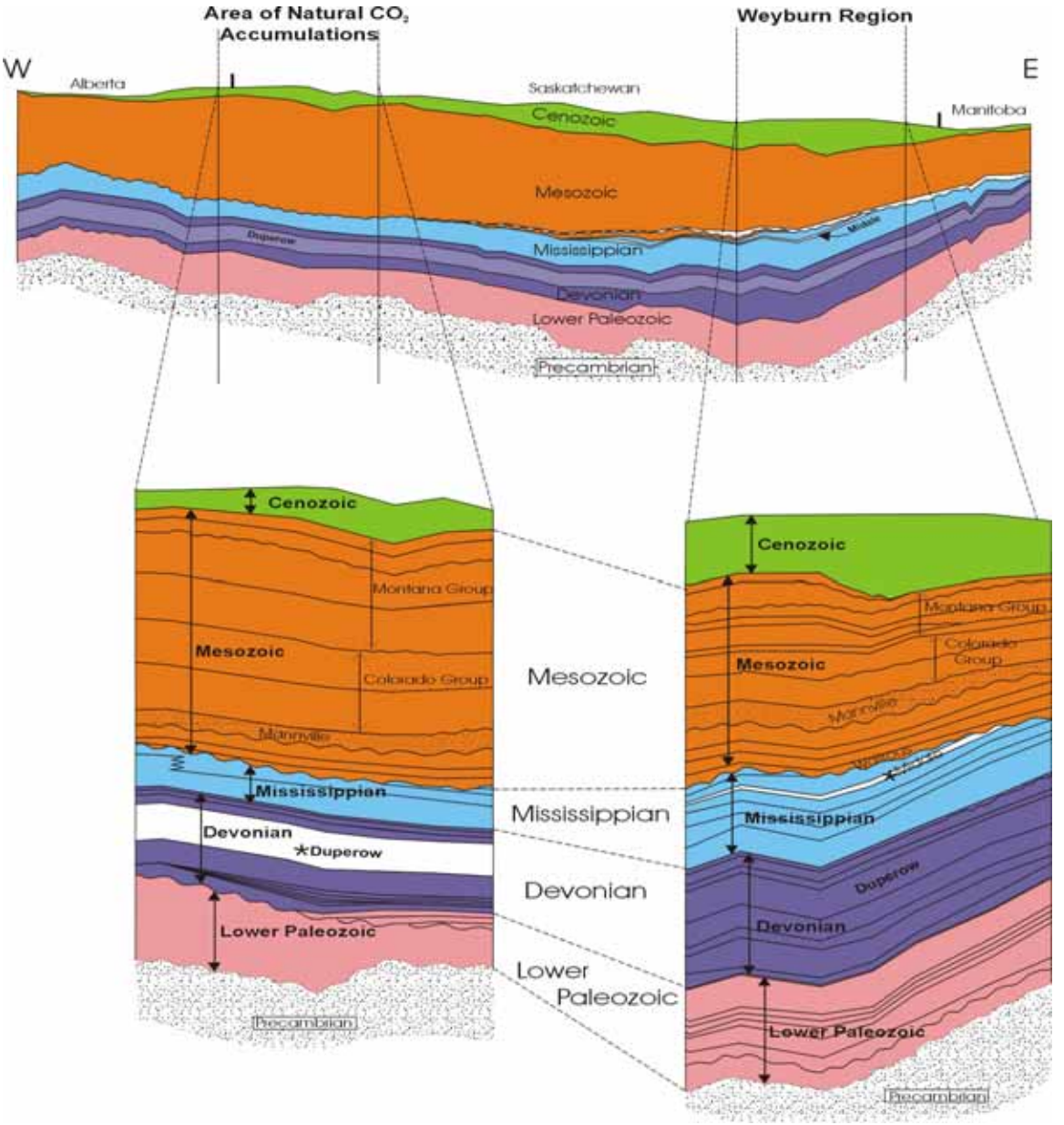

Figure 1.8: Comparison of the geological setting between the natural CO_2 sites in southwestern Saskatchewan (see Figure 1.1) and that of the Weyburn injection site. The top diagram depicts the relatively continuous strata across the intervening distance between the two areas. Note that the Mississippian Midale Beds are truncated at the Sub-Mesozoic Unconformity and are not present in southwest Saskatchewan. This cross-section runs east-west from Manitoba to Alberta through the Weyburn field and parallels the Canada–US border. The lower diagrams show detailed geological columns that indicate the broad similarity of geological setting in both areas. At each site, the CO_2 is contained in Paleozoic carbonate reservoirs capped by anhydrite layers and in turn overlain by approximately 1500 m of Mesozoic shales, siltstones, and sandstones. At the Weyburn site, anthropogenic CO_2 is being injected into the Mississippian Midale Beds, whereas in southwestern Saskatchewan naturally occurring CO_2 is found mainly in the Devonian Duperow Formation.

Theme 1: Geological Characterization

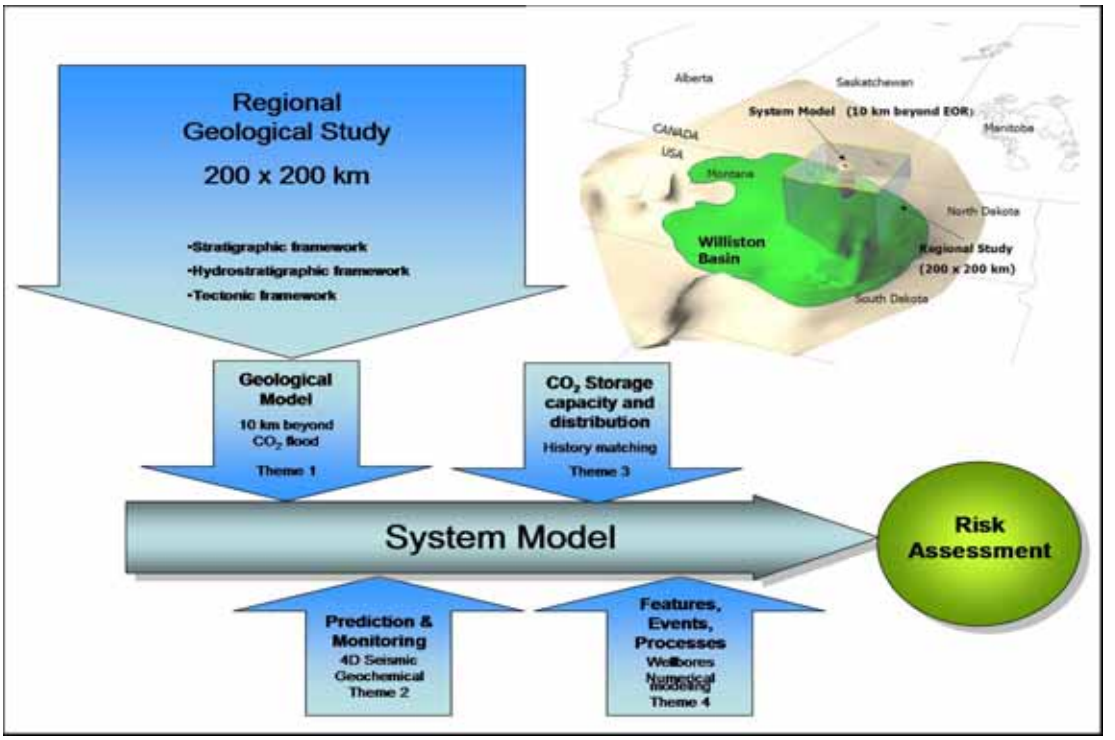

Figure 1.9: Relation of the geological model, and information gathered within other tasks of the project, to the overall System Model ultimately used for risk and performance assessment. The flow diagram indicates that the regional geological study provides data from geological, hydrogeological, and geophysical investigations required to construct the geological model and assess the appropriate spacial extent required for the geological model. The inset map depicts the regional study area within the Williston Basin, and shows the location of the System Model used in this study.

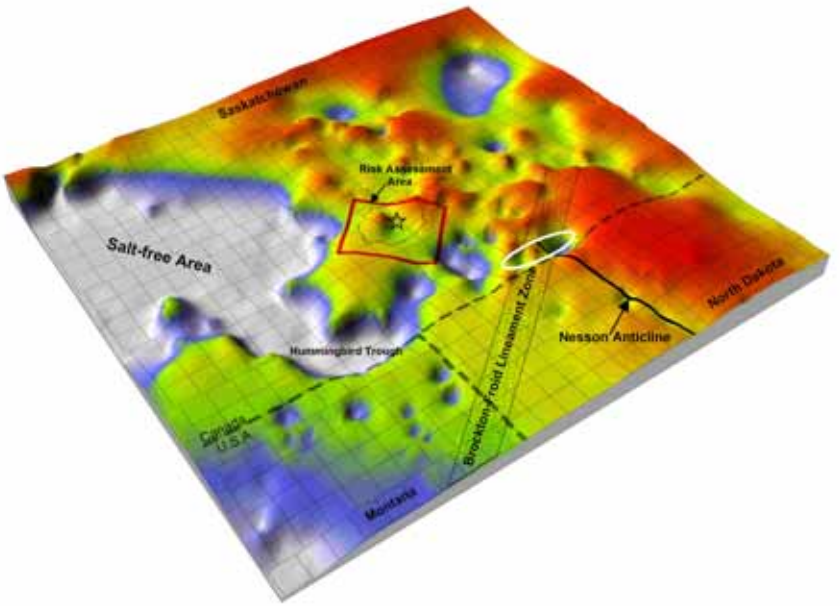

Figure 1.10: Surface map showing thickness variations in salt beds of the Devonian Prairie Evaporite Formation arising mainly from subsurface dissolution. The southern portion of the extensive salt-free region in the western map area defines the Hummingbird Trough, one of the most significant subsurface structures in the study region. More localized areas of dissolution are also present throughout the region, including a location (star) having about 30 m of salt removal within the limits of the Weyburn field and the area used in construction of the schematic diagrams of Figure 1.11, which lies within the oval outlined east of the Hummingbird Trough along the Canada – US border. This map is derived solely from well-based data, but other data, including seismic, are very useful in defining the locations and extents of dissolution areas where well information is sparse. Superimposed on this map are two basement structural features: the Nesson Anticline and the Brockton-Froid Lineament Zone, as defined on DEM and LANDSAT imagery in Montana and North Dakota (Penner et al., 2003) and projected into the Saskatchewan subsurface. Also outlined are the generalized trends of two basement structural features, the Nesson Anticline and the Brockton-Froid Lineament Zone.

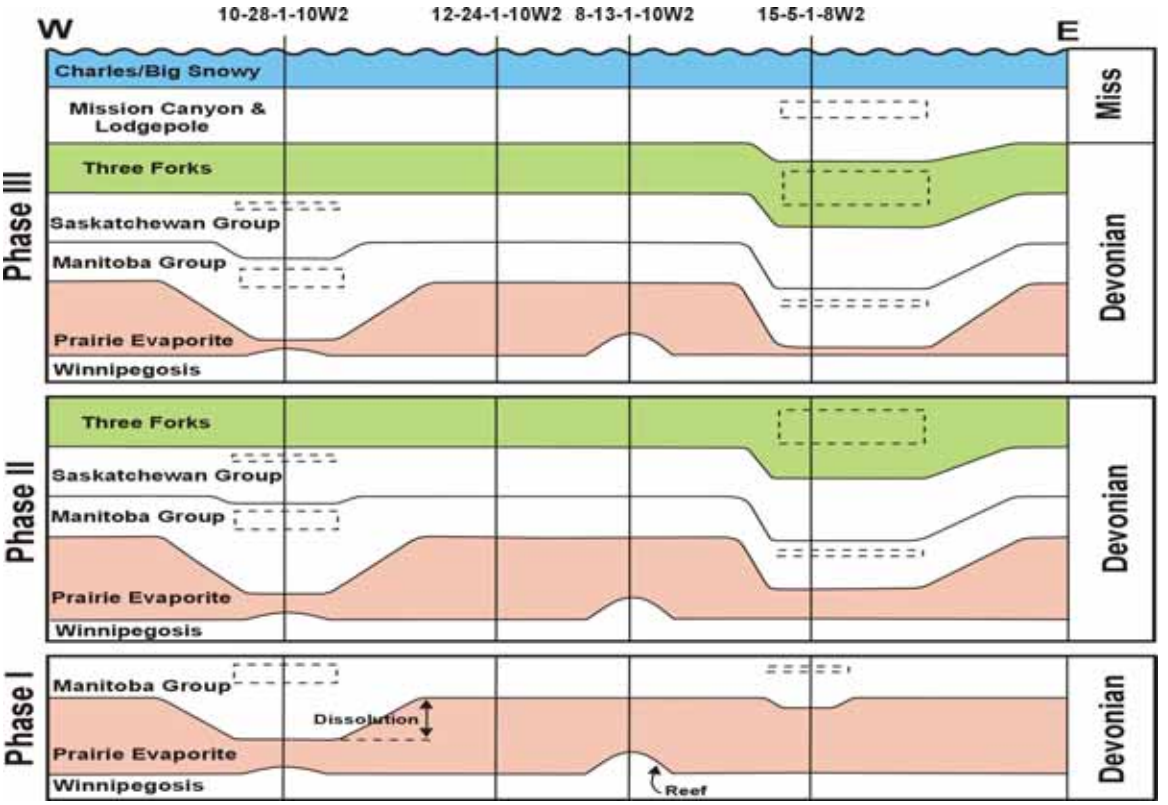

Figure 1.11: Schematic diagrams (not to true scale) depicting stages of salt dissolution and their effect on overlying strata in four wells in an area (white oval shown in Figure 1.10) south of Estevan. These diagrams indicate that the timing and extent of subsurface dissolution are not consistent throughout the basin and that significant differences in the nature of dissolution may occur within relatively restricted areas. Removal of material through dissolution of salts of the Middle Devonian Prairie Evaporite is compensated by localized thickening of sediments being deposited contemporaneously with dissolution. This provides information regarding the timing of dissolution and the possible vertical extent of strata potentially affected by collapse structures. Thickening of strata associated with underlying dissolution is depicted by dashed outlines. A Winnipegosis reef at 8-13-1-20W2 indicates that a thinner Prairie Evaporite sequence than observed regionally is due to depositional rather than post-depositional processes; similarly, a small buildup at 10-28-1-10W2 resulted in a decrease in original depositional thickness. In the 15-5-1-8W2 well, 21 m of "residual material" are all that is preserved within the Prairie Evaporite; in the other three wells, the Prairie Evaporite is composed of salts.

Theme 1: Geological Characterization

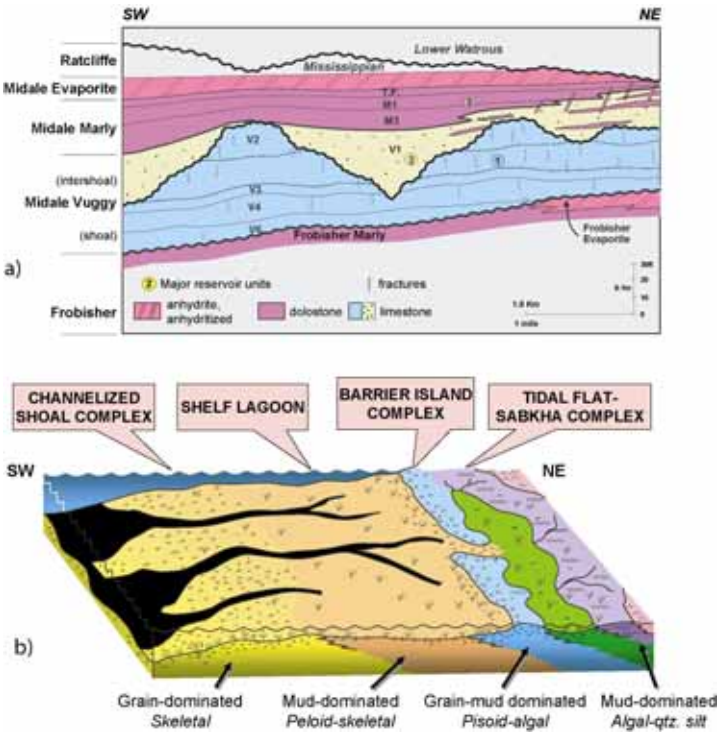

Figure 1.12: a) Generalized SW-NE cross-section through the Weyburn pool. The three major reservoir subdivisions are limestones of the Midale Vuggy shoal and intershoal and dolostones of the Midale Marly layer. More detailed subdivisions are indicated by V1, V2, etc., and these were used in developing the reservoir model for production and optimization of the CO_2 flood strategy. Note that fractures are most common in the shoal deposits of the Midale Vuggy. Anhydritization toward the up dip (NE) part of the reservoir is an important component of the sealing package that also includes the Midale Evaporite, Frobisher Evaporite, and Lower Watrous Member. b) Paleoenvironment of deposition of the Midale Beds of the Weyburn oil pool: grain-dominated rocks and shoal deposits form good-quality reservoir typical of the Vuggy, whereas Marly sediments were formed in quieter environments, such as lagoons; the Midale Evaporite, which forms the primary cap for the reservoir, formed within the tidal flat-sabkha complex. These diagrams are courtesy of EnCana Corporation and have been slightly modified.

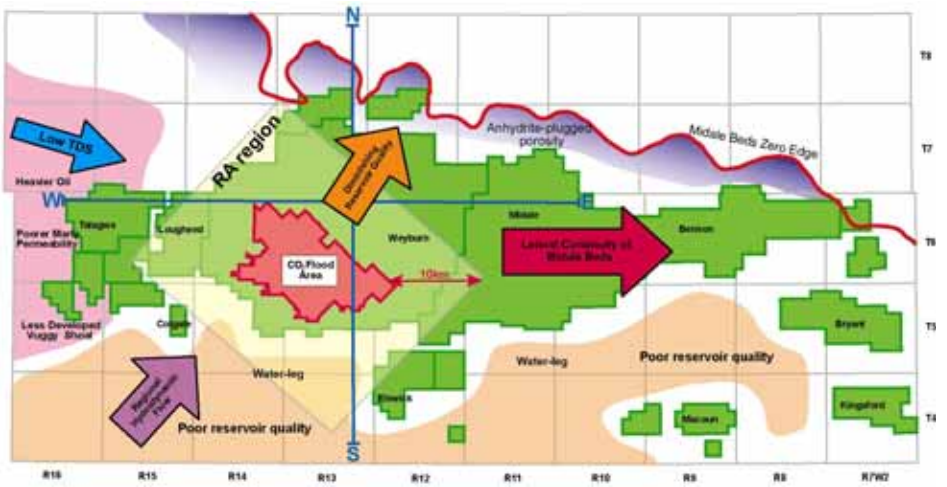

Figure 1.13: Bounding conditions of the Mississippian Midale Beds of the Weyburn field as shown in plan view. The Risk Assessment region is represented by the yellow rectangle and the projected area of CO_2 flooding is the red region in the western part of the Weyburn field. Various oil fields in Midale strata along the Mississippian subcrop trend are outlined in green. To the north of the Weyburn pool, the Midale Beds are truncated along the Sub-Mesozoic Unconformity (Midale Beds zero edge) where extensive porosity reduction has occurred through diagenetic processes. South (down dip) of the pool, reservoir quality is poorer and the rocks are generally water-charged (shaded light brown). West of the EOR region, the carbonate facies include more poor-quality intershoal areas and may have variably higher water saturations in the pink-shaded area. East of the EOR area, reservoir quality may slightly diminish, but overall facies are broadly similar to, and show considerable lateral continuity with, the Weyburn reservoir. Two cross-sections through this region, N-S and E-W, are shown in Figure 1.5.

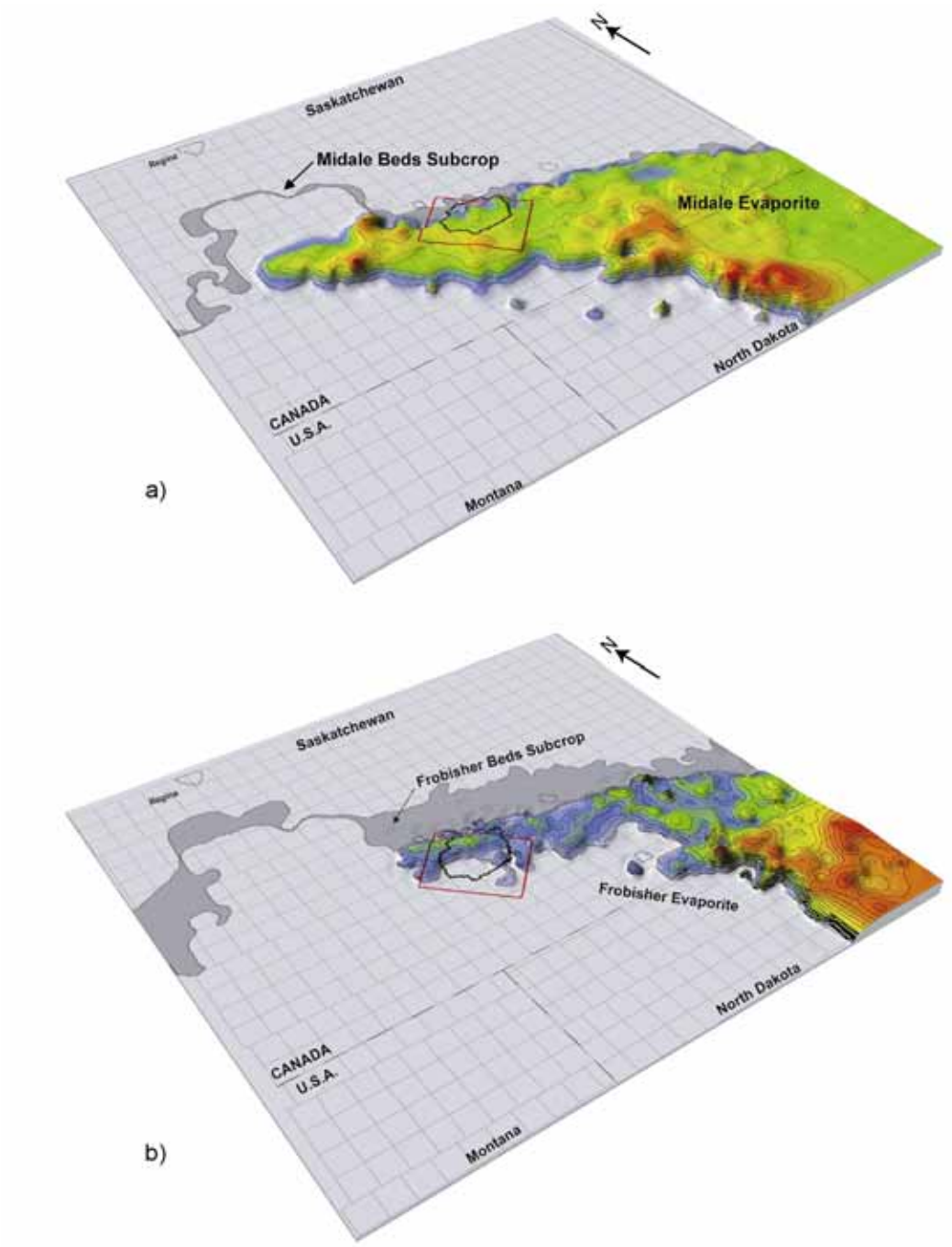

Figure 1.14: a) Map of the distribution and thickness variations of the Midale Evaporite that forms the important upper seal to the Weyburn reservoir. The subcrop region of the Midale Beds is also shown and is generally pervasively altered, resulting in porosity reduction. The subcrop of the Midale Beds is the region where the beds are truncated by the Sub-Mesozoic Unconformity (see Figure 1.5). In general, subcrop regions of Mississippian strata have markedly reduced porosity due to diagenetic alteration throughout much of southeastern Saskatchewan. b) Map showing the distribution and thickness variations of the Frobisher Evaporite that forms a bottom seal to the Weyburn reservoir in the northern portion of the pool. The subcrop region of the Frobisher Beds is shown. The Risk Assessment region is the red rectangle, and the Weyburn field is outlined in black.

Theme 1: Geological Characterization

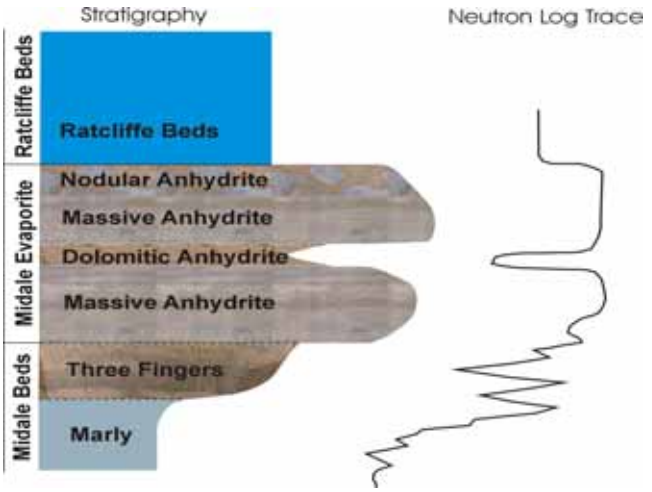

Figure 1.15: Generalized stratigraphic profile of lithotypes commonly observed in the Midale Evaporite, the upper seal to the Weyburn reservoir. The Three Fingers zone is a transitional unit between the upper part of the Midale reservoir and the anhydrite cap (see Figure 1.12b). The Three Fingers zone is considered part of the upper reservoir and is a low-permeability, patterned carbonate that only rarely exhibits oil staining. Massive and nodular anhydrite units comprise most of the Midale Evaporite. The thickness of the Midale Evaporite varies from approximately two to 11 m in the Weyburn pool. Dolomitic interbeds occur throughout and may form a distinct layer, as shown above. The trace of the neutron log on the right may be used to infer density, or porosity, variations within the cap. Deflections of the trace to the right indicate reduction in porosity. The pattern of fill used in the stratigraphic column is taken from photographs of the respective lithotype.

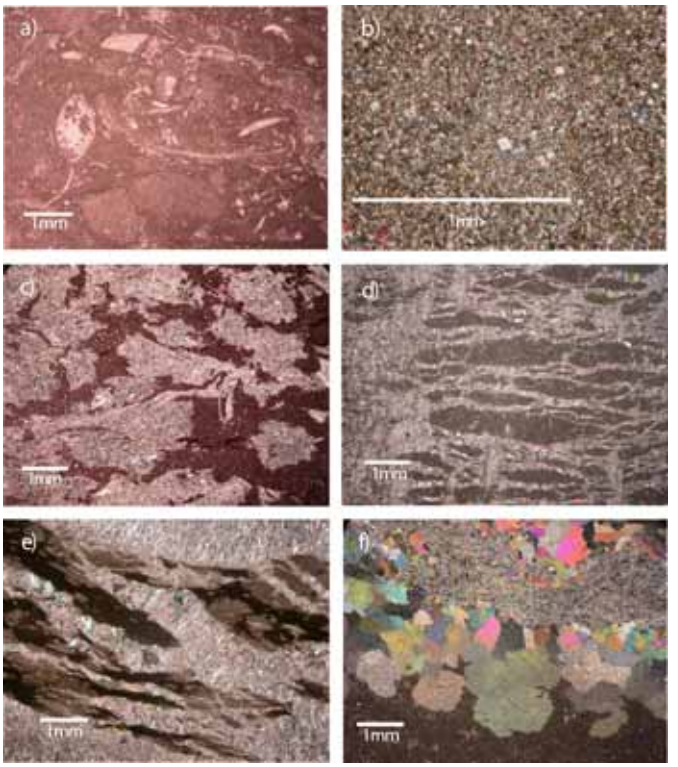

Figure 1.16: Photomicrographs of diagenetic facies within the altered zone taken from the Midale Beds at or near the Mississippian subcrop: a) biomicrite; skeletal and bivalve allochems are partially destroyed by the micritizing process; b) granular non-porous anhydritic dolomite; former skeletal grains may be apparent as 'ghosts', but are, for the most part, destroyed; c) nodular anhydrite in a micrite matrix; d) satin-spar anhydrite veins coalescing into an anhydrite nodule; e) typical horizontal satin-spar vein displaying vertically elongate fibrous anhydrite crystals; f) large crystals of metasomatic anhydrite surrounding a core of contemporaneous fibrous anhydrite.

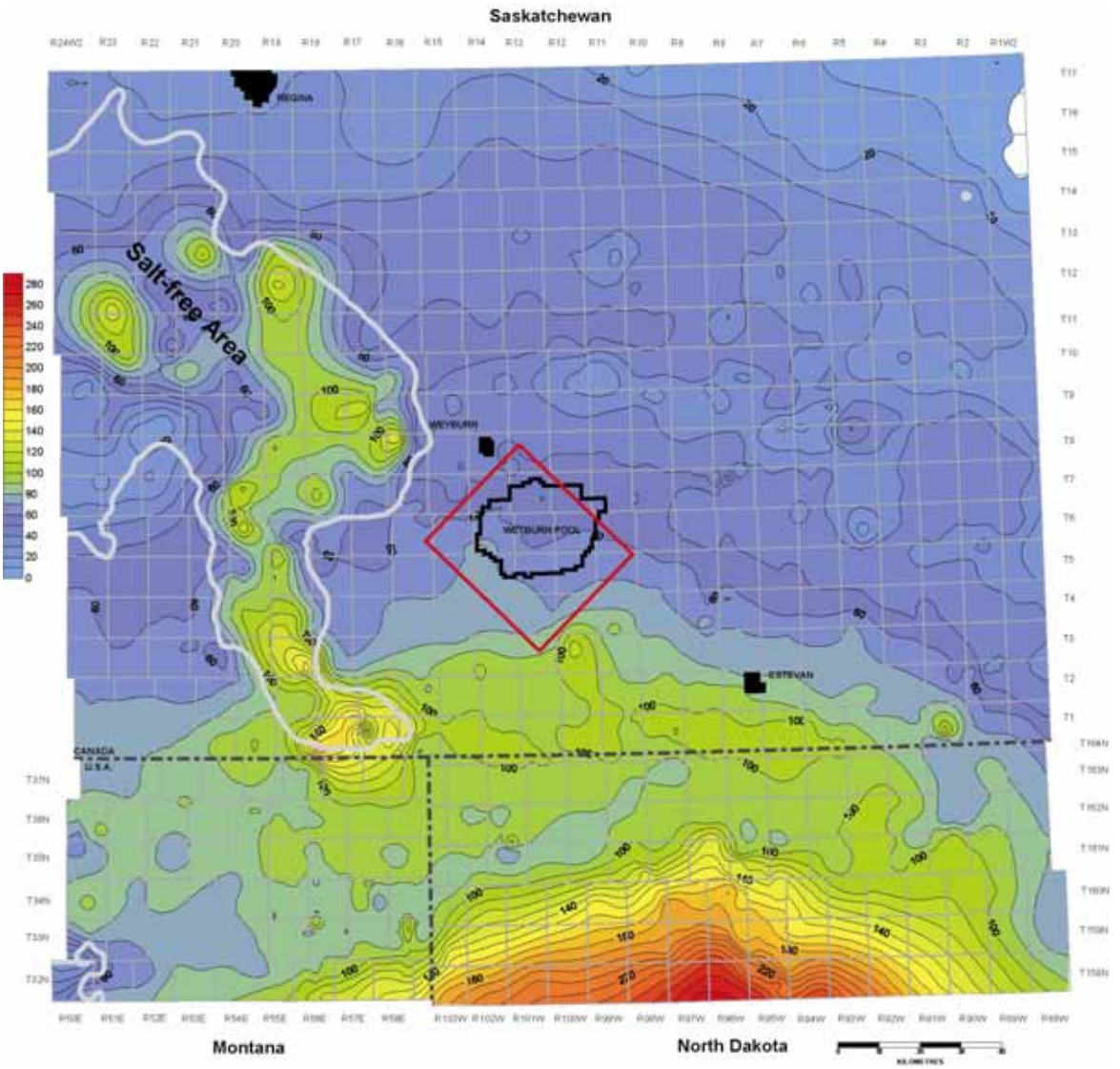

Figure 1.17: Isopach map of the Triassic Lower Watrous Member in the regional study area demonstrating the occurrence of thickened strata above an extensive area of Devonian salt dissolution (salt-free area) in the western part of the regional study area (see Figure 1.10). The Lower Watrous Member occurs immediately above the Sub-Mesozoic Unconformity and is an effective regional aquitard throughout the mapped area and one of the primary seals to the Weyburn pool. The thickness increase indicates that salt dissolution influenced deposition of strata during the Mesozoic and must be considered in assessing the integrity of geological storage systems in the Williston Basin.

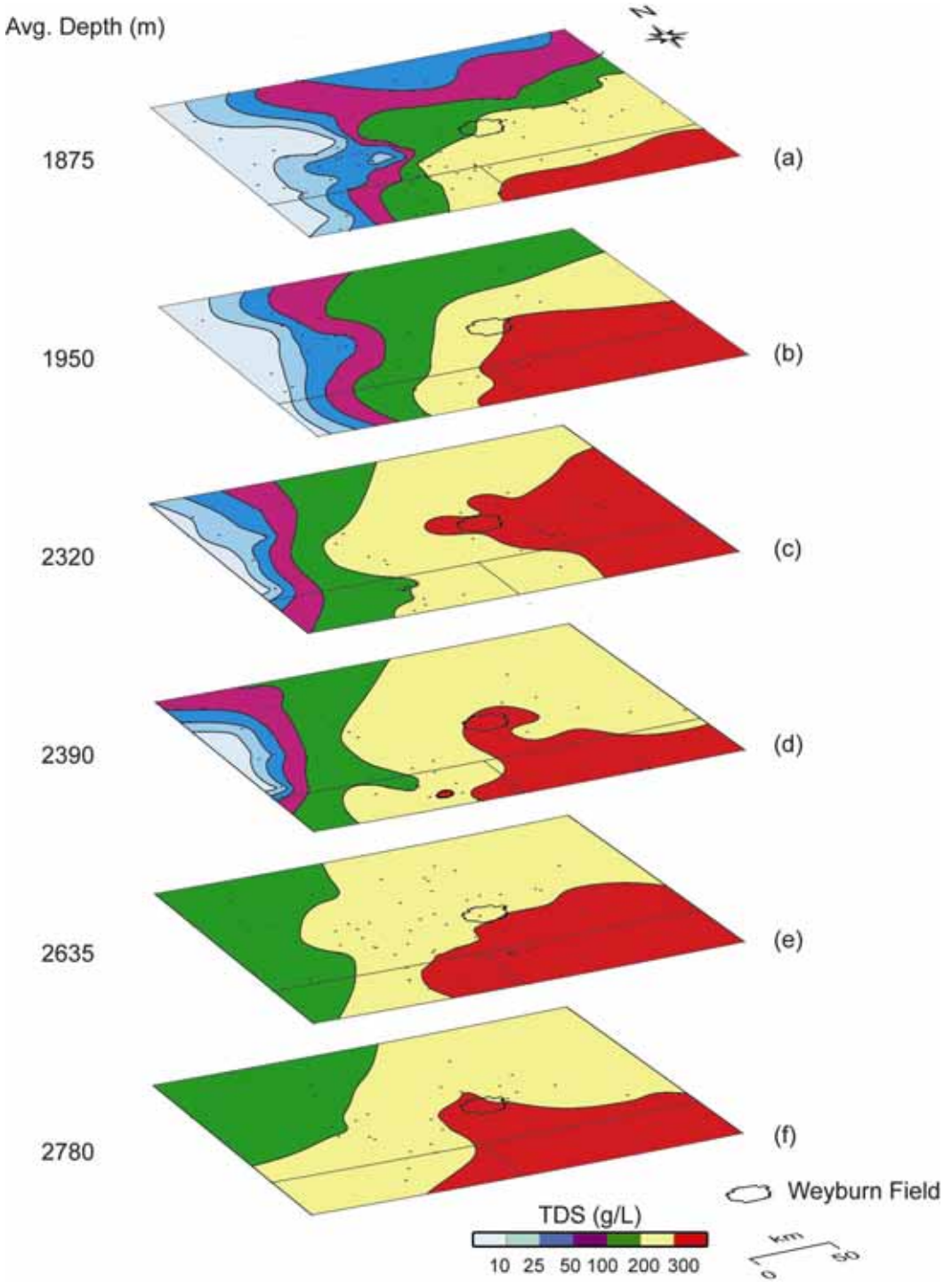

Figure 1.18: Vertical stack of Total Dissolved Solids maps for selected pre-Mississippian aquifers: a) Birdbear, b) Duperow, c) Winnipegosis, d) Ordo-Silurian, e) Yeoman, and f) Cambro-Ordovician. Note that different contour intervals are used in these maps. Average depth refers to the approximate vertical depth at the location of the Weyburn field. Colour scale also applies to Figures 1.19 and 1.20.

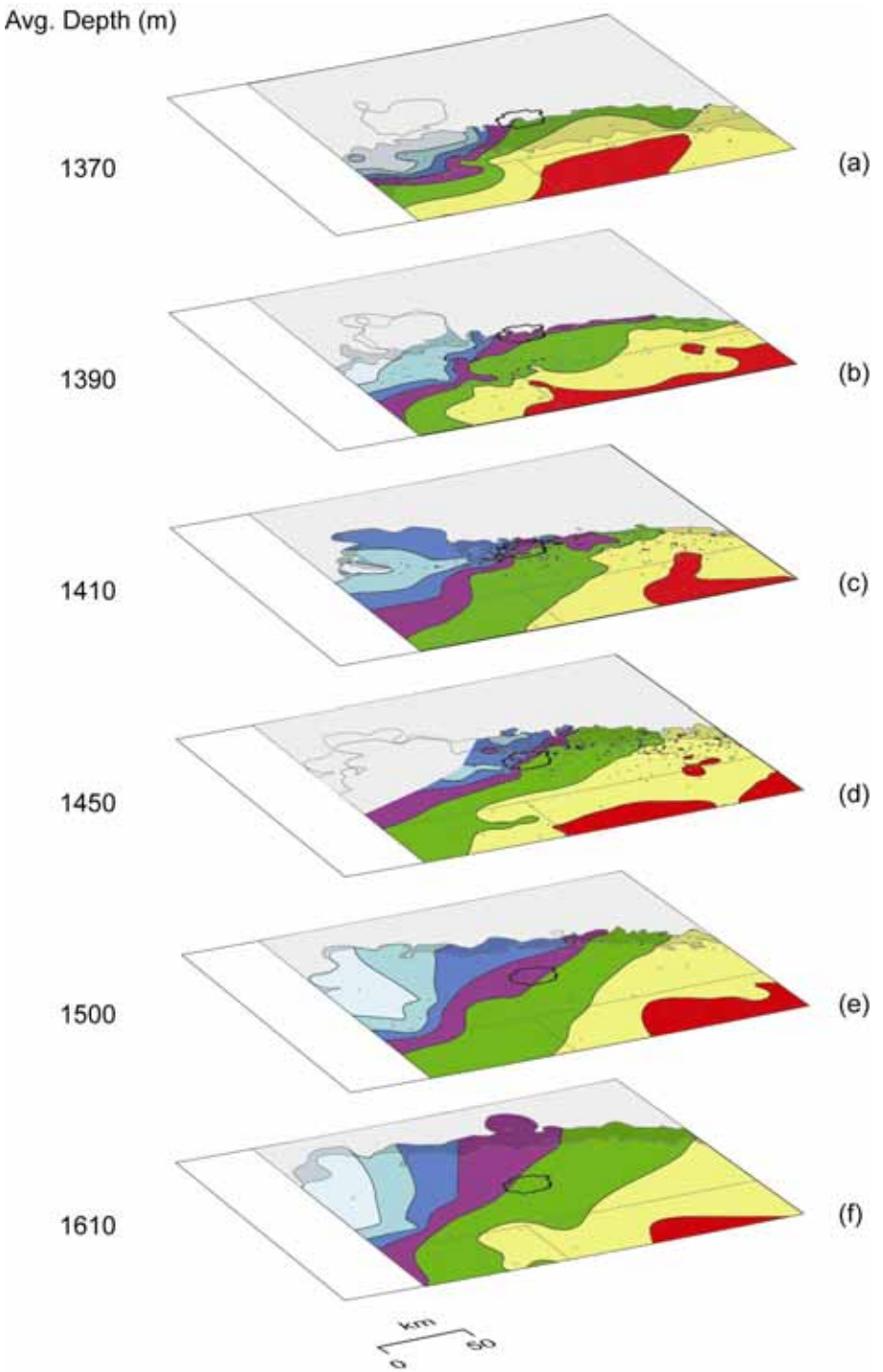

Figure 1.19: Vertical stack of Total Dissolved Solids maps for selected Mississippian aquifers: a) Poplar, b) Ratcliffe, c) Midale, d) Frobisher, e) Alida, and f) Tilston. See Figure 1.18 for colour scale.

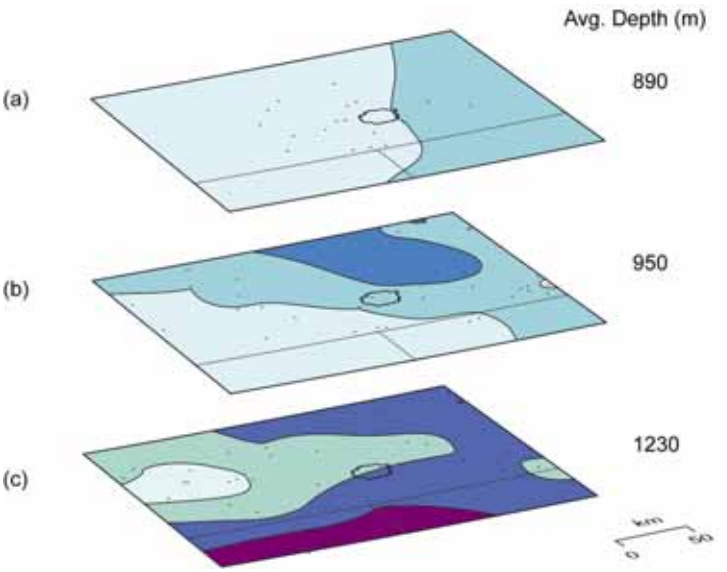

Figure 1.20: Vertical stack of Total Dissolved Solids maps for selected Mesozoic aquifers: a) Newcastle, b) Mannville, and c) Jurassic. See Figure 1.18 for colour scale.

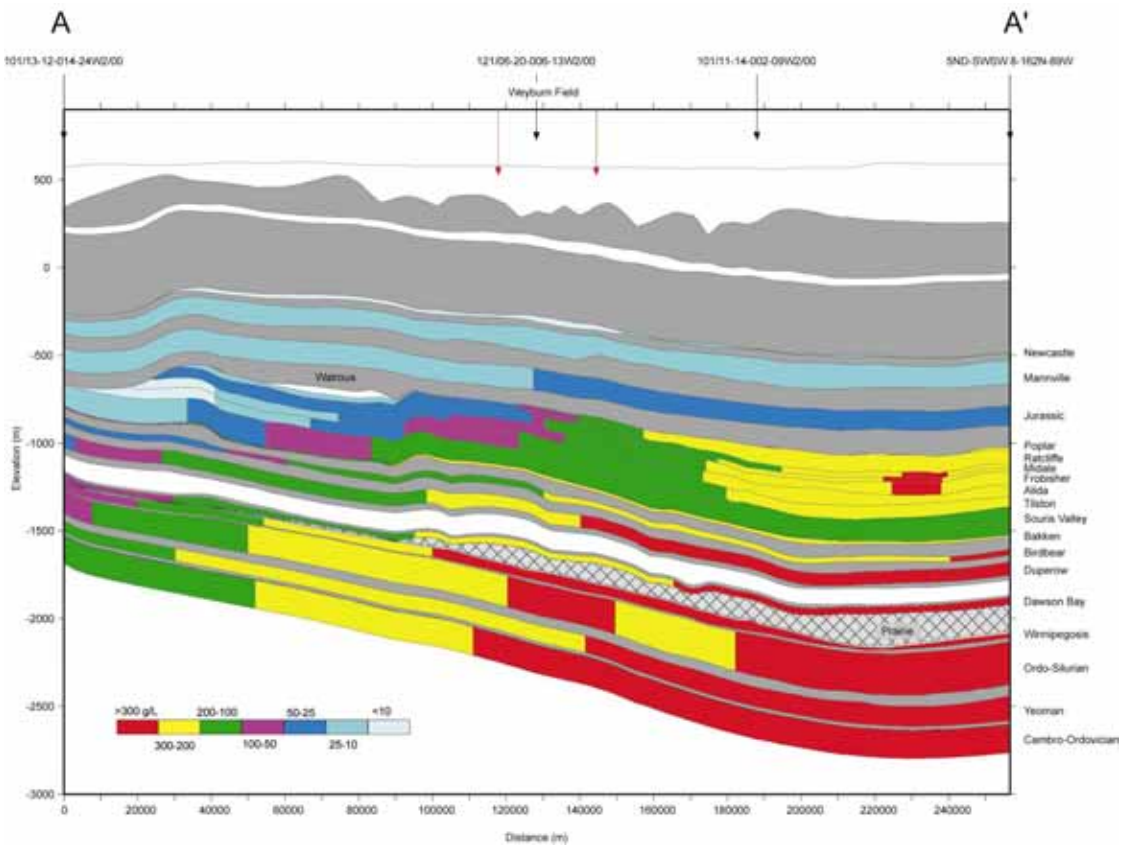

Figure 1.21: Cross-section A-A' with TDS distribution, hydrostratigraphy, and basin structure. Total dissolved solids are indicated by colour scale at bottom left. Individual aquifer units are labeled on right vertical axis. Aquitards are shaded grey. The extents of the Weyburn field are shown at top of the diagram. Note the fresh waters invading Mississippian and pre-Mississippian aquifers from the west (left) below the Watrous aquitard. The location of this cross-section is shown in Figure 1.2.

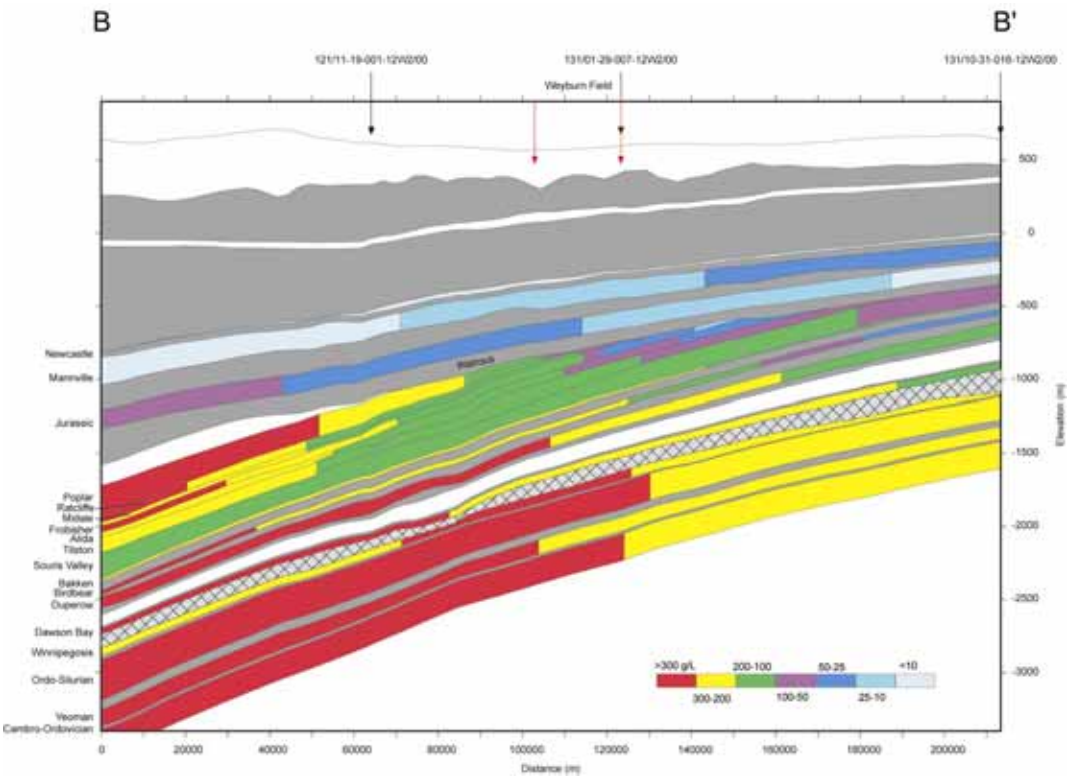

Figure 1.22: Cross-section B-B' with TDS distribution, hydrostratigraphy, and basin structure. Total dissolved solids are indicated by colour scale at bottom left. Individual aquifer units are labeled on left vertical axis. Aquitards are shaded grey. The extents of the Weyburn field are shown at top of diagram. The location of this cross-section is shown in Figure 1.2.

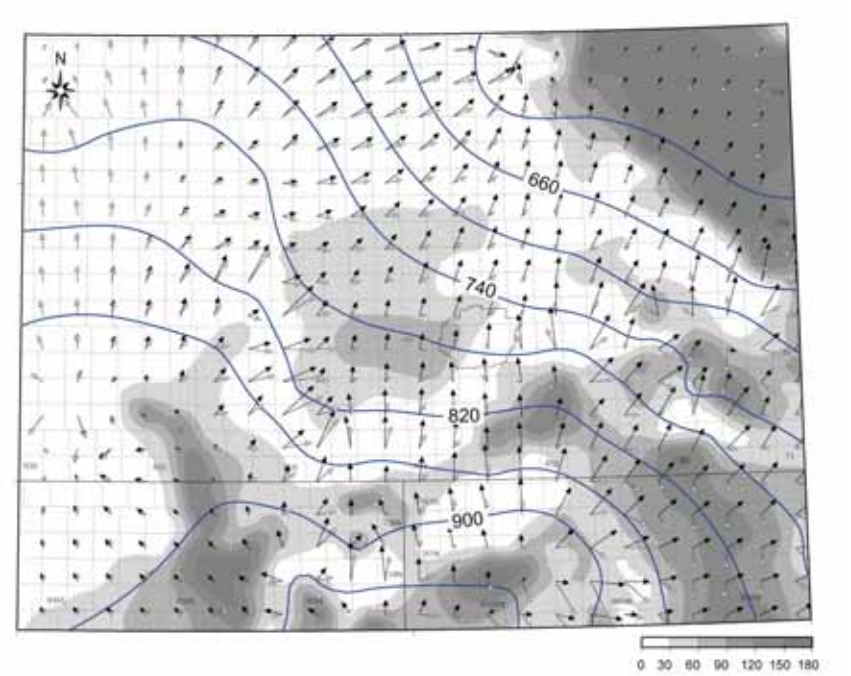

Figure 1.23: Water Driving Force (WDF) map for the Winnipegosis aquifer. Contours are equipotentials, or lines of constant EFWH, spaced at 40 m. Solid black vectors indicate hydraulic gradient driving force and grey arrows indicate total driving force (WDF) corrected for buoyancy effects. Darkness of shading indicates the degree of azimuthal error between these two driving forces resulting from increasing density-related flow effects.

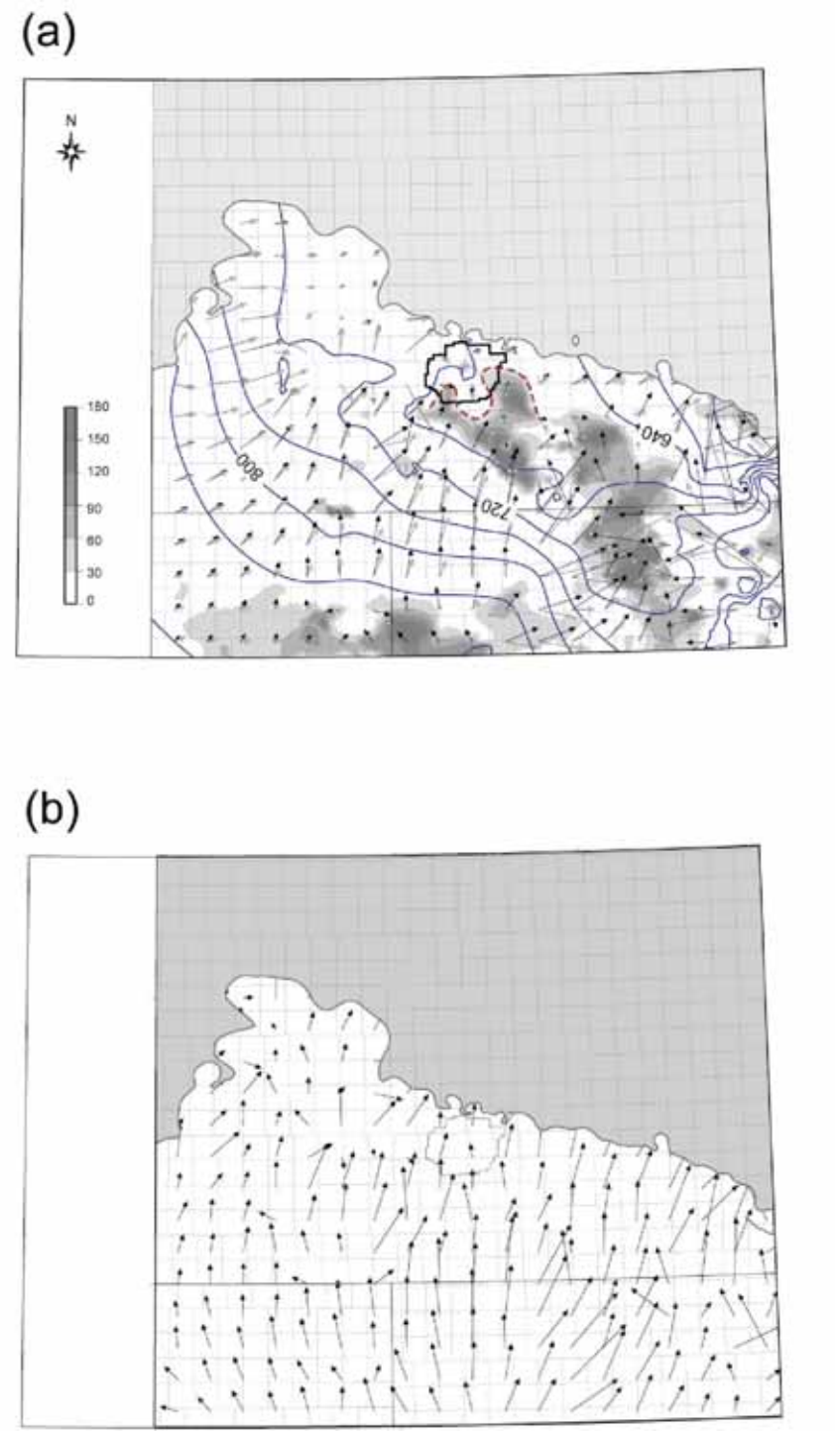

Figure 1.24: a) Water Driving Force (WDF) map for the Midale aquifer. Contours are equipotentials, or lines of constant EFWH, spaced at 40 m. Solid black vectors indicate hydraulic gradient driving force and grey arrows indicate total driving force (WDF) corrected for buoyancy effects. Red dashed line approximates the position where flow becomes dominated by density-related effects in the area southeast of the Weyburn field. CO_2 injection is planned for the western portion of the Weyburn pool. b) Predicted hypothetical trajectories of separate-phase CO_2 in the Midale aquifer. Separate phase CO_2 migration is primarily due to buoyancy drive.

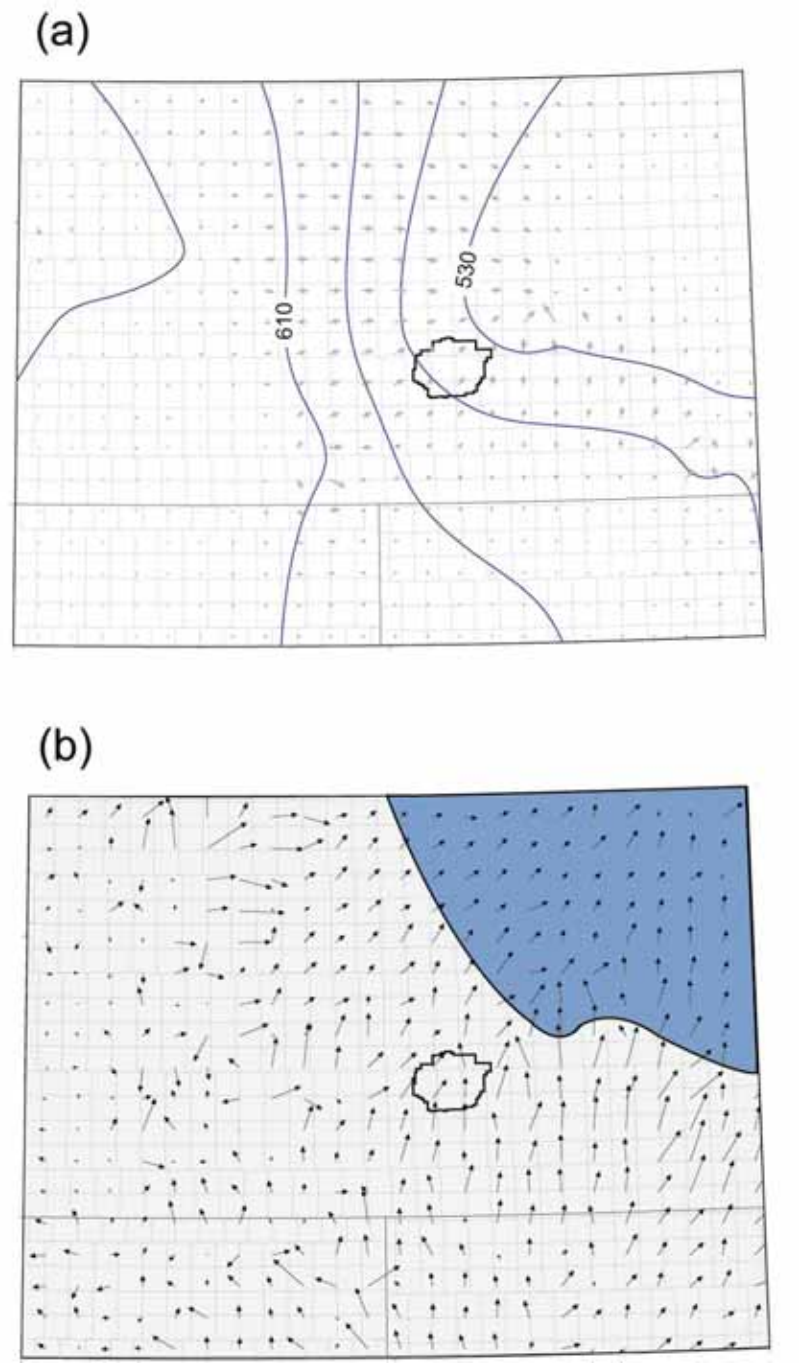

Figure 1.25: Mannville aquifer potentiometric surface with flow directions inferred from the gradient of EFWH alone; b) Predicted hypothetical trajectories of supercritical and gaseous (blue shaded area) CO_2 in the Mannville aquifer. Minor structural anomalies influence these trajectories.

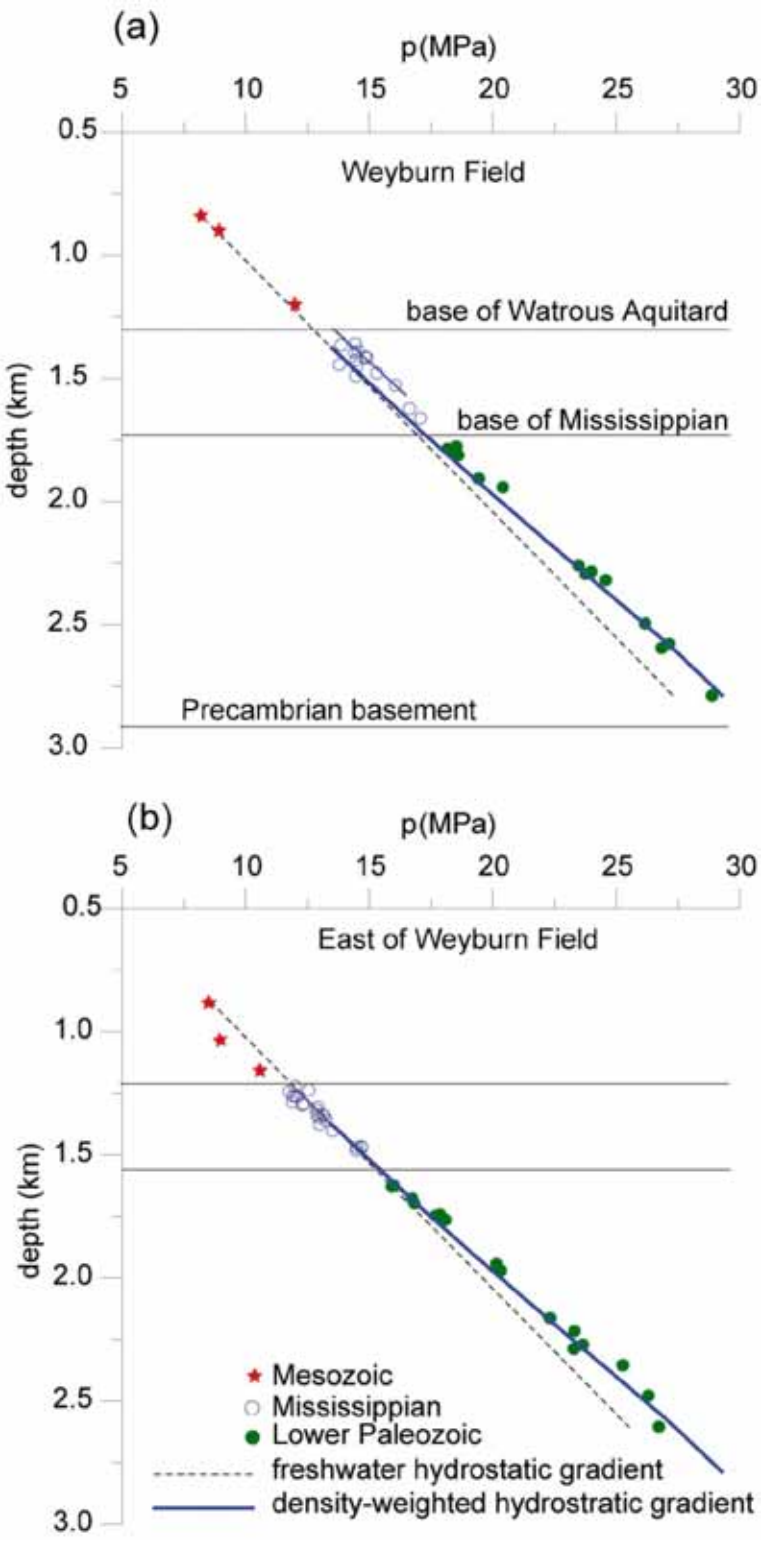

Figure 1.26: a) p[d] profile in the Weyburn field; b) east of the Weyburn field area. Areas represented by these profiles are shown in Figure 1.2. See discussion in text.

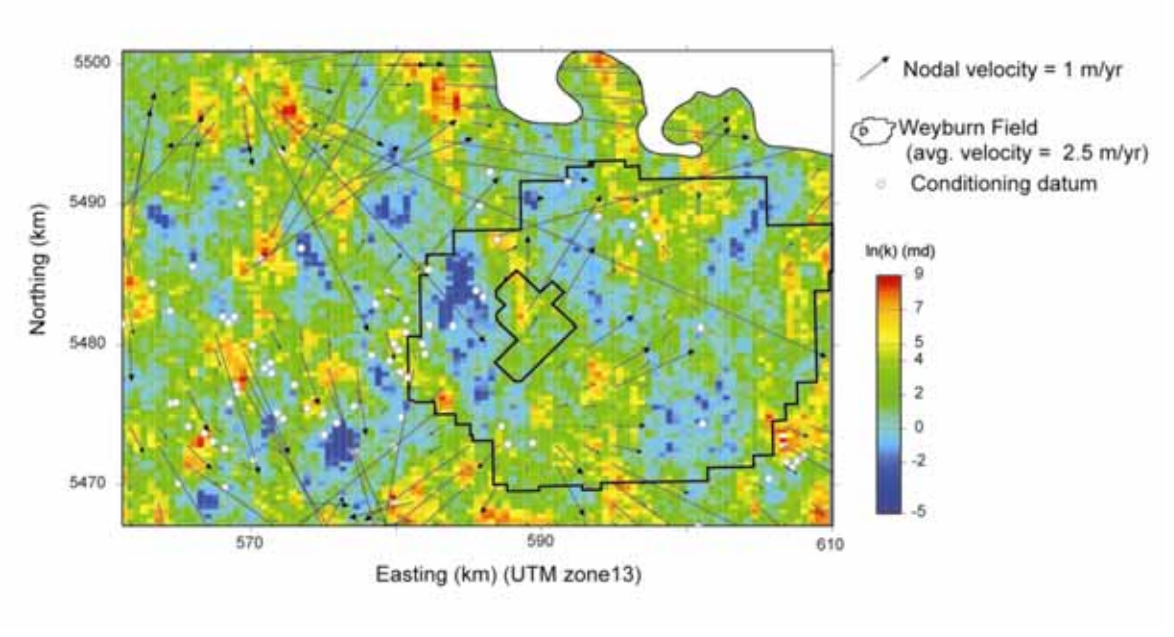

Figure 1.27: A single realization of the Midale aquifer permeability field over the Weyburn near-field area with calculated formation water flow velocities. Vectors represent calculated point water flow-velocities at grid nodes, assuming spatially constant porosity. Vector scaling is linear and a reference vector is shown. Note natural logarithmic transform of permeability magnitudes.

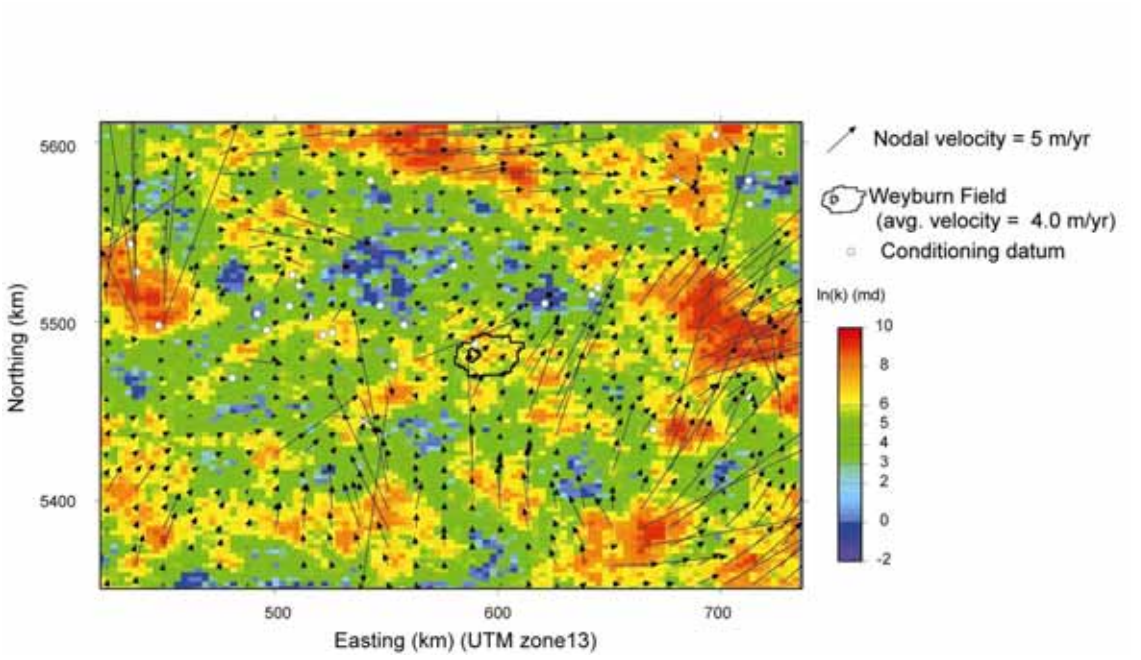

Figure 1.28: A single realization of the Jurassic aquifer permeability field over the entire map area and calculated formation water flow velocities. Vector scaling is linear, and a reference vector is shown.

Theme 1: Geological Characterization

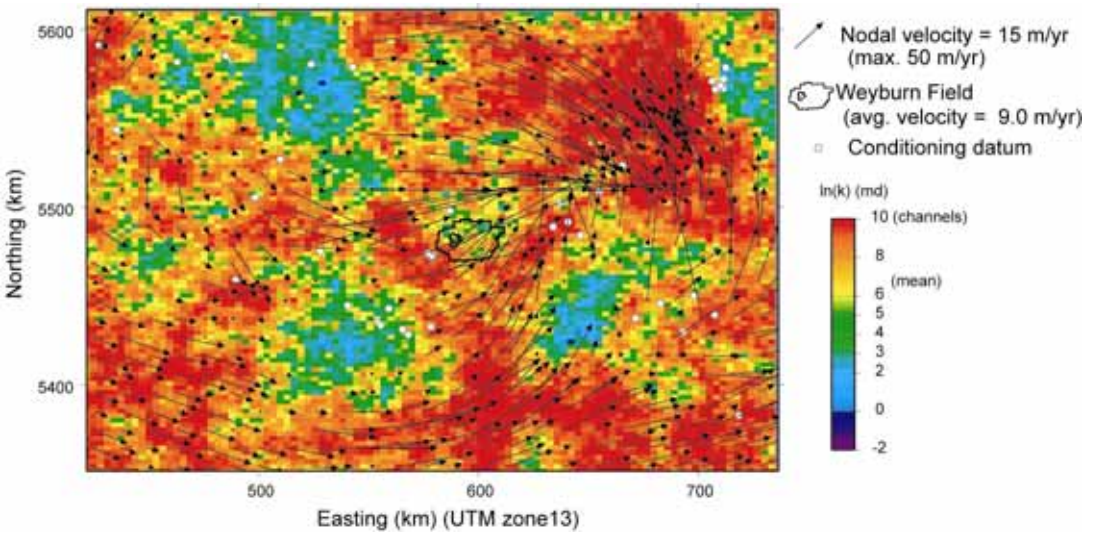

Figure 1.29: A single realization of the Mannville aquifer permeability field over the entire map area and calculated formation water flow velocities. Vector scaling is linear, and a reference vector is shown.

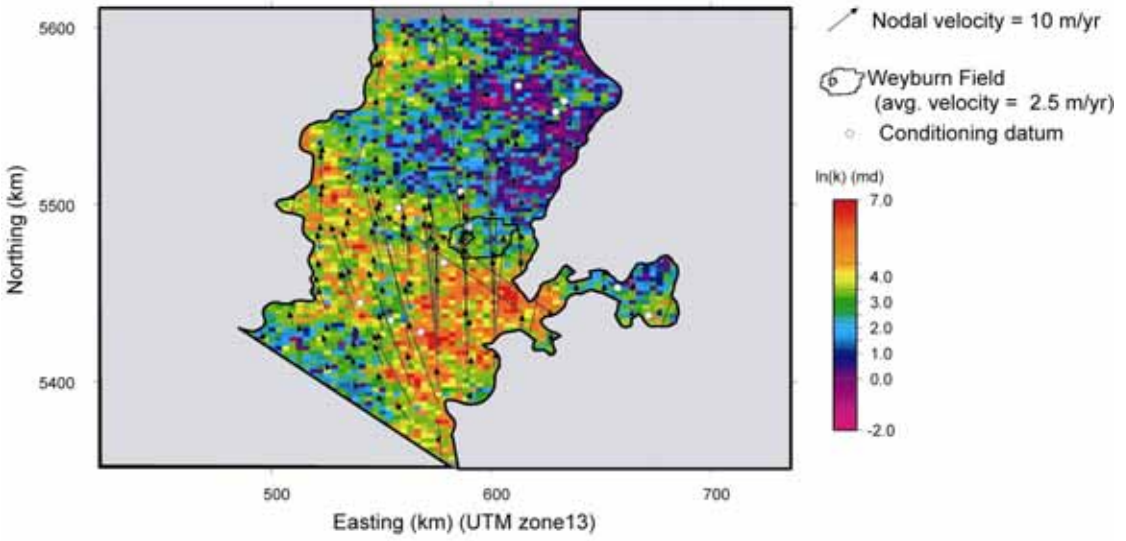

Figure 1.30: A single realization of the Newcastle aquifer permeability field over the entire map area and calculated formation water flow velocities. Vector scaling is linear, and a reference vector is shown. Grey shading indicates predominantly shale facies.

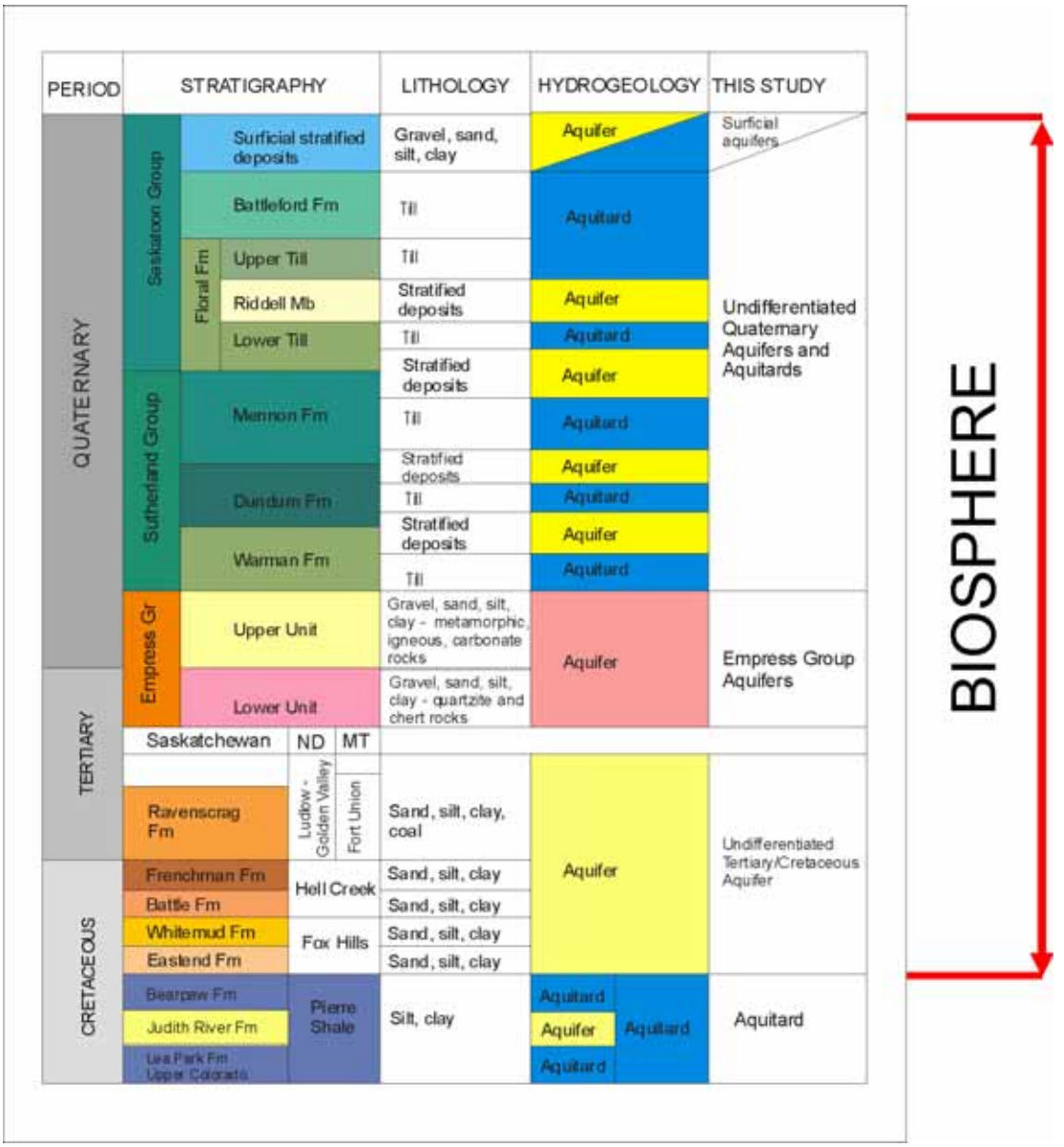

Figure 1.31: Stratigraphic framework of the shallow hydrogeological investigations. The general lithology of the various units is listed. The range of the biosphere as defined in this project is shown.

Theme 1: Geological Characterization

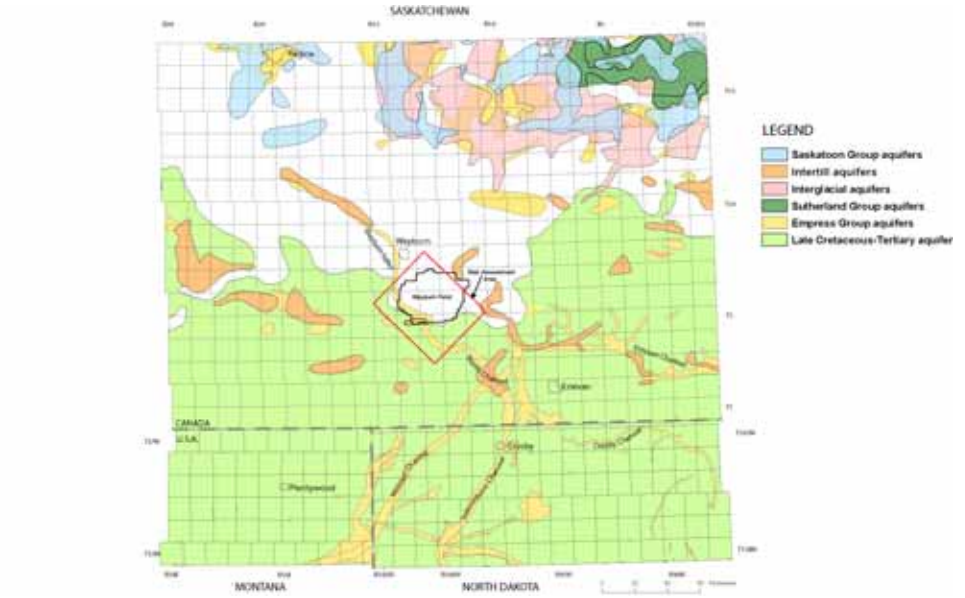

Figure 1.32: Distribution of shallow aquifers in the regional study area. See Figure 1.31 for the stratigraphic relationships among these aquifer groups. The Estevan buried valley system is one of the more extensive aquifer systems in the area and consists of the Estevan, North, Missouri, and Yellowstone Channels. The relation between the North and Weyburn Channels in the vicinity of the Weyburn field was the focus of a detailed study in this project. Figure 1.33 shows the revised pathway of the Weyburn Valley aquifer.

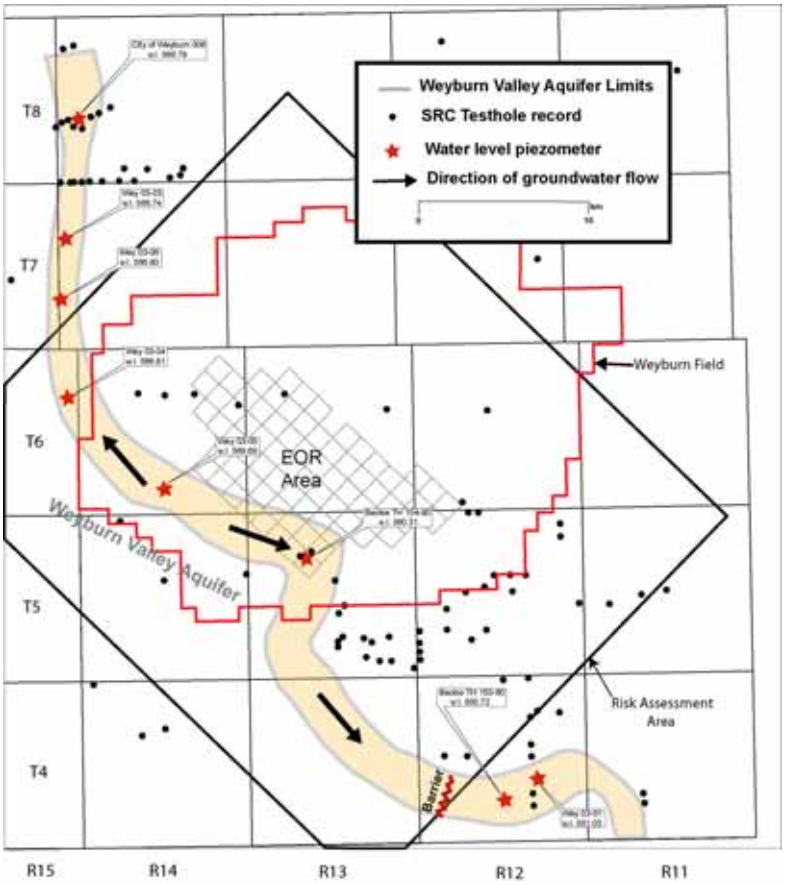

Figure 1.33: Extent of Weyburn Valley aquifer, selected testhole water elevations, and inferred flow directions (for August 8-2003). The Risk Assessment area is outlined in black. EOR Area represents the region that will ultimately be subjected to CO_2 injection.

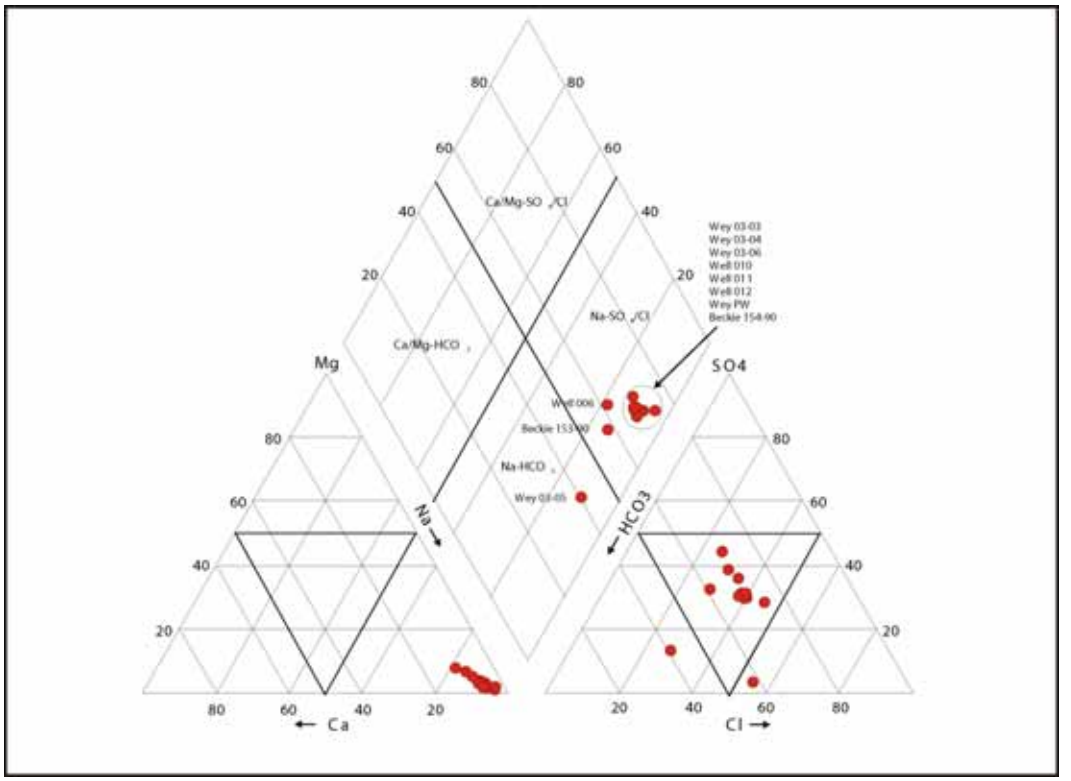

Figure 1.34: Hydrochemical facies of groundwaters collected from the Weyburn Valley aquifer.

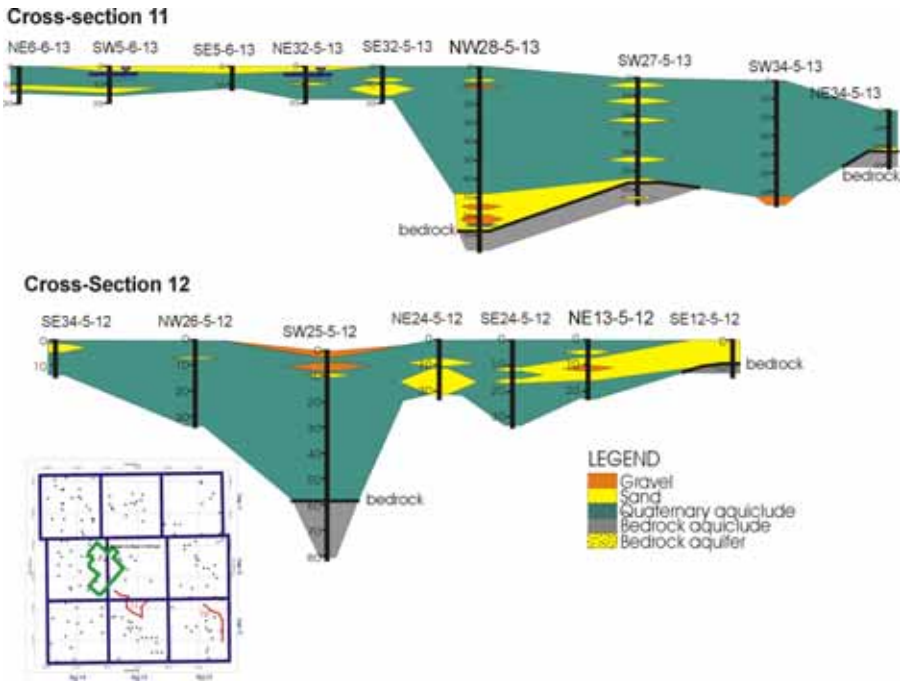

Figure 35: Typical near-surface lithological cross-sections from the Weyburn area showing the distribution of shallow Quaternary aquifers in the vicinity of the Weyburn field (see inset map). The shallow aquifers are generally isolated and of limited extent, but may be important sources of water for residential and agricultural use. The distribution of rock types shown is determined from well logs and drillers' reports.

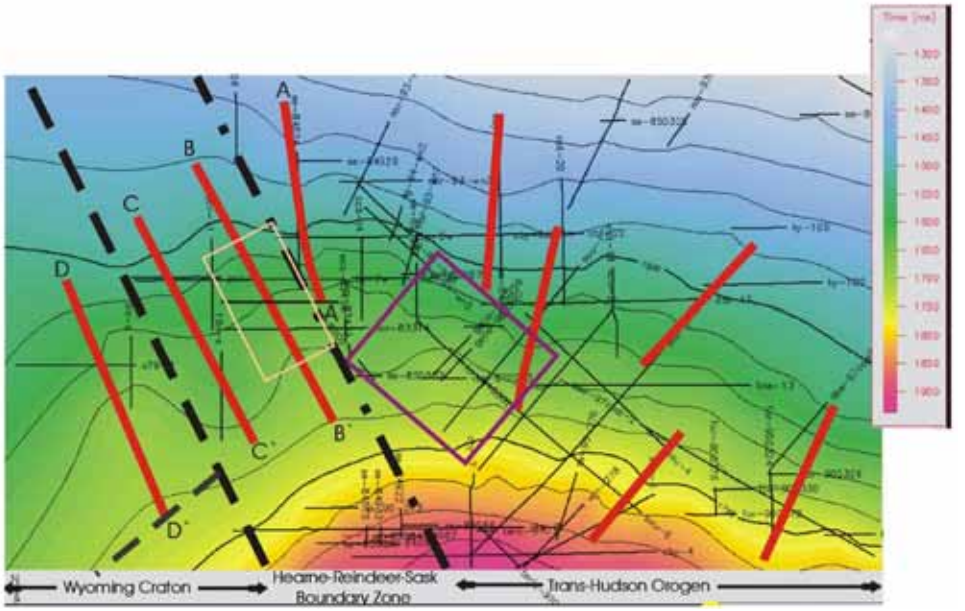

Figure 1.36: Structure of Precambrian surface in regional study area. The contours indicate a more irregular surface in the western portion of the map in the Hearne-Reindeer Zone and Wyoming Craton than within the Trans-Hudson Orogen. A radiating pattern of plunging anticlines and synclines, shown by thick red lines, is found on the surface of the Precambrian basement. The pink box outlines the location of seismic sections depicted in Figure 1.38.

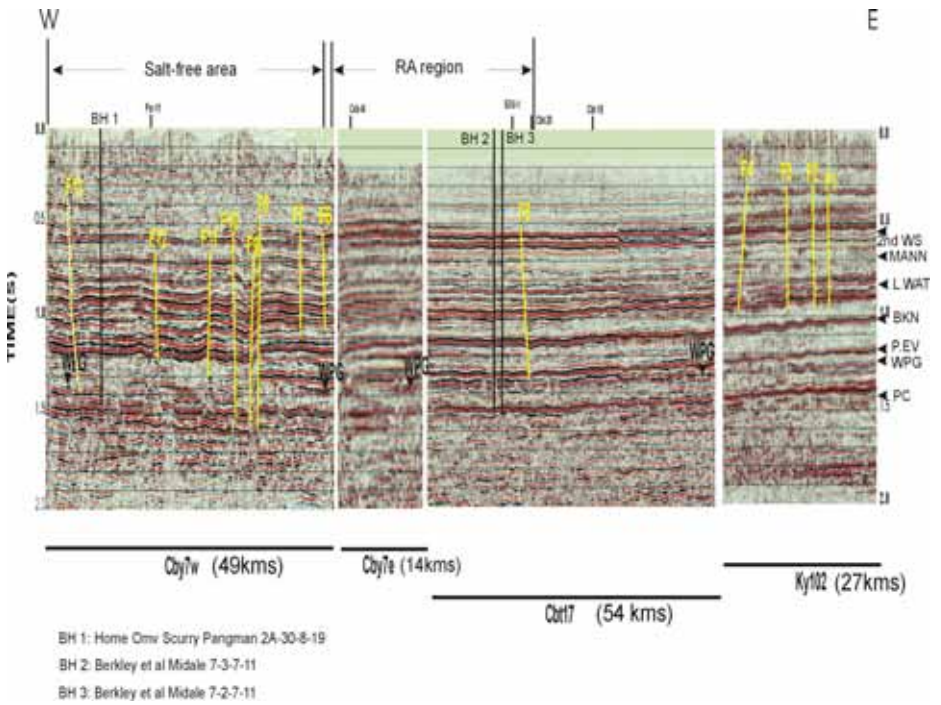

Figure 1.37: A regional east-west composite seismic section constructed from four individual 2D seismic lines (time-migrated). The line name and length is shown at the bottom of the section and the location of the lines is shown in Figure 2. Faults and fractures are identified in yellow and numbered from east to west. Most structures are observed near the east and west margins of the profile, including features associated with the Missouri Coteau (see Figure 1.43) and western margin of the Hummingbird Trough (F13), and in the area of extensive salt dissolution (F6-F12). In the central part of the profile near the Risk Assessment region, tectonic disturbances are more subdued. Specific reflectors are identified along the right vertical axis: 2nd WS: Cretaceous Second White Specks; Mann: Cretaceous Mannville Group: L. Wat, Triassic Lower Watrous Member; BKN: Devonian Bakken Formation; P.EV.: Devonian Prairie Evaporite; WPG: Devonian Winnipegosis Formation; PC: Precambrian. Calibration boreholes are identified as BH 1, BH 2, and BH 3 and identified on the diagram. The intersection of other seismic lines is shown along the top of the section by small vertical lines.

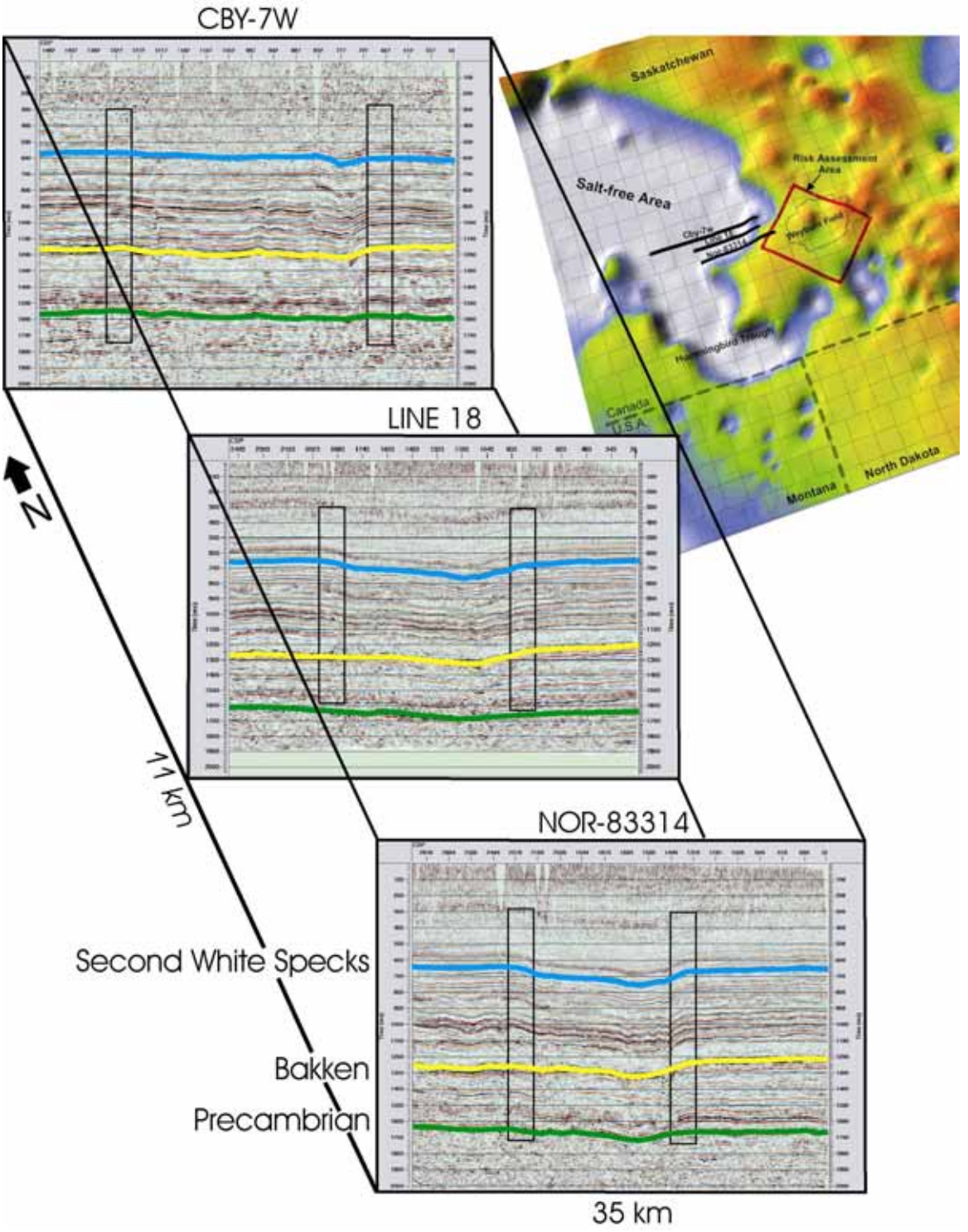

Figure 1.38: A series of three seismic profiles along the basement structure B-B' shown in Figure 1.36. The Precambrian basement is generally lower than regional values along this structure. Collapse of Phanerozoic strata through removal of Devonian salt is also suggested by these profiles. The locations of the seismic lines are superimposed on the inset map showing thickness variations in the Devonian Prairie Evaporite (as determined from well data only). The seismic data suggest that collapse was multistage and largely proceeded from north to south, where strata up to Late Cretaceous in age were affected.

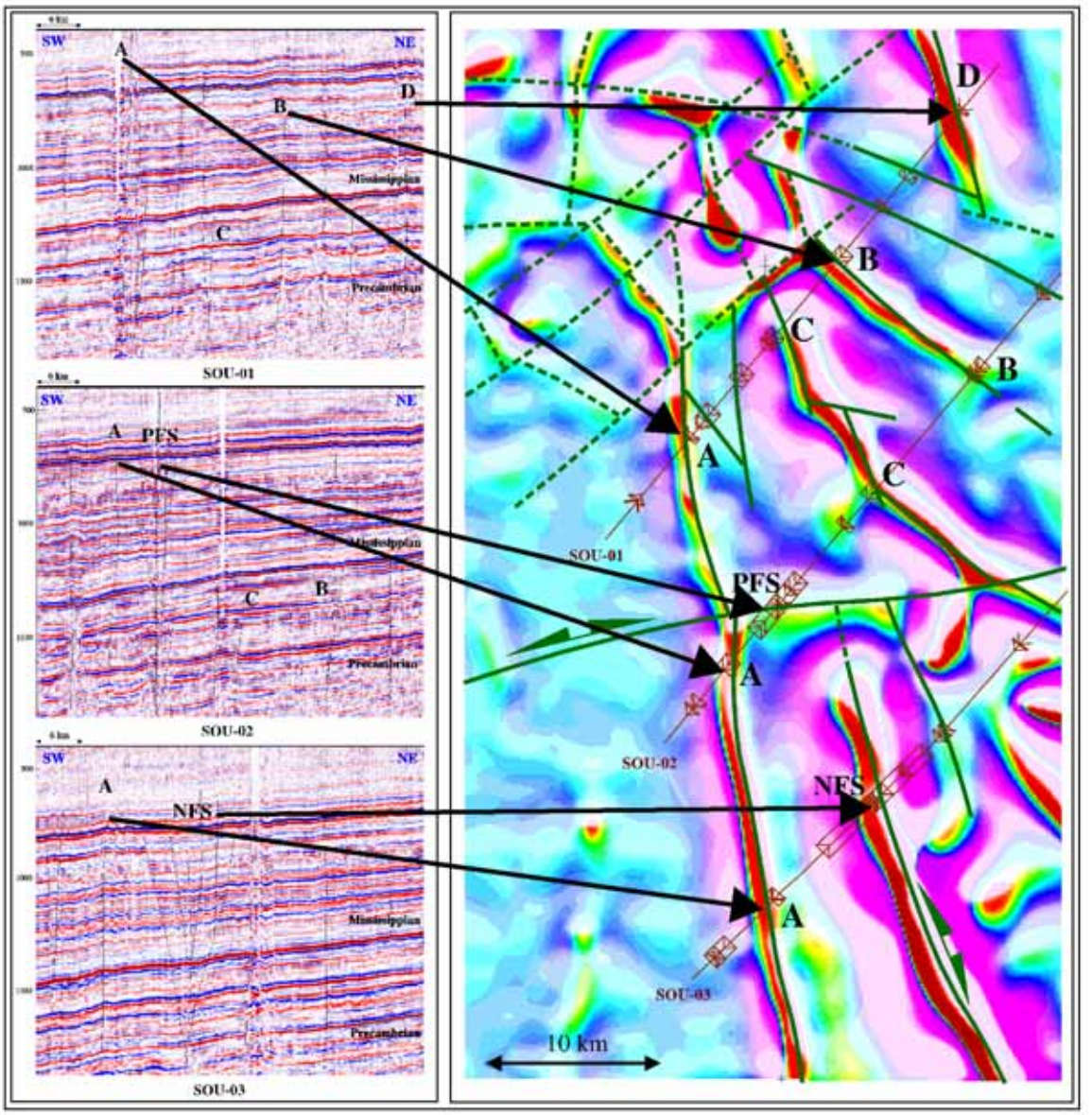

Figure 1.39: The relation of three 2D seismic profiles (time-migrated) on the left to a filtered magnetic anomaly map using HRAM data on the right. The magnetic characteristics revealed by the HRAM data help to correlate seismically identified subsurface faults and fracture zones. The locations of the three seismic sections are drawn on the HRAM map, and the positions of seismically identified faults are noted (as indicated by arrows). The relation among the faults (identified as A, B, C, D, PFS, and NFS) based on seismic data alone is uncertain. Using the basement trends and tectonic fabric revealed through HRAM analysis permits greater confidence in fault correlations. The solid green lines on the HRAM map represent fault or fracture trends based on seismic and HRAM data, whereas the dashed green lines represent fault or fracture trends based mainly on HRAM data only.

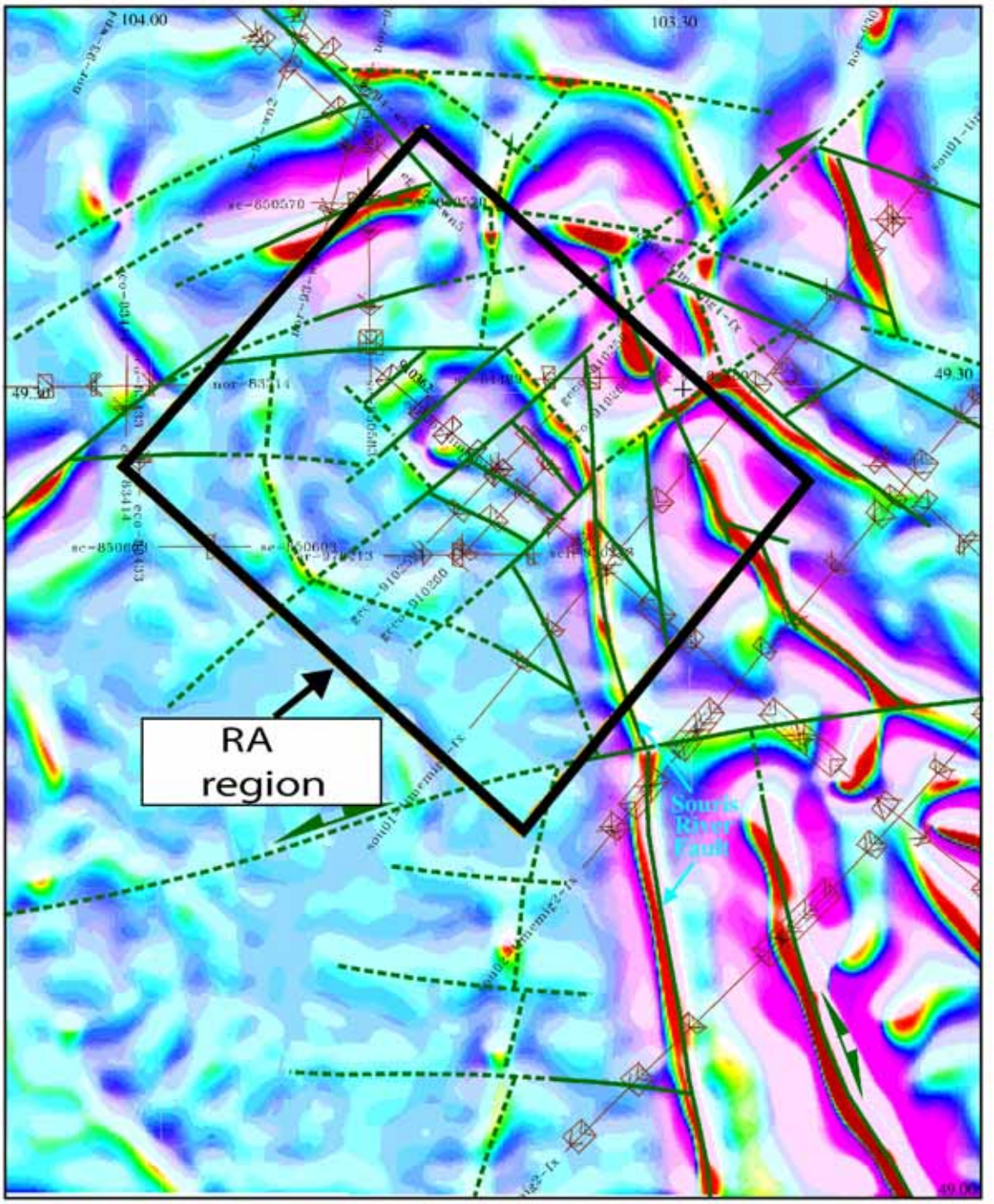

Figure 1.40: Map showing interpreted fault and fracture network in the vicinity of the Risk Assessment region. This interpreted network of faults and fracture zones was constructed by integrating seismic and HRAM data. Solid lines are faults identified through seismic and HRAM integration and dashed lines are features identified solely through HRAM interpretation.

Theme 1: Geological Characterization

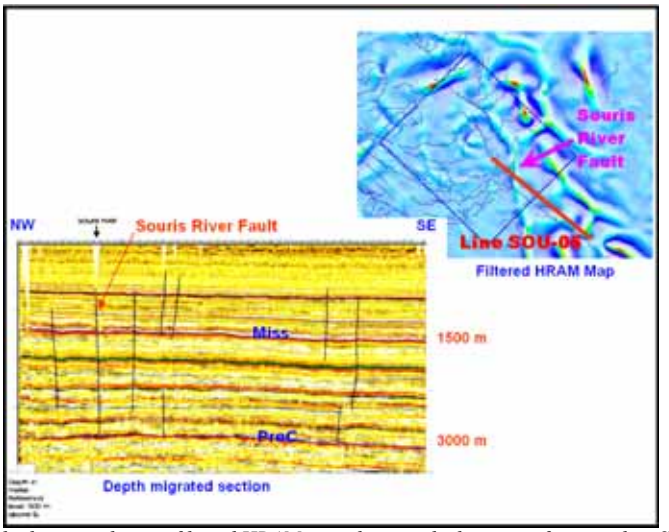

Figure 1.41: The upper right diagram shows a filtered HRAM map showing the location of seismic line SOU-6 (location also shown in Figure 1.2) and the Risk Assessment region as the blue rectangle. A seismically identified fault, as shown in the depth-migrated seismic profile on the lower left, corresponds to a magnetic anomaly trend on the HRAM map. This fault was labeled the Souris River fault in this project, and, while it demonstrates limited vertical offset, it was included in the geological model for risk assessment.

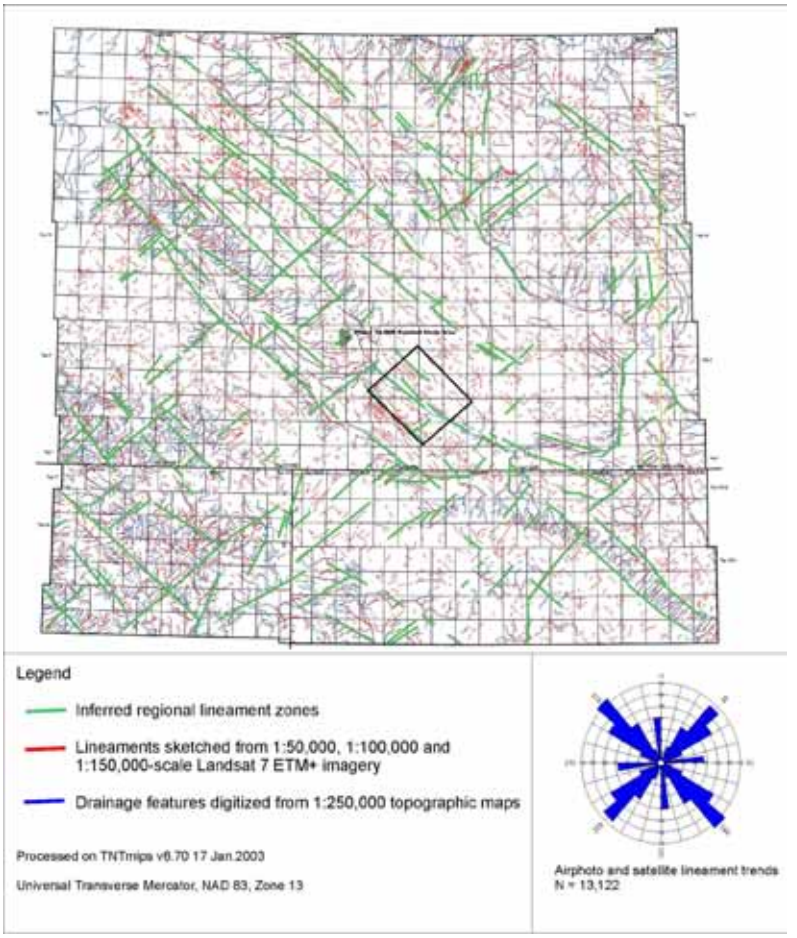

Figure 1.42: A map of the regional study area showing the location of surficial lineaments and lineament zones identified through Landsat 7 imagery analysis. The smaller red lines are individual surface lineaments that represent escarpments, valleys, and smaller drainage depressions. Clusters of individual lineaments are used to define the longer lineament zones, shown in green. The inset diagram depicts the preferred orientation demonstrated by the lineament trends in the study area using both Landsat and airphoto interpretation.

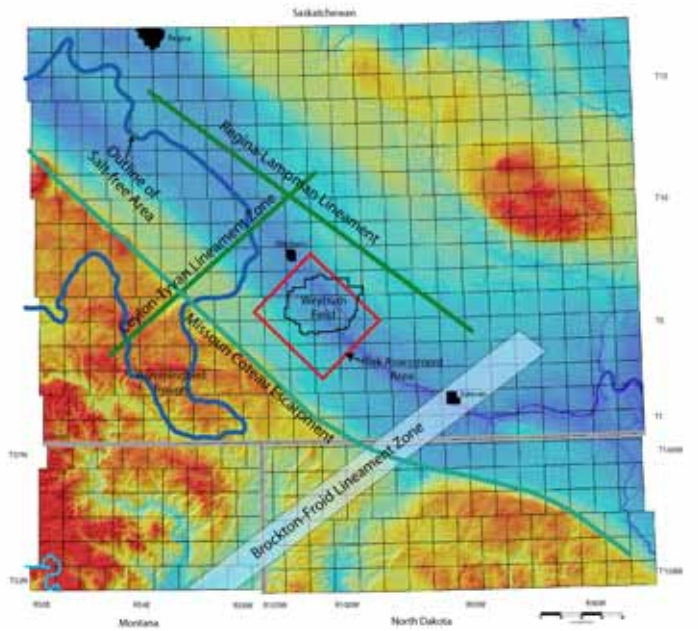

Figure 1.43: Map of the regional study area showing the topography using digital elevation data. Superimposed on this map are several major lineament trends, including the Missouri Coteau Escarpment, a prominent topographic feature in the area. Also shown are the surficial Regina-Lampman and Ceylon-Tyvan lineament zones. These lineament zones show a close correspondence to the edges of the salt-free area found in Devonian strata. The Brockton-Froid lineament zone refers to an interpreted region of linear trending fractures or faults in the basement. Surface lineaments identified exhibit a coincident orientation with this trend.

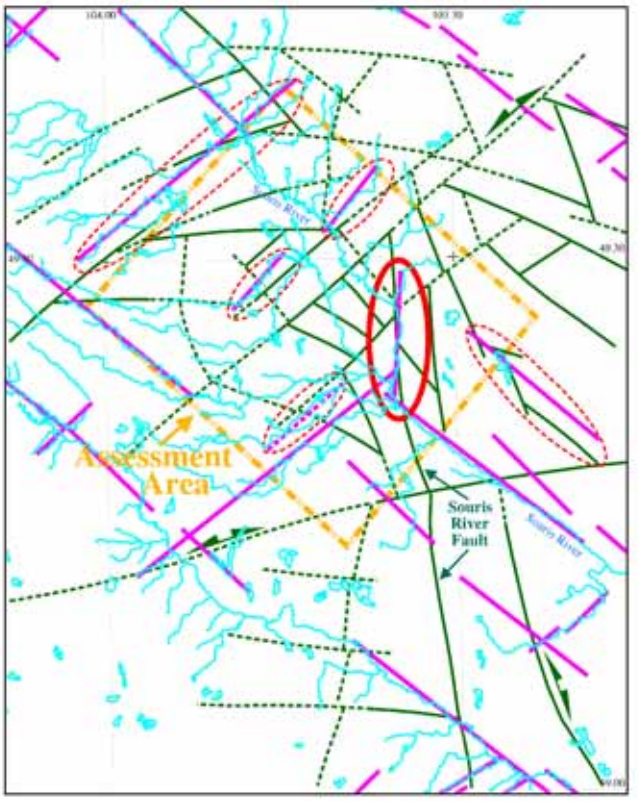

Figure 1.44: Map showing relation between seismically and magnetically identified faults and fracture zones and surface lineament zones around the Risk Assessment region. The solid green lines indicate fault trends interpreted using seismic and HRAM data, and the dashed lines are trends interpreted from HRAM data only. The purple lines are surface lineament zones. The solid red oval indicates a location where a fault identified using seismic and HRAM coincide with a surface lineament zone. This is the Souris Valley fault. The dashed red outlines are regions where slightly weaker correlations are found among the three data sets.

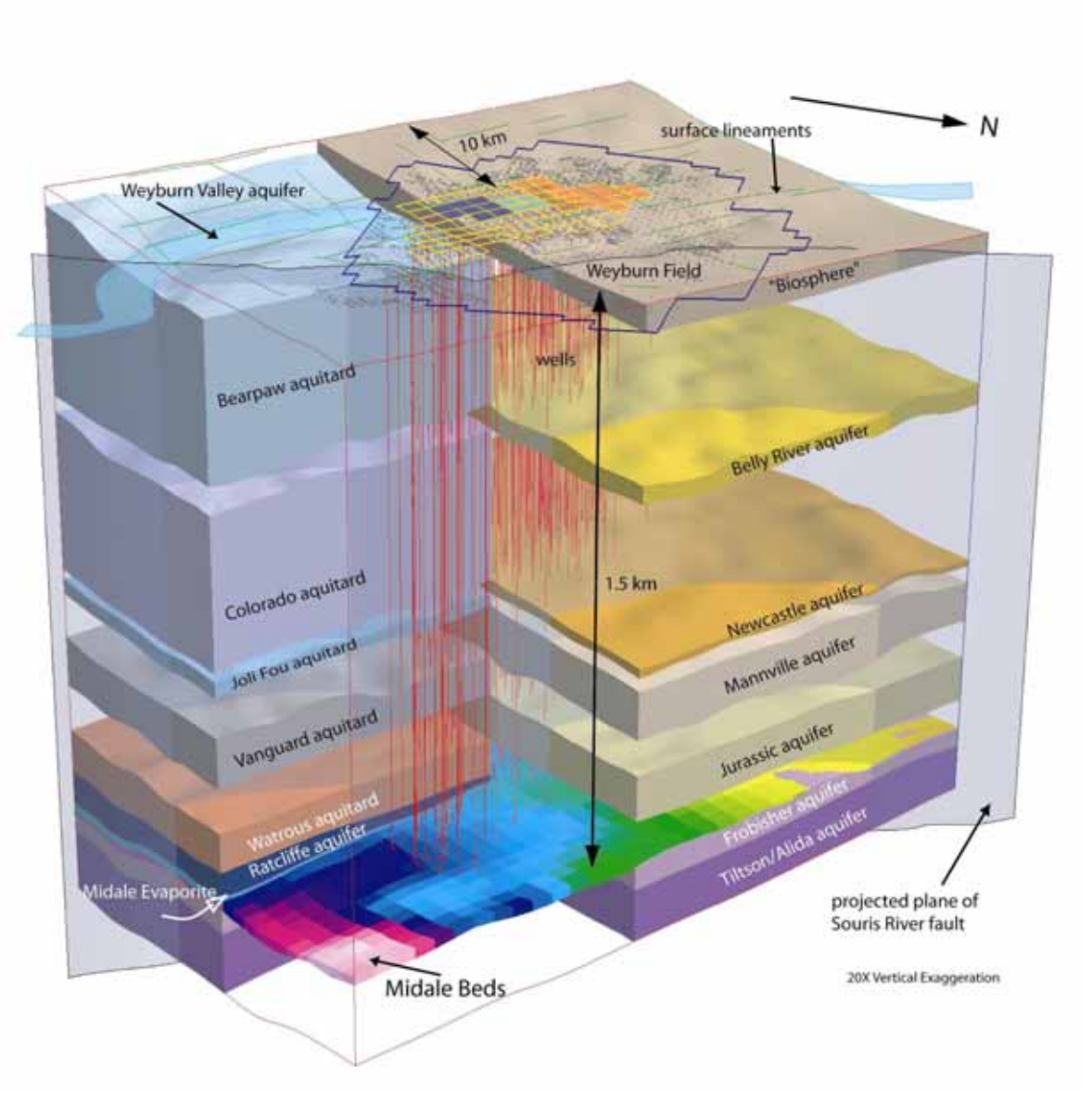

Figure 1.45: A cutaway block diagram depicting components of the System Model developed for the Weyburn Project. The expected area of CO_2 injection is shown by the yellow grid on the surface, and the areas already subjected to flooding are shown as filled colors within the grid. Surface lineaments identified through air photo analysis are shown as green lines. The revised distribution of the pre-glacial Weyburn Valley aquifer is depicted within the "biosphere." The layers on the left, above the Mississippian beds, are aquitards; the layers on the right are aquifers. The color variations of the Midale Beds, which are shown extending to the actual limits of the geological model, reflect differences of property values, in this instance, TDS content. All the layers in this model are similarly populated, with various properties where available. The plane of the Souris River fault is shown for reference. The System Model also contains information regarding anthropogenic features, such as wells, and pressure and fluid distributions related to oil-production methods. The extent of this model is approximately 10 km beyond the limits of the planned CO_2 injection area in the Weyburn field.

THEME 2: PREDICTION, MONITORING AND VERIFICATION OF CO_2 MOVEMENTS

THEME LEADER: D. J. WHITE
THEME AUTHORS: K. HIRSCHE, T. DAVIS, I. HUTCHEON, R. ADAIR, G. BURROWES, S. GRAHAM, R. BENCINI, E. MAJER, AND S.C. MAXWELL

1 SUMMARY

Seismic imaging and geochemical sampling methods have been applied to monitor the Weyburn CO_2 EOR flood within 19-patterns of the Phase 1A area. In each case, baseline surveys were acquired prior to the start of injection in order to establish a reference against which subsequent monitor surveys were applied. P-wave time-lapse travel time delay and amplitude difference maps clearly show the distribution of CO_2 within the reservoir at different times. The time-lapse seismic response proves highly sensitive to the presence of low levels (5-10 molar %) of a CO_2-rich component and less sensitive to increases at higher saturations. This allows confident identification of the CO_2-front, but makes accurate seismic-based volume estimation difficult. Improved history matching is demonstrated where discrepancies between seismic and reservoir simulation results are used to improve the simulation model. Time-lapse shear wave splitting maps and horizontal crosswell tomography identify prominent fracture networks in the reservoir that influence the spread of CO_2. Geochemical sampling of production fluids has identified short-term chemical processes in the evolution of the reservoir fluid geochemistry: 1) injected CO_2 dissolution into reservoir brine; 2) reservoir carbonate mineral dissolution; 3) increase in total dissolved solids in reservoir brine. These processes show good spatial correlation with the highest CO_2 injection volumes of the Phase 1A area and with the seismic anomaly maps. Passive seismic monitoring at the reservoir level shows a low level of microseismicity associated with the flood process. Magnitude –4 to –1 events are located at the reservoir level that are predominantly associated with production operations rather than CO_2-induced stress changes. Soil gas sampling and analysis above the injection site found gas fluxes (for CO_2, O_2, and CO_2) in the range of natural soils and comparable to an off-set reference location, indicating that there is no evidence so far for escape of injected CO_2 from depth.

2 OBJECTIVES AND ROLE IN CO_2 STORAGE ASSESSMENT

An underlying goal of the IEA GHG Weyburn CO_2 Monitoring and Storage Project is to optimize management of the reservoir for enhanced oil recovery and safe, efficient storage of CO_2. To accomplish this, an improved understanding is required of the reservoir properties and the nature of how the injected CO_2 spreads and interacts with the rock matrix and reservoir fluids. The specific objectives of this work are to 1) test and improve conventional geological-based simulator predictions of how the CO_2 flood will progress, 2) assess the chemical reactions that form the predicted mechanisms for long-term storage of CO_2 within the reservoir, 3) observe the dynamic response of the reservoir to CO_2 flooding, 4) develop and demonstrate robust methodologies for monitoring the CO_2 flood, and 5) determine the distribution and security of the CO_2 within the reservoir. Monitoring entails observing the physical and chemical effects of the CO_2 injection on the state of the reservoir system with a focus on tracking the spread of CO_2 within and potentially outside of the reservoir. Verification is the substantiation of the interpreted monitoring results to allow reliable estimation of the volume and distribution of CO_2 in the subsurface.

3 SCOPE OF INVESTIGATION

A broad spectrum of field observational methods over a wide-range of scales has been applied toward monitoring subsurface CO_2 movement and associated *in situ* stress variations during the injection process. For each of the field methods utilized, an attempt has been made 1) to establish the underlying basis for the sensitivity of the method to CO_2-induced changes within the subsurface, 2) to ascertain that the observed changes in the measured parametres are significant relative to the data uncertainties, and 3) to test the interpreted results using field production data and reservoir flow simulations. Ultimately, iterative comparison of the monitoring results and reservoir simulations are made to improve the accuracy of reservoir simulations and verify the monitoring results.

Initial predictions of how the CO_2 flood would progress were based on flow simulations using an existing reservoir model based on the well-bore geology from the dense network of wells in the Weyburn field. A variety of seismic and geochemical sampling methods have been subsequently used to monitor the CO_2 injection process and characterize the reservoir between boreholes. Seismic imaging of the CO_2 in the subsurface has been accomplished primarily through time-lapse 3D multi-component surface seismic reflection imaging complemented by time-lapse and static borehole seismic surveys. *In situ* stress variations are assessed by time-lapse shear-wave splitting analysis, passive seismic monitoring, and downhole pressure measurements. Rock/fluid property measurements, combined with reservoir simulation and production history matching including seismic constraints, have been used to calibrate the seismic observations to known CO_2 injection volumes and to update the reservoir simulation model. The geochemistry of produced oil, gas, and brine has been regularly monitored and analyzed for a broad range of chemical and isotopic parametres to infer injection-related chemical processes within the reservoir and to track the path of injected CO_2. Soil gas sampling is designed to detect injected CO_2 that may have escaped from the reservoir and percolated to the surface.

4 PREDICTION: A PRIORI KNOWLEDGE OF THE RESERVOIR AND PRE-INJECTION FORECASTING OF CO_2 FLOW

Knowledge of the reservoir in the CO_2 injection area is based on 50 years of production data and a large number of wellbores and associated geological and geophysical logging data. Reservoir characteristics from this knowledge base, as summarized in Section 4.1, formed the basis for designing the plan for enhanced oil recovery (EOR) through a miscible CO_2 flood as described in Section 4.2. Reservoir flow simulation results predicting the response of the reservoir to CO_2 flooding are described in Section 4.3.

4.1 The Reservoir

Weyburn oil reserves lie within a thin zone (maximum thickness of 30 m) of fractured carbonates in the Midale beds (see Figure 1.3 in Theme 1) of the Mississippian Charles Formation, which were deposited in a shallow carbonate shelf environment. The reservoir comprises two intervals (shown schematically in Figure 2.1), an upper Marly dolostone (0-10 m thick) and lower Vuggy limestone (0-20 m thick), that are sealed by anhydritic dolostones and anhydrites of the Midale Evaporite. The Midale Marly unit ranges from chalky dolomudstone to calcitic biofragmental dolostone with intervening thin beds of biofragmental limestone. The fractured, Vuggy unit includes a lower, peritidal 'shoal' sequence with common secondary (vuggy) porosity and an upper shallow marine 'intershoal' sequence dominated by fine grained carbonate sands. The Midale beds are naturally vertically fractured although fracture density is generally higher within the Midale Vuggy. The dominant fracture set within the reservoir strikes NE-SW, as determined from core and imaging logs (Bunge, 2000), and is sub-parallel to the regional trajectories of maximum horizontal stress (Bell and Babcock, 1986). The vertical stress at the reservoir level due to the lithostatic load is ~34 MPa, as estimated from a density log, and the minimum horizontal stress is ~18-22 MPa in this region (McLellan *et al*., 1992).

The reservoir is underlain by the Frobisher beds (Evaporite, Marly, and Vuggy), which are lithologically and depositionally similar to the Midale beds. The Frobisher Evaporite is not present in the southern half of the EnCana Weyburn field (Figure 2.2), where the original oil-water contact was in the upper part of the Frobisher Vuggy unit.

The focus of the monitoring study is the Phase 1A EOR area, shown in Figure 2.2, where the reservoir is at ~1450 m depth and has a mean temperature of ~63º C. Estimated pore pressures of ~14 MPa existed when the field was originally discovered, and during waterflooding, they ranged from 8-19 MPa. Recently measured pore pressures range from 12.5 MPa to 18 MPa with an average of ~15 MPa. Thickness maps of the Midale Marly and Vuggy units within the Phase 1A area are shown in Figure 2.3. The Marly unit is 3-10 m thick (mean of ~6 m), the Vuggy unit is 8-22 m thick (mean of ~17 m), and the total reservoir thickness is 18-29 m (mean of ~23 m). The Midale Marly unit has relatively high porosity (16 to 38%) and low permeability (1 to >50 milliDarcy), whereas the Midale Vuggy unit has relatively low porosity (8-20%) and high permeability (10 to >300 milliDarcy). The Vuggy shoal unit is more porous than the Vuggy intershoal unit (mean value of 15% as compared to 10%) and more permeable (mean value of 50 milliDarcy as compared to 3 milliDarcy).

4.2 Description of the CO_2 Flood EOR Process

The Weyburn field hosted an estimated 221 million m^3 (1.4 billion barrels) of oil at the time of discovery in 1954. Initial estimates of water saturation within the reservoir were ~35%. Primary production within the field continued until 1964, at which time the initiation of waterflooding resulted in oil production peaking at 7250 m^3/ day (46,000 barrels/day) in 1965. During the waterflooding, it was recognized that the Vuggy unit was swept preferentially due to its higher permeability, with estimates suggesting that as much as 90% of the injected water went into the Vuggy unit. In 1991, drilling of horizontal infill wells commenced, with 130 horizontal wells drilled by 1997. This drilling program was designed specifically to target the Marly unit. Approximately 24% of the original oil in place (OOIP) had been recovered by 2000.

To aid in further recovery of oil at the Weyburn field, PanCanadian (now EnCana), the field operator, developed an EOR plan based on a miscible CO_2 flood. In the Phase 1A area (Figure 2.2), CO_2 was to be injected into 19 well patterns at individual injection well rates of 0.04-0.3 million m^3/day (74-558 tonnes/day), with a planned total injection volume of 30% pore volume. Water injection would be continued at a ratio of 0.5-2.0 water/CO_2 (or 15-60% pore volume of water) on a reservoir volume basis. Wellhead injection pressures of 15 MPa were planned, with average reservoir operating pressures between 14 and 17 MPa. These conditions exceed the critical point pressure and temperature (7.4 MPa and 31º C) of CO_2, and, thus, the injected CO_2 initially exists as a dense fluid (*i.e.*, supercritical gas) in the reservoir. Gravity segregation (or *gravity override* effect) was expected to aid in sweeping the Marly unit.

The miscible CO_2 flooding at Weyburn is expected to result in incremental oil recovery of 13-19% (mean of 16%) of the OOIP. There are complementary effects that will enhance oil production. Weyburn oil swells with dissolving CO_2, resulting in a net volume increase of ~30% and a reduction in the viscosity of the oil. If the CO_2 saturation in oil could be achieved uniformly throughout the reservoir, it would result in the current oil-in-place swelling to 94%, by volume, of the oil volume at the time of discovery, and waterflooding of the swelled oil would hypothetically lead to a 23% increase in recovery. However, in practice, this recovery rate is not achievable. Instead, implementation of a miscible CO_2 flood improves the local displacement efficiency of the sweep by reducing the capillary forces that act to trap the oil in the pores of the rock.

The CO_2-based enhanced oil recovery (EOR) scheme was initiated in September of 2000 in 19 patterns of the EnCana Weyburn Unit at an initial injection rate of 2.69 million m^3/day (or 5000 tonnes/day). The source of the CO_2 is the Dakota Gasification Company's synthetic fuel plant located in Beulah, North Dakota. The CO_2 is transported 320 km via pipeline to the Weyburn field. By 2002, the rate of CO_2 injection in the Phase 1A area increased to 3.39 million m^3/day (6300 tonnes/day) including 0.71 million m^3/day (1320 tonnes/day) of CO_2 recycled from oil production. The CO_2 EOR has contributed over 788 m^3/day (5000 barrels/day) to a total daily production of 3240 m^3/day (20,560 barrels/day) for the entire

Weyburn Unit. As of May 30, 2003, cumulative CO_2 injected was 1.90 billion m^3 (3.5 million tonnes). The EOR plan for 2003 to 2008 includes expanding the CO_2 flood into a total of 75 patterns, with ~10.8 billion m^3 (20 million tonnes) of injected CO_2 anticipated over the lifetime of the project.

4.2.1 Miscible CO_2 flood

Pure CO_2 and oil are not generally miscible. As the CO_2 initially contacts the oil, it dissolves in the oil to produce an *oil-rich* phase until a molar fraction of ~0.66 CO_2 is achieved (for T=63° C, and P=15 MPa). Subsequently, if reservoir pressure is maintained above the minimum miscibility pressure (MMP~15-17 MPa for Weyburn crude) the pure CO_2 captures vapourized intermediate hydrocarbons from the oil, forming a *CO_2-rich* phase that is less viscous than the oil-rich phase. As the latter process progresses, the CO_2-rich phase and the oil-rich phase eventually become miscible, in which case the capillary forces holding the oil-rich phase in place are reduced enough to allow the trapped oil to be swept from the rock pores. This effect is achieved by reducing the interfacial tension between the two phases. At reservoir pressures less than the MMP, the CO_2-rich phase becomes increasingly enriched in lighter hydrocarbon components (*e.g.*, methane), resulting in poor miscibility.

The flood strategy within the Phase 1A area was designed specifically to target the Marly unit, which resides in the upper part of the reservoir (see Figure 2.1) and has been largely bypassed during the waterflooding. Gravity segregation supported by waterflooding is applied to accomplish this (see Figure 2.4). The relatively low density of CO_2 and the CO_2-rich phase means that these phases will naturally rise to the top of the reservoir. This natural tendency will be further enhanced by injection of water into the Vuggy unit, which should push the lighter CO_2 upward. The predominant injection pattern utilized within the Phase 1A area (15 of 19 patterns) is *separate but simultaneous injection of* CO_2 *and water* (SSWG; CO_2 and water in horizontal and vertical injectors, respectively). The remaining 5 patterns are either *Vuggy water alternating gas* (VWAG; using vertical injection wells) or *Marly and Vuggy water alternating gas* (MVWAG). The WAG strategies are appropriate in some cases because they allow the waterflood to push the swollen oil by limiting the formation of the highly mobile CO_2-rich phase. Further details of these injection strategies can be found in Theme 3.

4.3 Simulation Using the Existing Reservoir Model

Prior to the start of the CO_2 injection, reservoir simulation was conducted to forecast the likely production response of the reservoir to CO_2 injection, to determine which injection strategies were most appropriate in different parts of the field and to estimate required injection volumes and incremental oil recovery. 3D reservoir simulation models of up to 38,000 grid blocks were constructed for use with a compositional flow simulator (Eclipse 300). The simulation models were based on engineering data (injection profile logging, pressure transient, and vertical pulse testing) and a constructed geological model based on formation microscanner logs, repeat formation testing, and open hole wireline logs, as well as the logging and interpretation of 12,000 m of core from over 600 vertical wells and 2 horizontal wells. The constructed geological model did not explicitly contain fractures, but their implicit effect is accounted for in the reservoir flow simulation model by matrix permeability changes required to match the historical production data from decades of waterflooding. Pressure-volume-temperature properties determined for Weyburn oil complemented by slim tube and swelling experiments were incorporated into the simulation. The results of the compositional simulation were used as a guide for further modeling through a four-phase, four-component simulator with the Todd-Longstaff formulation to account for viscous fingering. Mixing parametres of 0.60-0.65 were used. Approximately 30% of the 75 pattern EOR project area was modeled. Based on this simulation study, the average forecast recovery for the CO_2 flood area is 16% of the OOIP. This is somewhat less than the 24% recovery predicted by coreflood displacement tests and waterflooding sweep efficiencies due to the adverse mobility ratio between oil and CO_2, the gravity override effects, and reservoir heterogeneity.

Porosity and permeability of the reservoir simulation model are depicted in Figures 2.5 to 2.7. The thinner, high-porosity Marly unit is clearly visible in Figure 2.6, which shows the porosity for vertical slices through the reservoir model. Similarly, in Figure 2.7, the very high permeability Vuggy shoal areas (red

colours) stand out. The predicted vertical distribution of CO_2 saturation within the Marly and Vuggy units is illustrated in Figure 2.8. CO_2 saturation at 2 years from the start of injection is shown in plan view for the entire reservoir interval (Figure 2.9) and for the Marly interval only (Figure 2.10). In general, CO_2 is more broadly distributed in the Vuggy unit due to the higher permeability, and in the VWAG patterns, the CO_2 resides exclusively in the Vuggy units.

Predicted pressure variations over the first two years of injection (Figure 2.11) indicate pressures increasing in almost all regions of the reservoir with the exception of the MVWAG pattern in the eastern part of Phase 1A. Pressures increase by as much as 10 MPa from starting pressures of 15 MPa. To 2002, the pressures in the northern region continue to increase and in the southern region the high pressures spread out. For further details of reservoir simulation, the reader is referred to Theme 3.

5 MONITORING: OBSERVING THE EFFECTS OF INJECTED CO_2 WITH TIME

A keystone of the IEA GHG Weyburn CO_2 Monitoring and Storage Project is the effort to monitor the changes in the state of the reservoir resulting from CO_2 injection. To facilitate this, an extensive effort was made to acquire robust baseline measurements against which all subsequent monitoring surveys could be compared, including the monitoring surveys presented here, but also any future monitoring surveys. This aspect of the project, and the extensive knowledge provided by the well-based monitoring that is done in the regular course of EOR operations, makes this project unique.

In this section, a description of the results is provided from the various monitoring methods applied at the Weyburn field. First, the physical and chemical bases underlying the adopted monitoring methods are described in Section 5.1, along with the supporting laboratory and modeling results. This is followed by results from the various monitoring methods (Section 5.2), including production data (Section 5.2.1), geochemistry of production fluids and gases (Section 5.2.2), seismic imaging methods (Section 5.2.3), microseismic monitoring (Section 5.2.4), and soil gas sampling (Section 5.2.5). Integrated interpretation of the monitoring results is presented in Section 5.3.

5.1 The Basis for Monitoring

Production data are the primary means of monitoring the effects of CO_2 injection at the reservoir. These data comprise regular sampling of downhole pressures as well as the volumes of injected and produced reservoir gases and fluids. Additional monitoring methods that have been implemented at the Weyburn field include 1) measurements of changes in reservoir fluid chemistry, 2) imaging changes in the seismic properties of the reservoir, 3) passive recording of microseismic activity in the reservoir, and 4) sampling of surface soil gas for traces of leaking CO_2. These methods provide distinctly different, but complementary, monitoring capabilities. For example, production and geochemical sampling is limited to the locations of wellbores, whereas time-lapse seismic monitoring provides uniform sampling between the wellbores. Geochemical sampling identifies the effects of CO_2 advancing ahead of the CO_2 bank, in contrast to time-lapse seismic images which are generally more directly linked to the spatial distribution of CO_2 at the time of measurement. The chemical and physical effects underlying these monitoring methods are described below.

5.1.1 Chemical reactions accompanying CO_2 injection

As CO_2 is injected into the reservoir, a number of important processes are likely to occur, including CO_2 dissolution ($CO_2 + H_2O \Leftrightarrow H^+ + HCO_3^-$), carbonate mineral dissolution ($H^+ + CaCO_3 \Leftrightarrow Ca^{2+} + HCO_3^-$; $CO_2 + H_2O + CaCO_3 \Leftrightarrow Ca^{2+} + 2HCO_3^-$), and eventually carbonate precipitation in the form of calcite or other carbonate minerals. Observing the resultant variations in calcium concentrations, total alkalinity, pH,

and carbon isotope ratios in the produced fluids and gases provides a measure of the degree of interaction taking place between reservoir fluids, injected CO_2, and reservoir rocks. The distinct isotopic signature ($\delta^{13}C$ value of –35 ‰ (V-PDB)) of the injected CO_2 from the synthetic fuels plant in North Dakota relative to the baseline reservoir HCO_3^- ($\delta^{13}C$ of –6 to –20 ‰) will allow the path of injected CO_2 to be traced as a precursor of the advancing CO_2 front.

5.1.2 Seismic sensitivity to the physical effects of CO_2 injection

The injection of CO_2 into the reservoir affects its seismic properties via a number of mechanisms. In saturated porous rocks, the net seismic characteristics of the rock are largely controlled by the characteristics of the rock matrix (*e.g.*, matrix stiffness, density, and porosity), the nature of the fluid occupying the pore space, and the effective stress (the difference of the confining pressure and the pore pressure). Injection of CO_2 modifies both the pore fluid and the pore pressure within the rock, and, thus, should change the associated seismic properties. To quantify these effects several sources of information are included. The seismic properties of different reservoir pore fluids are considered in Section 5.1.2.1. Ultrasonic measurements on fluid-saturated reservoir core samples (Section 5.1.2.2) allow investigation of the effects of pressure variation and fluid replacement for a limited range of porosities and fluid saturations. A common rock physics model (Gassmann, 1951; Sherif and Geldart, 1995) is adopted to use these observations as the basis for predicting seismic changes over the broader range of porosities observed in the reservoir (Section 5.1.2.3). Geophysical well logs (Section 5.1.2.4) provide the vertical distribution of lithologies and porosities for the initial fluid saturations and pressures. A means of assessing saturation and pressure effects in the seismic data is discussed in Section 5.1.2.5, followed by seismic resolution considerations (Section 5.1.2.6) and the potential for observing injection-related microseismicity (Section 5.1.2.7).

A central objective of the monitoring effort is to track and quantify the distribution of CO_2 in the subsurface over time. In light of this, an underlying theme in the following sections is the potential for seismic imaging techniques to accomplish this. As described in Section 4.2.1, during a miscible flood, brine and oil within the reservoir will be partially replaced by pure CO_2, a CO_2-rich phase, or an oil-rich phase. CO_2 can also dissolve in the brine, but its solubility in brine is very low (~1-2% molar fraction) as compared to its solubility in oil. In any of these scenarios (with the exception of brine replacing oil-rich phase), the pore fluid is being partially replaced by fluids containing a large molar fraction of CO_2. Thus, if it can be demonstrated that the seismic response is sensitive to either oil or water being replaced by fluid phases with large fractional CO_2, then the seismic images should be a proxy for the distribution of CO_2 in the reservoir.

5.1.2.1 Fluid properties

Compressional wave velocity (Vp) in a fluid is directly related to the fluid's bulk modulus (G) and inversely related to its density, where bulk modulus is a measure of a fluid's incompressibility. The bulk modulus and density of single-component reservoir fluids as determined by modeling are shown in Figure 2.12 and summarized in Table 2.1. Brine is the least compressible (G~3.0 GPa) of the reservoir fluids by a factor of at least 2, relative to oil (G~1.5 GPa), and by a minimum factor of 15 compared to pure CO_2 (G<0.3 GPa). The bulk modulus of an oil/CO_2 mixture decreases gradually with increasing CO_2 fraction until compositions of ~40 molar per cent CO_2 are achieved. For more CO_2-rich compositions, the bulk modulus decreases dramatically. Similarly, density decreases more rapidly above 40 molar per cent CO_2. Given the contrast in the bulk moduli values amongst the reservoir fluids (Table 2.1), and their contrast relative to values for representative reservoir rocks (10-15 GPa), it is clear that for intermediate-to-high porosity rocks, the overall rock stiffness will be strongly influenced by the composition of the pore fluid. The range in density amongst the fluids is smaller, and will, therefore, have a secondary effect on seismic properties. Thus, observable variations in seismic properties of the reservoir should be apparent in regions where the molar per cent of CO_2 exceeds 40%. Also, water displacement of oil by water (or *vice versa*) should result in significant changes.

Table 2.1 Reservoir fluid properties (for P=15-25 MPa; T=63 ^{o} C) summarized from Brown (2002).

Fluid	Bulk Modulus (GPa)	Density (kg/m^3)	Viscosity (relative to oil)	Solubility of CO_2 (molar %)
Oil	1.2-1.7	800-880	1	66
Brine	2.7-3.2	1020-1080	~1/10	1-2
CO_2	0.05-0.18	580-760	1/70	100

The single-component fluid behaviour depicted in Figure 2.12 is a simplification of reservoir conditions where multi-component fluids are likely present in general. In this case, if one of the components is significantly more compressible than the others (*e.g.*, pure CO_2 or a CO_2-rich phase), it will dominate the effective compressibility of the bulk pore fluid. As a consequence, the presence of even a small amount of the highly compressible component will reduce the compressibility of the bulk pore fluid enough to produce an observable reduction in the compressional wave velocity. This type of behaviour is hinted at in Figure 2.13a, which shows that for pressures below the *bubble-point* pressure, the bulk modulus of oil/CO_2 mixtures decrease dramatically, approaching the bulk modulus of pure CO_2. Beneath the bubble-point pressure, which increases with CO_2-saturation, CO_2 escapes from the oil, forming a separate component that dominates the effective bulk modulus of the two-component system. The implication of this behaviour is that the seismic measurements will be highly sensitive to reservoir situations where a CO_2-rich phase exists. This sensitivity of the seismic reflection response to gas is well-known (*e.g.,* Domenico, 1976; Batzle and Wang, 1992).

5.1.2.2 Rock core measurements

Direct measurements made on reservoir rock core samples provide a primary source of information in determining the effects of the CO_2 flood on the reservoir's seismic properties. The properties determined in this manner can be used as the basis for further modeling (see Section 5.1.2.3). However, it must be recognized that 1) these measurements exclude the effects of fractures that exist on a larger scale within the reservoir and 2) Vp measurements are frequency-dependant (*e.g.*, Batzle *et al.*, 2001). Figure 2.13 displays the velocity sensitivity to pore fluid substitution determined for a broad suite of carbonate rock cores from the Western Canada sedimentary basin. Notably, the majority of values exceed 5% (Figure 2.13a), demonstrating the feasibility of seismically monitoring gas injection in a carbonate reservoir (*e.g.*, see Hirsche *et al.*, 1997), although there is a broad variation and no obvious correlation with porosity (Figure 13b).

Similar rock property measurements have been made on several core samples from the Midale Vuggy and Marly units of the Weyburn field. Figure 14 demonstrates the effect of pore fluid composition on seismic velocities, both compressional wave velocity (Vp) and shear wave velocity (Vs), for a saturated Vuggy rock core that has a porosity of 13%. The effective pressure (Pconfining-Ppore) is kept constant to simulate a constant reservoir pressure, isolating the effect of fluid composition. As can be seen, a Vp decrease of 2-3% occurs for pore pressures of 15 to 25 MPa for brine replaced by CO_2, which is the fluid replacement that should have the largest effect. In contrast, Vs shows little sensitivity to pore fluid composition. The sensitivity of Vp and of Vs to pore pressure in the Vuggy unit is shown in Figure 15. Over the effective pressure range of 5-25 MPa, the pressure-induced variations of 1.5-1.8% for Vp and Vs are smaller than the maximum saturation-induced changes of up to 4% in Vp but are larger than the ~1% saturation-induced changes in Vs. Measurements for the Marly samples (porosities of 0.18 and 0.21) shown in Figures 2.16 and 2.17, suggest pressure-induced changes (~4%) in Vp and Vs that are comparable to the saturation-induced variations. It should be noted, however, that the Marly results are generally less consistent. The insensitivity of Vs to pore fluid saturation (at least in the Vuggy unit) has been noted (*e.g.*, Wang *et al*., 1998; Brown, 2002) and suggested as a potential means of discriminating pore pressure versus pore fluid saturation effects using a combination of P- and S-wave data. There are some classes of lower symmetry anisotropic media where this insensitivity of Vs to pore fluid saturation does not hold (Cardona, 2002).

The anisotropic nature of the Weyburn reservoir rocks is well documented, with aligned vertical fractures (Section 4.1) contributing significantly to the anisotropy. In anisotropic media, a phenomenon referred to as shear-wave splitting or birefringence often occurs. The sensitivity of shear-wave splitting to decreasing differential pressure for Vuggy and Marly samples is shown in Figure 2.18. For the Vuggy sample, shear-wave splitting exceeding 1% is only attained for differential pressures below 9 MPa. In contrast, for the Marly samples, shear-wave splitting lies in the range of 3-5.5% for similar differential pressures. The increase in splitting effect with reduced differential pressure is interpreted as resulting from the opening of oriented microcracks in the rock core. In the reservoir, this would correspond to increased pore pressure opening existing cracks or fractures at the scale observed in these core samples and also for larger scale fractures.

To summarize these and more extensive measurements made on reservoir fluids and rock samples from the Weyburn reservoir (Brown, 2002; Core Laboratories Canada, 1998; Wang *et al*., 1991), the following changes in seismic properties have been demonstrated. A median value of ΔVp=-6% due to brine-to-gas substitution is found for carbonates of the Western Canada basin. For the Weyburn samples: 1) Maximum magnitudes of ΔVp=-4 to -5% are found for brine-to-gas replacement; 2) Significant dissolved CO_2 (>25%) in an oil-rich phase is required to distinguish it from oil based on Vp; 3) Pressure related ΔVp=0 to -2% is observed for the Vuggy unit, although ΔVp comparable to saturation-induced effects (~-4%) arguably may occur for the Marly unit; 4) Vs is less sensitive to the composition of the pore fluid; 5) Vp does not uniquely distinguish fluid saturation from differential pressure effects, although Vs may, as it is insensitive to the pore fluid; 6) Shear-wave splitting increases (1-2%) in saturated Vuggy with decreasing differential pressure, whereas splitting increases are larger in the Marly (5-6%; based on dry sample); 7) Vp variations are insignificant for temperature variations in the range of T=45-65^{o} C.

5.1.2.3 Gassmann's rock physics model

The direct measurements made on fluid and rock core samples demonstrate the potential effects of fluid substitution and pressure changes at the reservoir. However, noting the limited scale over which these measurements are strictly valid and that the few samples tested are representative of only a small range of the large porosity and fluid saturation variations that occur in the reservoir, a means of more generally estimating the effects on seismic properties is required. For this purpose, Gassmann's rock physics model is used (Gassmann, 1951). This model allows prediction of the seismic properties of a fluid-saturated porous rock based on the rock porosity and seismic parametres of the pore fluid and rock matrix. This formulation is not strictly applicable to anisotropic rocks, and it generally tends to underestimate the effects of fluid substitution in carbonate rocks (*e.g.,* Wang *et al*., 1991; Hirsche *et al*., 1997). However, it provides a reasonable first-order basis for estimation (*e.g.*, compare the results in Table 2.2 for the isotropic and anisotropic model), recognizing that it provides a lower bound to expected fluid saturation effects. Comparison of the physical property measurements and Gassmann-based calculations for Vp shows that although Gassmann underestimates the Vp values, both results demonstrate comparable sensitivity to fluid substitution and pressure changes (Brown, 2002). Combining Gassmann's model with geophysical well logs allows prediction of the detailed seismic changes over the depth interval of the reservoir induced by CO_2 injection.

Table 2.2 Sensitivity of Vp and Vs to changes in fluid composition and pressure for Marly and Vuggy units. Based on a) Gassmann isotropic rock physics model (labeled Iso) from ultrasonic core testing and geophysical logs and b) anisotropic rock physics model (labeled Aniso). The anisotropic model is a generalization that attempts to account for fractures observed in core and image logs from the reservoir (Bunge, 2000). φ= porosity. Table is modified from Brown (2002).

Change	Marly Unit, φ=24%				Vuggy Unit, φ=10%			
	Iso	Aniso	Iso	Aniso	Iso	Aniso	Iso	Aniso
	ΔV_p (%)	ΔV_p (%)	ΔV_s (%)	ΔV_s (%)	ΔV_p (%)	ΔV_p (%)	ΔV_s (%)	ΔV_s (%)
Brine to oil	-3.3	-3.4	1.1	1.1	-2.2	-2.8	0.4	0.4
Brine to CO_2	-6.0	-6.3	-2.5	-2.5	-4.2	-5.6	1.0	1.0
1 MPa Δ(Pore Pressure) @ 15 MPa	-0.64	-0.65	-0.90	-0.90	-0.18	-0.16	-0.15	-0.15

5.1.2.4 Well log-based modeling

Having established the general sensitivity of the reservoir seismic properties to CO_2 injection (Sections 5.1.2.1 to 5.1.2.3), more detailed modeling of the seismic response can be implemented using well log properties in conjunction with the rock physics model (Section 5.1.2.3). Figure 2.19 shows the model-based change in well logs (Vp, Vs, density) due to CO_2 saturation in the reservoir interval 1400-1420 m.

The logs show a decrease in Vp of about 8% for both the Marly and Vuggy Formations, but as expected, much smaller changes of Vs occur. The higher sensitivity compared to the results of Table 2.2 is due to use of a change in saturation from 100% brine to 30% brine (here) as compared to 100% brine to 100% gas (in Table 2.2). The 30% residual brine saturation has almost the same bulk modulus as the 100% gas case, but the density is higher due to the residual water, resulting in a further reduction in Vp.

Table 2.3 Rock properties for log modeling results shown in Figure 2.19. Fluid parametres used are: gas gravity of 1.22 API (for CO_2), oil gravity of 29.0 API, gas-oil ratio of 30, and brine salinity of 85,000 ppm. An effective pressure of 15 MPa and temperature of 63° C were assumed.

Unit	Lithology	Matrix Mineralogy	Density (kg/m^3)	Bulk Modulus (GPa)	Shear Modulus (GPa)
Marly	Dolomite	Dolomite	2870	94.9	45.0
Vuggy	Limestone	Calcite	2710	76.8	32.0

Figure 2.20a shows the resultant velocity logs vs. thickness (0-28m) of the CO_2 bank as the reservoir is filled downward from the top of the Marly unit. The average velocity change determined over the entire reservoir interval is from -1 to -8% as the CO_2 bank increases in thickness from 2 to 24 m. Figures 2.20b and c show the Vp logs for effective pressures ranging from 5 to 30 MPa for 80% CO_2 saturation and 100% brine saturation within the reservoir, respectively. As can be seen, the Vp decrease for the saturation effect is dominant over that due to the pressure effect, which is consistent with the results in Table 2.2.

Figure 2.21 depicts the effect on the seismic reflection waveform of CO_2 saturation vs. thickness (0-24m) as CO_2 saturates the reservoir downward from the top of the Marly unit. The difference seismogram in the vicinity of the reservoir (at ~1150 ms) changes drastically as CO_2 fills the upper 4 m, but does not change notably after. As CO_2 fills the high porosity Marly interval, the impedance difference of the Marly unit relative to the bounding units increases, accentuating the amplitudes of the negative peak associated with the Marly unit and the positive peak associated with the Vuggy unit. As the CO_2 bank spreads downward into the Vuggy, the seismic response changes very little, reflecting the lesser sensitivity of the seismic response to CO_2 saturation in the Vuggy unit. The lower sensitivity to Vuggy CO_2 saturation is further

emphasized in Figure 2.22, which shows that CO_2 saturation begins at the top of the Vuggy unit and expands downward and into the underlying Frobisher Marly unit. Relatively little change in the seismic response occurs until the CO_2 reaches the Frobisher unit, which has characteristics comparable to the Midale Marly unit. Thus, the seismic response measured at the Frobisher Marly is also sensitive to CO_2 entering the Frobisher Marly.

The sensitivity of the seismic response to a free gas component in the pore fluid is demonstrated in Figure 2.23, which shows that a small amount of CO_2 (10%) is seen to produce the same effect as much larger amounts. This suggests that determination of the CO_2 saturation within the reservoir from the time-lapse seismic data will be problematic in situations in which a free gas component exists. However, it is important to note that this result assumes a uniform mixture of gas and liquids in the reservoir. If this is not the case, then variable saturation will be more detectable. Pressure vs. saturation effects on the seismic response are shown in Figure 2.24. The largest differences, by far, both in time delay and amplitude at the Marly level, are caused by increased CO_2 saturation (compare a *vs*. b) rather than pressure (compare traces within either a or b).

Figures 2.25 and 2.26, respectively, depict the amplitude difference measured at the Marly horizon and the travel time delays determined from the modeling results of Figure 2.21. Fractional Marly amplitude differences (Figure 2.25) exceed 30% by the time the CO_2 saturates the entire Marly interval, after which they gradually increase to ~40%. As CO_2 enters the Frobisher, the Marly amplitude actually decreases somewhat, demonstrating the effects of thin bed superposition (see Section 5.1.2.6). The travel time delays (Figure 2.26) show behaviour similar to the amplitude differences, with delay times increasing rapidly for CO_2 flooding in the Midale or Frobisher Marly units but with gradual increases as the CO_2 saturates the Midale Vuggy unit.

5.1.2.5 Saturation *vs*. pressure effects

The travel time delay modeling results (Figure 2.26) provide a means of estimating the effects of saturation vs. pressure. For a constant porosity layer saturated with CO_2, there is a non-linear relationship between the associated travel time delay and CO_2-induced fractional seismic velocity decrease within the layer. Then, for a given fractional velocity decrease, a linear relationship exists between time delay and layer thickness, as shown in Figure 2.27. Comparison of these curves to the best-fit line determined for the time delays of Figure 2.26 suggests that the travel time delays defined for the entire reservoir interval are consistent with a fractional velocity decrease of ~9%. This estimate of the average velocity decrease produced within the reservoir due to saturation effects can be compared with the time delays observed in the surface seismic data to assess whether additional pressure contributions are required to explain the velocity decrease. This is done in Section 5.3.1 below.

5.1.2.6 Seismic resolution

The modeling in Section 5.1.2.4 showed an example in which the seismic amplitudes measured at the Midale Marly level of the reservoir were affected by CO_2 saturation 18 m below in the Frobisher Marly unit. This is a consequence of attempting to measure properties of a reservoir that is thin relative to the length of the seismic wavelet that is being used as a probe, and this raises the issue of seismic resolution. Conventionally, vertical resolution is defined in terms of the minimum thickness of a thin bed that can be seismically detected. This thickness is estimated to be $\lambda/4$ to $\lambda/8$ (Widess, 1973; p. 468 of Yilmaz, 1999; p. 174 of Sheriff and Geldart, 1995), where λ is the dominant wavelength of the seismic wavelet, $\lambda = V_p / f_c$, and f_c is the central frequency of the seismic wavelet. When the aggregate thickness of the beds of interest is less than $\lambda/4$, the zone is considered a *thin bed*. In such cases, the reflections from the top and bottom of the thin bed interfere so that 1) it difficult to identify the individual reflections if the thickness is less than $\lambda/4$ and 2) the amplitude of the composite reflection decreases with the layer thickness. Lateral resolution is defined by the Fresnel radius for unmigrated data, $(F=(\lambda z/2)^{1/2})$, where z is depth, and for accurately migrated data (*i.e.*, when the subsurface seismic velocity is accurate), the lateral resolution is λ.

For the P-wave surface seismic data considered here, f_c= 60 Hz, Vp=3500-5000 m/s. Thus, λ=56-80 m λ/4=14-20 m, and the Fresnel radius is 200-240 m. In the Phase 1A area, the Marly unit is 3-9 m thick (mean of ~5 m), the Vuggy unit is 8-21 m thick (mean of ~16 m), and the total reservoir thickness is 17-28 m (mean of ~23 m). Thus, the Marly and Vuggy units (and in some areas the reservoir interval) constitute thin beds. The limited depth extent of the reservoir units means that the time-lapse seismic response will be a superposition of the effects of CO_2 flooding the individual units, and, thus, the response of the individual units will not generally be resolved. However, there are methods, such as, impedance inversion, (Oldenburg, 1983), that have potential for improving the depth resolution of the time-lapse seismic data.

5.1.2.7 Microseismicity associated with stress changes in the reservoir

CO_2 injection will modify pore pressures (by up to 10 MPa) within the reservoir, resulting in a dynamic response of the reservoir rock matrix. Seismic deformation associated with the reactivation or creation of fractures can result from a number of mechanisms, including hydraulic fracturing, shearing associated with stress or pressure changes, reservoir compaction, or material property changes. Discrete acoustic emissions (*i.e.*, microearthquakes) accompany deformation. Typical magnitudes of injection-related microseisms observed in other fields range from –4 to 0 (Maxwell *et al*., 2003; Maxwell and Urbancic, 2001, 2003). Fracture-related permeability within the reservoir may be altered by the injection process as pressure changes within the reservoir may open or close fracture systems. The spatial and temporal variations in the microseisms may be used to track pressure changes and, potentially, gas movement.

5.2 Monitoring Methods and Results

The schedule of CO_2 injection and monitoring is shown in Figure 2.28. Results from each element of the comprehensive monitoring program are described in the following sections. The monitoring effort is designed to document as much of the dynamic reservoir response as possible. Baseline static characterization of the reservoir (*e.g.*, porosity, permeability, fracture systems, fluid distribution) prior to injection is important in planning the flood and anticipating how it will proceed. As well, baseline measurements provide the reference against which all subsequent monitoring surveys can be compared. Following flood initiation, the goal is to track the saturation and distribution of CO_2 within the reservoir, assess the interaction of the CO_2 with the other reservoir fluids, determine pressure variations, identify off-trend flow so that the injection process can be adjusted accordingly, and ensure the security of CO_2 within the reservoir. Finally, monitoring provides a means of verifying the volume of CO_2 that resides within the reservoir. Efficient and complete access to the reservoir volume and avoidance of premature flow-through of CO_2 to producing wells is important whether either enhanced oil recovery or CO_2 storage is the ultimate goal.

5.2.1 Conventional production data

A significant advantage in conducting this study in a working oilfield is the access to fundamental production data. These data constitute the regular temporal sampling of variations in production parametres (*e.g.*, injected and produced volumes of gas, oil, and water and reservoir pressures) against which other monitoring methods are compared and calibrated.

The Phase 1A CO_2 injection history is summarized in Figure 2.29, which shows average monthly injection volumes of 43 to 71 million m^3 (1.5 to 2.5 BCF). As of June 1, 2003, 1750 million m^3 (61.7 BCF) of CO_2 were injected in the Phase 1A area. The cumulative volume of CO_2 injected in each of the Phase 1A patterns to the time of the Monitor 2 seismic survey is shown in Figure 2.30. The effectiveness of the CO_2 EOR operation is depicted in Figure 2.31, where the incremental oil production (actual production minus predicted production without injection) is shown to reach 800 m^3/day (5000 bbl/day). The direct correlation between injected CO_2 volume and oil production is shown for the total Phase 1A area in Figure 2.32 and on a pattern-by-pattern basis in Figure 2.33. As seen in Figure 2.32, daily oil production increased from 630

m^3/day to 1100 m^3/day (4000 bbl/day to 7000 bbl/day) by the time 570 million m^3 (20 BCF) of CO_2 were injected into the reservoir.

Production statistics monitored on a well-by-well basis allow the spread of CO_2 to be tracked over time, as demonstrated in Figure 2.34 wherein a dramatic increase in oil production and decrease in water rate are observed several months after the onset of CO_2 injection (September, 2000). Subsequently, a CO_2 response at the well is observed in July, 2001. Figure 2.35 depicts CO_2 responses over the Phase 1A area. In the first 4 months (September to December, 2000) following the onset of injection, CO_2 response was limited to a single horizontal production well. From January to June, 2001, responses were seen in 5 horizontal producers, including one within a MVWAG pattern in the eastern corner of the Phase 1A area. An additional 6 horizontal producers, all within the SSWAG patterns, began to exhibit responses during the last half of 2001. In 2002, CO_2 responses were observed in 14 vertical production wells, mostly in the vicinity of horizontal producers that had responded previously. Areas that were notably void of CO_2 response by the end of 2002 are in the VWAG patterns in the northern region of Phase 1A and in the southernmost region of the flood.

Reservoir pressures have been sampled in a subset of wells across the Phase 1A area. The resulting values are shown as contour plots in Figures 2.36 to 2.38. From 2000 to 2001, reservoir pressures actually declined (compare with the predicted pressure variations in Section 4.3) in the row of patterns that immediately borders the SE boundary of the Phase 1A area. In contrast, pressures increased dramatically in the northern patterns. From 2001 to 2002, pressures increased significantly in the southern region of the Phase 1A area.

5.2.2 Geochemistry of production fluids and gases

The methodology employed in the geochemical monitoring phase of the project is to sample produced fluids before (baseline) and during the injection of CO_2 (see Figure 2.28 for monitoring schedule) and analyze them for a wide array of chemical and isotopic parametres and then to use the results to interpret the chemical processes in the Midale Weyburn Reservoir. Ten monitoring trips occurred between August 2000 and September 2003. As of autumn 2003, over 500 samples of produced brines, gas, and oil samples were collected and analyzed. Changes in the chemical and isotopic values (Table 2.4) provide a wealth of information on processes that are taking place in the reservoir as a result of CO_2 injection.

Table 2.4 Concentrations of selected geochemical parametres prior to the start of injection and following 930 days of injection.

	Pre-injection		930 days of Injection		
	Mean	Standard Deviation	Mean	Standard Deviation	%Change
pH	6.7	0.2	6.7	0.3	-1
Total Alkalinity (mg/L)	429	104	1094	375	155
Ca (mg/L)	1372	186	1913	298	39
Mg (mg/L)	374	27	597	69	60
Resistivity (ohm m)	0.149	0.023	0.104	0.014	-43
$\delta^{13}C_{HCO3}$	-2.8	2.7	-5.7	4.7	N/A
Cl (mg/L)	38440	7930	39530	7410	3
SO_4 (mg/L)	3465	207	3596	252	4

As expected, three short-term chemical processes are readily observed in the time evolution of the reservoir fluid geochemistry: 1) Injected CO_2 dissolution within reservoir brine ($CO_2 + H_2O \Leftrightarrow H^+ + HCO_3^-$) results in decreased pH; 2) The resultant low pH (*i.e.*, acidic) fluid reacts with the reservoir carbonates (predominantly calcite ($CaCO_3$) in the Vuggy unit and dolomite ($CaMg(CO_3)_2$) in the Marly unit) leading to mineral dissolution ($H^+ + CaCO_3 \Leftrightarrow Ca^{2+} + HCO_3^-$ and $2H^+ + MgCa(CO_3)_2 \Leftrightarrow Mg^{2+} + Ca^{2+} + 2HCO_3^-$) and increased alkalinity [HCO_3^-]; 3) Mineral dissolution produces an increase in total dissolved solids in the reservoir brine as well as an increase in pH, $\delta^{13}C_{HCO3}$, Mg^{2+}, and Ca^{2+}.

Carbon isotopes ($\delta^{13}C_{HCO3}$ or abbreviated as $\delta^{13}C$) provide a means of tracking the spread of trace amounts of injected CO_2 as a precursor of the advancing CO_2 "front." This is possible due to the distinct isotopic

signature of CO_2 ($\delta^{13}C$ value of –35 ‰) delivered from the synthetic fuels plant that reduces the $\delta^{13}C$ values of the injected CO_2 to ~ –20 ‰ (Figure 2.39). This is significantly depleted relative to the baseline $\delta^{13}C$ values and the $\delta^{13}C$ values of the reservoir carbonate minerals.

Following the start of injection, reaction of injected CO_2 with formation water was apparent within six months. At 10 months time, the $\delta^{13}C$ values of reservoir fluids had decreased dramatically from the original values of -1 to -7 per mil to values of -4 to -11 per mil (Figure 2.40). The decrease in $\delta^{13}C$ values is most easily attributable to the dissolution of injected CO_2. The effects of mineral dissolution were recognized by 10 months time, as indicated by increases in alkalinity, $[Ca^{2+}]$, and total dissolved solids (Figure 2.41, 2.42, and 2.43). These indicators of mineral dissolution continued to increase to 21, and then to 31, months time and show good spatial correlation with the highest CO_2 injection volumes of the Phase 1A area. The effect of mineral dissolution on the $\delta^{13}C$ values can be seen in Figure 2.40, which shows that the values at 21 months increased from the 10-month survey.

The observed increase in electrical conductivity of reservoir fluids over time (Figure 2.48) may be related to the increased dissolved ions due to dissolution of the reservoir rock, although it could, alternatively, indicate that the CO_2 flood is extracting fluid of higher salinity from reservoir zones (Midale Marly) that were inaccessible from primary and secondary (waterflooding) production. Mass balance calculations will attempt to quantify the amount of reservoir material that has been dissolved.

5.2.3 Seismic imaging results

A variety of seismic imaging methods have been applied to monitor the CO_2 flood. In each case, baseline data were acquired prior to the start of the CO_2 flood to provide a reference for future comparison. Subsequently, repeat (or monitor) seismic data were acquired during the first 2 years of the CO_2 flood (see Figure 28 for monitoring schedule) to determine changes in the seismic properties of the reservoir relative to the baseline survey. This methodology is commonly referred to as *time-lapse* imaging, or in the case of 3D seismic data, *4D imaging*, where time represents the 4^{th} dimension. Time-lapse seismic data acquired include 1) surface 3D 3-component seismic reflection surveys for the entire Phase 1A area, 2) surface 3D 9-component seismic reflection surveys for 4-patterns within the Phase 1A area, and 3) 3D 3-component vertical seismic profiles (VSP) for a single well within the Phase 1A area. In addition, several non-repeat seismic surveys were conducted, including horizontal and vertical crosswell tomography surveys and vertical seismic profiles. Some of the key results from these monitoring efforts are highlighted below.

5.2.3.1 Pre-injection seismic measurements and reservoir characterization

A section through the P-wave 3D data volume from the baseline 3-component survey is shown in Figure 2.44. The geological horizons identified in this data set and the subsequent monitoring surveys form the basis for much of the time-lapse analysis described below. The top of the reservoir horizon (Midale Marly) is indicated, along with several other horizons of interest. Identification of the various geological horizons with seismic events is based on correlation of the seismic data with well log-generated synthetic seismic data (Figure 2.45). As can be seen, it appears that both units of the reservoir (Midale Marly and Vuggy) can be detected in the seismic section, at least locally.

A horizontal crosswell survey was acquired (Figure 2.46) prior to the start of CO_2 injection (Majer *et al*., 2001; Washbourne *et al*., 2001; Li *et al*., 2001). The original intent was to conduct a follow-up monitoring survey for time-lapse imaging, but logistical problems prevented acquisition of this monitoring survey. The frequency band of the seismic source (200-2000 Hz) in the horizontal crosswell survey was an order of magnitude higher than for the surface seismic source, allowing imaging of reservoir property variations on the scale of metres. To our knowledge, this was the first-ever deployment of a large-scale crosswell survey between horizontal wells.

The horizontal crosswells were located within the Marly unit (see Figure 2.1) of the reservoir. This layer has a much lower velocity (3.5 km/s) than the bordering layers (~5.5 to 6.0 km/s), and, thus, acts as a

waveguide for seismic energy propagating across the layer. A tomographic imaging approach was developed to use this guided or trapped wave energy. An attenuation tomogram for 500 Hz energy is shown in Figure 2.46a, with an attempt at integrating this result with the existing reservoir model shown in Figure 2.46b. The tomogram has been converted from an attenuation image to permeability within the depth slice by using porosity and fluid viscosity from the reservoir model and by using Biot relationships (Biot, 1956) to calculate the permeability. The resulting permeability values clearly depend on the parameters from the reservoir model and the assumed attenuation mechanisms, but the observed trends are robust. The permeability values obtained range from 50 to 150 milliDarcy, which is comparable to the range of permeabilities measured within this unit (10 to 500 milliDarcy). Notably, the spatial trends in the calculated permeability are at an angle to the horizontal injection wells (oriented along-trend) and are also oblique to the local seismic impedance and porosity trends (cf., Li *et al*., 2001), suggesting the presence of off-trend zones of enhanced permeability. This is discussed further in Section 5.3.

The shear-wave data from the baseline 9-component 3D survey were used to determine the shear wave velocity anisotropy map for the reservoir interval in a 4-pattern sub-region, as shown in Figure 2.47. Seismic shear wave anisotropy derived from the amplitude ratios of split shear waves is a robust measure of fracture density. The high negative anisotropy areas are interpreted as zones of higher fracture density of northwest or off-trend fractures in the reservoir.

5.2.3.2 Time-lapse seismic results

The time-lapse P-wave seismic results are illustrated in Figure 2.48, where the Baseline, Monitor 2 and Baseline-Monitor 2 data are shown for a vertical slice through the 3D data volume. The amplitude differences (colour background) are most prominent at the reservoir level and beneath. The large differences well below the reservoir are artifacts (*i.e.*, do not represent geological changes at this depth), as they are due to the time-delay introduced by changes at the reservoir level that produce misalignment of the baseline and monitor waveforms everywhere beneath. Travel time delay maps determined at the Bakken horizon for the Monitor 1 and 2 surveys are shown in Figure 2.49 and compared to a static reference horizon, the Lower Gravelbourg horizon located above the reservoir, in Figure 2.50. Significant delay time anomalies are readily apparent around the horizontal injection wells, with maximum delay time values of ~2 ms. The delay time map at the Bakken horizon represents the cumulative travel time delay due to CO_2 effects at the overlying reservoir level. The small thickness of the reservoir precludes resolving the Marly and Vuggy units based on travel time delays. Minimum fractional velocity changes determined from the travel time delays for the complete reservoir thickness (Figure 2.51) show values of up to ~10%. Fractional velocity decreases may actually be greater if the CO_2 is restricted to a sub-interval of the reservoir.

Amplitude differences are somewhat more sensitive than the travel time delay maps and allow difference maps to be determined for the horizons in the immediate vicinity of the reservoir. Figure 2.52 shows the amplitude difference map for the Monitor 2 survey determined at the Marly horizon, along with the corresponding difference map determined at the reference horizon (Figure 2.53).

The magnitudes of the travel time (Figure 2.49) and amplitude anomalies (Figure 2.52) and their areal coherence exceed that observed at the LGVB reference horizon (Figures 2.50 and 2.53). Comparing the seismic anomalies (Figures 2.49 and 2.52) with the injection pattern types and injected volumes (to 2002 in Figure 2.54) a number of general observations are made. In all patterns where there has been injection of only small volumes of CO_2 (<2% HCPV), there are no significant seismic anomalies. An exception to this is pattern 1602 where there appears to be a significant amplitude anomaly. Travel time and amplitude anomalies are pronounced in all of the SSWAG patterns where there has been significant volume of CO_2 injected (~3-14% HCPV). The travel time delays show a strong correlation with the horizontal injections wells, generally forming a halo around the injector with the largest anomalies occurring directly over the well trajectory. There is generally good agreement between the injection volumes and the areal extent and/or magnitude of the anomaly. Exceptions to this are patterns 1623 and 0619, where the amplitude anomalies are not as prominent as the travel time anomalies. In contrast to the SSWAG patterns, seismic anomalies are less prominent in the VWAG patterns in the northern part of the Phase 1A area, and in the MVWAG pattern (1618), even though large volumes of CO_2 (up to 13% HCPV) have been injected. Comparison with the production pressure data (Figures 2.36 to 2.38), reveals that the northern Phase 1A

area, where the seismic anomalies are smallest, has experienced large pressure increases from 2000 to 2001, whereas pressures in the southern parts of the Phase 1A area actually dropped during this period. If pressure were largely responsible for the observed seismic anomalies in the Monitor 1 map, a positive correlation between travel time delays, positive amplitude anomalies, and pressure would be expected. No such correlation is apparent, indicating that the alternative (*i.e.*, CO_2 saturation effects) is primarily responsible for the observed anomalies.

The shear-wave splitting maps for the reservoir level determined from the Baseline and Monitor 2 shear wave data are depicted in Figure 2.55. Shear waves are very sensitive to fractures and associated changes in these fractures due to CO_2 flooding. Changes are largely due to changes in effective stress, but they could also be due to geochemical changes in the reservoir. Note the zone of increased anisotropy that forms a curvi-linear pattern along the SE and NE sides of the diagram. Also shown, in Figure 2.56, is the map of S-wave amplitude differences for the Monitor 2 survey. With the exception of a strong amplitude anomaly in the southern pattern, the amplitude anomalies are relatively weak. In contrast to the P-wave amplitude anomalies (Figure 2.52), there does not appear to be a strong spatial correlation with the horizontal injection wells.

5.2.4 Passive seismic monitoring

An array consisting of 8 triaxial geophones was cemented in a vertical well 101/06-08 (see Figure 2.57 for location) of the Phase 1B flood area. As part of EnCana's normal operation, this well was being abandoned and replaced with a new, vertical CO_2 injection well (121/06-08) within approximately 50 m of the monitoring well. This offered an unique passive monitoring scenario in which a seismic array could be installed close to the reservoir and cemented as part of the normal well abandonment and then used to monitor injection at close proximity to the array.

Background seismicity was recorded with the array between August, 2003, and January, 2004, (see Table 2.5 for a summary) prior to the start of CO_2 injection in well 121/06-08. Figure 2.57 shows a map around the monitoring well, including vertical and horizontal patterns of production and injection wells. Also shown in Figure 2.57 is an expected detection range (orange circle) of about 400 m, based on previous passive monitoring examples (Maxwell and Urbancic, 2003). As indicated in the figure, there are no specific injection wells close the monitoring well prior to the drilling of the new, 121/06-08 WAG (water alternating gas) injector. Nevertheless, several events were recorded during this background period, the majority of which were related to completion procedures of the new well.

Table 2.5 Summary of seismicity detected over 8 months of recording.

Time Period	No. of detected events	No. of Days
12/08/03-18/09/03	6	38
19/09/03-19/11/03	6	60
20/11/03-18/12/03	15 (includes events during completion of well 121/06-08	29
19/12/03-01/02/04	16 (15 start after start of CO_2 injection on Jan. 21)	45
02/02/04-29/02/04	4	28
01/03/04-31/03/04	15	31

In January, 2004, CO_2 injection began in the 121/06-08 well, resulting in associated microseismicity. Figures 2.58a and 2.59a show locations of events recorded in the five week period following the start of injection. The events were concentrated in a region between the injector and the closest active production well (191/11-08). Figure 2.60 shows a comparison between the gas injection and microseismic activity rates. The seismicity began near the start of CO_2 injection, but upon close inspection, actually occurred as a set of events during the final stages of water injection and a second set of events during the transition from water to CO_2 injection. Figure 2.60a shows the production data from the 191/11-08, where a significant increase in gas production occurred with the introduction of the CO_2 in 121/06-08.

Subsequent to the swarm of events near the start of CO_2 injection, low activity rates were recorded until March 18-19, 2004, when 15 events were detected (see Figures 2.58b and 2.59b) with locations near production well 191/09-08. At this time, production was shut-down in this well (Figure 2.60b). A similar seismic response was observed in September, 2003, when this well was shut-down. Based on the temporal correlations of microseismicity with production history, most seismic events appear to be associated with changes in production (well shut-down) or injection changes (water to gas) where local pressure transients might be expected. Otherwise, microseismicity is low during the intervening periods of CO_2 injection. The lower limit of detectable seismic events with distance from the recording array is shown in Figure 2.61.

5.2.5 Soil gas sampling

Soil gas studies were undertaken (see Figure 2.62 for locations) with the primary objectives of measuring the natural background concentrations and ascertaining if there is a leak of CO_2, or associated tracer gases, as a direct result of the solvent flood presently occurring at the EnCana Weyburn oilfield. There were three periods of sampling between July, 2001, and October, 2003. Sampling of the 360 point grid above the injection area over this time range showed CO_2, O_2, and CO_2 flux values in the range of natural soils, and these observed levels can be explained by standard metabolic pathways that normally occur in the shallow soil horizon. The spatial anomaly distributions of these gases (Figure 2.63) are reasonably reproducible from year-to-year and season-to-season, despite the fact that the range of values varies from high concentrations in the hot, wet summer of 2001 to low concentrations found in the autumns of 2002 and 2003 (Figure 2.64). In contrast to these biologically active species, the statistical and spatial distribution of radon and thoron is very similar from one sampling season to the next. This provides support for the assumption that leakage is not taking place, as one would expect to see high radon during the periods of high CO_2 if the latter were acting as carrier for the former, which is a more trace gas. Hydrocarbon values were found to be within normal ranges in October, 2003, but the previous two seasons showed elevated values that were not fully expected. In fact, ethylene and propane showed a statistical distribution over the three years that is quite similar to that of CO_2, whereas methane and ethane had relatively constant values, except for more concentrated outliers during the first and second seasons. As the heavier hydrocarbons do not normally originate via shallow biological reactions, it is difficult to reconcile these results with those of the other gases.

A comparison of the grid data with that of the background site, located in similar surface geology but outside the Weyburn oilfield, shows a very similar statistical distribution for all monitored parameters. This result supports the interpretation that the observed gas concentrations are not due to deep leakage (Figure 65). In particular, both sites have a very similar CH_4 / (C_2H_6 + C_3H_8) ratio. This value is low and in the range of the thermo-catalytic regime; however, the fact that such a value was found both within and outside of the oilfield implies that the origin of these gases is not necessarily a deep oil reservoir.

Highly detailed horizontal profiles performed across radon and CO_2 anomalies defined during the first-year sampling of the main grid were used both to select sites for the installation of the long-term radon monitoring probes, as well as to study in detail the elevated soil gas concentrations and to relate them to surface lineaments. The work conducted on these profiles showed reproducible trends for CO_2, CO_2 flux, and, to a lesser extent, radon, with anomalies occurring in correspondence with low lying areas and surface water. Although some of these coincide with mapped lineaments, which could, in theory, be the surface expression of deep faults, it is more likely that these lineaments are shallow features that accumulate water and nutrients and thus produce biologically created anomalies.

Background measurements were also made at a remote site located 10km NW of the main soil gas study area. In general, the background site showed a similar range of soil gas concentrations to the main study grid, with radon, thoron, and some heavier hydrocarbon gases having slightly higher values (Figure 2.65). This confirms that the levels seen within the CO_2 injection area are normal for such prairie soils and lends further support to the body of evidence indicating a biogenic origin for the CO_2.

Finally, work was also performed on a number of sites that could represent possible vertical migration pathways, including two decommissioned wells, a river lineament, and a salt collapse structure with its

associated faulting. Soil gas concentrations for the two wells were well within the range of data from the main soil gas grid, but the suspended well had, on average, somewhat higher CO_2 values, and the completely abandoned well slightly higher methane and ethane contents than the grid. However, sites around the wells with higher CO_2 or methane/ethane were not associated with higher levels of other gases, such as the highly mobile tracer gas helium, radon, or other hydrocarbons. Although small scale leakage cannot be entirely ruled out, there is no strong evidence for it. Further investigation would, however, be warranted to better understand the results. The river lineament shows some weak CO_2 anomalies, but their positions, and the general lack of accompanying higher levels of other gases, support a biogenic origin, rather than being indicative of deep gas escape. There are some He anomalies on one profile across the lineament that could be considered for more detailed future follow-up work. The salt collapse structure has generally low concentrations of soil gases and no significant levels, except for some anomalous He results on one profile, that merit further investigation.

Overall, there is no evidence so far for escape of injected CO_2 from depth. Further monitoring of soil gases is necessary to verify that this remains the case in the future and more detailed work is required to better understand the causes of variation in soil gas contents, and to investigate further possible conduits for gas escape.

5.3 Integrated Interpretation of Monitoring Results

5.3.1 Pressure versus saturation effects in seismic monitoring

A variety of evidence indicates that CO_2 saturation effects dominate over pressure-induced effects in the P-wave time-lapse seismic images. Although core sample measurements (Table 2.2) indicate that changes in Vp due to pressure increases can be comparable to saturation effects for pressure changes in the observed range (5-10 MPa, Figures 2.16 to 2.19), both the detailed seismic modeling (Figures 2.21 to 2.24) and the comparison of the seismic results with the production data indicate that this is not generally the case.

First, small magnitude P-wave seismic anomalies occur in the areas of the Phase 1A area where the largest changes in reservoir pressures have occurred during injection. In contrast, the area where the most areally extensive and largest magnitude anomalies are found corresponds to a region where pressures decreased, which should result in anomalies of the opposite type to what was observed. Second, predicted CO_2 thickness maps (Figure 2.66) determined by converting the delay times to CO_2 thickness for a range of fractional velocity changes compare best with expected reservoir thickness when velocity change is estimated between 10 and 14%. Velocity changes of up to 10% can be accounted for by saturation effects (see Section 5.1.2.5). Regions on the map where the difference is negative correspond to areas where the modeled saturation relation does not adequately account for the observed travel time delays within the thickness of the reservoir. These local discrepancies could be due to unaccounted pressure contributions responsible for maximum fractional velocity decreases of 3 to 4%. Finally, the absence of correlation between the P-wave and S-wave time-lapse anomalies (compare Figures 2.52 and 2.55) suggests that the prominent P-wave anomalies are primarily saturation-related. If pressure contributions were comparable, a similar anomaly pattern would be expected on the S-wave anomaly maps as the S-wave velocities are generally less sensitive to pore fluid saturation.

5.3.2 CO_2 distribution within the reservoir

Geochemical and seismic monitoring maps are compared to the injection volumes and reservoir geology in Figure 2.67. Recognizing the difference in spatial sampling of the geochemical and seismic anomaly maps, strong regional correlations are apparent between them as well as with some of the primary geological features of the reservoir. The former observation increases confidence in the ability of the monitoring techniques to track the distribution of CO_2 within the reservoir, and the latter strongly suggests that the spread of CO_2 is controlled by specific geological features within the reservoir (*e.g.*, depositional facies and fracture systems). A number of observations have been noted. First, there is a very strong correlation between the Vuggy shoal thickness (Figure 2.67a) and the trends on the geochemical maps (Figures 2.67.b and c), suggesting that the geochemical sampling is most sensitive toward CO_2 distribution within the Vuggy unit. Second, the seismic (Figure 2.67e and f) and geochemical maps (Figures 2.67b and c) both indicate that little CO_2 is present within the northern side of the Phase 1A area, consistent with the smaller injection volumes (Figure 2.67d) in patterns 1624, 0630, 0625, 0626, and 1626. Also, relatively low porosities occur in this region (particularly in the Marly unit) and most of the CO_2 injected here is predicted to reside in the Vuggy interval (see simulation results in Figures 2.9 and 2.10). Both of these factors contribute to a reduced seismic response (see Table 2.2). Third, the strongest anomalies on the $\delta^{13}C$ and the seismic anomalies occur within the same area (patterns 1612 and 0613). Fourth, both seismic and $\delta^{13}C$ maps indicate intermediate amounts of CO_2 within the southwest part of Phase 1A (patterns 1602 and 0611), although the Ca distribution suggests a high degree of mineral dissolution here. Fifth, the largest degree of mineral dissolution (as indicated by the Ca distribution map) corresponds to the region where the largest volume of CO_2 has been injected. Sixth, intermediate values on the geochemical maps occur in the northwesternmost patterns (0623, 1623, and 0626) where there is little seismic response. Again, the lack of a significant seismic response is probably due to CO_2 residing primarily in the Vuggy interval.

Figure 2.68 provides a comparison of the seismic anomalies (amplitude and travel time delay) and the distribution of CO_2 response wells. Comparing the amplitude and time delay anomaly maps (Figures 2.68a,b and c,d), the distribution of travel time anomalies corresponds reasonably well with the large amplitude anomalies but show fewer fine details or spurs extending away from the injectors. This is consistent with the reduced sensitivity of the travel times as compared to the amplitude anomalies. By the time of the Monitor 1 survey (15 months post injection start-up), CO_2 responses had occurred exclusively in horizontal production wells. This is reasonable, as in most cases horizontal wells are the nearest producers to the horizontal injection wells. Of the 13 wells that showed CO_2 responses by the time of Monitor 1, 12 are connected to the nearest production well by seismic amplitude anomalies, providing a ready explanation of the flow path. The one horizontal well (labeled "C") that showed a response but no clear path actually has a seismically determined path on the higher resolution 4-pattern images (see Figure 2.70). However, a number of horizontal production wells have associated amplitude anomalies by Monitor 1, but do not show CO_2 responses (*e.g.*, A, B, D, E, and F). Three of these wells (A, B, and D) are located along the edges of the seismic coverage and, thus, may be considered less reliable, leaving two wells (E and F) with apparently false positive results. These may be the result of data uncertainties or could indicate that the anomaly is actually associated with CO_2 within the underlying Vuggy unit, which has by-passed the horizontal producers in the overlying Marly interval.

In contrast to the Monitor 1 amplitude anomalies, only 4 of 13 response wells are connected to CO_2 injectors by time delay anomalies (Figure 2.68c). However, there are no cases in which the time delay anomalies occur at production wells where no CO_2 response is observed (*i.e.*, no false positives). The absence of time delay anomalies but presence of amplitude anomalies where CO_2 responses have been recorded indicates that the CO_2 resides within a restricted interval of the reservoir that is insufficient to produce a delay time anomaly. Based on the amplitude modeling, this interval likely lies within the Marly unit. This is supported by impedance inversion results from the 4-pattern area (Figure 2.69) where a strong spatial correlation exists between the large magnitude impedance changes in the Marly interval and the amplitude anomalies, in contrast to the Vuggy impedance changes which are more diffuse.

By the time of the Monitor 2 survey (28 months post injection start-up), the correspondence between 2001 CO_2 response wells and seismic delay time anomalies increased to 6 of 13 and showed good

correspondence for 3 of the 7 2002 vertical producers (away from the perimeter) that have a CO_2 response. Four wells (G, H, and 2 at I) do not have clear seismic anomalies connecting them to injection zones. Lack of a corresponding seismic anomaly for response wells may be due to access to the producer through the Vuggy unit, to which the seismic response is less sensitive, or access may be via a narrow fluid pathway that is not imaged. The better correlation of the amplitude anomaly maps, as compared to the time delay anomaly maps, with the horizontal producers with CO_2 responses, supports the conclusion that the amplitude anomaly maps are more sensitive to mapping the CO_2 within the Marly interval.

In addition to the main amplitude anomalies, there are also smaller off-trend anomalies that suggest that channeling of the CO_2 is occurring in some areas. One example, in which an E-W spur is observed emanating from the main anomaly, is highlighted in Figure 2.70 (see arrow). A similar trend is observed on the spatially coincident attenuation (or calculated permeability) image from Figure 2.46 (inset in Figure 2.70) and to a lesser extent on the S-wave amplitude difference map (Figure 2.55). These observations imply the presence of enhanced permeability, which may be part of a larger pattern as described below.

A curvi-linear pattern of S-wave identified anisotropy correlates spatially with a similar pattern on the $\delta^{13}C$ map in Figure 2.71. This correlation is highlighted for a sub-area (red rectangle), which is expanded in the inset of Figure 2.71. There, zones of high anisotropy (outlined by heavy black lines) generally follow the contours along the fringe of the $\delta^{13}C$ map. Furthermore, this pattern generally follows the salt dissolution edge (white dashed line in inset of Figure 2.71) of the underlying Prairie evaporite, suggesting that a network of fractures may exist within the reservoir in association with salt dissolution. Alternatively, the observed anisotropic zone may be associated with depositional facies-controlled features as it approximately corresponds to the transition from intershoal to shoal depositional facies in the Vuggy unit. In any case, both the seismic and geochemical results strongly suggest that the CO_2 flood is advancing preferentially along this zone of enhanced permeability.

5.3.3 Seismic detection limits

An important question that arises in monitoring is "What is the smallest volume of CO_2 injected that can be detected?" This will depend on a variety of factors, including the porosity and fluid saturation of the injection formation, the repeatability of the seismic measurements (determined by noise, surface recording conditions, *etc*.) and, fundamentally, the frequency content of the seismic wavelet and the seismic wavespeed (V_p for compressional waves) of the subsurface. For the purposes of this discussion, the Midale reservoir units are considered.

Both seismic time-lapse travel time delays and amplitude differences have been utilized for monitoring, and they have different detection capabilities. The travel time delay measures a cumulative effect (*i.e.*, the product of fractional travel time change x thickness) and, thus, is capable of detecting local zones with relatively high fractional velocity change (*e.g.*, CO_2 saturation within the reservoir unit) or a thicker zone with low fractional velocity change (*e.g.*, either due to lower porosity or low CO_2 saturation). However, it is incapable of resolving thin layers (*e.g.*, the Marly from the Vuggy). In contrast, amplitude differences implicitly have greater potential for resolving thin zones (*e.g.*, Marly from the Vuggy) but are less sensitive to low fractional velocity changes over a larger depth interval.

In the case of travel time delays, the vertical resolution is determined by the minimum travel time difference that can be reliably identified combined with the travel time sensitivity to changes in the geological unit. Observing the travel time differences for the monitoring surveys at a reference horizon, where no travel time delays are expected (the Lower Gravelbourg; see Figure 2.50), shows travel time delay standard deviations of ~0.4 ms. Using the travel time modeling results (Figures 2.26 and 2.27, where 80% CO_2 is assumed) this delay corresponds to ~4 m in the Marly unit (porosity of 29%) or ~12 m in the Vuggy unit (porosity of 8%). Taking the product of the fractional porosity, fractional CO_2 saturation, and the thickness provides a thickness of CO_2 of 0.96 to 1.17 m at reservoir conditions. The minimum detectable volume is then the product of this thickness with the lateral resolution estimate. For wavelength, Fresnel radius, or smoothing interval, these areas are 60mx60m=3600 m^2, 200m radius=125664 m^2, and 120mx120m=14,400 m^2. Thus, the minimum detectable volume estimates range from 3500 m^3, 121000 m^3,

to 14000 m^3 at reservoir conditions. Converting these to standard conditions, the obtained values are 1 million m^3 (1900 tonnes), 35 million m^3 (65000 tonnes), and 4 million m^3 (7500 tonnes), respectively. The size of the smoothing operator (between the wavelength and Fresnel zone estimates) provides a reasonable estimate of the detection volume – 4 million m^3 or 7500 tonnes. If the CO_2 is present as a free gas so that saturations as low as 10% (as compared to 80%) produce a similar response, then these detection limits may be reduced by a factor of eight. This *proviso* also applies to the amplitude calculations in the next paragraph.

The amplitude modeling tests (Figures 2.21) show detectable amplitude differences for 80% CO_2 saturation over a 2 m interval in the high porosity Marly unit and smaller, but detectable, amplitude differences for 80% saturation over a 5 m interval in the lower porosity Vuggy unit. These correspond to CO_2 thicknesses of 0.46 m and 0.32 m, respectively. Using the same lateral resolution estimates as for the travel time analysis, the minimum detectable volumes in the reservoir interval are 1150 m^3, 40000 m^3, and 4600 m^3 at reservoir conditions. Converting these to standard conditions, the values obtained are 0.34 million m^3 (620 tonnes), 11.7 million m^3 (22000 tonnes), and 1.4 million m^3 (2500 tonnes), respectively. Again, using the size of the smoothing operator, the estimated detection volume is 1.4 million m^3 or 2500 tonnes.

5.3.4 CO_2 containment within the reservoir

In addition to monitoring the spread of CO_2 within the reservoir, the seismic data provide a means of assessing potential leakage of CO_2 into the overlying strata, subject to certain assumptions and limiting uncertainties. First, there are leakage scenarios that would be difficult to detect seismically. For example, if CO_2 were dispersed at low saturation levels over a large depth interval above the reservoir or if CO_2 were to migrate vertically through narrow conduits. Also, the seismic response to CO_2 in the overlying strata is not well known. However, using the seismic response observed at the reservoir level, and recognizing that the overlying strata above the Midale evaporite seal will be water-saturated (*i.e.*, generally devoid of hydrocarbons), and thus conducive to the presence of CO_2 as a free gas, some preliminary estimates can be made.

Toward this end, amplitude and time delay anomaly maps (Figure 2.72) for the reservoir interval (~1150 ms or 1400 m) were compared against those in the overlying 200 m, including the Watrous (1100 ms or 1300 m), Lower Gravelbourg (~1080 ms or 1230 m), and Lower Vanguard (~1000 ms or 1130 m) horizons. As seen in Figure 2.72, away from the edges of the seismic coverage, where the results are unreliable, there are no seismic time delay or amplitude anomalies that are comparable in areal extent or magnitude to the anomalies observed at the reservoir level. This provides some reassurance that the vast majority of the injected CO_2 remains within the reservoir and that the anomalies observed at the reservoir level are highly significant. There are, however, present at the various horizons, small magnitude anomalies with limited spatial extent that could be due to either data uncertainties or to CO_2 leakage. Assessment of the significance of anomalies of this scale is highly subjective. But to provide a first-order estimate of an upper limit on potential CO_2 leakage, assume these anomalies are assumed to be real. Considering the travel time anomaly at the Watrous horizon, which should include the integrated travel time effects of the entire overlying column, the area covered by values exceeding the threshold at this horizon represents ~3% of the area of the time delay anomaly observed at the reservoir level. This does not account for the magnitude by which the time delays exceed the threshold value, which would further reduce the significance of the time delay observed at the Watrous horizon. Taken at face value, but recognizing the simplifying assumptions that have been made, this result suggests that the maximum amount of CO_2 that may have migrated above the Watrous horizon is <2-3% of the injected volume. Note that there is no independent evidence to suggest that any significant volume of CO_2 has actually migrated above the reservoir.

6 VERIFICATION: MAPPING OF THE VOLUME AND DISTRIBUTION OF INJECTED CO_2

6.1 First-order Volumetrics

It is clear that the P-wave time-lapse seismic images at the reservoir largely depict CO_2 saturation as opposed to pressure changes (Section 5.3.1). To further scrutinize this conclusion, and to assess the volumetric implications to be drawn from the seismic results, focus is placed on a 4-pattern area within the Phase 1A region (Figure 2.70). As seen, the areal extent of the anomalies surrounding each of the four dual-leg horizontal injection wells is proportional to the net cumulative amount of CO_2 injected, whether the comparison is made for different injectors in the same monitoring survey or for the same injector in subsequent monitoring surveys.

To obtain a first-order sense of whether the reservoir volumes implied by the areal size of the seismic anomalies are reasonable compared to the volume of injected CO_2 volumes and whether the volume differences implied by the seismic anomalies are proportional to the temporal and spatial variations of injected CO_2 volumes, it is useful to consider some simple end-member volumetric calculations. Using the average reservoir porosity and thickness values in the immediate vicinity of the 4-patterns in conjunction with the area of the seismic anomalies on a pattern-by-pattern basis, the reservoir volume associated with the seismic anomalies can be determined. This volume exceeds the volume of injected CO_2 (see Tables 2.6 and 2.7) by a factor of 4.6 to 5.5, implying mean CO_2 saturation values of 0.19 to 0.23 for the entire reservoir interval. Higher mean CO_2 saturations of ~0.3-0.5 are estimated if the CO_2 is restricted to the Marly or Vuggy units. It is implicitly assumed in these volumetric calculations that the CO_2 exists as a free gas. In reality, the actual volume occupied by the injected CO_2 will be affected by the degree to which it is dissolved in the other reservoir fluids. Due to the contrast in solubility of CO_2 in brine versus oil at reservoir conditions (see Table 2.1), this effect should be most significant where large quantities of oil are encountered, and least significant where the pore fluid is largely brine.

The net injected volume of CO_2 over the 4-pattern area increases by 70% between the Monitor 1 and Monitor 2 surveys, whereas the ratio of seismic volume estimate to the injection volume (see Tables 2.6 and 2.7) varies by 17%, reflecting a direct but inaccurate relationship between the areal size of the seismic anomalies and the net volume of injected CO_2. On a pattern-by-pattern basis, there is more variability with mean increase in net CO_2 injection volume of 59 ± 18%, and a mean change in seismic/injection ratio of 23 ±11%. A similar comparison of these quantities between patterns within the same monitoring survey shows less consistency in the relationship between injection volume and areal extent of the seismic anomaly. This increase in variability may reflect heterogeneity in the reservoir that is unaccounted for in these simple calculations.

Table 2.6 Ratio of the net CO_2 injection volumes to 2001 from production data versus from seismic estimation. The seismically estimated volumes are based on mean thickness and porosity values for the Marly, Vuggy, and combined Marly-Vuggy (Table 2.8) within the 4-pattern area of Figure 70 and the area covered by the seismic anomalies. The assumption is that the entire pore space is filled by CO_2, and, thus, in this regard, the seismically determined volume estimate represents a maximum estimated volume. Reservoir pressure and temperature used for the calculations are 15 MPa and 63° C, respectively.

	Seismic vol./CO2 vol. Ratio			Mean Saturation		
Pattern	Marly Only	Vuggy Only	Marly & Vuggy	Marly Only	Vuggy Only	Marly & Vuggy
0618	2.37	2.92	5.28	0.42	0.34	0.19
1613	3.86	4.75	8.61	0.26	0.21	0.12
1612	2.44	3.00	5.44	0.41	0.33	0.18
0613	1.41	1.73	3.14	0.71	0.58	0.32
Mean (excl. 1613)	2.07	2.55	4.62	0.51	0.42	0.23

Table 2.7 Ratio of the net CO_2 injection volumes to 2002 from production data versus from seismic estimation. The seismically estimated volumes are based on mean thickness and porosity values for the Marly, Vuggy, and combined Marly-Vuggy (Table 2.8) within the 4-pattern area of Figure 2.70 and the area covered by the seismic anomalies. The assumption is that the entire pore space is filled by CO_2, and, thus, in this regard the seismically determined volume estimate represents a maximum estimated volume. Reservoir pressure and temperature used for the calculations are 15 MPa and 63° C, respectively.

	Seismic vol./CO2 vol. Ratio			Mean Saturation		
Pattern	Marly Only	Vuggy Only	Marly & Vuggy	Marly Only	Vuggy Only	Marly & Vuggy
0618	2.80	3.45	6.25	0.36	0.29	0.16
1613	5.66	6.97	12.63	0.18	0.14	0.08
1612	2.78	3.42	6.19	0.36	0.29	0.16
0613	1.78	2.20	3.98	0.56	0.46	0.25
Mean (excl. 1613)	2.45	3.02	5.48	0.43	0.35	0.19

Table 2.8 Mean properties for reservoir units in the 4-pattern area of Figure 2.70. The reservoir properties (thickness and porosity) were determined from the detailed geological model.

Unit	Mean fractional Porosity	Mean thickness (m)
Marly	0.23	6
Vuggy	0.10	17
Marly & Vuggy	0.13	23

Applying the same volumetric analysis to the larger 9-pattern area (see Figure 2.2 for location relative to 4 –pattern area), mean CO_2 saturation levels of ~0.20-0.25 are indicated (Figure 2.73) for most of the patterns. This is consistent with results from the simulator, which indicate that mean CO_2 saturations are ~0.2 in the simulated results when mean CO_2 saturation is determined over the areas where simulated values exceed 0.05 at the time of the Monitor 2 survey. The largest discrepancies occur for the VWAG patterns, as noted previously. More sophisticated volumetric comparisons that account for such heterogeneity are provided in Section 6.2.

6.2 Reservoir Simulation/History Matching With Seismic Constraints

An iterative process of reservoir simulation, comparison of simulated and seismic–derived CO_2 distribution, and modification of the reservoir permeability model has been conducted using the P-wave results from the Phase 1A area. This iterative methodology is depicted schematically in Figure 2.74. The potential advantage of using the seismic data is the interwell detail of the CO_2 distribution that is provided. Although the time-lapse seismic data do not uniquely resolve CO_2 distribution within the Marly and Vuggy units, the modeling results of Section 5.1.2.4 suggest that the time delay anomalies are sensitive to CO_2 in the Marly or Vuggy, whereas the amplitude anomalies determined at the Marly horizon are particularly sensitive to CO_2 in the Marly unit. Thus, the areal extent of Marly amplitude anomalies is used as a proxy for the presence of CO_2 in the Marly unit and the time delay maps as a more general indicator of CO_2 distribution in the reservoir. This approach provides some discrimination of the vertical distribution of CO_2 within the reservoir.

Figures 2.75 and 2.76 show a comparison of the CO_2 areal distribution within the Marly unit predicted by the seismic data at the time of the Monitor 2 survey compared to the distribution from the reservoir simulator obtained using the original reservoir model. As seen, there is relatively good agreement in the immediate vicinity of the horizontal injection wells (Figure 2.75), but there are also significant areas of disagreement. A total of 10 iterations of model updates were performed with local changes to permeability applied to improve the fit of the reservoir simulations to the production and seismic data. In each of these iterations, the time delay map was used as a constraint against the gas saturation in the combined Marly and Vuggy Formations. Subsequently the focus changed to matching the amplitude data with the CO_2 distribution in the Marly unit, where the reservoir simulator predicted larger areas of gas saturation in the Marly around the majority of horizontal injection wells (see Figure 2.77). This next stage was implemented on a pattern-by-pattern basis in the central 9-pattern area (see Figure 2.2 for location), as described below. After the majority of patterns had significantly improved, a final full field simulation was run. The results shown in Figure 2.78 and Figure 2.79 illustrate the mismatch by pattern and iteration. As can be seen, the

attempts to better match the simulator and seismic saturation estimates have been successful in most patterns but not all. The volume of injected CO_2 from production data vs. seismic is shown in Figure 2.80. For five of the patterns, the seismic estimate is within 20% of the known volume of injected CO_2, consistent with the earlier simple volumetric calculations. For the other five patterns, the seismic estimate is very different than the injected volume, in some cases overestimating and other cases underestimating.

The need to focus on the simulation pattern-by-pattern is demonstrated by injection Pattern 06-13-006-14W2. Figure 2.81 shows a comparison of the Monitor 2 seismic anomaly for the Marly horizon and the simulation result in the vicinity of this injector. As can be seen, the simulated CO_2 distribution within the Marly is much broader than indicated by the seismic anomaly. The model behaviour in this part of the field was dominated by the presence of an extremely low permeability interval that inhibited the downward migration of CO_2 into the Vuggy unit, resulting in a broad distribution of CO_2 within the Marly unit. Careful examination of the injection pressure histories suggested that there may be a vertical permeability pathway, in the area of the CO_2 injection well, associated with either fractures or crossflow between existing vertical wells that spanned the Marly and Vuggy zones. Based on this observation, the vertical permeability was increased near the injection well, resulting in a reduced volume of CO_2 in the Marly unit (Figure 2.82b and Figure 2.83) and leading to an improved match between the simulated production and the production history (compare Figures 2.84 and 2.85). This demonstrates the potential for improving the reservoir model using the additional constraints provided by seismic.

An alternate approach to seismic-based reservoir simulation within the Weyburn field attempts to explicitly account for the fracture permeability within the reservoir (Terrell, 2004). In this case, shear wave anisotropy is used to identify the distribution of fracture networks within the reservoir, which then form the basis for constructing a fracture permeability model for flow simulation (Figure 2.86). The resulting flow simulation produced an improved history match for the water and CO_2 floods. Incorporating shear wave anisotropy into reservoir modeling and simulation represents a promising and important new contribution to work in the Weyburn field. Previously, the only way to include fracture permeability was through well testing, reservoir simulation, and history matching. These models that explicitly incorporate fracture permeability are important not only for history matching, but also for forward prediction. Early prediction of these fracture networks would help in well planning and flood pattern rollout.

6.3 Improved Prediction

Improved knowledge of the reservoir provided by the various monitoring techniques should ultimately provide an improved reservoir model leading to more accurate flow simulations. Flow-simulator predictions can be used as the basis for optimizing the flood management for the field. It allows various injection and production scenarios to be tested. As an example, Terrell (2004) used the fracture-permeability model to forecast production under two scenarios (Figure 2.87) within the Phase 1A four-pattern area focused on by CSM. One scenario was to continue using only the current four horizontal injectors. The second scenario involved converting several vertical wells, in between the horizontal injection patterns, to CO_2 injectors. In addition, a vertical well, as yet undrilled, was added to the unswept central area. The result projects an 80,000 m^3 increase in oil production over a ten-year period. This incremental recovery would pay for the seismic survey costs 10 to15 times over. Another cost savings is a reduction in the amount of carbon dioxide processed and recycled.

7 CONCLUSIONS AND RECOMMENDATIONS FOR FUTURE WORK

7.1 Conclusions

The ability of seismic and geochemical sampling methods to monitor physical and chemical changes in the Weyburn reservoir induced by CO_2 injection has been clearly demonstrated. Both methods are capable of determining the areal distribution of CO_2 within the reservoir, although at different levels of detail. A number of conclusions have been drawn from this work.

Comparison of time-lapse anomalies from independent P-wave data sets and at horizons above the reservoir, where no changes are expected, demonstrates that the seismic observations are robust, clearly exceed background noise levels, and show good repeatability. Generally, the areal extent of the seismic anomalies surrounding any of the dual-leg horizontal injection wells in the SSWG patterns is directly related to the net cumulative amount of CO_2 injected.

Rock and fluid property measurements, log-based synthetic seismic modeling, and reservoir simulation/production history matching with seismic constraints all indicate that P-wave time-lapse seismic monitoring is highly sensitive to the presence of a CO_2-rich gas phase within the reservoir, even at low levels of saturation (5-10%), whereas pressure effects are a secondary factor. Estimated maximum saturation effects include Vp decreases of 4-10%, and reflection amplitude decreases of 30-40%, as compared to Vp decreases of < 3% for pressure effects. This sensitivity to low-saturation CO_2 makes the P-wave time-lapse images very good at mapping regions of the reservoir where CO_2 is present and at identifying the CO_2–front, but makes accurate seismic-based volume estimates difficult. Reliable seismic-based volume estimates can only be made in conjunction with CO_2 saturation estimates from reservoir flow simulations.

Volumetric analysis suggests a mean CO_2 saturation of ~20% over the entire reservoir interval in the areas identified by the P-wave seismic amplitude anomalies. This is similar to mean values determined from the reservoir simulator results when calculated over areas where the simulated CO_2 saturation exceeds 5%.

Smaller off-trend anomalies in the P-wave images have been identified, suggesting that channeling of CO_2 is occurring in some areas. This observation is further supported by S-wave data, which have identified anisotropic zones potentially associated with fracture systems. Spatial correlation of such zones with geochemical anomalies, and more locally with a horizontal crosswell image, suggests a network of fractures exists within the reservoir with enhanced permeability that allows preferential advance of the CO_2 flood.

The seismic data do not uniquely resolve the upper (Marly) and lower (Vuggy) units of the reservoir. However, the heightened sensitivity of the amplitude response to changes in the Marly unit allows partial discrimination of vertical CO_2 distribution using a combination of amplitude and time delay anomaly maps. The geochemical maps appear to be most sensitive to CO_2 distribution within the Vuggy unit.

1.4 million m^3 (at standard conditions or 2500 tonnes) or 4 million m^3 (at standard conditions or 7500 tonnes) are estimates of the smallest amounts of CO_2 at the reservoir level that could be detected using the time-lapse P-wave amplitude differences or travel time delays, respectively. These estimates may be overly conservative by a factor of 8, based on the sensitivity of the seismic anomalies to low saturations of CO_2.

Based solely on the seismic results, it is estimated that the maximum amount of CO_2 that may have migrated above the reservoir is <2-3% of the total injected volume. However, there is no independent evidence to suggest that any significant volume of CO_2 has actually migrated above the reservoir. There is no evidence from the soil gas sampling for migration of measurable amounts of CO_2 into the overburden or to the surface.

Approximately 60 microseismic events with magnitudes ranging from –3.0 to –1.0 were recorded during 6-months of monitoring with a seismic array just above the reservoir. Almost all of the events appear to be associated with changes in production or injection changes (*e.g.*, water-to-gas), where local pressure

transients might be expected. Magnitudes and occurrence frequency of microseismicity are low during periods of CO_2 injection and appear to be equal to or less than values characteristic of microseismicity associated with waterflooding that has been ongoing for more than 30 years.

An integrated approach, linking simulation history matching with time-lapse seismic, has been applied, resulting in reduced non-uniqueness in the time-lapse seismic interpretation and more efficient (*i.e.*, fewer iterations to match) history matching. The potential for seismic-based improvement of reservoir modeling and prediction has been demonstrated further by using the pre-injection spatial variability of anisotropy to estimate fracture permeability. A fracture-enhanced single porosity reservoir model provides significantly improved history matches to waterflood breakthrough responses and predicted CO_2 saturation anomalies that replicate the shape and distribution of time-lapse anomalies seen in the seismic data.

Geochemical monitoring identified the reaction of injected CO_2 with formation water (*i.e.*, CO_2 dissolution; $CO_2 + H_2O \Leftrightarrow H^+ + HCO_3^-$) occurring within six months, and becoming significant within 10 months. Reservoir rock reactions with injected CO_2 (carbonate mineral dissolution; $H^+ + CaCO_3 \Leftrightarrow Ca^{2+} + HCO_3^-$ and $2H^+ + MgCa(CO_3)_2 \Leftrightarrow Mg^{2+} + Ca^{2+} + 2HCO_3^-$) was apparent within approximately 20 months. There is conclusive evidence of CO_2 storage as bicarbonate in water and within the oil phase, both of which represent viable long-term storage methods. Permanent storage of CO_2 in carbonate minerals depends on reactions of CO_2 with silicate minerals; there has been no evidence for the occurrence of these reactions over the initial 24 months of monitoring, which is consistent with the reaction rates being too slow to be observed directly within the span of this study.

The path of injected CO_2 can be traced geochemically due to distinct isotopic signatures associated with the injected CO_2 ($\delta^{13}C$ value of –35 ‰ versus the higher pre-injection $\delta^{13}C$ value of –6 to –20 ‰). Regions of lower $\delta^{13}C$ values correspond to the regions of maximum CO_2 injection, although the values are also affected eventually by the competing effect of mineral dissolution.

7.2 Gaps and Suggestions for Future Work

There are a number of knowledge gaps that, if filled, would advance the understanding of the reservoir response to CO_2 injection and the ability to monitor the associated changes. A large uncertainty exists in the mixing and solution state of fluids within the reservoir, which translates into significant uncertainty in interpreting the time-lapse seismic results. For example, most of the time-lapse results described here are based on an assumed presence of a CO_2-rich free gas component. This is reasonable in regions where brine is the dominant fluid component but is less accurate where large volumes of oil that will dissolve the CO_2 reside. Further work involving detailed seismic modeling and reservoir simulation is required to better quantify these effects. It is concluded that the monitoring results track the spread of CO_2 in the reservoir and identify zones of enhanced permeability. There is a general need to further verify these conclusions. Spinner, geochemical tracer surveys, and selective drilling, coring, and logging of vertical slimholes could be used to test the seismically determined CO_2 distribution and flow-path details along the lengths of horizontal wells and in the interwell regions. Interpreted prominent fracture zones (both in the reservoir and in the overburden) could be tested by selective drilling. Improved understanding of the seismic images would be achieved by *in situ* time-lapse geophysical logging and by further modeling of the seismic response. Isotope mass balance should be included as an additional constraint in reservoir simulations. A test of conformance control could be conducted and monitored seismically to determine how well it works, and follow-up work on using seismic data to monitor dissolution and the effects of mineral precipitation along high permeability fracture networks would be useful.

8 REFERENCES

Batzle, M. and Z. Wang, 1992, Seismic properties of pore fluids, *Geophysics*, 57, pp. 1396-1408.

Batzle, M., R. Hofmann, D. H. Han, and J. Castagna, 2001, Fluids and frequency dependent seismic velocity of rocks, *The Leading Edge*, 2, pp. 170-171.

Bell, J. S. and E.A. Babcock, 1986, The stress regime of the western Canadian Basin and implications for hydrocarbon production, *Bulletin of Canadian Petroleum Geology*, 34, pp. 364-378.

Biot, M. A., 1956, Theory of propagation of elastic waves in fluid-saturated porous solids, *Journal of the Acoustical Society of Applied Physics*, 26, pp. 182-185.

Brown, L.T., 2002. *Integration of Rock Physics and Reservoir Simulation for the Interpretation of Time-Lapse Seismic Data at Weyburn Field, Saskatchewan*, M.Sc. Thesis, Reservoir Characterization Project, Colorado School of Mines, Golden, Colorado, 208p.

Bunge, R. J., 2000. *Midale Reservoir Fracture Characterization Using Integrated Well And Seismic Data, Weyburn Field, Saskatchewan,* M.Sc. Thesis, Reservoir Characterization Project, Colorado School of Mines, Golden, Colorado, 204p.

Cardona, R., 2002. *Topics On The Seismic Characterization Of Fractured Reservoirs,* Ph.D. Thesis, Reservoir Characterization Project, Colorado School of Mines, Golden, Colorado, 218p.

Core Laboratories Canada Ltd., 1998. *Advanced Rock Property Study*, unpublished report for PanCanadian Resources, 59p.

Davis, T. L, M. J. Terrell, R. D. Benson, R. Cardona, R. R. Kendall, and R. Winarsky, 2003, Multicomponent seismic characterization and monitoring of the CO_2 flood at Weyburn Field, Saskatchewan, *Leading Edge*, 22, pp. 696-697.

Domenico, S. N., 1976, Effect of brine-gas mixture on velocity in an unconsolidated sand reservoir, Geophysics, 41, pp. 882-894.

Fuck, R. F., 2003, The latest on shear wave volumes: *RCP Spring Meeting Report*, pp. 20-21.

Gassmann, F., 1951, Uber die Elastizitat poroser Medien, Vier. *Der Natur*. Gesellschaft in Zurich, 96, pp.1-23.

Herawati, I., 2003, *The Use Of Time-Lapse P-Wave Impedance Inversion To Monitor A CO2 Flood At Weyburn Field, Saskatchewan*, M.Sc. Thesis, Reservoir Characterization Project, Colorado School of Mines, Golden, Colorado, 153p.

Hirsche, K., M. Batzle, R. Knight, Z. Wang, L. Mewhort, R. Davis, and G. Sedgwick, 1997, Seismic monitoring of gas floods in carbonate reservoirs: From rock physics to field testing, *67th Ann. Internat. Mtg: Soc. Of Expl. Geophys*., pp. 902-905.

Li, G., G. Burrowes, E. Majer, and T. Davis, 2001, Weyburn field horizontal-to-horizontal crosswell seismic profiling: Part 3 – Interpretation, *Society of Exploration Geophysicists 2001 Annual Meeting*, San Antonio, Expanded Abstract, 4 p.

Majer, E., V. Korneev, T. Daley, G. Li, T. Davis, J. Washbourne, and H. Merry, 2001, Weyburn field horizontal-to-horizontal crosswell seismic profiling: Part 1 – Planning and data acquisition, *Society of Exploration Geophysicists 2001 Annual Meeting*, San Antonio, Expanded Abstract, 4 p.

Maxwell, S. C. and T. I. Urbancic, 2001, The role of passive microseismic monitoring in the instrumented oil field, *The Leading Edge*, p. 636.

Maxwell, S. C., T. I. Urbancic, M. Prince, and C. Demerling, 2003, Passive imaging of seismic deformation associated with steam injection in Western Canada, *Society of Petroleum Engineers Annual Technical Conference and Exhibition*, Denver, Expanded Abstract *SPE* 84572, 8 p.

Maxwell, S. C. and T. I. Urbancic, 2003, Passive imaging of seismic deformation associated with injection for enhanced recovery, *SEG Annual Meeting*, Dallas, Texas.

McLellan, P. J., K. Lawrence, and K. Cormier, 1992, A multiple-zone acid treatment of a horizontal well, Midale Saskatchewan, *Journal of Canadian Petroleum Technology*, 31, pp. 71-82.

NIST Thermophysical properties of hydrocarbon mixtures database (SUPERTRAPP), Version 3.1, 2002.

Oldenburg, D. W., T. Scheuer, and S. Levy, 1983, Recovery of the acoustic impedance from reflection seismograms, *Geophysics*, 48, pp. 1318-1337.

Sheriff, R. E. and L.P. Geldart, 1995, *Exploration Seismology*, University of Cambridge Press, Cambridge, 592 p.

Terrell, M. J., 2004, *Fracture Permeability Characterization At Weyburn Field: From Shear Wave Anisotropy Through Flow Simulation*. Colorado School of Mines, PhD Thesis, 211 p

Wang, Z., W. K. Hirsche, and G. Sedgwick, 1991, Seismic velocities in carbonate rocks, J*ournal of Canadian Petroleum Technology*, 30, pp. 112-122.

Wang, Z., M. E. Cates, and R. T. Langan, 1998, Seismic monitoring of a CO_2 flood in a carbonate reservoir: a rock physics study, *Geophysics*, 63, pp. 1604-1617.

Washbourne, J., G. Li, and E. Majer, 2001, Weyburn field horizontal-to-horizontal crosswell seismic profiling: Part 2 – data processing, *Society of Exploration Geophysicists 2001 Annual Meeting*, San Antonio, Expanded Abstract, 4 p.

White, D. J., G. Burrowes, T. Davis, Z. Hajnal, K. Hirsche, I. Hutcheon, E. Majer, B. Rostron, and S. Whittaker, 2004, Grennhouse gas sequestration in abandoned oil reservoirs: The International Energy Agency Weyburn pilot project, *GSA Today*, 14, pp. 4-10.

Widess, M. B., 1973, How thin is a thin bed? *Geophysics*, 38, pp. 1176-1180.

Yilmaz, O., 1999. *Seismic Data Processing, Investigations in Geophysics Series, V. 2*, Society of Exploration Geophysicists, Tulsa, 526p.

Theme 2: Prediction, Monitoring, and Verification of CO_2 Movements

FIGURES

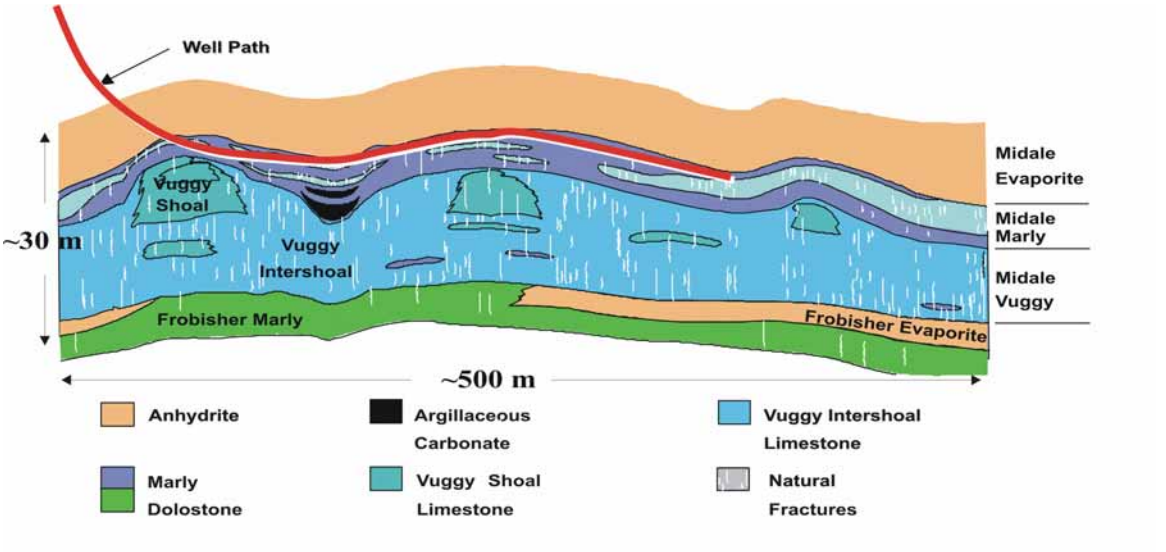

Figure 2.1: Schematic reservoir geology.

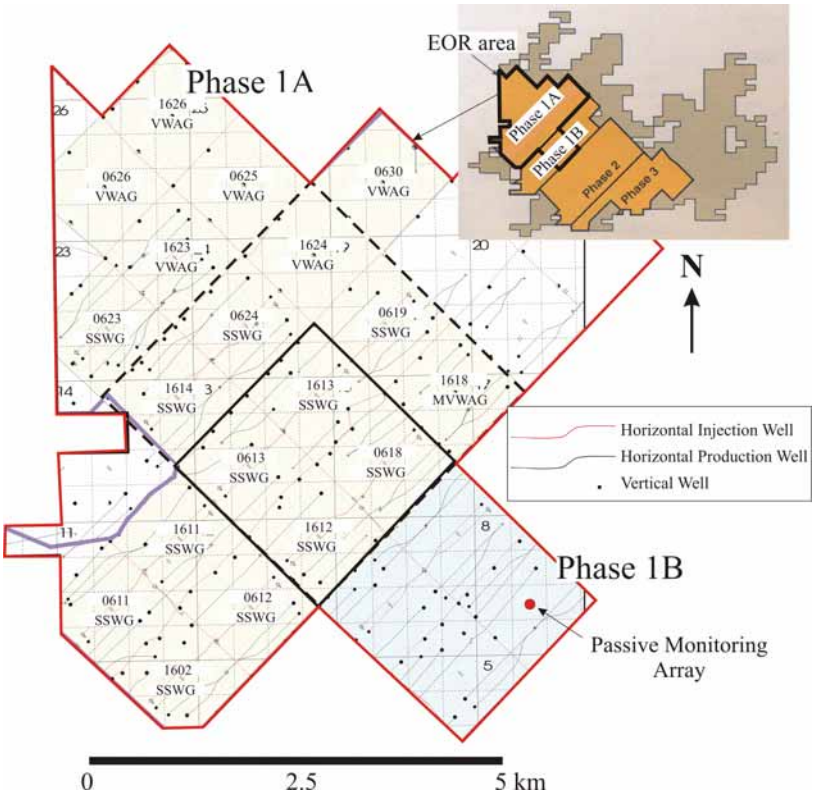

Figure 2.2: Location map (inset) showing the CO_2 Flood/EOR area. The larger map shows the 19-patterns of the Phase 1A injection area that have been monitored using time-lapse 3D P-wave seismic data. Highlighted is the 9-pattern area (dashed box) where the seismic data have been used in history matching. Also shown is a 4-pattern sub-area where complementary 9-component time-lapse 3D seismic surveys were conducted. The location of the well in Phase 1B that holds the passive seismic monitoring system is indicated. The thin lines represent horizontal injection (red) and production (black) wells. Black dots indicate vertical well locations. The patterns are numbered for reference, and the type of injection strategy being used in each pattern is also annotated.

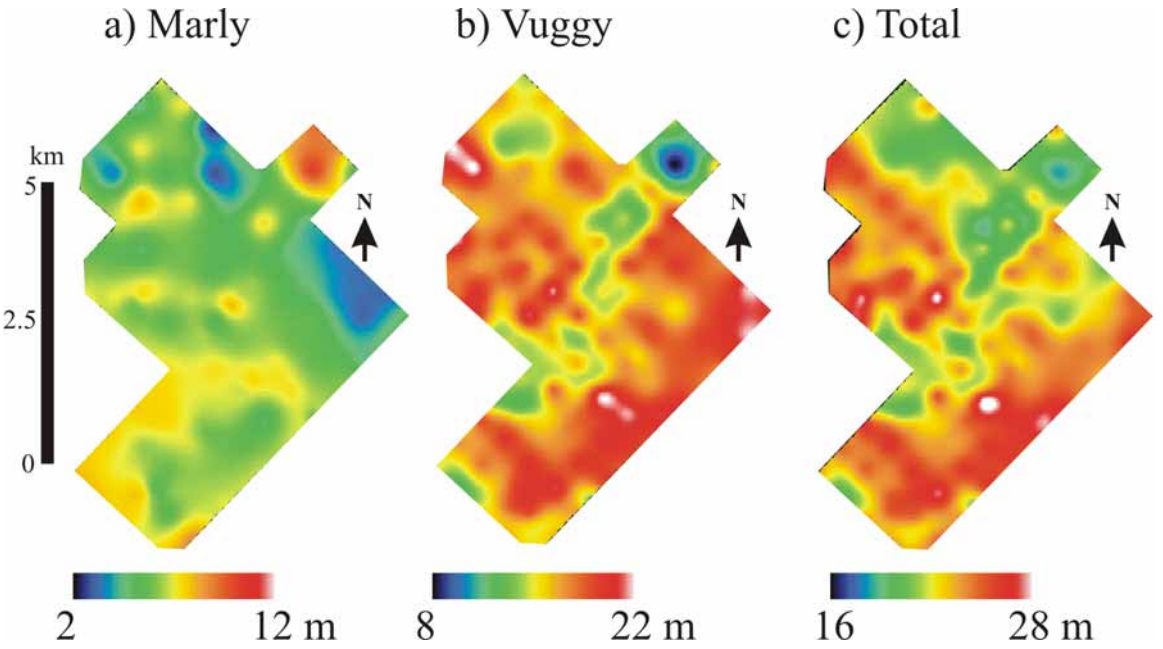

Figure 2.3: Thickness of reservoir units in the Phase 1A area from the geological model. a) Marly unit, b) Vuggy unit, and c) combined Marly and Vuggy.

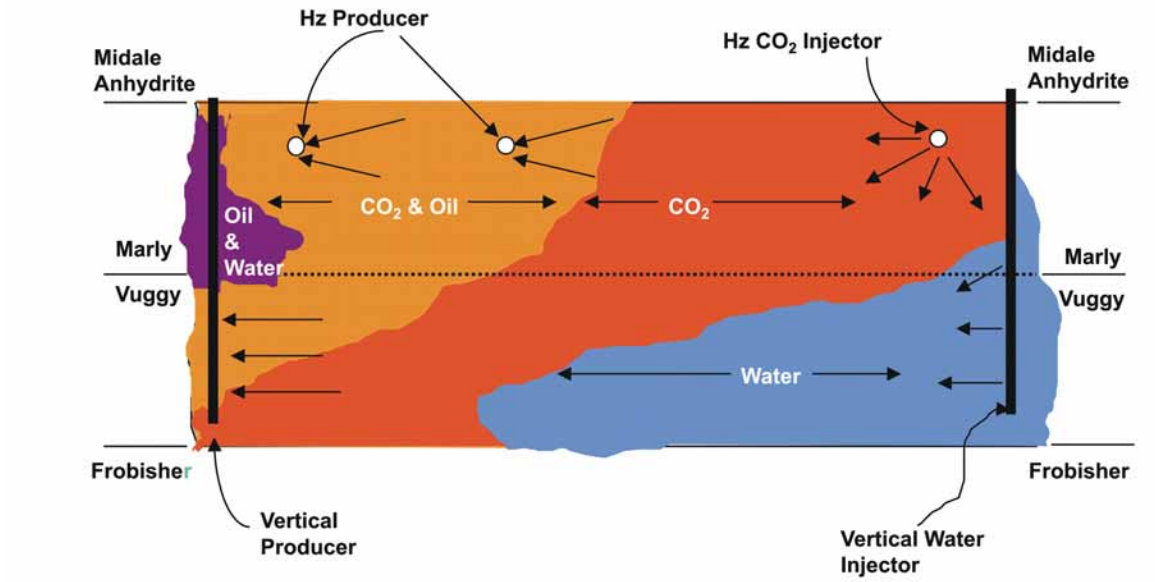

Figure 2.4: Schematic of the CO_2 flood process.

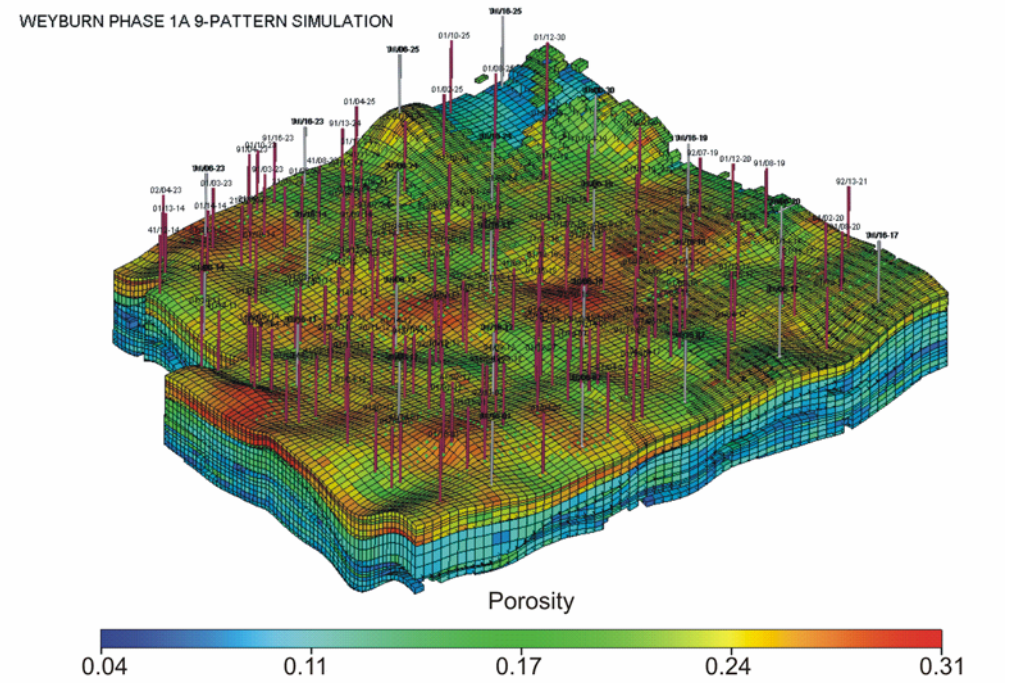

Figure 2.5: Reservoir simulation model: 3D perspective view of porosity. The vertical bars represent wells.

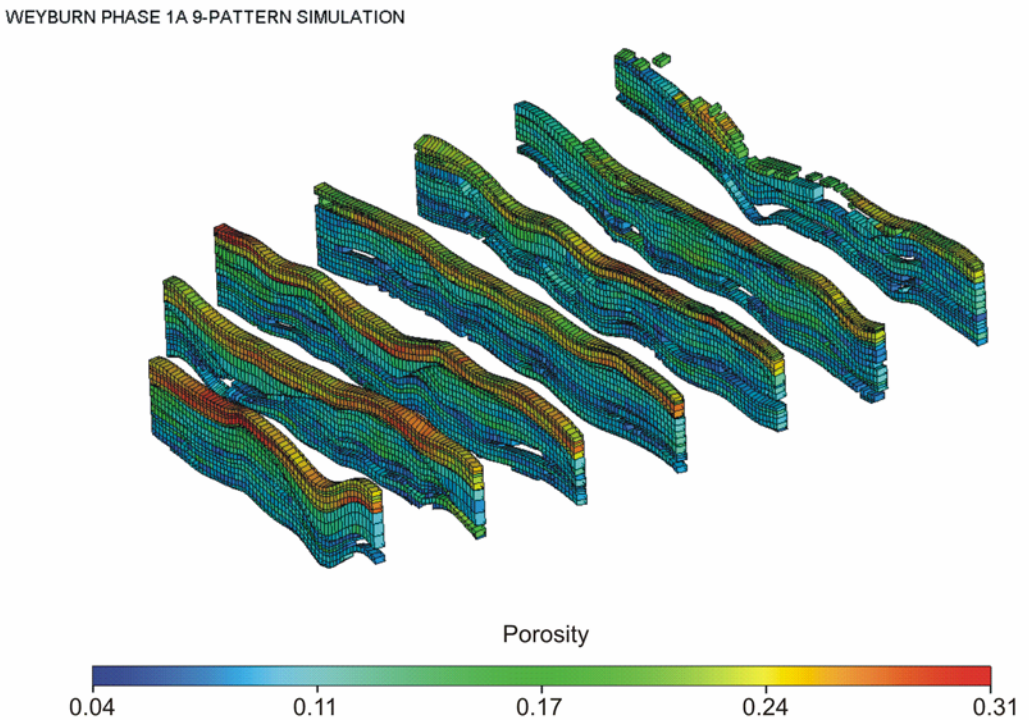

Figure 2.6: Reservoir simulation model: Fence diagram of porosity

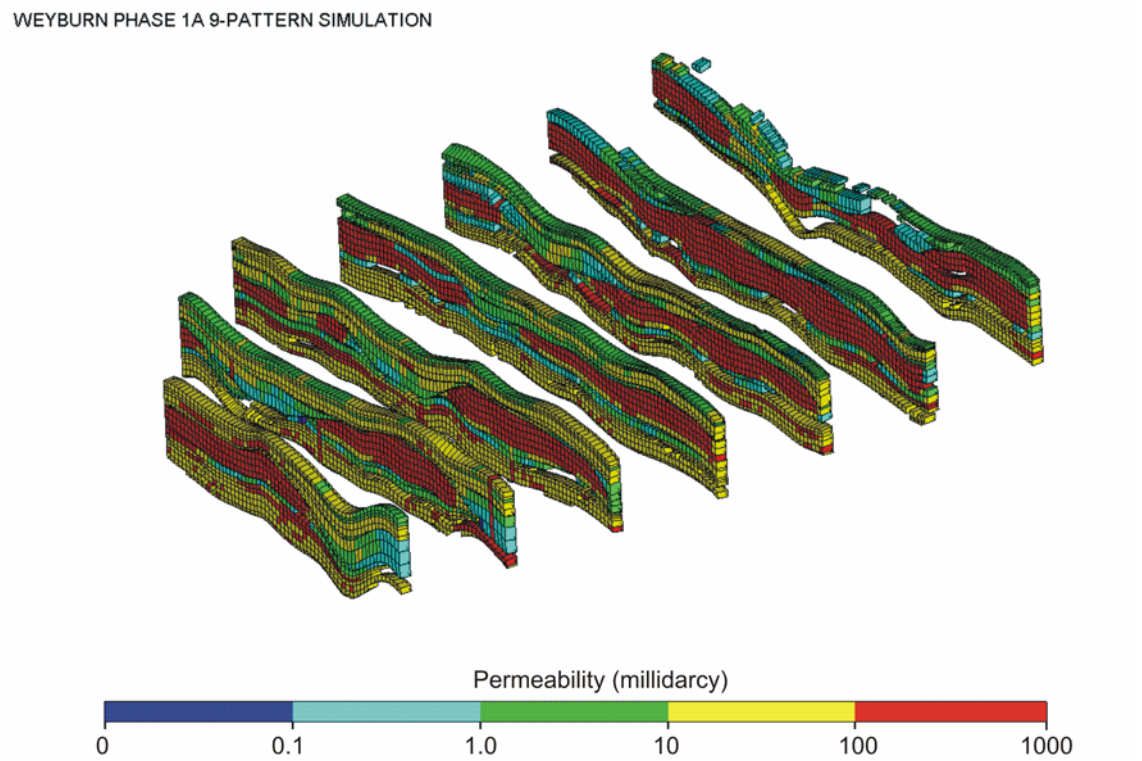

Figure 2.7: Reservoir simulation model: Fence diagram of permeability.

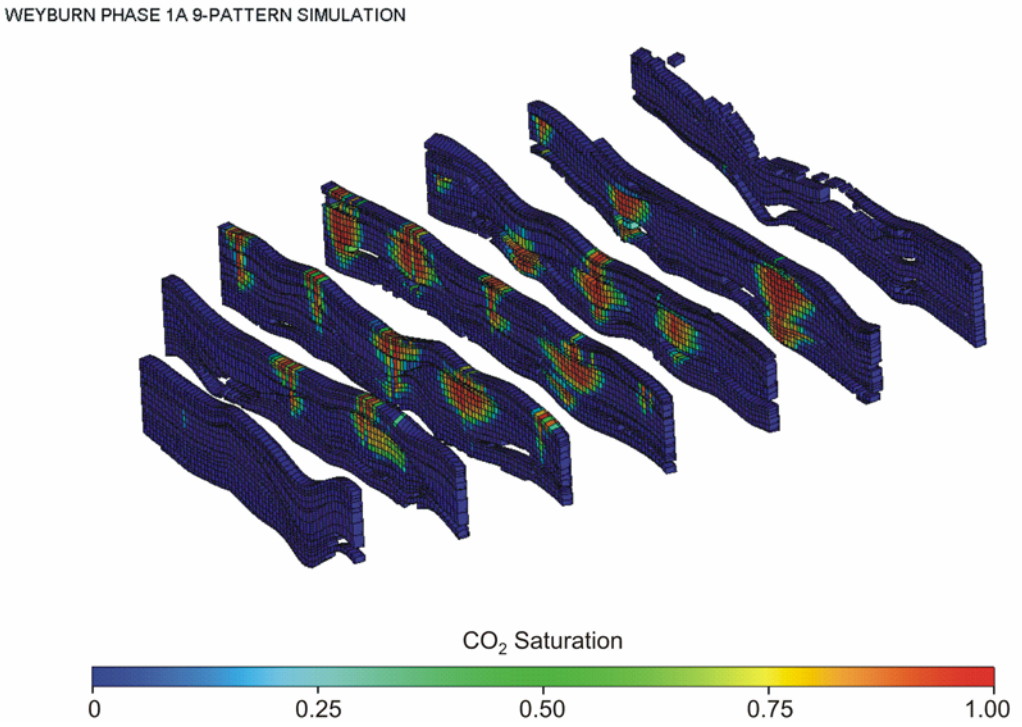

Figure 2.8: Reservoir simulation model: Fence diagram of predicted CO_2 distribution at 2 years from start of injection.

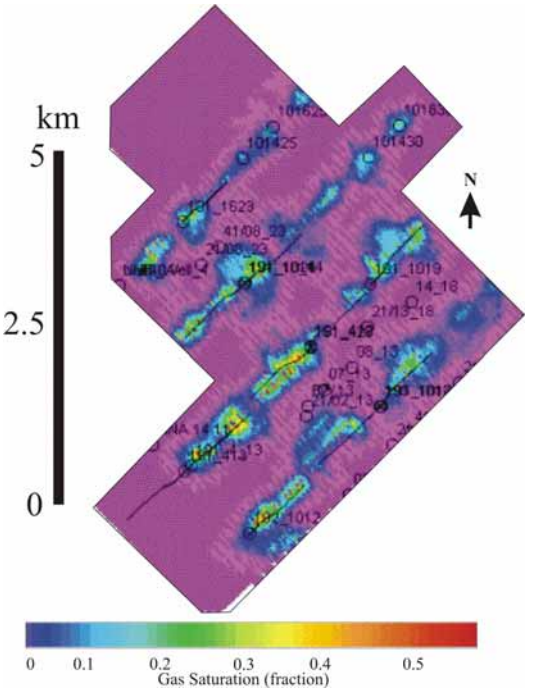

Figure 2.9: Reservoir simulation model: plan view of predicted CO_2 saturation at 2 years after start of injection. Saturation is for the entire reservoir interval. Note that the northern 2 patterns were not included in the simulation. Some well locations are marked and annotated.

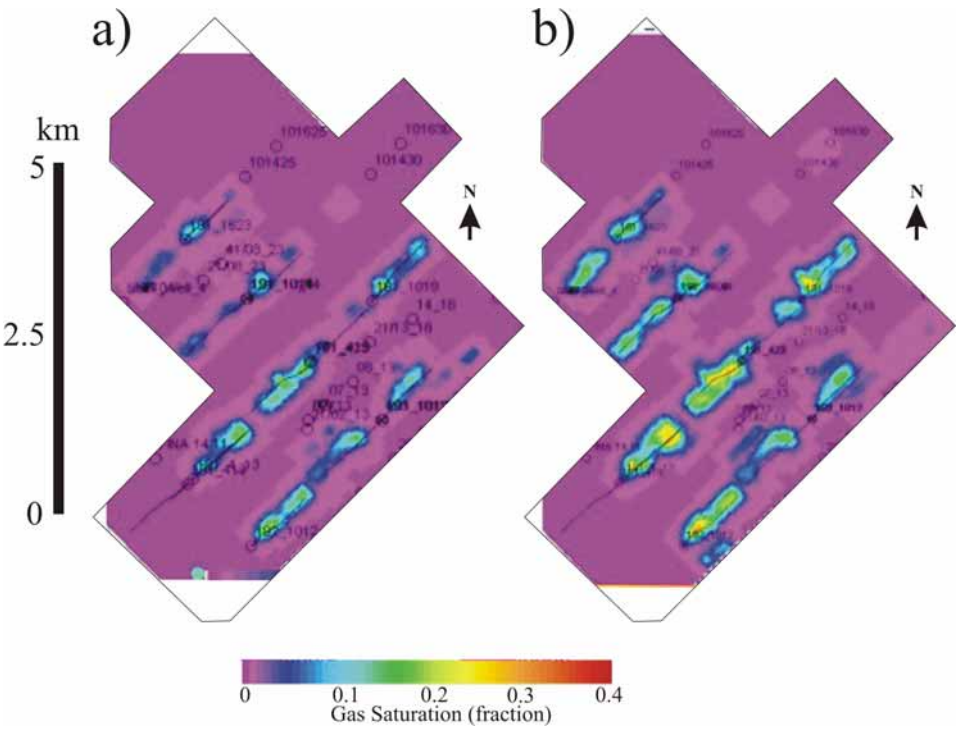

Figure 2.10: Reservoir simulation model: plan view of predicted CO_2 saturation at a) 1 year and b) 2 years after start of injection. Saturation is shown for the Marly interval only. Note that the northern 2 patterns were not included in the simulation. Some well locations are marked and annotated.

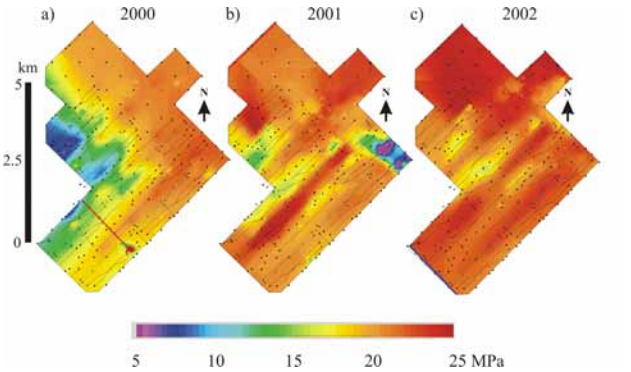

Figure 2.11: Reservoir simulation model: Plan view of predicted reservoir pore pressures at the Marly Horizon at time of a) baseline survey (2000), b) Monitor 1 Survey, and c) Monitor 2 Survey (2002). Horizontal injection (green) and production (black) wells are shown in addition to vertical wells (dots).

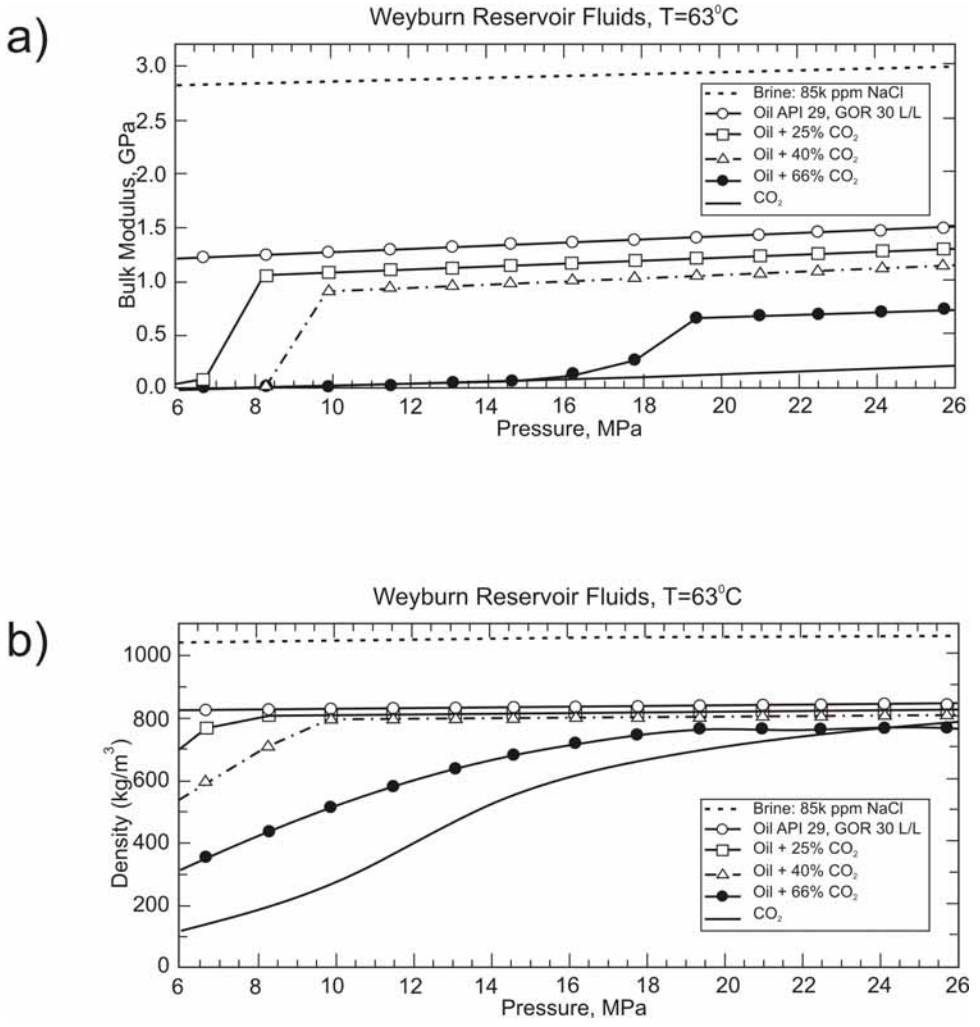

Figure 2.12: Effect of CO_2 saturation on a) fluid bulk modulus and b) fluid density. For an ideal fluid, $Vp=(G/\rho)^{1/2}$, where Vp is P-wave velocity, G is bulk modulus and ρ is density. Parameters determined by modeling with STRAPP and FLAG are plotted as functions of composition and pressure for a reservoir temperature of 63° C. FLAG (Fluid Acoustics for Geophysics) is a modeling program based on acoustic property relations described in Batzle and Wang (1992), and STRAPP (NIST, 2002) is an equation of state-based thermophysical modeling program for hydrocarbon mixtures. Figure modified from Brown (2002).

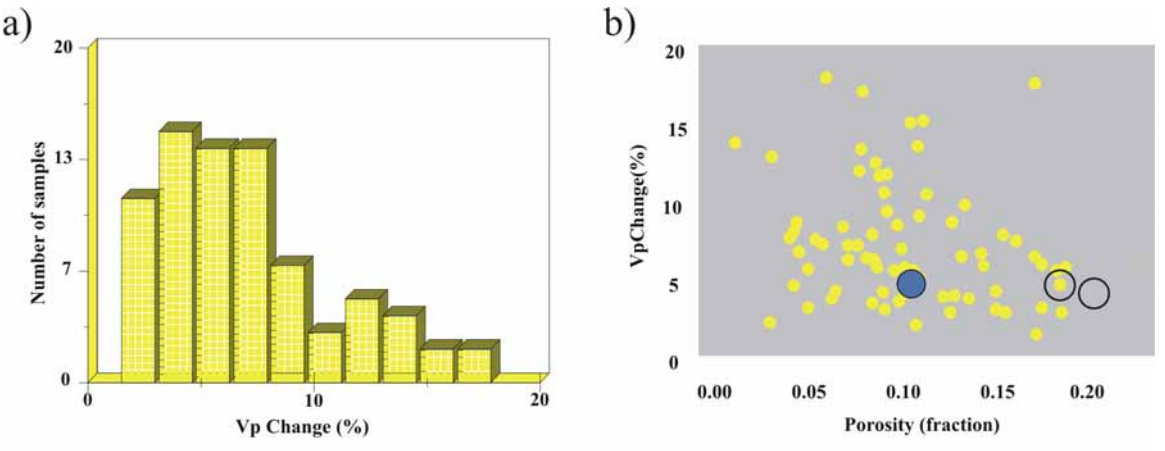

Figure 2.13: a) Histogram of Vp changes resulting from pore fluid change from gas to 30 degree API "dead" oil for 90 carbonate samples from the Western Canadian basin (Wang et al., 1991). Effective pressure is 20.7 MPa. b) Vp change vs. porosity for pore fluid change from gas to brine for the same set of samples. The large solid dot represents the result for the Vuggy limestone sample from Figure 2.14, and the open dots show the results for the Marly dolomite samples from Figures 2.16 and 2.17.

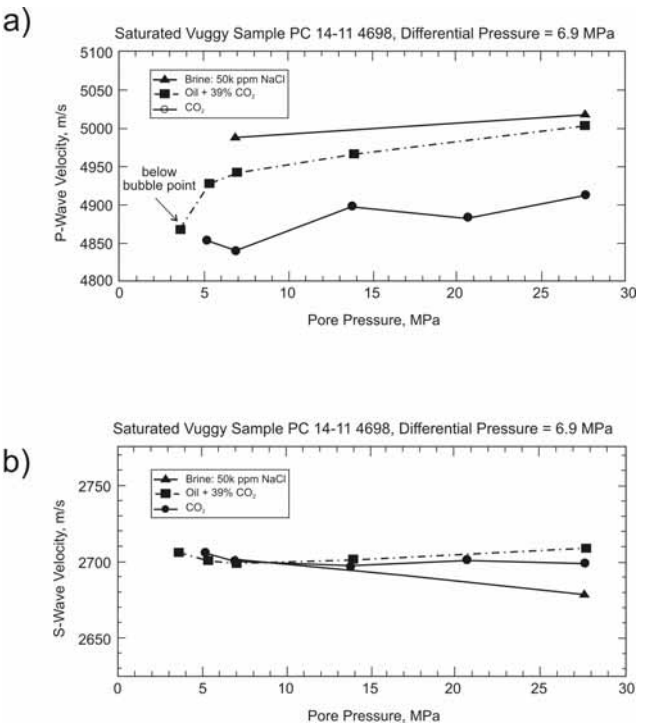

Figure 2.14: Variation of a) Vp and b) Vs vs. pore pressure at a constant differential pressure of 6.9 MPa for a Vuggy sample with porosity of 13%. Modified from Brown (2002).

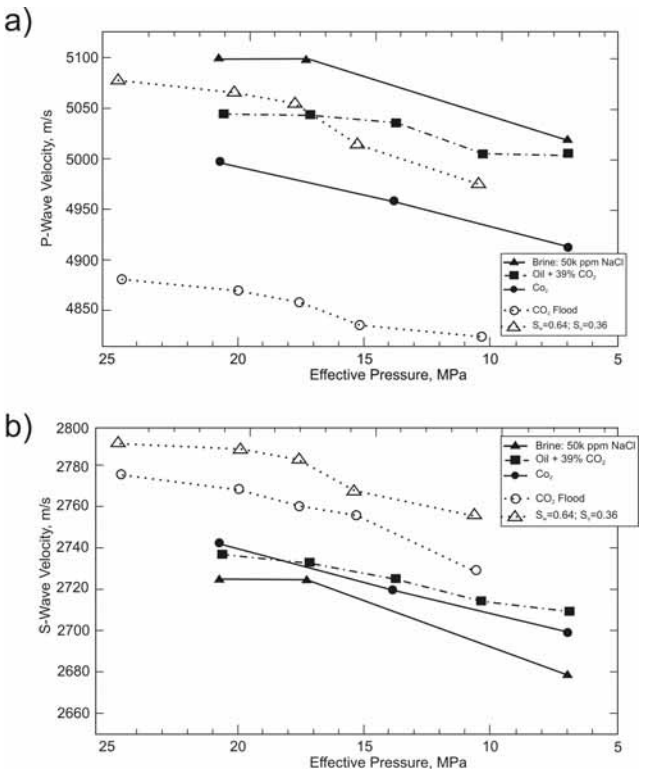

Figure 2.15: Variation of a) Vp and b) Vs vs. effective pressure for saturated Midale Vuggy core samples. The solid symbols are for the Vuggy sample of Figure 2.13 (porosity of 13%), and the open symbols are for a Vuggy sample with porosity of 14% from Core Laboratories Canada (1998). The measurements were made at constant confining pressures of 34.5 MPa and 32.1 MPa, respectively. S_W=fractional water saturation. S_O=fractional oil saturation. Effective pressure is the difference of the confining pressure and the pore pressure.

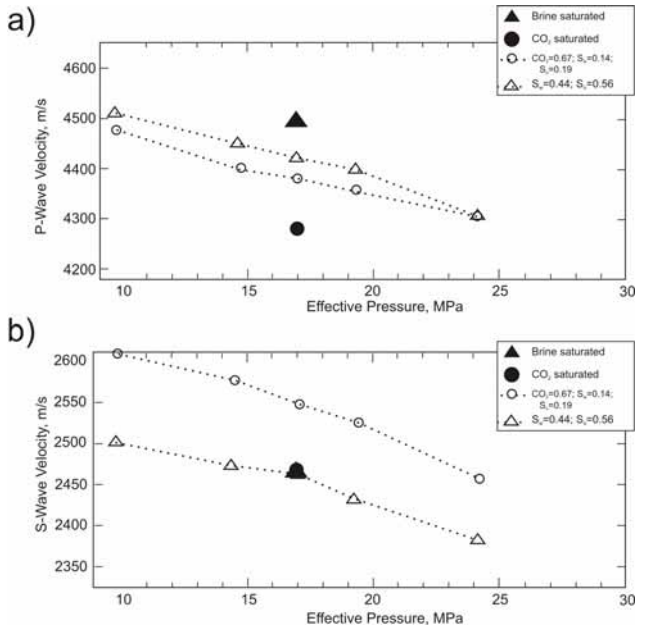

Figure 2.16: Variation of a) Vp and b) Vs vs. effective pressure for Midale Marly core sample with porosity of 18% from Core Laboratories Canada (1998). The measurements were made at a constant confining pressure of 32.1 MPa. S_W=fractional water saturation. S_O=fractional oil saturation. Effective pressure is the difference of the confining pressure and the pore pressure.

Theme 2: Prediction, Monitoring, and Verification of CO_2 Movements

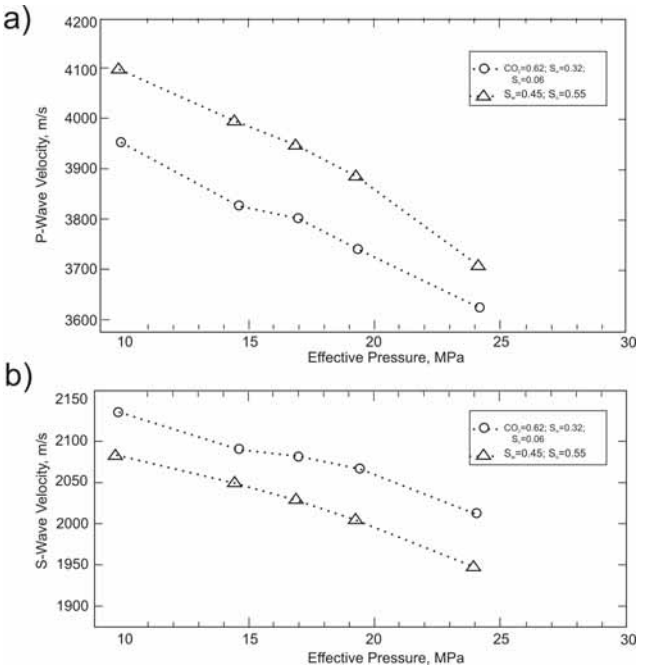

Figure 17: Variation of a) Vp and b) Vs vs. effective pressure for Midale Marly core sample with porosity of 21% from Core Laboratories Canada (1998). The measurements were made at a constant confining pressure of 32.1 MPa. S_W=fractional water saturation. S_O=fractional oil saturation. Effective pressure is the difference of the confining pressure and the pore pressure.

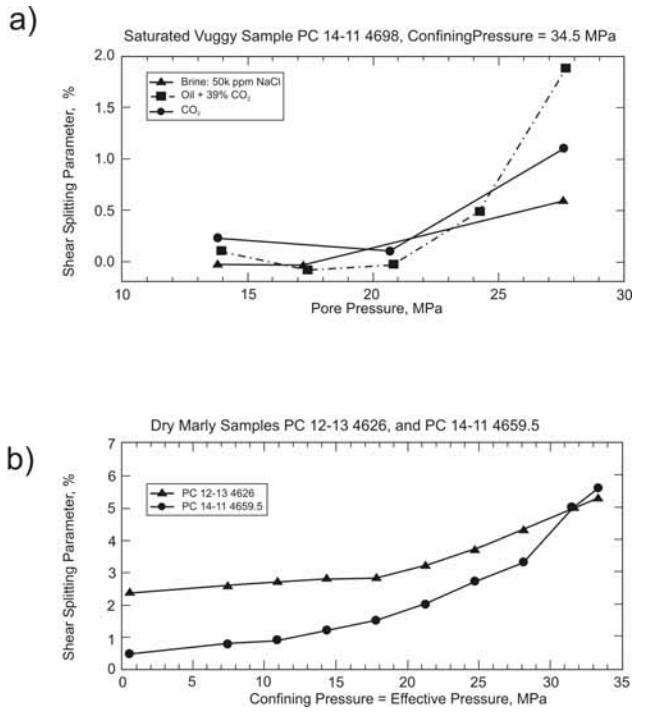

Figure 2.18: Variation of shear-wave splitting vs. differential pressure for a) the Vuggy sample of Figure 2.13, and b) two Marly samples (porosities of 29% and 33%, respectively). In a), the sample was fluid saturated, whereas in b) the sample was dry. Modified from Brown (2002).

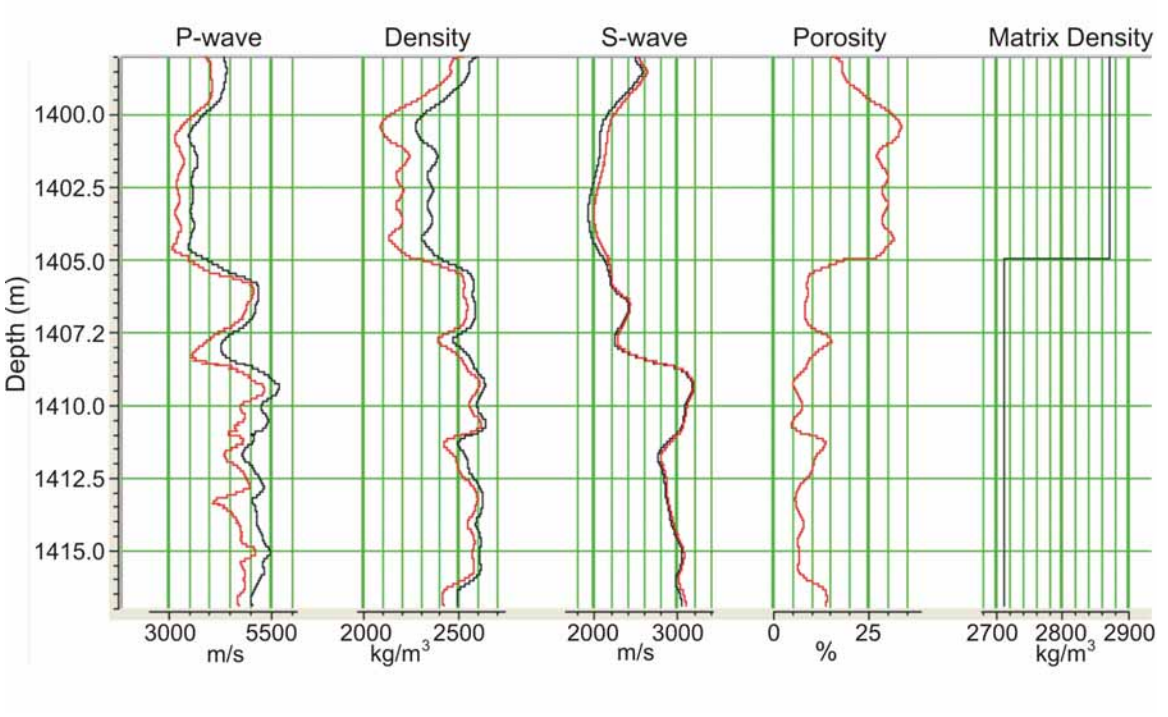

Figure 19: Fluid substitution results calculated using the Gassmann equation over the entire Marly and Vuggy interval. Original logs are shown in black and logs with simulated CO_2 injection (substitution of 100% brine with 30% brine and 70% gas) are shown in red. The rock and fluid parameters are provided in Table 2.3. The bulk fluid properties were determined using the method of Batzle and Wang (1992).

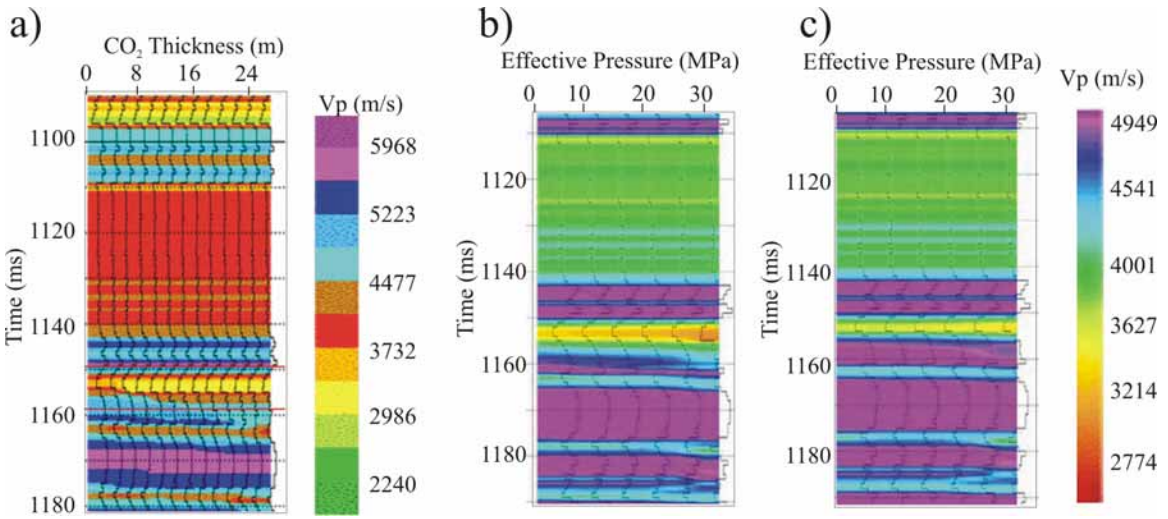

Figure 2.20: a) Vp logs vs. CO_2 thickness measured from the top of the Marly unit, assuming 80% CO_2 saturation in the interval where it is present. b) Vp log for 80% CO_2 saturation and variable effective pressure. c) Vp log for 100% brine saturation and variable effective pressure. In b) and c), the pressure-dependence of the dry rock matrix properties has been accounted for using core sample data from Brown (2002). The pressure-dependent properties used are from a Marly sample that shows the largest pressure effect. Thus, the pressure effect may actually be overestimated in the case of the Vuggy unit.

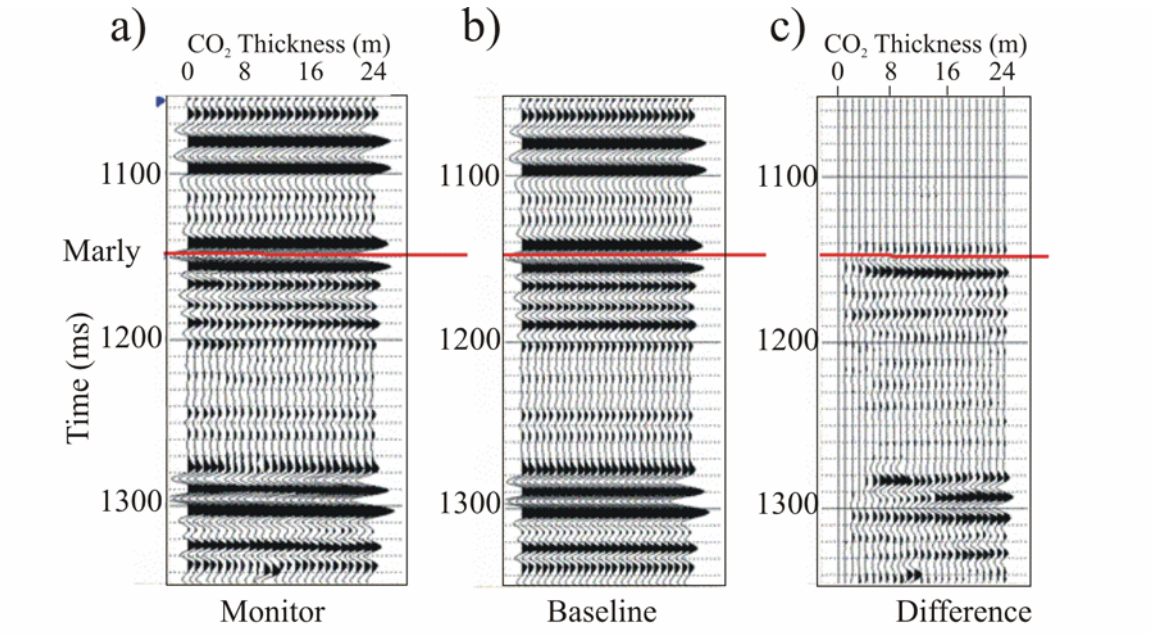

Figure 2.21: Monitor, baseline, and difference synthetic seismograms for an injected CO_2 bank that starts at the top of the reservoir and increases in thickness from 0 to 24 m (results from left to right in a and c). The Marly horizon is labeled.

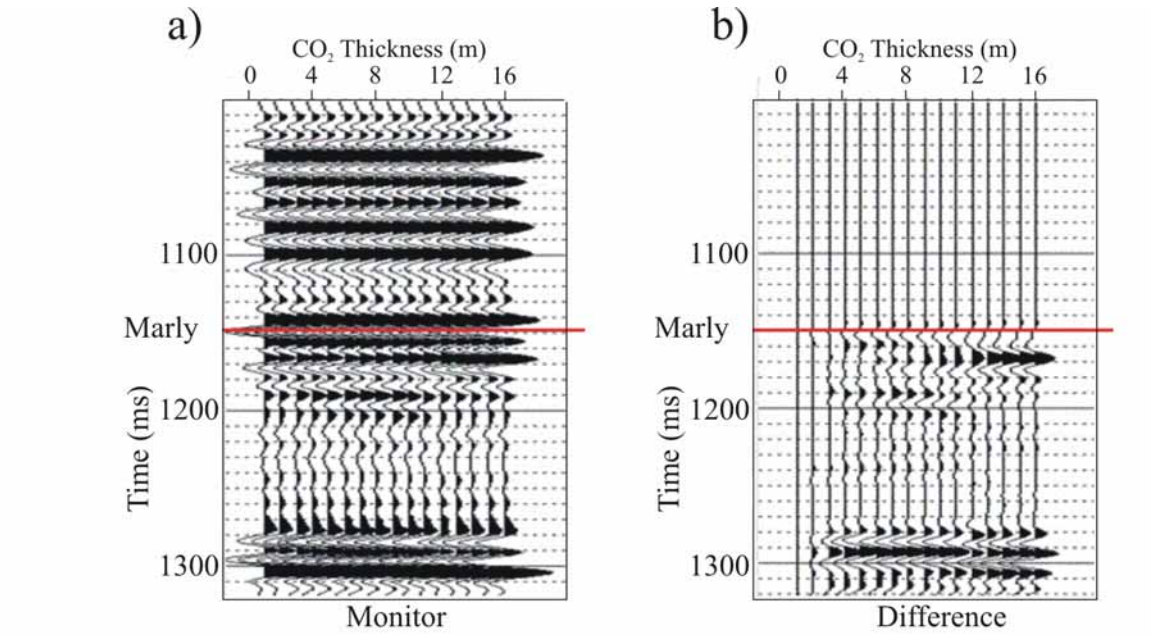

Figure 2.22: Monitor and difference synthetic seismograms showing the effect of a CO_2 bank of variable thickness (from 0 to 16 m, left to right) present only in the Vuggy interval. The Marly horizon is labeled.

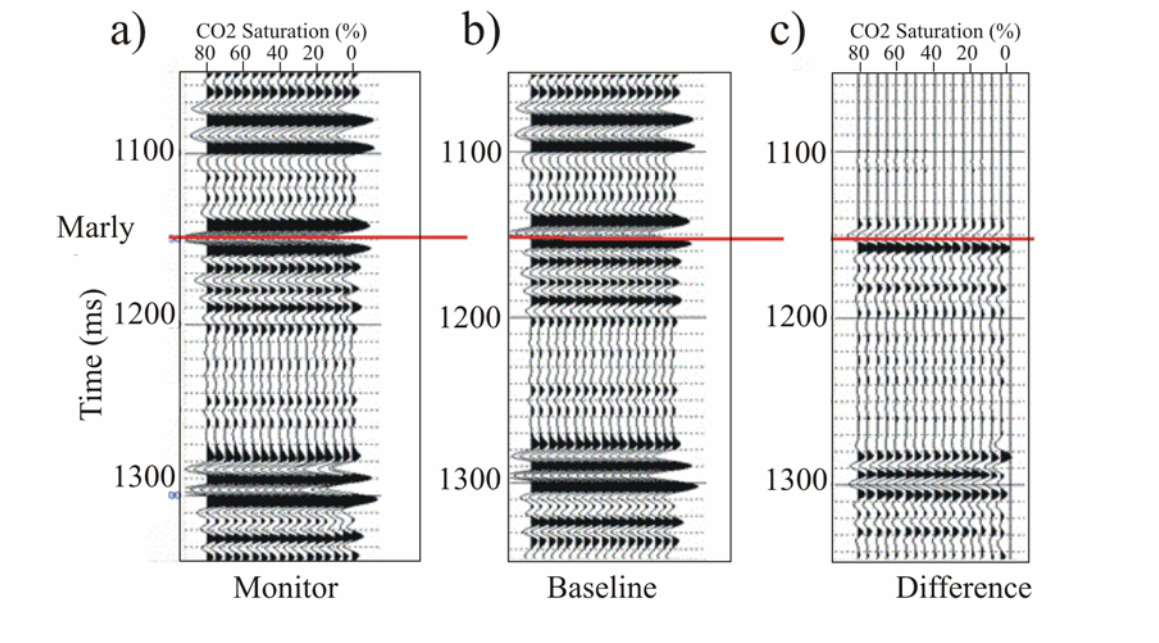

Figure 2.23: Monitor and baseline synthetic seismograms for a 20 m thick CO_2 bank with CO_2 saturation ranging from 80% to 0%. The Marly horizon is labeled

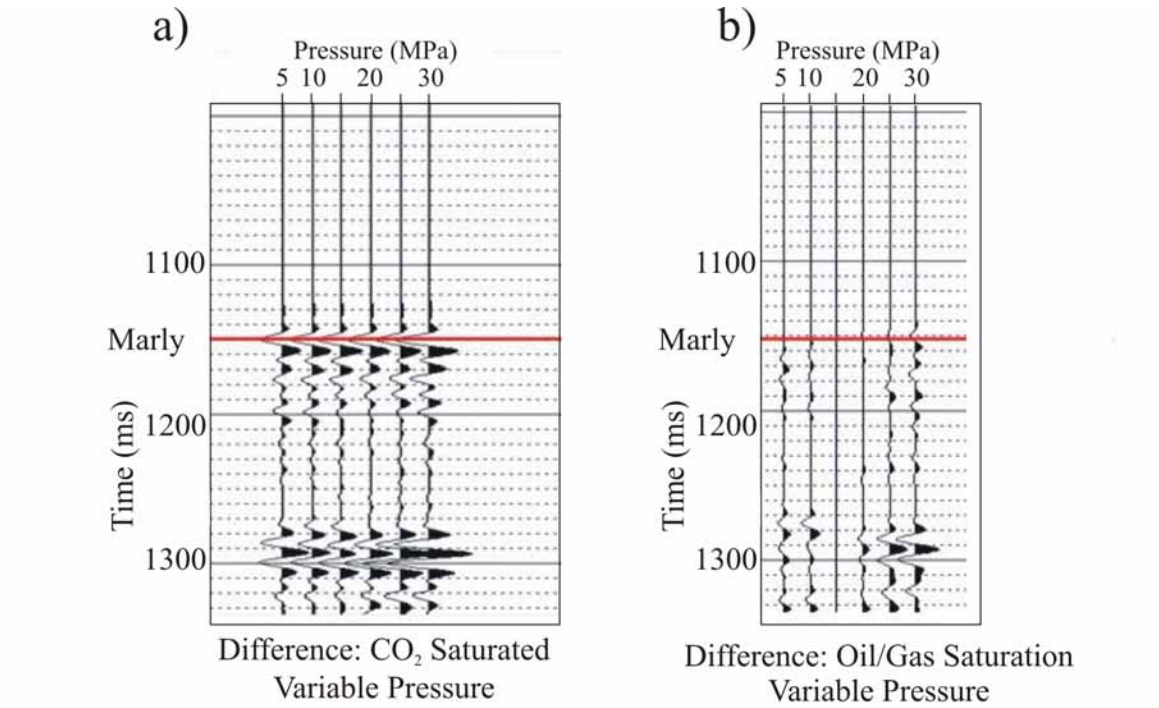

Figure 2.24: Difference synthetic seismograms showing the effect of variable reservoir pressure (ranging from 5 to 30 MPa) for CO_2 saturated (left) and oil/brine saturated (right) conditions. The initial conditions were oil/gas saturation at 15 Mpa reservoir pressure. The difference traces were created by subtracting the base survey synthetic trace (P=15 MPa, and 0% CO_2 saturation) from the traces determined for variable pressure and CO_2 saturation. The Marly horizon is labeled.

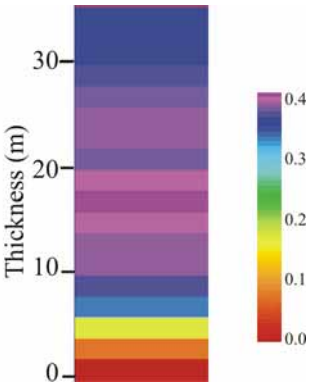

Figure 2.25: a) Normalized amplitude difference determined at the Marly horizon vs. CO_2 thickness (0-36m) as measured from the top of the Midale Marly unit. The amplitude differences shown were determined for the synthetic seismograms shown in Figure 2.21. The RMS amplitude is measured using a 5ms window centred on the horizon, and the fractional amplitude change (shown) is derived by taking the ratio of the difference amplitude divided by the average of the base and monitor amplitudes.

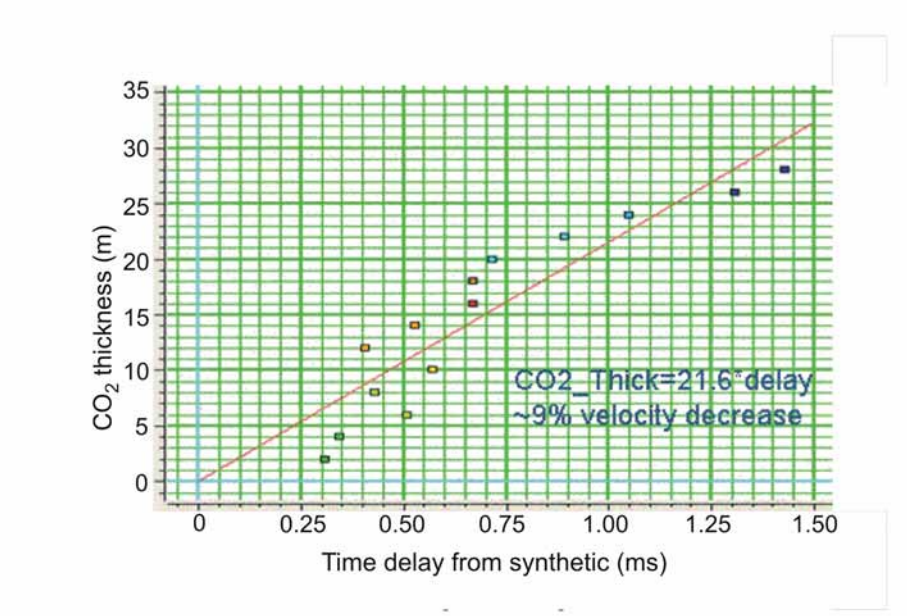

*Figure 2.26: Thickness of CO_2-saturated interval vs. travel time delay as determined by modeling for the same case as shown in Figure 2.21. The CO_2 interval thickness is measured downward from the top of the Marly Unit. The travel time delays are determined at the Bakken Horizon (at ~1300 ms), which reflects the time shifts introduced by passage through the reservoir interval where the actual property changes are occurring. The red line (CO_2 thickness = 21.6*travel time delay) is a linear regression determined for the complete set of points and, thus, represents an average dependency of travel time delay on CO_2 thickness for the entire vertical interval.*

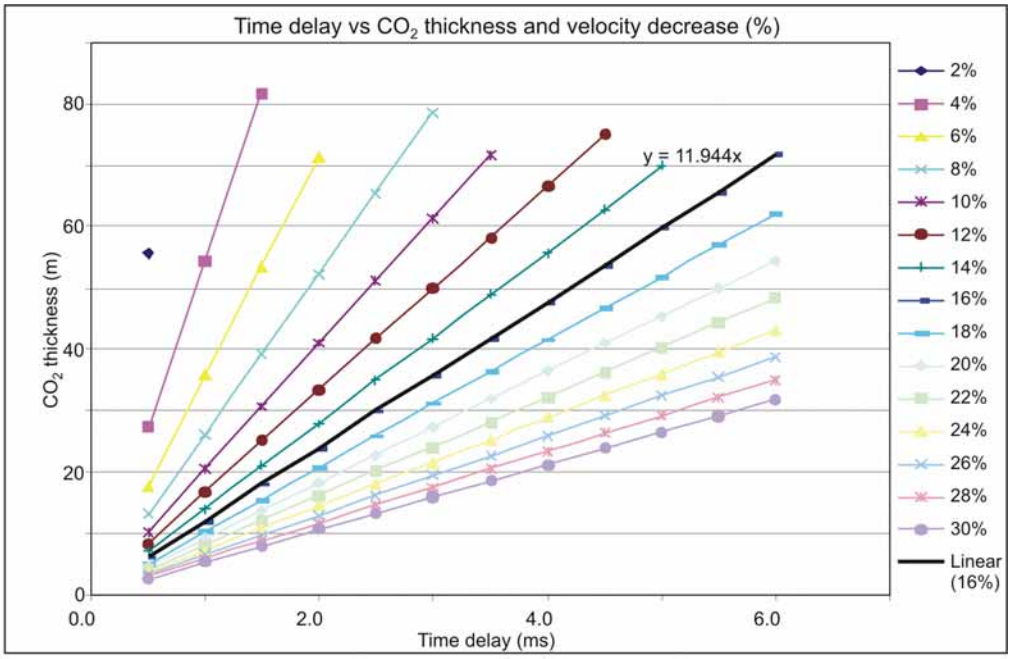

Figure 2.27: Time delay vs. CO_2-saturated layer thickness. The various lines show the linear relationship for various assumed %velocity decreases.

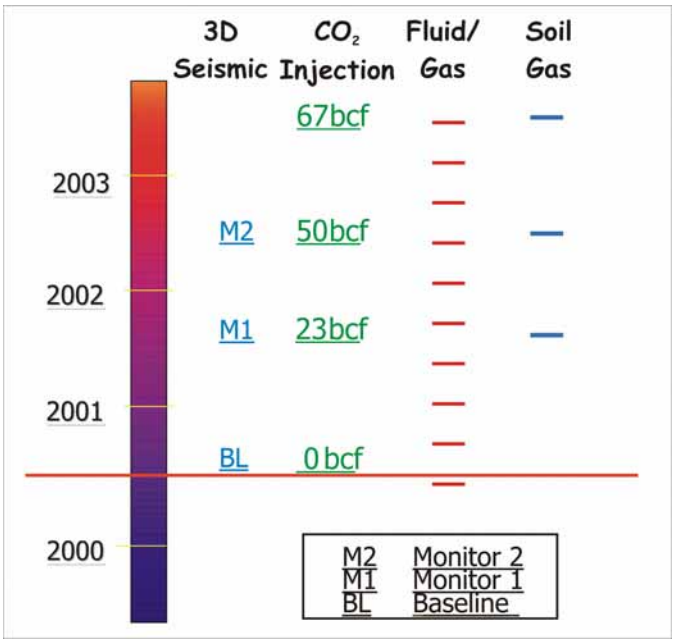

Figure 2.28: CO_2 injection and monitoring schedule. Note that the 3D Seismic monitoring actually included independent multi-component seismic surveys for each of the Baseline, Monitor 1, and Monitor 2 surveys. The first set of surveys were conducted by EnCana Corporation and entailed 3D surveys using 3-component geophones recording dynamite shots over the entire 19-patterns of the Phase 1A area. The P-wave results reported here are primarily from this data set. The second set of surveys were conducted by the Reservoir Characterization Project (Colorado School of Mines) and constituted 3D surveys using 3-component Vibroseis energy sources recorded by 3-component geophones (i.e., 9-components) over a 4-pattern sub-area of Phase 1A (see Figure 2.2 for location). This data set provided the S-wave results that are presented here. The independent surveys were acquired within 2 months of each other at each of the monitor times.

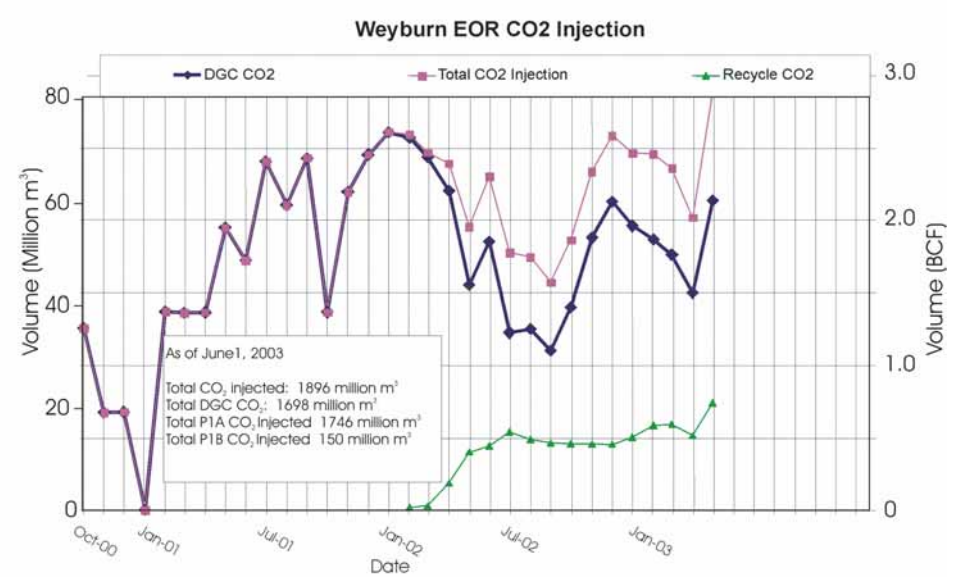

Figure 2.29: Phase 1A CO_2 injection history on a monthly basis. The total CO_2 injected is the sum of that delivered from the Dakota Gasification Company (DGC) and CO_2 recycled from production.

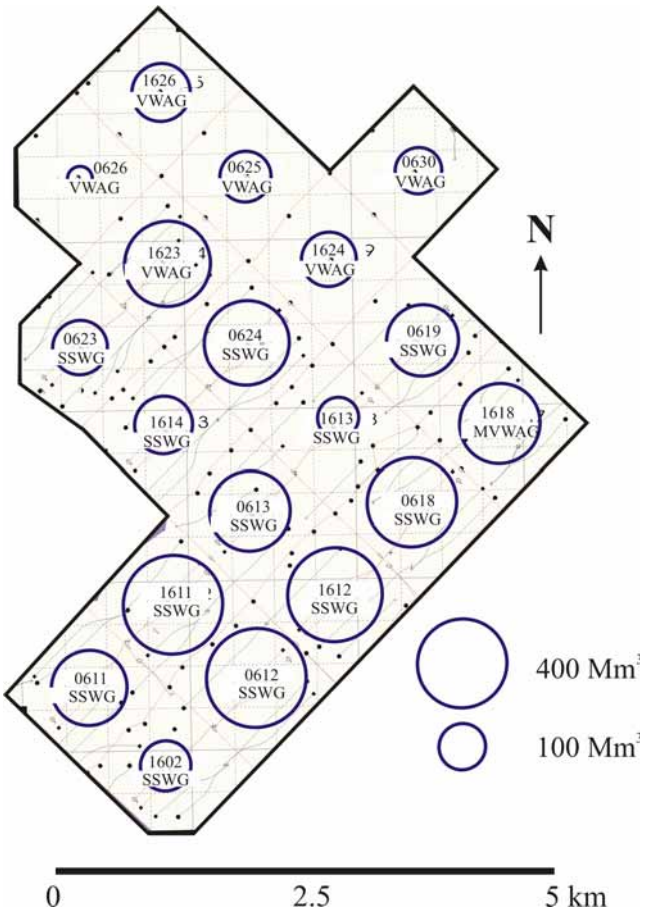

Figure 2.30: Phase 1A gross injection volumes of CO_2 by pattern to 2002. Note that volumes are calculated for reservoir conditions (P=15 MPa and T=63^o C). Area of the circles is proportional to the injected volume.

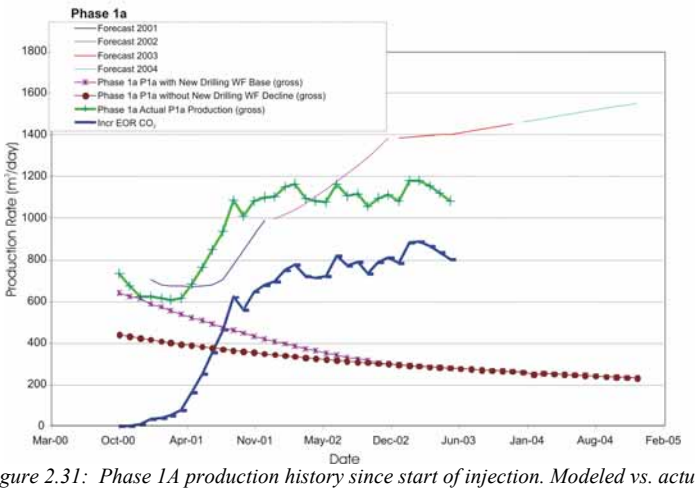

Figure 2.31: Phase 1A production history since start of injection. Modeled vs. actual.

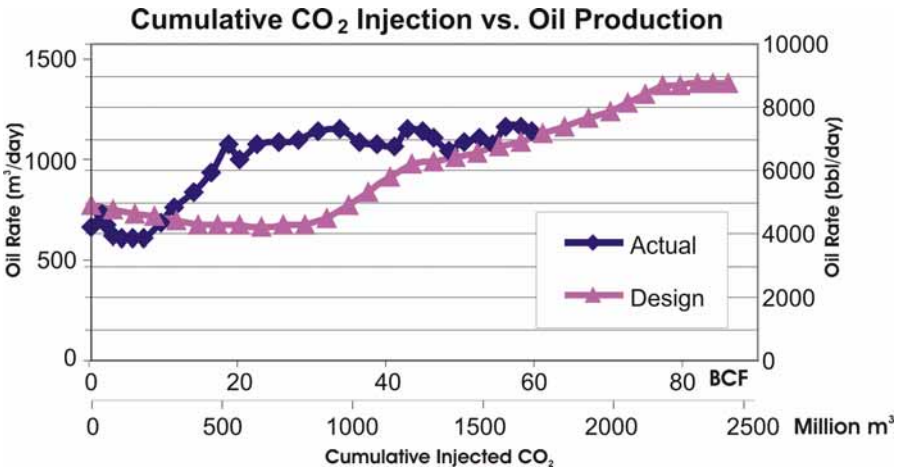

Figure 2.32: Phase 1A performance. CO_2 injection volume vs. oil production.

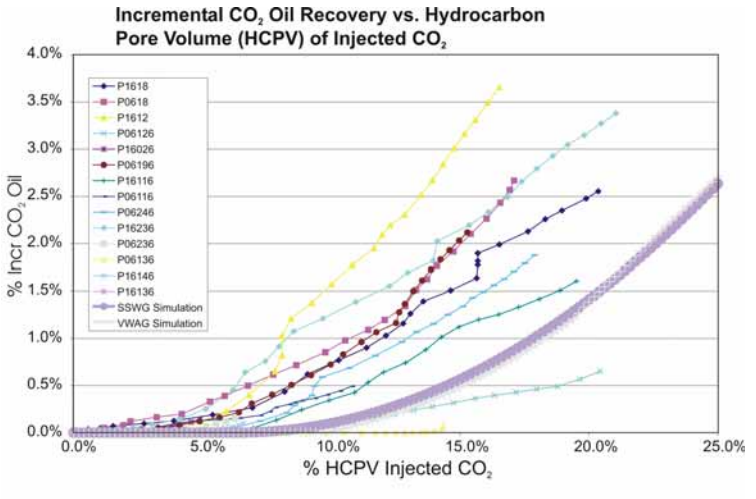

Figure 2.33: Phase 1A performance. Incremental oil production vs. CO_2 injection by production well.

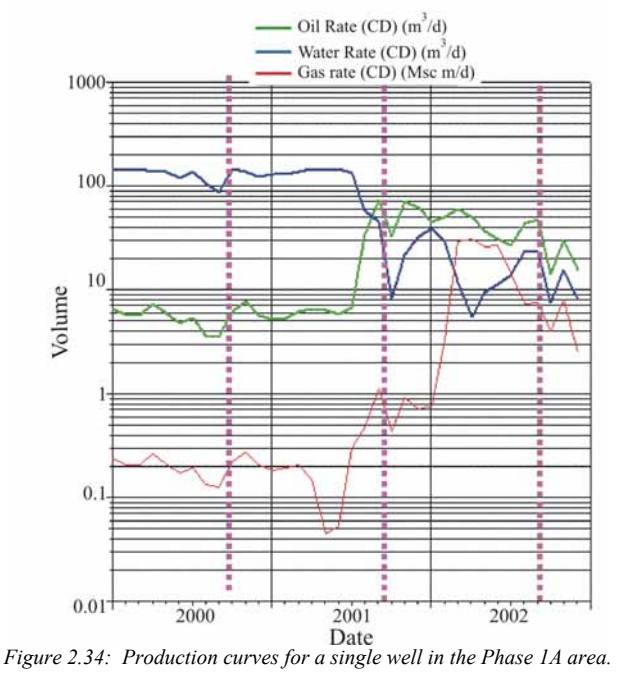

Figure 2.34: Production curves for a single well in the Phase 1A area.

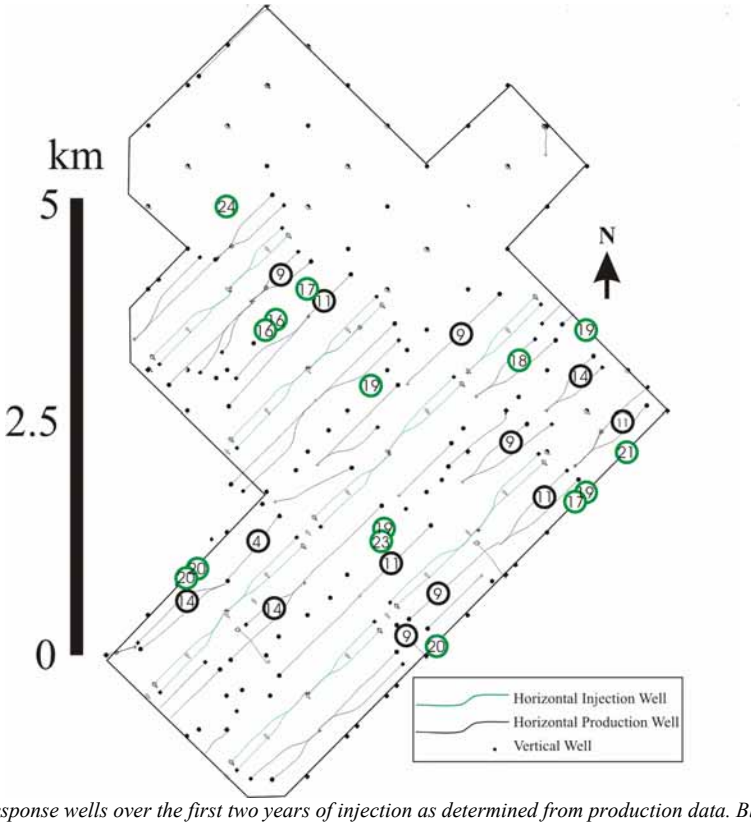

Figure 2.35: CO_2 response wells over the first two years of injection as determined from production data. Black circles indicate response within the first year following start of injection, and the green circles are responses within the following 12 months. The number in each circle indicates the time of response in months since the start of CO_2 injection. In the case of horizontal production wells, the location along the well where CO_2 contacts the well is unknown.

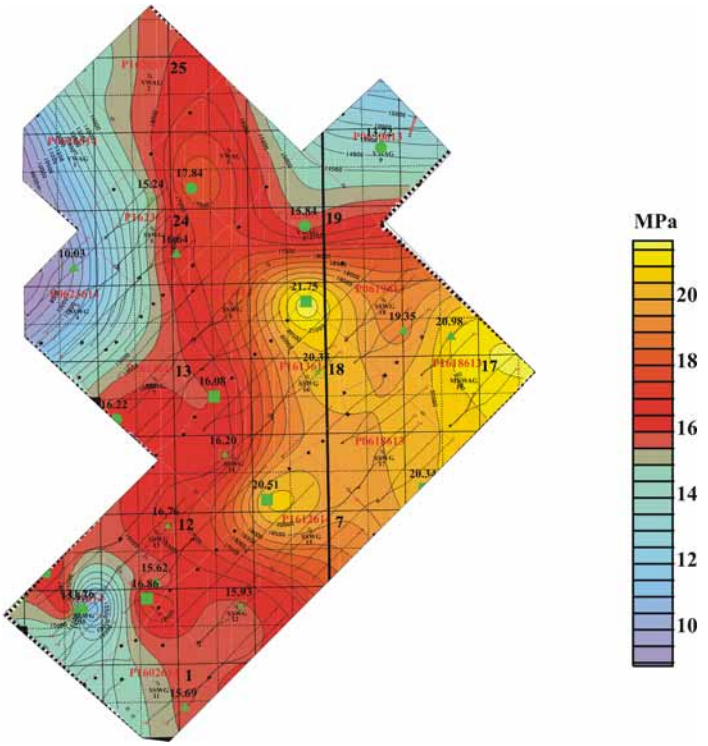

Figure 2.36: 2000 reservoir pressure data based on sparse well measurements. Locations of the wells where measurements were made are indicated by the green markers.

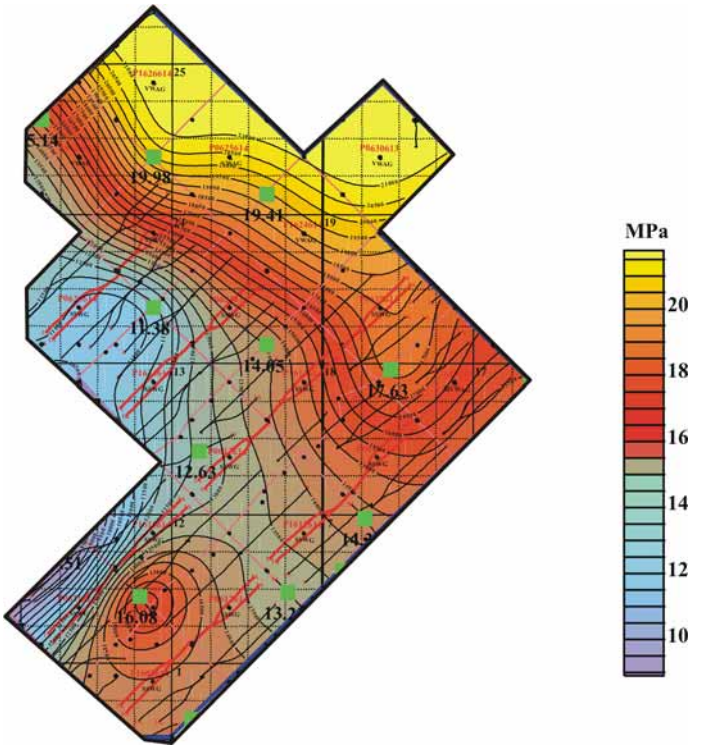

Figure 2.37: 2001 reservoir pressure data based on sparse well measurements. Locations of the wells where measurements were made are indicated by the green markers.

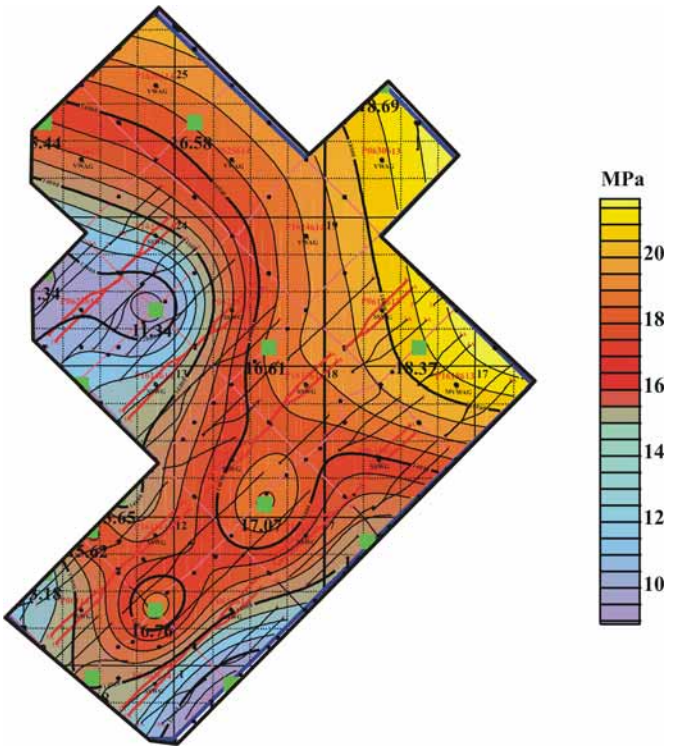

Figure 2.38: 2002 reservoir pressure data based on sparse well measurements. Locations of the wells where measurements were made are indicated by the green markers.

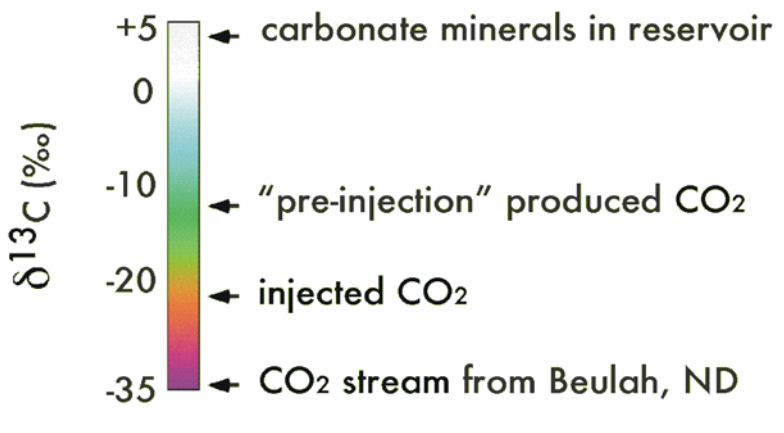

Figure 2.39: $\delta^{13}C$ values for reservoir rock, pre-injection produced CO_2, injected CO_2, and the CO_2 source from Beulah. Mineral dissolution drives produced CO_2 and dissolved CO_2 (as bicarbonate) $\delta^{13}C$ values to a more positive value. Conversely, dissolution of injected CO_2 drives produced CO_2 $\delta^{13}C$ values to a more negative value.

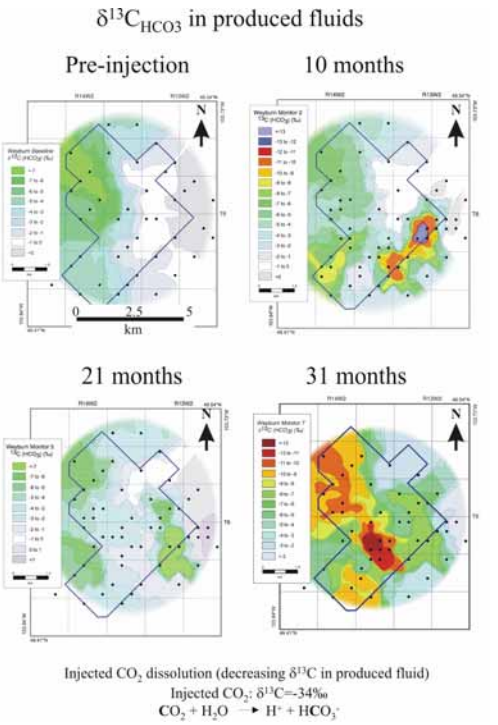

Figure 2.40: $\delta^{13}C[HCO_3]$ in produced fluids. The well locations (black dots) represent the locations of data points that are used to produce the contour plots.

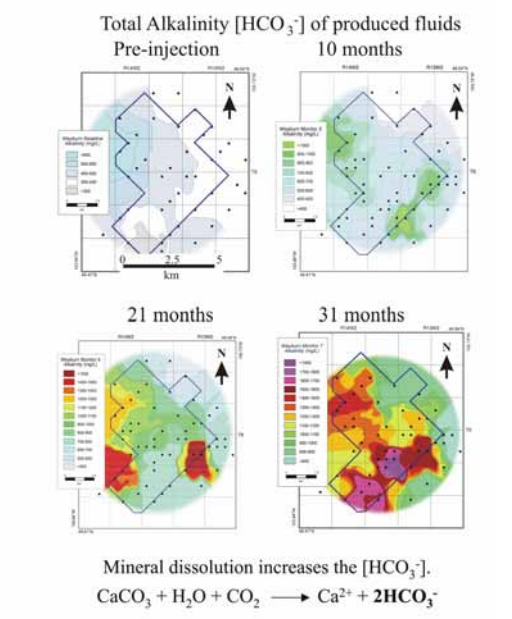

Figure 2.41: Total Alkalinity [HCO_3^-] of produced fluids. The well locations (black dots) represent the locations of data points that are used to produce the contour plots.

Theme 2: Prediction, Monitoring, and Verification of CO_2 Movements

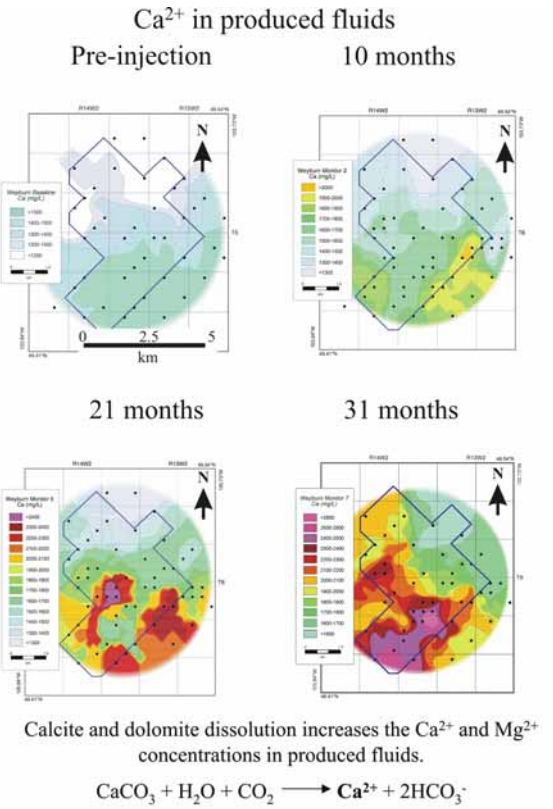

Figure 2.42: Ca^{2+} in produced fluids due to mineral dissolution. The well locations (black dots) represent the locations of data points that are used to produce the contour plots.

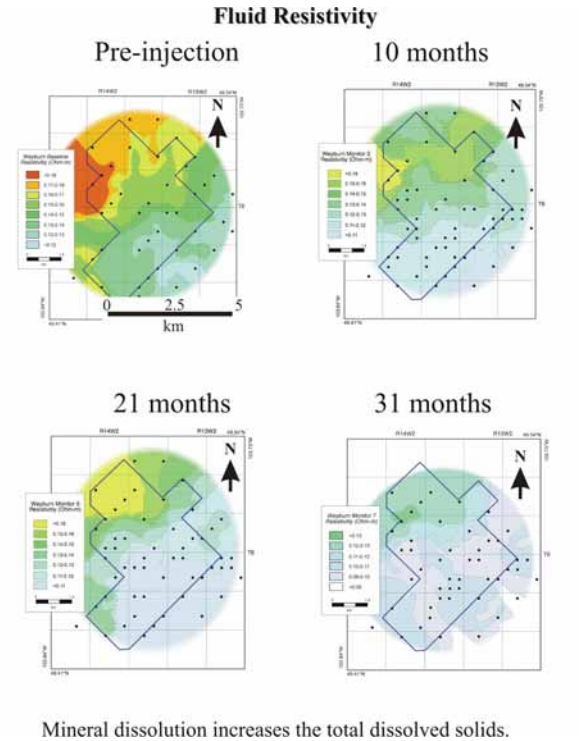

Figure 2.43: Fluid electrical conductivity. The well locations (black dots) represent the locations of data points that are used to produce the contour plots.

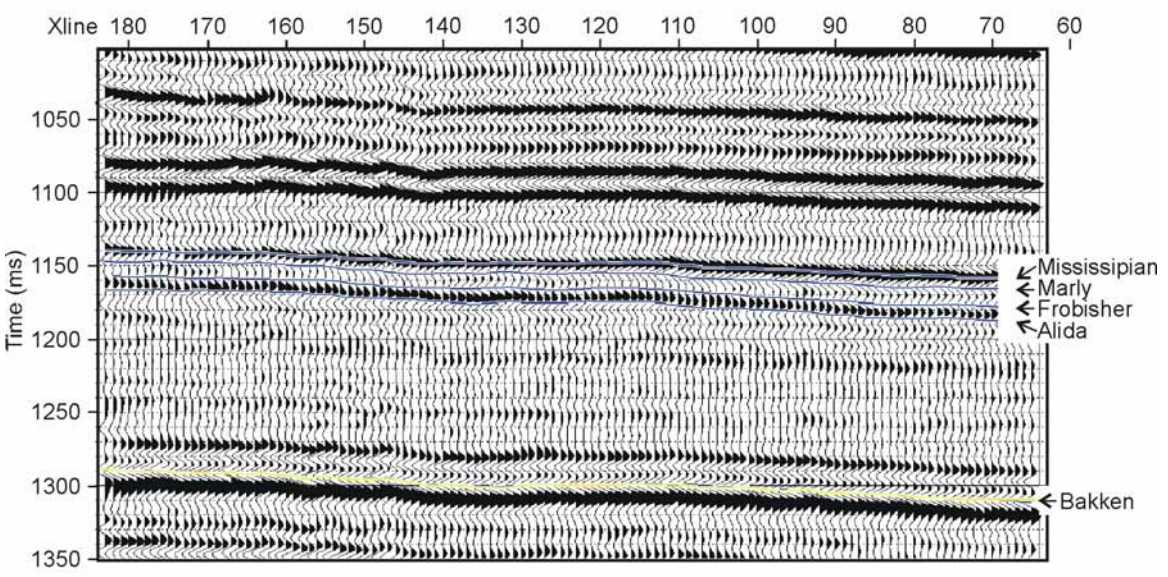

Figure 2.44: Example cross-section through the P-wave 3D data volume identifying the horizons of interest. These data are from the Baseline 19-pattern survey, which were acquired using dynamite sources and 3-component geophones. The bin-size for processing was 40x60 m, which has subsequently been interpolated to 40x40 m bins.

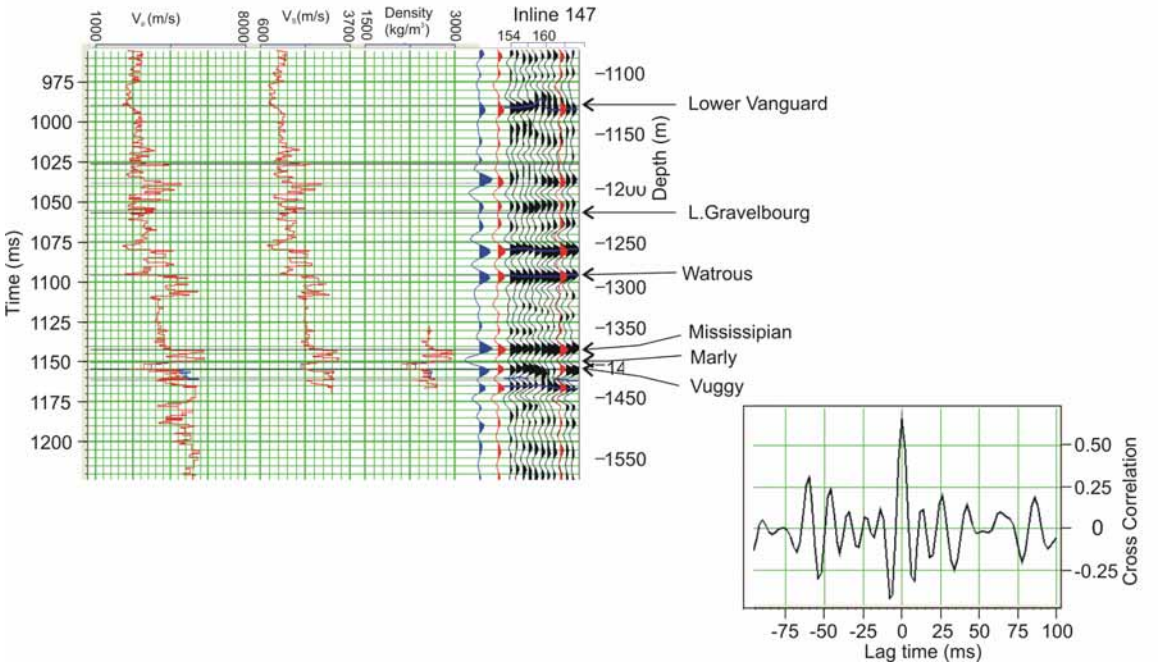

Figure 45: Comparison of P-wave surface seismic data and well log-generated synthetic seismic trace. The cross-correlation of the synthetic trace with the observed data (inset) has a zero-lag value of 0.66, indicating a good "tie" of the data to the well log. The wavelet used in constructing the synthetic seismic traces was extracted from the surface seismic data shown in Figure 2.44.

Theme 2: Prediction, Monitoring, and Verification of CO_2 Movements

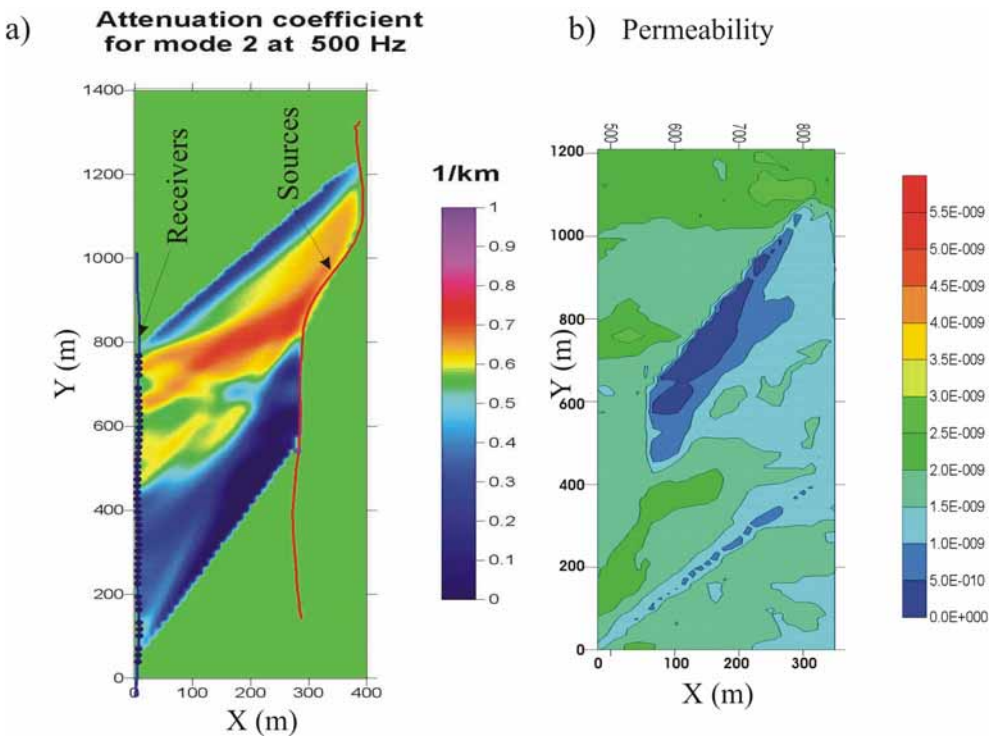

Figure 2.46: a) Horizontal crosswell attenuation tomogram for a sub-horizontal slice through the Marly unit (see Figure 2.70 for orientation). The tomogram is determined for energy with a centre frequency of 500 Hz. Data were acquired using a piezoelectric source deployed in one well and a 48-level hydrophone string in the opposite well. b) Permeability calculated using the attenuation values from a), based on the Biot (1956) relationship and using parameters (porosity and fluid viscosity) from the existing reservoir model. Units are in cm^2 (1 Darcy= $0.987x10^{-8}$ cm^2).

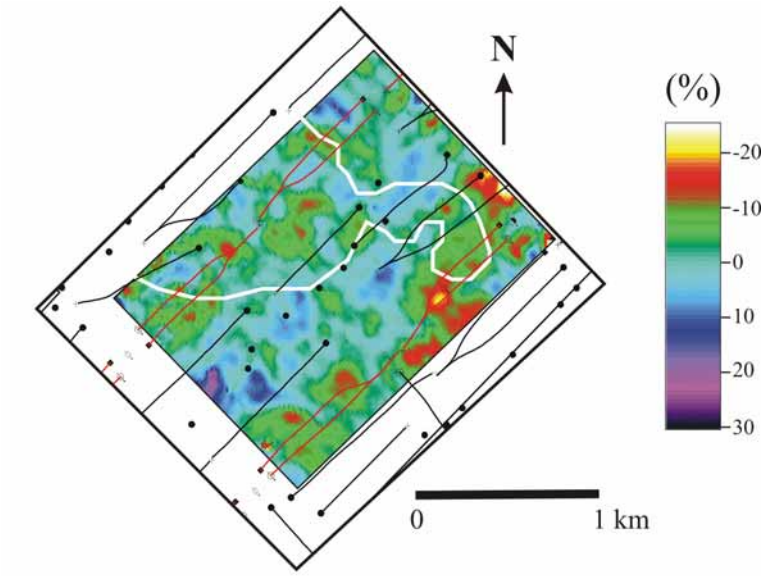

Figure 2.47: Shear wave anisotropy (%) map for the reservoir interval for the 4-pattern baseline survey in 2000 (from Fuck, 2003). The white line delineates the boundary of salt dissolution of the Prairie Evaporite, which resides below the reservoir.

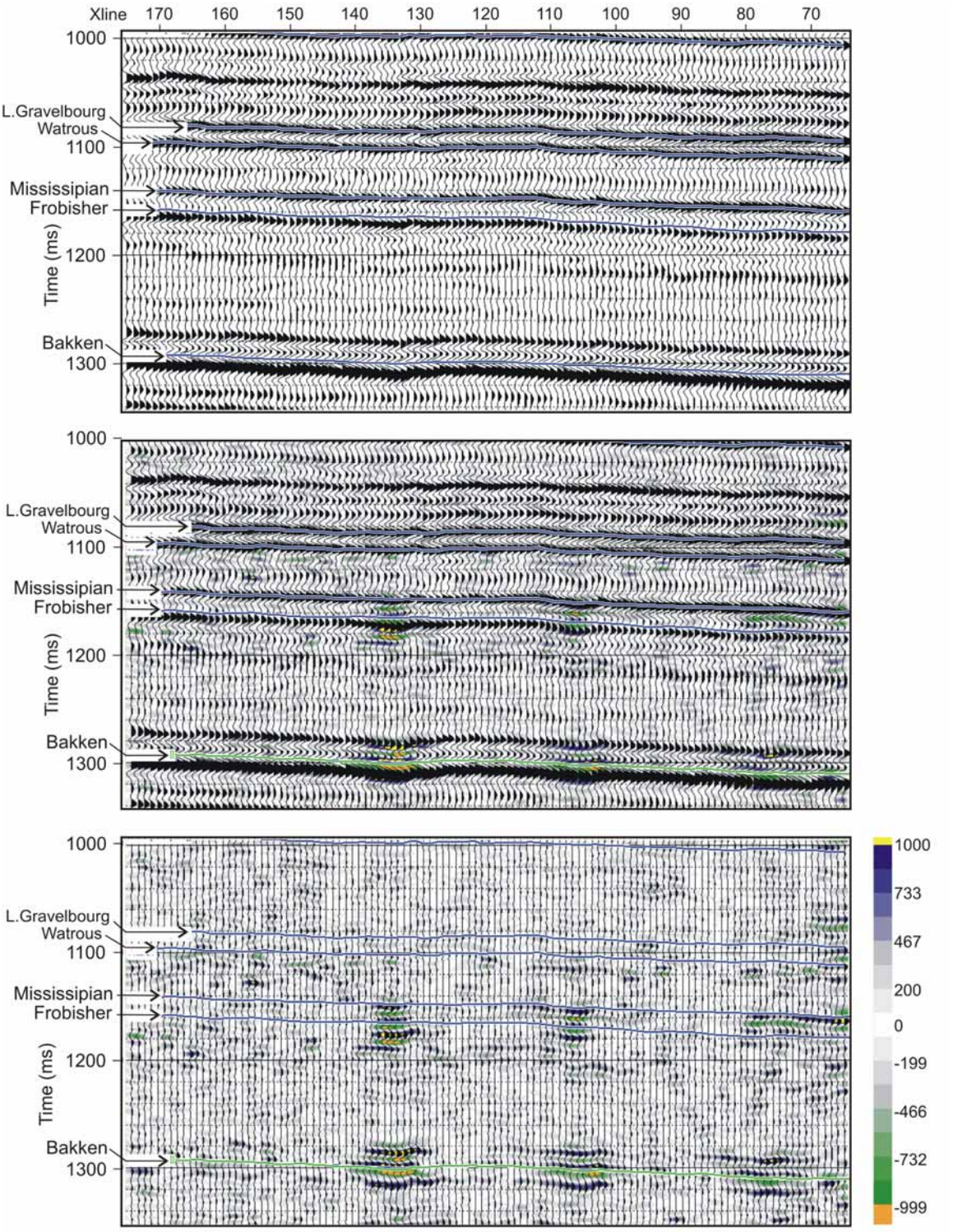

Figure 2.48: Baseline (top), Monitor 2 (middle), and difference (i.e., Baseline-Monitor 2; bottom) for a vertical section (in-line 128) through the 19-pattern 3D P-wave data volume. The colour underlay represents the difference amplitude.

Theme 2: Prediction, Monitoring, and Verification of CO_2 Movements

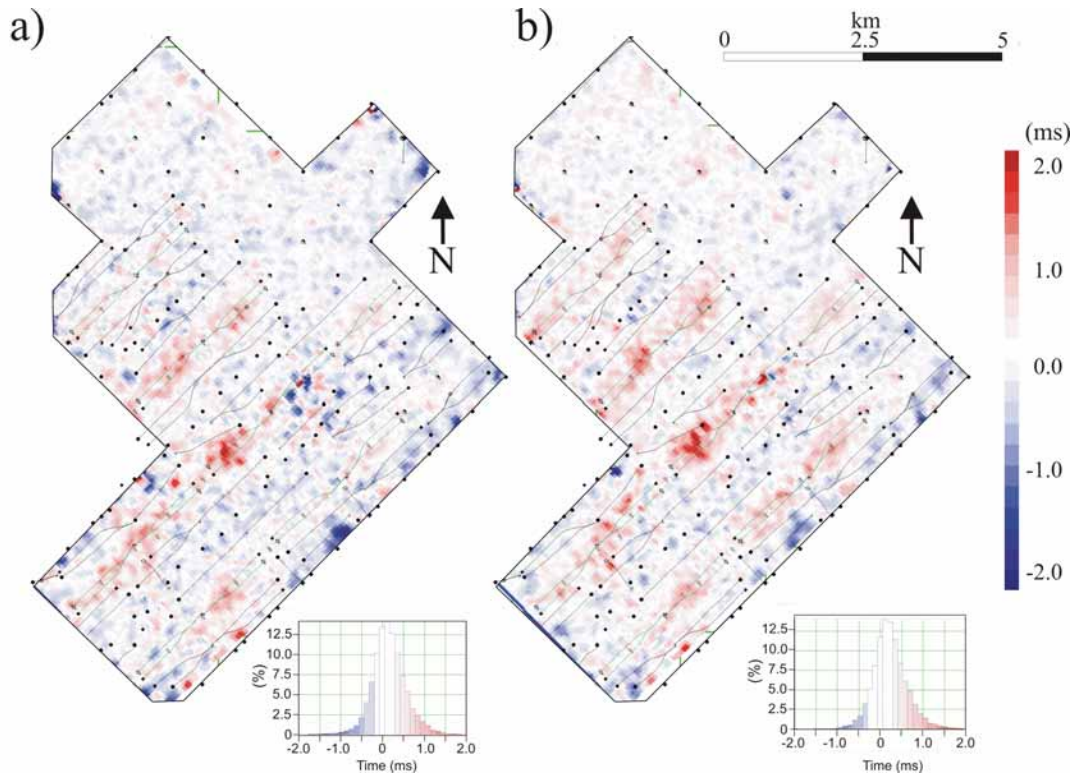

Figure 49: Travel-time delay maps for the Monitor 1 (2001) and Monitor 2 (2002) surveys relative to the Baseline survey. The time delays are determined at the Bakken horizon below the reservoir, which reflects the time delay for reflections passing through the reservoir while experiencing minor variations in the waveform. The determination of travel time delays in the immediate vicinity of the reservoir (using either the Vuggy or Marly horizons) is complicated by changes in the waveform introduced at the reservoir horizons. Insets show histograms of the travel time delays.

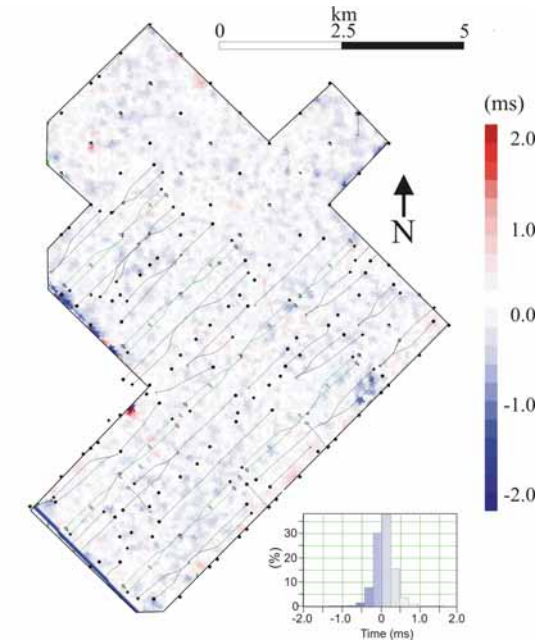

Figure 2.50: Travel-time delay map for the Monitor 2 survey relative to the Baseline survey determined at the Lower Gravelbourg horizon that is located above the reservoir. This horizon is used as a static reference level to determine the uncertainty levels in the delay map (i.e., travel time delays that are less than those observed at the Lower Gravelbourg should not likely be considered significant). Inset shows a histogram of the travel time delays.

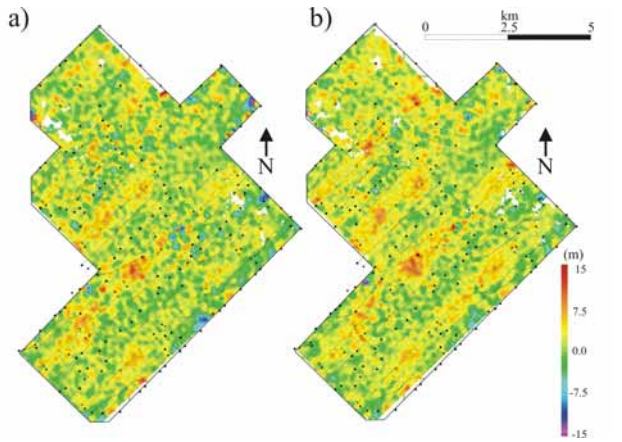

Figure 2.51: Estimated fractional velocity decrease map for the reservoir. The velocity decrease is estimated using the known reservoir thickness and the observed time delays (from Figure 2.49) to obtain a fractional velocity decrease based on the travel time delay-CO_2 thickness curves of Figure 2.27. That is, this fractional velocity decrease map represents the average velocity decrease corresponding to the observed travel time delay if the travel time delay is associated with the entire reservoir thickness (i.e., if the CO_2 fills the whole vertical reservoir column). In this sense, this map represents the minimum fractional velocity decreases within the reservoir required to produce the observed travel time delays. Fractional velocity decreases may be greater if the CO_2 is restricted to a sub-interval of the reservoir.

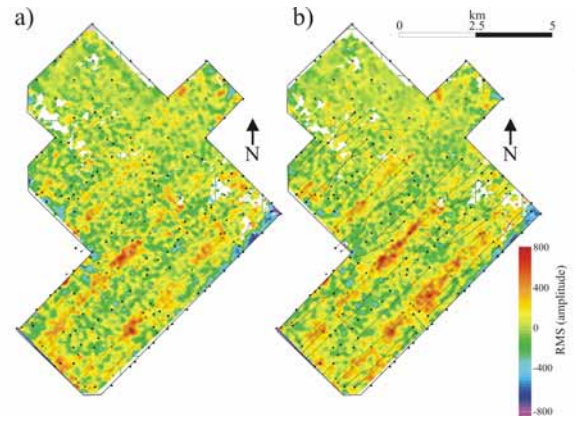

Figure 2.52: Amplitude difference map at the Midale Marly horizon for the Monitor 1 and 2 surveys relative to the Baseline survey. The amplitudes are RMS values determined using a 5 ms window centred on the horizon.

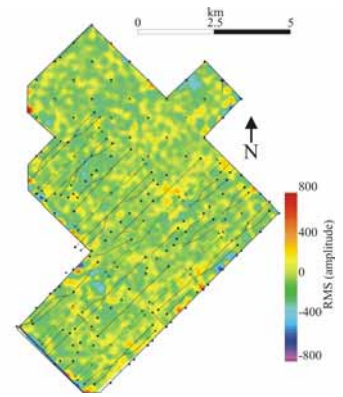

Figure 2.53: Amplitude difference map at the Lower Gravelbourg horizon for the Monitor 2 survey relative to the Baseline survey. The amplitudes are RMS values determined using a 5 ms window centred on the horizon. This horizon is used as a static reference level to determine the uncertainty levels in the amplitude difference map (i.e., amplitude differences that are less than those observed at the Lower Gravelbourg should not be considered significant).

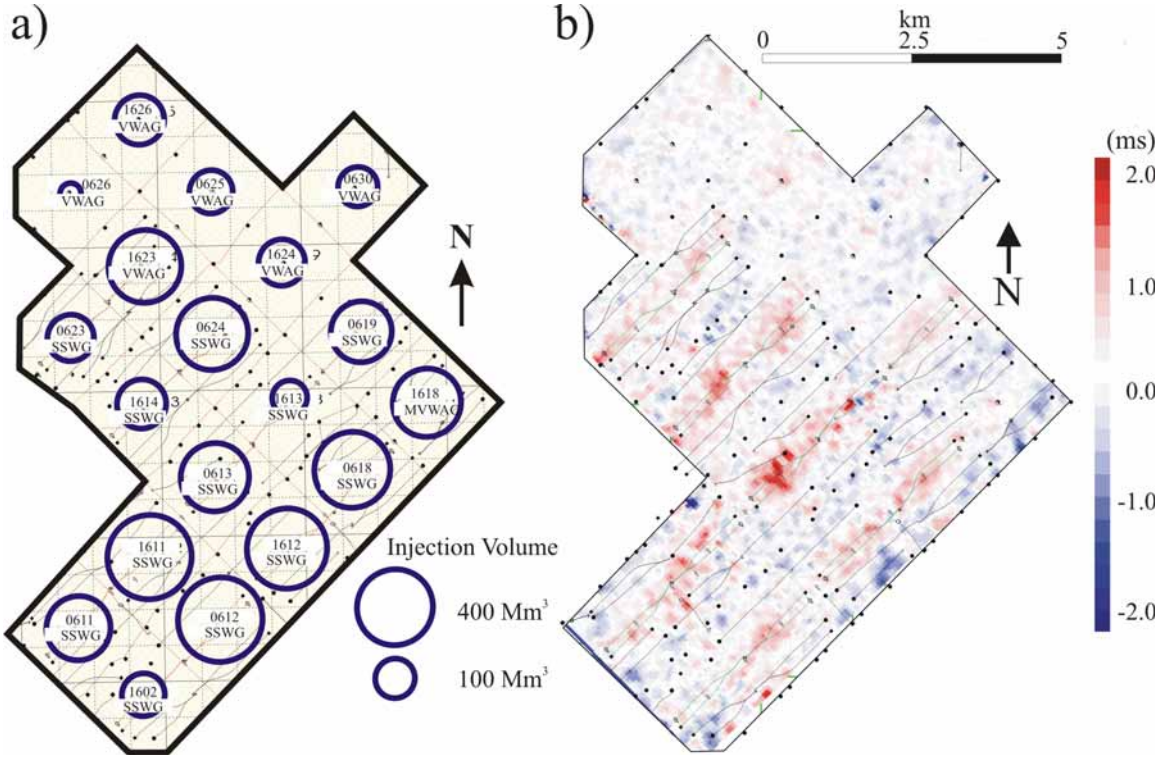

Figure 2.54: Comparison of a) gross CO_2 injection volumes (at approximate reservoir conditions) by pattern to the time of the Monitor 2 survey, and b) travel time delay anomalies for the Monitor 2 survey.

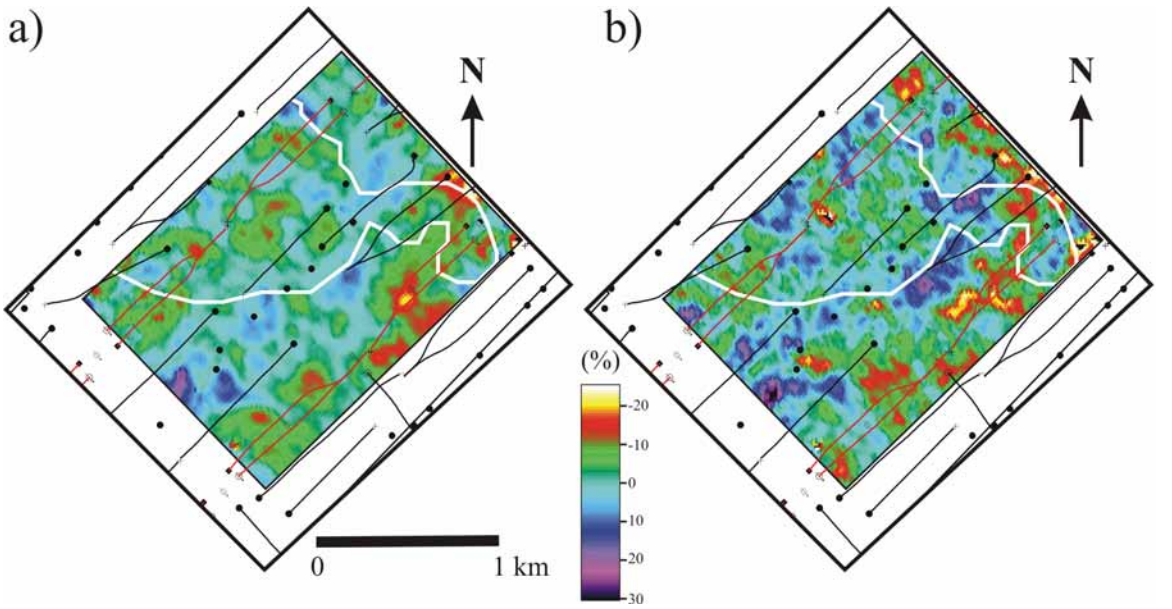

Figure 2.55: Comparison of the shear-wave splitting maps from a) Baseline survey and b) Monitor 2 survey for the 4-pattern sub-region of Phase 1A. The white line delineates the boundary of salt dissolution of the Prairie Evaporite, which resides below the reservoir.

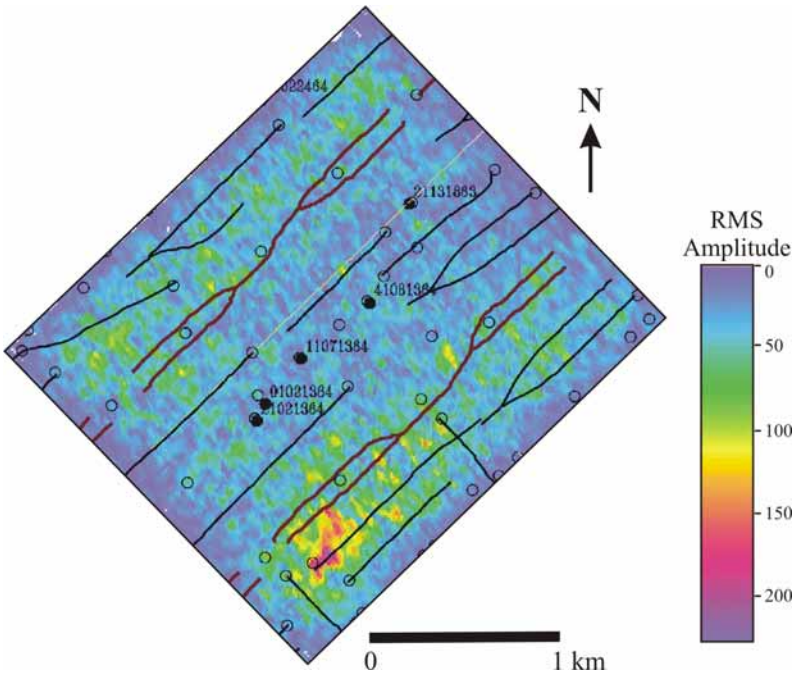

Figure 2.56: S-wave amplitude differences for the Monitor 2 survey relative to the Baseline survey for the 4-pattern sub-region of Phase 1A (after Davis et al., 2003).

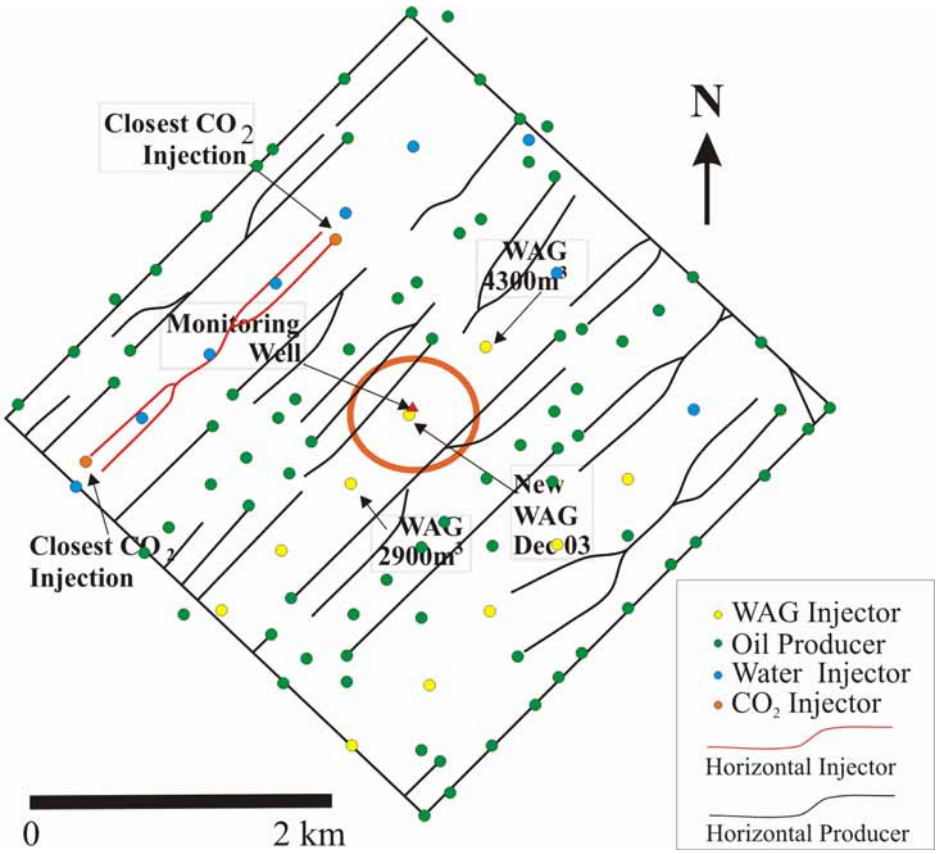

Figure 2.57: Map of wells in the vicinity of the Phase 1B passive monitoring well. Horizontal and vertical lines represent township lease boundaries spaced at 1600 m for scale. See Figure 2.2 for the location of Phase 1B relative to Phase 1A.

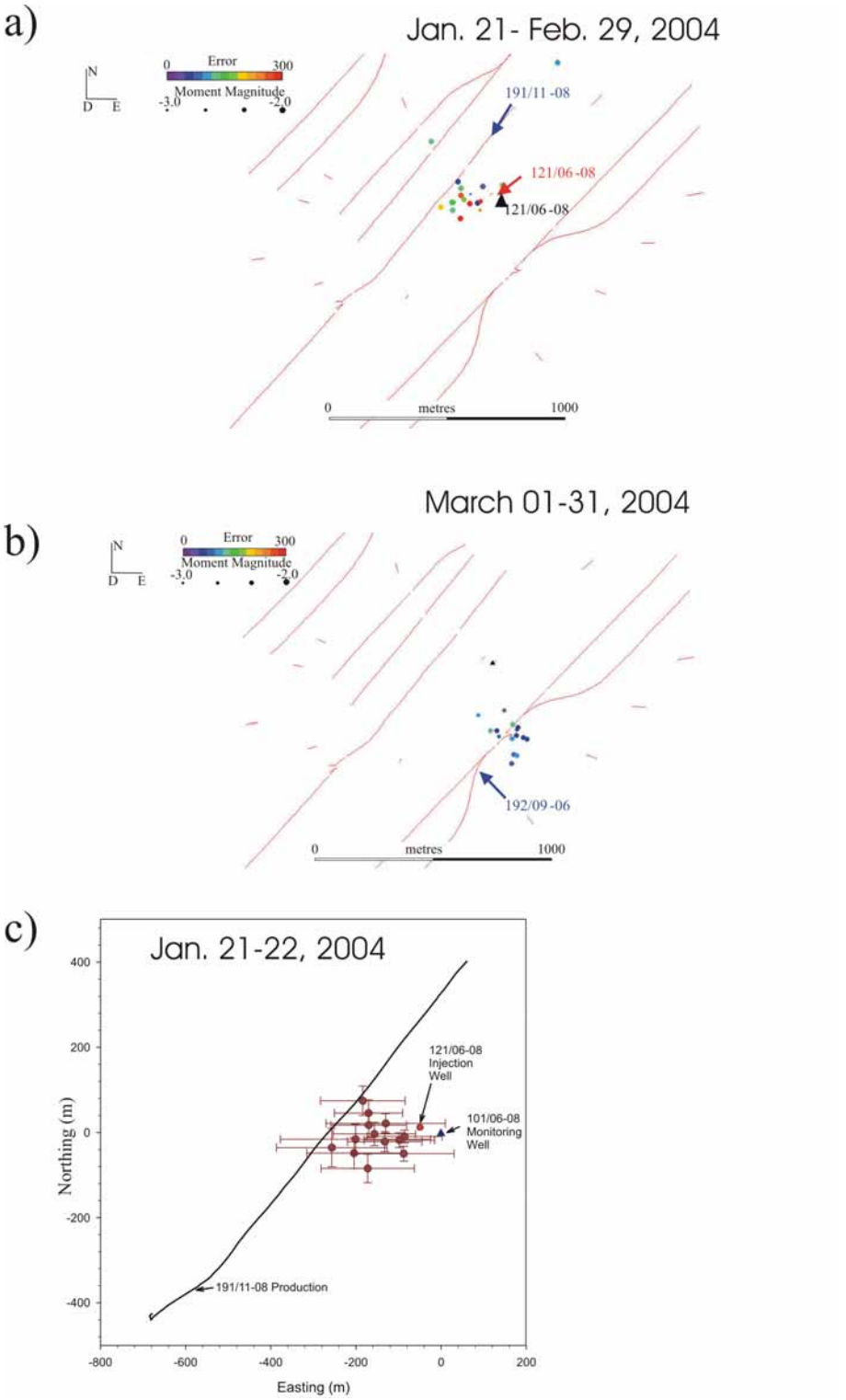

Figure 2.58: Plan view of microseismic events (circles) recorded during a) Jan. 21-Feb. 29, 2004, b) Mar. 1-Mar. 31, 2004, and c) locations with uncertainty bars for cluster of events occurring Jan. 21-22, 2004. Geophones are represented by a black triangle. The uncertainty bars represent 95% confidence limits determined for the following estimated data uncertainties: p-wave arrival times (±5 ms), s-wave arrival times (±8 ms), and source azimuth direction (±10°).

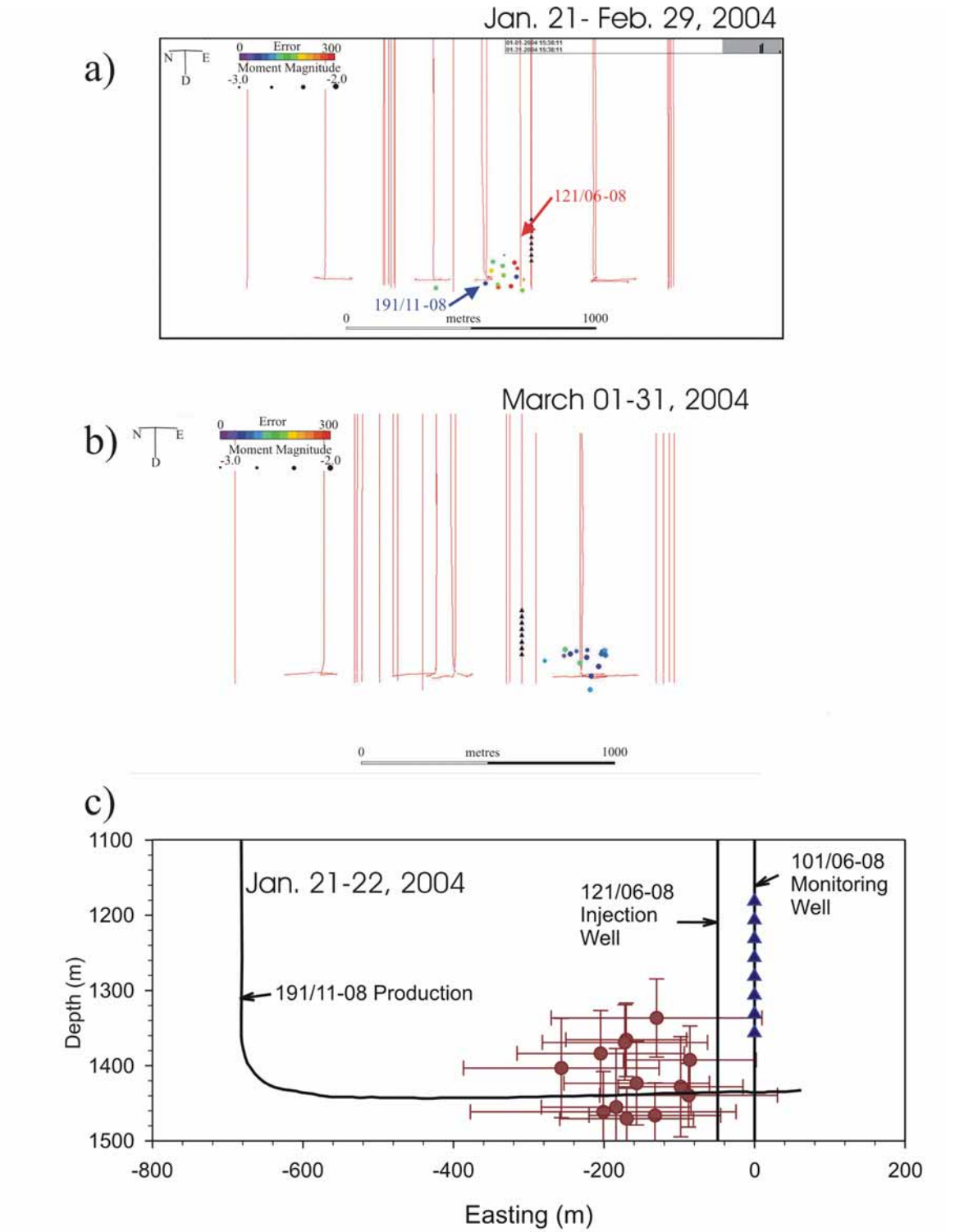

Figure 2.59: Sectional view of microseismic events (circles) recorded during a) Jan. 21-Feb. 29, 2004, b) Mar. 1-Mar. 31, 2004, and c) locations with error bars for cluster of events occurring Jan. 21-22, 2004. Geophones are represented by a black triangle. The uncertainty bars represent 95% confidence limits determined for the following estimated data uncertainties: p-wave arrival times (±5 ms), s-wave arrival times (±8 ms), and source azimuth direction (±10°).

a)

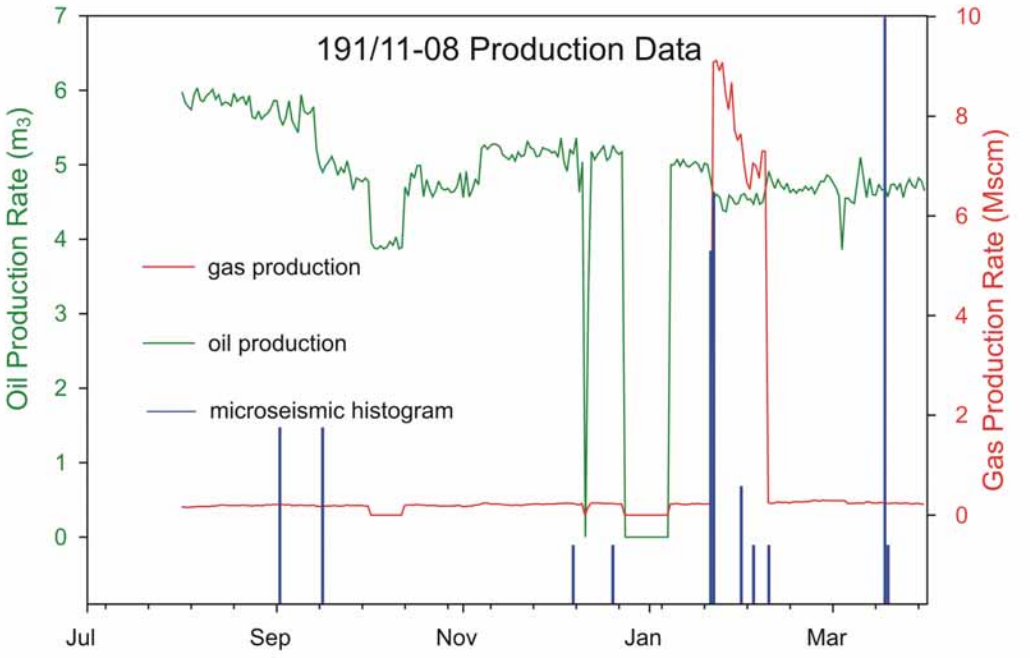

b)

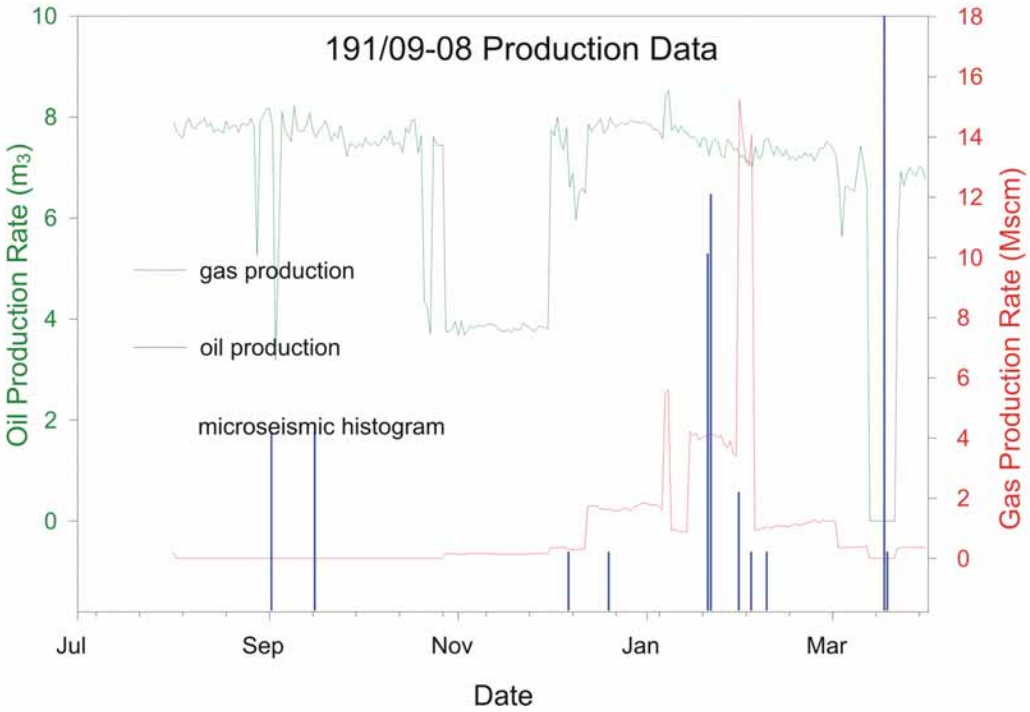

Figure 2.60: Injection and production rates from neighbouring horizontal wells compared to histograms of microseismicity. a) Well 191/11-08, and b) well 191/09-08. See Figures 2.57 to 2.59 for well locations relative to the monitoring well.

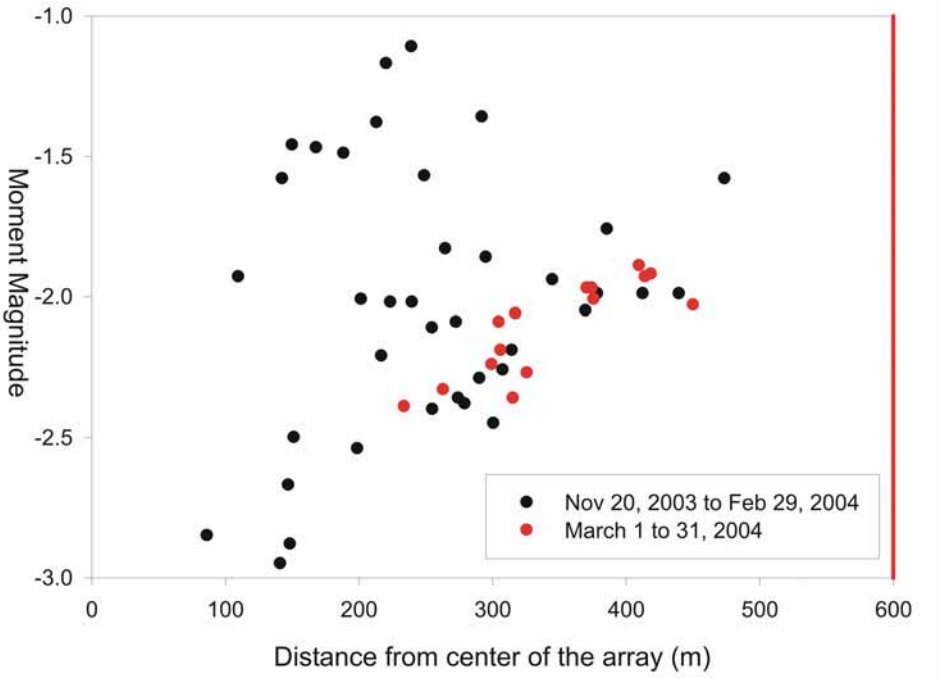

Figure 2.61: Moment magnitude versus distance from seismic array for all events detected between Nov. 20, 2003, and Mar. 31, 2004, defining the limit of sensitivity of the seismic array for events for a given distance.

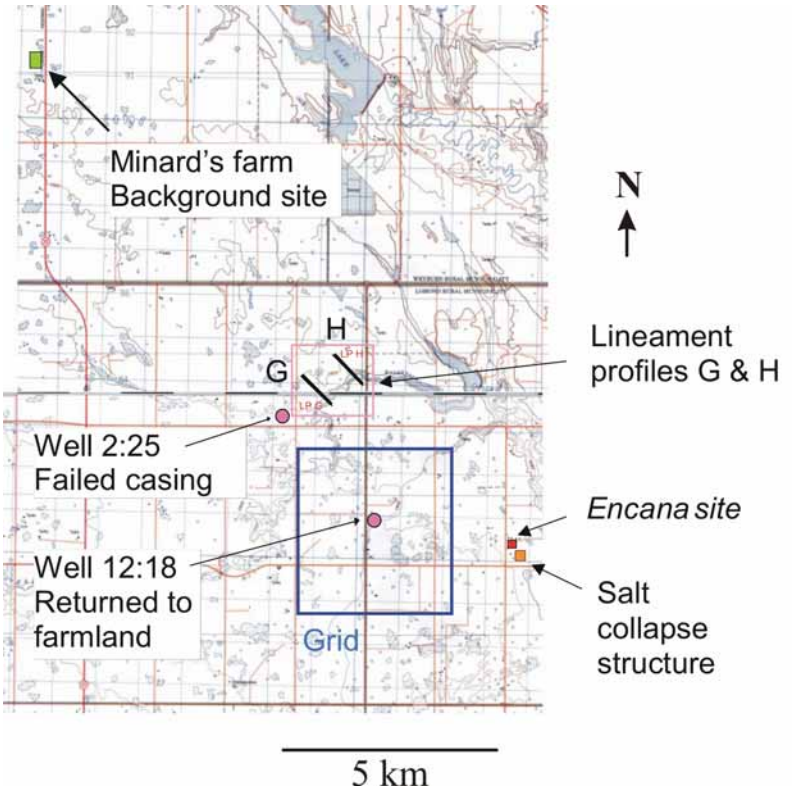

Figure 2.62: Map showing the locations of the various soil gas sampling sites.

Theme 2: Prediction, Monitoring, and Verification of CO_2 Movements

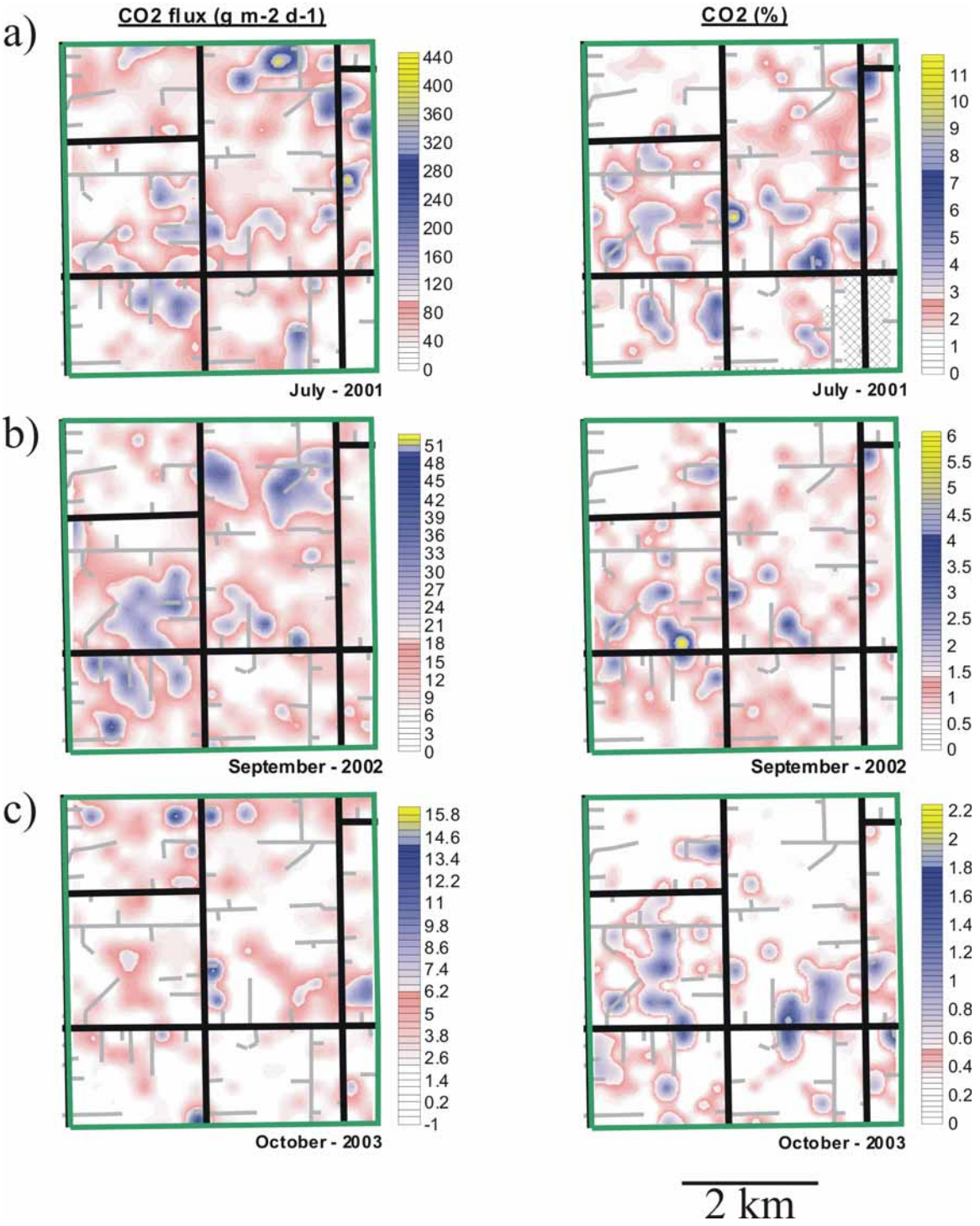

Figure 2.63: Contoured distribution of CO_2 flux (left column) and soil gas CO_2 (right column) for the three sampling campaigns: a) July, 2001, b) September, 2002, and c) October, 2003.

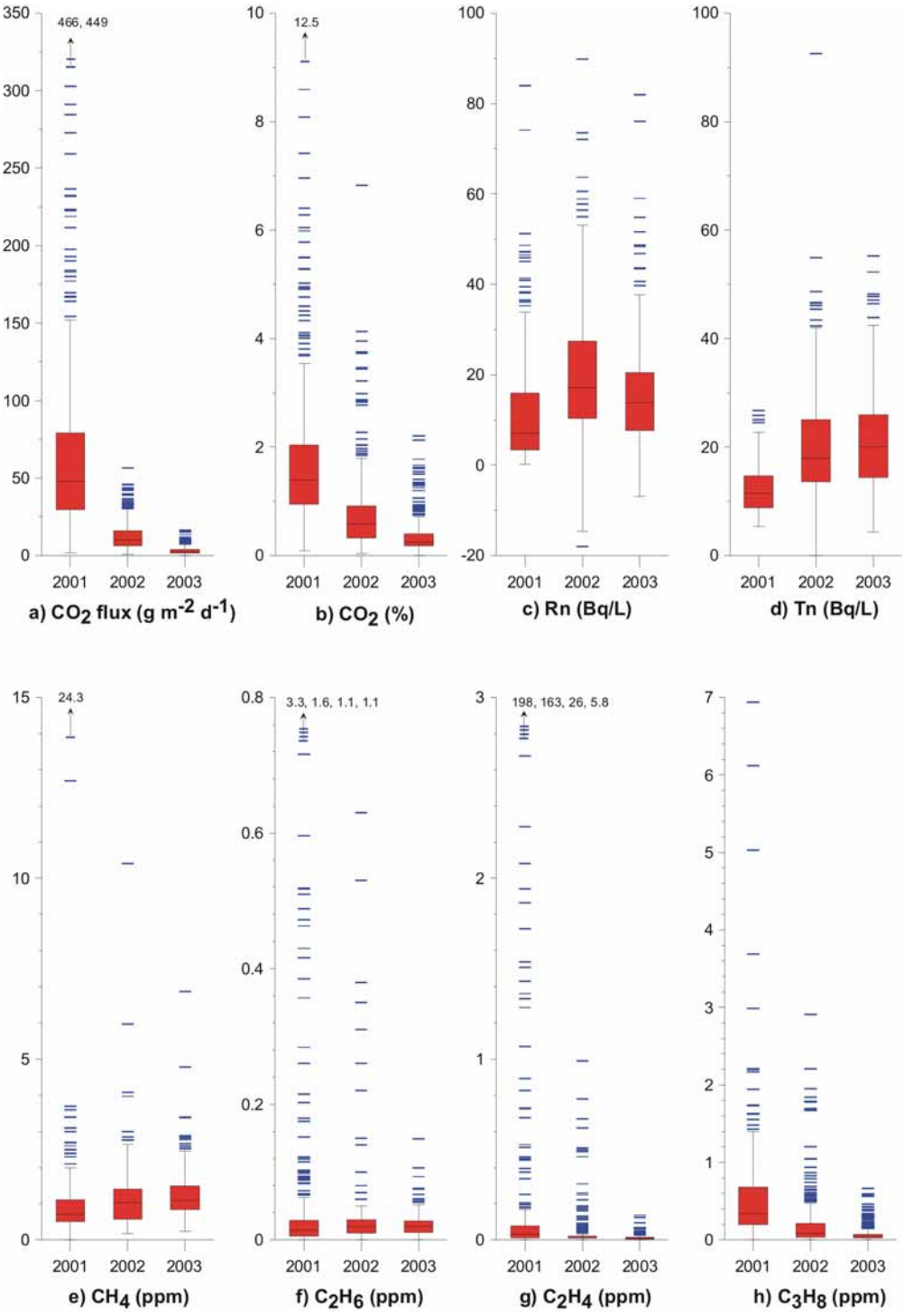

Figure 2.64: Box and whisker plots for gas flux and some of the soil gases measured on the main grid for each of the three years of the project. CO_2 flux, CO_2, ethylene, and propane all decrease substantially with each successive field campaign, whereas radon and thoron are relatively constant and methane and ethane decrease primarily only in the outlier values. Note that off-scale values are represented with an arrow and the respective numerical value(s). The units of the various measurements are indicated in the parentheses of the label that identifies each plot. The following are included in the Box and whisker plot format: median value with 25th and 75th percentiles (shaded box and horizontal line within), 5th and 95th percentile (vertical line with end-dashes), and outlying values (isolated dashes).

Theme 2: Prediction, Monitoring, and Verification of CO_2 Movements

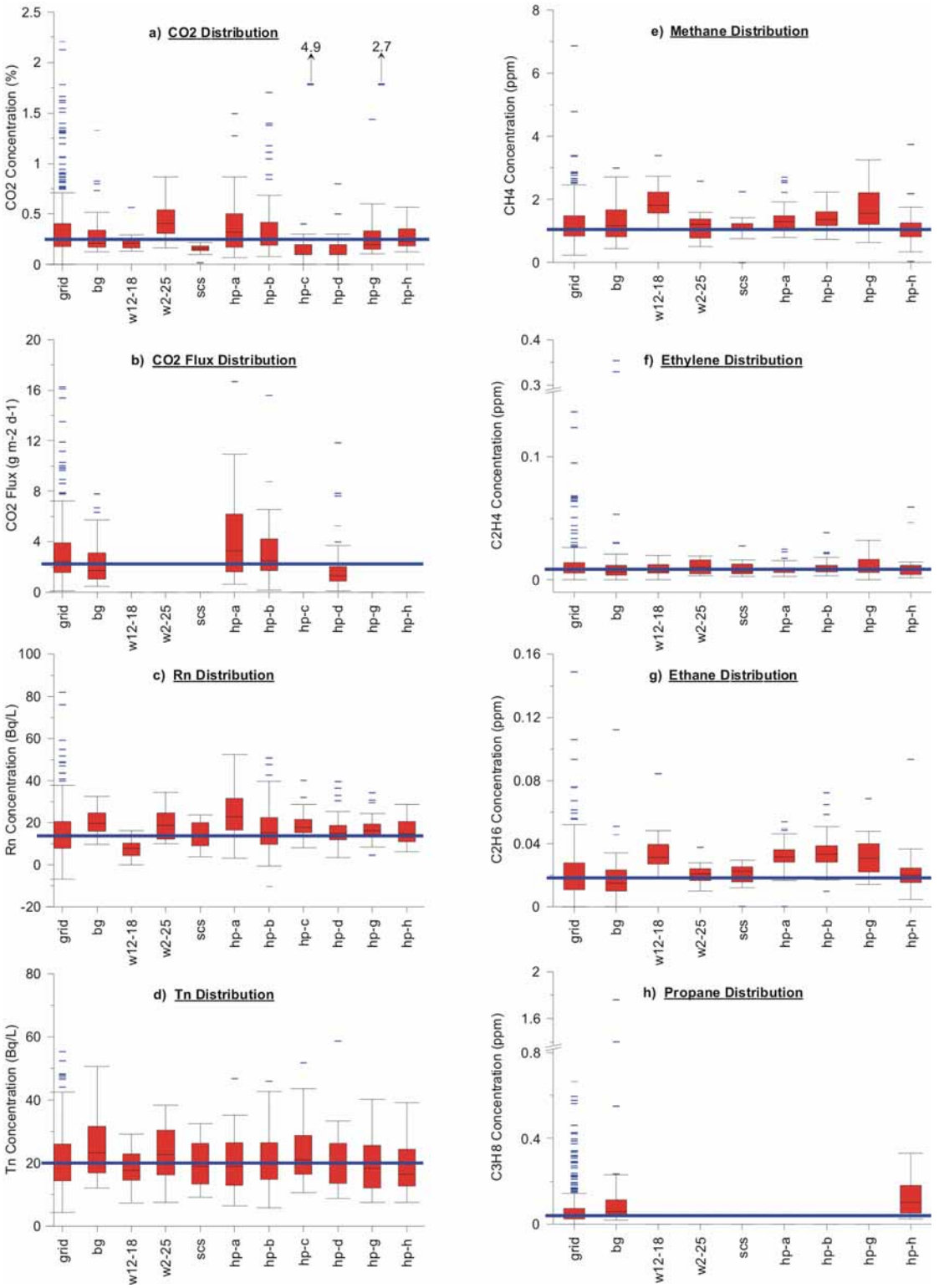

Figure 2.65: Box and whisker plots showing the statistical distribution of the various measured parameters for each of the 11 sites sampled during the October 2003 campaign. Note that the long horizontal blue line, which represents the median of the main grid data set, has been added to aid in comparisons. The abbreviated site labels (see Figure 2.62 for locations) are: bg=background, w12-18=well 12:18, w2-25=well 2:25, scs=salt collapse structure, and hp=highly detailed horizontal profiles. The following are included in the Box and whisker plot format: median value with 25th and 75th percentiles (shaded box and horizontal line within), 5th and 95th percentile (vertical line with end-dashes), and outlying values (isolated dashes).

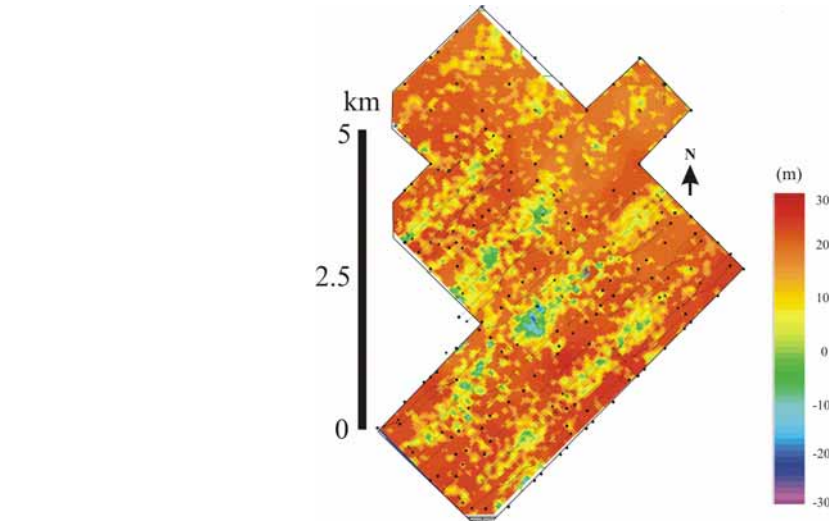

Figure 2.66: Difference map of the true reservoir thickness (from the geological model) minus the CO_2 thickness estimated from the travel time delay map. The thickness of the CO_2 column is predicted from the observed travel time delay map converted to thickness using an estimated fractional velocity decrease of 10% where CO_2 saturation occurs. The assumption is that the CO_2 occupies a vertical interval of the reservoir ranging from zero to the full reservoir thickness. Regions where the difference is negative correspond to regions where the modeled saturation relation does not adequately account for the observed travel time delays within the thickness of the reservoir. This could be due to 1) unaccounted pressure effects, 2) CO_2 saturation within a column exceeding the reservoir thickness (e.g., CO_2 extending into the Frobisher unit), or 3) inaccuracy of the model-based regression relationship. The latter possibility may be the result of large-scale fractures that affect travel times observed at the seismic survey scale that are not represented in the core-scale measurements.

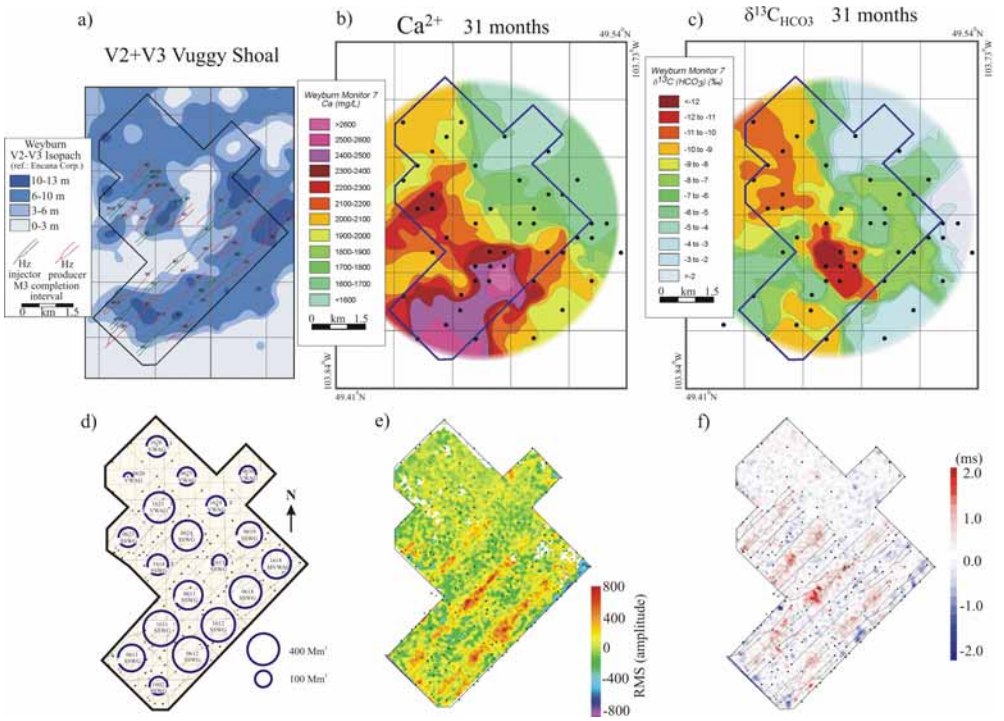

Figure 2.67: Comparison of geochemical and seismic monitoring maps, gross injection volumes, and the thickness of the Vuggy shoal unit.

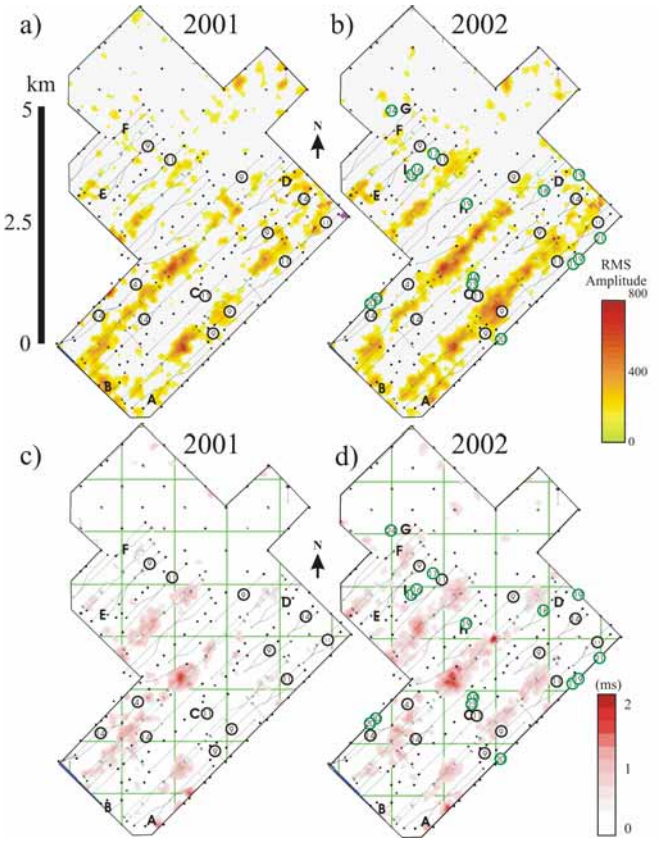

Figure 2.68: Comparison of P-wave time-lapse seismic anomaly maps and CO_2 well responses as determined from production data for the Monitor 1and Monitor 2 surveys. a,b) Amplitude difference maps determined at the Marly horizon with a threshold of 175 amplitude units applied. c,d) Travel time delay maps determined at the Bakken horizon with a threshold of 0.5 ms applied. The circles denote production wells that have recorded a CO_2 response. The number in each circle indicates the time of response in months since the start of CO_2 injection. Black circles indicate responses in the first 12 months, and green circles indicate responses after the first 12 months.

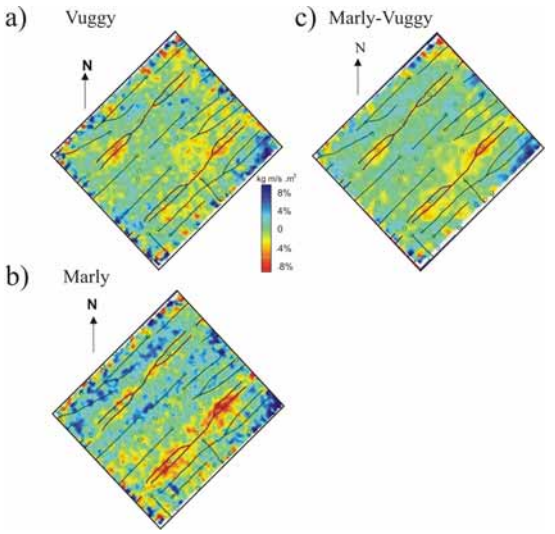

Figure 2.69: Impedance changes for the a) Vuggy, b) Marly, and c) combined Marly and Vuggy as determined by inversion of the Baseline and Monitor 2 P-wave data for the CSM 4-pattern area (see Figure 2.2 for location) from Herawati (2003).

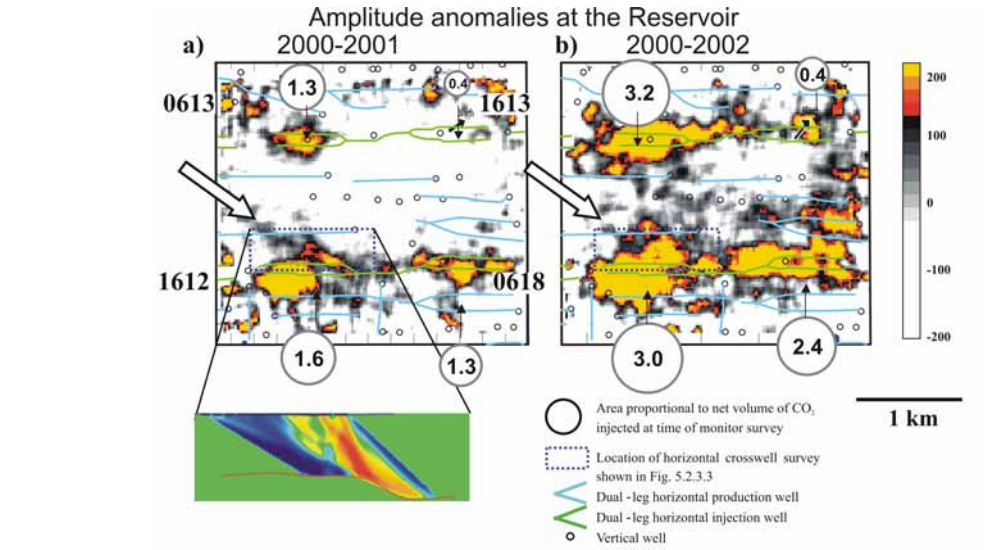

Figure 2.70: P-wave amplitude difference maps for a) Baseline minus Monitor 1 and b) Baseline minus Monitor 2 surveys, determined from the 3D P-wave surface seismic data from the 4-pattern sub-region of Phase 1A (after White et al., 2004). Note that this Monitor 2 survey was acquired 2 months earlier than the Monitor 2 survey for the full 19-pattern area. The amplitudes were determined as the arithmetic mean over a 5 ms window centered on the reservoir horizon. The large circles represent the cumulative net volume of CO_2 (at reservoir conditions in units of 10^6 m^3) that had been injected at the time of the monitor survey for each of the 4 dual-leg horizontal injectors. The large arrows indicate interpreted zones of off-trend CO_2 spread. In a), the attenuation tomogram from Figure 2.46 is shown in an expanded panel emanating from its position on the amplitude map.

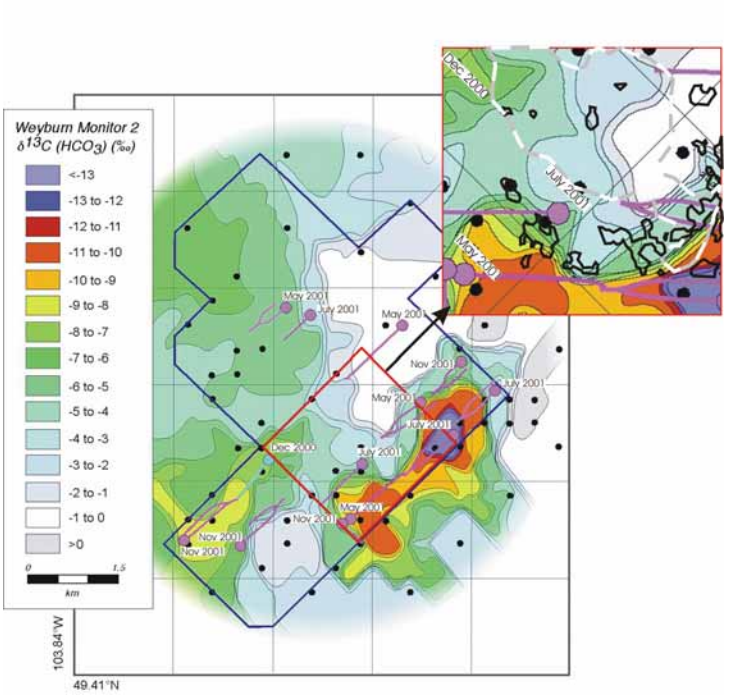

Figure 2.71: Contour map of the $\delta^{13}C$ values from the Monitor 2 fluid sampling survey (July, 2001). Black dots identify well locations where fluid/gas sampling was conducted within the 9-pattern Phase 1A flood area (dark outline). The larger dots and horizontal well legs that are coloured purple identify wells where a significant CO_2 response was observed within 4 months following the sampling survey. For comparison, the red rectangle identifies an area (shown in detail in the expanded inset panel, upper right) where the gamma parameter (or shear-wave splitting map) has been determined from the S-wave data for the Monitor 2 seismic survey (2002). The gamma parameter is a measure of the % difference between the velocities of the fast and slow (split) shear waves and can be used to estimate fracture density and direction. In the inset, zones indicated by heavy black outlines identify negative anomalies where the gamma parameter map (not shown) values are <-10%. The heavy white dashed line is the salt dissolution edge.

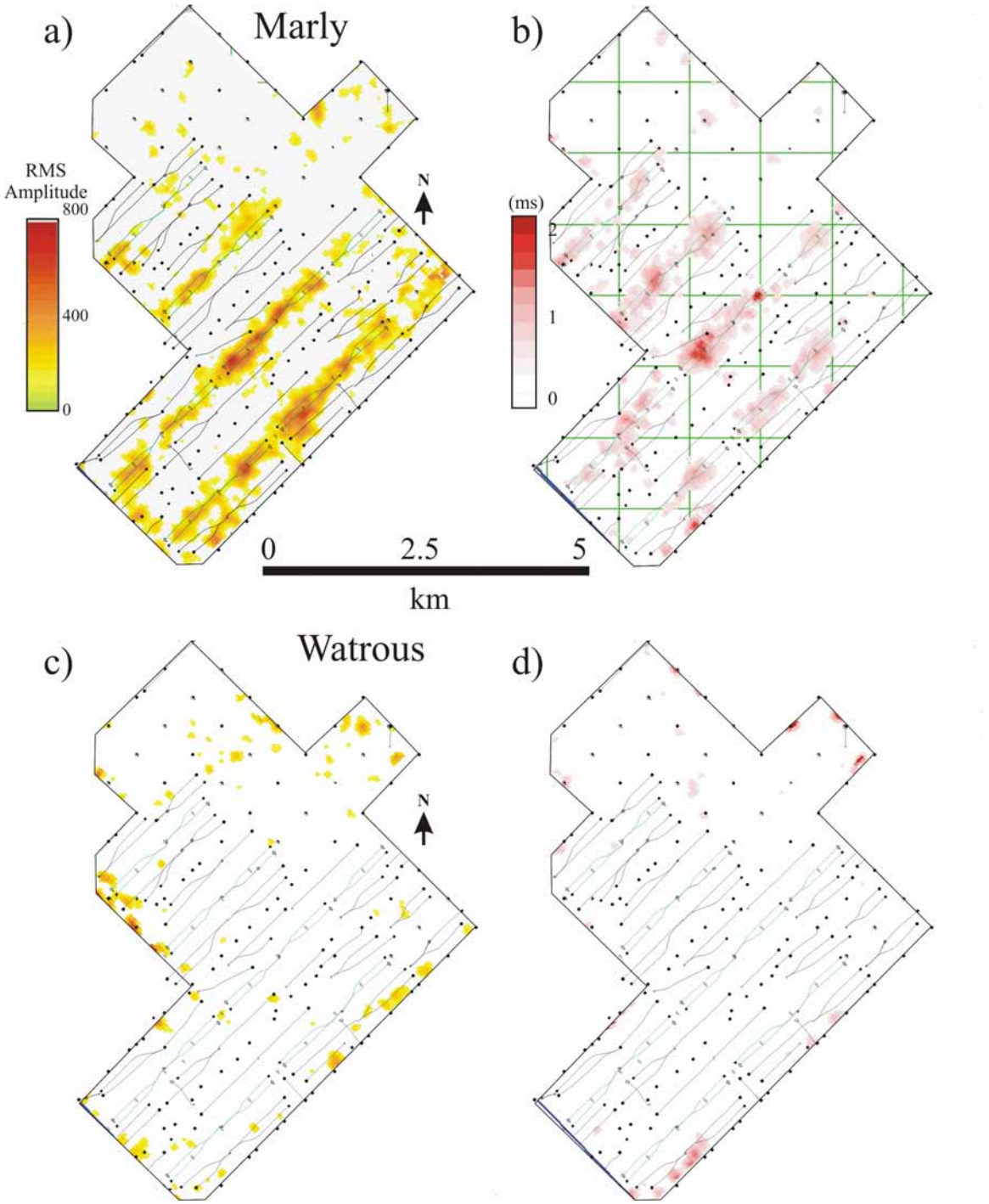

Figure 2.72 (part 1): Amplitude difference maps (left column) and travel time delay maps (right column) for the Monitor 2 (2002) survey relative to the Baseline survey at the following horizons (from top to bottom): a,b) Marly, c,d) Watrous, e,f) Lower Gravelbourg, and g,h) Lower Vanguard. The same amplitude and time delay threshold levels have been applied as in Figure 2.68.

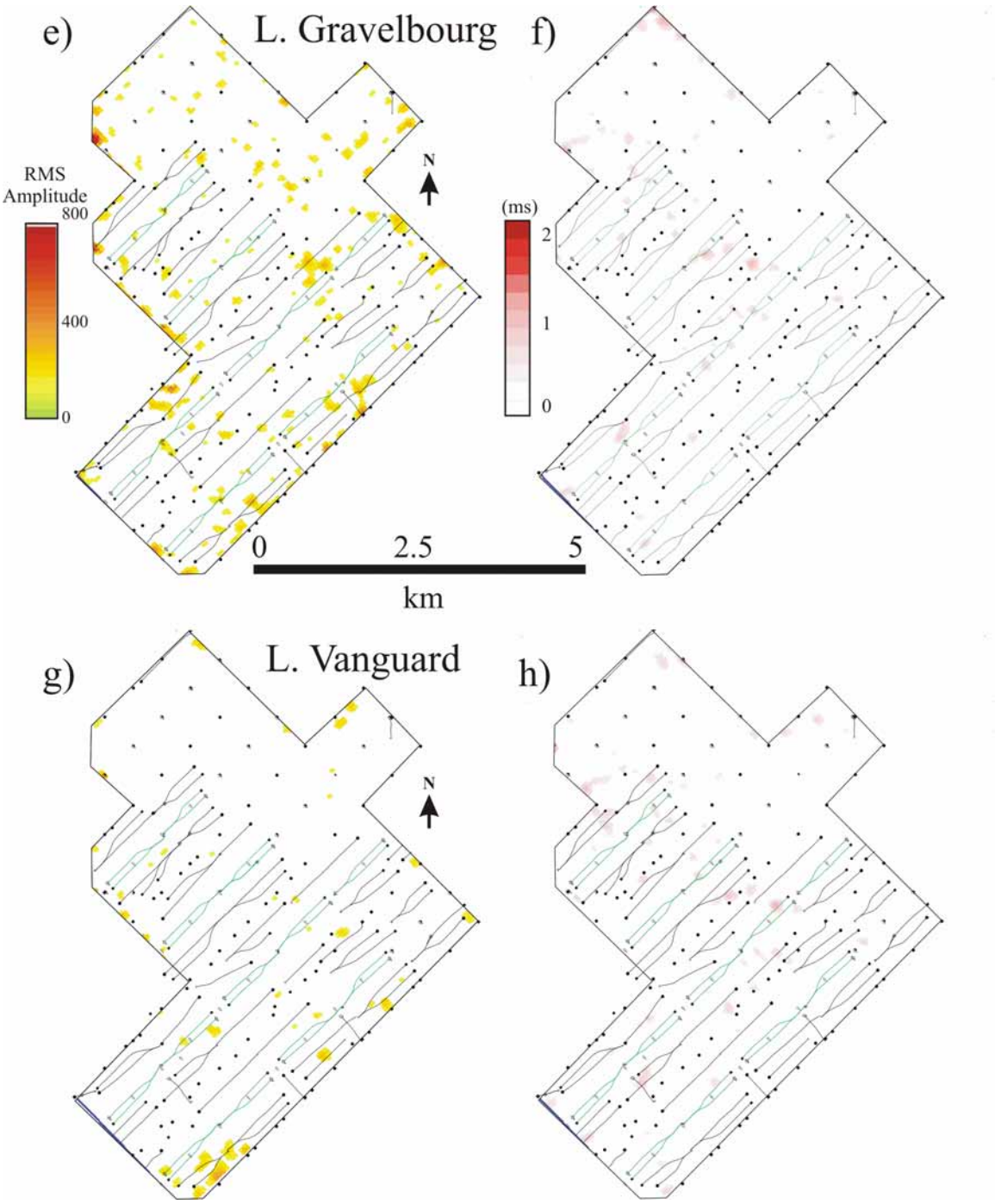

Figure 2.72 (part 2): Amplitude difference maps (left column) and travel time delay maps (right column) for the Monitor 2 (2002) survey relative to the Baseline survey at the following horizons (from top to bottom): a,b) Marly, c,d) Watrous, e,f) Lower Gravelbourg, and g,h) Lower Vanguard. The same amplitude and time delay threshold levels have been applied as in Figure 2.68.

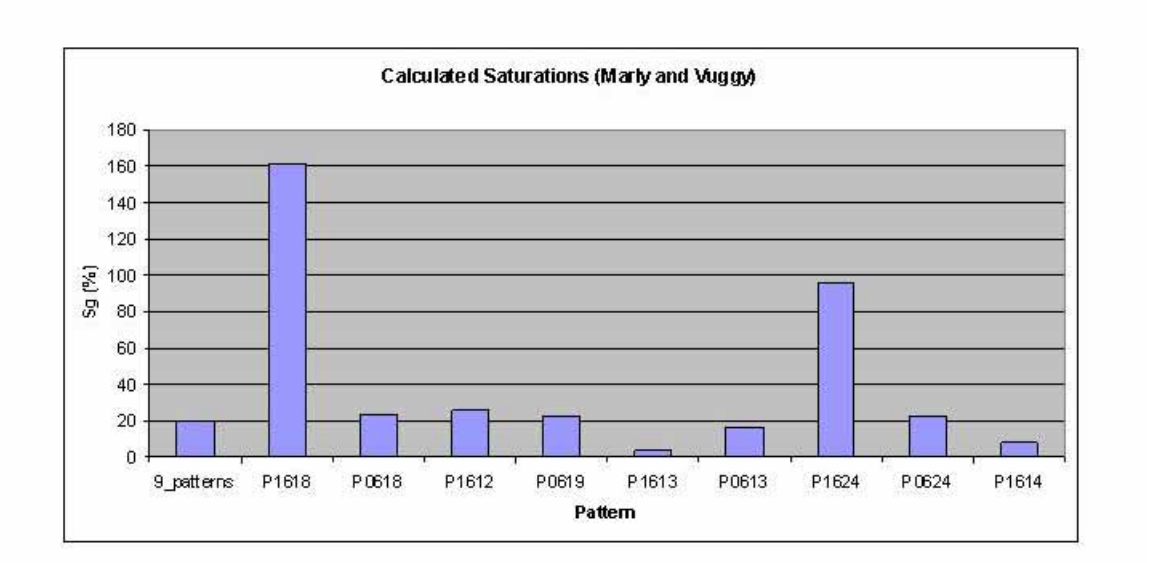

Figure 2.73: Calculated mean gas saturation by pattern determined from volumetrics for the Monitor 2 P-wave amplitude map.

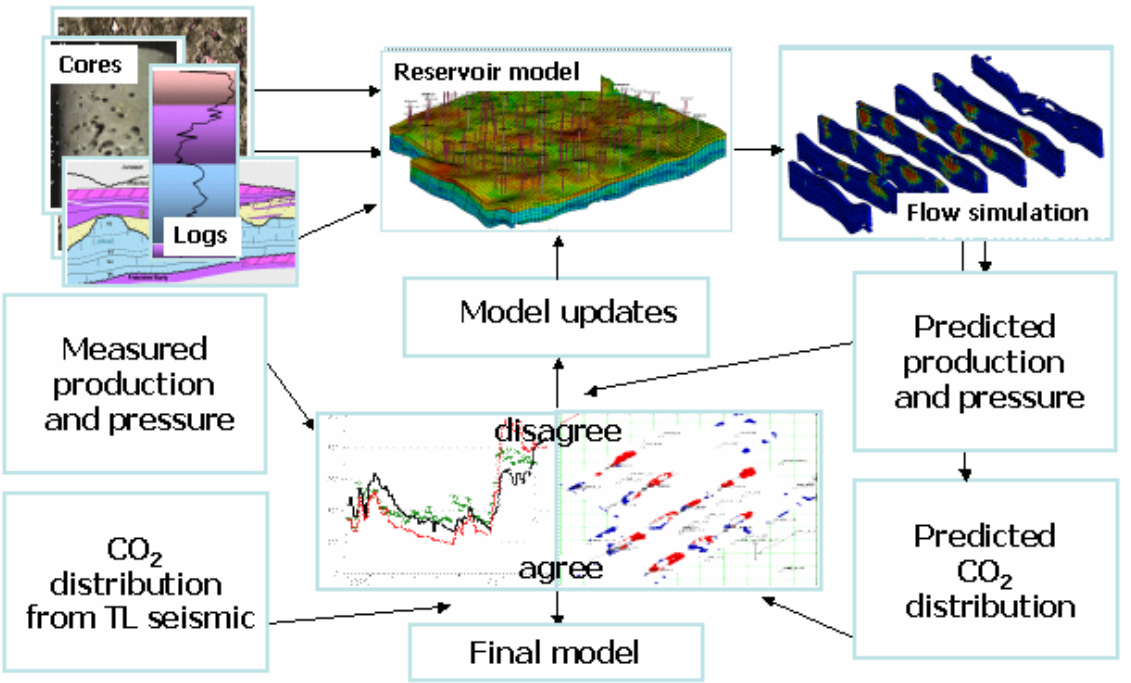

Figure 2.74: Schematic process flow for history matching including direct use of the seismic information.

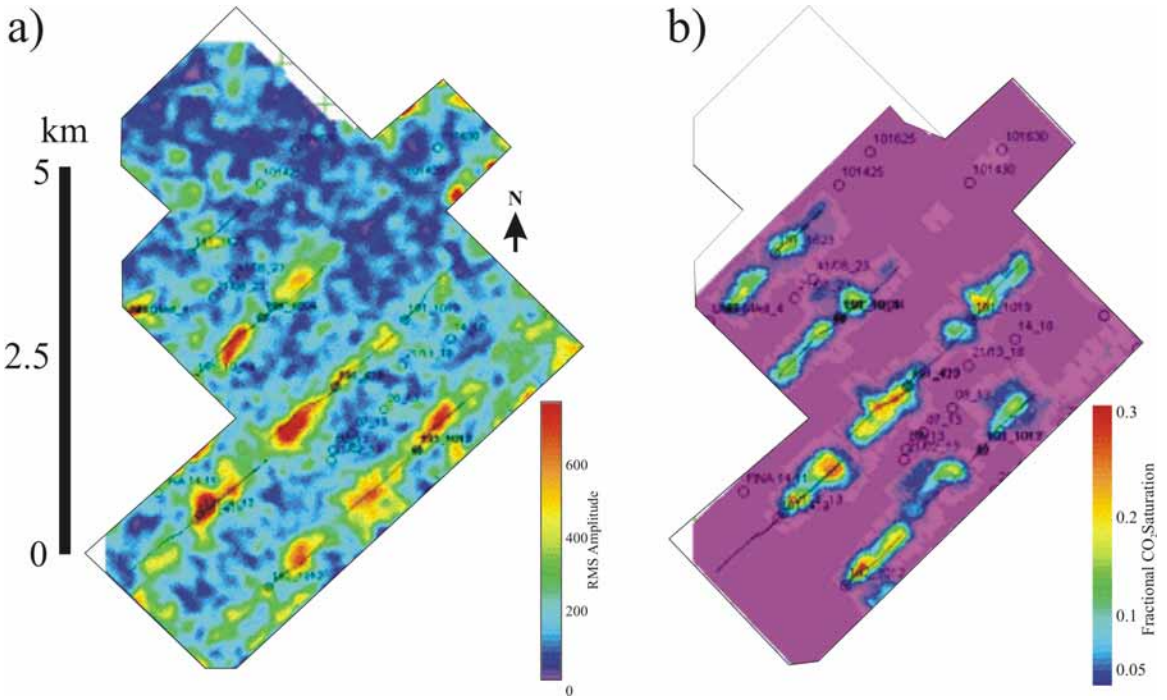

Figure 2.75: Comparison of CO_2 distribution at the Marly level at the time of the Monitor 2 survey as derived from the a) P-wave time-lapse time delay map and b) original reservoir simulation model.

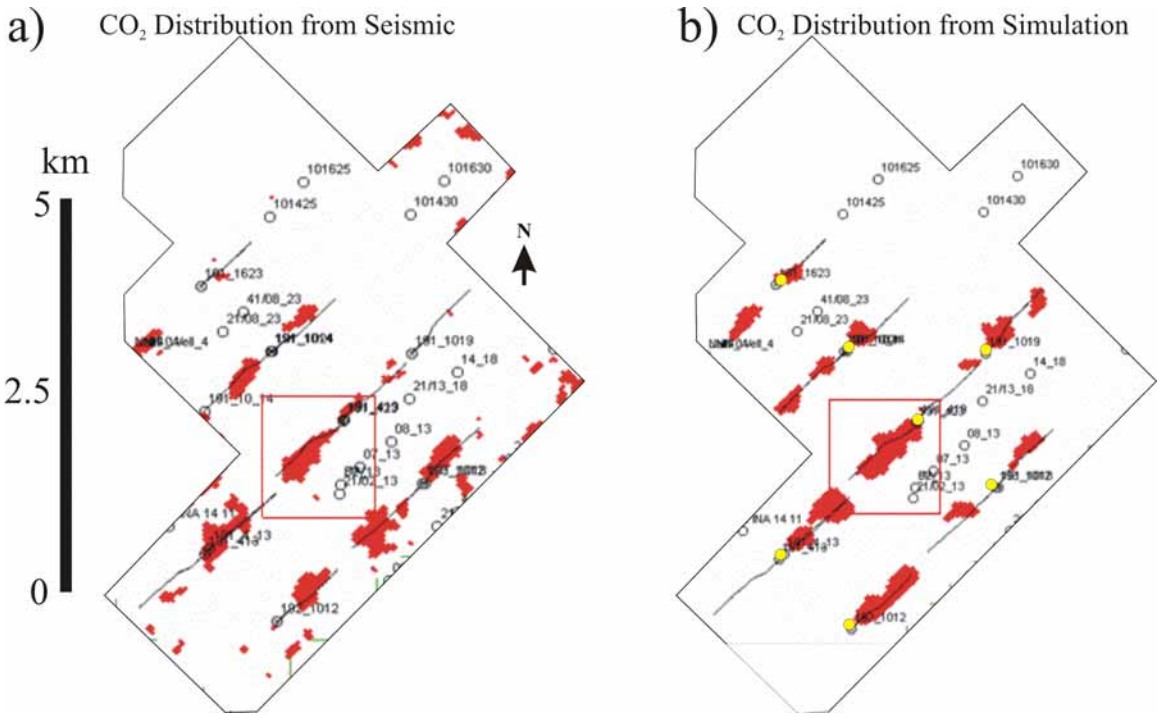

Figure 2.76: CO_2 distribution at the time of the Monitor 2 Survey as predicted by a) the P-wave amplitude difference map and b) the starting reservoir simulation model shown in Figure 2.75. In a), the CO_2 distribution is determined by applying a threshold of 1.5 standard deviations of the amplitude map. In b), the CO_2 distribution represents areas where CO_2 saturation exceeds 10 molar per cent. The choice of threshold values is subjective, but the results are not overly sensitive to the value used for two reasons; first, the gas saturation distribution from the simulator changes quickly in the vicinity of the CO_2 front, and second, the seismic response is very sensitive to the presence of CO_2 in small amounts (5-10%), but it less sensitive for increases to higher saturation levels. Thus, in either case, significant variations in the chosen threshold lead to small changes in the estimated position of the CO_2 front.

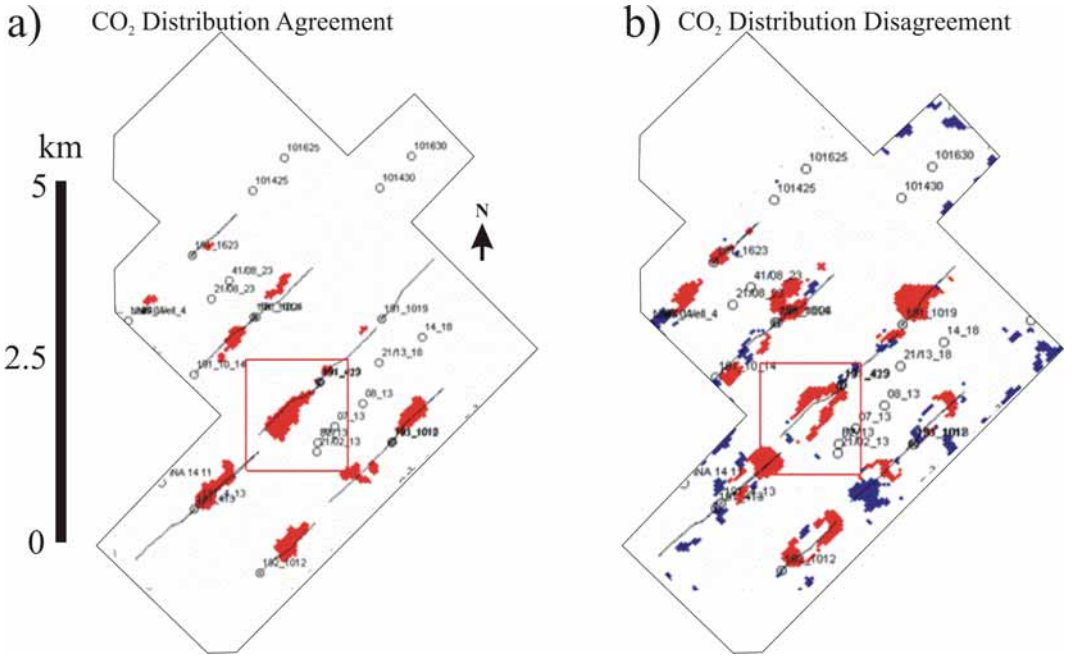

Figure 2.77: Comparison maps of the seismic and simulator gas distributions for the history match 11 model update. See Figure 2.76 (caption) for description of how distributions were determined. a) Red zones indicate areas of agreement between the CO_2 distributions from seismic and reservoir simulation. b) Areas where the CO_2 distributions from seismic and starting reservoir simulation disagree. Red zones are where the simulator predicts CO_2 saturation that is not observed in the seismic map, and blue zones are where the seismic predicts CO_2 saturation that is not observed in the simulator CO_2 distribution map.

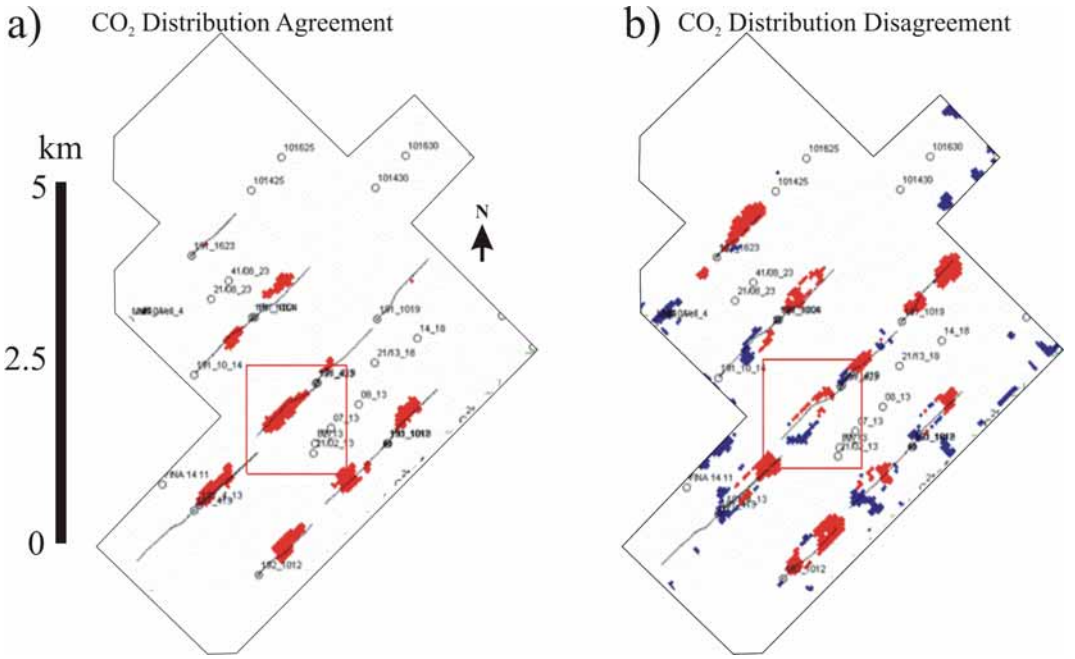

Figure 2.78: Comparison maps of the seismic and simulator gas distributions for the history match 16 model update. See Figure 2.76 (caption) for a description of how distributions were determined. a) Red zones indicate areas of agreement between the CO_2 distributions from seismic and reservoir simulation. b) Areas where the CO_2 distributions from seismic and starting reservoir simulation disagree. Red zones are where the simulator predicts CO_2 saturation that is not observed in the seismic map, and blue zones are where the seismic predicts CO_2 saturation that is not observed in the simulator CO_2 distribution map.

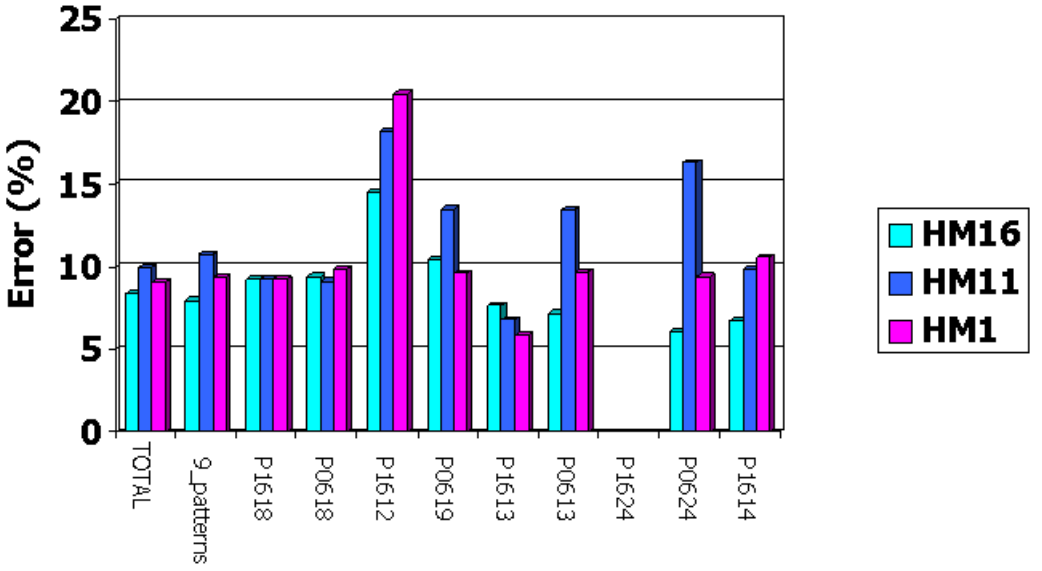

Figure 2.79: Percentage of grid cells that disagree between the seismic and simulator binary maps on a pattern-by-pattern basis for the Monitor 2 survey.

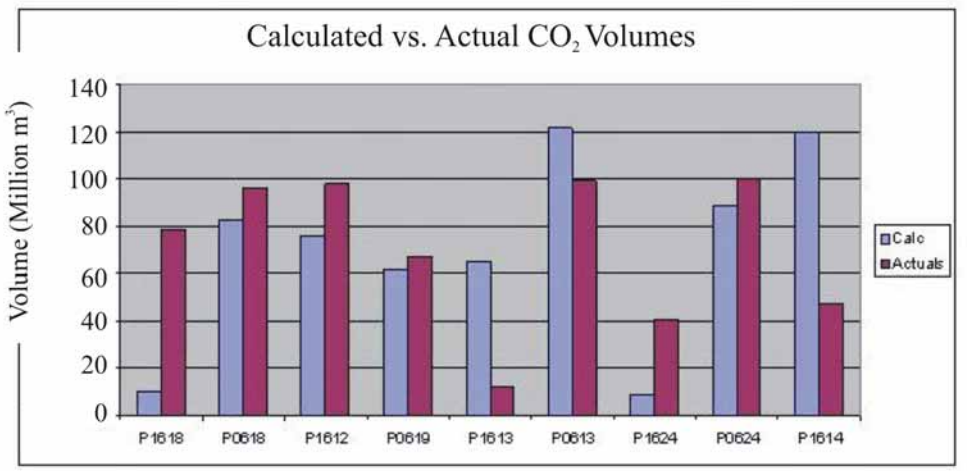

Figure 2.80: Actual net CO_2 volumes compared to estimated CO_2 volumes from the Monitor 2 seismic volumetrics, assuming a gas saturation of 20%.

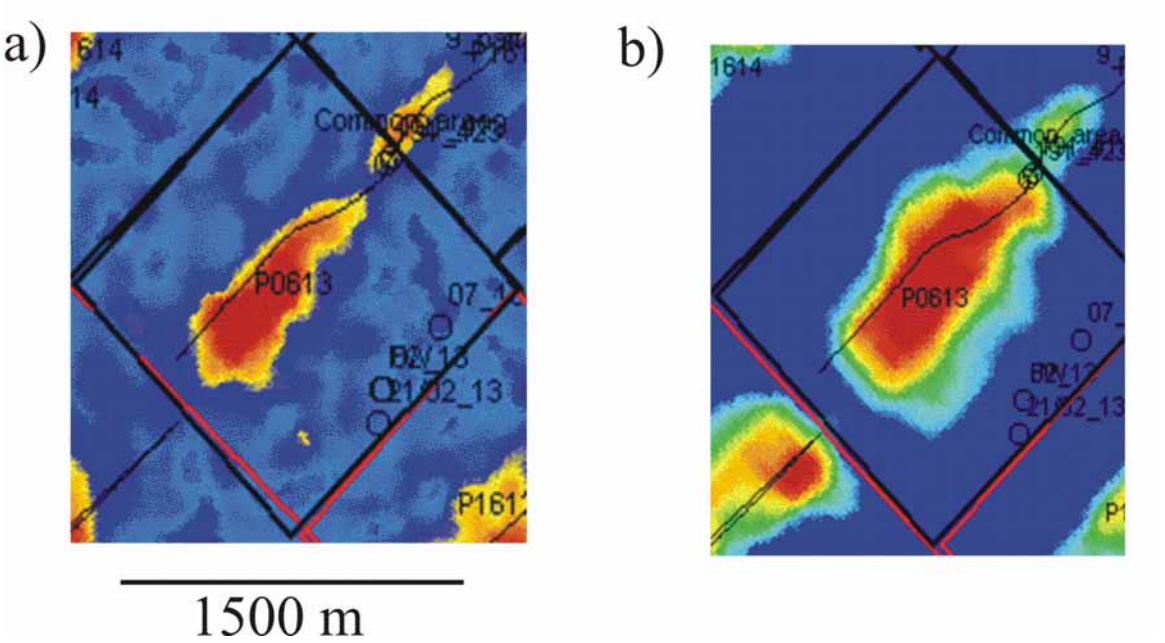

Figure 2.81: Comparison between Monitor 2 Marly amplitude difference map and free gas saturation in the Marly Formation from reservoir simulation.

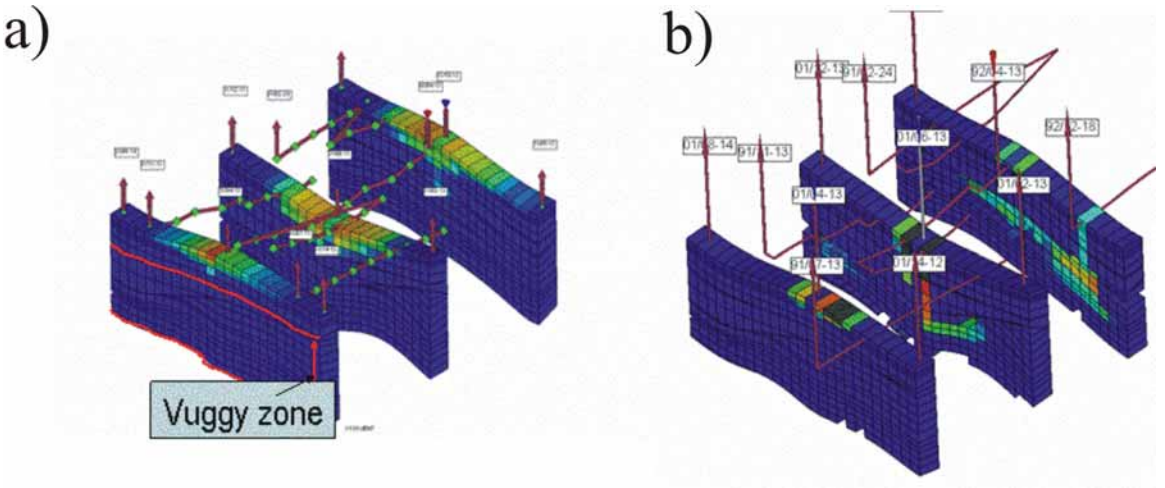

Figure 2.82: Pattern 06-13 simulated gas saturation for a) history match 11 and b) after model update.

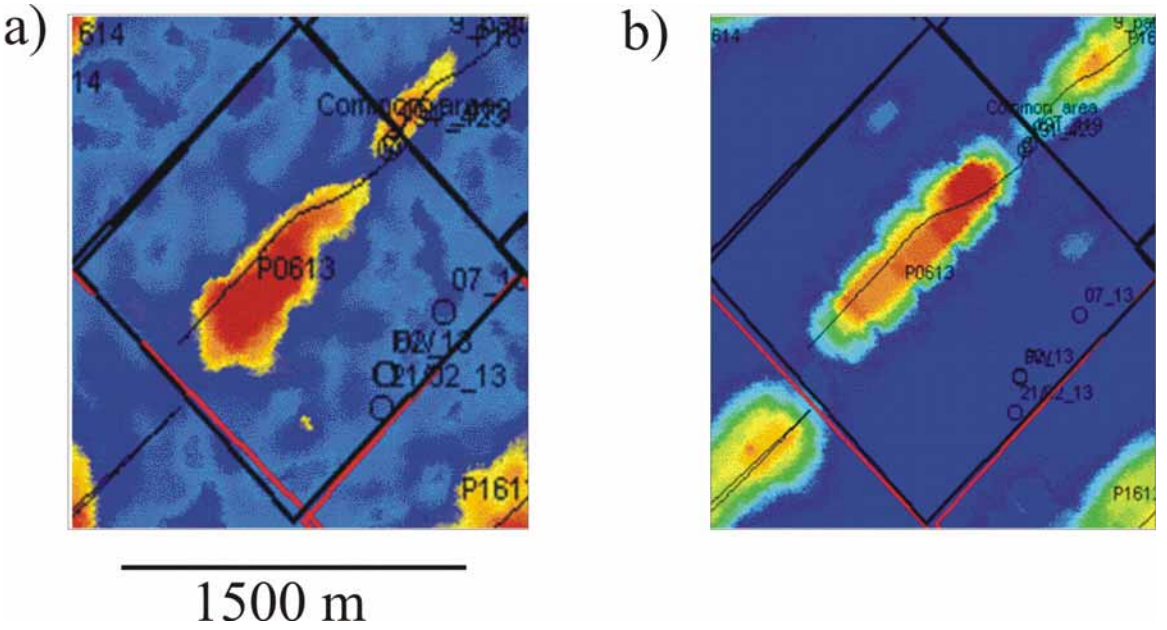

Figure 2.83: Comparison between Monitor 2 Marly amplitude difference map and free gas saturation in the Marly Formation from reservoir simulation history match iteration 16.

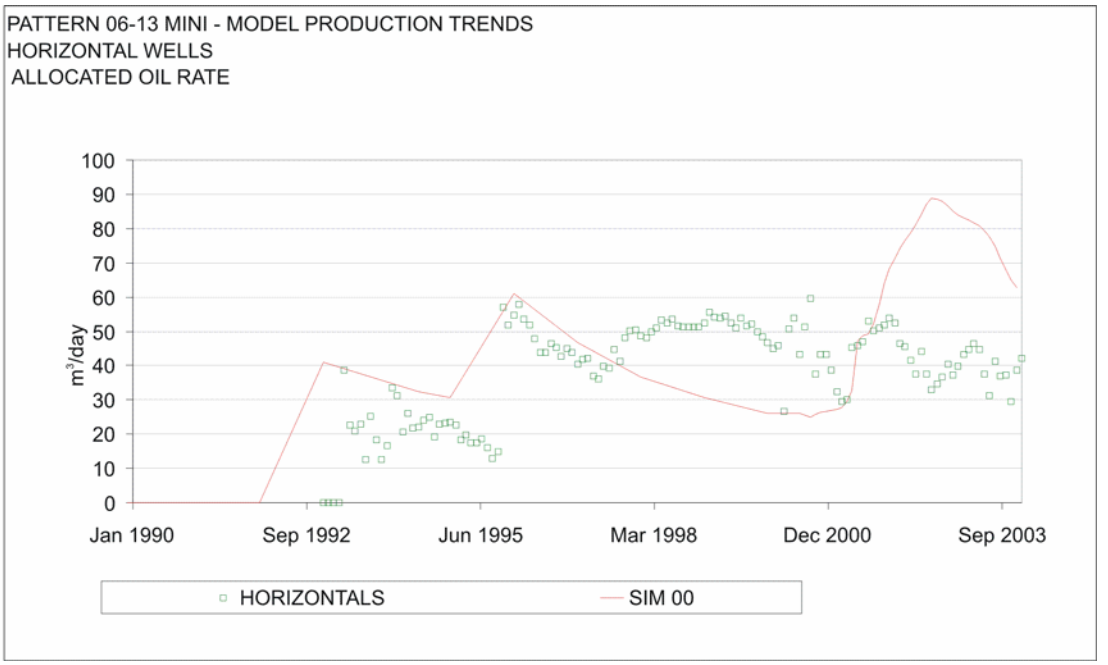

Figure 2.84: Production rate of horizontal wells before model update

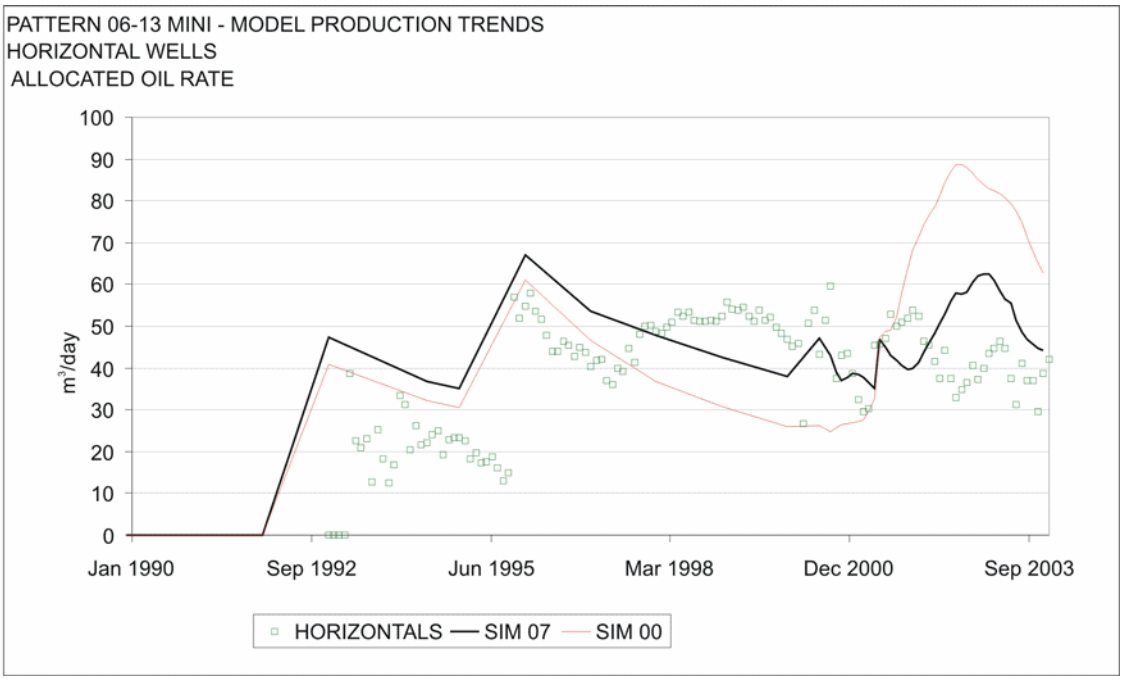

Figure 2.85: Oil production rate for horizontal wells in Pattern 06-13 after model update.

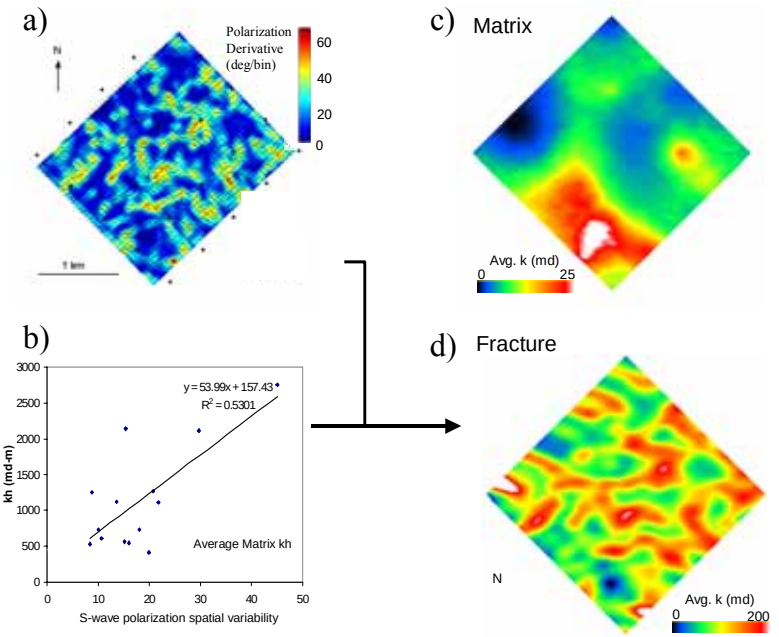

Figure 2.86: Seismic anisotropy is used to guide the prediction of fracture permeability so that a reservoir model can be created and flow simulated (from Terrell, 2004). a) Spatial derivative of the fast shear-wave polarization. The warm colours represent areas where fracture sets are likely to be interconnected and, thus, feature higher permeability. b) Cross-plot of the total flow capacity (kh) calculated from vertical well production data vs. the polarization derivative. c) Modeled matrix permeability for each layer. Note the generally low permeability of the matrix. d) Modeled fracture-enhanced permeability constrained by the derivative of the fast shear-wave polarization. Note the increased lateral heterogeneity over the matrix permeability.

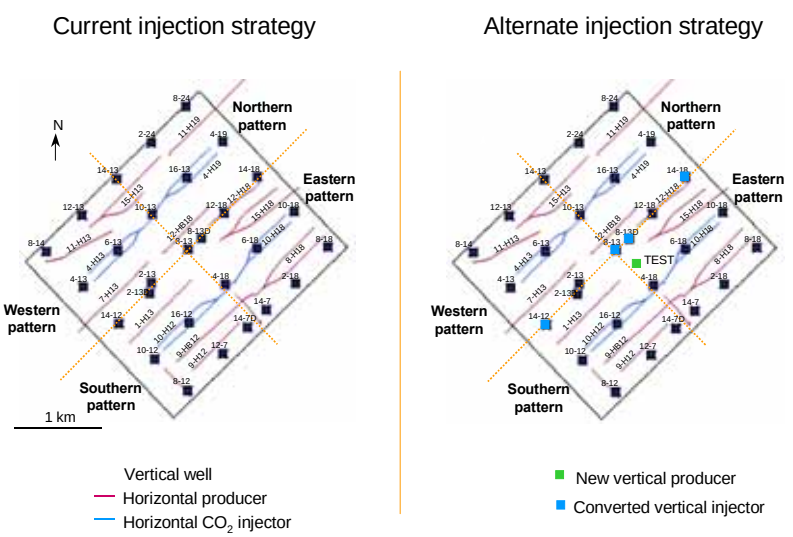

Figure 2.87: Two production scenarios forecast from the new reservoir model that incorporates fracture permeability (from Terrell, 2004).

THEME 3: CO_2 STORAGE CAPACITY AND DISTRIBUTION PREDICTIONS AND THE APPLICATION OF ECONOMIC LIMITS

THEME LEADER: DAVID LAW
THEME AUTHORS: SAM HUANG, NORMAN FREITAG, ERNIE PERKINS, FRED WASSMUTH, BOB DUNBAR, KOOROSH ASGHARI

1 SUMMARY

Weyburn oil properties and CO_2-oil phase equilibrium behaviour has been measured using oil samples collected periodically from various wells. These laboratory measurements provided information to tune the equation-of-state (EOS) parameters in the PVT model used in the reservoir simulation. The reservoir simulation model used to predict the CO_2 storage capacity in the Weyburn Unit reservoir has been successfully validated based on both laboratory-scale and field-scale simulations. In the laboratory-scale simulation, CO_2-coreflood experiments conducted with different oil samples were history-matched. In the field-scale simulation, field production histories in three different patterns with different CO_2 injection strategies were history-matched. Reservoir simulation started with fine-grid, individual well patterns and were gradually up-scaled to a coarser, 75-pattern grid for the simulation of the entire area slated for CO_2-enhanced oil recovery (EOR). Good history matching was achieved with actual production data. Also, the prediction of 23 million tonnes (MT) of total CO_2 stored matched reasonably well with EnCana Corporation's (EnCana's) internal estimates. Other CO_2 storage cases were also investigated, including continuing with CO_2 injection past the termination of the commercial EOR project (approximately year 2033), while continuing to produce incremental oil from wells still operating under a pre-determined gas-oil ratio (GOR) limit and disposing of produced water elsewhere to make room for the additional CO_2 injected. Storage gas credits were assumed to be initiated at the start of this phase of the operation. The Storage Economic Model was then run to determine the economic limit for such an operation. Of the significant amount of additional CO_2 that can be physically stored in this manner, the model predicted various limits of CO_2 volumes that could be economically stored as a function of the amount of CO_2 credits received and the desired rate of return for the operation.

Conformance control treatments developed in this project predicted a substantial improvement in volumetric sweep efficiency from the application of specially-formulated gel treatments to the best candidate wells. If such technology were to be successfully applied, it may contribute an additional 10% recovery of the total EOR oil from the treated wells. This, in turn, could accommodate 1.83 MT of additional CO_2 stored, assuming a case in which 20% of the EOR patterns would have received a gel treatment.

Long-term CO_2 solubility and ionic and mineralogical trapping potential in the Weyburn Unit reservoir have been estimated based on preliminary geochemical modeling. It was found that even in a carbonate reservoir, such as Weyburn, silicate minerals are present in sufficient quantity to react with CO_2-charged fluid, with a total of approximately 45.15 MT of CO_2 potentially stored by this trapping mechanisms. This amount was significantly higher than the purchased amount of 20 MT planned by EnCana for the EOR project. This calculation assumes complete availability of CO_2 for the reactions and complete reaction of the silicate minerals.

2 THEME OBJECTIVES AND ROLE IN CO_2 STORAGE ASSESSMENT

The Theme 3 objectives were to demonstrate that the maximum CO_2 storage capacity that could be achieved physically and economically at a geological storage site can be estimated, that CO_2 distribution and trapping mechanisms within the storage site can be predicted, and that CO_2 storage performance could be improved through the application of conformance control treatments.

The role of Theme 3 in the CO_2 storage assessment was to demonstrate the technical and economic feasibility of sequestration of CO_2 in geological formations with a focus on oil reservoirs. An unique methodology for reservoir simulation has been developed in this Theme, and it has met the challenge of assessing CO_2 storage capacity in a very large-scale CO_2-EOR operation, such as the one taking place at Weyburn. The approach began with very detailed fine-grid single-pattern simulations and concluded with a coarse-grid 75-pattern simulation. In addition, a CO_2 storage economic model that takes carbon taxes and credits into account has been developed, and it can provide a credible assessment of the point at which, after CO_2-EOR, a CO_2 storage project reaches its economic limit. Work from this Theme, notably the reservoir simulation, including predictions of final CO_2 distribution and reservoir conditions at the end of the CO_2-EOR and the storage operations, also provided important information for the risk assessment of potential CO_2 leakage and migration in Theme 4.

3 SCOPE OF INVESTIGATION

Since the scope of Theme 3 encompassed three major areas – prediction of CO_2 storage capacity, prediction of CO_2 distribution within the reservoir, and prediction of economic limits to storage – a broad range of investigations were carried out.

Phase behaviour of CO_2 in the Weyburn Oil System was studied to determine whether or not the conditions required for miscibility of the injected CO_2 with the reservoir oil change with continuing field operation, which could potentially affect both oil recovery and the CO_2 storage capacity of the reservoir. The investigations involved periodically collecting and analyzing oil samples from different wells in the Weyburn reservoir. This investigation also provided a data set by which the necessary parameters were determined in order to accurately represent the oil and gas/fluid phases during reservoir simulation (*i.e.*, tuning of a PVT model) of the possible fate of the CO_2 remaining or added to the reservoir area.

CO_2-coreflood laboratory experiments were conducted to determine the impact of the changing composition of oil and recycled gas (*i.e.*, CO_2, CH_4, H_2S, *etc*.) on oil recovery and CO_2 movement. CO_2-coreflood tests were conducted using oil samples collected from the field. The reservoir simulator used in the prediction of CO_2 storage capacity in the Weyburn field was validated by history matching the CO_2-coreflood tests. Experiments were also conducted in order to understand viscous fingering effects on the CO_2-EOR recovery process.

Reliable predictive tools and methodology for CO_2 storage performance were developed and used to predict CO_2 movement and distribution and storage performance in the Weyburn reservoir. These tools were also applied to the investigation of alternative CO_2 storage cases after EOR, with a focus on promoting additional CO_2 storage.

The geochemical modeling was used to make long-term CO_2 trapped volume estimates. The long-term (1,000 – 10,000 years) chemical impact on CO_2 sequestration through dissolution and precipitation of minerals locally in the Weyburn field and regionally was predicted using geochemical models in conjunction with thermodynamic and kinetic data. The findings were used to identify whether or not permanent sequestration occurs through the precipitation of carbonate minerals, such as calcite, in the basin.

Conformance control (sweep efficiency) was studied to evaluate its application in improving oil production and increasing CO_2 storage. The fundamentals, performance, and placement of commercially available systems for mobility control were evaluated through laboratory experiments in anticipation of field trials.

A comprehensive economic model was developed in order to compare the relative merits of incremental oil recovery and CO_2 storage for the Project. The model was used to conduct economic analysis/sensitivity studies and assess the impact of economic limits on oil production and CO_2 storage.

4 PHASE BEHAVIOUR OF THE CO_2-WEYBURN OIL SYSTEM

4.1 Oil Sample Collection and Analysis

Phase behaviour of the CO_2-Weyburn oil system was investigated based on the measurement of the oil- and CO_2-based fluids collected periodically from the Weyburn reservoir. Oil samples were obtained from six wells in the Phase 1A area, as shown in Figure 3.1. The monitored wells were chosen to span the range of oil densities, between 921 and 858 kg/m^3 (22 and 33°API), that occur naturally across the Weyburn field, with the lightest oil being found at the northwest end of the field. In the Phase 1A area, all the oil had densities of less than 903 kg/m^3 (25°API). The samples were analyzed to obtain fluid composition, oil molecular weight, oil viscosity, oil density, saturation pressure, gas-oil-ratio (GOR), and minimum miscibility pressure (MMP).

The results for the two most informative wells are shown in Figures 3.2 to 3.4. Figure 3.2 shows the concentrations of the three main gases found in the samples from the horizontal well (91/1-11-6-14W2M), located in the region with denser oil. It was found that CO_2 breakthrough occurred in about July, 2002, when the second sample from this well was taken. Figures 3.3 and 3.4 show the concentration of the gases taken from the second sampling site, a vertical well (101/12-19-6-13W2M) in the lighter-oil area. Even by the end of March, 2004, CO_2 breakthrough had still not occurred at this well. However, the samples taken in January and March, 2004, showed that the CO_2 concentration was gradually beginning to rise and that the concentrations of hydrogen sulfide (H_2S) and the heavier hydrocarbon gases had decreased sharply. Evidently, some compositional changes were occurring in the vicinity of this well, and CO_2 breakthrough appeared to be imminent.

Figure 3.5 shows the history of the oil density for the two wells (91/1-11-6-14W2M and 101/12-19-6-13W2M) and also for the well first used to monitor the heavier oil area (101/8-12-6-14W2M). A relatively large drop in the produced oil density occurred a few months after breakthrough at horizontal well 91/1-11-6-14W2M. This change represents strong evidence that complete miscibility did not occur at all times; if all the oil had been extracted by the CO_2, it would all have been recovered unchanged. In addition, recombination tests (in which the produced oil and gas were recombined to oilfield conditions) demonstrated that the produced fluids were not fully miscible for several months after breakthrough.

The above behaviour, however, was transient and, therefore, not considered serious. The change in oil density diminished somewhat with time. The remaining change was attributed to the development of miscibility around the injection wells through multiple contact of the CO_2 with oil and to pressure drawdown below the bubble point in a small region around the production well. In addition, any precipitation of asphaltenes in the reservoir would also be reflected as a permanent reduction in the density of the produced oil.

Overall, the phase-behaviour tests established that the miscible or near-miscible conditions needed for successful enhanced oil recovery from the Weyburn field were being maintained. This was confirmed by another series of tests that measured the minimum miscibility pressure (MMP) of the oil blends towards CO_2. The blends were prepared by mixing various boiling-point cuts of Weyburn oil to reproduce the estimated average composition of the oil still in the drainage area of the production area at the time of sampling. Before breakthrough, the produced oil was used instead of a blend because there was no reason to believe that it differed significantly from the oil still in place. The results showed that the MMPs were nearly constant, barely rising over time.

4.2 Development of the PVT model

Based on detailed analysis of the composition of the collected oil samples, a seven-component Pressure-Volume-Temperature (PVT) model was developed. Pure CO_2 was selected as the first component, C_1 and N_2 (*i.e.*, potential contaminating gases) as the second component (*i.e.*, a pseudo-component), C_2, C_3, and H_2S (*i.e.*, other gases) as the third component, C_4 to C_6 and C_7 to C_{12} (*i.e.*, light ends of the oil phase) as the fourth and fifth components, respectively, and C_{13} to C_{30} and C_{30+} (*i.e.*, heavy ends of the oil phase) as the

sixth and seventh components, respectively. The grouping process was performed using Computer Modelling Group's (CMG's) Equation of State (EOS) Program, WINPROP®. Pseudo-component properties were determined from those of the pure components in the group. The measured oil properties, such as density, saturation pressure, gas-oil-ratio (GOR), and minimum miscibility pressure (MMP), were then used to tune the Peng-Robinson EOS (Peng and Robinson, 1976) parameters in the PVT model. Very good agreements were obtained between the measured and the predicted values by the PVT model. An example, for the comparison of the oil density, is given in Figure 3.6. The modified Pedersen viscosity correlation (Pedersen and Fredenslund, 1987) was used to fit the oil viscosity measurement, and Henry's law was used to estimate the solubility of CO_2 in water.

As the CO_2-flood process is a dynamic process, the composition and properties of both oil and gas phases are constantly changing. The capability of the PVT model to predict the change of properties in such a dynamic process was tested, and it was necessary to conduct multi-contact tests since later than expected CO_2 breakthrough at the monitored wells resulted in small changes in most of the collected oil samples. The multi-contact test procedure is shown in Figure 3.7. For the 1st contact test, which mimicked oil-CO_2 interaction when pure CO_2 was first injected, Weyburn oil at reservoir-like conditions was equilibrated with CO_2 in the test cell. Some CO_2 dissolved into oil, and some of the light ends of the oil were extracted into the CO_2-rich phase. In the 2nd forward contact test, that mimicked oil-CO_2 interaction at the CO_2 front, the mixture of CO_2 and oil light ends from the first contact test was equilibrated with fresh reservoir oil in the test cell. In the 2nd backward contact test, which mimicked oil-CO_2 interaction near the injection well, the oil, which lost some of the light ends from the 1st contact test, was equilibrated with pure CO_2 in the test cell. Compositions and properties of both the oil-rich and the CO_2-rich phases in each test were measured. It was found that CO_2 mol% in the oil-rich phase could be as high as 70%, which was lower than the range of 80 - 90% in the CO_2-rich phase. These phase compositions have been reasonably matched by the PVT model's prediction (to within a few %). Figure 3.8 shows an example of reasonable agreement between the measured and predicted phase properties based on density of the oil-rich phase. The PVT model correctly predicted an increase in oil-rich phase density in the backward contact tests due to light ends being extracted by the supercritical CO_2. However, the difficulty in obtaining a perfect match was believed to be due to the limitation of the cubic EOS in handling the CO_2 properties near the sensitive supercritical region.

Using the PVT model, it is possible to shed some light into the phase behaviour of Weyburn oil-CO_2 mixtures. Oil samples collected at Well 101/8-12-6-14W2M were mixed with CO_2 at 17.5 MPa and 61°C, and the relative volume of the gas phase (*i.e.*, CO_2 immiscible phase) as a function of CO_2 global mol% is shown in Figure 3.9. When the CO_2 global mol% was less than 60%, the mixture was completely miscible with all CO_2 dissolved in the oil. When the CO_2 global mol% was larger than 60%, the immiscible CO_2 phase appeared, and its volume increased from 0% to 100% as the CO_2 global mol% increased to 100%. It is noted that the supercritical CO_2 immiscible phase has a liquid-like density and a gas-like viscosity. This phase behaviour enables an understanding of the flows of CO_2 and oil in the Weyburn reservoir under different conditions.

5 LABORATORY INVESTIGATION OF CO_2-EOR PERFORMANCE

5.1 CO_2-Coreflood Experiments

Several CO_2-coreflood tests using oil samples collected from the field were conducted to assess the potential impact of changing oil composition on oil recovery/CO_2 storage. In these coreflood tests, sandstone Berea cores 2" (5.1 cm) in diameter and 12" (30.0 cm) long were used. The core was first flooded with brine, which was then displaced by dead oil. Each test included three stages: waterflood, CO_2-flood, and extended waterflood. In general, each test lasted 2 – 3 days. The operating conditions and test results for all the coreflood tests are summarized in Table 3.1. Overall, the effect of natural permeability variations between cores overwhelmed the effect of differing oil composition. However, the coreflood results can still be used to validate the capability of the numerical simulator to model the CO_2-EOR process in the laboratory-scale simulation.

Table 3.1 Summary of CO_2-coreflood test conditions and oil recoveries

Test #	Sample from Well #	Sample Time	API	Oil	Init. Oil Sat.	Core Permeability (md)	Recovery by CO_2 (%OOIP)
Test – 1	101/8-12-6-14W2M	08/00	28.3	Live	0.556	72	24.5
Test – 2	101/8-12-6-14W2M	04/01	28.3	Dead	0.692	146	29.7
Test – 3	101/12-25-6-14W2M	08/00	32.7	Live	0.532	110	22.3
Test – 4	101/12-25-6-14W2M	04/01	32.7	Dead	0.403	400	9.4
Test – 5	101/7-11-6-14W2M	10/01	28.4	Dead	0.589	80	46.2
Test – 6	101/12-19-6-13W2M	10/01	33.3	Dead	0.643	270	2.3
Test – 7	191/1-11-6-14W2M	05/02	29.5	Dead	0.620	139	5.3
Test – 8	191/1-11-6-14W2M	11/02	28.4	Dead	0.604	158	33.4

5.2 Numerical History-Match of CO_2-Coreflood Experiments

A total of eight coreflood tests, as shown in Table 3.1, were history matched. In the first attempt, 1-D simulation using 30 grid blocks of 1 cm along the core was reasonably successful in matching the initial waterflood results but failed to match the following CO_2-flood results. In order to improve the history match, 2-D simulation using a very fine grid system of 60 × 50 with grid block size in the order of millimetres was used. The purpose of the very fine resolution grid system was to capture the feature of viscous fingering which was believed to be the dominant mechanism for CO_2 movement in the CO_2-coreflood tests. In the 2-D simulation, the permeability distribution was generated from a lognormal distribution, with the peak at the average value and with a specified variance. For example, the permeability distribution for Test #5, which has an average value of 80 md, is shown in Figure 10, together with the profiles of CO_2 distributions as CO_2 mole fractions in the oil phase at different times during the CO_2-flood period. For Test #5, the three stages were waterflooding (0 – 0.9 days), CO_2-flooding (0.9 – 1.54 days), and extended waterflooding (1.54 – 2.68 days). The CO_2 profiles demonstrated the development of viscous fingers (Gardner and Yuma, 1984), which channeled through the core, resulting in poor sweep efficiency. Figure 3.11 shows the comparison between the measured and predicted oil production for Test #5, indicating that very good agreement can be achieved from the 2-D simulation not only during the initial waterflooding period, but also during the following CO_2-flood and extended waterflooding periods.

All coreflood tests were successfully matched using 2-D simulation, and viscous fingers, which channeled through the core due to permeability heterogeneity, were predicted in all laboratory tests. This pattern of CO_2 displacement is the result of the permeability distribution. The viscosity contrast between the low viscosity CO_2 and the oil leads to faster flow of CO_2 in the high permeability paths. However, it is uncertain how significant the viscous fingering effect is in the field-scale operation in the Weyburn reservoir. There is abundant evidence that permeability heterogeneity dominates viscous fingering, both at laboratory-scale and at field-scale, though the length scales of permeability variations will be entirely different in these two cases. Thus, history matches of coreflood tests should be used with extreme caution for field-scale predictions.

6 CO_2 STORAGE CAPACITY AND DISTRIBUTION PREDICTIONS

GEM® (CMG, 2002), a multi-phase, multi-component compositional reservoir simulation model developed by CMG was used to predict the CO_2 storage capacity during the CO_2-EOR operation in the Weyburn Unit reservoir (Hancock, 1999). The approach taken in modeling the size and complexity of 75 EOR patterns was to begin with fine-grid single-pattern simulations and conclude with a coarse-grid 75-pattern simulation that captures the overall injection, production, and fluid distribution within each single pattern, but does not capture the details for each individual well. The justification for using this coarser simulation approach was based on a methodology involving three levels of upscaling: (1) from a detailed geological model of the Weyburn reservoir to a fine-grid reservoir simulation model; (2) from 3 fine-grid single-pattern models to coarse-grid models of the same patterns; and (3) from 3 coarse-grid single-pattern models to a 75-pattern model using the same grid resolution.

6.1 Fine-Grid Single-Pattern Numerical Simulation

The capability of the reservoir simulation model to simulate the CO_2-EOR process is validated, based on 3 very detailed simulations, by matching of up-to-date pre-CO_2 and post-CO_2 field production history in 3 selected single patterns in the 19-pattern Phase 1A area, followed by predictions for the CO_2 distribution and storage performance at the end of EOR. The 3 patterns (P1612614, P1624614, and P1618613) are shown in Figure 3.12 and will be referred to hereafter as Pattern 1, Pattern 2, and Pattern 3, respectively. The CO_2-injection strategies used in these patterns represent 3 of the 4 strategies, which are tuned to varying geological characteristics in different parts of the field, planned for the Weyburn field. For Patterns 1, 2, and 3, the respective recovery strategies are: "simultaneous but separate water and gas injection (SSWG)," as shown in Figure 13, "Vuggy water-alternating-gas (VWAG)," as shown in Figure 3.14, and "Marly, Vuggy water-alternating-gas (MVWAG)," as shown in Figure 3.15. The fourth CO_2 injection strategy is the "straight gas injection (SGI)," as shown in Figure 3.16, but at the time of this project, it had not yet been applied to any pattern in the field. During the CO_2-flood stage, the SSWG strategy employed a horizontal CO_2 injector, together with vertical water injectors, with the main goal of preferentially flooding the upper, Marly zone, which contained significantly higher remaining oil-in-place than the Vuggy zone underlying it. Implementation of the SSWG strategy entailed drilling a new horizontal injection well, which is oriented NE-SW and has two legs, one on each side of the central, vertical water injector. The VWAG strategy was targeted at parts of the field having a relatively thin Marly zone. It employed vertical water/CO_2 injection wells in a line drive configuration to implement the WAG process in a 9-spot pattern. The MVWAG strategy also employed this technique. In addition, two new horizontal production wells were added to the pattern. Fluids were injected into only the Vuggy zone for VWAG, while fluids were injected into both the Marly and Vuggy zones for MVWAG. The SGI strategy will employ vertical CO_2 injection wells in a line drive configuration to implement the straight gas injection process.

The upscaling from EnCana's Phase 1A 2001 Stratamodel to the fine-grid simulation model primarily involved coarsening the vertical description from the Stratamodel to 9 layers that represent different flow units within the upper Marly and lower Vuggy zones in the Weyburn reservoir (Figure 3.17 and Table 3.2), while retaining the areal grid resolution with a grid block size of 57.4 m × 57.4 m. CMG's ModelBuilder® was used to incorporate well trajectory and completions information for all Phase 1A wells into the simulation input file. Then, 3 selected individual patterns, together with the surrounding buffer zones (Figure 3.12), in the 19-pattern Phase 1A area were cut from the reservoir model.

A simple approach was taken to upscaling absolute permeability values from the 2001 Stratamodel to the fine-grid system. Based on EnCana's previous 9-pattern reservoir simulation and history matching experience in the Weyburn field, all permeabilities were first multiplied by 0.6 to convert from air permeability to liquid permeability. Horizontal permeability of a simulation block was calculated as the weighted arithmetic mean of its constituent geological layer permeabilities, and vertical permeability was calculated as the weighted harmonic mean of the layer permeabilities. Porosity was upscaled by simple arithmetic averaging of the finer geological layer values. However, this procedure still did not capture several realities of reservoir heterogeneity. Firstly, fine-scale laminations and baffles typically reduced

vertical permeability significantly – beyond that captured by the harmonic upscaling. In the case of Weyburn, EnCana estimated that the vertical to horizontal permeability (k_v/k_h) ratio was approximately 0.1. Hence, a correction was made by reducing all previously calculated vertical permeabilities by this factor. After this correction, the "starting-point" distributions of permeability and porosity throughout the Phase 1A area for reservoir simulation were obtained. A second significant correction made to the grid block permeability values was due to the effect of fracturing. The reservoir was extensively fractured (Elsayed *et al.*, 1993), particularly in the Vuggy. This led not only to enhanced permeability, but also to permeability anisotropy – permeability was generally expected to be higher in the NE-SW "ontrend" direction. In this case, permeability enhancement factors were applied to adjust the "starting-point" distributions both globally and locally as part of the history-matching process.

Table 3.2 Naming Convention for Midale Flow Units in EnCana's Stratamodels

			PHASE 1A (2001)		WEYBURN FIELD (1999)	
			NAME	LAYER	NAME	LAYER
Flow Units in Geological Model	Zone Above		Evaporite	1	Evaporite	1
			3-Fingers	2		
	Midale	Marly	M1	3	M1	2
			M3	4	M2	3
					M3a	4
					M3b	5
					M3c	6
		Vuggy	V1	5	V1	7
			V1a	6	V2a	8
			V1d	7	V2b	9
			V2	8	V3	10
			V3	9	V4	11
			V4	10	V5	12
			V6	11	V6	13
					V7	14
	Zone Below		Frobisher	12	Frobisher	15

All 3 fine-grid single-pattern simulations with an areal grid block size of 57.4 m × 57.4 m provided a good history-match of the pattern production through the primary stage (1956 to 1964), secondary waterflood (1964 to 2000), and a little more than 2 years of tertiary CO_2-flood (2000 to 2002). Figures 3.18 to 3.20 show the matches of oil and water production, with corresponding surrounding buffer zones, as oil production rate and water cut for Patterns 1, 2, and 3, respectively. Individual well matches were not as good as the overall pattern match, but most are reasonably good. Examples of good and poor matches for individual wells are shown in Figures 3.21 and 3.22, respectively.

Seismic data offered the chance of "ground-truthing" simulation predictions between wells, where there was little other chance of confirmation. The comparison of seismic images and reservoir simulation results was, however, not entirely straightforward, since the seismic data did not directly measure the parameters used in reservoir simulations, such as saturations, compositions, and pressures. Rather, a typical seismic image reflected the sonic properties of the reservoir, which in turn depended in some complex way on the typical simulator properties. Nonetheless, the seismic data collected to date has shown a spatial distribution

clearly attributable to movement of CO_2 through the reservoir. Figures 3.23 and 3.24, for example, show EnCana's four-dimensional (4D), three-component (3C) surface seismic response images for both the Marly and Vuggy zones throughout the Phase 1A area after 1 year and 2 years of CO_2-flood, respectively. "Anomalies" attributable to CO_2 could be seen around most injectors. There are reasonable similarities between the numerical simulation images of global CO_2 mole fractions, shown for layers 2 (M3) and 6 (V2), and "anomalies" attributable to CO_2 in the Marly and Vuggy zones. A more detailed numerical history match for 9 patterns in the Phase 1A area with improvements gained from using the seismic data as constraints has been conducted by EnCana and is reported in Theme 2.

Based on the successful match of pattern history, including the significant oil rate increases and water cut reductions during the first 2 years of the CO_2-flood, the simulations were extended in predictive modes for all 3 patterns for an additional 23 years after the "history" period, which ended in October 2002. Therefore, a total of 25 years of post-waterflood operation were simulated. Operational guidelines recommended by EnCana were considered during the predictive CO_2-flood period. These guidelines are: inject CO_2 only for approximately 1 year or until CO_2 breakthrough; after the CO_2-only injection period, for Pattern 1, start a SSWG process with injection of equal volumes of CO_2 and water simultaneously, and for Patterns 2 and 3, start a VWAG or MVWAG process with 3 months water and 3 months CO_2 injection (equal reservoir volumes in each slug); maintain (*i.e.*, for SSWG) or increase (*i.e.*, to speed up VWAG and MVWAG) total fluid production rates to be comparable with those at the end of waterflooding; inject fluid to replace voidage; keep pattern pressure above 18 MPa for miscibility (< 27 MPa); after CO_2 breakthrough, keep CO_2 production to a maximum of 70% of injection by cutting back rates on high CO_2 producers.

CO_2 storage capacity and EOR performance for 3 EOR cases were investigated for all 3 patterns. Case I encompassed following the guidelines with no GOR control at the producers. Case II was the same as Case I but with gas injection stopped after ~50% hydrocarbon pore volume (HCPV) CO_2 injection and continuation with water injection only. Case III was also the same as Case I but with GOR control at the producers and with vertical producers shut-in when GOR > 2,000 m^3/m^3 and horizontal producers shut-in when GOR > 4,000 m^3/m^3.

Figure 3.25 shows examples of CO_2 inventory for Pattern 1 for the aforementioned cases. Qualitatively, very similar results were observed for Patterns 2 and 3. Details for CO_2 storage capacity and EOR performance are given in Table 3.3. The performances differed considerably, depending on the CO_2 injection strategies. In general, oil recovery response was faster in Pattern 1, with the SSGW injection strategy, and the CO_2 storage performance was also better, due to more CO_2 being injected into this pattern from the horizontal injector. It is estimated that CO_2 storage in the order of 100,000 to 500,000 tonnes can be achieved in each individual pattern. Figure 3.26 demonstrates, for Case I, CO_2 distribution at the end of EOR (2025) for the 3 patterns.

Table 3.3 Numerical prediction of CO_2 storage capacity and EOR performance for different cases for Patterns 1, 2, and 3 (fine-grid single-pattern simulation)

(a) Pattern 1 (SSWG)

	Pattern 1 (P1612614) - SSWG		
	Case I	Case II	Case III
	CO_2 Inventory (tonnes) @ 2025/01/01		
In Gas	212,750 (56.3%)	28,036 (15.7%)	275,630 (52.9%)
In Oil	82,286 (21.7%)	78,813 (44.2%)	141,950 (27.2%)
In Water	83,080 (22.0%)	71,524 (40.1%)	103,940 (19.9%)
Total	378,116	178,373	521,520
Recycled	~ 80.7%	~ 85.7%	~ 60.5%
	Total Oil Recovery (%) OOIP – 2,535,010 m^3		
Primary + Waterflood	34.7% (@ 2000/09/01)		
CO_2-EOR (Additional)	55.6% (20.9%)	54.1% (19.4%)	54.6% (19.9%)

(b) Pattern 2 (VWAG)

	Pattern 2 (P1624614) - VWAG		
	Case I	Case II	Case III
	CO_2 Inventory (tonnes) @ 2025/01/01		
In Gas	69,998 (40.0%)	34,359 (25.3%)	42,244 (30.6%)
In Oil	47,997 (27.5%)	46,458 (34.2%)	48,326 (35.0%)
In Water	56,832 (32.5%)	54,904 (40.5%)	47,402 (34.4%)
Total	174,827	135,721	137,972
Recycled	~ 76.3%	~ 79.2%	~ 53.4%
	Total Oil Recovery (%) OOIP – 1,313,887 m^3		
Primary + Waterflood	32.3% (@ 2000/09/01)		
CO_2-EOR (Additional)	41.3% (9.0%)	40.6% (8.3%)	38.2% (5.9%)

(a) Pattern 3 (MVWAG)

	Pattern 3 (P1618613) - MVWAG		
	Case I	Case II	Case III
	CO_2 Inventory (tonnes) @ 2025/01/01		
In Gas	158,570 (46.6%)	36,017 (18.3%)	144,600 (41.3%)
In Oil	94,350 (27.7%)	91,316 (46.5%)	121,140 (34.6%)
In Water	87,286 (25.7%)	69,079 (35.2%)	84,197 (24.1%)
Total	340,206	196,412	349,937
Recycled	~ 80.7%	~ 83.1%	~ 60.7%
	Total Oil Recovery (%) OOIP – 1,736,165 m^3		
Primary + Waterflood	29.1% (@ 2000/09/01)		
CO_2-EOR (Additional)	50.8% (21.7%)	48.3% (19.2%)	47.2% (18.1%)

6.2 Up-scaling from Fine-Grid to Coarse-Grid Single-Pattern Simulation

The fine-grid single-pattern simulations were upscaled to coarse-grid simulations of the same patterns. The fine-grid system had an areal grid block size of 57.4 m × 57.4 m and 9 vertical layers representing the 9 flow units within the upper Marly and the lower Vuggy zones. On the other hand, the coarse-grid system had an areal grid block size of 133.9 m × 133.9 m and 2 vertical layers representing the Marly and the Vuggy zones. The goal of the upscaling was to reproduce the important features of the finer description using a coarser description and then determine the upscaling pseudo-functions (*e.g.*, absolute and relative permeabilities) for patterns with different CO_2 injection strategies. The 3 coarse-grid single-pattern simulations were used as building blocks to carry out simulations of the entire 75 patterns as the same grid resolution (*i.e.*, an areal grid block size of 133.9 m × 133.9 m) is applied.

The "starting-point" distributions of permeability and porosity for the coarse-grid system are upscaled from those for the fine-grid system. Similarly, horizontal permeability of a simulation block for the coarse-grid system was calculated as the weighted arithmetic mean of the layer permeabilities of the fine-grid system, and vertical permeability was calculated as the weighted harmonic mean of the layer permeabilities.

Porosity was upscaled by simple arithmetic averaging of the layer values of the fine-grid system. For the coarse-grid system, the permeability enhancement factors to the "starting-point" distributions, both globally and locally, are determined based on history-matching process of the field data and comparison of the fine-grid simulations.

The upscaling methodology has been validated by demonstrating reasonable agreement when comparing the numerical results during the pre-CO_2 and CO_2-flood periods between the fine-grid and the coarse-grid simulations. The upscaling from fine-grid to coarse-grid, in general, was not dramatic, as horizontal grid block size was increased only slightly more than 2 times. There were only slight differences between the absolute permeability used in the fine-grid and the coarse-grid systems. Also, the relative permeability curves used in the fine-grid simulations can be used in the coarse-grid simulations. All the wells in a given pattern in the fine-grid simulation can be represented by 3 pseudo-wells – 1 producer, 1 water injector, and 1 gas injector – in the coarse-grid simulation. In this case, each pseudo-well acted as a multi-lateral horizontal well with perforations coincided with the actual perforations from the different wells it represented. Figure 3.27 shows an example of good agreement when comparing the oil production for Pattern 1 (SSWG) between the fine-grid and the coarse-grid simulations. For the fine-grid simulation, oil recovery from Pattern 1 was predicted as 7.3%, 34.6%, and 55% OOIP after the primary production (1956 – 1964), the waterflood (1964 – 2000), and the CO_2-flood (2000 – 2025), respectively. On the other hand, for the coarse-grid simulation, oil recovery was predicted as 8.1%, 29.9% and 52.4% OOIP after the primary production, the waterflood and the CO_2-flood, respectively. Figure 3.28 shows a comparison of CO_2 distribution, as CO_2 global mole fractions (indicated as "CO_2 saturation" in the figures), in the Marly and Vuggy zones for Pattern 1 (SSWG) between the fine-grid and the coarse-grid simulations.

The upscaling methodology was applied in the 75-pattern simulation, which enabled the prediction of the final CO_2 storage capacity to be carried out in a manageable manner.

6.3 75-Pattern Numerical Simulation

The only geological model available for the 75-pattern simulation was EnCana's Weyburn Field 1999 Stratamodel, which is the older version of the 2001 Stratamodel used in the single-pattern simulations (*i.e.*, both fine-grid and coarse-grid). The 1999 Stratamodel had a total of 15 flow units with 13 units located within the Weyburn reservoir, as shown in Table 3.2, as compared to a total of 12 flow units with 9 units located within the Weyburn reservoir for the 2001 Stratamodel. The upscaling from EnCana's Weyburn Field 1999 Stratamodel to the coarse-grid 75-pattern simulation model was very similar to the upscaling from EnCana's Phase 1A 2001 Stratamodel to the fine-grid simulation model, then to the coarse-grid simulation model. The Schlumberger GeoQuest program FloGrid® was first used to convert the initial geological data into simulation grid data. The selected horizontal resolution of the simulation grid was 133.9 m × 133.9 m (same as the coarse-grid single-pattern simulations), which was slightly coarser than the 57.4 m × 57.4 m resolution of the geological model. The simulation grid was oriented NE-SW and NW-SE to capture the field's well geometry, whereas the geological grid was oriented N-S and E-W. This grid block dimension produced a well spacing between 9-spot wells of close to 5 grid blocks (or 9 × 9 grid blocks for a single pattern). On the other hand, the selected vertical resolution of the simulation grid was 15 flow units in the geological model in Step 1. Then, an area of 15 × 10 patterns was cut out, as shown in Figure 3.29. This encompasses the 75 EOR patterns and the surrounding 23 buffer patterns. During the second step of the upscaling, CMG's Modelbuilder® was used to upscale the 15 vertical flow units to 2 layers representing the upper Marly and the lower Vuggy zones (Figure 3.39), while the horizontal resolution was retained. Comparing the original-oil-in-place (OOIP) of Patterns 1, 2, and 3 (*i.e.*, the building blocks) in the 75-pattern simulation model with those in the coarse-grid single-pattern simulation indicated that the two Stratamodels were reasonably consistent, at least in the Phase 1A area.

There was a total of 24,300 grid blocks in the 75-pattern simulation, 21,658 of which were active blocks and 2,642 of which were null blocks. The simulation area included 75 EOR patterns and 23 surrounding buffers, as shown in Figure 3.29. There was a total of 271 pseudo-wells. Three pseudo-wells (*i.e.*, 1 producer, 1 water injector, and 1 gas injector) were in each EOR pattern and two (*i.e.*, 1 producer and 1 water injector) were in each buffer pattern. Fluid production and injection rates were provided by EnCana for each pattern (or each pseudo-well). These rates were determined by summing the rates for all the wells

in the pattern. In the case of a fraction well located at the boundary, a geometric factor was applied (*e.g.*, ¼ for a corner well and ½ for an edge well). Figure 3.30 shows pseudo-wells representing the 9-spot vertical wells during the primary and waterflood stages for each pattern, and Figure 3.31 shows pseudo-wells representing the well configurations for different CO_2 injection strategies during the CO_2-flood stage. It was also attempted to have the pseudo-wells represent, as closely as possible, the well configuration during the in-filling stage, before the CO_2-flood, when vertical and horizontal in-filled wells were added to the pattern. Figure 3.32 shows examples of realistic CO_2 distributions after CO_2 injection into the SSWG and MVWAG patterns using the pseudo-well approach in the 75-pattern simulation.

Due to the complications of dealing with the 75-pattern simulation, several simplifications were made. Even though oil properties vary throughout the Weyburn field, the same oil properties were used for all patterns. The oil properties for the oil samples collected in the Phase 1A area were used. Two sets of relative permeability curves, one for the upper Marly zone and one for the lower Vuggy zone, were used for all patterns (*i.e.*, end points remain the same for all patterns). Constant rate constraints were assigned to each pseudo-well as much as possible (liquid production rate for producer and water and gas injection rates for water and gas injectors, respectively). Within the limited scope of this study, it was not feasible to alter the rate input for each pattern with time. Hence, CO_2-EOR performance may not be optimized in the numerical prediction. All WAG patterns alternated gas and water injection at the same time. It is assumed that there were no activities in any wells outside of the 75 EOR and buffer patterns. Approximately 25 years of CO_2-EOR operation for each pattern were assumed; hence, the EOR operation terminated in 2033.

These assumptions are justified, as the main objective of the 75-pattern simulation is to provide the final CO_2 distribution and reservoir conditions at the end of EOR, which are the initial conditions for the risk analysis model of the geosphere in Theme 4. The 75-pattern simulation is not capable of predicting the performance of detailed day-to-day EOR field operation.

To validate the upscaling methodology, numerical prediction from the 75-pattern simulation was first compared with the up-to-date pre-CO_2 and post-CO_2 field production history. Then, predictions were made for the CO_2 storage capacity at the end of EOR following EnCana's planned field operating guidelines as closely as possible (base case). These guidelines are: pattern CO_2 injection strategy as shown in Figure 3.33 (a list of the name and type of the 75 EOR patterns is given in Table 3.4); pattern roll out plan as shown in Figure 3.34; the injection plan is to inject 50 – 60% HCPV; a maximum CO_2 supply of 2.69×10^6 m^3/d (95 MMscf/d); an operating reservoir pressure of > 18 MPa for miscibility; the depletion plan is water flush of depleted patterns to liberate some of the CO_2 for recycling; the recycle plan is approximately 60% of total CO_2 injection.

Table 3.4 EOR pattern ID and type and roll out date

75 EOR Patterns								
ID	Name	Type	ID	Name	Type	ID	Name	Type
1	P0626614	VWAG	26	P0601614	SSWG	51	P1610613	MVWAG
2	P1626614	VWAG	27	P1636514	MVWAG	52	P0629513	MVWAG
3	P0625614	VWAG	28	P0606613	MVWAG	53	P1620513	MVWAG
4	P0623614	SSWG	29	P1601614	SSWG	54	P1629513	MVWAG
5	P1623614	SSWG	30	P0620613	VWAG	55	P0628513	MVWAG
6	P0624614	SSWG	31	P1619613	VWAG	56	P0633513	MVWAG
7	P1614614	SSWG	32	P0629613	VWAG	57	P1628513	MVWAG
8	P1624614	VWAG	33	P1620613	VWAG	58	P1633513	MVWAG
9	P0630613	VWAG	34	P0617613	SSWG	59	P0634513	MVWAG
10	P0611614	SSWG	35	P1608613	SGI	60	P1634513	MVWAG
11	P1602614	SSWG	36	P0616613	SGI	61	P0635513	MVWAG
12	P0612614	SSWG	37	P0609613	SGI	62	P1627513	SGI
13	P1611614	SSWG	38	P1609613	SGI	63	P0611613	SGI
14	P0613614	SSWG	39	P0615613	SGI	64	P1603613	SGI
15	P1612614	SSWG	40	P1630513	MVWAG	65	P1602613	SGI
16	P1613614	SSWG	41	P0631513	MVWAG	66	P0602613	SGI
17	P0618613	SSWG	42	P1631513	MVWAG	67	P1626513	SGI
18	P0619613	SSWG	43	P0632513	MVWAG	68	P1635513	SGI
19	P1618613	MVWAG	44	P0605613	MVWAG	69	P0601613	SGI
20	P0607613	SSWG	45	P1632513	MVWAG	70	P1601613	SGI
21	P1607613	SSWG	46	P1605613	MVWAG	71	P0636513	SGI
22	P1606613	MVWAG	47	P0604613	MVWAG	72	P1636513	SGI
23	P0608613	MVWAG	48	P1604613	MVWAG	73	P0606612	SGI
24	P1617613	VWAG	49	P0603613	MVWAG	74	P0631512	SGI
25	P0621613	VWAG	50	P0610613	MVWAG	75	P1631512	SGI

For the base case, it was also necessary to verify the final CO_2 storage volume in the Weyburn reservoir with EnCana's estimated purchases of approximately 20 million tonnes (MT) and to verify EnCana's prediction of an oil recovery factor of 46% OOIP, which will be increased from 30%, achieved with conventional waterflooding.

An initial goal of the 75-pattern simulation was to match the HCPV of the entire 75 EOR patterns in the simulation to that of EnCana's estimation by adjusting the initial water saturation in the patterns. The initial water saturation for each pattern was adjusted according to the pattern type. The simulator HCPV of 1.5268×10^8 m^3 for the entire 75 patterns is only 3.2% higher than the EnCana's oil field management (OFM) value of 1.4794×10^8 m^3.

Figure 3.35 shows % HCPV of CO_2 injection for each individual pattern in the EOR base case 75-pattern simulation. The CO_2 injection period for each pattern was approximately 25 years, and CO_2 injection for each pattern was to be maintained at a constant rate as much as possible, with only a few exceptions. Therefore, the 75-pattern simulation started at 1955 and ended at 2033. In the simulation, it was found that at the end of EOR (*i.e.*, 2033), a total of 45.91% HCPV of CO_2 had been injected into the 75 patterns. Oil and water production rates and cumulative oil production are shown in Figures 3.36 and 3.37, respectively. Matching of the pre-CO_2 injection field production history was found to be reasonable. The simulation predicted an oil recovery of 26% OOIP in the 75 EOR patterns before CO_2 injection and an oil recovery of 47.2% OOIP at the end of CO_2-EOR. If the buffer patterns were also considered, the oil recoveries before CO_2 injection and at the end of the CO_2-EOR were 24.3% and 42.8%, respectively. The oil recovery predictions agreed reasonably well with EnCana's forecast of 30% and 46%, respectively. Figure 3.38 shows oil recoveries for individual patterns, and Figure 3.39 shows oil recoveries for different pattern types. It was found that 46.7%, 24.4%, 22.6%, and 8.3% of the total oil recovery were from the MVWAG, SSGW, SGI, and VWAG patterns, respectively.

Figure 3.40 shows CO_2 injection and recycle rates. The difference between the CO_2 injection and recycle rates is the amount of CO_2 needed to be purchased. It was found that the CO_2 purchased was always less than the maximum CO_2 supply of 95 MMscf/d. The total amount of CO_2 needed to be purchased was

23.2 MT, as shown in Figure 41. The predicted total CO_2 recycled is 58.2% of the total CO_2 injected. Figure 3.42 shows CO_2 storage in different pattern types. For the total CO_2 storage of 23.2 MT, 13.1%, 6.5%, 34.6%, 37.1%, and 8.7% are stored in the SSWG, VWAG, MVWAG, SGI, and buffer patterns, respectively. More CO_2 was stored in the SGI patterns mainly because these patterns were the latest to start CO_2 injection; thus, the least CO_2 was being flushed out for recycle. On the other hand, less CO_2 was stored in the SSWG patterns mainly because these patterns were the earliest to start CO_2 injection; thus the most CO_2 was being flushed out for recycle. Figure 3.43 shows CO_2 inventory in the 75 plus buffer patterns. By the end of CO_2-EOR, 23.2 MT of CO_2 are stored. Total CO_2 stored in the reservoir water is about 5.87 MT, or 25.3% of the total inventory. On the other hand, total CO_2 stored in the oil and gas (immiscible) phases are 10.25 MT and 7.09 MT, or 44.2% and 30.5% of the total inventory, respectively. Figure 3.44 shows CO_2 distribution as CO_2 global mole fractions in the Marly and the Vuggy zones at the end of CO_2-EOR.

In general, predictions from the CO_2-EOR base case have matched many of EnCana's guidelines and forecasts. However, within the limited scope of this study, "fine tuning" of the operating strategy for each pattern was not attempted. It may result in the CO_2 injection and oil production in each pattern during the initial stage of the CO_2-EOR not being optimized and a CO_2 purchase schedule differing from EnCana's forecast. Therefore, the numerical prediction for the CO_2-EOR base case presented here is not an absolutely definitive simulation of EnCana's CO_2-EOR project. Nevertheless, the CO_2-EOR base case was considered sufficiently accurate to provide realistic initial reservoir conditions, in terms of CO_2 storage/distribution, pressure, and amounts of unrecoverable oil and water, for the risk analysis model of the geosphere to assess the potential CO_2 leakage and migration in Theme 4.

Alternative CO_2 storage cases after EOR were also investigated, with a focus on promoting additional CO_2 storage. The 75-pattern simulation was extended from 2033 after EOR to 2055 for alternative CO_2 storage cases. Two types of CO_2 storage cases were investigated. Cases II and IIa involved continued injection of fresh CO_2 with all pseudo-producers (one per pattern) shut-in. A maximum injection pressure of 29.5 MPa was chosen for an average depth of 1,450 m for the Weyburn reservoir with a safety margin of 90%. Cases III and IIIa involved continued injection of fresh CO_2, with gas-oil ratio (GOR) control at pseudo-producers (one per pattern). Producers were shut-in when GOR > 1,500 m^3/m^3.

Alternative Cases II and III were conducted after the CO_2-EOR base case. Alternative Cases IIa and IIIa were conducted after a CO_2-EOR alternative case with more CO_2 storage than the base case. A summary of the CO_2-EOR alternative case performances is given in Table 3.5.

Figure 3.45 shows CO_2 inventory in the 75 plus buffer patterns for CO_2 storage alternative Case II. By the end of the CO_2 storage process (2055), 29.08 MT of CO_2 were stored, which is an additional CO_2 storage of 5.87 MT after EOR. Without any production in this case, pressure of the reservoir built rapidly with continuous CO_2 injection and reached the maximum allowed pressure of 29.5 MPa within 3 years. Thus, very little CO_2 could be stored after the maximum allowed pressure had been reached. Figure 3.46 shows CO_2 distribution as CO_2 global mole fractions in the Marly and the Vuggy zones at the end of the CO_2 storage process. Figure 3.47 shows CO_2 inventory in the 75 plus buffer patterns for CO_2 storage alternative Case III. By the end of the CO_2 storage process (2055), 54.85 MT of CO_2 are stored, which is an additional CO_2 storage of 31.64 MT after EOR. With continuous oil production in this case, an additional 7.1% OOIP could be recovered at the end of the CO_2 storage process. The net CO_2 utilization ratio during the CO_2 storage process (alternative Case III) was 1,462, which is significantly higher than 416 for the CO_2-EOR base case. Figure 3.48 shows CO_2 distribution as CO_2 global mole fractions in the Marly and the Vuggy zones at the end of the CO_2 storage process. A summary of the EOR and storage performance for the EOR base case and the subsequence CO_2 storage alternative cases is given in Table 3.5. Also shown in Table 3.5 is the summary of storage performance for CO_2 storage alternative cases IIa and IIIa following the CO_2-EOR alternative case.

Table 3.5 Numerical prediction of CO_2 storage capacity and EOR performance for baseline and alternative scenarios (75-pattern simulation)

	Baseline EOR Case (2000 – 2033)		Alternative EOR Case (2000 – 2033)	
CO_2 Injected, %HCPV	45.9%		59.7%	
CO_2 Recycled, % Injected	58.2%		56.9%	
CO_2 Stored, million tonnes	23.21		30.05	
Oil Recovery after water flood, %OOIP	26%		26%	
Oil recovery after EOR, %OOIP	47.2%		50.3%	
Net CO_2 Utilization Ratio*, m^3/m^3	416		496	
	Alternative Storage Cases (2033 – 2055)		Alternative Storage Cases (2033 – 2055)	
	Case II	Case III	Case IIa	Case IIIa
CO_2 Stored (Additional), million tonnes	29.08 (5.87)	54.85 (31.64)	37.2 (7.2)	60.7 (30.60)
Oil Recovery @2055 (Additional), %OOIP	----	54.3% (7.1%)	----	54.7% (4.4%)
Net CO_2 Utilization Ratio*, m^3/m^3	----	1,462	----	2,585

* m^3 of CO_2 stored / m^3 of additional oil recovery in 75 EOR patterns

7 LONG-TERM CO_2 TRAPPED VOLUMES ESTIMATES FROM GEOCHEMICAL MODELING

Geochemical modeling is a prediction tool that can be used to provide an assessment of the amount of CO_2 that will be stored in the reservoir through solubility trapping, ionic trapping, and mineralogical trapping. In conjunction with detailed reservoir and flow modeling, these predictions will determine the amount and nature of CO_2 storage in the reservoir. Data needed for geochemical modeling included formation and injection fluid compositions and detailed mineralogical assessments of each of the major flow units in both the Vuggy and Marly zones in the Weyburn reservoir.

7.1 Mineralogy of the Weyburn Reservoir

Microscopic examination, X-Ray Diffraction (XRD), and LPNORM (a linear programming model that performs normative calculations) analysis of approximately 100 samples established the presence and abundances of minerals for each of EnCana's reservoir flow units. Midale Evaporite "Three Fingers Zone" (TFZ), Midale Marly, and Frobisher Marly were composed of finely crystalline dolomite, minor calcite, and anhydrite. The uppermost Midale Marly and the TFZ were the intervals, where the greatest volumes of reactive silicate minerals were found, as shown in Figure 48. The mineral content was 16.8% quartz and 17.1% silicate. In Figure 3.49, minerals with heavier elements are brighter shades of grey. Figure 3.49a shows a TFZ sample with abundant silicates, such as quartz (qtz), illite (ill), and K-feldspar (ksp). Dolomite (dol), with traces of later anhydrite (anh), comprises the bulk of the rock. Figure 49b shows a sample of the flow unit, V6, with large irregularly shaped vugs partially filled with later anhydrite (anh), dolomite (dol2), and calcite (cc2). The rock was predominantly calcite (cc), with traces of silicates and dolomite. Marly and TFZ porosity was generally submicroscopic, with little pore filling mineralization.

Midale Vuggy shoal and intershoal flow units were predominantly calcite with relatively low (<10 wt.%) silica and silicate mineral abundances. Potentially reactive silicate minerals, such as illite and feldspar, were limited throughout the reservoir, averaging 4 wt.% and 1 wt.%, respectively. Vuggy flow units were characterized by variable pore sizes (up to 2 mm long) that were most commonly filled with carbonate and

anhydrite. Anhydrite cementation and anhydrite replacement of microcrystalline calcite was more common toward the erosional contact above the Frobisher beds.

The mineralogical normative results showed that, even in a carbonate reservoir such as at Weyburn, silicate minerals were present in sufficient quantity (Table 3.6) to react with CO_2-charged fluid.

Table 3.6 Summary of average mineral modes for each of EnCana's flow units sampled during the reservoir mineralogy program.

Unit	Samples	Flow Unit	Weight Per cent Minerals (Wt.%)									
			Calcite	Dolomite	Anhydrite	Quartz	K-Feldspar	Plagioclase	Illite	Kaolinite	Anatase	Apatite
Midale Evaporite – Three Finger Zone	8	ME-TF	0.7	60.0	5.3	16.8	9.1	3.0	4.7	0.0	0.3	0.0
Midale Marly	11	M0	11.7	65.9	6.3	7.4	4.9	1.6	2.2	0.0	0.1	0.0
	4	M1	24.4	47.9	20.2	3.6	2.7	1.0	0.1	0.0	0.1	0.0
	15	M3	21.8	62.7	5.2	4.6	3.5	1.3	0.7	0.2	0.1	0.0
Midale Vuggy	7	V1	82.3	11.6	2.8	1.5	0.9	0.6	0.3	0.0	0.0	0.0
	12	V2	89.9	5.0	3.6	0.7	0.3	0.4	0.0	0.0	0.0	0.0
	6	V3	76.7	16.1	2.5	2.2	1.5	0.8	0.0	0.0	0.0	0.0
	12	V4	77.5	13.3	3.3	2.2	2.0	0.9	0.7	0.1	0.1	0.0
	6	V6	68.8	14.6	12.8	1.8	0.5	0.3	0.2	0.9	0.0	0.0
Frobisher Marly	10	FM	4.5	72.7	8.1	6.9	4.4	2.0	1.3	0.0	0.1	0.1
Frobisher Evaporite	2	FE	23.5	15.9	59.1	0.8	0.4	0.3	0.0	0.0	0.0	0.0

7.2 Estimates of Trapping Potential in Weyburn Reservoir

Although there were differences in mineralogy between the 8 different flow units, the reactions that would occur over time were predicted to be similar. Up to approximately 10 years, there was precipitation of calcite and kaolinite, and dissolution of anhydrite and the various silicate minerals. At approximately 10 years, a major change is predicted to occur, with the precipitation of dawsonite (a sodium aluminum carbonate) and minor amounts of anhydrite and the dissolution of calcite and all of the remaining silicates. Other "minor" mineralogical reactions occurred. During this period, the pH generally decreased (became more acidic), and the total dissolved carbon in solution, calcium, and potassium concentrations increased (potassium later than calcium due to the slower silicate reactions). Sodium concentrations decreased. The very short-term results (less than 1 year) included precipitation of carbonate and sulphate minerals, driven by degassing of produced fluids in the surface facilities and by mixing with the make-up water. The short-term modeling results are consistent with the results from the fluid monitoring program and the experiments undertaken by the British Geological Survey (Rochelle *et al.*, 2004) and the Geological Survey of Denmark and Greenland Ministry of the Environment (Olsen and Stentoft, 2000).

One of the critical modeling parameters is the speed at which the supercritical CO_2 dissolves into the formation water. This parameter controls the mineralogical reactions, and over the simulation period, the potential amount of sequestered CO_2. It was estimated by observing the compositional and isotopic changes of the produced water measured in the Theme 2, Fluid Monitoring Program. Some of the produced

water compositions had nearly reached isotopic equilibrium over three years. The results indicate that the supercritical CO_2 will nearly saturate the water in the formation during the EOR process over a period of 3 to 10 years, thereby becoming available for mineralogical storage reactions.

The primary storage and trapping mechanism was phase trapping – trapping supercritical CO_2 as a separate phase. This would be enhanced through the geochemical reactions occurring in the reservoir, such as those summarized above. Additional storage would occur through solubility trapping (storage through gas dissolution in the water), through ionic trapping (storage through the carbonate, bicarbonate, and other ionic species in the water), and through mineral trapping (precipitation of new phases containing carbon in their structure). Using estimates of the porosity, the volume of each of the flow units, and the reactions determined through the modeling, the maximum potential amount of trapping in each flow unit could be estimated, (Table 3.7). Integrating these results over the entire reservoir yields a total of approximately 45.15 MT with 22.65 MT, 0.25 MT, and 22.25 MT of CO_2 potentially stored through solubility, and ionic and mineralogical trapping mechanisms, respectively. Because approximately 20 MT of CO_2 was planned to be injected as part of the EOR process, the Weyburn Midale reservoir has excess storage capacity in these stable forms.

These estimates of storage capacity are for the long-term case and are based on a number of assumptions. The most critical assumptions were that there was just sufficient supercritical CO_2 for reaction in each of the flow units and that complete or significant reaction of the silicate minerals would occur over 5,000 years. However, in reservoir simulation of single patterns and of the 75 patterns, this was not the case shown not to be the case, primarily due to the density of supercritical CO_2 and its tendency to rise in the reservoir. Complete reaction of the silicate minerals is unlikely over the simulation period, as the carbonate and sulphate minerals armor a number of the silicate minerals. The initial dissolution of the carbonates and sulphates will remove some of the armoring, allowing more silicates to react. The impact of incomplete silicate reactions can be easily estimated – if only 50% of the silicates are available to react, the mineralogical trapping of CO_2 will decrease by 50%.

Table 3.7: Estimation of maximum potential amount of CO_2 trapping

Flow Units	Trapping Mechanisms in Each of Flow Units in Weyburn Reservoir			
	Solubility (MT CO_2)	Ionic (MT CO_2)	Mineral (MT CO_2)	% Mineral Trapping
M0	1.22	0.0128	1.87	60%
M1	3.57	0.0452	3.90	52%
M3	4.14	0.0347	5.73	58%
V1	3.65	0.0426	2.97	45%
V2	3.87	0.0683	1.51	28%
V3	1.40	0.0155	1.44	50%
V4	2.38	0.0206	2.90	55%
V6	2.42	0.0175	1.93	44%
Total	22.65	0.2572	22.25	49%

Nevertheless, subject to the assumptions inherent in this approach, the reservoir simulation estimates of CO_2 distribution in the reservoir could be combined with the geochemical modeling of long-term reactions to obtain a preliminary estimate of the CO_2 distribution in the Weyburn reservoir after 5,000 years. Based on the CO_2 storage capacity of 23.2 MT for the baseline scenario, approximately 10.25 MT remains in the oleic phase, 6.50 MT and 0.07 MT is sequestered through solubility and ionic trapping in the aqueous phase respectively, and 6.38 MT is sequestered through mineral trapping (Figure 3.50). It is predicted that there would not be a free supercritical CO_2 gas phase present in the reservoir after 5,000 years.

7.3 Potential Trapping in Adjacent Formations

A limited potential exists that leakage of fluids could occur from the Weyburn reservoir to other formations above and/or below. If leakage occurred, then reactions between the fluid and the minerals in these formations could occur and may potentially trap more carbon dioxide. In order to assess this, detailed mineralogy of these formations must be known.

Microscopic examination, X-ray diffraction (XRD), X-ray fluorescence (XRF), Scanning Electron Microscope (SEM), and micro-probe analyses were undertaken on almost 100 samples taken from 19 formations in the stratigraphic column surrounding the Weyburn Midale reservoir. The data was combined and evaluated using LPNORM methodology. Approximately 60 of the analytical data sets were used to describe the Bearpaw, Belly River, Lea Park, 2nd White Specs, Viking (top), Viking (base), Lower Colorado, Mannville, Vanguard, Upper Shaunavon, Upper and Lower Gravelbourg, Upper and Lower Watrous, Poplar, Ratcliffe, Frobisher, Kisbey, and Alida Formations. The major constituents of these formations are listed in Tables 3.8 and 3.9.

Table 3.8 Regional Formation mineralogy, Part 1

Unit	Quartz	Albite	Anorthite	k-Feldspar	Kaolinite	Illite	Illite-Smectite
Bearpaw	31.5	2.8	0.0	2.6	6.7	6.1	41.5
Belly River	45.1	3.0	0.0	2.9	4.8	2.1	36.8
Lea Park	24.8	3.0	0.0	2.9	9.1	16.7	33.0
2nd White Specks	26.6	3.0	1.5	0.7	0.0	2.6	8.5
Top Viking	31.9	1.9	0.0	2.0	45.2	2.3	15.1
Base Viking	39.5	3.2	1.6	0.0	6.3	11.0	20.1
L. Colorado	33.6	3.5	2.4	3.8	8.2	10.8	27.0
Mannville	50.0	2.0	0.2	2.1	18.7	6.6	14.9
Vanguard	33.7	2.1	0.2	1.8	7.2	10.3	12.0
U. Shaunavon	25.6	3.8	0.0	2.9	5.2	11.2	9.8
Upper Gravelbourg	11.4	1.3	0.0	0.0	1.1	2.6	11.4
Lower Gravelbourg	9.7	0.0	0.0	0.4	0.0	0.0	17.1
Upper Watrous	9.5	1.6	0.0	0.2	0.0	0.0	18.2
Lower Watrous	10.6	3.4	0.0	3.1	0.5	3.8	0.0
Poplar	8.1	2.2	0.1	4.4	0.0	2.8	3.3
Ratcliffe	3.0	0.5	0.0	0.6	0.0	1.2	0.0
Frobisher	3.6	1.2	0.0	1.7	0.2	0.0	0.0
Kisbey	15.3	0.8	0.0	1.7	0.0	8.4	0.0
Alida	0.9	0.4	0.0	0.3	0.0	0.0	0.0

The formations range widely in composition, from an almost pure limestone (Alida Formation) to extremely clay rich units (Viking (top) – 45% kaolinite, Bearpaw – 47% illite/smectite) to feldspar rich units (lower Colorado - ~10% combined feldspars) to dolomite-anhydrite units (Ratcliffe, Poplar, Watrous). A number of formations had measurable amounts of iron oxides, with more than 5% observed in the lower Colorado. This wide range of mineralogical normative results indicates the potential for a variety of different reactions, each of which had to be evaluated in detail in order to assess CO_2 trapping potentials.

Table 3.9 Regional Formation mineralogy, Part 2

Unit	Calcite	Ankerite	Dolomite	Magnesite	Siderite	Anhydrite	Hematite
Bearpaw	0.0	4.1	0.0	0.0	3.6	0.0	0.0
Belly River	0.0	2.0	0.0	0.0	2.7	0.0	0.0
Lea Park	0.0	0.0	3.4	0.0	5.8	0.0	0.0
2nd White Specks	53.8	0.0	0.0	0.0	0.0	1.6	0.5
Top Viking	0.0	0.2	0.4	0.0	0.4	0.0	0.0
Base Viking	3.8	1.7	0.0	0.0	11.2	0.2	0.0
L. Colorado	0.4	0.8	0.0	0.7	2.2	0.0	5.1
Mannville	0.2	1.1	0.0	1.0	0.0	0.0	0.6
Vanguard	23.3	1.5	1.1	0.7	4.4	0.0	0.4
U. Shaunavon	0.0	3.0	32.6	3.1	0.0	0.1	1.3
Upper Gravelbourg	67.1	3.5	0.0	1.2	0.0	0.0	0.0
Lower Gravelbourg	67.5	4.7	0.0	0.3	0.0	0.0	0.0
Upper Watrous	12.4	0.0	28.0	0.0	1.5	27.4	0.0
Lower Watrous	23.3	0.4	40.2	0.0	0.1	13.3	0.2
Poplar	11.2	0.9	40.6	2.1	0.0	23.7	0.3
Ratcliffe	42.9	0.1	21.1	0.5	0.2	29.5	0.0
Frobisher	79.1	0.7	10.8	0.8	0.0	1.4	0.0
Kisbey	17.5	0.0	54.5	0.0	0.0	1.3	0.2
Alida	96.9	0.1	0.0	1.3	0.0	0.0	0.0

Using the mineralogical normative results and a “model leakage fluid” based on the results of injected CO_2 and water reactions with the M0 units of the Weyburn reservoir after 10 years, the potential reactions in each of the 19 different formations were predicted for a period up to 5,000 years.

The potential mineralogical changes were quite diverse, resulting in very different reaction mechanisms occurring in each of the formations. The formations with iron oxides typically formed siderite (iron carbonate), resulting in mineral trapping of CO_2. Formations with significant amounts of calcium silicate minerals (primarily anorthite) formed additional calcite (calcium carbonate), resulting in mineral trapping of CO_2. If significant amounts of magnesium-containing minerals were present, then a mineralogical shift from calcite to dolomite was observed. All formations with significant amounts of reactive silicate minerals resulted in pH buffering of the fluid as they reacted, leading to late stage formation of carbonate minerals.

One major difference between these calculated results and those for the Weyburn reservoir was the absence of Dawsonite (a sodium aluminum carbonate) formation. Three of the Formations (Alida, Ratcliffe, and Lower Gravelbourg) are not anticipated to experience the formation of additional carbonate minerals, but rather some of the existing carbonate minerals would be dissolved. These Formations have a very limited amount of silicate minerals, no iron oxides, and are primarily composed of calcite/dolomite/anhydrite.

A summary of the modeling results, in terms of potential CO_2 storage or release, is given in Table 3.10. The maximum potential change is shown as tonnes of CO_2 per cubic meter of reservoir based on the assumptions that all of the rock is accessible for reaction within the necessary time frame and that the “leakage fluid” is an aqueous fluid derived from the M0 unit in the Weyburn reservoir.

Table 3.11 Potential amount of CO_2, which could be stored in each adjacent Formation

Formation	Tonnes CO_2 Precipitated (+) or Released (-) per cubic meter of Formation
2nd White Specks	1.16×10^{-2}
Alida	-1.43×10^{-4}
Bearpaw	1.51×10^{-2}
Belly River	1.50×10^{-2}
Frobisher	2.70×10^{-3}
Lower Colorado	1.50×10^{-2}
Upper Watrous	1.94×10^{-2}
Lower Watrous	8.06×10^{-3}
Viking Top	1.55×10^{-2}
Base Viking	1.45×10^{-2}
Vanguard	1.49×10^{-2}
Upper Shaunavon	2.38×10^{-2}
Ratcliffe	-7.09×10^{-4}
Poplar	1.42×10^{-2}
Mannville	4.48×10^{-3}
Lea Park	1.50×10^{-2}
Kisbey	4.89×10^{-3}
Upper Gravelbourg	7.71×10^{-5}
Lower Gravelbourg	-6.00×10^{-4}

The potential mineralogical storage for most of these Formations ranges from about 1 kilogram of CO_2 to about 24 kilograms of CO_2 per cubic meter of formation.

These conclusions are based on identical assumptions to those discussed for geochemical reactions in the Weyburn reservoir, with one additional constraint. The flow velocity/path through each of these Formations must be slow enough for the geochemical reactions involving the precipitation of carbonate minerals to come to completion.

With the exception of the 3 previously mentioned Formations, all of the Formations surrounding the Weyburn oilfield can permanently store CO_2 from "leakage fluids" as mineral matter. This could increase the security of this field if it were to be considered as a greenhouse gas repository.

8 CONFORMANCE CONTROL

In the Weyburn Midale reservoir, two oil-bearing intervals, the Vuggy and the Marly, have different fracture characteristics, extents of water invasion, and degrees of heterogeneity. Since this reservoir was characterized by trending fractures and alternating layers of high and low permeability, conformance control of the injected CO_2 was crucial in optimizing the oil recovery and enhancing the storage capacity of the reservoir. Once miscibility was achieved in-situ between the injected CO_2 and the displaced oil, conformance control was the key factor in conducting an economic displacement flood. Since there is an obvious synergism between improved oil recovery and increased CO_2 storage capacity, recovery optimization is an essential aspect of this type of storage project.

Two forms of conformance control have already been implemented in the Weyburn reservoir. Injecting the CO_2 in water alternating gas (WAG) mode controls the mobility of the gas between more viscous slugs of water. This method has both positive and negative effects. The water reduces the CO_2 mobility, but it also traps oil, increases water flow, and decreases extraction of lighter hydrocarbons from the oil by the CO_2 (Bernard *et al.*, 1980). A mechanical form of conformance control has been achieved by placing the horizontal injection and production wells such that the overall fluid flow is in the off-trend fracture direction. However, even in the off-trend direction, fractures with generally smaller apertures could be found, resulting in CO_2 channeling between the injector and producer. Additional conformance control measures for the CO_2 injection project needed to be implemented in order to achieve maximum oil recovery efficiency. The overall scope of this study was to evaluate the performance of commercially available conformance control technologies from laboratory tests to field applications. These technologies were all based on chemical formulations, which can be categorized into mobility control agents or foams (Chou *et al*., 1994; and Hanssen *et al.*, 1995), blocking and diverting agents or gels (Borling, 1994; Hild and Wackowski, 1998; and Sydansk and Southwell, 2000), and hybrids thereof, namely gel-foams (Friedman *et al.*, 1997; and Wassmuth *et al.*, 2001).

Review of previous field applications showed that blocking and diverting gel applications seem to be the most practical and long lasting in improving conformance control in areas where fluid flow is dominated by fractures. Foam and gel-foam field applications were not reliable or effective in providing conformance control in reservoirs with high permeability contrasts. Gel applications for CO_2 conformance control in the nearly depleted Wertz field (Borling, 1994) and in the Rangely field (Hild and Wackowski, 1998) were economically successful. In both cases, numerous large injector treatments were implemented. Payout of the gel treatments occurred within 3 to 8 months. There seemed to be no negative effects on injectivity or oil production. From the eight foam applications for CO_2 conformance control (Hanssen *et al.*, 1995) that were reviewed, only one was successful. Foam could be used for near wellbore injection profile modification. However, for in-depth reservoir profile modification, the current foam technology was not suitable. One gel-foam application in the Rangely field was reviewed. Even though on a volume basis, the gel-foam was more economical in comparison to a straight gel application, the gel-foam did not impart a long lasting conformance effect.

During the waterflood period in the Weyburn reservoir, EnCana has applied 14 gel applications of various sizes to several horizontal and vertical wells to try to improve the sweep efficiency. Generally, logging techniques were used to pinpoint the zone of water influx in the wellbore. The identified zone was isolated and the gelant was injected only into the isolated zone. After the initial three gel applications in 1996, 11 additional gel applications followed in 1997. The subsequent production profiles show that 4 of the 13 gel treatments were fully successful in increasing the oil production rate and decreasing the water rate. In addition, 4 gel treatments successfully reduced the water production rate and maintained the oil production rate. Any water that was not produced at the treated well was diverted to a neighboring well to produce additional oil. Thus, a success rate of 60% was achieved with these treatments. During the 14 gel treatments, a total of 3,200 m^3 of gel was injected at an approximate cost of $550,000. Based on our reserve estimates, the gel treatments increased reserves by 95,000 m^3 (590,000 barrels), which results in a finding and development cost of $0.92/bbl (from the gel costs alone).

8.1 Laboratory Investigation of Conformance Control Technologies

The initial goals of this task were to screen out and optimize conformance control formulations through laboratory bench tests for the different technologies mentioned above. Secondly, the impact of the optimized formulations on CO_2 conformance control was evaluated through coreflood tests in two types of media, homogeneous matrix core and artificially fractured core, which was made by cutting a matrix core into two halves and using a spacer to create a fracture with an aperture of approximately 80 mm. The ultimate result of these experiments is recommendations for when and under what conditions the various conformance control technologies should be applied.

Foams:

Foamability studies indicated that the most suitable surfactant to generate CO_2-foam under Weyburn reservoir conditions was Chaser CD-1045, when compared to other surfactants, such as Surfonic N-95, Surfonic L-24 9, and Bio-Terge AS-40. This commercially available surfactant was formulated to provide superior foam stability with CO_2 in the presence of oil. A surfactant concentration of 0.5 wt% is recommended to overcome in-situ adsorption levels and to maintain the surfactant concentration of its critical micelle concentration of 0.2 wt%.

Coreflood tests in the matrix core indicated that a foam quality of 80% generates foams with the highest mobility reduction of the gas phase. Mobilities for foams at different foam qualities are shown in Figure 3.51. Effects of temperature and pressure on foam mobility were also studied. It was found that increases in temperature or decreases in pressure resulted in the decrease of foam mobility.

Regular foam was not effective in displacing oil from the fractured core. The effective viscosity of the foam in the fractured core was measured at 10 mPa.s at low flow rates, while in the matrix core, the same foam generated viscosities with several hundred mPa.s. After foam injection ended, the conformance control effects of the foam were easily eroded with chase fluids in the fractured core.

Gels:

Chromium crosslinked polyacrylamide gels were found to be suitable for blocking and diverting purposes in the Weyburn reservoir. The gelation time could be delayed through the addition of sodium lactate to the basic gel formulation. Thus, the gelation time was varied from 4 to 8 hours, resulting in gel formulations more suitable for field applications.

For the gel applications in fractured cores, incremental oil was produced after the gel had aged in-situ during subsequent miscible CO_2 and water injection. The oil saturation was monitored along the length of the core before and after the gel treatment (Figure 3.52). After the gel treatment, CO_2 and water were diverted into the top- and bottom-half matrix cores to displace previously bypassed oil, and an incremental 24 to 30% OOIP was recovered. The breakdown of oil recovery before and after gel treatment in a fractured core is shown in Figure 3.53. With the gel placement in the fractured core, it was possible to achieve an ultimate oil recovery in a fractured core similar to miscible flood recovery in the homogenous, matrix core.

Gel-Foams:

An optimized CO_2-gel-foam formulation was developed for application in Weyburn reservoir conditions. The liquid component of the gel-foam formulation incorporated the optimized surfactant CD1045 at a concentration of 0.75% with the chromium crosslinked polyacrylamide gel plus sodium lactate for gelation delay. This formulation has both mobility control behaviour during injection and blocking/diverting actions after the gel-foam has set. During gel-foam injection into the fractured core, an incremental 10% OOIP was produced. The effective viscosity of the gel-foam in the fractured core was approximately 10 times higher than regular foam at the same flow rates. The gel-foam does provide sufficient viscosity so that, during the injection, CO_2 and water was forced into the matrix and recovered incremental oil.

Based on the laboratory and field trial results, gel applications are predicted to be the most likely to succeed in CO_2 conformance control applications for the Weyburn reservoir. During a gel treatment, the injected gel will be extruded along the fracture path and will block a large number of the fractures. Subsequent injection of CO_2 and water will sweep out parts of the reservoir that have not been blocked by the gel. In the reviewed field trials, there were no indications that injectivity was a significant problem after the gel applications. This seems to indicate that the placed gel did not shut-off all the fractures or that some fractures were only partially blocked.

8.2 Design and Prediction of Treatment Performance in the Weyburn Reservoir

A stage-gating process was setup to progress the conformance control technologies from laboratory to field application. This stage-gating process, summarized in Figure 3.54, shows the individual steps that need to be completed before the field application could be implemented. Once the literature review and most of the experimental work was completed, candidate selection, reservoir scale treatment simulations, and conformance problem identification were carried out.

GOR values and oil production and water production rates were used as screening criteria to select candidates for a conformance control program. Out of 600 wells, 20 with the highest GORs were identified (highlighted in Figure 3.55 with blue markers). Wells characterized by higher GOR values were located in specific areas of the field, as indicated by trend circles in the Phase 1A area. The next step in the target well selection process was to establish which injection wells were contributing to the quick CO_2 breakthrough leading to uneconomic CO_2 recycling and high GORs.

In June 2003, a tracer study was conducted to help diagnose the conformance problems in three SSWG Patterns (P1613614, P0618613, and P0619613) in the Phase 1A area. Six of the horizontal wells were sampled for tracer breakthrough at regular intervals. The results from this tracer study would enable direct correlations between injectors and producers to be established. The total injected tracer volume at breakthrough was a measure of the pore volume in the high permeability zone. This measure would be used to size the gel treatment.

Reservoir simulations on Pattern 1 (P1612614) were used to demonstrate the impact of conformance control treatments on oil recovery in a horizontal well pattern (Figure 3.56). The simulation results obtained from the fine-grid single-pattern simulation were used as the base case (without gel treatment). The gel treatment simulation followed a multi-step approach. First, the permeability between the injector and producer was modified, mimicking a conformance control application. The permeability was reduced by a factor of 10. Second, the impact of the permeability modification on injection rates and oil production for the target pattern was studied. Third, the size of conformance control treatment required to modify the rock permeability by plugging the fracture volume was calculated. Finally, the economic impact of the conformance control treatment was calculated.

The simulation predicted the performance of an injector (93/10-12-006-14W2) treatment on two near-by horizontal producers (91/01-13-006-14W2 and 93/10-12-006-14W2). A total pore volume (PV) of 80,000 m^3 was assumed to be treated with 1,000 m^3 gel, as gel placement was limited to fractures, which are approximately 1% PV. The impact of the gel treatment on cumulative oil and gas production for two near-by horizontal producers is shown in Figure 3.57. The simulation indicated an incremental oil recovery of 20,000 m^3, corresponding to a 10% increase in oil recovery. Based on the void space made available from the incremental oil recovery, an additional 25,000 tonnes of CO_2 can be stored. If this preliminary estimate is extended over the entire field (75 patterns), assuming a 10% increase in total oil recovery and assuming that only 20% of the EOR patterns would undergo gel treatments, it is estimated that an additional 1.7 MT of CO_2 could be stored in all the patterns. Such a gel treatment would cost C$200,000 to $500,000. Assuming that the netback value of the oil would be $100/$m^3$, the revenue from the incremental oil production would approach $2.0 million. Thus, gel conformance treatments would be economically attractive in such scenarios.

9 ECONOMIC LIMITS OF CO_2 STORAGE

9.1 Description of Storage Economic Model

The CO_2 storage economic model was developed by Canadian Energy Research Institute (CERI) for the purpose of performing economic evaluations of specific CO_2 storage opportunities. This model provides users with the ability to evaluate the preliminary economics of a specific CO_2 storage opportunity for a specific CO_2 supply source, a specific CO_2 transportation system, and a specific CO_2 storage project (either stand-alone or in conjunction with an EOR project), to evaluate the impact of changing fiscal provisions (*i.e.*, royalties, taxes, subsidies, and grants) on storage economics, to evaluate the impact of CO_2 credits and penalties and associated tax applications for each of the capture, transportation, and storage modules, and to examine the sensitivity of the results to various economic parameters (*i.e.*, oil prices, capital costs, operating costs, and fiscal regimes). Some sensitivity tests are automatically performed in each model run, and the user can test many other cases and combinations.

The CO_2 Economic Model can be used as a tool in assessing the economics of specific wells associated with the project, the overall project itself, and any other potential CO_2-EOR or storage project. The user's inputs, such as financial inputs or physical properties, can be tailored to suit many regions of interest. This makes the model applicable over a wide range of situations. CERI used information and data from its Study No. 106 (CERI, 2002) to provide the underlying assumptions for calculation of CO_2 capture, transportation, and storage costs. The structure of the model, which consisted of three different modules (CO_2 capture module, CO_2 transportation module, and CO_2 storage module), is given in Table 3.12.

Table 3.12 Modular structure of CO_2 storage economic model

CO_2 Capture Module	CO_2 Transportation Module	CO_2 Storage Module
• Several CO_2 capture prototypes with representative capital cost, operating cost and technical parameters	• CO_2 transportation model with representative capital cost, operating cost and technical parameters	• CO_2 storage framework - requires capital cost, operating cost and technical parameters derived from an EOR technical screening model, numerical or laboratory simulation, or field trial
• Ability to adjust capital cost, operating cost and technical parameters as new information becomes available	• Ability to adjust capital cost operating cost and technical parameters as new information becomes available	• Ability to adjust fiscal parameters - carbon taxes/credits, royalties, income taxes
• Ability to insert actual capital cost, operating cost and technical parameters	• Ability to insert actual capital cost, operating cost and technical parameters	
• Ability to insert actual CO_2 prices	• Ability to insert actual transportation tolls	

9.2 A Demonstration Case

The capability of the CO_2 storage economic model has been demonstrated in a "demo run," based on the total oil production and CO_2 injection predictions from the 75-pattern simulation EOR base case (Table 3.5).

In the simulation, the CO_2-EOR phase operated by EnCana in the Weyburn region was assumed to be in operation from the beginning of 2001 to the end of 2033. It was assumed that, as at present, CO_2 is captured from the Dakota Gasification Company, south of Weyburn in North Dakota, and transported by a 320 km pipeline to the Weyburn field. CO_2 was injected into and around the 75-pattern oil-producing region to enhance oil recovery. The Weyburn EOR region (*i.e.*, 75 patterns) has an OOIP estimate of 139 million cubic meters. Secondary recovery during the EOR years was assumed to total 5% of OOIP (7 million cubic meters). Incremental recovery over the EOR period is estimated at 21 million cubic meters (*i.e.*, additional oil recovery from EOR minus oil recovery estimated for continuous waterflooding). It is estimated that another 7 million cubic meters could be recovered during the years 2034 to 2053 during the CO_2 storage phase. Figure 3.58 shows cumulative incremental oil production.

CO_2 would be produced during operations and recycled, or re-injected, into the reservoir. The amount of CO_2 stored is the amount injected minus the amount produced. The amount stored is also the amount that must be delivered, or purchased. EnCana has stated that it has contracted 95 million cubic feet per day (4,981 tonnes/day or 20 MT over the 33 EOR years) of CO_2 from Dakota Gasification Company (DGC). From the 75-pattern simulation EOR base case, the total purchase and storage of CO_2 (injected and recycled) was 25 MT from 2001 to 2033, with a peak storage rate of 3,881 tonnes/day in 2008. In the last few years of operations, CO_2 injection rates are predicted to fall as ramp-down occurs. Most of the CO_2 injected during the ramp-down phase was recycled CO_2. Figure 3.59 shows cumulative CO_2 purchased/stored.

After EOR operations, additional CO_2 storage and oil production is possible. This area could be operated as a storage facility, with oil production as a by-product. This predicted oil production, as seen from Figure 58, produces a significant revenue stream after EOR. Figure 3.60 shows daily oil and CO_2 rates for both the EOR and the post-EOR phases from 2001 to 2053 for the Weyburn Unit.

The storage economic model was run for the years 2001 to 2033 (EOR phase) first, to estimate the economics of EnCana's EOR project. It was found that the EOR project was economic, generating a 10% internal rate of return (real) at an oil price of US$22.61 (or C$30.15 with an exchange rate of $0.75 US/Cdn) based on a dollar valuation in 2000. With the project assumed to operate for 33 years, from 2001 to the end of 2033, the delivered CO_2 cost was calculated to be C$29.85/tonne. The total CO_2 stored over the 33 years is 25 MT, and the total incremental oil produced is 21 million cubic meters (or 133 million barrels). The total CO_2 storage cost, including capital costs and the cost of CO_2 purchased, was calculated to be C$1.32 billion. CO_2 credits and penalties were not incorporated in this run. By the supply cost method, all discounted costs must be balanced by discounted revenues. Oil production is the only revenue stream in this example, and the result was C$151.49 per tonne of CO_2 stored (not avoided).

The storage economic model was then run for the years 2034 to 2053 (post-EOR phase) with an oil price of C$30.15 per barrel and delivered cost of CO_2 at C$29.85, as estimated from above. Assuming the CO_2 storage rates and oil production rates above, for the years 2034 to 2053, varying credits for CO_2 emission storage (based on amount of CO_2 stored and not CO_2 avoided) were tested. Assuming a refurbishment cost of C$0.25 million per well at 2033, the calculated internal rates of return are given in detail in Table 3.13. In this case, construction is assumed to take place in 2033 in order to continue the operational flow from the EOR phase to the post-EOR phase. The capital cost of CO_2 compression equipment (to handle higher recycle volumes) was estimated to be C$20 million in 2033. A total of 189 wells, horizontal and vertical, would have to be re-opened (refurbished) after EOR (they were assumed to be shut-in towards the end of EOR) to increase injection volumes. This resulted in an estimation of the initial capital expenditures of C$67 million. The sustaining capital costs were assumed to continue after EOR at C$7 million per year. Operating costs were assumed to be a fixed cost of C$16 million per year plus a variable cost, dependent on oil production, at C$3.75 per barrel produced. All other financial assumptions, such as income taxes and royalties, were the same as those used for the EOR phase run (Table 3.14).

As would be expected, it was found that, with no credits, operation beyond 2033 would not be economic. Depending on costs and years of storage operation, CO_2 credits of C$8/tonne would be needed to make at least a 10% real rate of return on the investments required for extended operations, and the storage operations must last for at least 8 years. In the case of only 5 – 7 years of storage operations, higher credits per tonne stored would be required under the simulated conditions.

Table 3.13 Economic evaluation of rate of return for a CO_2 storage process

Rate of Return given Credit for CO_2 Stored (C$/tonne) $0.25 million/well cost at 2033 ($67 million initial capex in year 2033)																	
Year of Post EOR	Credit for Stored CO_2																Additional Post EOR CO_2 Storage (MT)
	$0	$5	$6	$7	$8	$9	$10	$11	$12	$13	$14	$15	$16	$18	$20	$25	
20	< 0	< 0	< 0	< 0	11%	14%	16%	19%	21%	23%	25%	27%	29%	32%	36%	45%	26.2
15	< 0	3%	7%	10%	12%	15%	17%	19%	21%	23%	25%	27%	29%	32%	36%	45%	20.6
14	< 0	5%	8%	10%	13%	15%	17%	19%	21%	23%	25%	27%	29%	32%	36%	45%	18.8
13	< 0	6%	8%	11%	13%	15%	17%	19%	21%	23%	25%	27%	28%	32%	36%	45%	17.1
12	< 0	6%	9%	11%	13%	15%	17%	19%	21%	23%	25%	26%	28%	32%	36%	45%	15.3
11	< 0	7%	9%	11%	13%	15%	17%	19%	21%	22%	24%	26%	28%	32%	36%	45%	14.1
10	< 0	6%	9%	11%	12%	14%	16%	18%	20%	22%	24%	26%	28%	31%	35%	45%	12.9
9	< 0	6%	8%	10%	12%	14%	16%	17%	19%	21%	23%	25%	27%	31%	35%	44%	11.2
8	< 0	4%	6%	8%	10%	12%	14%	16%	18%	20%	22%	24%	26%	30%	33%	43%	9.5
7	< 0	2%	4%	6%	8%	10%	12%	14%	16%	18%	20%	22%	24%	28%	32%	42%	7.8
6	< 0	< 0	< 0	1%	3%	5%	8%	10%	12%	14%	16%	18%	20%	24%	29%	39%	7.1
5	< 0	< 0	< 0	< 0	< 0	< 0	< 0	2%	4%	6%	9%	11%	13%	18%	23%	34%	6.4

Table 3.14 Overview of physical and financial assumptions for EOR phase used for "demo run"

Start year of operation - 2001	
2 years of construction	
Exchange Rate - $0.75 US/Cdn	
Inflation Rate - 2% per annum	
Discount Rate - 10% per annum for each module	
Natural Gas Price - $4.25 Cdn per gigajoule	
Electricity Price - $50 per megawatt hour	
Electricity Emission Factor - 0.75 tonnes per megawatt hour	
Gas Fuel Emission Factor - 50 tonnes per terajoule	
Emission Credits - $0.00 per tonne of CO_2	
Emission Penalty - $0.00 per tonne of CO_2	
Capture:	High Purity Source
	CO_2 Concentration (wet vol. %) - 54%
	Operating Factor - 90%
	CO_2 Recovery Factor - 99%
	Federal Tax Rate - 35%
	Regional Tax Rate - 10.5%
	Capital Cost Allowance if Canada - 30%, Recovery Period if US - 5 years
	Admininstrative & General costs - 10% of initial capital costs
	Abandonment & Reclamation costs - 3% of initial capital costs
	30 years in operation
Pipeline:	Length of Pipeline - 290 kilometres
	Year-to-year Operating Costs - 4% of initial capital costs
	Federal Tax Rate - 21%
	Capital Cost Allowance if Canada - 6%, Recovery Period if US - 5 years
	Regional Tax Rate - 17%
	Admininstrative & General costs - 10% of initial capital costs
	Abandonment & Reclamation costs - 3% of initial capital costs
	30 years in operation
Storage:	Initial Capital Costs - $350 million
	Sustaining Capital Costs - $7 million per operating year
	Total Delivered Cost of CO_2 - $739 million over the lifetime of the project
	Total Cost of CO_2 Storage: $1.3 billion over the lifetime of the project
	Operating Costs: $7.50 per barrel of oil produced
	Abandonment & Reclamation costs - 3% of initial capital costs
	Federal Tax Rate - 21%
	Regional Tax Rate - 17%
	Capital Cost Allowance if Canada - 30%, Recovery Period if US - 5 years
	Royalty Rate - 25% of net revenue
	33 years in operation

10 CONCLUSIONS AND RECOMMENDATIONS FOR FUTURE WORK

Based on periodically collecting and analyzing oil samples from different wells in the Weyburn reservoir, it is confirmed that the CO_2-EOR process is operating under miscible or near-miscible conditions. A PVT model has been developed based on measurements of the oil sample, and it is capable predicting the equilibrium phase behaviour of the CO_2-Weyburn oil system accurately during reservoir simulation. The reservoir simulation model, which was validated by both laboratory-scale and field-scale simulation, has been successfully used to predict the CO_2 storage capacity and distribution in the Weyburn reservoir. A reservoir simulation methodology accounting for the size and complexity of the 75 EOR patterns has been developed. The approach, which began with fine-grid single-pattern simulations and ended with a coarse-grid 75-pattern simulation, involved three levels of upscaling: (1) from a detailed geological model of the Weyburn reservoir to a fine-grid reservoir simulation model, (2) from 3 fine-grid single-pattern models to coarse-grid models of the same patterns, and (3) from 3 coarse-grid single-pattern models to a 75-pattern model using the same grid resolution.

Using the predicted CO_2 distribution in the Weyburn reservoir at the end of EOR, a geochemical model has been applied to provide a preliminary assessment of the amount of CO_2 that will be stored in the reservoir through different trapping mechanisms (solubility and ionic and mineralogical trappings).

Conformance control treatments for the Weyburn field have been developed and tested. Simulated application of specially-formulated gel treatments to the best candidate wells predicted a substantial improvement in volumetric sweep efficiency from the application. This in turn would result in additional CO_2 stored.

A storage economic model has been developed and used to determine the economic limit of the CO_2 storage operations after EOR. Of the significant amount of additional CO_2 that can be physically stored in this manner, the model predicted various limits of CO_2 volumes that can be economically stored as a function of the amount of CO_2 credits received and the desired rate of return for the operation.

Knowledge gaps identified include data from the implementation of conformance control field trials to establish levels of success and the collection of further performance data from the CO_2-flood to history-match the 75-pattern reservoir model (to date there are only three years of EOR production data available for history matching). These gaps also include an evaluation of a dual-porosity approach to reservoir simulation in recognition of the fractured carbonate nature of the Weyburn reservoir and implementation of a fully coupled approach between reservoir simulation and geochemical modeling for a more precise estimation of the long-term CO_2 trapping potential.

A number of recommendations for future work can be made. Currently, estimates of long-term CO_2 trapping based on geochemical modeling are very preliminary. Improved estimates can be achieved by considering more detailed assessments of production fluid compositions and by taking into account the dynamic flow of CO_2. Reservoir simulation and geochemical models can be coupled to allow more accurate estimates. Reactive transport modeling should be considered. Continuing with field fluid sampling is important. Field trials of conformance control could not take place in Phase 1. It is important that such trials take place in future studies. Currently, limited post-CO_2 breakthrough field fluid data is available and none is available for the light-oil sample collection site. There is still a question as to how the natural variation of fluid properties across the Weyburn Unit could be accommodated in fluid characterization so oil sample collection remains important. Currently, CO_2 storage is focused on the Weyburn Unit. Examination of surrounding aquifer storage potential may make subsurface storage more appealing, especially to power generators who may not have access to oil or gas reservoirs. Only single-porosity models have been used in the reservoir simulation, but due to the fractured nature of the carbonate reservoir in the Weyburn Unit, some consideration should be given to the application of dual-porosity models. Further evaluation of the total CO_2 storage potential of the Weyburn Unit and surrounding Midale Formation aquifers would be probative. Developing means of monitoring and verifying CO_2 storage outside the Weyburn Unit should be considered.

11 REFERENCES

Borling, D. C., 1994, Injection conformance control case histories using gels at the Wertz field CO_2 tertiary flood in Wyoming, *SPE Paper No. 27825*.

Canadian Energy Research Institute (CERI), 2002, Cost for capture and sequestration of carbon dioxide in western Canadian geologic media, *CERI, Study No. 106*.

Chou, S. I., S. L. Vasicek, D. L. Pisio, and J. A. Goodgame, 1994, CO_2-foam field trial at North Ward-Estes, *SPE/DOE Paper No. 27785*.

Computer Modeling Group (CMG) Ltd., 2002, *GEM, Advanced Compositional Reservoir Simulator, Version 2002 User's Guide*.

Elsayed, S. A., R. Baker, P. L. Churcher, and A. S. Edmunds, 1993, A multidisciplinary reservoir characterization and simulator study of the Weyburn Unit, Saskatchewan, Canada, *SPE Paper No. 25852*.

Friedman, F., T. L. Hughes, M. E. Smith, G. P. Hild, A. Wilson, and S. N. Davies, 1997, Development and testing of new foam-gel technology to improve conformance of the Rangely CO_2 Flood, *SPE Paper No. 38837*.

Gardner, J. W. and J. G. J. Yuma, 1984, An investigation of phase-behavior/macroscopic-bypassing interaction in CO_2 flooding, *SPE Journal*, pp. 508-520.

Hancock, S. K., 1999, Project brings commercial-scale CO_2 miscible flooding to Canada", *Oil & Gas Journal*.

Hanssen, J. E., L. M. Surguchev, and M. Dalland, 1995, Field experience with foam processes: a critical review, *Paper presented at 16th IEA Collaborative Project on Enhanced Oil Recovery, Chiba, Japan*.

Hild, G. P. and P. K. Wackowski, 1998, Results of injection well polymer gel treatment program at the Rangely Weber Sand Unit, Rangely Colorado", *SPE Paper No. 39612*.

Olsen, D. and N. Stentoft, 2000, The Weyburn Monitoring Project core analysis test to ascertain changes in fluid flow properties as a consequence of reaction with CO_2, *Research carried out as part of the EU Project No. ENK5-CT-2000-00304*.

Pedersen, K. S. and A. Fredenslund, 1987, An improved corresponding states model for the prediction of oil and gas viscosities and thermal conductivities, *Chem. Eng. Sci*., Vol. 42, No. 1, pp. 182-186.

Peng, D. Y. and D. B. Robinson, 1976, A new two-constant equation of state, *Ind. Eng. Chem. Eng. Fundam*., 15, pp. 59-64.

Rochelle, C. A., J. M. Pearce, D. J. Birchall, and K. Bateman, 2004, Experimental geochemical studies of CO_2-porewater-rock interaction, *The Weyburn Project: Summary Report for Task 3.1, British Geological Survey Commissioned Report CR/04/020*.

Sydansk, R. D. and G. P. Southwell, 2000, More than 12 years experience with a successful conformance control polymer-gel technology, *SPE Prod. & Facilities* 15, 4, pp. 270-278.

Wassmuth, F. R., L. A. Hodgins, L. L. Schramm, and S. M. Kutay, 2001, Screening and coreflood testing of gel foams to control excessive gas production in oil wells, *SPERE*, pp. 187-194.

FIGURES

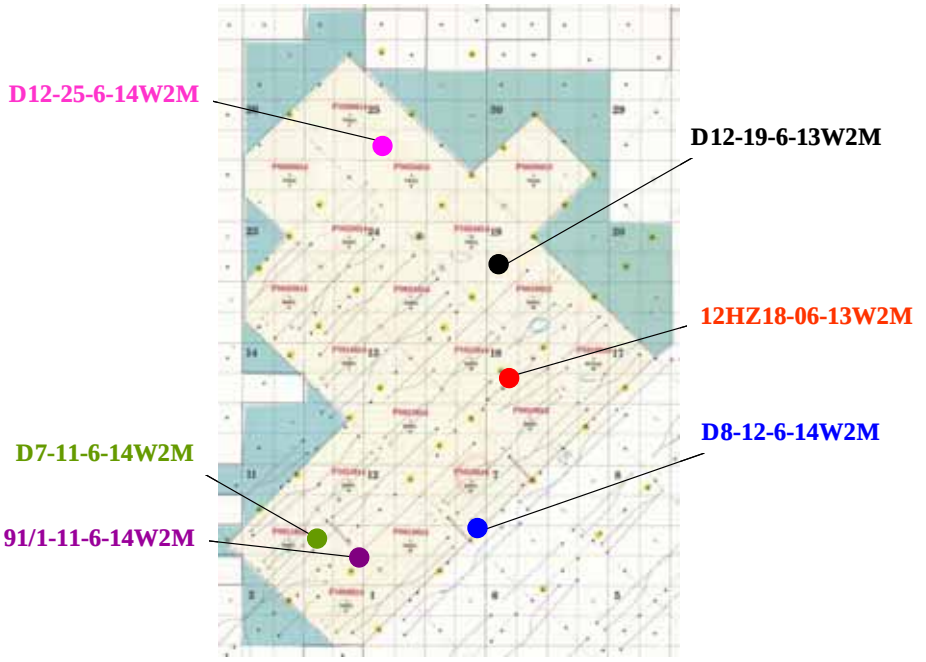

Figure 3.1: Locations of oil sample wells (samples from well 12HZ18-06-13W2M are collected by EnCana)

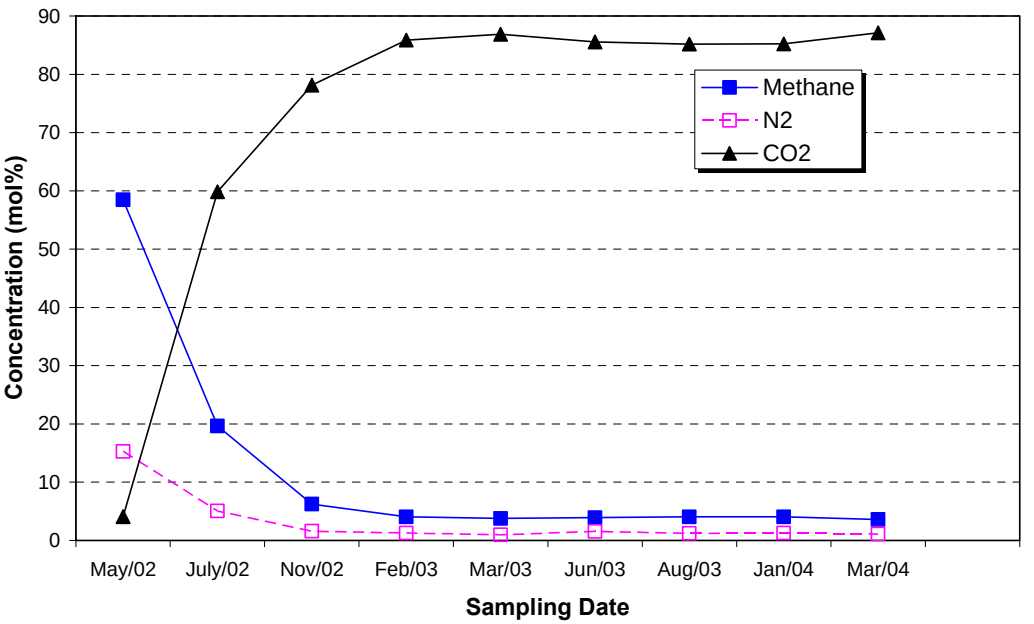

Figure 3.2: Main Components in Gas Samples from Well 91/1-11-6-14W2M

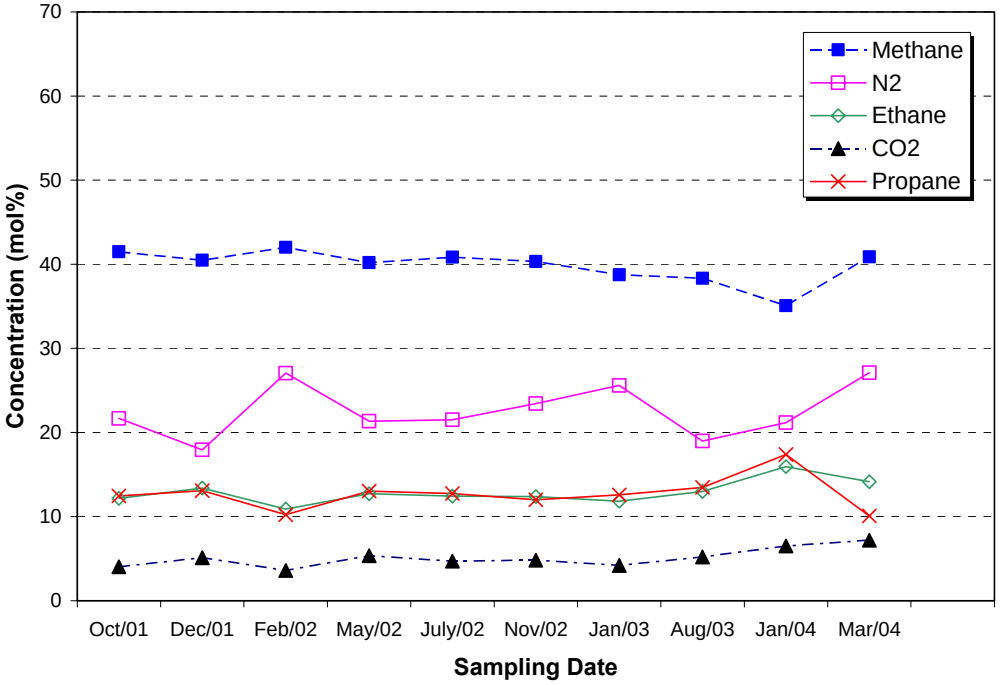

Figure 3.3: Main components in gas samples from Well 101/12-19-6-13W2M

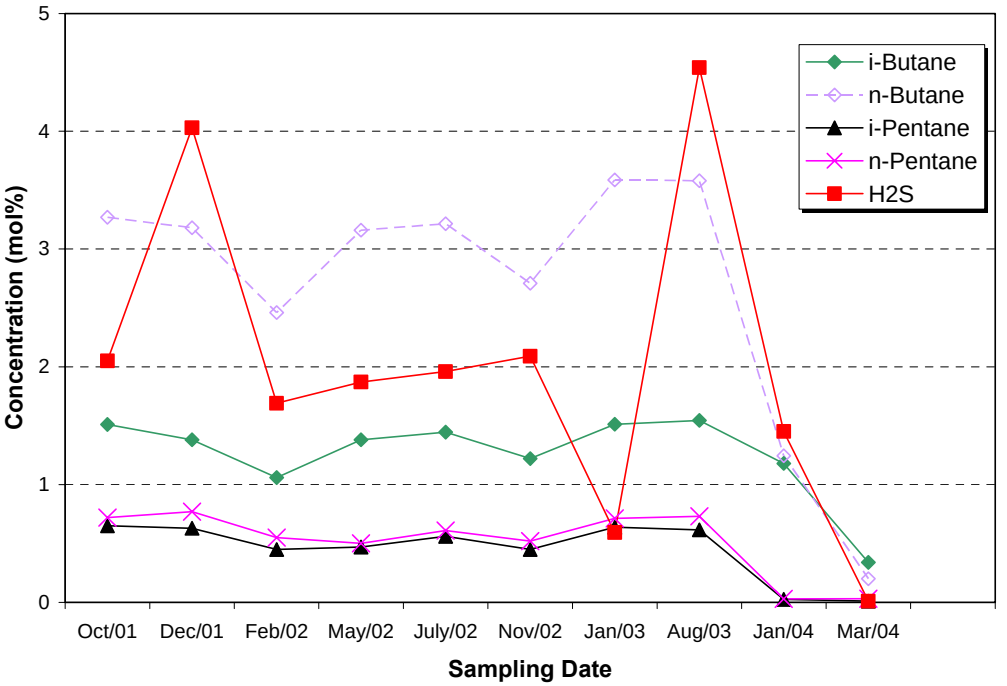

Figure 3.4: Minor components in gas samples from Well 101/12-19-6-13W2M

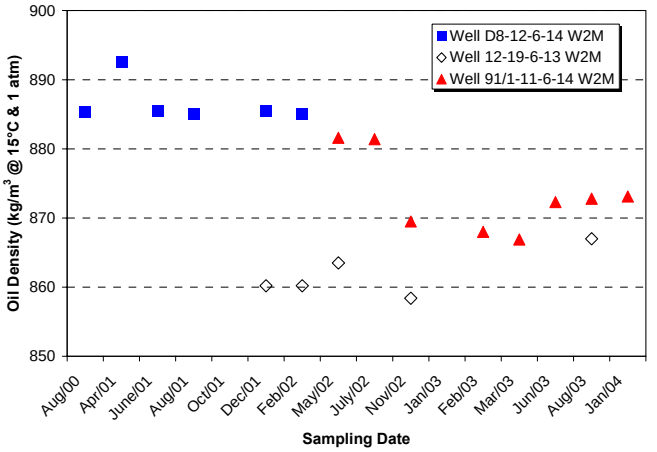

Figure 3.5: Densities of flashed oils from sampled wells

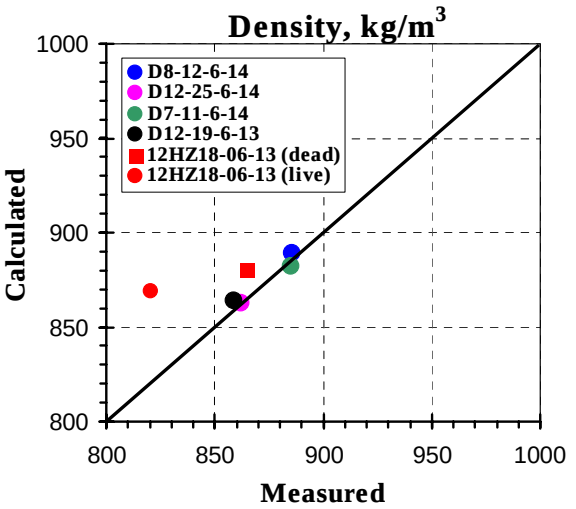

Figure 3.6: Comparison between measured oil phase densities and those predicted by PVT model

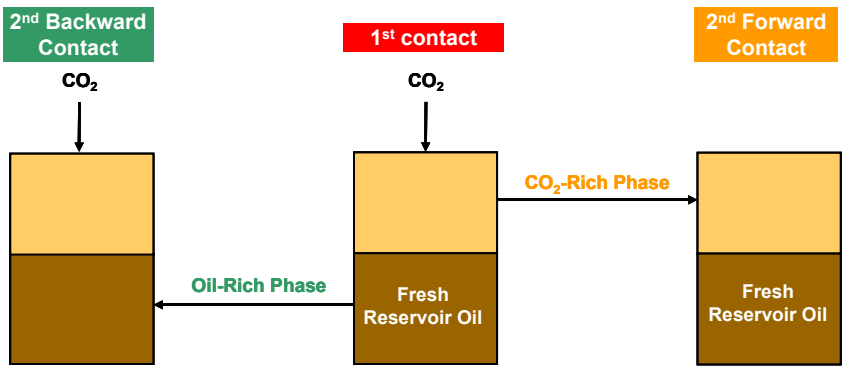

Figure 3.7: Procedure for multi-contact tests

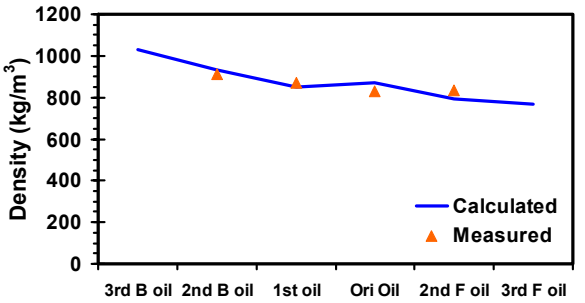

Figure 3.8: Comparison between measured densities in the oil-rich phase and those predicted by PVT model

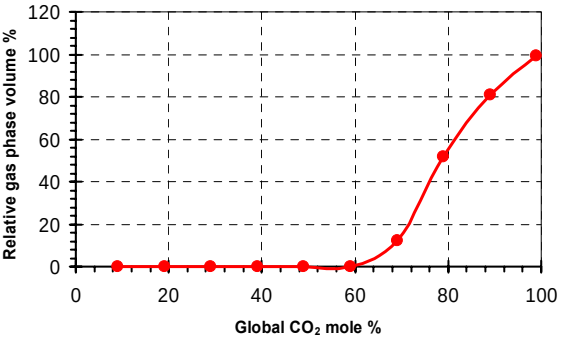

Figure 3.9: Relative gas phase volume for Weyburn oil-CO_2 mixtures at 17.5 MPa and 61 ℃ predicted by PVT model

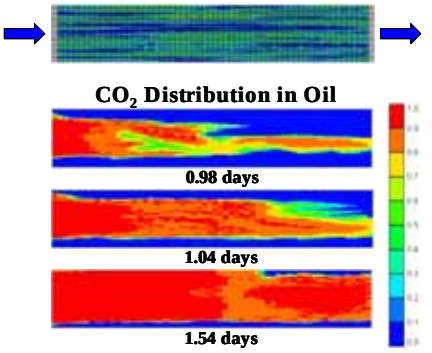

Figure 3.10: Permeability distribution and CO_2 distribution as CO_2 mole fraction in the oil phase for Test 5 using oil sample collected from Well 101/7-11-6-14W2M

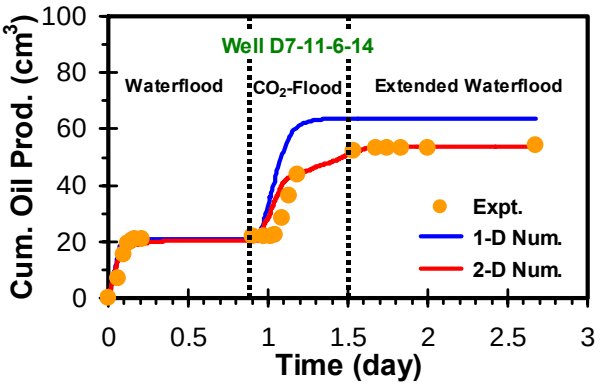

Figure 3.11: Comparison between measured and predicted oil production for Test 5 using oil sample collected from Well 101/7-11-6-14W2M

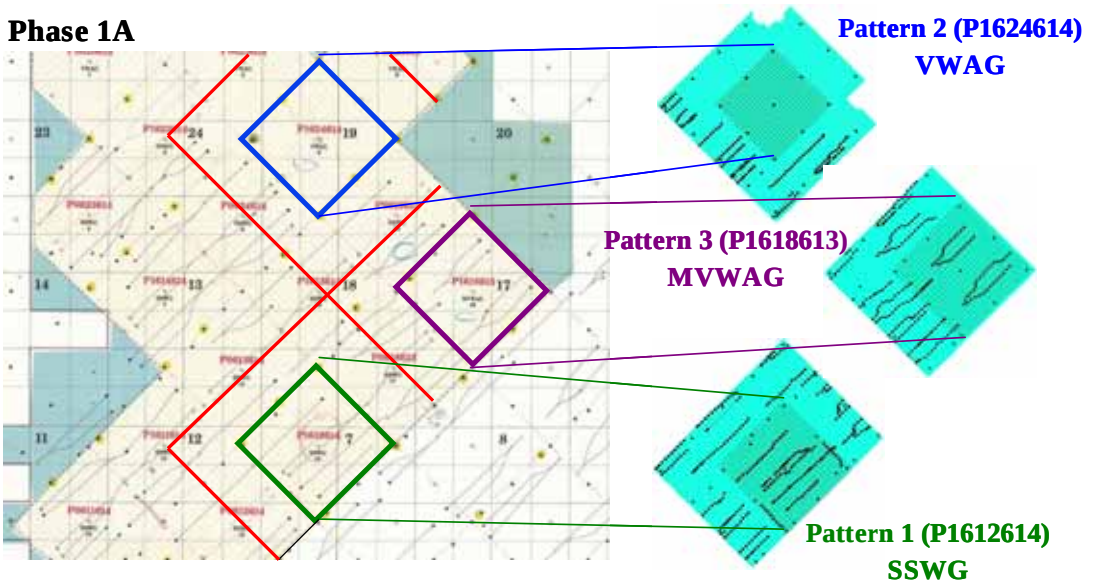

Figure 3.12: Single patterns selected for fine-grid simulations

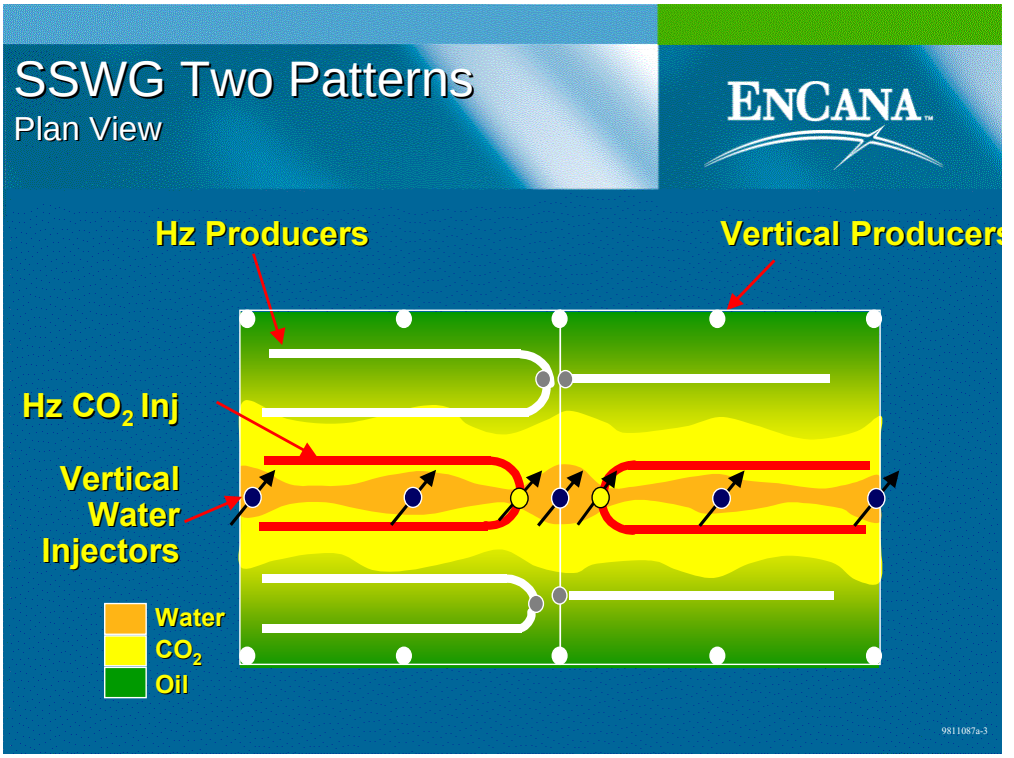

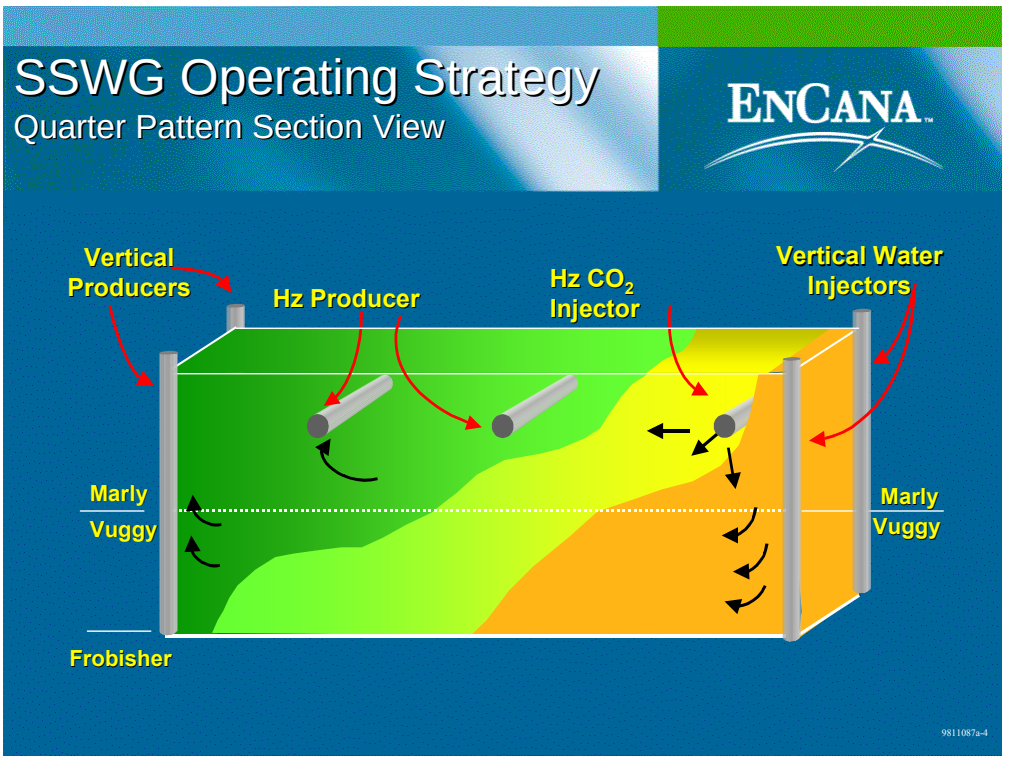

Figure courtesy of EnCana Corporation

Figure 3.13: "Simultaneous but separate water and gas injection, SSWG" miscible flood strategy (e.g. Pattern 1)

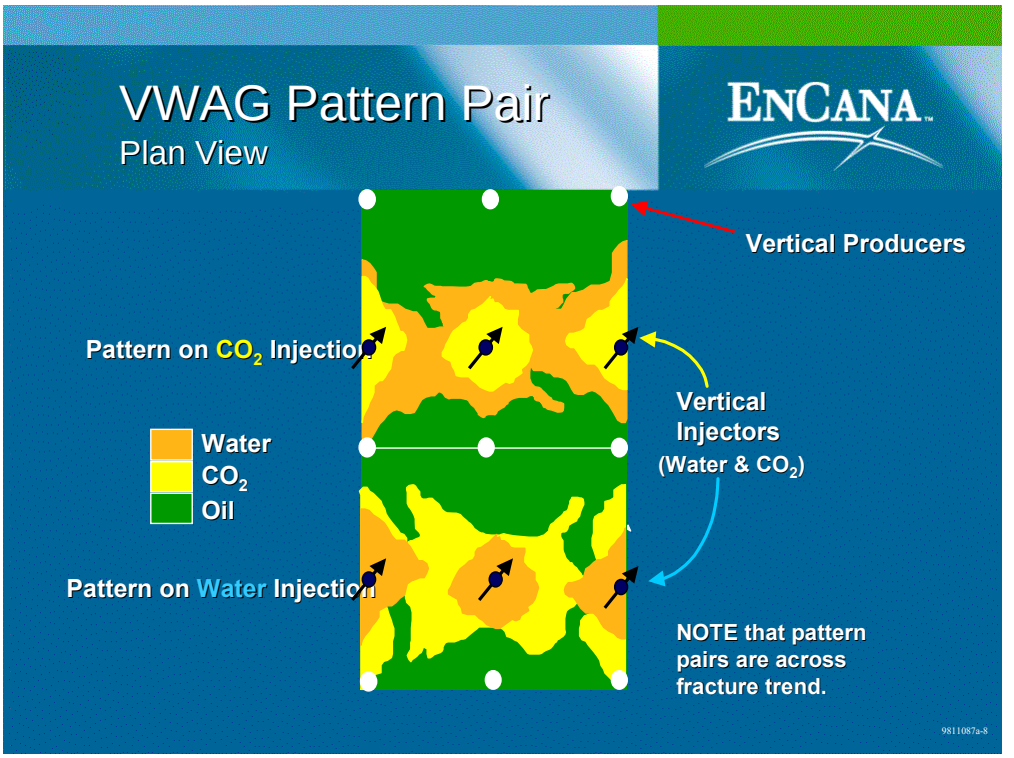

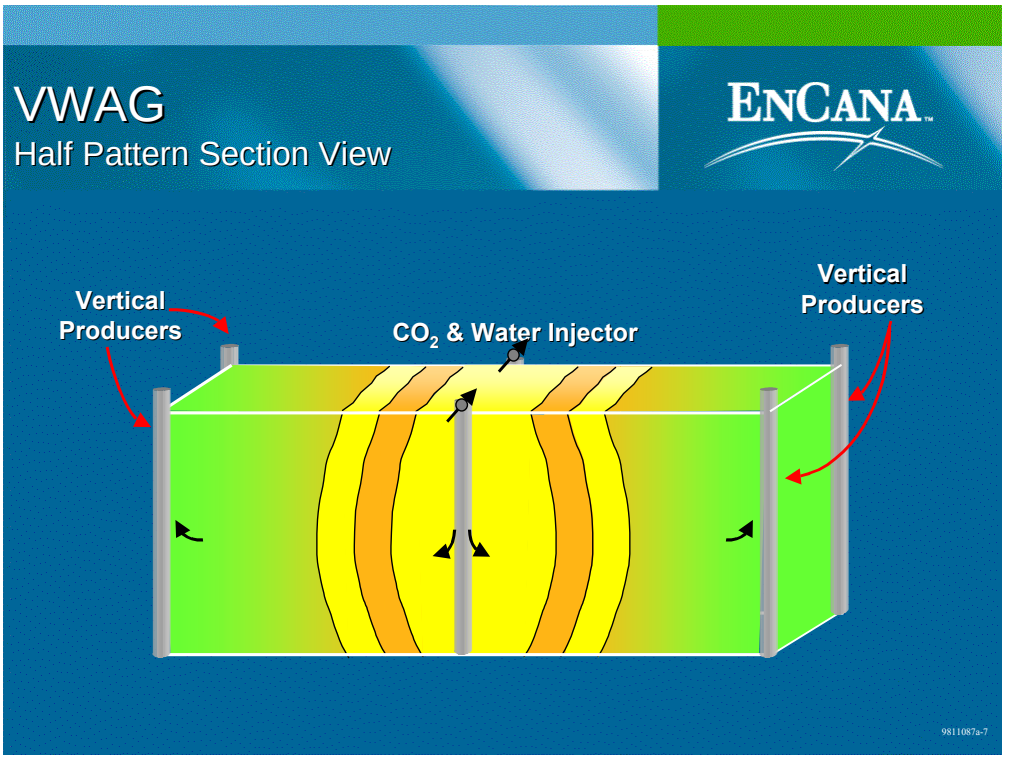

Figure courtesy of EnCana Corporation

Figure 3.14: "Vuggy water-alternating-gas, VWAG" miscible flood strategy (e.g. Pattern 2)

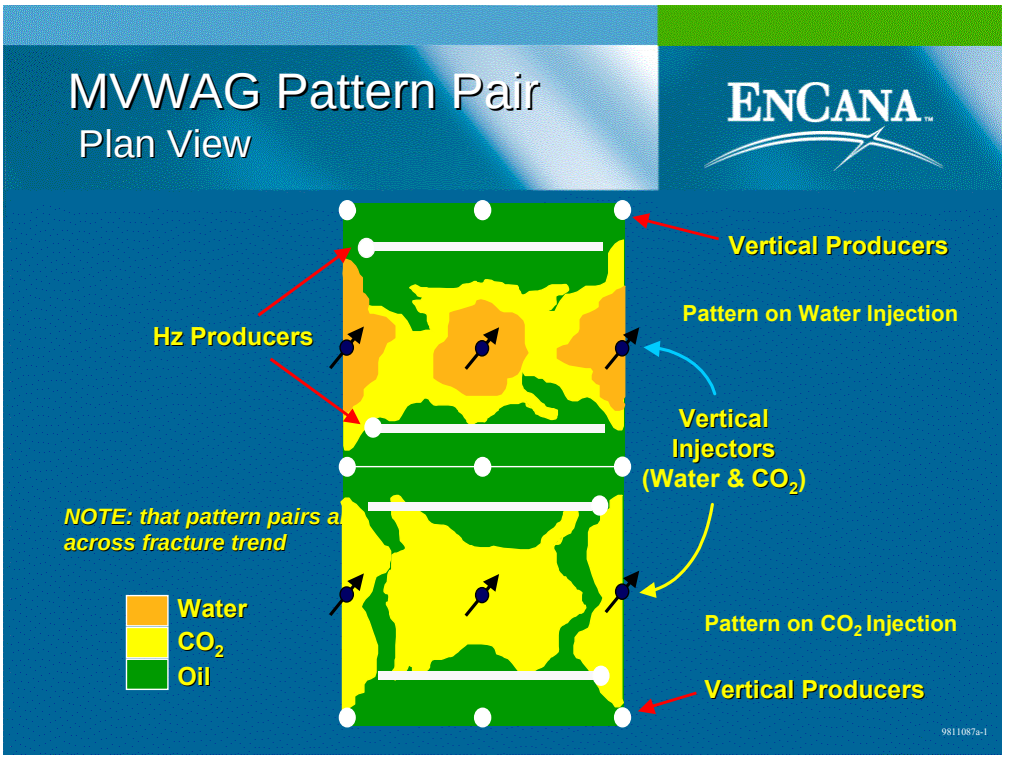

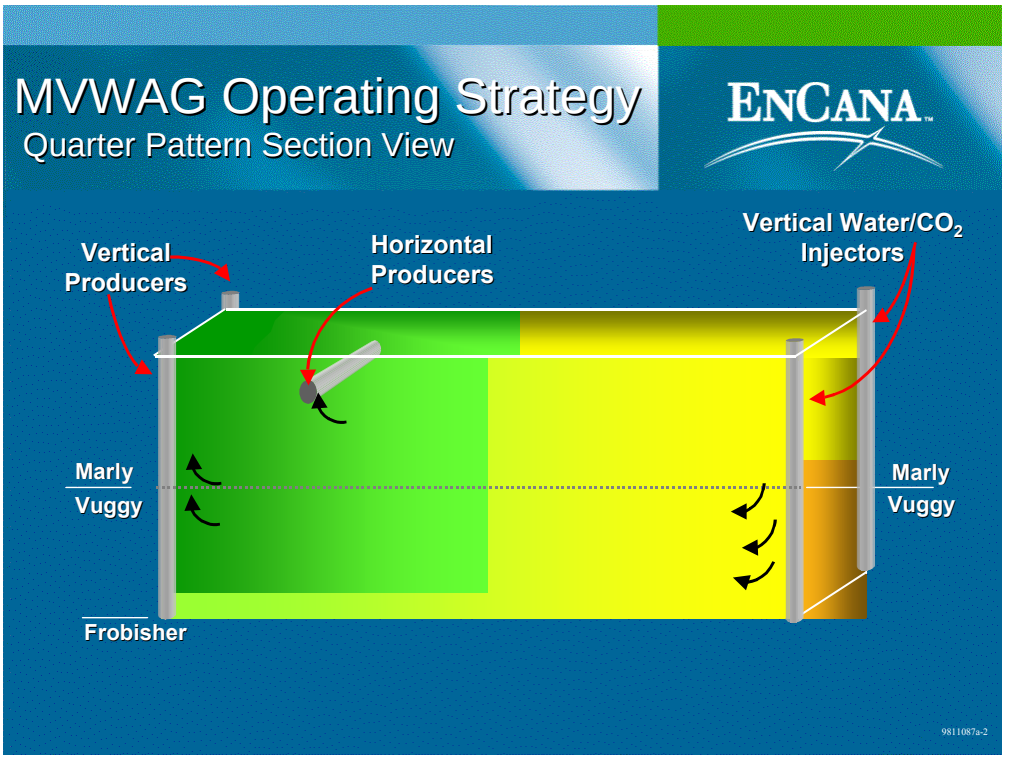

Figure courtesy of EnCana Corporation

Figure 3.15: "Marly, Vuggy water-alternating-gas, MVWAG" miscible flood strategy (e.g. Pattern 3)

Theme 3: CO_2 Storage Capacity and Distribution Predictions and Application of Economic Limits

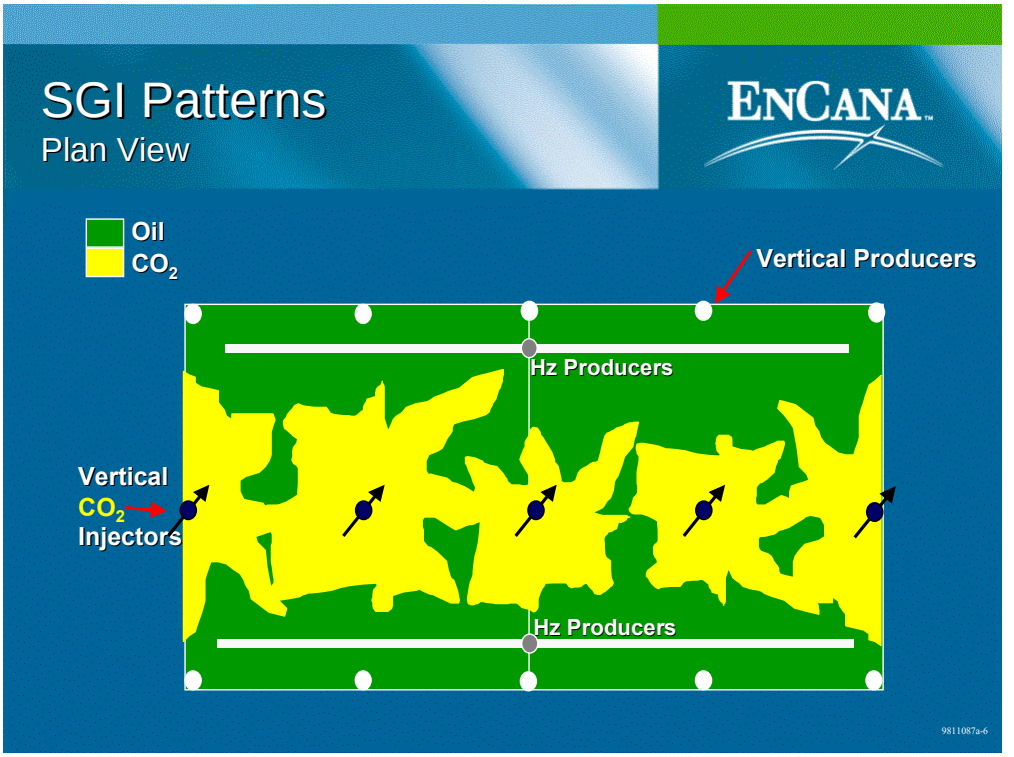

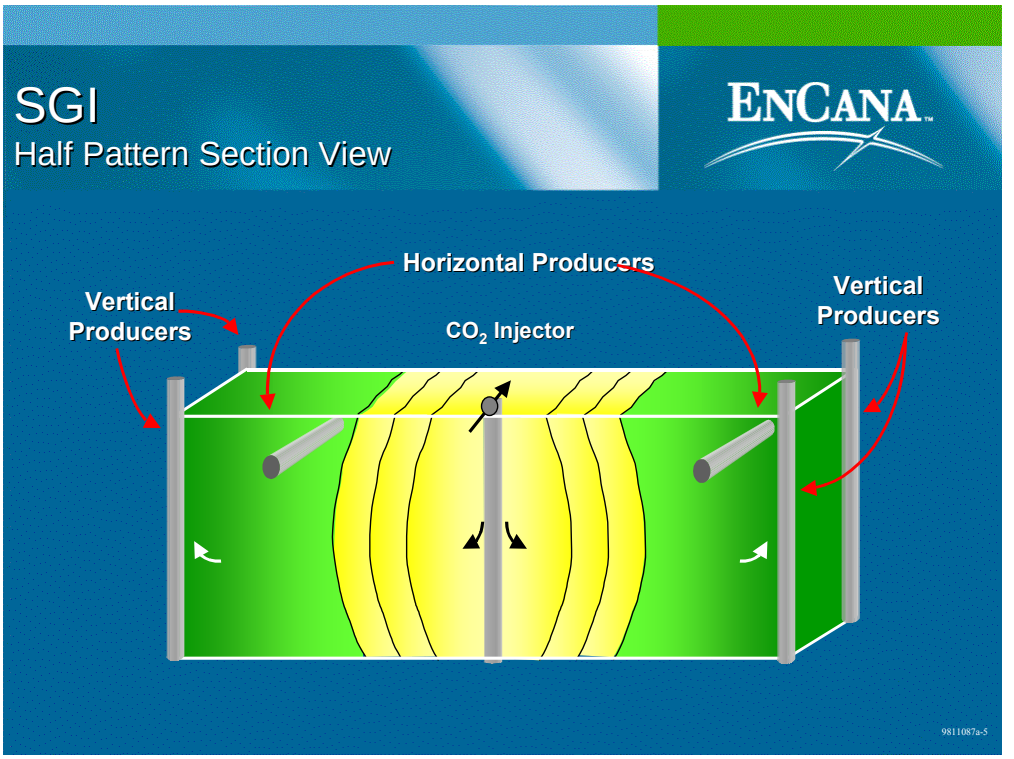

Figure courtesy of EnCana Corporation

Figure 3.16: "Straight gas injection, SGI" miscible flood strategy

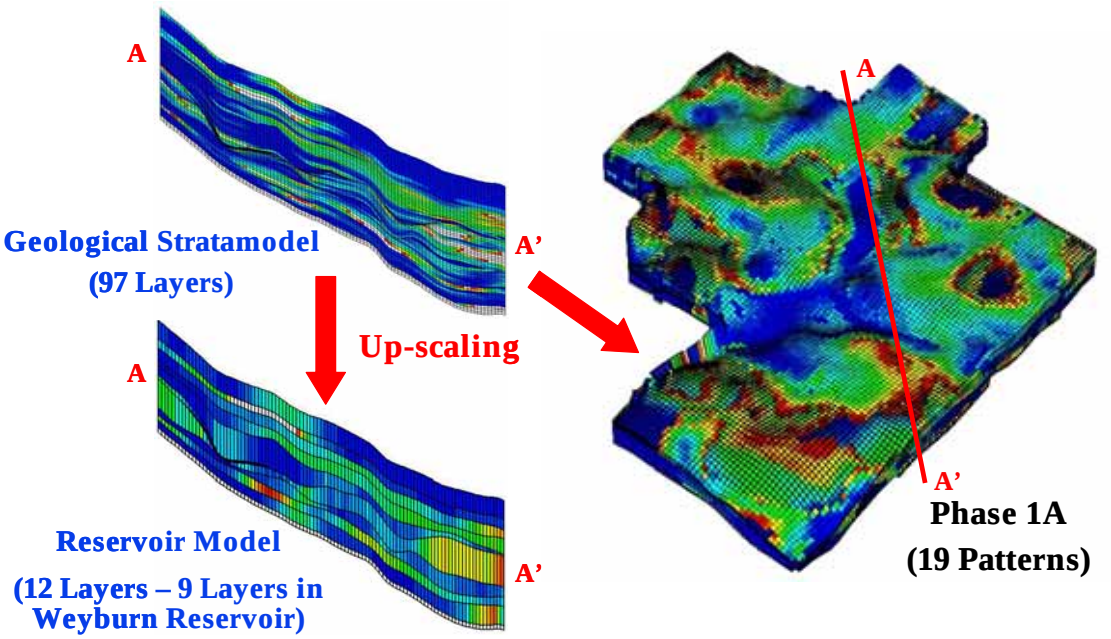

Figure 3.17: Upscaling from EnCana's Phase 1A 2001 Stratamodel to fine-grid simulation model

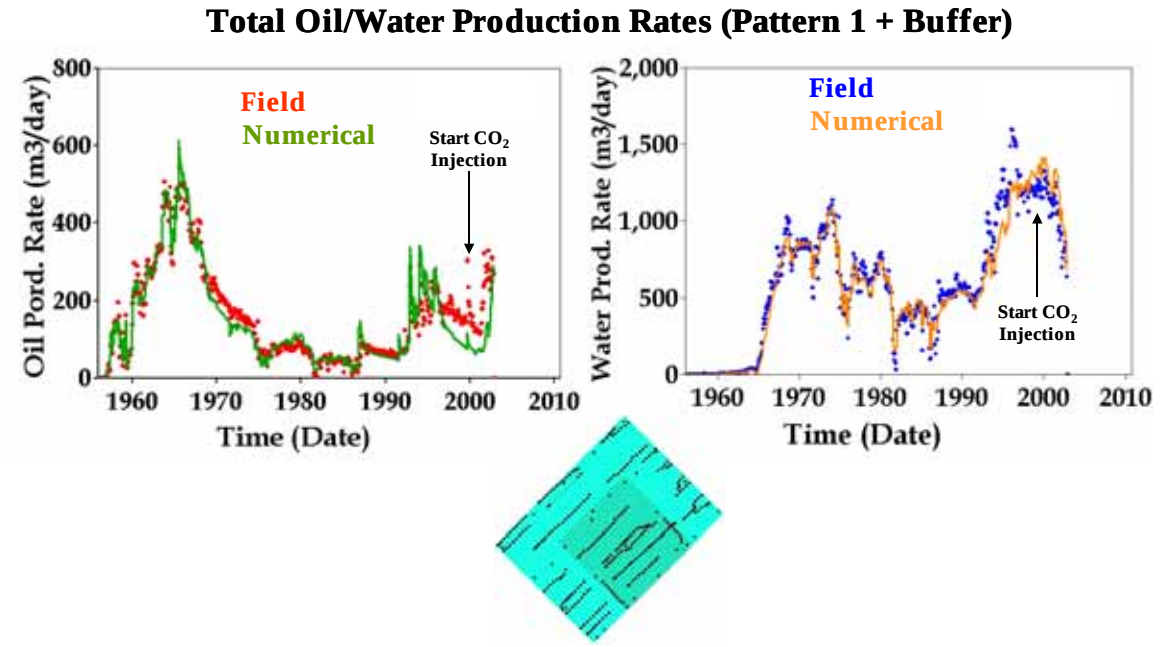

Figure 3.18: History match of oil and water production for Pattern 1 + buffer (fine-grid single-pattern simulation)

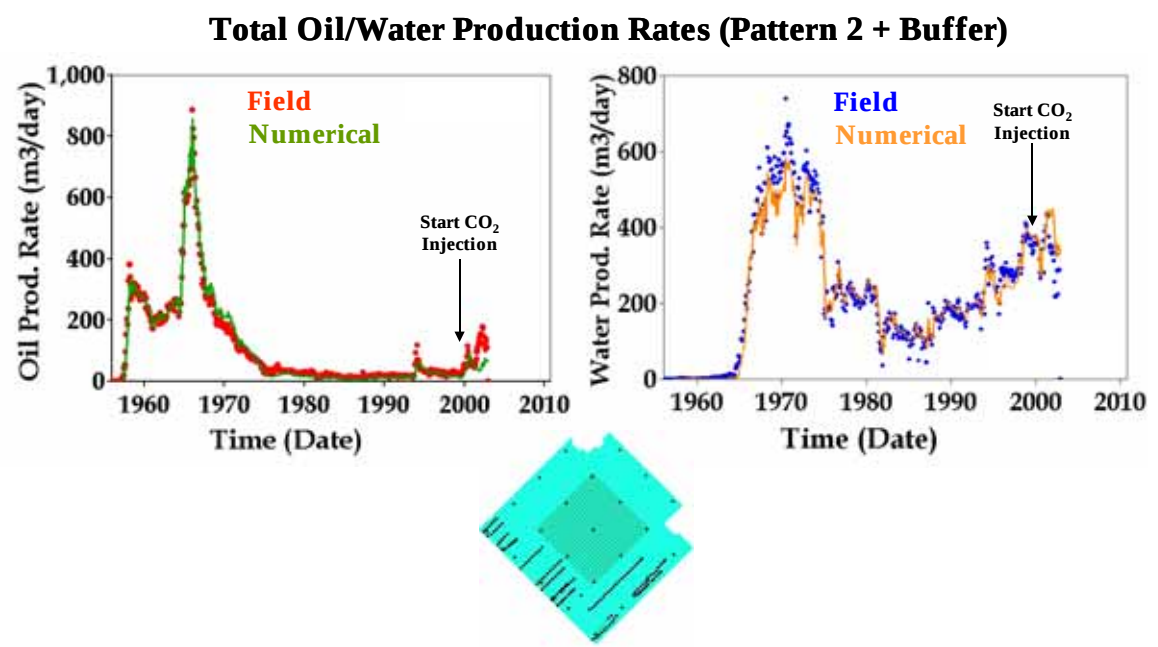

Figure 3.19: History match of oil and water production for Pattern 2 + buffer (fine-grid single-pattern simulation)

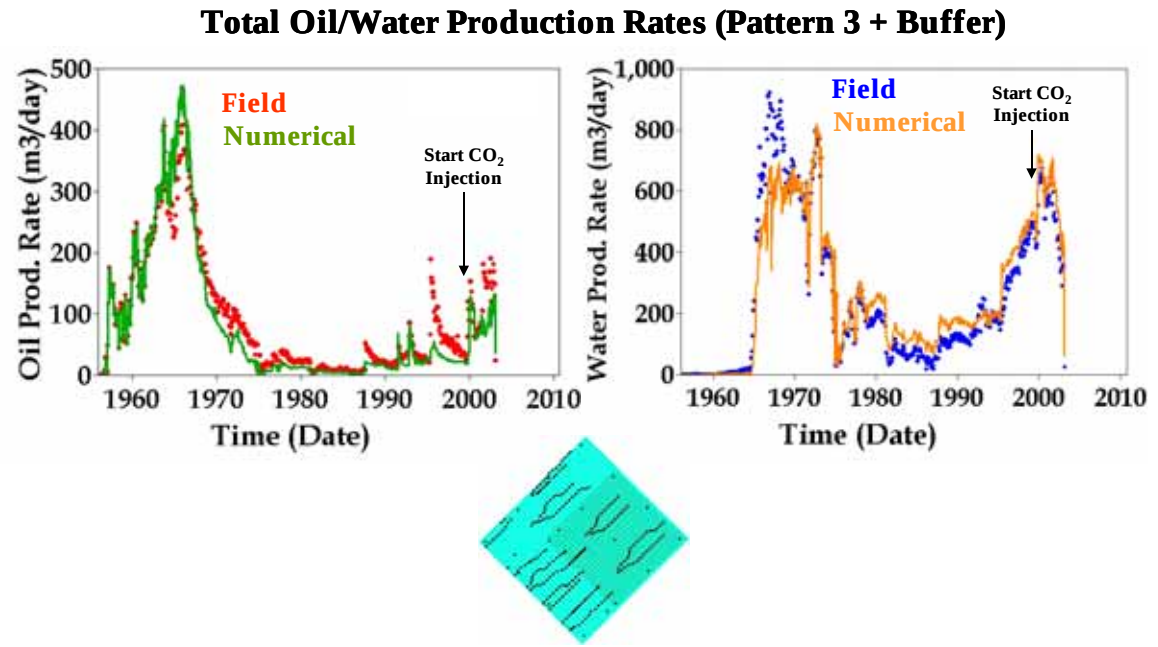

Figure 3.20: History match of oil and water production for Pattern 3 + buffer (fine-grid single-pattern simulation)

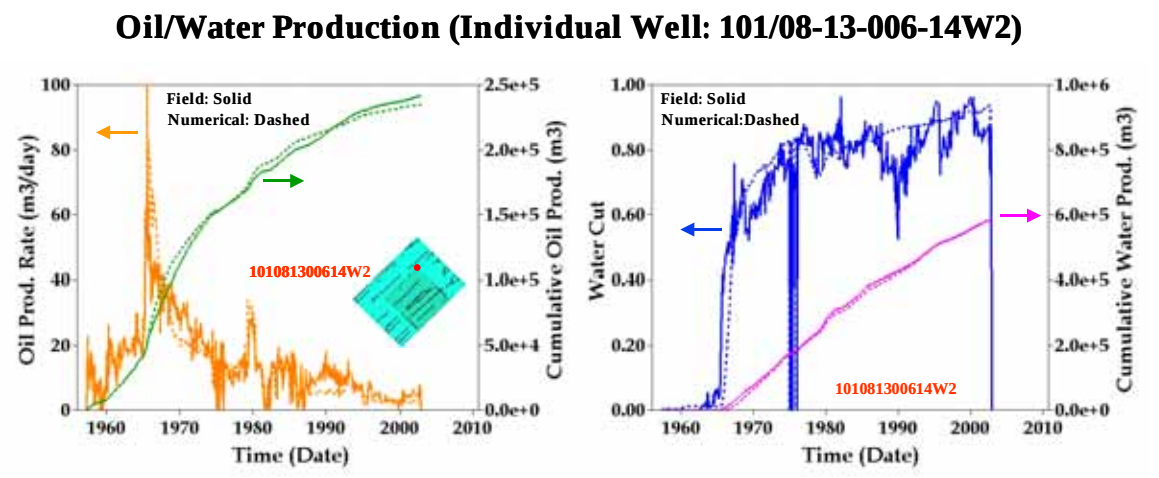

Figure 3.21: History match of oil and water production for individual well 101/8-13-6-14W2 in Pattern 1 (e.g., good match for fine-grid single-pattern simulation)

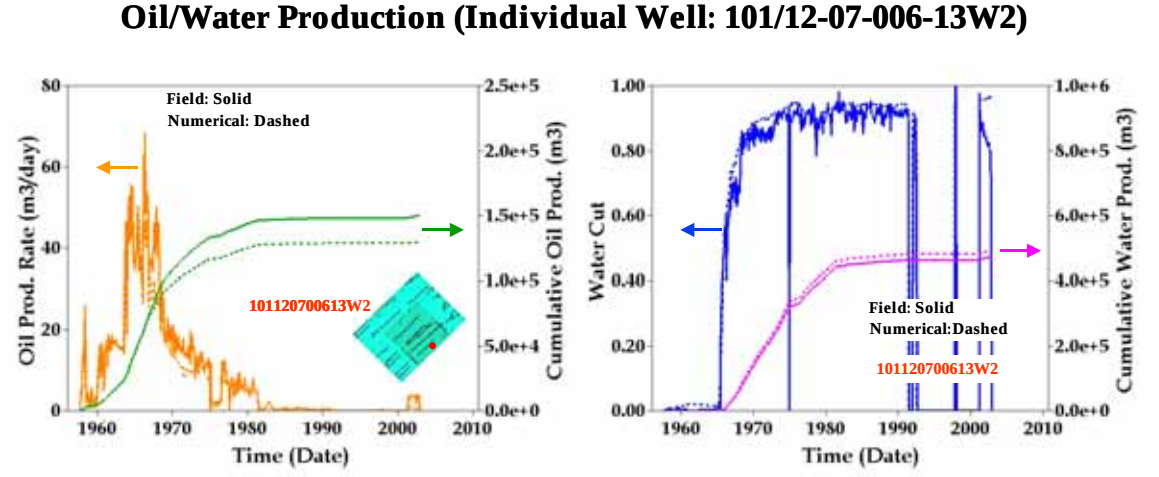

Figure 3.22: History match of oil and water production for individual well 101/12-7-6-13W2 in Pattern 1 (e.g., poor match for fine-grid single-pattern simulation)

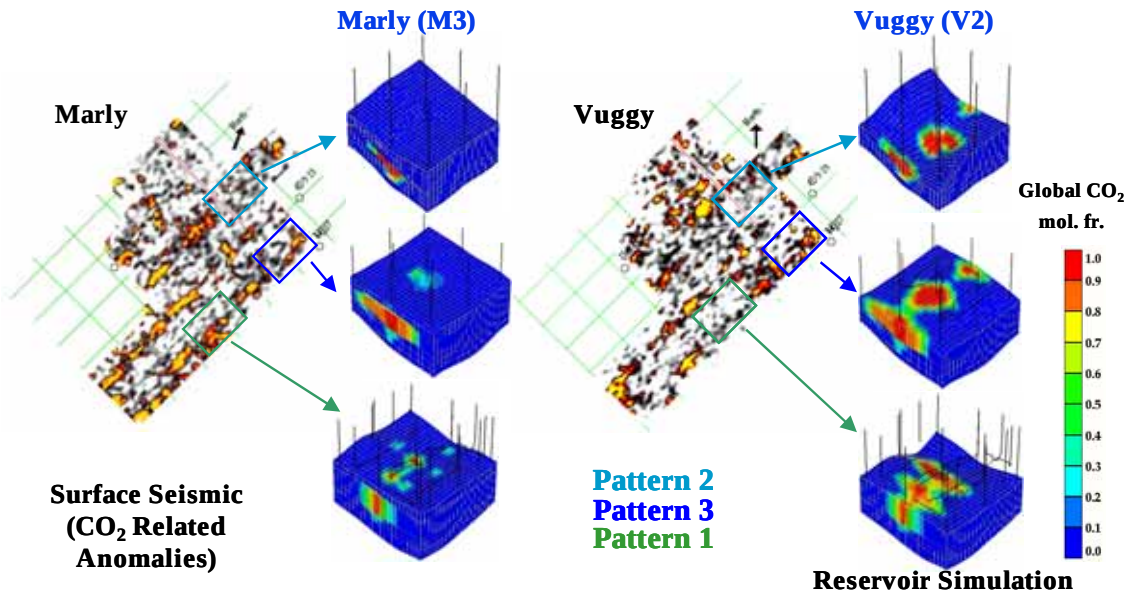

Figure 3.23: Comparison of numerical prediction of CO_2 distribution after 1 year of CO_2-flooding with EnCana's 4D 3C surface seismic observations (fine-grid single-pattern simulation)

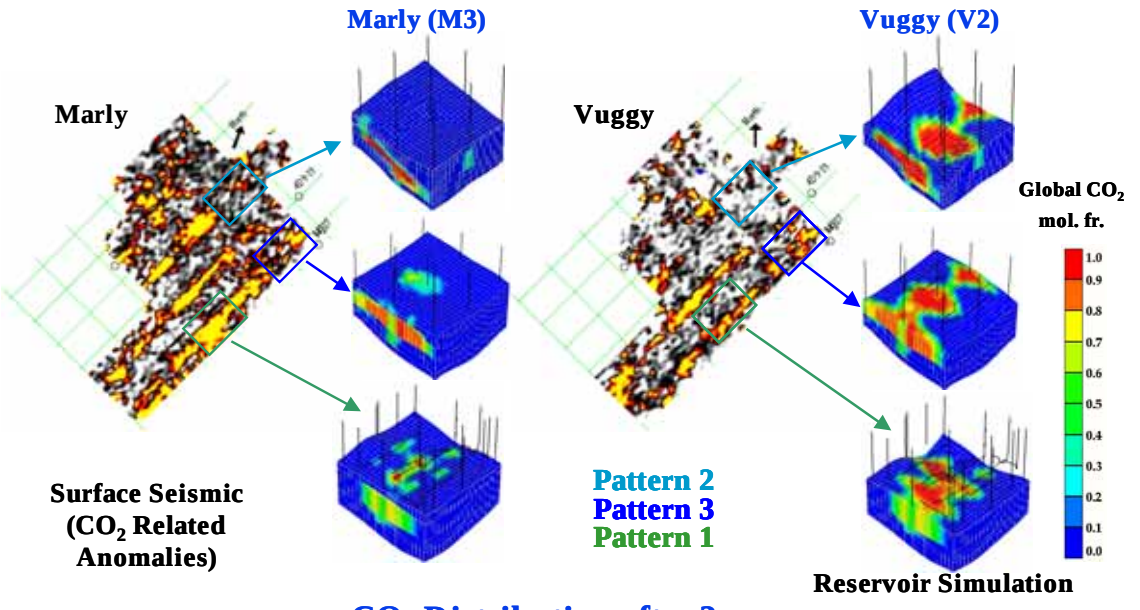

Figure 3.24: Comparison of numerical prediction of CO_2 distribution after 2 years of CO_2-flooding with EnCana's 4D 3C surface seismic observations (fine-grid single-pattern simulation)

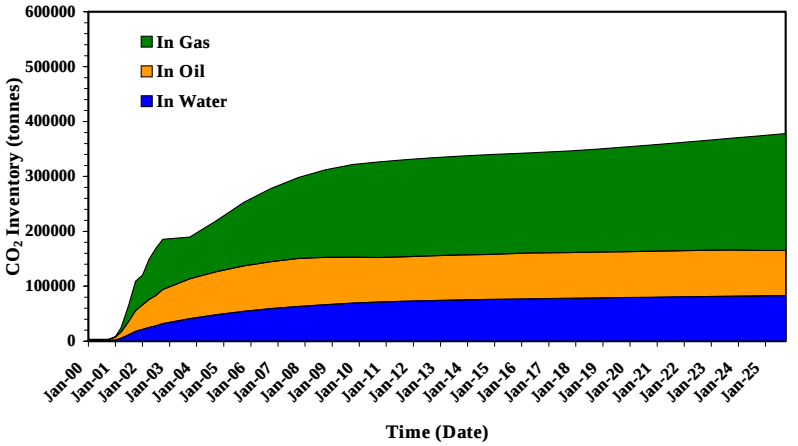

(a) Case I for Pattern 1 (SSWG)

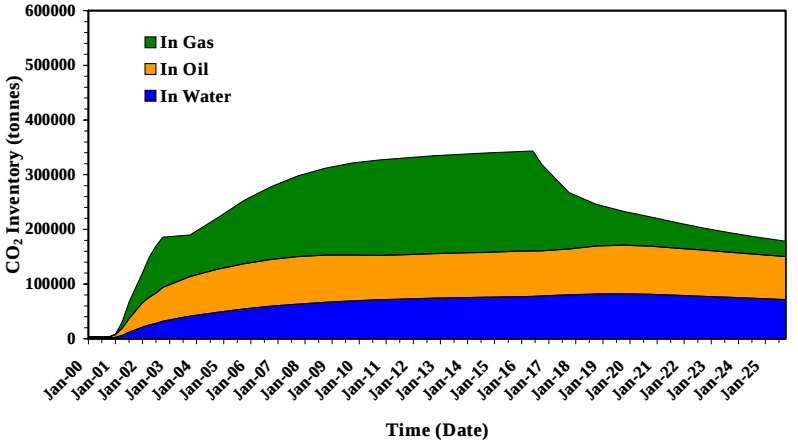

(b) Case II for Pattern 1 (SSWG)

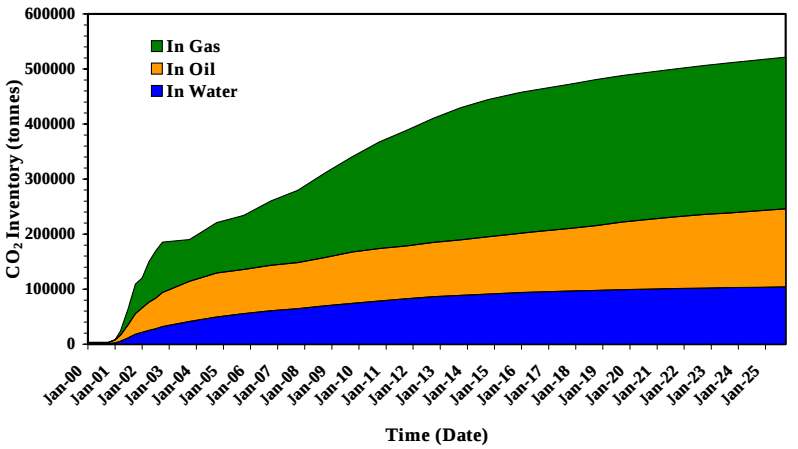

(c) Case III for Pattern 1 (SSWG)

Figure 3.25: CO_2 Inventory for Pattern 1 (SSWG) for three different EOR cases (fine-grid single-pattern simulation)

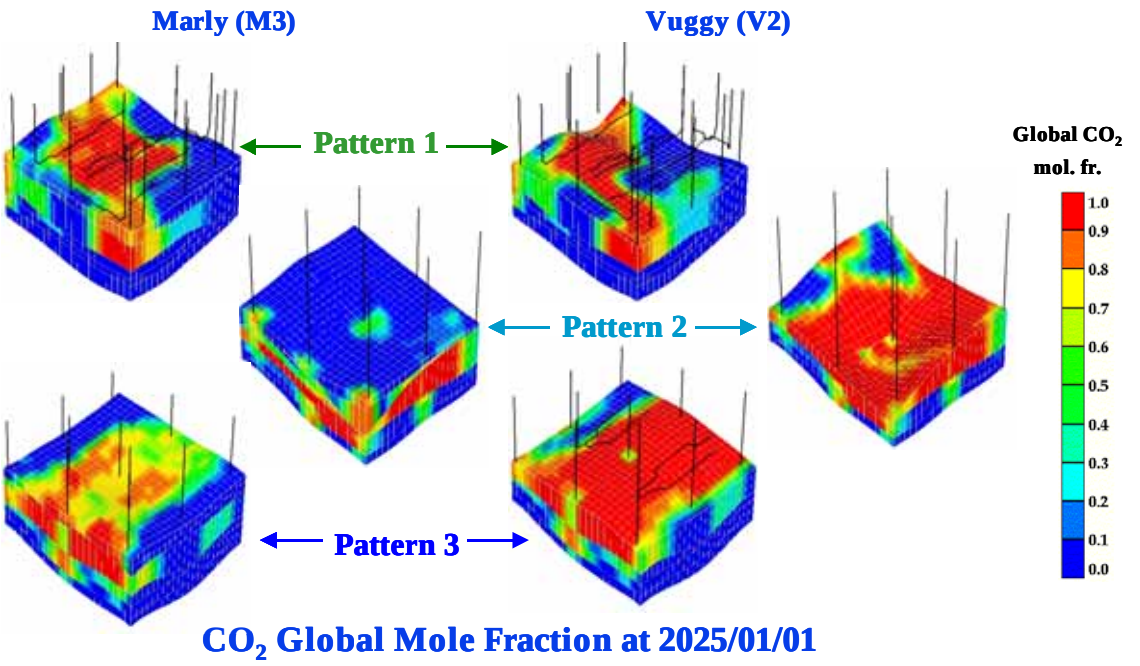

Figure 3.26: CO_2 distribution as global gas mole fraction for Case I for three different patterns (fine-grid single-pattern simulation)

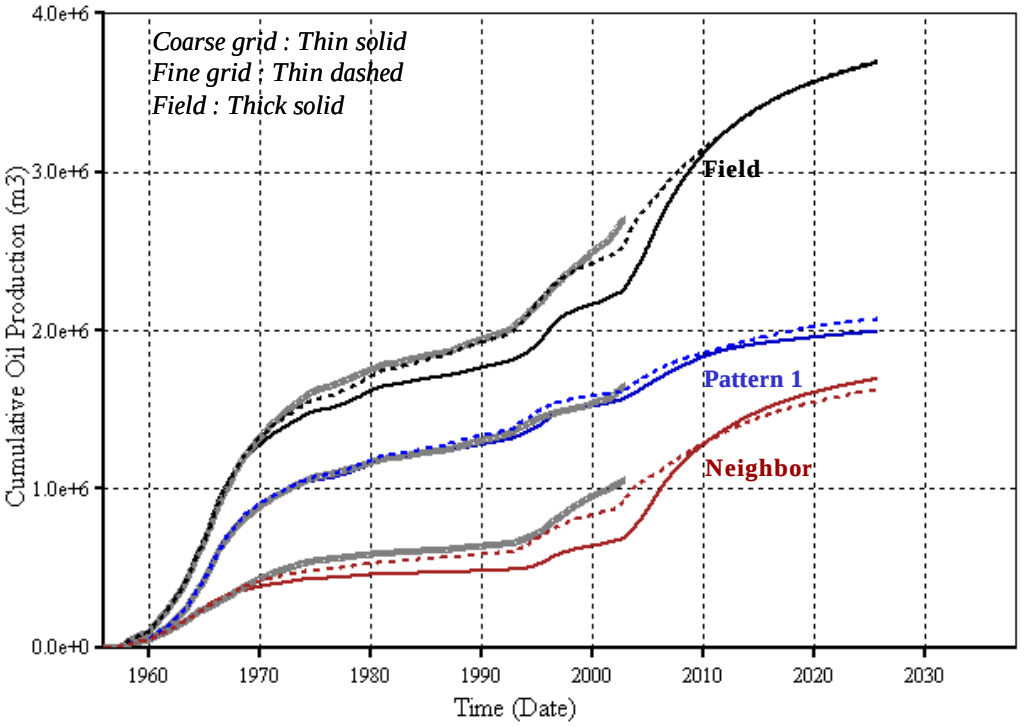

Figure 3.27: Comparison of oil production for Pattern 1 (SSWG) between fine-grid and coarse-grid single-pattern simulations

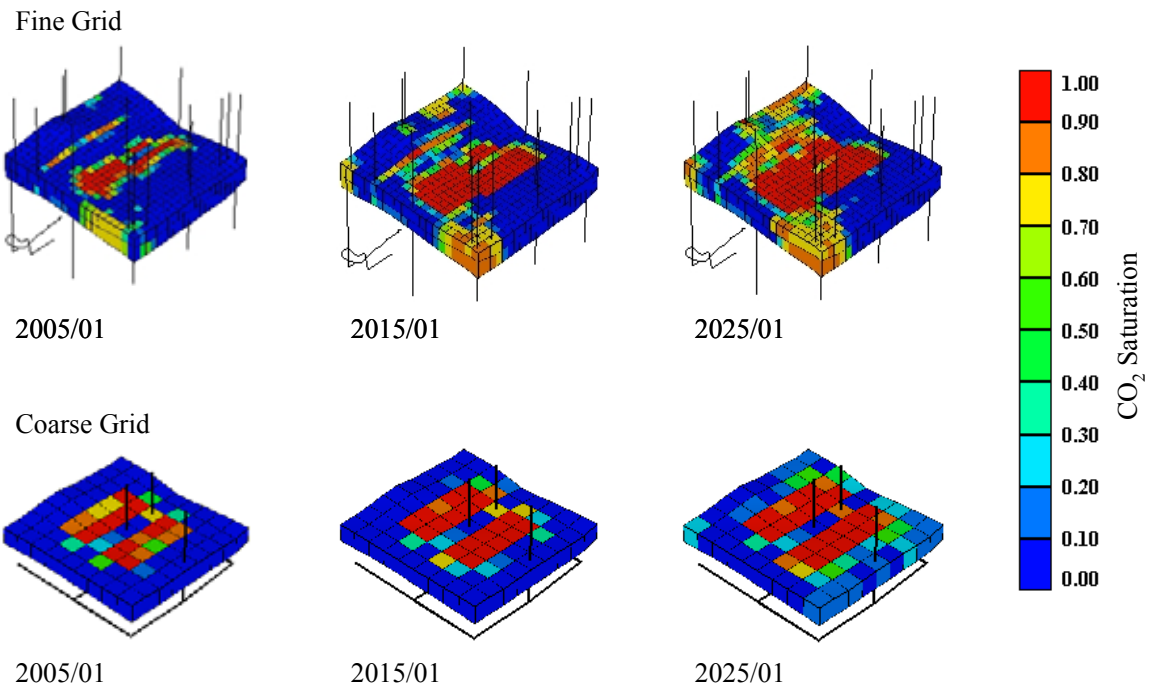

(a) Marly Zone (M3)

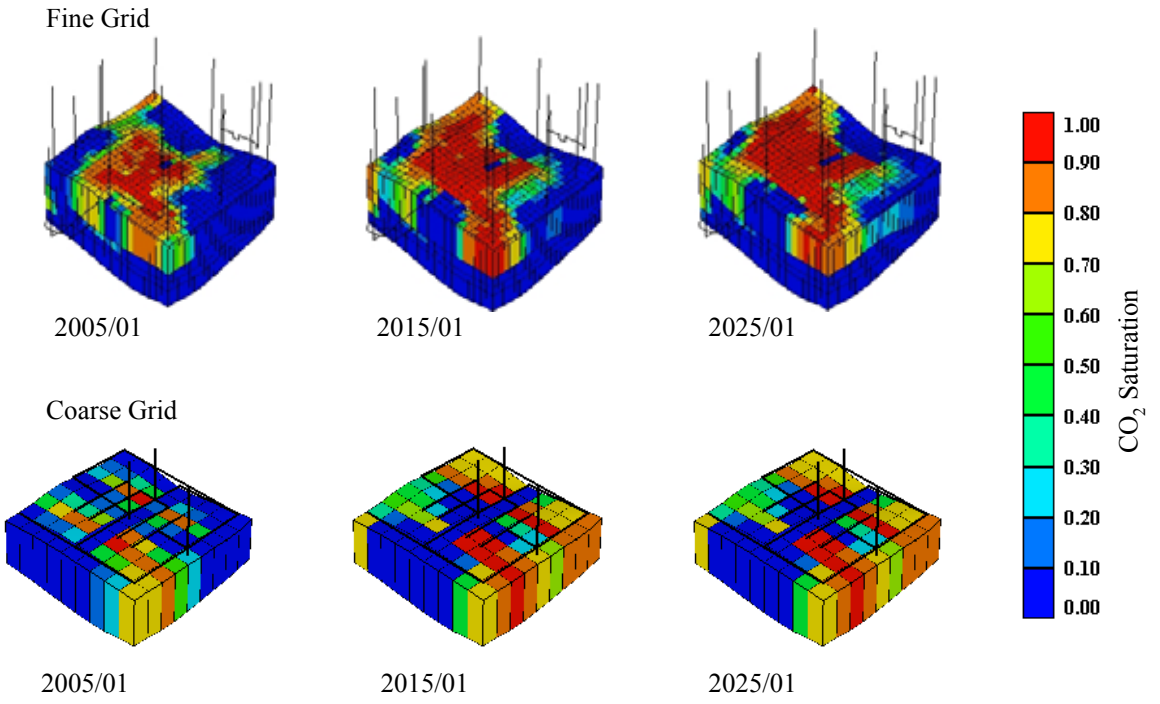

(b) Vuggy Zone (V2)

Figure 3.28: Comparison of CO_2 distribution for Pattern 1 (SSWG) between fine-grid and coarse-grid single-pattern simulations

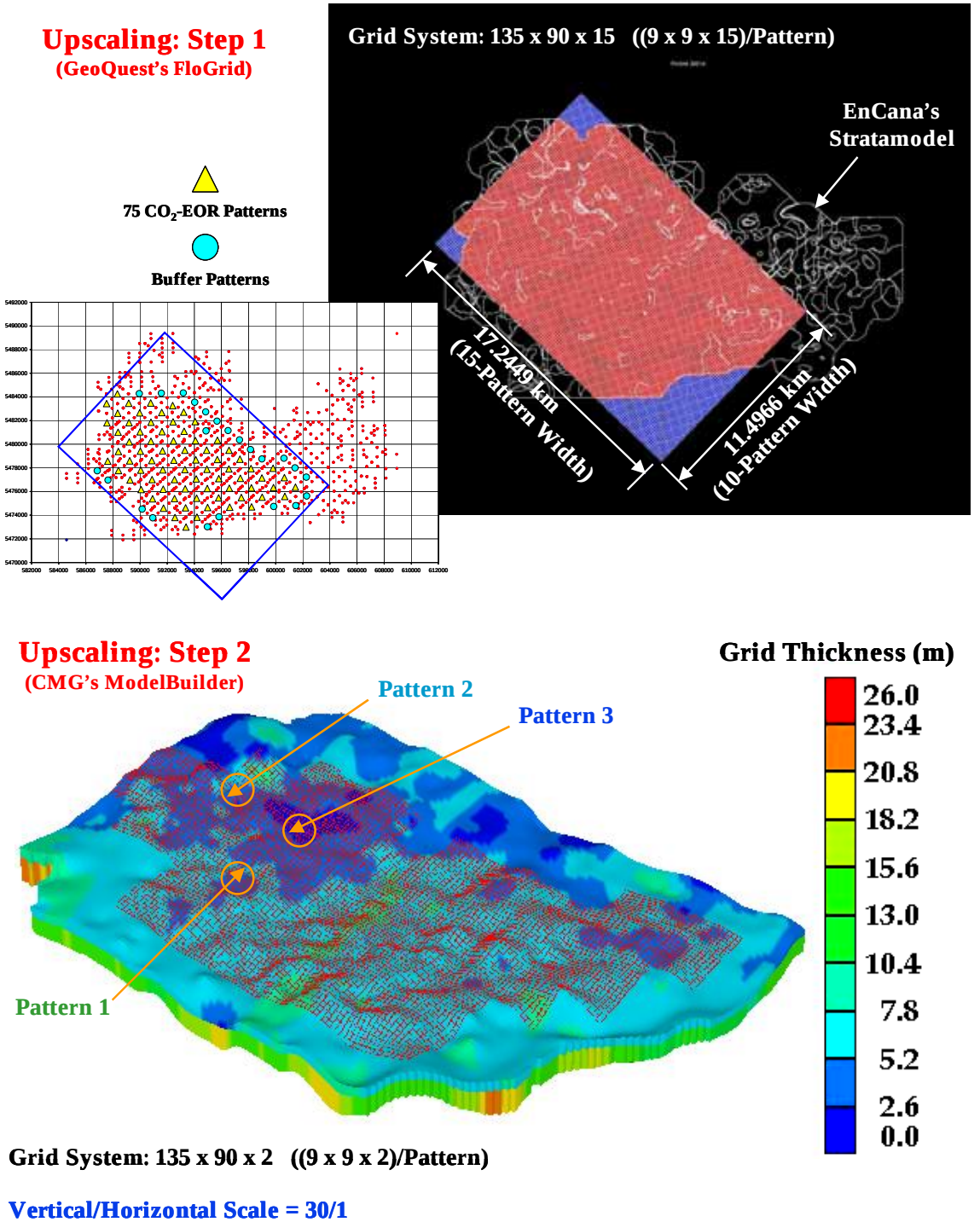

Figure 3.29: Upscaling from EnCana's Weyburn Field 1999 Stratamodel to 75-pattern reservoir model

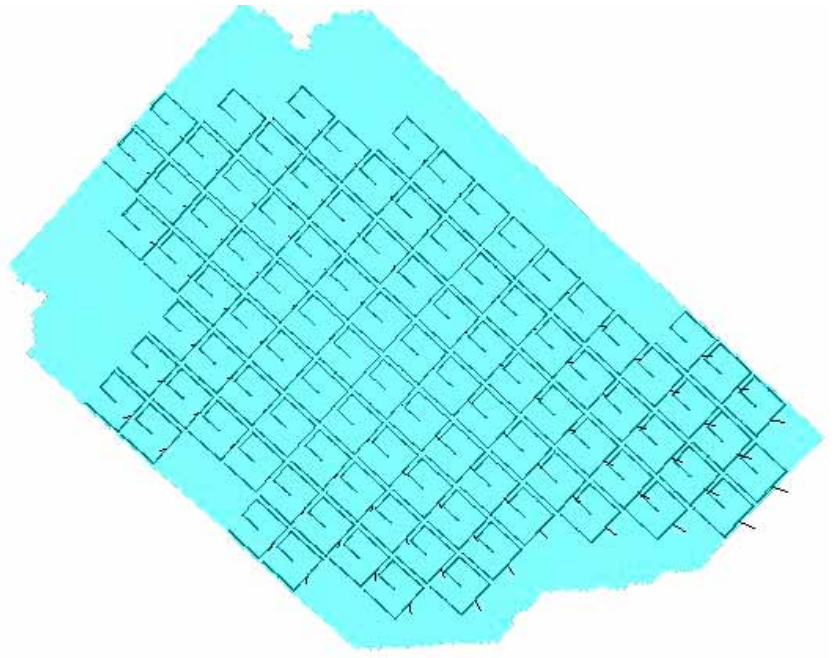

Figure 3.30: Pseudo-wells showing 9-spot wells (75-pattern simulation)

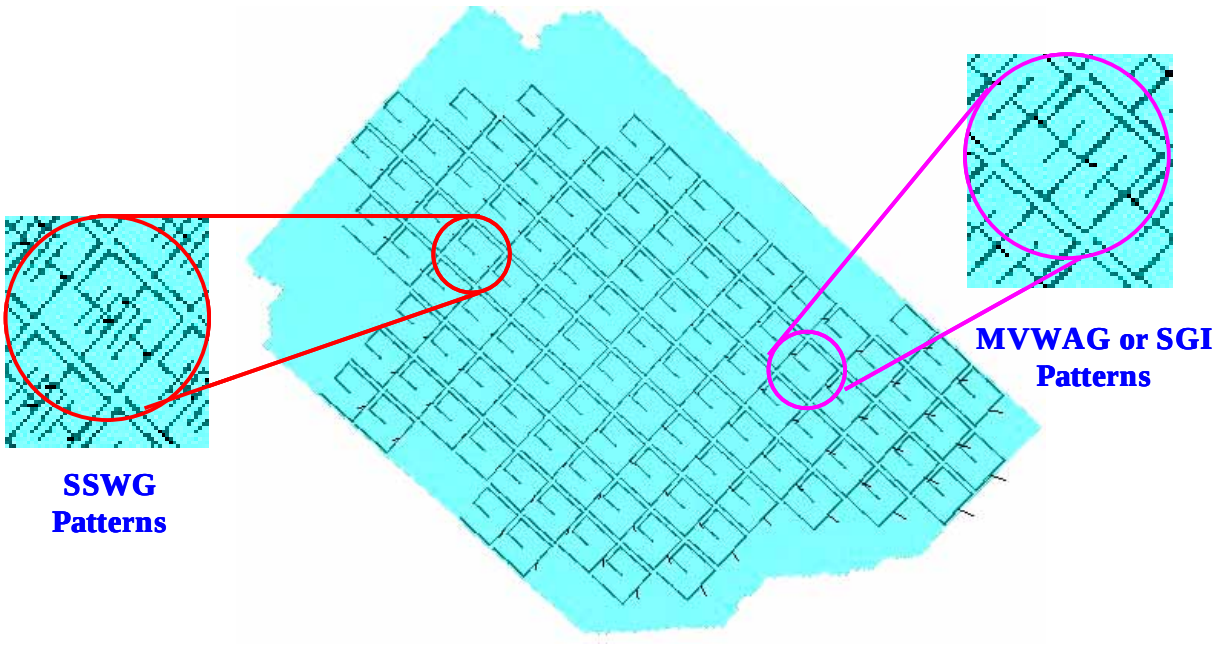

Figure 3.31: Pseudo-wells showing in-filled wells for different CO_2 injection strategies (75-pattern simulation)

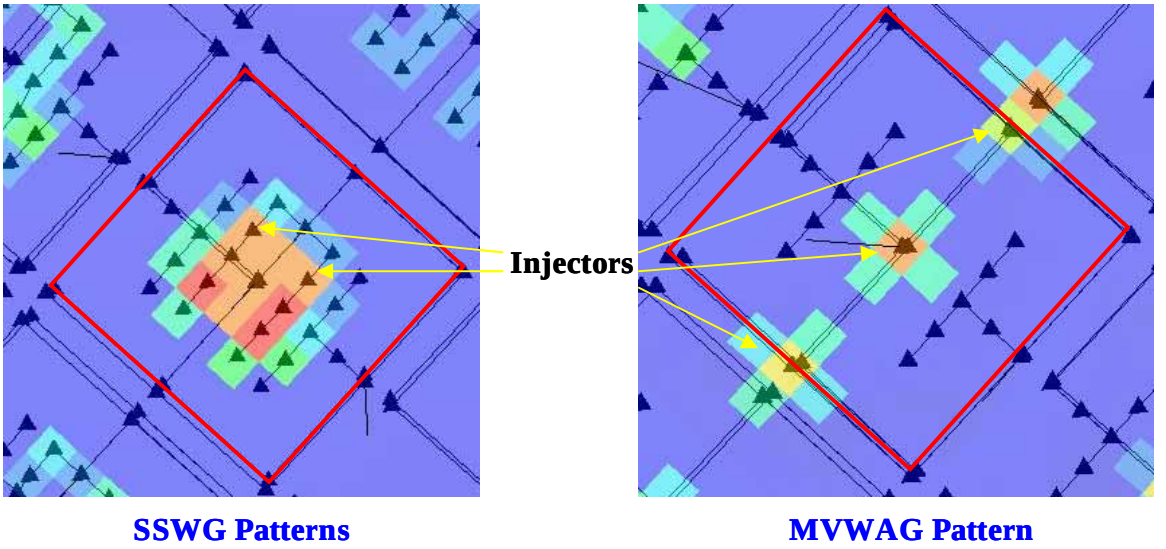

Figure 3.32: Examples for more realistic CO_2 distributions using pseudo-well approach (75-pattern simulation)

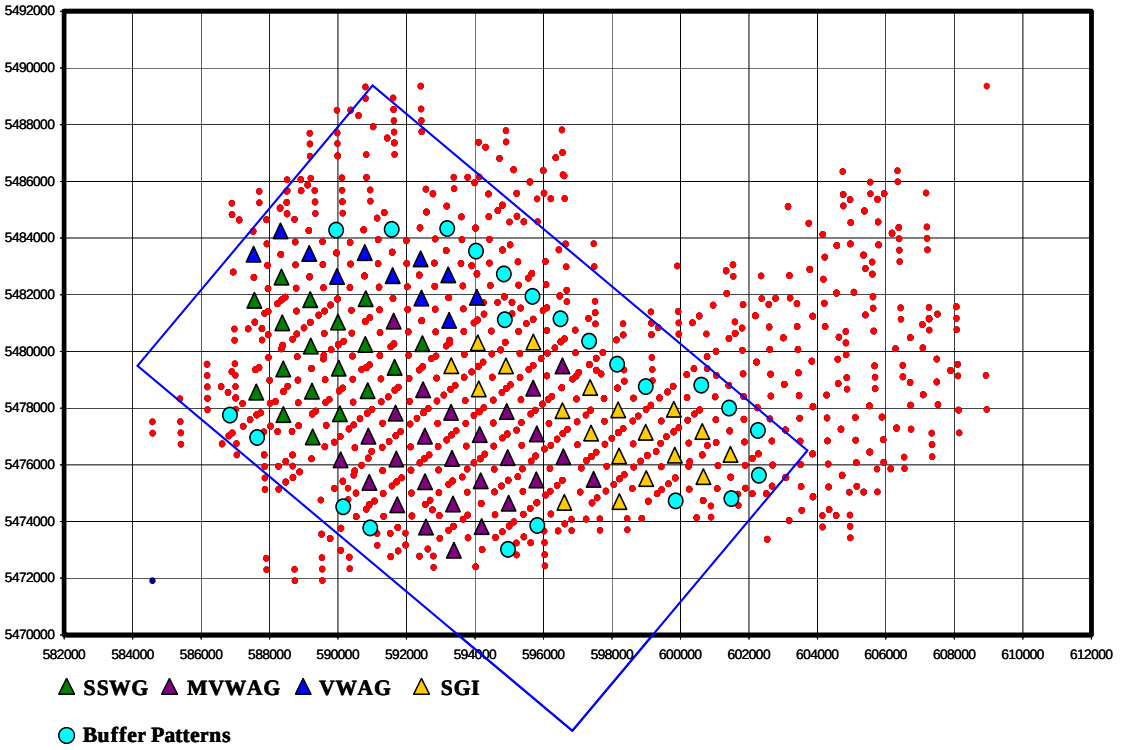

Figure 3.33: CO_2 injection strategies for 75-Pattern simulation (recommended by EnCana)

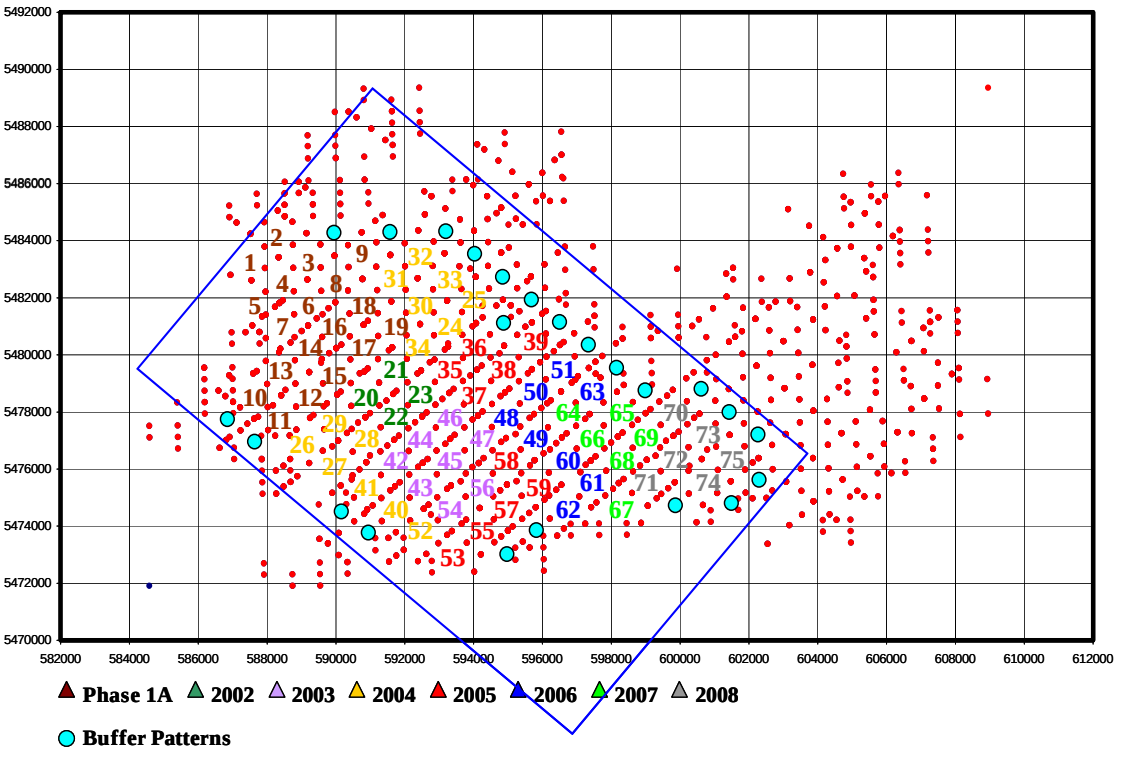

Figure 3.34: Rollout plan for 75-pattern simulation (recommended by EnCana)

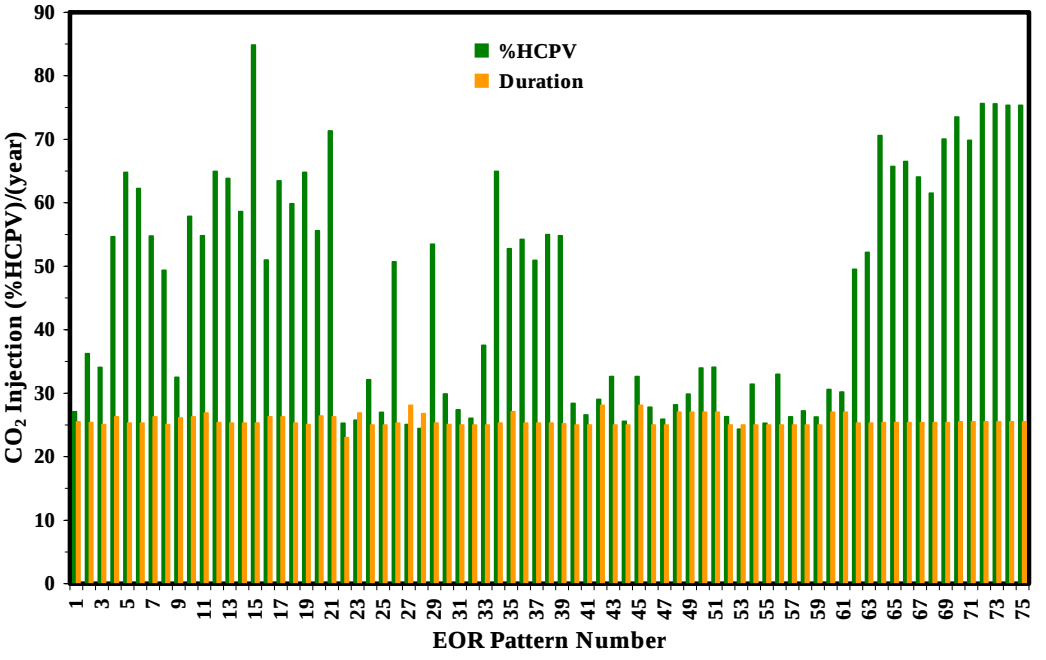

Figure 3.35: %HCPV of CO_2 injection in 75 EOR patterns (75-pattern simulation - EOR base case)

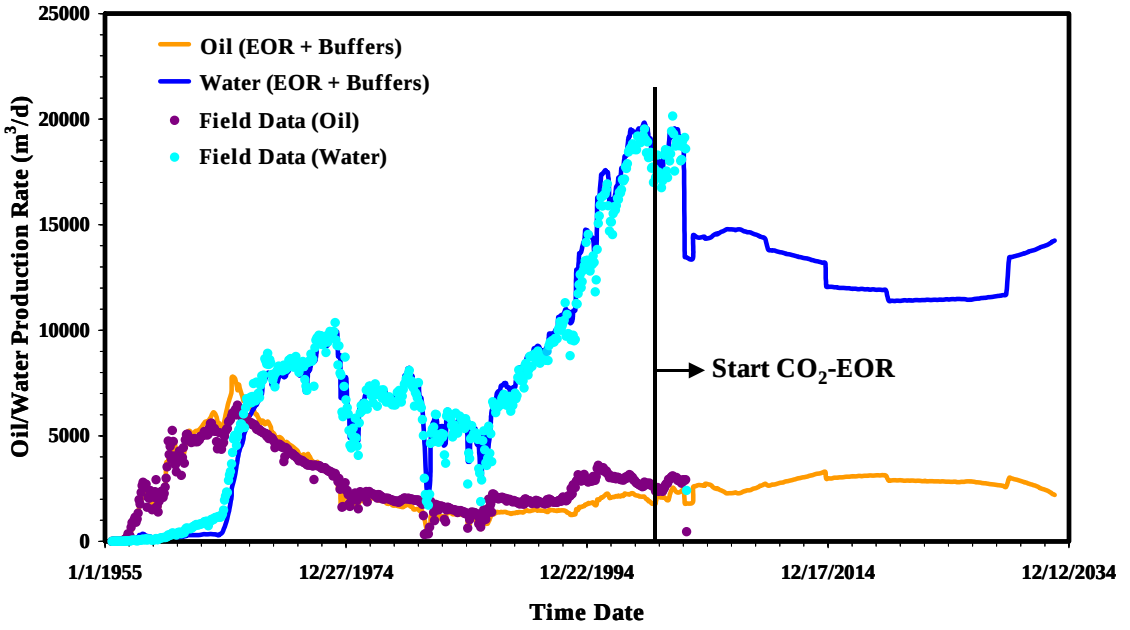

Figure 3.36: Oil and water production rates (75-pattern simulation - EOR base case)

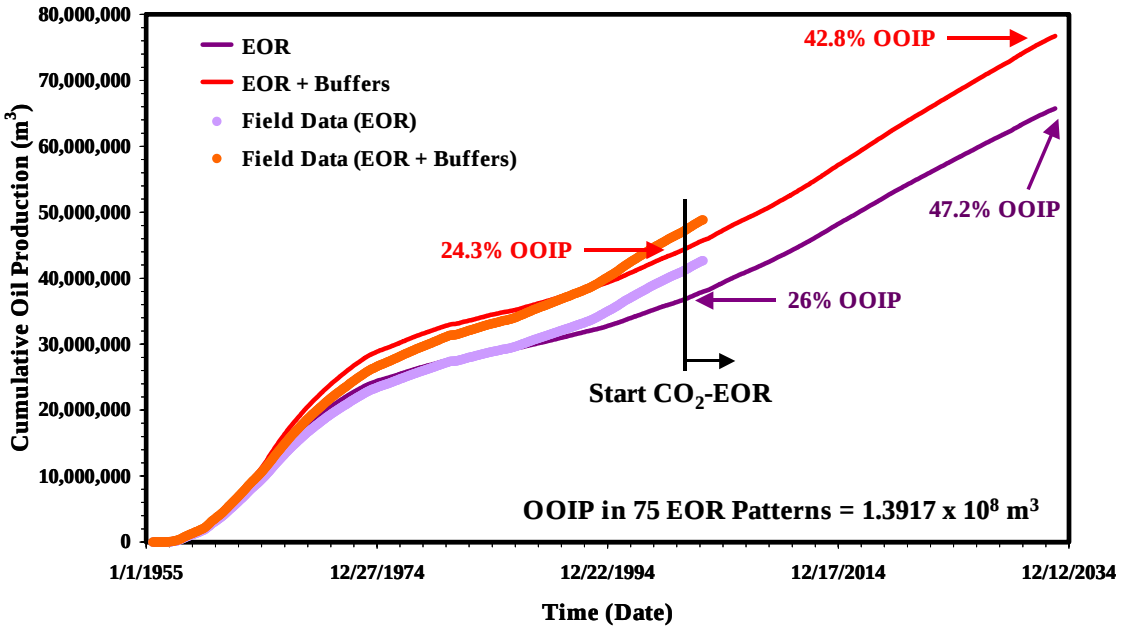

Figure 3.37: Cumulative oil production (75-pattern simulation - EOR base case)

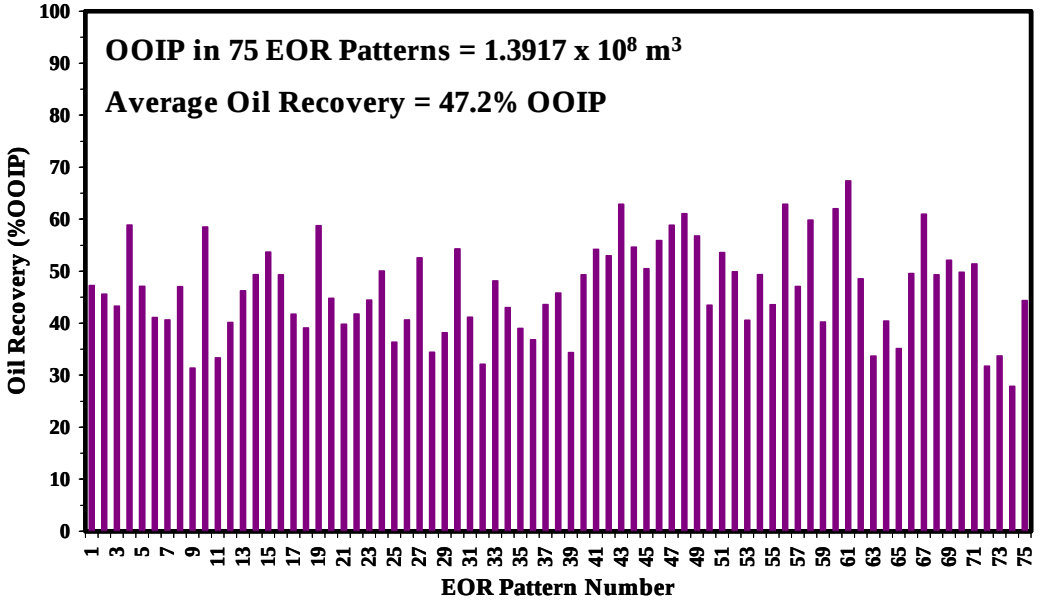

Figure 3.38: % oil recovery in 75 EOR patterns (75-pattern simulation - EOR base case)

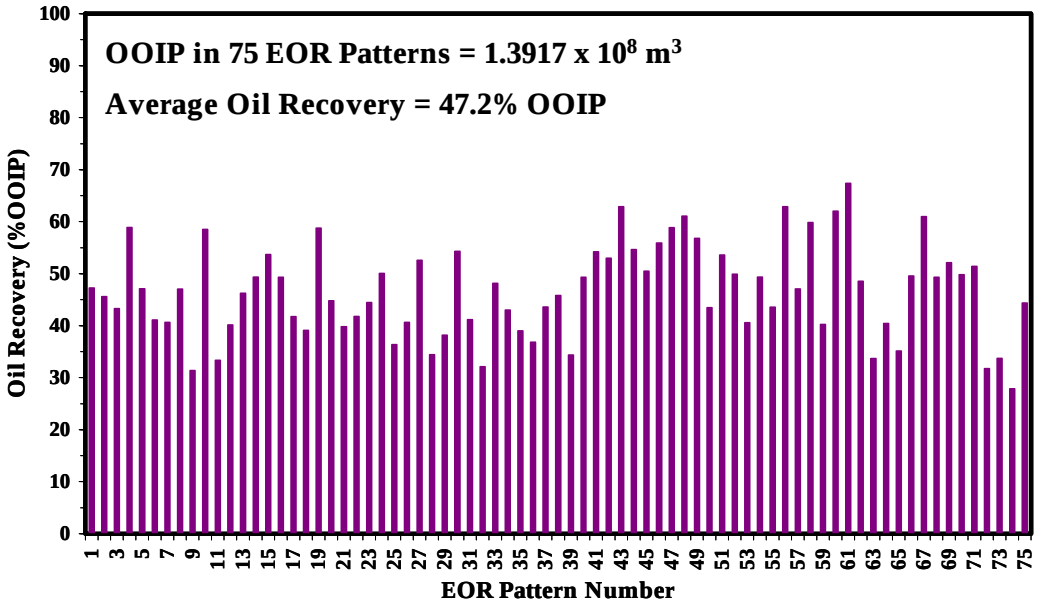

Figure 3.39: Cumulative oil production for different pattern types (75-pattern simulation - EOR base case)

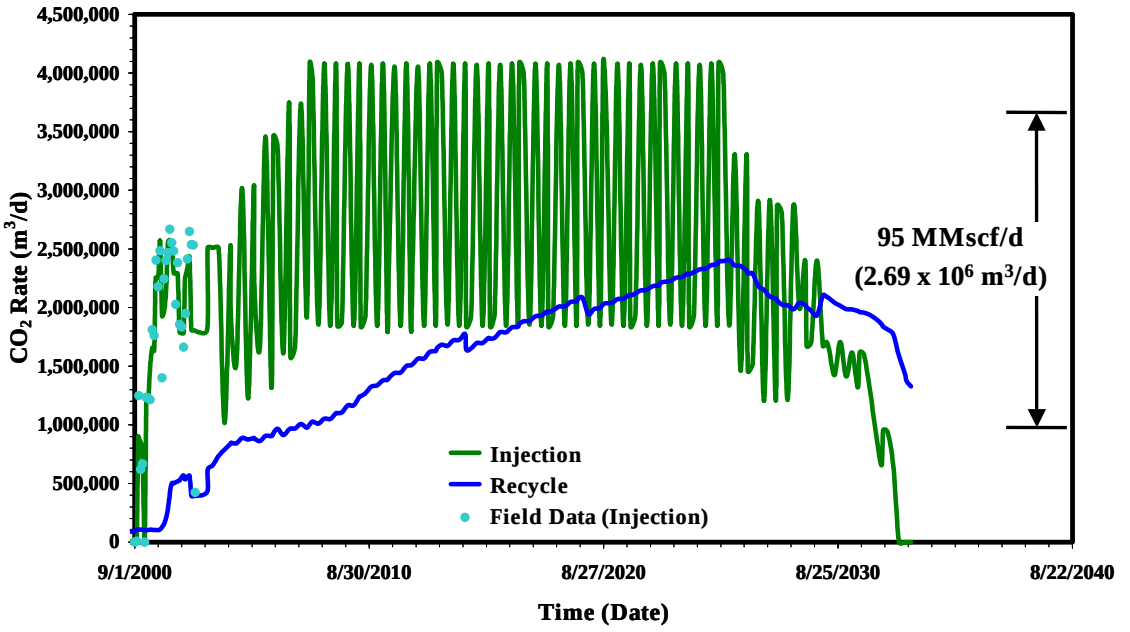

Figure 3.40: CO_2 injection and recycle rates (75-pattern simulation - EOR base case)

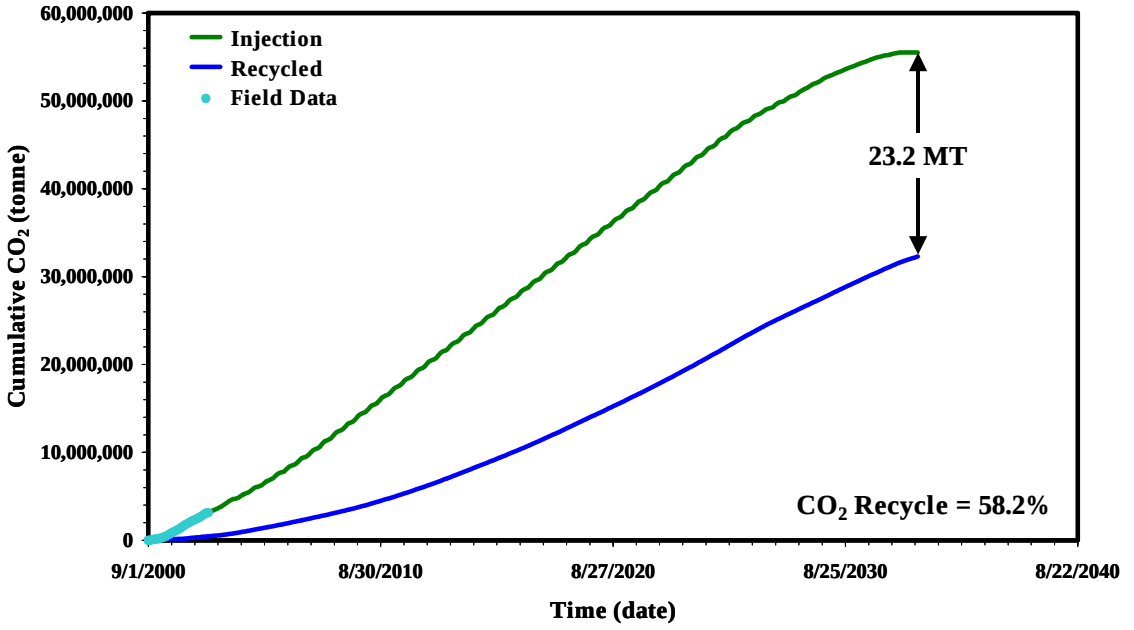

Figure 3.41: CO_2 storage capacity (75-pattern simulation - EOR base case)

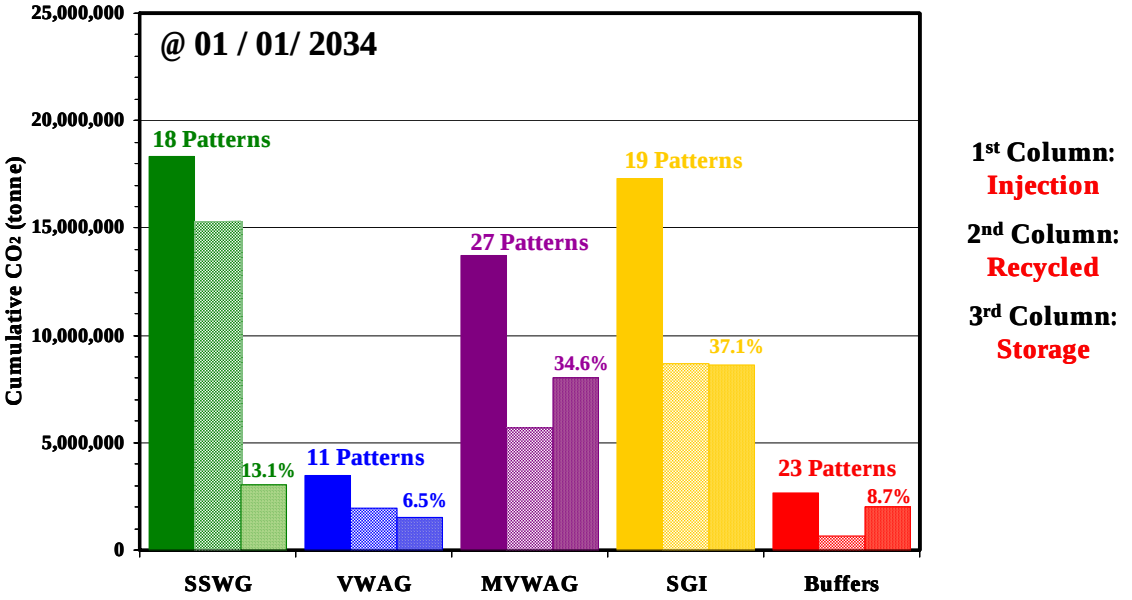

Figure 3.42: CO_2 storage capacity by pattern type (75-pattern simulation - EOR base case)

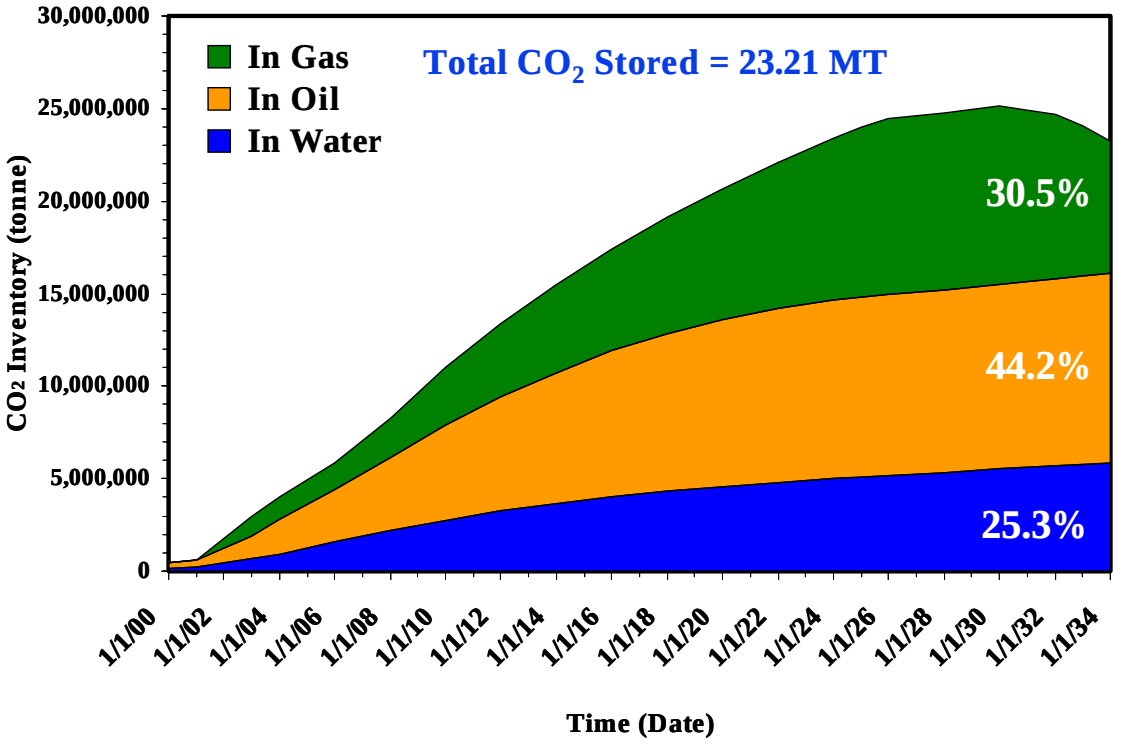

Figure 3.43: CO_2 inventory (75-pattern simulation - EOR base case)

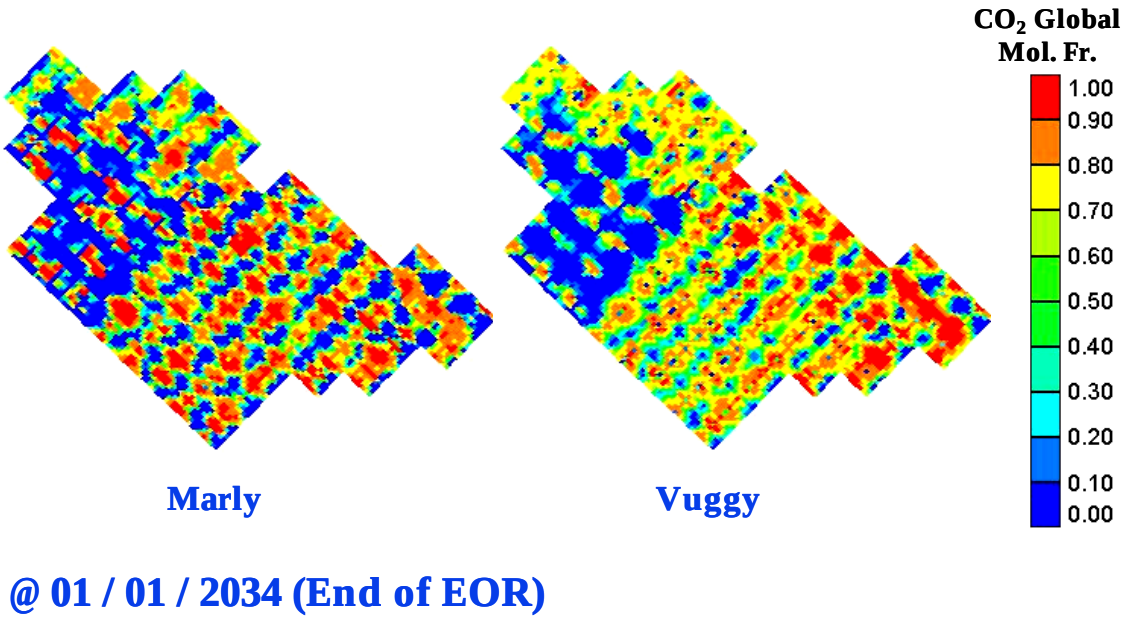

Figure 3.44: CO_2 distribution as global mole fraction at the End of EOR (75-pattern simulation - EOR base case)

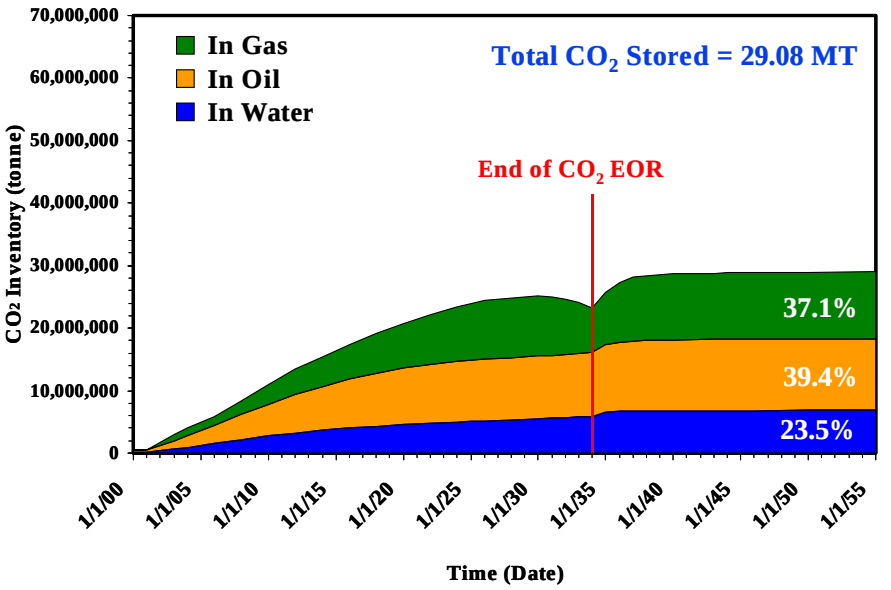

Figure 3.45: CO_2 Inventory (75-pattern simulation - CO_2 storage alternative Case II)

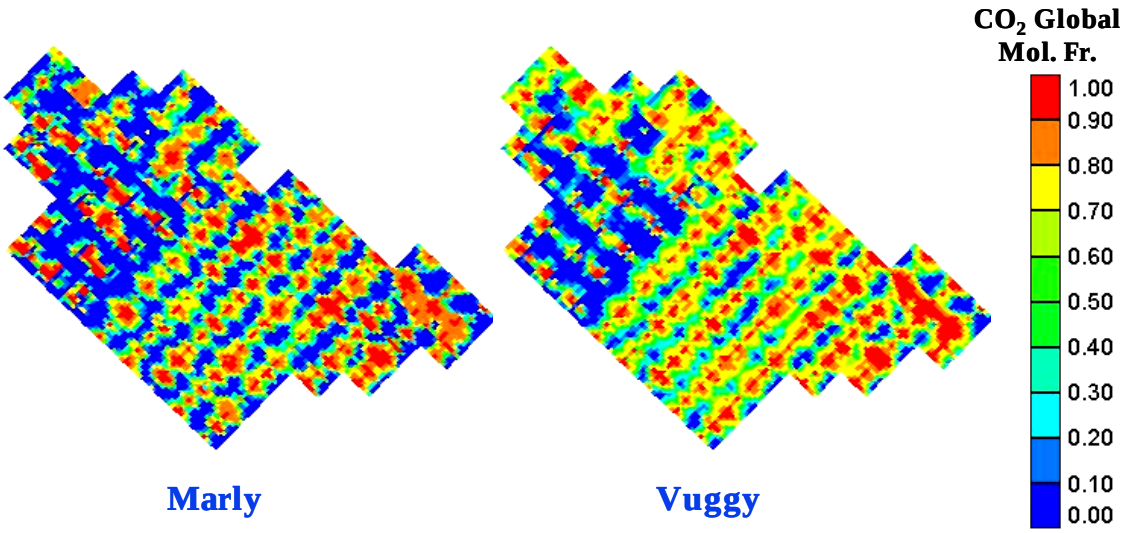

Figure 3.46: CO_2 distribution at the end of storage (75-pattern simulation - CO_2 storage alternative Case II)

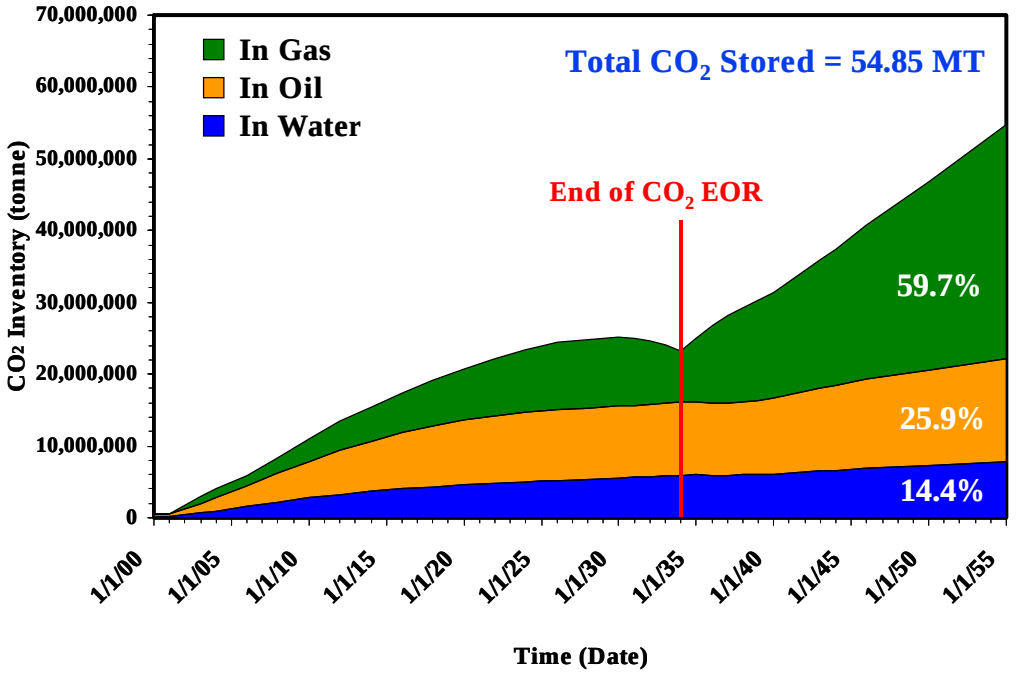

Figure 3.47: CO_2 inventory (75-pattern simulation - CO_2 storage alternative Case III)

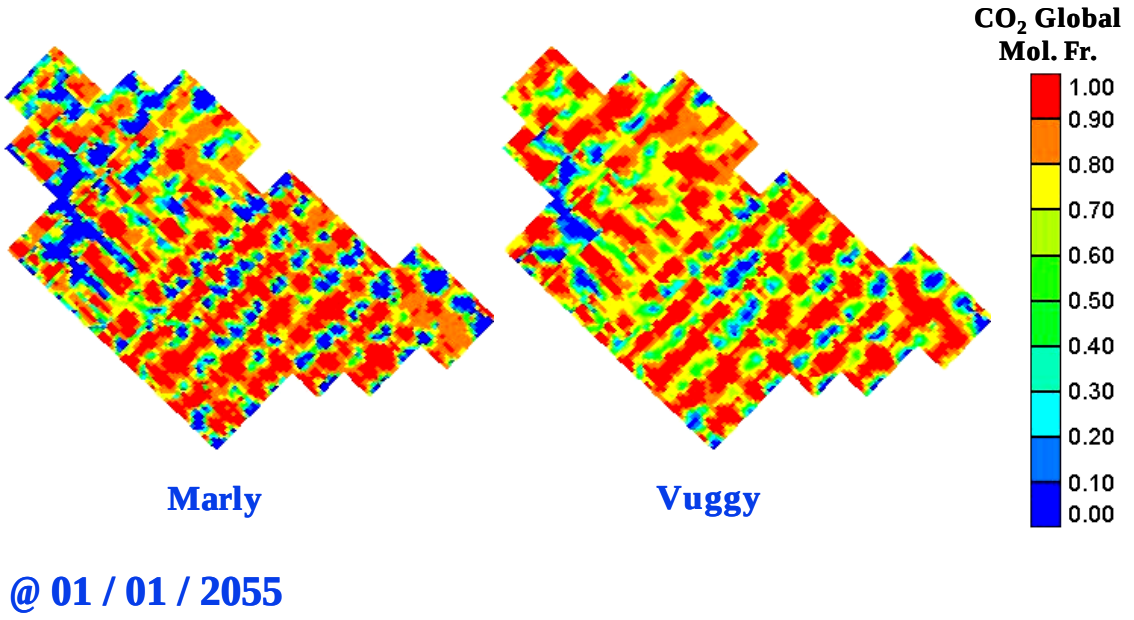

Figure 3.48: CO_2 distribution at the end of storage (75-pattern simulation - CO_2 storage alternative Case III)

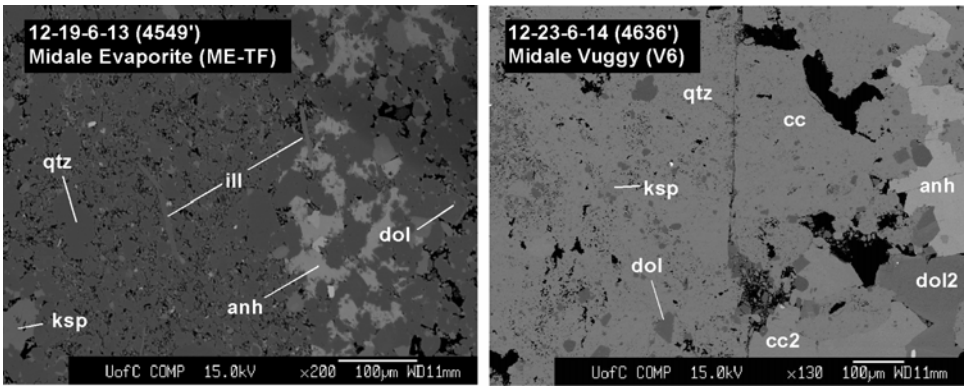

(a) *(b)*

Figure 3.49: Back-scattered electron (BSE) images from the electron-probe microanalyser (EPMA)

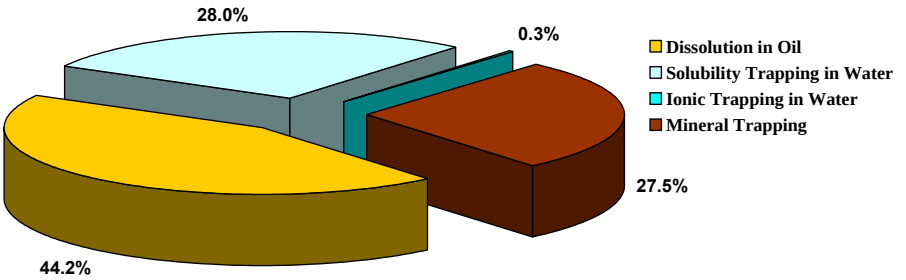

Figure 3.50: Preliminary estimation of CO_2 distribution in Weyburn reservoir after 5,000 years based on geochemical modelling of 75-pattern simulation EOR base case prediction

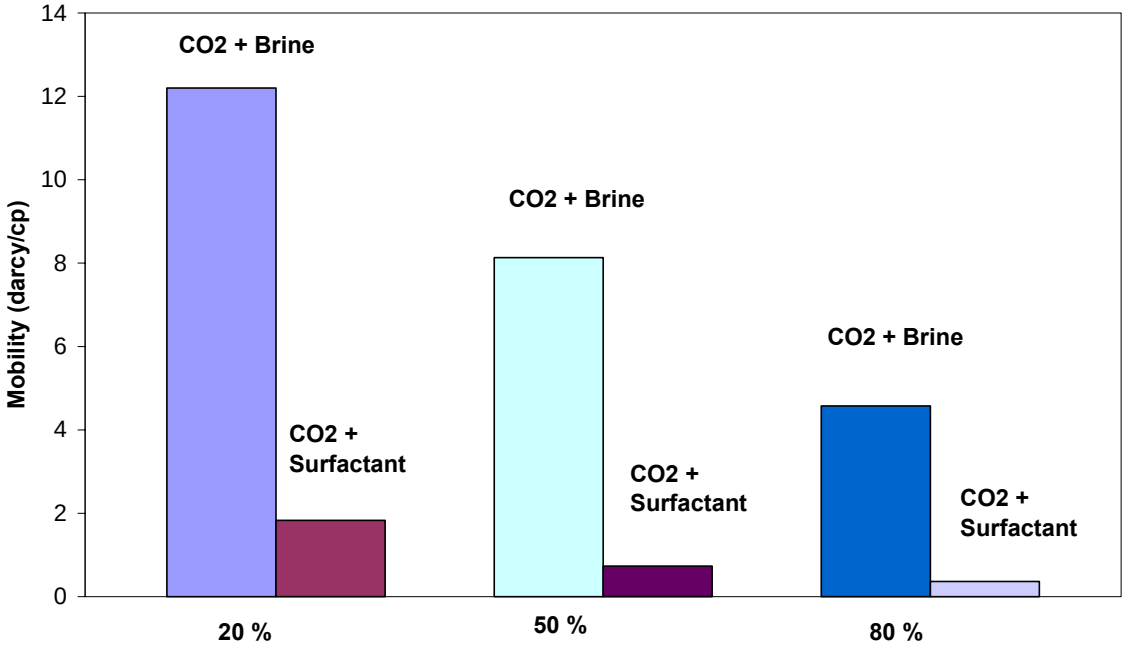

Figure 3.51: Mobility of CO_2-water and CO_2-foam at different CO_2 fractions

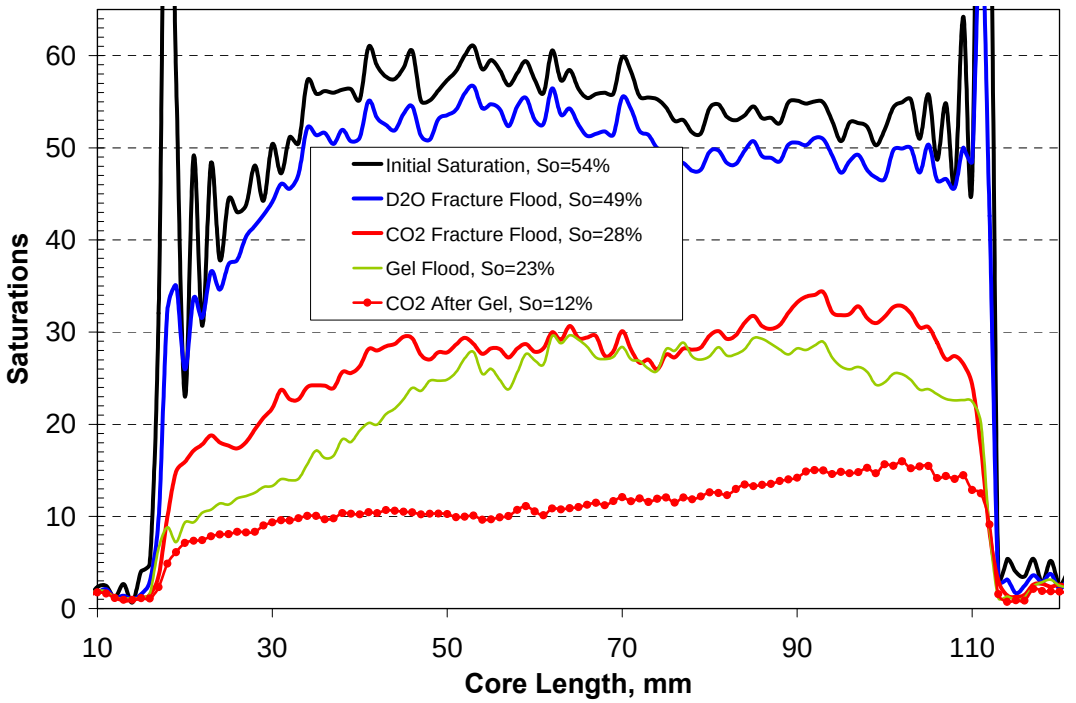

Figure 3.52: Oil saturation distributions in fractured core before and after gel treatment

Theme 3: CO_2 Storage Capacity and Distribution Predictions and Application of Economic Limits

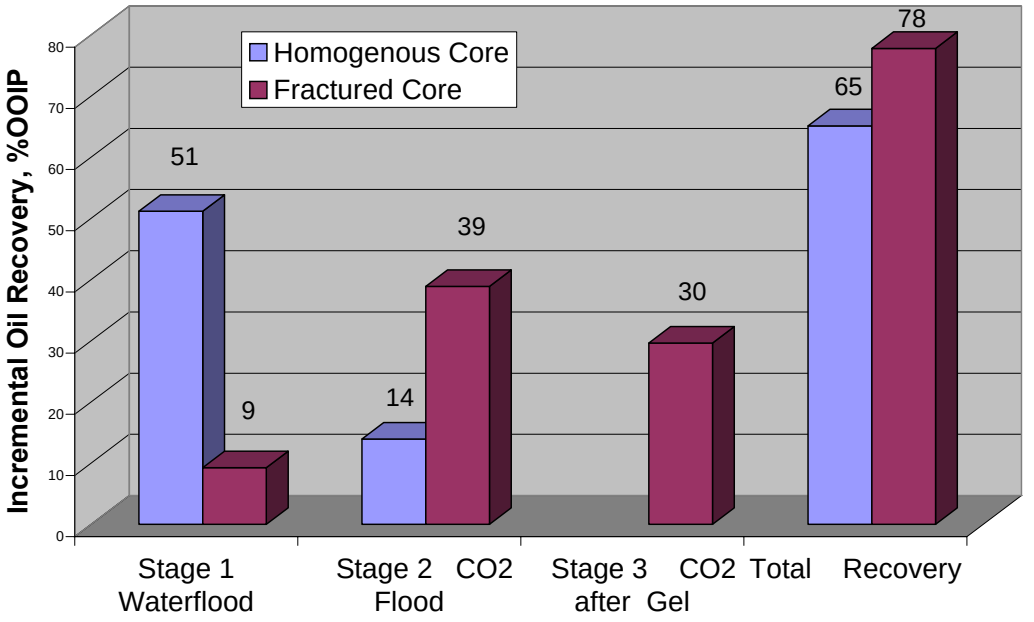

Figure 3.53: Oil recovery in fractured and homogenous core

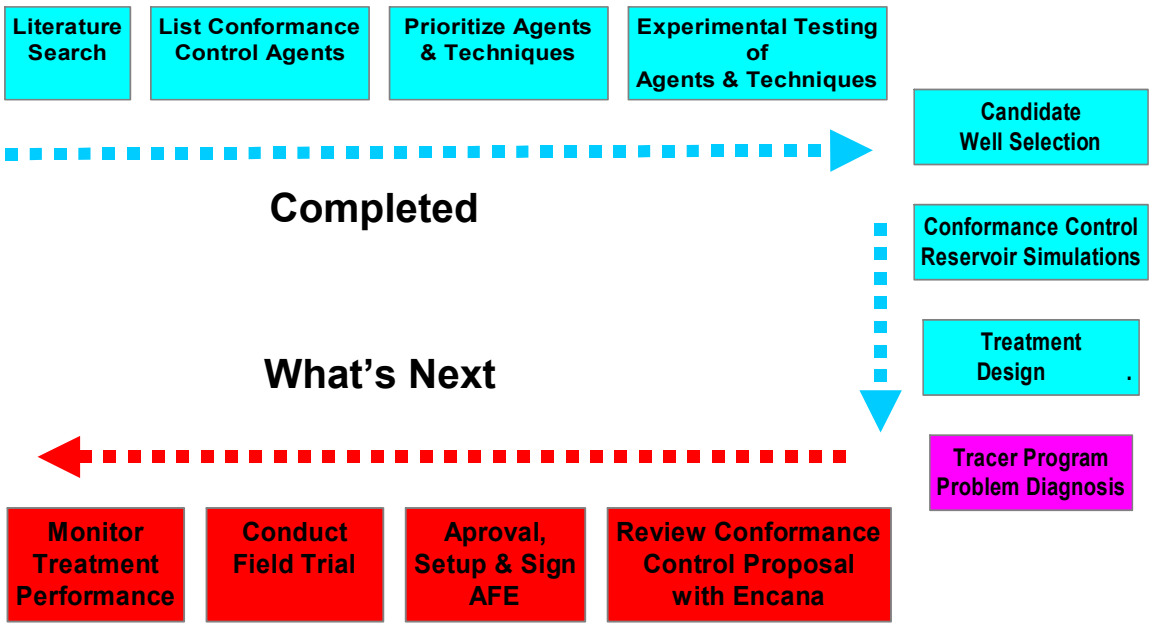

Figure 3.54: Stage gating process toward field application

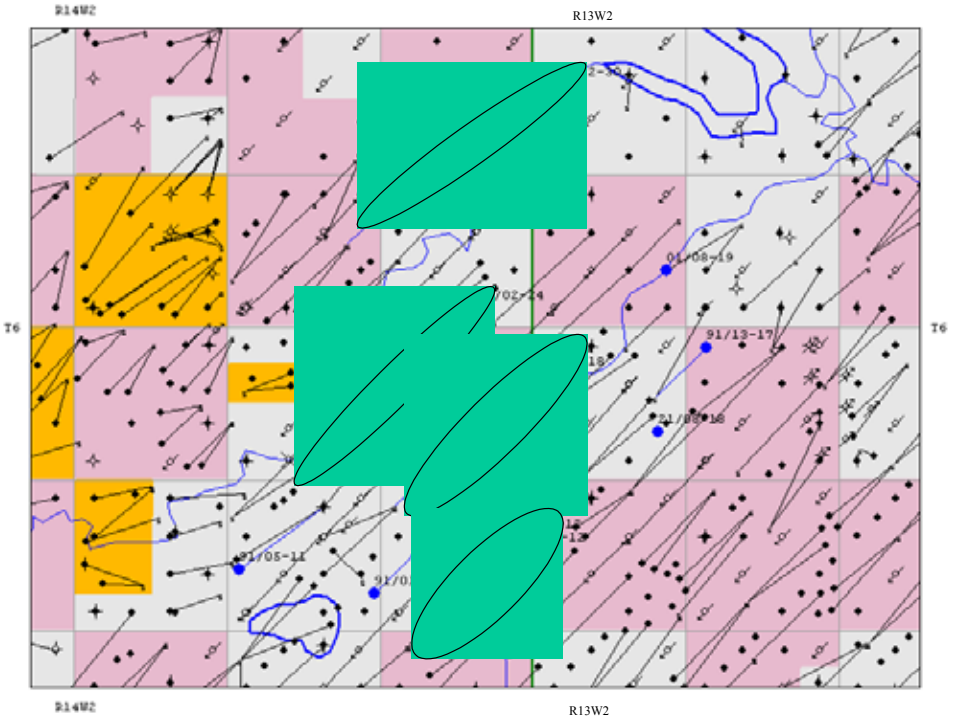

Figure 3.55: Higher GOR well candidates for gel treatment in Phase 1A area (blue markers: well; green circles: well trends)

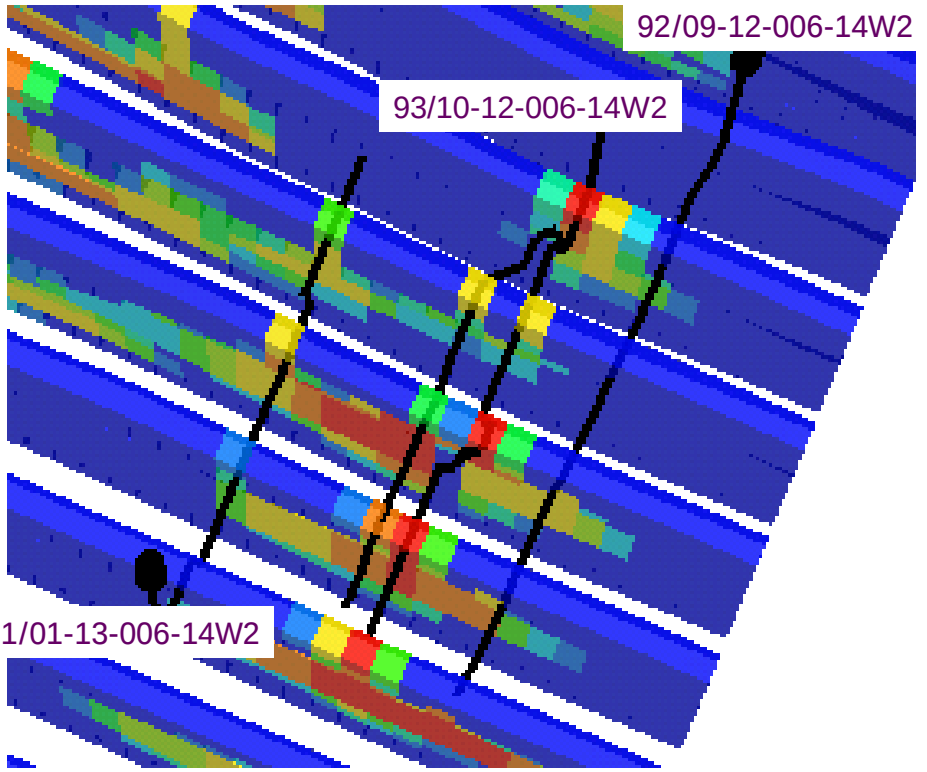

Figure 3.56: Well pattern for gel treatment numerical simulation in Pattern 1

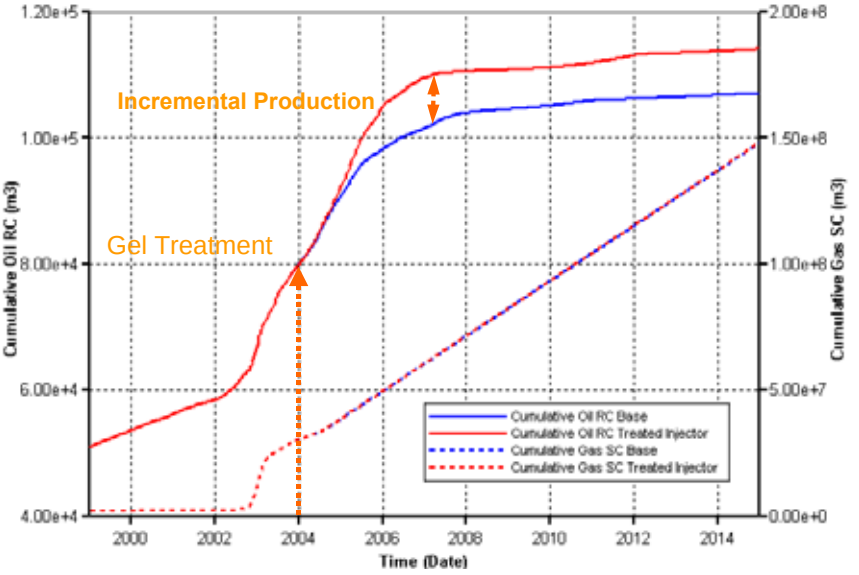

(a) 91/01-13-006-14W2

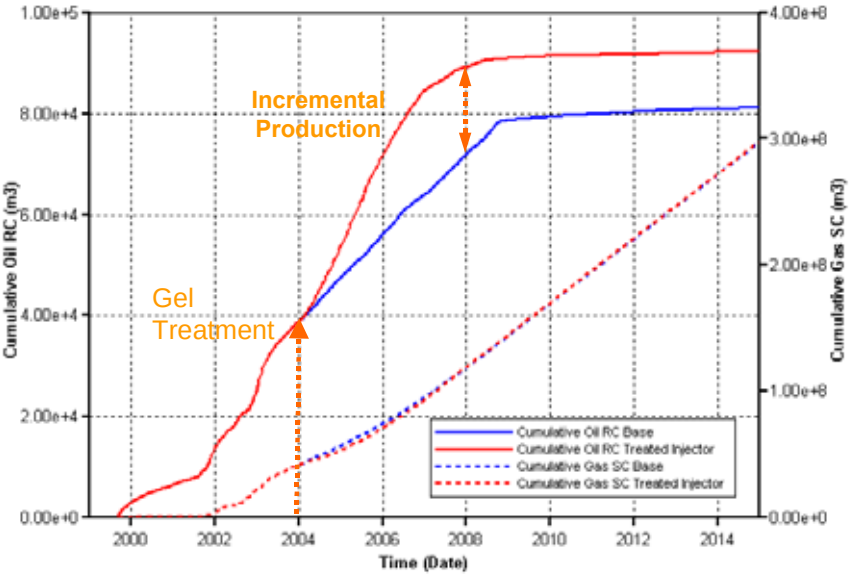

(b) 92/09-12-006-14W2

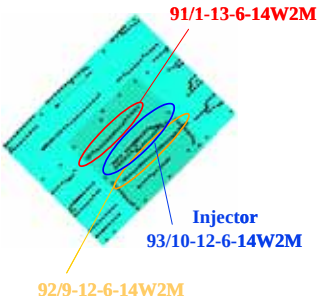

Figure 3.57: Impact of conformance control treatment on two nearby producers

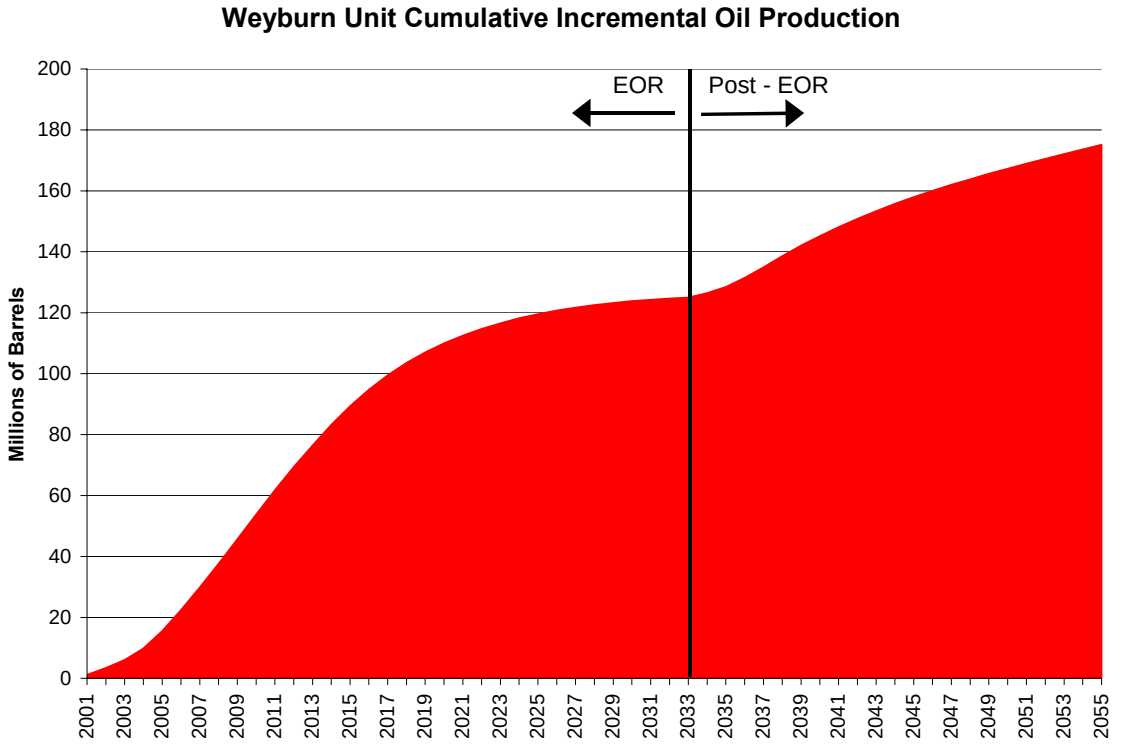

Figure 3.58: Weyburn Unit cumulative incremental oil production used for "demo run"

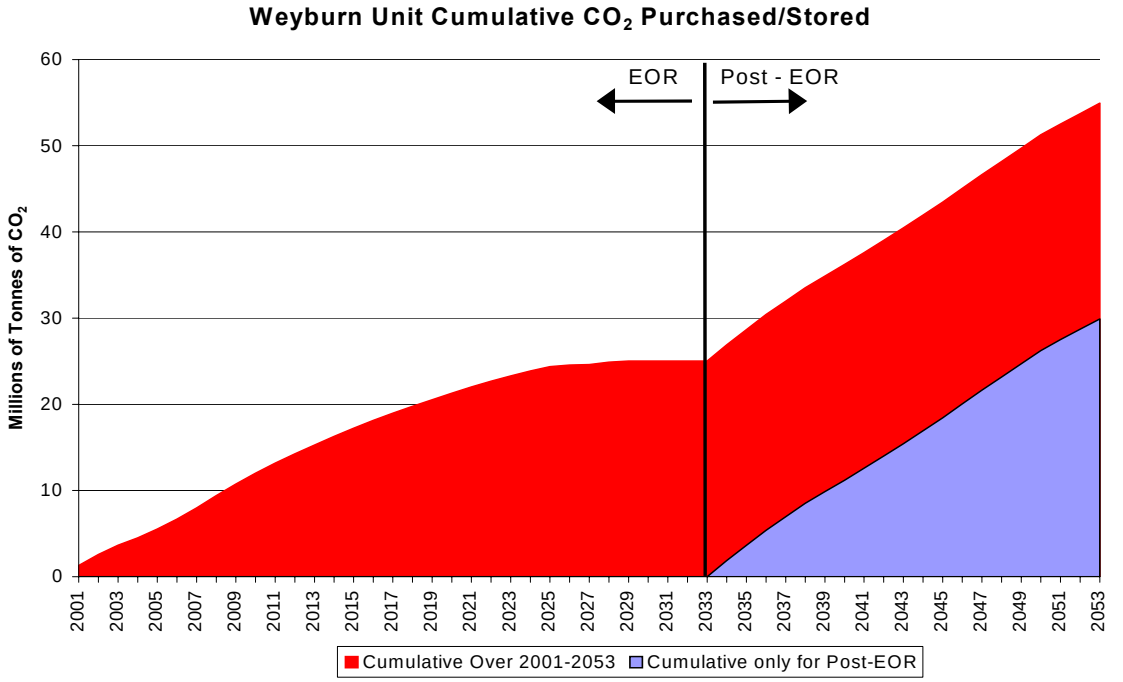

Figure 3.59: Weyburn Unit cumulative CO_2 purchased/stored used for "demo run"

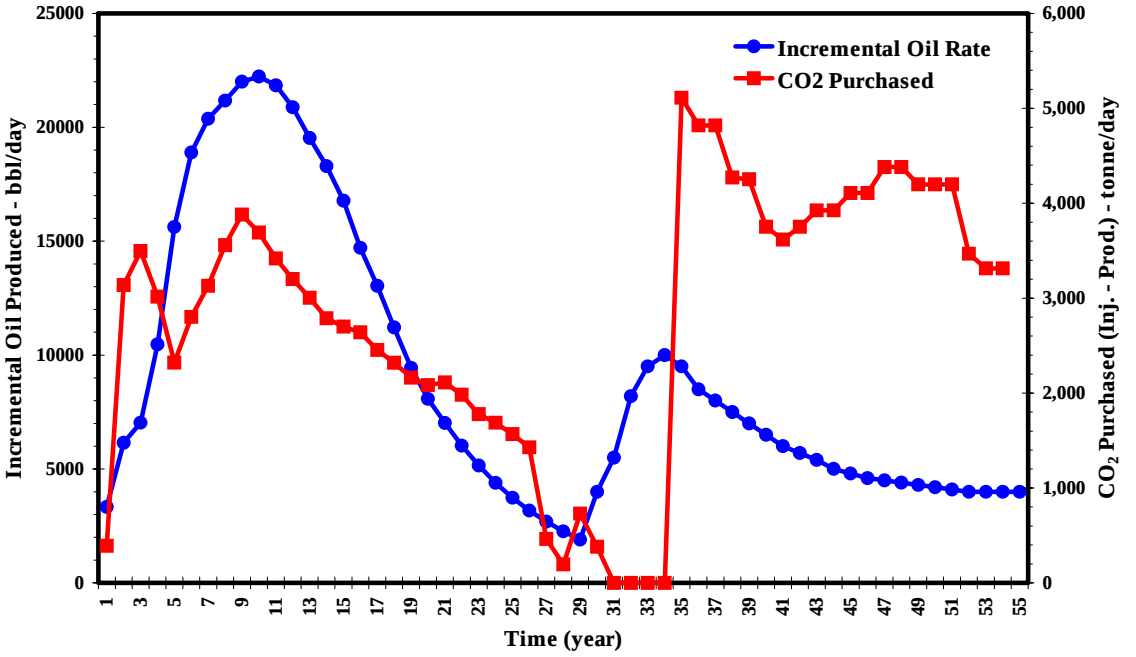

Figure 3.60: Weyburn Unit incremental oil production and CO_2 purchased used for "demo run"

THEME 4: LONG-TERM RISK ASSESSMENT OF THE STORAGE SITE

THEME LEADER: RICK CHALATURNYK
THEME AUTHORS: WEI ZHOU, MIKE STENHOUSE, MARSHA SHEPPARD, FRANK WALTON

1 SUMMARY

Performance assessment has been applied as the initial phase of an overall risk assessment process to evaluate the long-term fate of CO_2 injected into the Weyburn reservoir. The role of performance assessment within Phase 1 of the IEA GHG Weyburn CO_2 Monitoring and Storage Project was to identify the risks associated with geological storage and assess the ability of the Weyburn reservoir to securely store CO_2 for an extensive period of time. The performance assessments have also been utilized to identify and increase our understanding of crucial processes for CO_2-EOR and will form a critical component of the final risk assessment in Phase 2 of the Project.

As with many engineered or natural systems, the Weyburn "System," comprising the geology of the reservoir and overlying and underlying layers, varying well types, groundwater flow regimes, fluid characteristics, and so on, is very complex. This complexity was managed through the application of a rigorous and formal systems analysis approach. To assist in identifying the processes that could be relevant to the evolution or performance of the System, a list of features, events, and processes was developed. Their evaluation, including their interactions, lead to a description of how the System might evolve over the timeframe of the performance assessment and formed the foundation for the development of a scenario that describes how the system may be expected to evolve - the base scenario - in the far future and other scenarios that describe alternative, but feasible futures. Performance assessment in Phase 1 of the Project focused primarily on the base scenario.

Compositional reservoir simulations in support of early performance assessment studies were conducted for the time period of 5000 years starting from the end of EOR. They provided an initial understanding of CO_2 migration; the process and parameters that may be important to modeling its long-term fate. These studies involved increasingly more complex treatment of a conceptual model of the system. The early studies highlighted the importance of processes such as CO_2 diffusion in the oil phase, phase saturation distribution at the end of EOR, groundwater velocities within the reservoir zone, and the strong interplay between the coupled processes of pressure-driven flow, density-driven flow, and diffusion.

Geological characterization research led to the development of a detailed, three-dimensional System Model description. The geological components of the System Model were constructed by combining detailed stratigraphic divisions into broader hydrostratigraphic divisions, or flow units. The lateral extent of the model is approximately 10 km from the EOR boundary. Embedded within the System Model was the entire 75 EOR pattern area planned for CO_2-flood rollout and used to predict the CO_2 storage capacity in the Weyburn reservoir. These large-scale reservoir simulation results provided the necessary fluid phase and pressure distributions at the end of EOR for the long-term performance assessment for a period of 5000 years following the end of EOR.

Deterministic and stochastic approaches were adopted to assess the fate of CO_2 within the geosphere and the man-made pathways (*i.e.* the abandoned wellbores), respectively. CO_2 migration was controlled by the movement of gas, oil, and water phases and by the chemical distributions of CO_2 among these three phases. Early, relatively fast mass transfer was attributed to high pressure gradients across the boundary of the EOR region. Mass transfer of CO_2 slows down as the pressure decreases, followed by a change in rate, or a slight increase, in the case of lateral CO_2 migration, as the ambient pressure/flow field is restored at about 1000 years. Based on the final iteration of the System Model and described more fully below, cumulatively, over 5000 years, the total amount of CO_2 removed from the EOR area is 26.8% of the initial (~ 21 MT) CO_2-in-place at the end of EOR, of which 18.2% moves into the geosphere below the reservoir, 8.6%

migrates laterally in the Midale reservoir outside the EOR area, and 0.02% diffuses into the caprock above the reservoir. No CO_2 enters the potable aquifer(s) over the 5000-year period.

For the abandoned well leakage assessment, the estimated maximum cumulative leakage of CO_2 for an estimated 1,000 wells was ~0.03 MT or 0.14% of the total CO_2-in-place at the end of EOR over the 5,000 year period. The mean cumulative leakage was estimated to be less than 0.001% of the CO_2-in-place at the end of EOR.

In addition to deterministic/stochastic approaches to performance assessment simulations, probabilistic risk assessment techniques were used to investigate the potential application of these methods for geological storage projects. A generalized performance assessment model employing simplifying assumptions and a compartmental model approach, and characterized by analytical solutions, was developed for the probabilistic risk analyses. A full probabilistic risk analysis study of the 75-pattern area was not completed in Phase 1 of the Project. However, to demonstrate the capability and potential of the probabilistic risk assessment methodology and its ability to identify key processes or parameters, a benchmarking and focused case study using the results from a single pattern reservoir simulation was undertaken.

Benchmarking results showed that, despite the differences in numerical/analytical approaches, both the reservoir simulator and probabilistic program generally agreed on the total amount of gas phase released, that the fractional gas release to the surface was considerably smaller than the fraction dissolved in place, and that the leakage rate to the surface through failed well seals was relatively small in terms of the overall effectiveness of the storage system. For the case study, 4000 parameter combinations were evaluated and the results indicated that after 5000 years, the average cumulative release of CO_2 to the biosphere was predicted to be 0.2% of initial CO_2-in-place with a 95% confidence interval range of 0.005% to 1.3% of initial CO_2-in-place. The average CO_2 released to the geosphere surrounding the reservoir was predicted to be 16% of initial CO_2-in-place with a 95% confidence interval range of 6% to 34% of initial CO_2-in-place. There is a 95% probability that 98.7% to 99.5% of the initial CO_2-in-place will remain stored in the geosphere for 5000 years.

Synthesis of all available well information within the Phase 1A area of the project provided the performance assessment studies with ranges of well types and their associated transport properties. Cement degradation models, incorporating sulphate attack, mechanical fatigue, carbonation, and leaching, provided wellbore cement hydraulic conductivities in the order of $1x10^{-16}$ m^2 ($1x10^{-4}$ Darcy) for most well types. For historical injection and production pressures within aging wellbores, modeling has predicted minimal impact on the sealing capability of the wellbores over the life of the EOR project. Geomechanical performance assessments have shown that the integrity of the bounding seals has likely been maintained throughout the historical injection/production period preceding CO_2 injection. They are predicted to maintain their hydraulic integrity given the current CO_2 injection pressures, and future salt dissolution processes will likely have minimal influence on their integrity. Geomechanical testing on the bounding seals confirm their strength and low permeability. Permeability for the anhydrite caprock was determined to be in the range of 10^{-19} to 10^{-20} m^2 (10^{-7} to 10^{-8} Darcy).

All performance assessment studies conducted within Phase 1 area have shown clear support for the conclusion reached within the geological characterization studies – the geological setting at the Weyburn field is highly suitable for long-term subsurface storage of CO_2. These studies have highlighted the significant capacity of the geosphere surrounding the reservoir to effectively store CO_2 and prevent its migration to the biosphere.

2 THEME OBJECTIVES

The ultimate objective of the long-term risk assessment research tasks was to assess the performance and ability of the Weyburn reservoir to securely store CO_2. Performance, by design, includes both engineering and safety aspects, and so the performance assessment (which has been applied as the initial phase of an overall risk assessment process) also had a role in identifying the risks associated with the geological storage of CO_2 within the Weyburn reservoir.
The ultimate deliverable from this project is a credible assessment of the permanent containment of injected CO_2 as determined by formal risk analysis techniques including long-term predictive reservoir simulations. Results will help answer questions by regulatory bodies as to the security of large volume CO_2 storage not only in the Williston Basin but also at other sedimentary basins where CO_2 storage is contemplated.

3 SCOPE OF INVESTIGATION

There are two contexts in which the long-term assessment is being carried out:

- *Environmental*, whereby the assessment establishes whether the CO_2 injected into the reservoir leaks to the biosphere or environment and, if so, whether the leakage imposes any environmental risk.

- *Greenhouse gas reduction*, whereby the assessment establishes whether the injected gas leaks to the atmosphere and, if so, whether the leakage compromises greenhouse gas (GHG) reduction objectives.

The focus for Theme 4 was primarily on the environmental context. The timescale associated with the assessment goes far beyond what is considered in typical engineering projects, and consequently there are a number of unique challenges associated with the long-term assessment. Uncertainty will always be associated with modeling, and this project is no different. Uncertainties arise from heterogeneities in the system, limited large-scale information, limited simulation capability of large-scale systems, potential disruptive events in the future, and limited capacity to predict how society will evolve in the future.

As with many engineered or natural systems, the Weyburn "System," comprising the geology of the reservoir and overlying and underlying layers, varying well types, groundwater flow regimes, fluid characteristics, and so on, is very complex. This complexity was managed through application of a rigorous and formal systems analysis approach, firstly, to identify and define the System and, secondly, to define base and alternative scenarios for the long-term fate of CO_2 within the System. Scenarios are the plausible and credible ways in which the Weyburn System might evolve over decades to millennia. Integration of the performance assessment with the major research Themes of the project remains an essential element in its success. Geological characterization research has lead to a detailed, three-dimensional System Model description. Embedded within the System Model is the entire 75 EOR pattern area planned for CO_2-flood rollout and used to predict the CO_2 storage capacity in the Weyburn reservoir. These large-scale simulation results provide the necessary fluid phase and pressure distributions at the end of EOR for the long-term performance assessment out to 5000 years.

From an assessment perspective, the two main elements of the System Model are the geosphere and biosphere. The geosphere, which includes the reservoir, incorporates all geological, hydrogeological, and petrophysical information assimilated for the System Model. The biosphere extends to a depth of about 300 m below ground surface and includes soil, surface water, and the atmosphere and the flora and fauna found within these areas.

4 OVERVIEW OF RISK ASSESSMENT METHODOLOGIES

Risk management is now a well accepted tool for controlling risks from a wide variety of industrial and other human activities. It fits into a number of worldwide safety regulations and industry good practice policies. Thus the chemical and petroleum industries, the nuclear industry, the aviation and space industries, the waste handling industry, the military, and parts of the food industries are all using risk assessment and risk management as a core tool (Pitblado and Mossemiller, 2004). The goal of the risk management process is to establish the significance of the estimated risk, compare the costs of reducing this risk to the benefits gained, compare the estimated risks to the societal benefits derived from incurring the risk, and carry out the political and institutional process of reducing risk (Oldenburg and Unger, 2003).

Risk is generally defined as the combination of frequency or probability and the consequence from a specified hazardous event. There are several kinds of risk assessments that deploy all three aspects of this definition (defined event, likelihood, and consequence). Figure 4.1 shows that the three levels of risk assessment apply equivalently in the overall risk management process, but the tool to select depends on project complexity, uncertainties, and phase in the project lifecycle. Three broad classes of risk analysis include qualitative studies, deterministic (DRA), and probabilistic (PRA). Within the Project, deterministic/stochastic and probabilistic methodologies were applied.

Deterministic risk assessment employs a single set of values for parameters in the model used to estimate impacts of the system under study. It does not explicitly deal with uncertainty in parameter values. However, the selected set of values might be conditioned so as to provide risk estimates associated with (for example) worst-case conditions, expected conditions – a stochastic approach. If exhaustive stochastic analyses are included, the entire approach can come to resemble probabilistic risk assessment. Probabilistic risk assessment formally accounts for the effects of uncertainty. This approach typically uses probability density functions to describe the range of possible values for parameters in the model describing the system under study. Multiple simulations are then employed, and each simulation uses a set of parameter values that are randomly selected from their probability density functions. The result of these simulations is a probability distribution for the risk that reflects the underlying uncertainty specified for the model parameters.

A systems analysis approach was adopted as the framework for the assessment modeling conducted within this project for a number of reasons. It provides a systematic framework for conducting safety assessments. It can be used to identify features, events, and processes over hundreds to thousands of years – the timescales of relevance in this project. The approach has been tried and tested in the field of radioactive waste disposal in different countries. It is a useful method of documenting progress and reasons for particular decisions.

Systems analysis consists of several inter-related elements. It involves development of a list of features, events, and processes (FEPs) that together describe the particular system being studied – in this case, the CO_2 storage reservoir – and all the FEPs that could occur within this system. It also includes identification of those FEPs that belong to the system itself and those that can be regarded as external to the system. It then involves identification of interactions between these FEPs, construction of base and alternative scenarios; and description of how these interactions will be accommodated in the consequence analysis modeling to be undertaken for each scenario.

5 RISK ASSESSMENT TOOLS

For the risk analyses conducted within Phase 1 of the Project, two simulation tools were utilized, the Eclipse E300 reservoir simulator from GeoQuest and CQUESTRA, an analytical program developed for probabilistic simulations. The following sections provide a brief summary of these two risk assessment tools.

5.1 ECLIPSE E300 Compositional Reservoir Simulator

ECLIPSE 300 (E300), a compositional reservoir simulator developed by Schlumberger, was used to investigate the long-term CO_2 fate for the Project. E300 has the capacity to simulate enhanced oil recovery (EOR) using CO_2. The simulator, however, was not developed especially for modeling the long time frames associated with CO_2 geological storage. Currently, no computational tools exist for this specific modeling purpose, but for the risk analyses, E300 has several advantages. It has been extensively field tested and validated. It is being used by EnCana to simulate the CO_2-EOR flood. Because of the low critical pressure and temperature of CO_2, it is important to track fate of the CO_2 in a large (spatial extent is defined by assessment time scale) geosphere/biosphere system. This requires the capability of using equations-of-state (EOS). Reservoir simulators have an EOS feature through which one can simulate CO_2 by including CO_2 as if it were a hydrocarbon component. E300 is also able to model CO_2 dissolution in water, which is important in assessing CO_2 hydrodynamic trapping. Finally, it uses industry standard protocols for incorporating geological features through special interfaces with geological modeling tools, such as Gocad® and EarthVision® (Gocad was used in the IEA GHG Weyburn CO_2 Monitoring and Storage Project).

Despite their many advantages, however, reservoir simulators are generally not developed for simulating CO_2 geological storage. There are a number of disadvantages in using the E300 and, perhaps, other reservoir simulators. Selection of a "no-flow" boundary condition that is a good approximation of most reservoir conditions is not sufficient for simulating CO_2 migration. However, this can be remedied using various features provided by simulators to simulate communication between reservoirs and surrounding aquifers. CO_2 can become carbonate through geochemical reactions (*i.e.*, mineral trapping). CO_2 can also react with species in groundwater to lower the pH value of the water, which may dissolve some minerals and alter rock properties. E300, as with most reservoir simulators, does not couple geochemical reactions with flow and transport. Although reservoir simulators have many features for simulating well flow, these are developed for production and injection operations conducted in oil and gas fields and cannot be readily applied to abandoned well leakage. While reservoir simulators incorporate CO_2 dissolution in water, they may not correctly calculate water density change due to CO_2 dissolution. This feature may be important in simulating CO_2 injected into aquifers and in studying CO_2 distribution as a result of density gradient.

5.2 CQUESTRA Program

CQUESTRA is a generalized performance assessment program for the storage of CO_2 underground and represents the first stage in the development of a PRA program for the storage of CO_2. The present version of CQUESTRA, CQ-1, reflects a stage-wise strategy to develop a first generation model that simulates the processes that are most likely to have the largest impact on the success of the CO_2 storage concept. It uses simplifying assumptions, where practical, and a compartmental model approach. Buoyancy forces pertaining to the oil rich phases and the separate CO_2 phase are considered to be the primary driving forces for escape that could compromise the storage system. CQ-1 accounts for mass transport of both the dissolved aqueous phase and the buoyant phases of supercritical, liquid, gaseous, and oil rich CO_2, depending on depth and temperature, using a simplified approach. It is assumed that all forms of buoyant CO_2 collect in layers or cushions under aquitards that have sufficiently small permeability to prevent the buoyant phases from penetrating these aquitards.

Open fractures, fissures, and faults in the aquitards can provide pathways for buoyant CO_2 phases. Boreholes and the borehole annulus also provide preferential pathways. The movement of buoyant CO_2 through the borehole structures will be mediated by the degradation of cemented seals, cemented annuli, and the borehole casing. It is assumed that buoyant CO_2 rising in a borehole can dissolve in the water column through corroded casings and degraded cement or gaps in the annuli.

CQ-1 considers three limiting cases: 1) there is an initial number of defective annuli that provide a continuous pathway to the surface for movement of the buoyant phase(s); 2) at a distinct time, a number of borehole seals fail, allowing movement of the buoyant phases up those boreholes. At this time the flow up the annuli ceases. The casings in the boreholes are all intact; 3) at a distinct time, a number of borehole seals fail, allowing movement of the buoyant phases up those boreholes. At this time, the flow up the annuli

ceases. The casings in the boreholes are all corroded, allowing dissolution in the water column during upward migration.

CQ-1 does not undertake to model the relatively short-term post-EOR processes. CQ-1 takes as the starting conditions for its assessment the spatial distribution of the CO_2 in the major reservoir phases after the reservoir has achieved steady-state pressures. This input information can come from any reservoir simulator. CQ-1 does not currently model time-dependent processes such as the degradation of cement well components and corrosion of well casings in detail. Rather single failure times are used to quantify these processes. Uncertainty and variation in failure times are currently handled by parameter sampling. Additional verification studies are required to justify the application of these simplified treatments to a very complex process.

6 RISK ASSESSMENT PARAMETERS

The risk analyses conducted within Phase 1 of the Project required integration with all major research tasks. Consequently, much of the data required for risk analyses were obtained from many diverse subtasks within the Project. The detailed data are contained within final subtask reports submitted by each research subtask, and it is beyond the scope of this summary document to synthesize all these data. The subsequent sections provide the salient parameters embodied within the long-term risk assessment studies in Phase 1.

6.1 System Model

Detailed geological characterization of the system model region was completed in Theme 1 activities. Because the geological description forms the backbone of the long-term risk analyses, it is worthwhile to review the major elements of the Weyburn system. Characterization of the Weyburn geological system for CO_2 storage targeted the delineation of primary and secondary trapping mechanisms and the identification of any potential pathways of preferential CO_2 migration. To place these components within a regional or basin context, the geological framework was constructed for a region extending 200 x 200 km around the Weyburn field, an area that includes portions of Saskatchewan, North Dakota, and Montana. Increased detail was focused within an area extending 10 km beyond the limits of the CO_2-flood, which defines the limits of the System Model used in risk assessment. Figure 4.2 provides a three dimensional perspective highlighting the position of these regions within the Williston Basin.

The geological setting at the Weyburn field is highly suitable for long-term subsurface storage of CO_2. Primary seals enclosing the reservoir (including the overlying Midale Evaporite and a highly anhydritized altered zone and the underlying Frobisher Evaporite) are observed to be highly competent and exhibit only rare discontinuities, most of which formed shortly after deposition, are completely healed, and exhibit no visual evidence of fluid conductance. In addition, as part of the primary sealing package, the Lower Watrous Formation forms a regionally extensive aquitard that effectively separates a deep hydrogeological system (including the Midale Beds) from a shallower hydrogeological system. Overlying the Watrous Formation is over 1 km of predominantly clastic strata that contain several thick and regionally extensive aquitards providing additional barriers to upward fluid migration. Aquifers present within the shallow hydrogeological regime may have high flow velocities (m/yr). Within the Midale Beds, however, low flow velocities (cm/yr) and favorable flow directions suggest formation water is unlikely to be an effective transport mechanism for dissolved CO2. Fracture zones and regional tectonic elements are present within the study region, yet none were found to exhibit evidence of fluid conductance or influence over hydrogeological components. Salt dissolution also has occurred within the risk assessment study region and may have induced fracturing of overlying rocks, although with no apparent compromise of the geologic container. These elements of the geologic setting of the Project are illustrated in Figure 4.3.

The System domain can be divided into four broad groups of components based on their function within the System Model: 1) The biosphere is the component in which the interaction of CO_2 with potable aquifers, biota, and human health risks will be assessed. Within Phase 1 of the Project, preliminary assessments of these processes (consequences) were undertaken (see Section 10) and for System Model simulations, the

biosphere was modeled as a reservoir for the cumulative releases transported by the wells through the upper geosphere; 2) The upper geosphere includes all aquifers and aquitards above the reservoir and below the biosphere. The wells penetrate all of these formations. It is within these upper aquifer formations that the storage of any CO_2 that might leak from these wells can take place; 3) The wells consist of the wellbore, the annulus (at least partially cement filled), the cement seal plug, and the steel casing; 4) The lower geosphere includes the reservoir (*i.e.*, the Midale Formation, which is subdivided into the Marly and Vuggy layers) and the aquifers below the Midale evaporite or cap rock. CO_2 can remain stored within the reservoir or be stored within the lower aquifers.

Figure 4.4 provides a schematic representation of the elements contained within the System Model. The geosphere data for formations above the reservoir were taken from data supplied by Theme 1 tasks (Geoscience). The System Model was subdivided into hydrostratigraphic units (7 aquitards and 6 aquifers) and the mean thickness, depth, porosity, and permeability of these formations are provided in Table 4.1. The data for aquifer flow velocities were abstracted from the larger regional dataset developed in Theme 1 to provide better estimates of the near-field velocities and porosities.

Table 4.1 Geosphere Parameters (all parameters are mean values for the System Model - details provided in the Theme 1 geoscience research section)

Formation	Depth to Top (m)	Thickness [m]	Permeability [mDarcy]	Porosity	Aquifer Velocity [m/yr]
Potable (Intertill) aquifer	0	54	15	0.2	n/a
Bearpaw aquitard	54	359	0.189	0.05	
Belly River aquifer	413	60	15	0.2	n/a
Colorado aquitard	473	399	0.189	0.05	
Newcastle aquifer	872	27	19.5	0.24	n/a
Joli Fou aquitard	899	38	0.0063	0.05	
Mannville aquifer	937	135	3772	0.25	9.3
Vanguard aquitard	1072	100	0.0063	0.05	
Jurassic aquifer	1172	124	567	0.16	4.0
Watrous aquitard	1296	97	0.8	0.04	
Poplar & Ratcliffe aquifer	1393	26	1	0.06	
Midale aquitard	1419	7	0.00001	0.003	
Midale Marly	1426	13	79	0.14	0.8
Midale Vuggy	1439	11	74	0.125	0.8
Frobisher aquifer	1450	66	8	0.15	0.8
Alida aquifer	1516	156	5	0.12	0.8

6.2 Wellbores

Upon completion of the 75 pattern project that comprises the currently planned CO_2 injection area, it is expected that approximately 1072 wells will exist. These wells will include the following geometries: 660 vertical oil producing wells; 200 horizontal oil producing wells; 197 vertical injection wells; 15 horizontal injection wells.

When the 10 km area surrounding the EOR project area is included, the number of wells of all types, the majority being vertical wells, totals almost 2200 wells. The general configurations or completion geometries for wells within the project area are shown in Figure 4.5.

6.3 Wellbore Statistics for the Weyburn EOR area

Wellbore information was collected from two main sources, older well data obtained from historical wellfiles transferred to microfiche (records stored in the Saskatchewan Industry and Resources Department) and newer well data obtained from internal wellfiles (in paper format and electronic) provided by EnCana. In general, the same information was found in both places, but substantially more detailed well records were available in the newer, electronic wellfile records. Data existing for wellbores drilled in the last decade were more detailed and complete than the data available for those wells drilled in the early development of the Weyburn field.

Information on wells drilled in the 1950s is generally limited to registries for geometry of wellbore (diameter, length), casing (diameter, length, grade) and cement type and volume. On the other hand, information available for a typical wellbore perforated in the 1990s is very detailed and complete. Cementing data include records of cement type, volume, depth set, circulation pressures, spacer volume, casing reciprocation stroke length, and time. Casing data include casing length, grade, accessories number, and spacing. Daily drilling reports provide a detailed progress of perforation with information such as mud density, volume, pressure, and daily drilling advance. Figure 4.6 illustrates a select range of statistics for the wells within Phase 1A of the Project.

6.4 Assessment of Wellbore Transport Properties

An assessment methodology of wellbore integrity, from a hydraulic or transport properties perspective, was based on identifying key leakage paths within a wellbore system and the processes or mechanisms that influence the characteristics of these leakage paths. The wellbore system has been chosen to include all the major components of a wellbore – internal abandonment configuration (bridge plug and cement), casing corrosion, annular cement (between casing and formation), excavation damage zones in the near-wellbore formation region, and all the interfaces that exists between these components.

A full understanding of these mechanisms can be only obtained following a comprehensive review of the wellbore environment during the different stages in the life of the well. The main stages during a well's life, from a hydraulic integrity point of view, can be classified as drilling, completion, well history, and abandonment. The influence of each one of these stages on the final hydraulic integrity of the well can be further classified into four major groups: geomechanical damage, hydro-chemical damage, mud removal, and cement deterioration damage. Geomechanical damage encompasses any stress-induced changes in the hydraulic conductivity properties of materials within the wellbore system. Hydro-chemical damage refers to any alteration of hydraulic conductivity in the near-well formation region – typically called formation damage. The third group, the efficiency with which mud is removed from the annulus during cementing operations, addresses the development of mud channels and its impact on hydraulic integrity of the wellbore system. Cement deterioration refers to porosity alterations due to geochemical processes under *in situ* conditions and in the presence of CO_2.

6.5 Reservoir Simulations

The basis for long-term assessments of the fate of the CO_2 was the distribution of CO_2 (in all phases) predicted by the 75 pattern numerical simulation conducted in Theme 3. Details of the reservoir simulation approach for the 75 pattern simulation of the entire CO_2-EOR flood can be found in Theme 3– Section 6.3. It is important for the reader to be familiar with the results and approach taken in the reservoir simulations, and, as such, the reader is encouraged to review the entirety of the Theme 3 section of this report.

7 SYSTEMS ANALYSIS RESULTS

The following section summarizes the results of the system analyses undertaken prior to proceeding with risk analyses of the fate of CO_2 injected into the Weyburn reservoir. It incorporates all the risk assessment research completed on features, events, and process identification and scenario analysis that was used to identify conditions for the most likely scenario existing within Weyburn – a base scenario. As a part of this exercise, alternate scenarios that capture potential changes in the base scenario were also developed.

7.1 Features, Events and Processes (FEPs)

In 2001, a Weyburn-specific FEPs list was generated from a segment of a FEPs list prepared for radioactive waste disposal, but containing FEPs that are relevant to the geosphere (*i.e.* excluding all FEPs specific to radioactive waste and to the engineered barriers of such a disposal system). To this list were added FEPs specific to CO_2 storage in the Weyburn reservoir. Table 4.2 contains FEPs that describe and define the Weyburn CO_2 Storage System.

Table 4.2 provides the initial framework for all assessment calculations performed over the course of the entire project. The FEPs shown in Table 4.2, particularly those that together describe the 'System' being studied, do not exist in isolation, but rather, are inter-related. Each of the FEPs may affect the System by influencing another FEP in some way or by causing a more specific interaction on/with another FEP.

In addition to Weyburn specific FEPs, complementary risk assessment programs in associated Weyburn research projects conducted in an EU (European Union) program, developed a generic FEP database for the geological storage of carbon dioxide, with the chosen FEPs being included for their relevance to the long-term safety and performance of the storage system after injection of carbon dioxide has been completed and the injection boreholes have been sealed. Some FEPs associated with the injection phase are nevertheless considered where these can affect long-term performance. The OECD/Nuclear Energy Agency FEP database for radioactive waste provided the inspiration for this generic CO_2 database.

The database currently includes around 200 FEPs in a hierarchical structure, with individual FEPs grouped into eight categories. Each FEP has a text description and an associated discussion of its relevance to long-term performance and safety. Figure 4.7 illustrates the web template for a particular FEP associated with climate change. Key references from the published literature are included to enable retrieval of more detailed information for each FEP. The database is internet-enabled incorporating hyperlinks to other relevant sources of information (reports, websites, maps, photographs, videos, *etc*.), and is searchable in a variety of ways; it has the potential to provide a 'knowledge base' for the geological storage of carbon dioxide.

Potentially important scenarios for the future evolution of a geological storage system have been considered. These scenarios need to be addressed in systems-level models for the assessment of performance and safety. The use of the FEP database as an audit tool to evaluate the completeness of such models has also been demonstrated.

Table 4.2 Features, Events and Processes relevant to the Weyburn CO_2 Storage System.

Category	WEYBURN FEP TITLE
SYSTEM FEPs	
Rock properties	
	Mechanical properties of rock (including stress field)
	Mineralogy
	Organic matter (solid)
	Presence and nature (properties) of faults / lineaments
	Presence and nature (properties) of fractures
	Cap-rock integrity
Hydrogeological properties	
	Cross-formation flow
	Fluid characteristics of rock
	Geometry and driving force of groundwater flow system
	Groundwater flow (including rate and direction)
	Hydraulic pressure
	Hydrogeological properties of rock
	Pore blockage
	Saline (or fresh) groundwater intrusion
	Transport pathways
Chemical/Geochemical	
	Carbonation
	Colloid generation
	Degradation of borehole seal (cement / concrete)
	Dissolution of minerals/precipitates/organic matter
	Dissolution / exsolution of CO2
	Dissolved organic material
	Groundwater chemistry (basic properties)
	Methanogenesis
	Microbial activity
	Mineral surface processes (including sorption/desorption)
	Precipitation/Coprecipitation/Mineralisation
	Reactive gaseous contaminants
	Redox environment / heterogeneities
	Salinity gradient
CO2 Properties and Transport	
	Advective flow of CO2
	Colloid transport
	Diffusion of CO2
	Dispersion of CO2
	Gas flow
	Source term (CO2 distribution)
	Thermodynamic state of CO2
	Transport of CO2 (including multiphase flow)

Category	WEYBURN FEP TITLE
SYSTEM FEPs (continued)	
Other gas	
	Gas pressure (bulk gas)
	Release and transport of other gases
Geology	
	Seismicity (local)
	Temperature / thermal field
	Uplift and subsidence (local)
Abandoned Wells	
	Annular space (quality / integrity)
	Boreholes - unsealed (extreme case)
	Corrosion of metal casing (abandoned wells)
	Expansion of corrosion products (abandoned well metal casing)
	Incomplete borehole sealing / Early seal failure
	Incomplete records of abandonment / sealing
NON-SYSTEM FEPs	
EFEPs	
	Artificial CO2 mobility controls
	Climate change
	Cross-formation flow (fast pathways)
	Depth of future wells drilled
	Earthquakes
	EOR-induced seismicity
	Exreme erosion
	Fault activation
	Future drilling activities
	Glaciation
	Hazardous nature of other gases
	Hydraulic fracturing (EFEP?)
	Hydrothermal activity
	Igneous activity
	Major rock movement
	Metamorphic processes
	Mining and other underground activities
	Monitoring (future)
	Regional uplift and subsidence (e.g. orogenic, isostatic)
	Rock properties - undetected features (e.g. faults, fracture networks, shear zone, etc.)
	Sea-level change
	Seismic pumping
	Seismicity (EXTERNAL)

7.2 Scenario Analysis

Scenarios are designed to address the question "What if……?" Different scenarios are generated by the impact of some external processes on the System being assessed, in this case the Midale reservoir where CO_2 will be stored. Selection of these processes, either individually or in conjunction with one or more processes, will identify the nature of the scenario to be assessed. The first scenario usually investigated examines the expected evolution of the storage system itself. This scenario is called the "Base Scenario." In the context of the Project, the Base Scenario refers to the migration of CO_2 from the 75-pattern of the Weyburn reservoir, both within and beyond the primary formation (Midale Beds) into which the CO_2 was injected.

The Base Scenario developed for the Project includes a number of elements. The main reservoir area is that part of the reservoir which will undergo EOR using injected CO_2. The surrounding geosphere zone is the area within 10 km of the main reservoir area. The time frame being considered for risk analyses starts from the inception of EOR using injected CO_2 and extends out to 5,000 years. The Base Scenario includes the complete stratigraphic column, and the caprock (nominally the Midale Evaporite) may have natural

fractures or discontinuities, but it is assumed that all fractures are isolated or sealed such that caprock integrity is not impaired. The Base Scenario will consider physical trapping features, which have naturally contained the oil/gas within the reservoir. Another major element, the biosphere, extends to a depth of about 300 m below ground surface, and it includes soil, surface water, and the atmosphere and the flora and fauna found within these areas. The Base Scenario includes the presence of all wells found within the system model area. All wells have been deactivated following current standard field abandonment procedures applicable at the time of abandonment. Finally, the Base Scenario includes consideration of, but is not limited to, processes such as hydrodynamics, geochemistry, buoyancy and density driven flow, dissolution of CO_2 in water and residual oil, and pressure-temperature changes occurring within formations. In addition, alternate scenarios, which build on the base scenario definition but are meant to address future possibilities regarding how the system model area may be affected, were also developed and included the following scenarios: 1) Engineering options for EOR. This would include reservoir engineering options exploring the use of larger reservoir pressures for CO_2 injection, where over-pressurization and caprock fractures are possible problems, or employing a water flush at the end of EOR, which may decrease CO_2 storage potential; 2) Well abandonment options. Emphasis would be on the impact of different abandonment strategies and their influence on long-term risk of CO_2 leakage; 3) Impact of salt dissolution. Dissolution and subsidence may lead to development of fractures; 4) Fault activation/re-activation. This could represent a new and fast CO_2 transport pathway and could affect several formations; 5) Tectonic activity. This would include affects on the integrity of bounding seals to contain CO_2; 6) Human intrusion. This scenario would involve intrusion into the reservoir in search for CO_2 or petroleum. One option could be its impact on the uppermost seal in one or more wells. A second option would involve fluid extraction from a shallower resource that could lead to rapid release of CO_2 from CO_2 trapped in formations above the reservoir.

8 DETERMINISTIC/STOCHASTIC MODELING OF THE LONG-TERM MIGRATION OF CO_2

8.2 Description of Approach

The overlying philosophy involved in modeling over long timescales, particularly modeling associated with potential impacts to the environment, has been to adopt an acceptable and adequate approach, with careful recognition of important features, events, and processes and careful attention to the evolution of a realistic, defensible System Model throughout the tenure of the Project. Such a philosophy requires a conservative and robust treatment. A conservative treatment is one in which 'worst case' assumptions are made to construct conceptual models and 'worst case' parameter values are used in the calculations. In a Robust treatment, sensitivity analyses are used to identify controlling parameters – those parameters that have the greatest effect on CO_2 migration. If the results of sensitivity analyses warrant additional investigations, parameter uncertainty can be quantified and a probabilistic assessment carried out.

This conservative and robust treatment makes use of an iterative assessment approach, aimed at obtaining results that are acceptable to as broad an audience as possible. The associated level of effort in achieving a result is represented in Figure 4.8. There is an assumption that there is some exact solution to the modeling, but such a solution is impossible to achieve. Iterative or scoping calculations assist in guiding the modeling effort towards increasingly comprehensive or probabilistic analysis approaches.

At the outset of the Project, a substantial amount of detailed work was initiated within separate research tasks. Not all the detailed results from these tasks were, or could be, incorporated in the long-term assessment of CO_2 migration. The results from these studies were 'abstracted' into the long-term assessment.

8.2 Modeling with an Early Conceptual Model – Early Project Studies

In the early stages of the Project, insufficient geoscience data were available to construct a detailed System Model. Consequently, for early bounding/scoping calculations, an Early Conceptual Model was based on a straightforward treatment of CO_2 migration within the Midale Beds, the horizon of CO_2 injection. As shown in Figure 4.9, the Early Conceptual Model consisted of two parts: 1) the "reservoir," which constituted the EOR area where CO_2 was being injected and oil produced (the 75 pattern area) and 2) "outside the reservoir" is the area within the Midale Beds that would not experience CO_2 injection.

Both areas are partially saturated with hydrocarbons and water. Due to the high concentrations of CO_2 within the reservoir, CO_2 will have a tendency to move out of the reservoir after EOR ceases. The model simulates CO_2 movement under the natural gradient and the gradients left from EOR operations, for up to 5000 years after completion of EOR. ECLIPSE 300 was used to simulate diffusion/dispersion and advection of three components: hydrocarbon, CO_2, and water. Sensitivity analyses of some (key) parameters were also carried out.

The results from these early studies can be summarized as follows: 1) diffusion appears to play a key role in the migration of injected CO_2 out of the reservoir, especially at early times; 2) advection within Midale Beds will be important to the long-term migration of CO_2 injected in the reservoir; 3) salinity has little impact on CO_2 migration; 4) formation properties impact CO_2 migration due to the coupled processes of diffusion and density-driven flow; 5) initial (*i.e.*, at the end of EOR operations) distributions of fluid pressure, composition, and saturation will likely have an impact on CO_2 migration.

8.3 Modeling with an Intermediate Conceptual Model – Mid-Project Studies

As research progressed within the Project, additional data, in particular geoscience data, were utilized to refine the Early Conceptual Model into an Intermediate Conceptual Model. The main concern addressed by the assessment modeling was to evaluate how much lateral migration of CO_2 was possible, given that the Midale Evaporite (caprock) did not have a uniform thickness and, in some places, its thickness was negligible (early geoscience research results). In other words, the risk of the lateral migration of CO_2 reaching thin caprock regions and the potential for leakage in these regions was targeted.
This conceptual model refinement process was an early example of integration efforts among the many research tasks within the Project and the long-term performance assessment studies. The Intermediate Conceptual Model, illustrated in Figure 4.10, was developed based on the following refinements of the Early Conceptual Model: CO_2 migration due to up-dip geology was taken into account due to Theme 1 geoscience research progress; five components were used for the fluid model (light, medium, and heavy hydrocarbon components, plus CO_2 and water) based on early results from Theme 3 research tasks; initial distributions of pressure, compositions, and saturations were obtained from early reservoir simulations of the EOR patterns; modeling of CO_2 migration by dissolution into the aquifer at the bottom of the reservoir.
Three simulations were conducted, one reference case and two sensitivity cases. The reference case used nominal permeability values (10 md for the Midale Marly and 30 md for the Midale Vuggy), low capillary pressure values (< 0.015 bar), an ambient formation flow of 5 cm/yr, and maximum formation dip angles (1° within the EOR region and 1.7° outside the EOR region). The first sensitivity case investigated a maximum permeability case wherein the maximum permeability values found for the Midale Marly (150 md) and the Midale Vuggy (500 md) were used, while all other parameters were the same as the reference case. The second sensitivity case investigated the influence of a Higher Capillary Pressure. This second case used the reference case data, but incorporated a capillary pressure that was increased by two orders of magnitude above the reference case value.

8.3.1 Modeling results for reference and sensitivity cases

Figure 4.11 shows the aqueous CO_2 concentration profiles as a function of distance for different time periods after the end of EOR operations. The results show that the maximum distance from the reservoir boundary at 5,000 years is about 500 m (for reasons of symmetry, only half the width of the reservoir is included and the reservoir boundary is shown at 7,500 m). In terms of mass flux away from the reservoir, Figure 4.12 shows the variation in mass flux as a function of time. Also presented in this diagram, as a function of time, is the average reservoir pressure. The distinctive drop in flux after about 100 years follows the drop in average reservoir pressure. Prior to 100 years, average reservoir pressure is the dominant driving force for CO_2 migration; thereafter, ambient flow becomes dominant.

With respect to the sensitivity studies, Figure 4.13 shows a comparison of migration distances at 5,000 years after the end of EOR operations, represented by concentration profiles. The results show that using the maximum permeability values for the Midale Beds, the migration distance is ~ 1,000 m away from the reservoir, some 500 m further than the Reference Case. On the other hand, a higher capillary pressure (by a factor of 100) results in a shorter migration distance. Figure 4.14 shows corresponding results for the cumulative mass transfer of CO_2 from the reservoir. The change in gradient of each curve corresponds to the change from pressure-dominated to ambient flow-dominated transfer. Maximum permeability values for the Midale Beds result in a cumulative mass transfer of 0.1% (relative to the total amount of injected CO_2 in-place), slightly greater than the Reference Case calculations (~ 0.05%) and higher than the case with higher capillary pressure.

8.3.2 Role of Frobisher Aquifer in CO_2 migration

In order to continue examining the processes that may influence the long-term fate of CO_2 injected into the Midale Beds, downward migration of CO_2 into, and subsequent migration along, the Frobisher aquifer was evaluated. For these simulations, no geochemical interactions were considered. A uniform distribution of CO_2 was assumed as initial conditions (at the end of EOR operations) in the Weyburn field. For these simulations, only a portion of the field (equivalent to a single pattern) was taken as the source. It was assumed, however, that all the CO_2 in this pattern was available for dissolution in the Frobisher aquifer, with subsequent lateral migration.

Figure 4.15 shows the results of the calculations, presented in terms of the aqueous CO_2 concentrations in the Frobisher aquifer at 5,000 years after the end of EOR operations. These results indicate that the CO_2 'plume' has migrated several thousand meters, although the CO_2 concentration at a distance of about 7,500 m from the reservoir/field is in the range of ~ 1.5 to 2.0 g/l.

8.3.3 Summary of conceptual model results

For both the simple and intermediate conceptual models, the focus has been on CO_2 migration away from the reservoir, primarily through lateral migration along the Midale Beds and downward migration of CO_2 into, and subsequent lateral migration in, the Frobisher aquifer. The rationale for focusing on this part of the geosphere at this stage of the project was to evaluate both the maximum extent of lateral migration in the Midale Beds, which helps inform the scale to which geological characterization must be completed in Theme 1 research activities, and the potential for CO_2 migration in the Frobisher aquifer, which also impacts source conditions for artificial pathway modeling.

Integrating the simulation results from these early studies provides the following findings for CO_2 migration over a timescale of 5,000 years: 1) the predicted average migration distance in the Midale Beds may reach 500 m with a possible maximum lateral migration of 1 km if maximum permeability is assumed for the Midale Beds; 2) a total of ~ 0.1 % of total injected CO_2 could migrate out of the reservoir, although this is expected to be a minimum value since the System Models are approximate; 3) if no fast pathways (natural or artificial) are found within the Midale Beds and Frobisher aquifer, the reservoir will be able to store CO_2 for at least 5,000 years; 4) up-dipping reservoir strata slightly increases CO_2 mass transfer from the reservoir; 5) the initial pressure gradient following EOR increases mass transfer of CO_2 from the reservoir; 6) formation water flow rate controls the long-term CO_2 migration in both the Midale Beds and

the Frobisher aquifer; 7) high permeability increases migration distances; therefore, fracture trends, on a large scale, if found, will be important; 8) high capillary pressure retards migration; therefore, the 'worst case' should use a low capillary value.

8.4 Modeling with Final System Model

Modeling of the long-term fate of CO_2 within the final System Model involved an evaluation of the potential for CO_2 to migrate to the environment via both natural and man-made (wellbore) pathways, relying on the technical input from many disciplines, including geology and hydrogeology, geochemistry, geomechanics, reservoir simulation, seismic, and wellbore technology. Systems analysis was conducted to identify credible and potential scenarios of the storage system. The credible scenario, the Base Scenario, is defined as the expected evolution of the Weyburn system (reservoir plus surrounding geosphere plus biosphere). Within this scenario, CO_2 is expected to migrate via natural (geosphere) as well as man-made (abandoned wells) pathways under pressure, density, and concentration gradients.

The final System Model defines the spatial and temporal extents of the long-term fate assessment. The geological component of the System Model was constructed by combining detailed stratigraphic divisions into broader hydrostratigraphic or flow units. The model includes ten aquifers and six aquitards from about 100 m below the Weyburn reservoir to the ground surface or up to about 1800 m of sedimentary rocks. The upper aquifer includes the near surface potable aquifer system that is treated as part of the biosphere and constitutes one end-point for the assessment of local environmental impacts. The following sections present the modeling results for geosphere (no wells) simulations and for abandoned well leakage simulations.

8.4.1 Assessment of geosphere migration

A deterministic treatment to CO_2 migration in the geosphere has been adopted because 1) CO_2 migration depends on the coupled processes associated with a multiphase, multi-component system, and on geological features and hydrogeological conditions; 2) quantitative evaluation of this system requires a detailed model; 3) the available data and chosen modeling tool make it possible to construct a comprehensive model that meets most of the requirements. As for potential leakage through man-made pathways (as discussed in Section 7), the variability of abandoned wells necessitates a stochastic treatment. The primary source of variability for the geosphere modeling comes from the heterogeneity of both the CO_2 distribution and rock properties in the reservoir.

Figure 4.16 shows the geosphere migration model for predicting long-term CO_2 migration in the geosphere. Geological formations in the System Model extent are represented as flow units (aquifers) and barriers (aquitards). Laterally, this migration model extends to approximately 10 km beyond the EOR region, including the reservoir outside the EOR patterns. The migration model accommodates heterogeneous permeability. In the aquifers, the field pressure data, obtained from Theme 1 geoscience research tasks, are linked to the migration model and, together with the permeability distribution, define the flow fields of formation waters. In the Midale Marly and Vuggy layers, where the oil reservoir is located, the oil field data are also mapped to the migration model, defining oil and water saturation distributions in the reservoir.

The geosphere migration model considers three phases (oil, gas, and water) and seven hydrocarbon components including CO_2 and six pseudo hydrocarbon components with molecular weights ranging from 19 to 822. The modified Peng-Robinson equations-of-state are used to dictate fluid phase behavior and component mass partitioning. The migration model uses the default CO_2 solubility data in E300, which originate from an empirical relation valid at low pH values ($<< 7$) and are applicable to most reservoir conditions (Chang *et al*, 1996).

The long-term assessment begins at the end of EOR (in 2034), taking into account the CO_2-in-place, as well as pressure and fluid/component distributions in the field, predicted for the EOR period by reservoir simulation activities in Theme 3. In the central area of the System Model that incorporates the 75 patterns, the starting conditions are provided by the reservoir simulation results at the end of EOR, as described in

the summary of Theme 3 research activities. To avoid upscaling problems, this central area was refined to the same resolution as the reservoir simulation model. To ensure correct fluid-in-place determinations, pore volumes of the central area are made identical to those in the reservoir simulation model. This is a critical step in assuring that the transfer of simulation data from one program (and model) to another is done rigorously.

Various sources have contributed to relative permeability and capillary pressure data for aquifers, aquitards, and reservoir rocks used in the simulation, including field data for the reservoir provided by EnCana. For aquitards, data for consolidated material anhydrite were used (Christian-Frear, 1995). For the caprock, the "entry pressure" effect was included by adjusting the capillary pressure curve using laboratory-measured data (Dong, 2003). Wherever oil phase data were absent, but were needed as input, equations to derive oil relative permeability (Honarpour *et al*., 1982) were used. CO_2 diffusion coefficients are based on values reported in (Grogan *et al.*, 1986).

Key assumptions of the model include: (1) ignoring coupled geochemical reactions that could alter rock transport properties and (2) treating the fractured reservoir rock as an equivalent porous medium with permeability values interpreted from field data as well as history matching results.

The migration is simulated for up to 5000 years after completion of EOR. Figure 4.17 shows gas saturation distributions in the Midale Marly and Vuggy layers at the end of EOR and also at 100 years, 2000 years, and 5000 years after the end of EOR. It can be seen that CO_2-rich (with CO_2 mole fraction up to ~1.0) gas phase movement follows a general up-dip pattern and is trapped below the caprock, forming gas pockets. The gas pockets shrink with time due to loss of CO_2 by dissolution in the moving water. The oil phase also moves up-dip, accompanied by diffusion of hydrocarbon components (excluding CO_2) from the surrounding reservoir into the EOR area where much oil has been produced.

Both oil and gas phases inside the 75 patterns, however, are less mobile than the water phase and are largely confined within, and in the vicinity of, the 75-pattern area. Water movement is driven by pressure gradient during the early depressurization period and subsequently is controlled by the ambient flow field. Groundwater flow through the 75-pattern area picks up CO_2 from less mobile oil and gas phases, carrying dissolved CO_2 laterally outward and also downward into aquifers below the Midale layers, where it will take a geologically-significant time for the water to flow into the biosphere (*i.e*., a potable aquifer). This process accounts for most of the CO_2 removal from the 75 patterns. Once CO_2 is released into aquifers below the reservoir, the aqueous CO_2 would follow the hydrodynamic regime where it will be diluted, sorbed, and/or lost to carbonation reactions.

To summarize, CO_2 migration is controlled by the movement of gas, oil, and water phases and by the chemical distributions of CO_2 among these three phases. The complexities of migration justify the use of E300, or any similar simulators that have the capability to model coupled phase movement and mass partitioning processes with equations of state dictating phase behavior.

Figure 4.18 shows the rates at which CO_2 is removed from the 75-pattern area into the geosphere above, below, and within the Midale reservoir. It can be seen that the mass transfer of CO_2 is affected by the variation in pressure. Early, relatively fast mass transfer can be attributed to the high pressure gradient across the boundary of the EOR region. Mass transfer of CO_2 slows down as the pressure decreases, followed by a change in rate, or a slight increase in the case of lateral CO_2 migration, as the ambient pressure/flow field is restored at about 1000 years. The mass transfer rate generally decreases with time due to decrease in mass transfer driving force (pressure gradients, concentration gradients, *etc*.).

Cumulatively, after 5000 years, the total amount of CO_2 removed from the EOR area is 26.8% of the initial CO_2-in-place at the end of EOR (the CO_2 that is in the 75 patterns at 2034 is ~21 MT). Directionally, the movement of this 26.8% of initial CO_2-in-place can be described as follows: 18.2% of the initial CO_2-in-place is released into the geosphere below the reservoir primarily by hydrodynamic forces; 8.6% of the initial CO_2-in-place ends up in the Midale reservoir outside the EOR area; 0.02% diffuses into the Midale caprock; and no CO_2 enters the potable aquifer system over the 5000-year period.

8.4.2 Assessment of abandoned well leakage

The base scenario (see Section 7.2) defines man-made pathways for CO_2 migration as the existing wells plus those drilled prior to the completion of EOR, all of these abandoned upon completion of EOR. Abandoned wells, although sealed upon abandonment, may provide potential pathways for the injected CO_2 to return to the surface due to degradation of the sealing materials. There are thousands of wells within the System Model area, with most of these wells located outside the 75-pattern area. The geosphere migration results have shown that high CO_2 concentrations in all three phases occur within the 75 patterns, and, hence, the focus area for well leakage assessment is within the 75 patterns. Within the 75 pattern area, there are more than 800 existing wells and the drilling of additional wells may increase that number to over 1000 wells by the end of EOR.

Similar to the System Model, the well assessment model includes three-phases and seven-components, as well as pressure- and density-driven flow accompanied by CO_2 mass partitioning and molecular diffusion. Assessment of potential leakage was tackled using a unit cell approach combined with a stochastic treatment to address spatial variability of reservoir conditions. The unit cell model consists of a single well and a portion of the reservoir, its size (diameter) equal to the average well spacing (240 m) derived from UTM coordinates of all the existing wells in the focused area. Figure 4.19 illustrates the basic geometry for the unit cell model. The key assumptions of this approach include: 1) cement seal degradation corresponding to an increase in permeability from 0.001 mD (initially) to 1 mD at 100 years (Chalaturnyk *et al*, 2003); 2) at 100 years, the casing has completed corroded or corroded to an extent that it no longer acts as a hydraulic barrier; 3) no loss of CO_2 to flow inside the reservoir as well as within the formations surrounding the wellbore; 4) fast transport of CO_2 once it enters the open borehole (*i.e.*, rapid ascent of CO_2 to the surface as gas bubbles). It is considered that these assumptions result in a conservative assessment given the variability and uncertainty of the key parameters used in the model.

Existing data (Yu *et al*., 1993) for fresh concrete show that this material is extremely restrictive to flow (water phase becomes mobile at near unity saturation). The exceedingly high capillary pressure (>20 MPa at near unity water saturation) effectively blocks intrusion of non-aqueous phase fluids. While these properties are valuable to sealing performance, they may not be realistic for aged cement materials. Corresponding data are not available for aged cement, however. In this study, capillary pressure was estimated by combining the capillary pressure drop due to permeability increase using existing data for fresh cement together with a permeability-porosity relationship (Scheidegger, 1974).

The cement was assumed to be water-saturated, initially, and at the hydrostatic pressure of its depth. The initial conditions in the reservoir (Marly and Vuggy horizons) of the unit cell model were extracted from the results in the Midale Marly and Vuggy at 100 years after EOR predicted by the geosphere migration model. Spatial variability of the reservoir conditions was treated stochastically by populating the unit cell model across cells within the 75-pattern area. That is, in each unit cell calculation, the initial conditions of the Midale Marly and Vuggy corresponded to the geosphere results at 100 years for a given grid within the 75 patterns. In this way, the constraints on phase saturations and component concentrations dictated by the EOS can be honoured.

There are 6075 grids belonging to the 75 patterns. Of these grids, 287 grids were selected with a bias towards existing well locations, high CO_2-in-place, and high permeability values. Thus, although the range of CO_2-in-place of the selected grids is similar to that in the grids of the entire center area (75-patterns), the selected grids under-represent the population of low CO_2-in-place, which is a conservative treatment.

The unit cell model was activated for 287 calculations in which saturations, component concentrations, and permeability values in each of the 287 grids were used for individual runs. Since the reservoir pressure at 100 years is nearly hydrostatic, the average pressure in the 75-pattern area was used. The results show a large range in leakage rates; the maximum leakage rate ranges from 0 to 0.016 kg/day, and the time at which leakage reaches a maximum rate also varies. Figure 4.20 shows the 5%, mean, 95%, and maximum leakage rates as a function of time obtained from these (287) runs, along with leakage rates vs. time from selected runs. Further analysis found no apparent correlations between the maximum leakage rate and any one of the parameters in the reservoir surrounding a well. These parameters include horizontal and vertical

permeability, gas saturation, CO_2 gas concentration, *etc*., in both the Midale Marly and Vuggy layers. Some correlation is found between the maximum leakage rate and CO_2 aqueous concentration.

Figure 4.21 shows a scatter plot of the maximum leakage rates from the 287 runs against the total CO_2 mass in water in the corresponding 287 grids. The total CO_2 aqueous mass is the sum of the CO_2 mass in the water fraction of the Midale Marly and Vuggy layers, calculated using the corresponding water saturation, CO_2 aqueous concentration, density, and pore volume of each grid. It can be seen that, in general, the maximum leakage rate is associated with high CO_2 aqueous concentration. Nevertheless, high leakage is associated with high permeability values, high gas saturation, and high CO_2 concentrations in all three phases, while low leakage is associated with low permeability, zero gas saturation, and low CO_2 concentrations. The number of grids with extreme combinations of the key parameters, however, is small (<5% or >95%).

Variability in well leakage is also demonstrated in the cumulative leakage shown in Figure 4.22 as 5%, mean, 95%, and maximum cumulative leakage as a function of time. In general, the stochastic nature of reservoir conditions dictates stochastic behavior of leakage through abandoned wells across the focused area. However, when the cement permeability is low ($\leq$ 1 mD), the ultimate control of leakage lies in the cement permeability. When the cement permeability is higher (*e.g.*, > 10 mD), reservoir properties govern the rate and amount of CO_2 leakage. To confirm this conclusion, a few unit cell model runs were carried out using an increased cement permeability (10 mD), and the results indicated an increase in both the leakage rates and cumulative leakage, but only by a factor of about two.

Combining the *maximum* CO_2 flux through a wellbore (0.016 kg/day), with an estimated 1,000 wells over the 75-pattern area (currently ~875 wells), yields a total cumulative leakage of CO_2 of ~0.03 MT over 5,000 years. This total amount represents ~0.14% of the total CO_2-in-place (21 MT) at the end of EOR. This value is a highly-conservative upper estimate; however, as it assumes that the maximum flux is maintained throughout the 5,000-year period for all wells. Thus, a more representative value is the *mean* cumulative leakage, corresponding to less than 0.001% of the CO_2-in-place at the end of EOR.

9 PROBABILISTIC MODELING OF THE LONG-TERM MIGRATION OF CO_2

To assess long-term risk in complex problems, a methodology called probabilistic risk assessment (PRA) is the industry standard. Process-driven problems over long timeframes such as geological storage of CO_2 are very well suited to analysis using PRA. In the case of the IEA GHG Weyburn CO_2 Monitoring and Storage Project, a unique first generation program called CQUESTRA (CQ-1) was developed and applied to components of the project to elucidate the power of the PRA approach. This program was described in Section 5.2.

9.1 Description of Probabilistic Conceptual Model

The Probabilistic Conceptual Model (PCM) consisted of two components. The first was the Model domain, which defined the geological setting of the model including the Weyburn reservoir. The second component was the Model processes, which includes the physical and chemical processes that define the mass transport and storage of the CO_2 within the PCM domain. The PCM domain is shown schematically in Figure 4.23.

While Section 5.1 described most of the elements of the Model domain, it is repeated below for clarity and to reaffirm its similarity with the deterministic modeling. The Model domain was divided into the same four broad groups of components based on their function within the PCM: 1) the biosphere is the component in which the interaction of CO_2 with potable aquifers, biota, and human health risks will be assessed; 2) the upper geosphere includes all aquifers and aquitards above the reservoir and below the biosphere. The wells penetrate all of these formations, and it is within these upper aquifer formations that storage of CO_2 leaking from the wells can take place; 3) The wells consist of the wellbore, the annulus (at least partially cement filled), an 8 m long cement seal plug and the steel casing; 4) The lower geosphere includes the reservoir (*i.e*. the Midale Formation, which is subdivided into the Marly and Vuggy layers) and

the aquifers and aquitards below the Midale evaporite or cap rock. CO_2 can remain stored within the reservoir or be stored within the lower aquifers.

Local variability in formation porosity, permeability, Darcy flow velocity, *etc*., are all incorporated into probability distribution functions (PDFs) to capture the uncertainty in all of a PCM domain's features and processes. Once the physical PCM domain is fully described, the CQ-1 program quantifies the main driving forces pertinent to the storage of CO_2 in a reservoir. A flow diagram showing the interconnectivity of the PCM domain components with the Model processes is shown in Figure 4.24. Table 4.3 provides an overview of the major processes included in CQ-1 and associated with the Model domain components shown in Figure 4.23.

Table 4.3 Features, Events and Processes relevant to the Weyburn CO_2 Storage System.

Category	WEYBURN FEP TITLE
SYSTEM FEPs	
Rock properties	
	Mechanical properties of rock (including stress field)
	Mineralogy
	Organic matter (solid)
	Presence and nature (properties) of faults / lineaments
	Presence and nature (properties) of fractures
	Cap-rock integrity
Hydrogeological properties	
	Cross-formation flow
	Fluid characteristics of rock
	Geometry and driving force of groundwater flow system
	Groundwater flow (including rate and direction)
	Hydraulic pressure
	Hydrogeological properties of rock
	Pore blockage
	Saline (or fresh) groundwater intrusion
	Transport pathways
Chemical/Geochemical	
	Carbonation
	Colloid generation
	Degradation of borehole seal (cement / concrete)
	Dissolution of minerals/precipitates/organic matter
	Dissolution / exsolution of CO2
	Dissolved organic material
	Groundwater chemistry (basic properties)
	Methanogenesis
	Microbial activity
	Mineral surface processes (including sorption/desorption)
	Precipitation/Coprecipitation/Mineralisation
	Reactive gaseous contaminants
	Redox environment / heterogeneities
	Salinity gradient
CO2 Properties and Transport	
	Advective flow of CO2
	Colloid transport
	Diffusion of CO2
	Dispersion of CO2
	Gas flow
	Source term (CO2 distribution)
	Thermodynamic state of CO2
	Transport of CO2 (including multiphase flow)

Category	WEYBURN FEP TITLE
SYSTEM FEPs (continued)	
Other gas	
	Gas pressure (bulk gas)
	Release and transport of other gases
Geology	
	Seismicity (local)
	Temperature / thermal field
	Uplift and subsidence (local)
Abandoned Wells	
	Annular space (quality / integrity)
	Boreholes - unsealed (extreme case)
	Corrosion of metal casing (abandoned wells)
	Expansion of corrosion products (abandoned well metal casing)
	Incomplete borehole sealing / Early seal failure
	Incomplete records of abandonment / sealing
NON-SYSTEM FEPs	
EFEPs	
	Artificial CO2 mobility controls
	Climate change
	Cross-formation flow (fast pathways)
	Depth of future wells drilled
	Earthquakes
	EOR-induced seismicity
	Exreme erosion
	Fault activation
	Future drilling activities
	Glaciation
	Hazardous nature of other gases
	Hydraulic fracturing (EFEP?)
	Hydrothermal activity
	Igneous activity
	Major rock movement
	Metamorphic processes
	Mining and other underground activities
	Monitoring (future)
	Regional uplift and subsidence (e.g. orogenic, isostatic)
	Rock properties - undetected features
	(e.g. faults, fracture networks, shear zone, etc.)
	Sea-level change
	Seismic pumping
	Seismicity (EXTERNAL)

9.2 Description of Approach

Input to CQ-1 represents the integration of data provided by a number of research providers within the Project and includes reservoir model and simulation results generated in Theme 3 research tasks. Also included are reservoir simulation data abstracted from E300 output runs, hydraulic transport properties for wells, geosphere and reservoir property data generated in Theme 1 research tasks, and geochemical model results generated in Theme 2 research tasks. Process models and data for the PCM come from other tasks within the Project. The following is a summary of process models and/or data and their sources.

The reservoir model and CO_2 inventories are abstracted from GEM® EOR predictions generated in Theme 3 research tasks. The GEM® data at the end of EOR are used as input data for E300 simulations. E300 computes the impact of reservoir depressurization on CO_2 phase inventories and redistribution due to buoyancy. These latter data are then abstracted into CQ-1 as the starting inventory for PRA studies. Reservoir property data used in the PRA study were obtained from Theme 1 research results. In some cases, experimental or field data were not available for some input parameters, and, thus, reliance was placed on "expert RP opinion" for these parameters. Data on CO_2 phase mass fraction, density, viscosity, end-point saturation, and relative permeability in the reservoir are not available; these data were abstracted from the EOR output data from either the GEM® or E300 models, which use Equations of State (EOS) to calculate these properties given the phase composition. Formation data for the intrinsic permeability, porosity, temperature, free-water diffusion constant for dissolved CO_2, aquifer Darcy velocity, and salinity were taken from data obtained from Theme 1 research results.

The well model and data are supplied by tasks described earlier in this discussion of the Theme 4 research area. Currently, the well model consists of cement permeability data for the well annulus and plug as a function of time, well type, and vertical location within the geologic strata. Well cement permeability data are currently abstracted into CQ-1 as a PDF. There is currently no recommended model for corrosion of the steel well casing. A well casing failure time in the form of a PDF is currently used in CQ-1. A well database has been compiled that contains well type and location with the Weyburn reservoir. These latter data have been abstracted into CQ-1 as a PDF that contains information for both well type and frequency of occurrence within the reservoir.

The geosphere data for formations above the reservoir were taken from data obtained from Theme 1 research results and are a combination of limited field data and "expert RP opinion." The model has simplified many of the geological formations by grouping them into 7 aquitards and 6 aquifers, as described in Section 5.1. Table 4.1 provides the formation thickness and depths. The data for aquifer flow velocity, porosity, and salinity were generated in Theme 1 research activities and included the Midale, Jurassic, and Mannville and Newcastle aquifers. These data were abstracted from a larger regional data set to provide better estimates of the near-field velocities and porosities. In addition, "expert RP opinion" was used to provide aquifer flow velocities for the remaining aquifer formations. In order to calculate CO_2 solubilities in formation waters, a vertical temperature gradient of 0.035 $^oC/m$ was used.

The geochemical model includes the impact of geochemistry on CO_2 transport properties, dissolution in the aquifers, and mineralization rates. The main geochemical parameters in CQ-1 are the density of water as a function of temperature, pressure and salinity, the solubility of CO_2 as a function of temperature, pressure, density of water, and salinity, the surface tension of the gas phase in formation water as a function of pressure and temperature, and the rate of mineralization in each formation. Algorithms for calculating the first two parameters (density of water and solubility of CO_2) were provided from Theme 3 geochemistry research tasks.

9.3 Comparison of Deterministic and Probabilistic Risk Analyses

For Phase 1 of the Project, full integration of the deterministic and probabilistic results for a 5000 yr simulation on the final System Model was not achieved. To provide some measure of comparison between the two models, however, a benchmarking study was undertaken in an attempt to validate the methodology adopted for the risk analyses. It is often essential from the standpoint of computational efficiency to develop a simplified PRA approach that captures the major processes taking place during the post-EOR

evolution of the reservoir, but leaves out second-order effect details that do not significantly contribute to assessing risk. To verify the assumptions involved in this simplification process, it is essential to compare the simplified PRA program to a more complex solution technique. The benchmarking process was used to test the PRA program and/or to identify processes that need to be included.

In formulating a benchmarking strategy, it was necessary to select a set of conditions that emphasized features in the current programs that could be compared and to avoid conditions that would emphasize known differences in the programs. The other fundamental condition for this benchmark study was to use the same starting data for the two approaches, where possible. The underlying basis of the study was to simulate the evolution and fate of the CO_2 stored in Pattern 1 in the Phase 1A area of the Project, at the end of a simultaneous but separate water and gas injection EOR recovery strategy. The benchmark case studies were divided into two broad categories designed to examine the benchmarking system models BSM) without the influence of wells and to compare various aspects of the simulation of well behaviour.

9.3.1 Models with no wells present

With no wells or fractures present in the Midale aquitard (*i.e.*, the reservoir cap rock), the only means of CO_2 migration from the reservoir is diffusion upward through the cap rock into the Poplar-Ratcliffe aquifer and diffusion laterally or vertically downward into aquifers adjacent to the Midale (*e.g.*, the Frobisher aquifer). The objective of the "no wells" case study was to compare predicted CO_2 inventories in these adjacent aquifers after a period of 5000 years.

The E300 simulations used in this benchmark study assumed zero Darcy flow within the Midale or in the overlying aquifers or the underlying Frobisher aquifer (as indicated earlier, final System Model simulations with E300 included Darcy flow within all stratigraphic units of the system model). Within CQ-1, it is not possible to run a zero flow case, even for benchmarking simulations. In the simplest terms, CQ-1 was developed using the assumption that Darcy flow was present in all aquifers and that transport from stationary bodies containing CO_2 (*e.g.*, wells) to mobile aqueous phases (*i.e.*, flow within an aquifer) is controlled by a mass transport equation, which is flow rate dependent. This latter analytical equation is not valid for zero Darcy flow; hence, a very low flow must be specified in order to obtain meaningful predictions. Rather than providing predictions at some arbitrarily specified Darcy flow, a series of calculations for a range of low Darcy flow rates were supplied. CQ-1 uses starting CO_2 inventory data supplied by E300, which avoids the need for calculating the impact of the post-EOR reservoir depressurization on CO_2 phase distributions within P1. For this benchmark study, the CO_2 starting inventory data was supplied from E300 for a time 100 years after the end of EOR when pressure equilibration is predicted to be essentially complete.

Calculated CO_2 inventories resulting from migration out of the Weyburn reservoir over the 5000-year period of the no-well case study are summarized for both the Midale and Poplar-Ratcliffe Beds in CQ-1 in Table 4.4. A graphical comparison of these same results is given in Figure 4.25. Given the differences in their modeling methodologies, the agreement between CQ-1 (Darcy velocity of 0.0001 m/a) and E300 is reasonable.

Table 4.4 Overview of Major Processes and Assumptions in the CQ-1 PRA Model.

System Component	Process	Notes
Reservoir	Model of gas phase for prediction of gas cushion area and height.	Cushion area is used to predict the number of intersecting wells. Gas density is used to predict buoyancy forces that control vertical migration.
	Detailed model of buoyancy driven flow to well inlet	Permeability in the Marly M1 layer can control gas phase migration up a leaky well.
	Diffusion and dissolution	These processes control the losses from the reservoir to aquifers below and above the Midale aquitard.
	Equation of State and pressure history are not included in this version	The starting data for CQ-1 calculations is taken at the end of depressurization
Well	Model includes mass transfer through cement annulus and plug.	CQ-1 does not include the time-dependent variation of cement properties. Variations in cement properties are currently handled by sampling during PRA calculations. The onset of plug leakage is defined by a PDF.
	Corrosion time for steel well casing	The long-term failure rate for the steel well casing is currently unknown. Its failure time is defined by a PDF.
	Steady-state model for movement of the gas phase upwards though the cemented annulus around the well bore and dissolution of CO_2 from the annulus to the surrounding formations	The effects of salinity, temperature and pressure are also accounted for.
	Mass transport of CO_2 bubbles in the water-column within the well and dissolution of CO_2 into the surrounding formations through corroded well casings are predicted	Diffusion of the CO_2-saturated water from the well water column through well components and leakage into adjacent aquifers is a significant sequestration process. Rate of bubble rise and mass transport from bubbles in the wellbore is modeled.
Geosphere	Horizontal advection, dispersion and diffusion in aquifers	The steady state advection-dispersion equation is solved to determine loss rate of dissolved CO_2 into formations.
	Mineralization in aquifers	A simple first order mineralization reaction is assumed in CQ-1 at this time in the absence of a more complex geochemical model.
	Diffusion through the Midale aquitard and subsequent transport of dissolved CO_2 in the Ratcliffe aquifer by flowing water	Although the Midale aquitard has a very low permeability and resists advective flow, porosity still allows some vertical diffusion of water-dissolved CO_2.
Biosphere	A CO_2 release rate up the wellbore to the biosphere and a surface flux are calculated	These parameters can be used in a biosphere-related risk analysis.
	A CO_2 release rate to the upper potable aquifer is calculated	The Intertill aquifer is assumed to be representative of a potable aquifer. It is possible to use this release rate in future models to calculate the potential for heavy metal release and other factors related to the quality of potable water.

Table 4.5 CQ-1 data for 100 year starting time – benchmark study

CQ-1	**CO_2 MIGRATION at 5000 years (kg)**		
Darcy Velocity (m/a)	**Midale**	**Poplar**	**Total**
1.00E-07	1.30E+05	3.46E+04	1.65E+05
1.00E-05	1.31E+06	3.46E+05	1.65E+06
1.00E-04	***4.3E+06***	***1.11E+06***	***5.37E+06***
1.00E-03	1.67E+07	4.15E+06	2.09E+07

9.3.2 Models with wells present

This phase of the benchmarking program was intended to compare well-related loss rates from the P1 gas cushion as predicted by the CQ-1 and E300 programs. Unfortunately, the programs and their associated BSM used two different starting conditions so that predicted release rates could not be compared quantitatively. Qualitatively, the differences between the two programs were as would be expected by the differences in their starting conditions and other model parameters. Despite these differences, both programs agreed on the total amount of gas phase released to within an order of magnitude, and both programs predicted that the fractional gas release to the surface was considerably smaller than the fraction dissolved in place. Both programs indicated that the leakage rate to the surface through failed well seals was relatively small in terms of the overall effectiveness of the storage system.

9.4 Pattern 1 Case Study for PRA Approach

Owing to timing issues in completing a full System Model simulation out to 5000 years using the E300 program, the results of which would serve as input to a PRA of the 75-pattern EOR rollout of the Weyburn field, a full PRA study of the 75-pattern area was not completed in Phase 1 of the Project. However, to demonstrate the capability and potential of the PRA methodology and its ability to identify key processes or parameters, a PRA case study using the results from Pattern 1 history matching simulations (Phase 1A area of the Project) was undertaken.

9.4.1 Starting conditions for the Pattern 1 study

A plan view of the layout of Pattern (P1) with its ½-pattern buffer zone, as used by Cuthiell and Law (2003) to model EOR operations using GEM®, is shown in Figure 4.26. The EOR strategy for P1 consisted of "simultaneous but separate water and gas injection" (SSWG). Additional details concerning SSWG patterns can be found in Section 6.1 of Theme 3. E300 calculations for P1 showed that gas from the surrounding cells had displaced the brine followed by gas saturations essentially matching those in the rest of the gas cushion by about 600 years after EOR. Gas cushion inventories at this point in the post-EOR evolution of P1 were selected as the starting condition for the Pattern 1 PRA study.

Figure 4.26 also shows the superposition of the CO_2 gas-phase cushion on the map of P1. The cross sectional area of the gas cushion at the interface between the cushion and the cap rock is calculated directly from gas saturation data supplied by E300. The CO_2 gas-phase inventory was calculated from the sum of the contiguous gas phase inventories in the Marly layers (M1, M3) and the upper Vuggy layer (V1). These inventories totaled 1.27E+08 kg with the CO_2 gas inventory in the M1 layer representing 90% of this total.

CQ-1 requires the maximum gas cushion height and the capillary pressure as input. Neither of these parameters are available from E300 or GEM® input or output files. CQ-1 has built-in functions that allow the user to estimate gas cushion area and height based on gas density, formation porosity, end-point fractional saturation, and capillary pressure. By "history matching" with the above area, estimates of gas cushion height and capillary pressure were obtained.

Due to well positions within P1 and the gas cushion distribution, it was assumed that only one well intersected the gas cushion during the 5000 year simulation. The impact of additional wells intersecting the gas cushion and variations in cushion geometry is examined as part of this PRA study.

9.4.2 CQ-1 case study – deterministic calculations

The case study uses the best estimate of parameter values based on field or laboratory data or expert opinion in this deterministic simulation. This study represents the collective best estimate of the fate of the CO_2 in P1 during the first 5000 years after EOR. In terms of the leakage of well components, lack of an established model for corrosion of the steel casing at the time of the simulation made it difficult to execute a deterministic simulation. For this illustrative case study, it was assumed that the casing failed at (simulation) time = 0 (*viz*. 600 years after EOR) and that the cement plug begins to leak at (simulation) time = 50 years (600 + 50 = 650 years after EOR). The results of this base case deterministic simulation are shown in Figure 4.27.

In this study, 84.1% of the CO_2 Mass-In-Place (MIP) remains in the reservoir and only 0.2% MIP has been released by the well to the biosphere. The remaining CO_2 is stored in the geosphere. Of the starting CO_2 MIP, 11.9% is stored in the lower geosphere aquifers and 3.8% is stored in the six aquifers in the upper geosphere. The amount stored in the upper geosphere is a function of the leakage characteristics of the well. During the first 50 years of the simulation, the transport of the CO_2 to the upper geosphere is through the cement annulus. All of the CO_2 passing up the annulus during the first 50 years of the simulation is dissolved in the upper aquifers, and there is no release to the biosphere, as shown in Figure 4.27. At 50 years, there is an increase in the rate of dissolved CO_2 storage in the upper aquifers and there begins to be some release of the CO_2 up the wellbore to the biosphere. These latter changes in rates coincide with the start of leakage of the well cement plug. Because the casing was assumed to have failed at simulation time = 0, the CO_2 in the wellbore can be transported horizontally by diffusion from the wellbore through the corroded casing and the annulus to the aquifers surrounding the well.

9.4.3 CQ-1 case study – probabilistic study

A Monte Carlo simulation method was used to sample the PDF's for CQ-1 input parameters. A statistical summary of 4000 different CQ-1 simulations is presented in the following sections.

9.4.3.1 Releases to the biosphere

Figure 4.28 is a trend chart showing the fractional MIP release of CO_2 to the biosphere as a function of simulation time. The solid black line shows that the mean fractional release at 5000 years is about 0.002 (0.2%) of the starting MIP. The 70% (green) and 95% (blue) certainty levels (confidence intervals) are skewed about the mean. The reason for this is also illustrated in Figure 4.28 as a frequency histogram for the fractional MIP release of CO_2 to the biosphere at a simulation time of 5000 years. Both the mean and median fractional releases are shown. Although the mean is 0.002, the median value is 0.0008 (0.08%) – more than a factor of 2 lower than the mean. This median indicates that 50% of the simulations had a release to the biosphere lower than 0.08% of the MIP. The histogram indicates that the number of parameter combinations that produce higher releases decreases sharply with the size of the fractional release.

A simplified sensitivity plot showing the top four parameters at simulation times of 500, 1500, and 5000 years is given in Figure 4.29. Of the four parameters, two are positively correlated with the fractional release (Marly permeability and time of casing failure) and two are negatively correlated (time to leakage of wellbore and Mannville Darcy velocity). The parameter with the highest sensitivity is the Marly permeability.

The flow rate of the CO_2 from the gas cushion to the wellbore is controlled by the Marly permeability; hence, the fractional release to the biosphere is dominated by this parameter throughout the whole simulation. Note that the fourth parameter, casing failure time, refers to the time of the onset of the cement plug (used to abandon a wellbore) leakage and not to structural casing failure.

9.4.3.2 Fraction of CO_2 stored in aquifers

Aquifers in the upper and lower geosphere portions of the System Model play similar, but different roles with respect to CO_2 storage. Within the reservoir, storage can reduce the inventory of CO_2 before it can escape vertically by diffusion through the caprock or by means of leakage through wells or fracture systems. Aquifers above the caprock can mediate any vertical migration of CO_2. The trend plot in Figure 4.30 indicates that at 5000 years, the mean inventory of CO_2 stored in both the upper and lower aquifers is about 23% of the total starting inventory.

The 95% confidence interval (blue) bands give a range between 6% and 34% of the starting inventory – depending on the combination of parameters used in the simulation. The CO_2 inventory stored in each aquifer at the end of any interval of time reflects not only the relative effectiveness of the aquifer to store CO_2, but also the integrated effect of changes in the leakage rate from the various well components and other competing processes within the System Model. These competing processes include the size and rate of rise of CO_2 bubbles within the wellbore, the mass transfer rate of CO_2 from the bubbles to the surrounding fluid, and the gas flow rate through the competing annular and wellbore pathways. A post-processing algorithm in CQ-1 can be used to generate concentration gradient plots for the dissolved CO_2 in each aquifer surrounding the well.

Figure 4.31 shows the dissolved CO_2 in each of the six aquifers at 100 years of simulation time. With the exception of the Ratcliffe aquifer, these plots show that there is significant displacement and dilution of the CO_2 concentration gradient plume downstream of the well when advection is the dominant transport process. Figure 4.31 illustrates that lateral displacement is restricted to several meters near the well, but extension of the axes of the plot shown in Figure 4.31 would show that this broadens to 10 to 20 meters when the plume has reached a point hundreds of meters downstream.

10 GEOMECHANICAL PERFORMANCE ASSESSMENTS

Geomechanical response of the reservoir and the bounding seals to CO_2 injection may influence the hydraulic integrity of the bounding seals and may provide a mechanism to influence the hydraulic integrity of the wells. As well, alternative scenarios such as future salt dissolution processes can impart geomechanical effects (stress change and deformations) upon the storage environment and may impact the long-term integrity of CO_2 storage. To assist in the performance assessment studies of this project, geomechanical investigations on reservoir response to historical production and waterflooding, salt dissolution, fracture characterization, and constitutive behaviour of the anhydrite caprock were undertaken. The results of these investigations are discussed below.

10.1 Mechanical Earth Model

In order to perform geomechanical analyses, a mechanical earth model (geomechanical model) must be developed by gathering information from geological models – Theme 1 – as well as laboratory testing, certain geophysical techniques such as dipole shear sonic logs, and direct or indirect *in situ* stress measurements.

The Weyburn field is a naturally fractured reservoir with a medium to low permeability matrix. Therefore, fractures are a main control in production and the design and/or operation of any EOR process, including CO_2 flooding. These factors have led to a large number of fracture studies in the Weyburn field (Beliveau, 1991, and Bunge, 2000), and this information has been integrated for use in addressing geomechanical concerns with the caprock.

It is difficult to integrate the results of all these studies into a unified model of fracture spacing or densities for each formation, considering that two slightly different fields were studied, with different techniques, and even different assumptions about what a fracture is (some studies only considered open ones, others both open and sealed). However, it is clear that the Intershoal Vuggy is the most fractured of the formations, followed by the Marly, and finally the Shoal Vuggy. In addition, most of the fractures have a

short length, with an average of 30 cm in both fields, with only a very small percentage over 1 m. No fractures were observed crossing from the Vuggy to the Marly. The dominant direction of fracturing is NE-SW, and most of the fractures are vertical to sub-vertical.

The Williston Basin is currently not a tectonically active region, and the most disruptive active events during its depositional history were salt dissolution in the Prairie evaporites, erosive phenomena at different times, and glaciation. *In situ* stresses in the Weyburn field have not been measured thus far, and there is no clear evidence of breakouts and/or tensional failures during drilling activities in the history of the field. Therefore establishing the state of stress in the field is difficult.

The vertical stress can be obtained by integrating density logs, and it was found to be around 33 to 34 MPa. Mud density employed during drilling was in the order of 1.5 g/cm^3 and, for a depth of 1500 m, translates to a bottomhole static pressure of 22.5 MPa. Because of the lack of problems such as lost circulation during drilling, it is possible to say that 22.5 MPa may be a very low bound for the minimum *in situ* stress.

Finally, a simple geomechanical model was built with the assistance of Saskatchewan Industry and Resources, which included salt dissolution and the erosive event at the end of the Devonian and the Mississippian. The thickness of deposits removed during the erosive events were assumed to be 50 m in the Devonian and 200m in the Mississippian. This model showed that salt dissolution has probably not influenced the *in situ* stresses in Phase 1A of the Weyburn field, but may have altered the stress state in regions of the field closer to the salt dissolution area. Figure 4.32 illustrates the variation in the ratio of the horizontal to vertical effective stresses during these events.

Because of the lack of structural disturbance and relatively flat-lying character of the strata in this basin, it is reasonable to assume that the vertical stress is one of the principal stresses. Because of the direction of the dominant fractures in the reservoir (NE-SW), and the verticality of the fractures, it is likely that the other two principal stresses have a NE-SW direction for the maximum and NW-SE for the minimum. It is estimated that K_o lies between 1.0 and 1.5.

10.2 Fractures in Caprock

The presence of fractures inside the reservoir is well documented, where the presence of a NE-SW trending set controls the flow, but there is also a secondary set in the NW-SE direction. In order to gain confidence in the caprock integrity, it is necessary to understand the mechanisms that lead to the creation of these fractures. Although there has not been complete agreement to the causes of the fracturing, it is generally believed the fractures have a tectonic origin. Tectonic activity induced a change in *in situ* stresses from a fairly uniform *in situ* stress of state in a circular Williston Basin by early Mississippian times to a dominant compressive force in the WSW-ENE direction across the present-day elliptic basin (Redly, 1998). These stress changes can lead to tensional failure and are accompanied by rotation and dragging of pre-existing structures (Redly, 1998). Evidence of widespread fracturing in the basin occurs not only in the Weyburn (Whittaker and Rostron, 2003; Burrowes, 2001; Bunge, 2000) and Midale fields (Beliveau *et al*. 1991), but in the Little Knife field (Narr and Burruss, 1984), and in sediments from the Late Cretaceous to Late Pleistocene in Saskatchewan, eastern Montana, and western North Dakota (Stauffer and Gendzwill, 1987).

Such a mechanism of fracturing must have lead to widespread fracturing in the basin, with fracture densities controlled by tensional strength of the rock and local variations of *in situ* stresses. Nevertheless, plastic materials like shales or salts would have self-healed by creep, and a large number of fractures would have been closed by mineralization. Paleomagnetic studies (Cioppa, 2003) showed how there was hydraulic communication between the oil-bearing beds and the Watrous Formation around the late Cretaceous or early Tertiary, while the fractures in Little Knife are dated as post-Mesozoic (Narr and Burruss, 1984). Therefore, there is evidence of fracture formation and paleoflow from oil bearing beds around the same time that tectonic changes were occurring in the basin. However, there is no evidence of recent flow from the oil bearing beds into upper formations, and there is no evidence of conductive fractures in the caprock from any fracture study, repeat formation tests (RFT), or any overpressuring in the aquifers below the Watrous Formation, so it is possible to state with reasonable confidence that the caprock was a competent bounding seal at the time production began in the field in the late 1950s.

10.3 Influence of Historical Injection/production in Weyburn Field

Exploitation and production of an oil field may threaten the hydraulic integrity of its caprock through geomechanical phenomenon such as deformation, hydraulic fracturing, and shear failure. Therefore a geomechanical analysis was carried out using the mechanical earth model for Weyburn, described above, and the reservoir pressures extracted from a history match analysis of pre-CO_2 production. The analysis showed that the caprock and the reservoir have maintained their integrity, despite the aggressive exploitation and production of the field, due to the competence of the formations that make up the system. In addition, the large stiffness of the reservoir makes the displacements uniform throughout the stratigraphic column. This also appears to indicate that the likelihood of affecting the mechanical integrity of wellbores from formation displacements is low.

Given the lack of evidence of existing conductive features and the minor influence of historical injection/production on caprock integrity, the Midale Evaporite (caprock) can be treated as a competent bounding seal at the time CO_2 injection began in September, 2000.

10.4 Impact of High CO_2 Injection Pressures

To investigate the influence of elevated CO_2 injection pressures on caprock performance, a geomechanical analysis was performed wherein injection pressures were maximized "synthetically." The synthetic injection pressures were generated by scaling the historical waterflood injection pressure record, illustrated in Figure 4.33. Scaling involved maintaining the relative position of the points within the pressure record, but proportionally increasing their magnitude in order to produce a synthetic pressure record. The modeling indicated that hydraulic fracturing, as opposed to shear failure, will likely be the mechanism that will control the maximum permissible injection pressure while optimizing the volume of CO_2 that can be stored. This implies that once EOR activities cease, field operators may need to monitor injection pressures closely to maximize the stored volume through uniform pressurization of the field.

10.5 Influence of Ongoing Salt Dissolution Processes

Once pressure decays inside the reservoir to the original *in situ* pressure, flow will be density driven and the likelihood of creating or reactivating conductive features in the caprock will be small. Moreover, natural long-term hydraulic gradients are low, and, thus, up-dip fluid driving forces are weak and/or directed inward toward the reservoir. However, there can be events or processes that may affect the long-term stability of the caprock, such as tectonic activity or, in the case of Weyburn, salt dissolution processes. Geomechanical analyses exploring the impact of salt dissolution provide indications that the area of existing dissolution of the underlying salt formations will have to advance to within a kilometre of the reservoir to threaten the hydraulic integrity of the bounding seal units, an event that will not occur within the time-frame of the predictive models.

10.6 Hydro-Geomechanical Properties of Bounding Seals

In order to establish more accurately the geomechanical and hydraulic properties of the Midale Evaporite, a laboratory testing program including mechanical testing in the form of unconfined compression and triaxial compression tests, cyclic triaxial loading, and permeability measures before shearing, while shearing, and in one test, permeability after shearing was completed.

The unconfined compression test (vertically loaded specimens with no lateral confinement) resulted in brittle failure, which was characterized by vertical failure planes. The specimen had an unconfined compressive strength of 20.5 MPa with a Young modulus of 21.5 GPa. Two monotonic triaxial compression tests were carried out at confining pressures of 8 and 30 MPa.

At a confining stress of 8 MPa, the specimen exhibited brittle failure behaviour. The sample developed a clear shear plane, the result of the coalescence of microfractures throughout the sample. The sample failed at a maximum deviatoric stress of 30.5 MPa, and its Young modulus was 12.9 GPa. Once the sample had failed, permeability was measured through the shear plane. For well-defined failure planes, it is expected the permeability will be a function of the effective confining stress. However, the enhancement in permeability was very low because the plane was very rough, some gouge developed, and, apparently, the contact area remained intact.

The sample tested at 30 MPa confining stress unfortunately could not be failed because of limitations in the equipment available. The sample exhibited elastic behaviour throughout the test. The measured Young's modulus was 12.3 MPa. Similarly, no change in permeability or specific storage occurred. The permeability of the intact specimen was on the order of 10^{-20} m^2 (~ 10^{-8} Darcy).

Finally, a cyclic-loading triaxial test was carried out at 3 MPa confining stress, with the purpose of inducing gradual damage to the sample. These results are illustrated in Figure 4.34. Plastic strains accumulated throughout the test and the evolution of elastic properties due to cycling (softening) provided clear evidence of mechanical damage occurring in the sample. However, the values tended towards a constant value, indicating that the rate of induced damage was decreasing with load cycles. Permeability was monitored during the test, and it showed that permeability increased approximately one order of magnitude from 10^{-19} m^2 to 10^{-18} m^2 (10^{-7} to 10^{-6} Darcy) due to damage resulting from the cyclic loading. It appears from this test that damage of the sample in the pre-failure range does not affect significantly the hydraulic properties of the anhydrite, which has positive implications inside a reservoir that has been exploited, stimulated, and produced for long time periods, such as the Weyburn reservoir. Table 4.5 summarizes the result obtained from the mechanical tests carried out on Midale Evaporite specimens.

Table 4.5. Summary of geomechanical tests carried out in Midale Evaporites

Test No.	Well	σ_3 (MPa)	E (GPa)	σ_f (MPa)	ε_f (%)
1	-	0	21.5	20.5	0.40
2	8-13-006-14W2	3	12.0	-	-
3	8-13-006-14W2	8	12.9	30.6	0.30
4	-	30	12.3	-	

Legend: σ_3 = confining stress, E = Young's Modulus, σ_f = net axial stress at failure, ε_f = axial strain at failure

10.7 Mineralogy Testing of Caprock

Midale Evaporite samples available for geomechanical and hydraulic testing were analyzed chemically using X-ray Fluorescence (sulfates were determined using UniQuant method) and are provided in Table 4.6. The results showed large heterogeneity in the mineralogical content of different samples, even from the same well.

Table 4.6 Mineralogical Components of Different Midale Evaporite Samples.

	Test No. 1		Test No. 2		Test No. 3		Test No. 4	
Well	8-13-006-14W2		8-13-006-14W2		15-11-006-14W2		Unknown	
Depth	1392.32 -1393.24		1399.03 -1400.25		1418 -1420		Unknown	
Interpreted Mineralogical Content (%)								
Minerals	Dolomite	9.43	Dolomite	0.00	Dolomite	21.55	Dolomite	39.80
	Fe(OH)3	0.21	Fe(OH)3	0.04	Fe(OH)3	0.25	Fe(OH)3	0.54
	Kaolinite	1.44	Kaolinite	0.00	Kaolinite	1.67	Kaolinite	2.60
	Quartz	1.02	Quartz	0.00	Quartz	0.20	Plagi oclase	1.35
	Calcite	0.00	Gypsum	3.01	Gypsum	15.85	Quartz	7.18
	Anhydrite	81.48	Calcite	0.00	Calcite	0.00	Gypsum	15.06
			Anhydrite	92.08	Anhydrite	59.19	Calcite	2.39
							Anhydrite	29.57
	Total	93.58	Total	95.13	Total	98.72	Total	98.49
X-Ray Fluorescence (mass fraction)								
Oxides	SiO2	1.69	SiO2	0.00	SiO2	0.98	SiO2	9.32
	TiO2	0.01	TiO2	0.00	TiO2	0.00	TiO2	0.11
	Al2O3	0.57	Al2O3	0.48	Al2O3	0.66	Al2O3	1.29
	Fe2O3	0.16	Fe2O3	0.03	Fe2O3	0.19	Fe2O3	0.40
	MgO	2.06	MgO	0.00	MgO	5.10	MgO	8.70
	CaO	36.43	CaO	38.91	CaO	36.10	CaO	30.53
	Na2O	0.00	Na2O	0.00	Na2O	0.00	Na2O	0.16
	K2O	0.00	K2O	0.00	K2O	0.00	K2O	0.00
	P2O5	0.00	P2O5	0.00	P2O5	0.00	P2O5	0.00
	SO3	53.24	SO3	59.55	SO3	42.18	SO3	24.39
	LOI	5.24	LOI	0.64	LOI	13.90	LOI	23.70

11 Health, Environment and Safety Assessments

While the primary effort for Phase 1 of the Project was risk analyses with a focus on performance assessment, a preliminary study was undertaken to determine what may be considered an 'acceptable limit' for geosphere flux, based on a consideration of one type of health, environment, and safety (HSE) impact (Stenhouse *et al.*, 2004), namely, an increase in CO_2 concentration of indoor air as a result of CO_2 leaking directly from the subsurface into a dwelling. Additional consideration of a change in water chemistry of a potable aquifer as a result of direct CO_2 leakage into a (subsurface) aquifer may be considered another type of health, environment, and safety impact. However, only potential CO_2 concentrations in indoor air from a specified, 'nominal' geosphere flux were considered. Then, based on what is regarded as an 'acceptable CO_2 concentration' for indoor air, the corresponding limiting geosphere flux can be calculated.

11.1 CO_2 Leakage Issues for Indoor Air CO_2 Concentrations

The intention has not been to carry out detailed modeling of CO_2 movement or exchange within the biosphere. Models exist to follow CO_2 movement within the carbon cycle (Foley *et al.*, 1996), and one or more subsets of these models could be used to follow the key movements of CO_2 once it reaches the biosphere. More specifically, detailed modeling of CO_2 movement within the unsaturated zone of the biosphere has been performed by Altevogt and Celia (2002) and Oldenburg and Unger (2003). However, scoping-type calculations were considered sufficient for this stage of the HSE component of the long-term assessment. More detailed modeling may be warranted for future study if the implications of the scoping calculations are not definitive when integrated with the results of CO_2 migration modeling in the geosphere.
Increased CO_2 Concentration of Indoor Air from Point Source

The CO_2 concentration in indoor air may increase as a result of CO_2 leakage from the geosphere directly into a dwelling via a crack in the basement or foundations. Here, the source of leakage is considered as a point source, where the leaking CO_2 is localized and migrates vertically upwards. Figure 4.35 shows a schematic diagram of this geometry.

Under such circumstances, and, based on an analogous equation for determining indoor concentration of a hazardous gas based on an incoming gas flux (Grogan *et al.*, 1992), the CO_2 concentration in indoor air is given by the following equation:

$$C_{CO_2} = 100 \bullet \frac{\chi_{CO_2} A_{point\ source}}{\lambda_v V_{house}} \qquad (1)$$

where C_{CO2} = concentration of CO_2 in indoor air [%];

χ_{CO2} = flux of CO_2 released from geosphere [$m^3\ m^{-2}\ y^{-1}$];

$A_{point\ source}$ = area of source of leakage. *i.e.* wellbore [m^2][1];

λ_υ = ventilation rate within dwelling [air exchanges y^{-1}]; the frequency at which a volume of air equal to that in a dwelling, is replaced by outdoor air.

V_{house} = volume of dwelling [m^3]

Equation (1), above, is considered robust for this particular case, since it assumes that all the CO_2 that is leaking from a failed wellbore enters a dwelling via the upper soil layer, with no mass transport resistance or attenuation. In this respect, the calculation can be considered bounding for this type of source.

Wellbore data compiled as part of the performance assessment research tasks yields an average wellbore diameter of 228 mm, equivalent to a value of $4.08 \bullet 10^{-2}$ m^2 for $A_{point\ source}$. From previous assessment work carried out in Canada (Kozak *et al.*, 2000), the following values have been used for the non-CO_2 parameters above, *viz.*

λ_v = 8800 y^{-1} (~ 1 air exchange $hour^{-1}$) (UNSCEAR, 1988);

V_{house} = 250 m^3 (UNSCEAR, 1988).

The volume of a house corresponds to a single-storey dwelling. Based on the above equation and assumptions, and using the above parameter values, a 'nominal' CO_2 geosphere flux of 1 $m^3\ m^{-2}\ y^{-1}$ yields an indoor CO_2 concentration of $1.9 \bullet 10^{-6}$ %.

11.2 Acceptable Indoor Air Concentrations of CO_2 - Specific Recommendations

Several detailed studies have been conducted on the health/safety effects of elevated levels of CO_2 in indoor air. Firstly, as a reference basis, the U.S. National Institute for Occupational Safety and Health has issued Occupational Exposure Standards for CO_2 in the same way as for other chemicals. In Table 4.7, the Recommended Exposure Limits (REL), based on a time-weighted average (TWA), are given for CO_2 concentration over a 10-hour workday during a 40-hour week. The term "STEL" refers to a Short-Term Exposure Limit, which is a 15-minute time-weighted average CO_2 concentration that should not be exceeded at any time. Finally, "IDLH" signifies Immediately Dangerous to Life or Health concentrations.

[1] In the original citation (Grogan *et al*., 1992), 'A_{source}' refers to 'A_{house},' *i.e.* area of dwelling situated directly over the release/leakage point. In this case, however, the area of leakage from the surface is greater than the area of a dwelling. Here, in the particular Weyburn case, the leakage point is considered to be a failed wellbore, with cross-sectional area significantly (orders of magnitude) less than that of a dwelling. It is assumed that only one wellbore contributes to the CO_2 influx to a single dwelling.

Table 4.7 U.S. Occupational Exposure Standards (National Institute for Occupational Safety and Health, 1997).

	CO_2 concentration (ppm; %)	Circumstances
REL*	5,000 ppm (0.5%)	TWA*, 10-hour day, 40-hour week
STEL*	30,000 ppm (3%)	15-minute TWA
IDLH*	40,000 ppm (4%)	Immediately dangerous to life/health

NOTE: REL = recommended exposure limits; STEL = short-term exposure limit; IDLH = immediately dangerous to life and health. TWA = time-weighted average. See text for additional discussion.

Clearly, the CO_2 concentration applicable to REL is most relevant to an acceptable indoor CO_2 concentration, although applicable to a working day. More restrictive requirements might be expected for a domestic building, where people may spend a longer time indoors (longer than 10 hours a day, or 40 hours per week). For example, infants and children spend, on average, 85% to 95% of their time indoors (Samet *et al.*, 1993). The corresponding value for a limiting CO_2 concentration in a home for someone who remains there for 24 hours per day would be approximately half the workday value.

Health Canada (1989) quotes an "acceptable long-term exposure range (ALTER) for CO_2 in residential indoor air" of ≤ 3,500 ppm (≤ 0.35%). ALTER is defined as "that concentration range to which it is believed from existing information that a person may be exposed over a lifetime without undue risk to health." In making its recommendation, Health Canada attempted to take into account the sensitivity of particular groups of people, such as those with incomplete development (children), or deterioration of physiological processes. The particular vulnerability of children is recognised.

In other studies of the effects of indoor air CO_2 concentrations, Snodgrass (1992) notes that infants and children breathe more air than adults relative to their body size. Consequently, infants and children are more susceptible to respiratory exposures. Rice (2003) concluded, from a review of studies of health impacts from elevated CO_2 concentrations, that prolonged exposure, even to concentrations ≤ 1%, could significantly affect health in the general population.

Indoor Air Concentrations of CO_2 – Recommended Value Adopted for This Study

Based on the discussion above, including the recommendations of NIOSH (1997) and Health Canada (1989), and the conclusions of Rice (2003) and Snodgrass (1992), a CO_2 concentration of 0.35% in air has been used here as a recommended *acceptable indoor air concentration of CO_2*, for long-term exposure for assessment purposes. Using this value of 0.35% for CO_2 in Equation (1), the corresponding limiting flux of CO_2 from the geosphere to the biosphere, *in the context of indoor air concentration*, is $2.4 \bullet 10^4$ m^3 m^{-2} y^{-1}, assuming a ventilation rate of 1140 air exchanges y^{-1} (based on Shaw, 1987). For comparison with numbers quoted below, this annual flux is equivalent to a daily flux of $\sim 1.3 \bullet 10^5$ g m^{-2} d^{-1}.

11.3 Background CO_2 Flux from Soil Gas Studies at Weyburn

Several series of soil gas measurements have been made at Weyburn, allowing the opportunity to determine a 'background flux' for CO_2 (from soil) in the Weyburn field. Thus, Riding (2003) cites a measured CO_2 flux of 12.7 g m^{-2} d^{-1} in 2002 and of 65.8 g m^{-2} d^{-1} in July, 2001. Clearly, in the context of these data, the 'acceptable' geosphere CO_2 flux calculated to produce an indoor air concentration of 0.35% from a wellbore source is significantly greater than background.

Diffuse Geosphere Source - More Restrictive Geosphere Flux of CO_2

The 'acceptable' geosphere flux of CO_2 calculated above in the context of a wellbore source is relatively large because the flux occurs across a small area only – the cross-sectional area of a wellbore. For a more diffuse geosphere flux, over an area greater than the area of the house, the corresponding limiting

geosphere flux in the context of indoor air CO_2 concentration would be proportionately smaller, equivalent to ~ 35 g m^{-2} d^{-1}, more in the range of the measured background CO_2 flux. The origin of such a diffuse source could be a subsurface fault of fracture zone, but the likelihood of resistance to mass transport for such a diffuse source is significantly greater than for a wellbore source.

12 CONCLUSIONS AND RECOMMENDATIONS FOR FUTURE WORK

12.1 Conclusions

Performance assessment has been applied as the initial phase of an overall risk assessment process to evaluate the long-term fate of CO_2 injected into the Weyburn reservoir. Its role within Phase 1 of the Project was to identify the risks associated with geological storage and assess the ability of the Weyburn reservoir to securely store CO_2. Assessment of the complex natural system of the Weyburn reservoir and the CO_2-EOR process was managed through application of a rigorous and formal systems analysis approach.

Compositional reservoir simulations supporting early performance assessment studies were conducted for a time period of 5000 years, starting from the end of EOR, and were conducted to provide an initial understanding of CO_2 migration – the process and parameters that may be important to modeling its long-term fate. These early studies highlighted the importance of processes such as CO_2 diffusion in the oil phase, phase saturation distribution at the end of EOR, groundwater velocities within the reservoir zone, and the strong interplay between the coupled processes of pressure-driven flow, density-driven flow, and diffusion.

Deterministic and stochastic approaches were adopted to assess the fate of CO_2 within the geosphere and the man-made pathways (abandoned wellbores), respectively. Cumulatively, after 5000 years, the total amount of CO_2 removed from the EOR area is 26.8% (~ 5.6 MT) of the initial 21 MT CO_2-in-place at the end of EOR, of which, 18.2% (~3.8 MT) moves into the geosphere below the reservoir, 8.6% (~1.8 MT) migrates laterally in the Midale reservoir outside the EOR area, and 0.02% (~ $88 \cdot 10^3$ T) moves to the geosphere above the reservoir; no CO_2 enters the potable aquifer system over the 5000-yr period.

For the abandoned well leakage assessment, the estimated maximum cumulative leakage of CO_2 for an estimated 1,000 wells was ~0.03 MT or 0.14% of the total CO_2-in-place at the end of EOR over the 5,000 year period. The mean cumulative leakage was estimated to be less than 0.001% of the CO_2-in-place at the end of EOR.

In addition to deterministic/stochastic approaches to performance assessment simulations, probabilistic risk assessment techniques were pursued to investigate the potential application of these methods for geological storage projects. A full probabilistic risk analysis study of the 75-pattern area was not completed in Phase 1 of the Project. However, to demonstrate the capability and potential of the probabilistic risk assessment methodology and its ability to identify key processes or parameters, a benchmarking and focused case study using the results from a single pattern reservoir simulation was undertaken.

Benchmarking results showed that despite the differences in numerical/analytical approaches, the reservoir simulator and probabilistic program generally agreed on the total amount of gas phase released, that the fractional gas release to the surface was considerably smaller than the fraction dissolved in place, and that the leakage rate to the surface through failed well seals was relatively small in terms of the overall effectiveness of the storage system. For the case study, 4000 parameter combinations were evaluated and the results indicated that over 5000 years, the average release of CO_2 to the biosphere was 0.2% of initial CO_2-in-place with a 95% confidence interval range of 0.005% to 1.3% of initial CO_2-in-place. The average CO_2 released to the geosphere surrounding the reservoir was 16% of initial CO_2-in-place with a 95% confidence interval range of 6% to 34% of initial CO_2-in-place. This modeling predicts that there is a 95%

probability that 98.7% to 99.5% of the initial CO_2-in-place will remain stored in the geosphere for 5000 years.

Cement degradation models incorporating sulphate attack, mechanical fatigue, carbonation, and leaching have been used to estimate wellbore cement permeabilities of approximately $1x10^{-16}$ m^2 (10^{-4} Darcy) for most well types. For historical injection and production pressures within aging wellbores, modeling has predicted minimal impact on the sealing capability of the wellbores over the life of the EOR project. Geomechanical performance assessments have shown that the integrity of the bounding seals are maintained throughout the historical injection/production period preceding CO_2 injection, they maintain their hydraulic integrity given the current CO_2 injection pressures, and future salt dissolution processes will probably have minimal influence on their integrity. Geomechanical testing on the bounding seals confirm the strength and low permeability. Permeability for the anhydrite caprock was determined to be in the range of 10^{-19} to 10^{-20} m^2 (10^{-7} to 10^{-8} Darcy).

All performance assessment studies conducted within Phase 1 of the Project have shown that the geological setting at the Weyburn field is highly suitable for long-term subsurface storage of CO_2. These studies have highlighted the significant capacity of the geosphere region surrounding the reservoir to effectively store CO_2 and prevent its migration to the biosphere.

12.2 Recommendations for Future Research

Areas of potential future research identified from Theme 4 research activities include: assessing the validity and accuracy of upscaling, especially over the long time frames required for risk assessment; determining the degradation characteristics of well construction materials (cement and casing), including abandoned well sealing materials; to develop a statistical database on well sealing degradation rates and annulus cement quality; establishing the relationship between caprock topography, a primary control on hydrostratigraphic trapping mechanisms, and CO_2 leakage predictions through wellbores; quantifying the upper aquitard/aquifer characteristics and aquifer flow rates, especially near the wellbore; fully exploiting the power of risk assessment in determining the ability of the Weyburn reservoir to securely store CO_2, future by refining and auditing the input data for key System Model parameters (*e.g.*, Midale caprock capillary pressure or cement relative permeability curves), by including geochemical reactions within the model used for risk analysis and by revising and, most importantly, conducting field verification of wellbore transport models using well testing techniques or downhole cement core retrieval; evolving the base scenario from performance assessment to risk assessment, wherein both probability of an occurrence and the consequence are quantified; completing the risk assessment of the alternative scenarios; developing a verified probabilistic risk assessment model that contains the relevant physics to evaluate geological storage; assessing whether CO_2-EOR processes may influence the hydraulic conductivity of the fault found within the System Model; investigating the impact of temperature changes resulting from the injection of CO_2 on wellbore transport properties, reservoir behavior, and the integrity of the bounding seals; increasing understanding of the geomechanical consequences of geological phenomena such as salt dissolution, "mild" tectonic activity, erosive periods, or glaciation in order to inform long-term risk assessment studies; evaluating multiphase flow of CO_2 and water through fractures under changing stress and temperature conditions to help to compute how much CO_2 will actually leak in presence of such discontinuities; conduct experimental evaluation of initial and evolving permeability, degradation mechanisms and rates, capillary pressure, pH effects, and carbonation processes for oil field cements.

13 REFERENCES

Altevogt, A. S. and M. A. Celia, 2002, Modeling carbon dioxide transport in unsaturated soils. In: (Hassanizadeh *et al*. eds.): *Proc. XIVth International Conference in Computational Methods in Water Resources*, pp. 41-47.

Beliveau, D. A., D. A. Payne, and M. Mundry, 1991, Analysis of the waterflood response of a naturally fractured reservoir. *66th Annual Technical Conference and Exhibition of the Society of Petroleum Engineers*, SPE 22946.

Bunge, R. J. 2000, *Midale Reservoir Fracture Characterization Using Integrated Well And Seismic Data, Weyburn Field, Saskatchewan*. M.Sc. Thesis, Colorado School of Mines.

Burrowes, G. 2001, Investigation CO_2 storage potential of carbonate rocks during tertiary recovery from a billion barrel oil field, Weyburn, Saskatchewan: Part 2 – Reservoir geology (IEA Weyburn CO_2 Monitoring and Storage Project). *Summary of Investigations 2001*, 1, pp. 64-71.

Chalaturnyk, R., F. Moreno, J. Jimenez, N. Deisman, and S. Talman, 2003, A*ssessment of wellbore transport properties – Weyburn CO_2 Storage and Monitoring Project, 2003 Report: Task 3.4.2*.

Chang, Y. B., B. K. Coats, and J. S. Nolen, 1996, *A Compositional Model for CO_2 Flood including Solubility in Water*, SPE 35164.

Christian-Frear, T., 1995, Salado Data/Parameters: Anhydrite Two-Phase Parameters, *SAND 94-0472*, Sandia National Laboratory, Albuquerque, New Mexico, USA.

Cioppa, M. T. 2003, Magnetic evidence for the nature and timing of fluid migration in the Watrous Formation, Williston Basin, Canada: a preliminary study. *Journal of Geochemical Exploration*, Vol. 78-79, pp. 349-354.

Cuthiell, D. L. and D. H. S. Law, 2003, *Numerical Simulation of CO_2 Movement in a Weyburn Pattern, Year 2 Report: Task 5.4*.

Dong, M. 2003, Personal communication within the IEA GHG Weyburn CO_2 Monitoring and Storage Project.

Foley, J. A., I. C. Prentice, N. Ramankutty, 1996, An integrated biosphere model of land surface processes, terrestrial carbon balance, and vegetation dynamics, *Global Biogeochem. Cycles*, 10, pp. 603-628.

Grogan A. T., V. W. Pinczewski, G. J. Ruskauff, and F. M. Orr Jr., 1986, Diffusion of carbon dioxide at reservoir conditions: models and measurements, *SPE/DOE* 14897.

Grogan, H. A., K. J. Worgan, G. M. Smith, and D. P. Hodgkinson, 1992, Post-disposal implications of gas generated from a repository for low and intermediate-level wastes. *NAGRA Technical Report* NTB 92-07. Swiss Radioactive Waste Management Agency, Wettingen, Switzerland.

Hancock, E., P. Norton, and R. Hendron, 2002, Building America System Performance Test practices: Part 2, air-exchange measurements. *National Renewable Energy Laboratory Technical Report* NREL/TP-550-30270. NPEL, Golden, Colorado.

Health Canada 1989, Exposure Guidelines for Residential Indoor Air Quality. *Report of the Federal-Provincial Advisory Committee on Environmental and Occupational Health. First published April 1987, revised July 1989*. Ministry of Supply and Services, Canada.

Hoek, E. and E. T. Brown, 1997. Practical estimates of rock mass strength. *International Journal of Rock Mechanics and Mining Sciences*. 34, 8, pp. 1165-1186.

Hoek, E., C. Carranza-Torres, and B. Corkum, 2002, Hoek-Brown Failure Criterion - 2002 Update. *Rocscience*, 7 p.

Honarpour, M., L. F. Koederitz, and A. H. Harvey, 1982, Empirical Equations for Estimating Two-Phase Relative Permeability in Consolidated Rock, *SPE* 9966.

Jimenez, J. A. and R. J. Chalaturnyk, 2003, Are disused hydrocarbon reservoir safe for geological storage of CO_2? *Greenhouse Gas Control Technologies*, 1. pp. 471-476.

Jimenez, J. A., R. J. Chalaturnyk, and K. Kreis, 2004, Role of salt dissolution in the long-term performance assessment of CO_2 storage in the Weyburn field. *Seventh International Conference on Greenhouse Gas Control Technologies*.

Jimenez, J. A., R. J. Chalaturnyk, S. G. Whittaker, and G. Burrowes, 2004, A mechanical earth model for the Weyburn CO_2 Monitoring and Storage Project and its relevance to long-term performance assessment. *Seventh International Conference on Greenhouse Gas Control Technologies*.

Khan, D. K. and B. J. Rostron, 2003, Regional fluid flow in the Weyburn CO_2 project area: Implications for CO_2 sequestration. *Poster presented at the PTRC Meeting.*

Kozak, M. W., M. J. Stenhouse, and R. H. Little, 2000, Reference activity levels for disposal of Ontario Power Generation's low level waste. *Ontario Power Generation Technical Report* 05386-REP-03469.3-10000-R00. OPG, Toronto, Ontario, Canada.

Narr, W. and R. C. Burruss, 1984, Origin of reservoir fractures in Little Knife field, North Dakota. *AAPG Bulletin*, Vol. 68, No. 9, pp. 1087-1100.

National Institute for Occupational Safety and Health 1997, NIOSH Pocket Guide to Chemical Hazards. *DHHS (NIOSH)* Publication No. 97-140. U.S. Government Printing Office, Washington DC. http://www.cdc.gov/niosh/npg/npg.html.

NEA/OECD. 1998, Water-Conducting Features in Radionuclide Migration, Barcelona, Spain, June 10-12.

Oldenburg, C. M. and A. A. Unger, 2003, Transport and dispersion processes for CO_2 in the unsaturated zone and surface layer. *Paper presented at 2nd Annual Conference on Carbon Sequestration*, Alexandria, VA.

Pitblado, R. and M. Mossemiller, 2004, Risk Assessment Methods for Geosequestration of CO_2. *Technical Report* 700112 for PTRC, Det Norske Veritas (U.S.A.), 58 p.

PTRC. 2004, IEA GHG Weyburn CO_2 Monitoring and Storage Project*: Summary Report on Phase I.*

Redly, P. 1998, *Tectonostratigraphic Evolution of the Williston Basin*. Ph.D. Thesis University of Saskatchewan.

Rice, S. A. 2003, Health effects of acute and prolonged CO_2 exposure in normal and sensitive populations. Poster presentation, *NETL Second Annual Conference on Carbon Sequestration*, Alexandria.

Riding, J. B. 2003, Editor (with multiple contributors), Weyburn CO_2 Monitoring Project: *Project Management Interim Report 4 (months 13-24)*. EC Report, Contract ENK5-CT-2000-00304.

Samet J. M., W. E. Lambert, B. J. Skipper, A. H. Cushing, W. C. Hunt, S. A. Young, L. C. McLaren, M. Schwab, and J. D. Spengler 1993, Nitrogen dioxide and respiratory illnesses in infants. *Am. Rev. Respir. Dis.* 148, pp. 1258-1265.

Scheidegger, A. E. 1974, *The Physics of Flow through Porous Media*, University of Toronto Press, Toronto, Canada.

Shaw, C. V. 1987, Mechanical ventilation and air pressure in houses. *Canadian Building Digest* CBD-245.

Snodgrass, W. R. 1992, Physiological and biochemical differences between children and adults as determinants of toxic exposure to environmental pollutants. In: P. S. Guzelain, C. J. Henry, and S. S. Olin, eds. *Similarities and Differences Between Children and Adults: Implications for Risk Assessment*. ILSI Press, Washington DC., pp. 35-42.

Stauffer, M. R. and D. J. Gendzwill, 1987, Fractures in the northern plains, stream pattern, and the mid-continent stress field. *Canadian Journal of Earth Sciences*, 24, pp. 1089-1097.

Stenhouse, M. J., R. Arthur, and W. Zhou, 2004, Assessment of the limiting CO_2 flux from geosphere based on specific environmental impacts. *Monitor Scientific Report* MSCI-2301-9v2 to IEA GHG Weyburn CO_2 Monitoring and Storage Project.

UNSCEAR 1988, Sources, Effects and Risks of Ionizing Radiation. Report of United Nations Scientific Committee on the Effects of Atomic Radiation. UNSCEAR, New York, USA.

Whittaker, S. G. and B. Rostron, 2003, Geological storage of CO_2 in a carbonate reservoir within the Williston Basin, Canada: an update. *Greenhouse Gas Control Technologies*, 1. pp. 385-390.

Yu, A. D., C. A. Langton, and M. G. Serrgato, 1993, Physical Properties Measurement, *WSRC-RP-93-894*, Westinghouse, Savannah River Company.

FIGURES

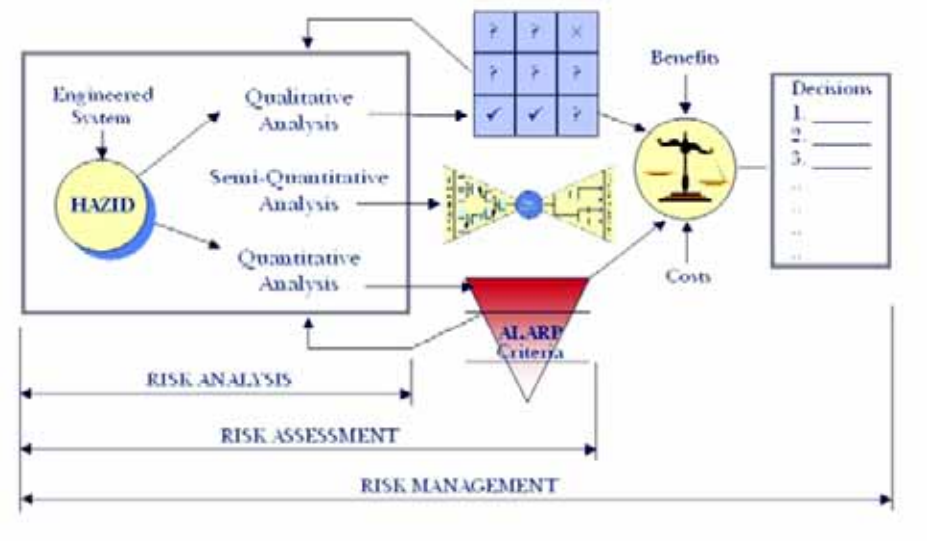

Figure 4.1: Three levels of risk assessment apply equivalently in the overall risk management process but tool selection depends on project complexity, uncertainties, and phase in project lifecycle

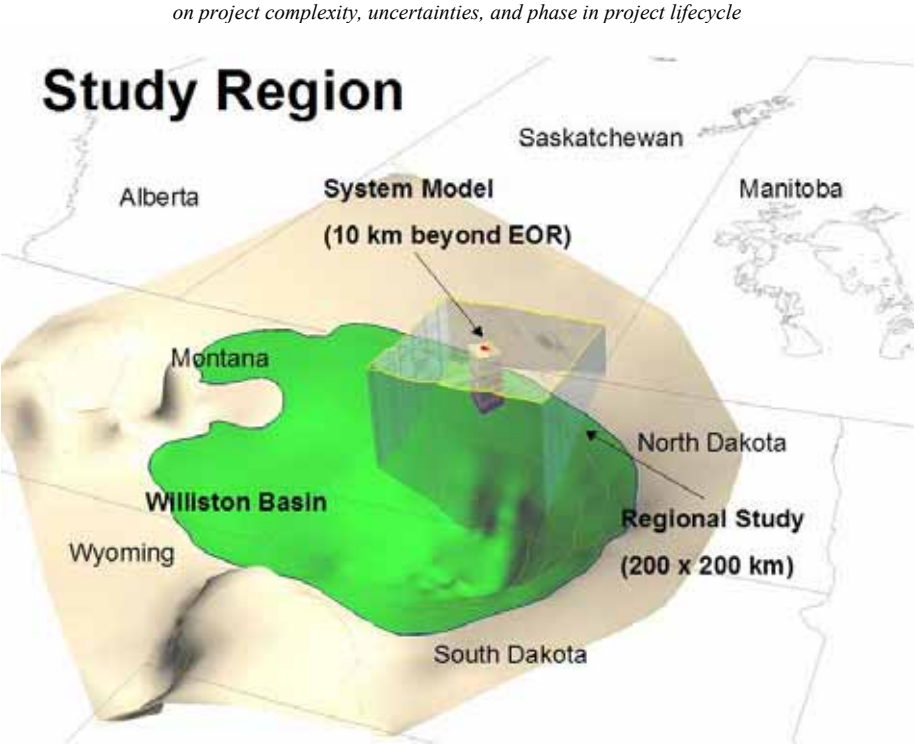

Figure 4.2: Relative position of the System Model within the overall regional study area of the Project

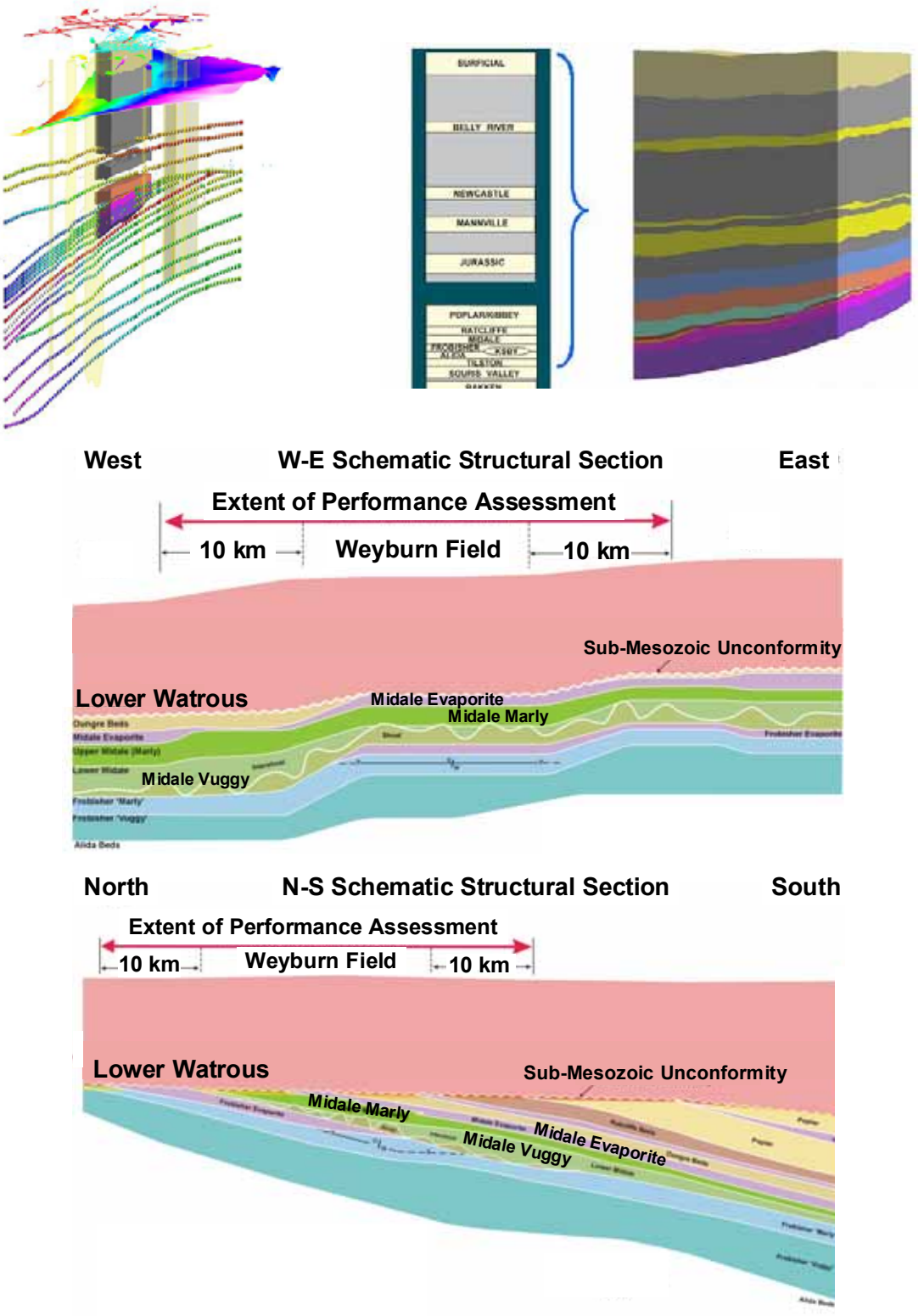

Figure 4.3: Geological Elements of the Risk Assessment System Model (see Theme 1 for detailed discussion on geological elements of the System Model)

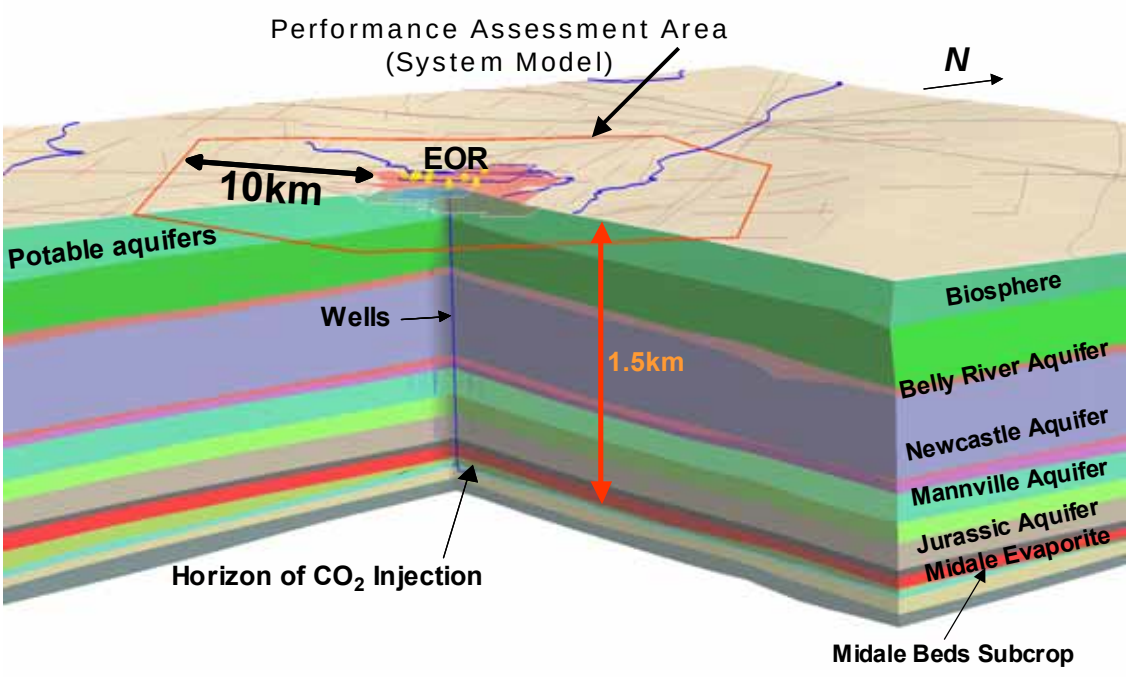

Figure 4.4: Diagrammatic representation of the system model consisting of the Weyburn Reservoir (enhanced oil recovery area), overlying and underlying geological layers, wells and the biosphere.

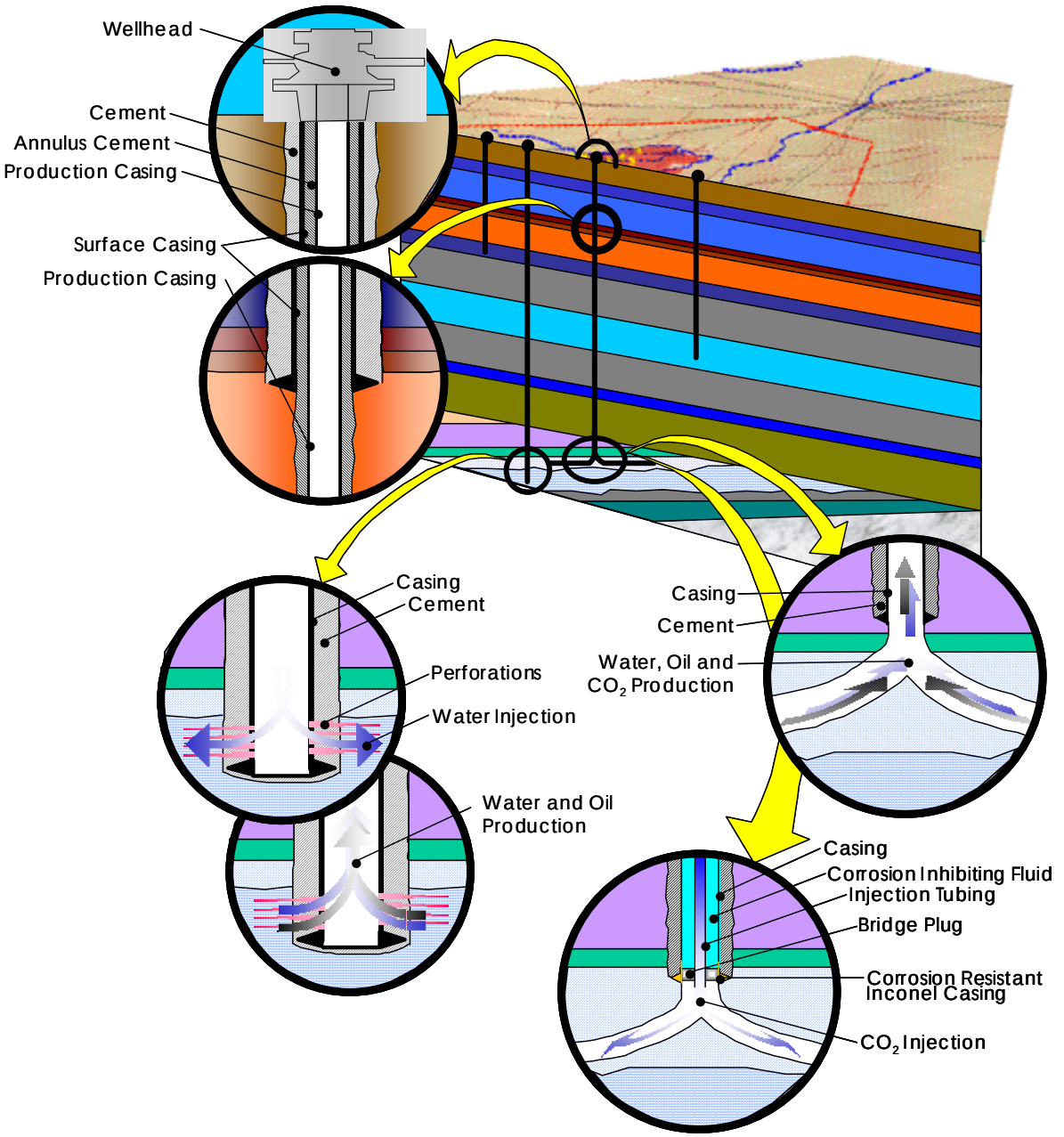

Figure 4.5: Range of well types within the Weyburn Project

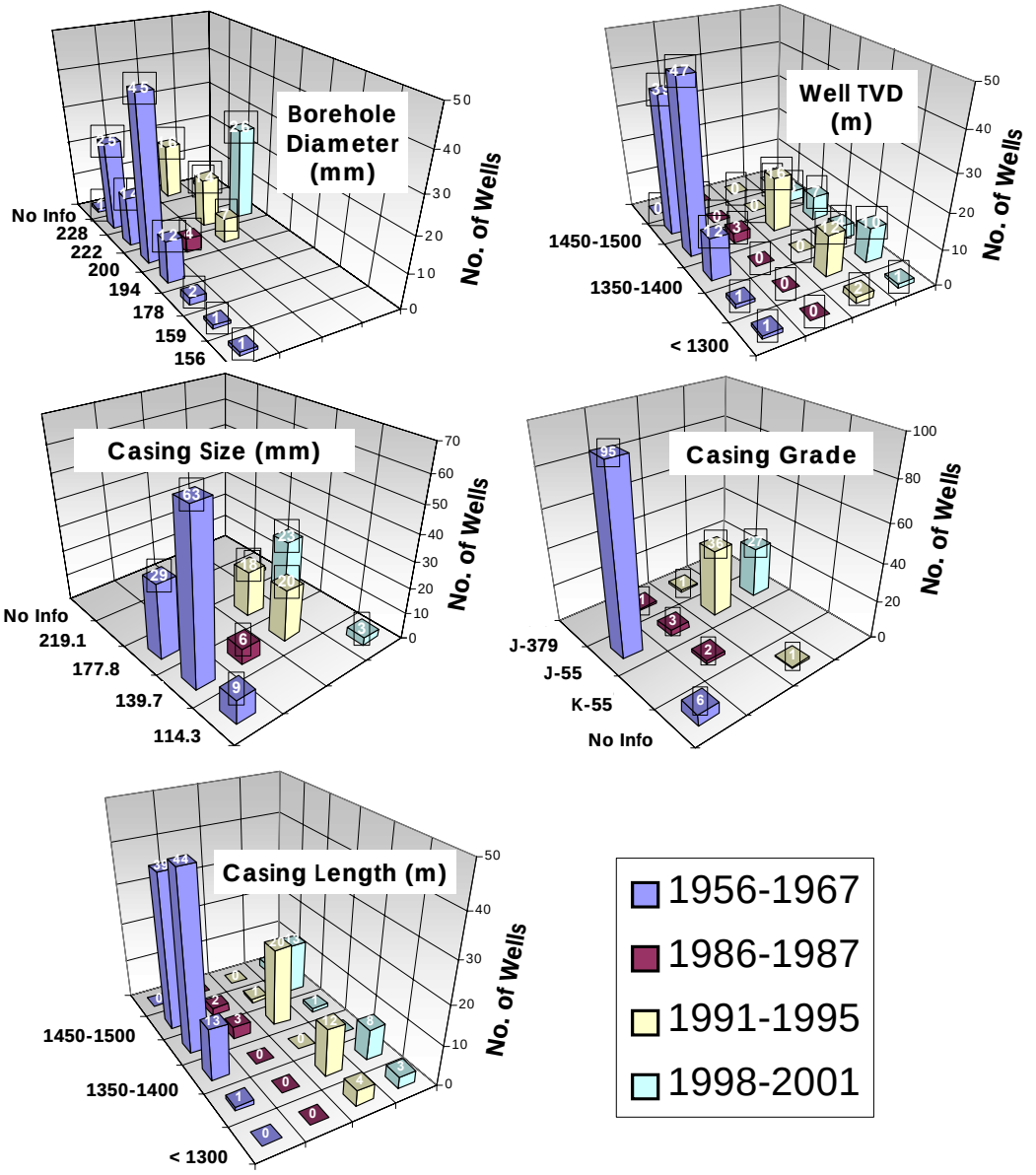

Figure 4.6: Wellbore statistics for wells within the Phase 1A area

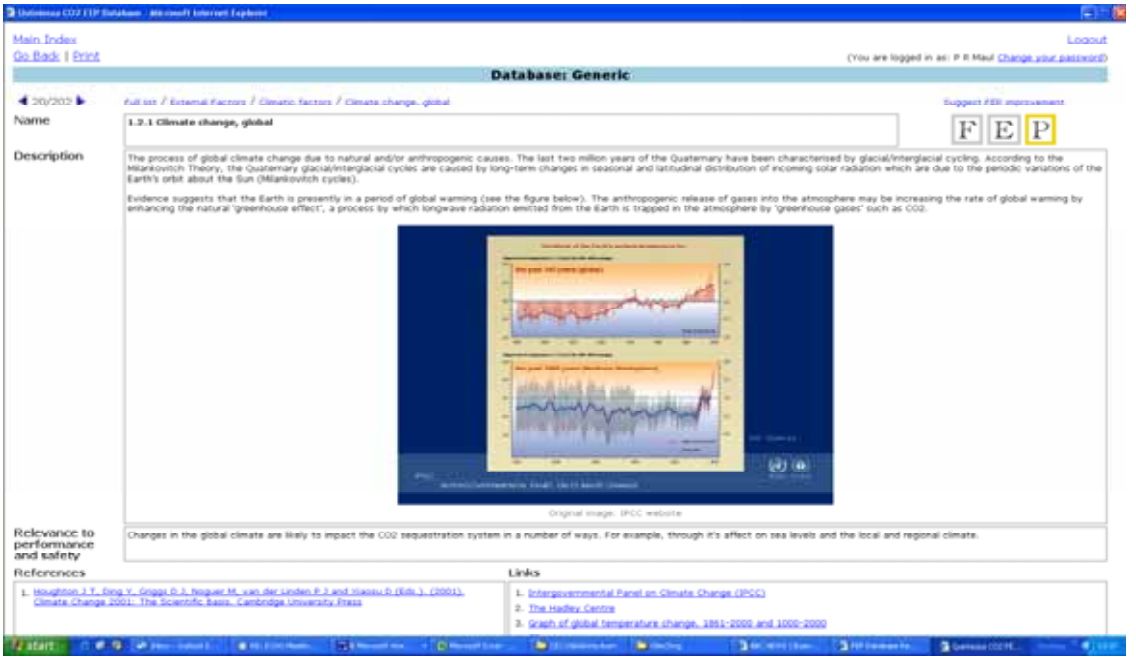

Figure 4.7: An example of a Feature, Event and Process (FEP) entry in the generic geological storage FEP database

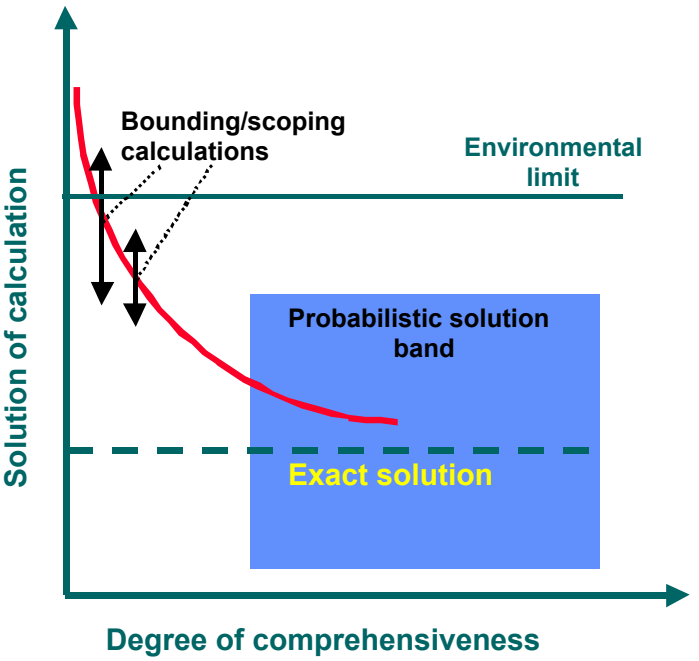

Figure 4.8: Relationship between level of effort and 'accuracy' of solution

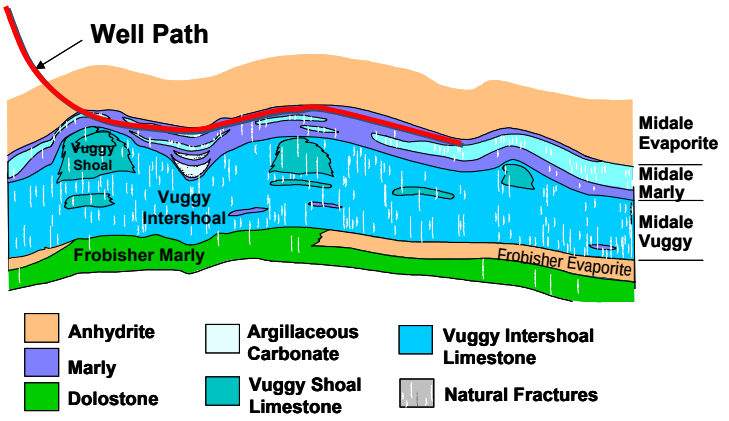

Conceptualization of Midale Bed

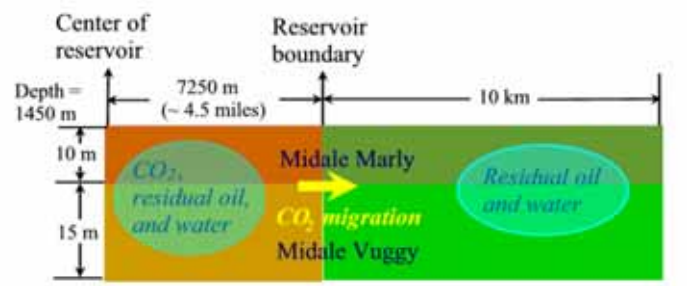

Figure 4.9: Conceptualization of Early Conceptual Model

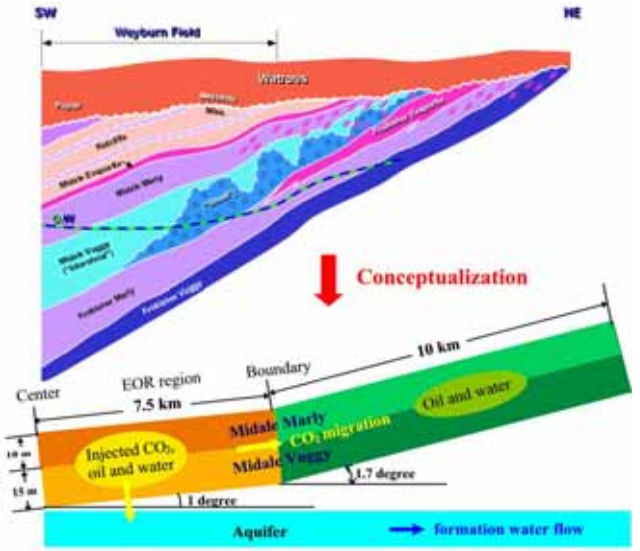

Figure 410: Intermediate Conceptual Model for 2002 modeling of Base Scenario (natural pathways)

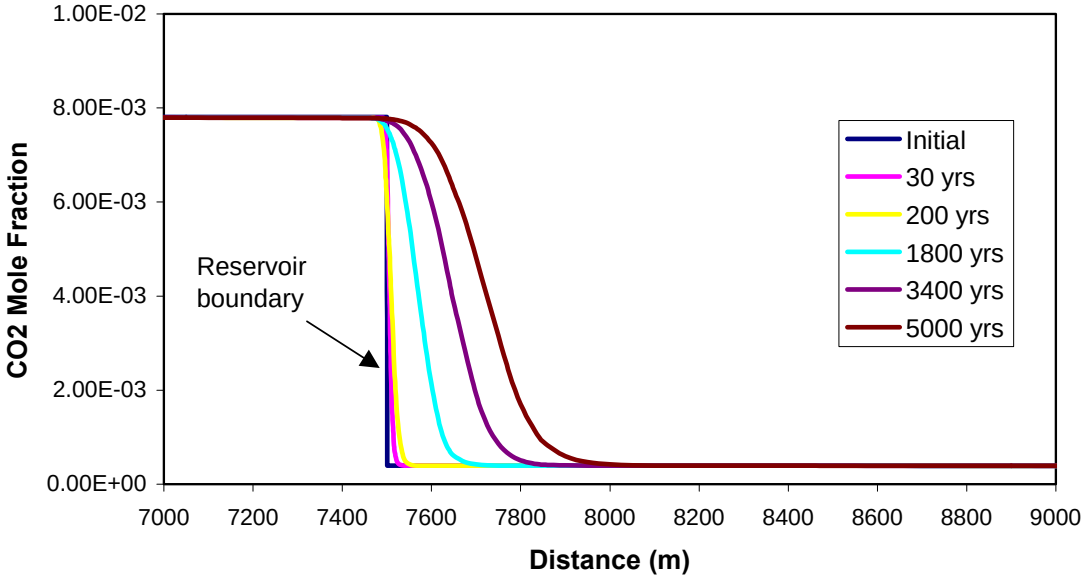

Figure 4.11: Aqueous CO_2 concentration profiles in the Midale Beds for different time periods after the end of EOR operations

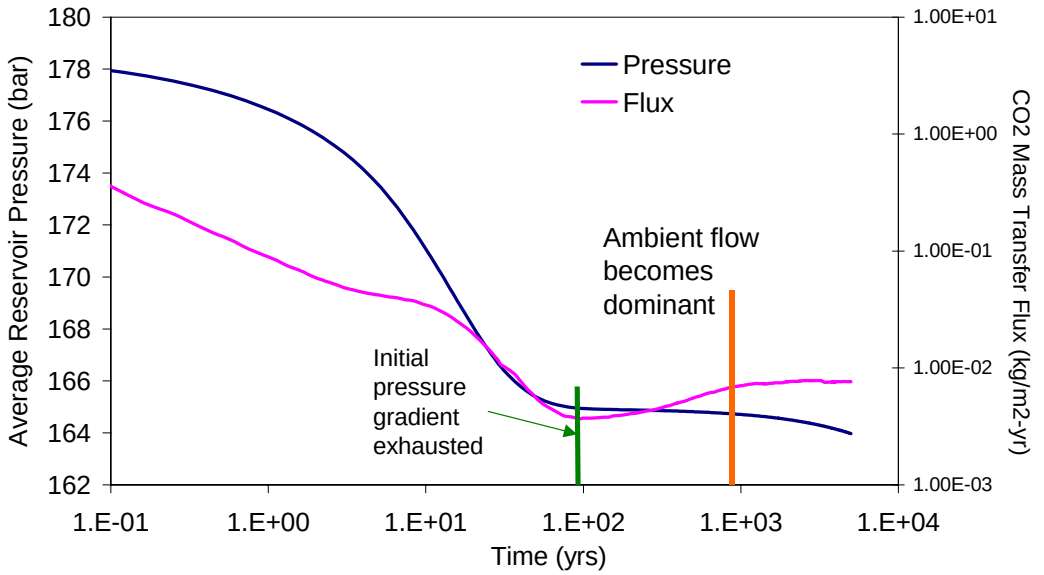

Figure 4.12: CO_2 mass transfer flux from the reservoir as a function of time (1 bar = 0.1 MPa)

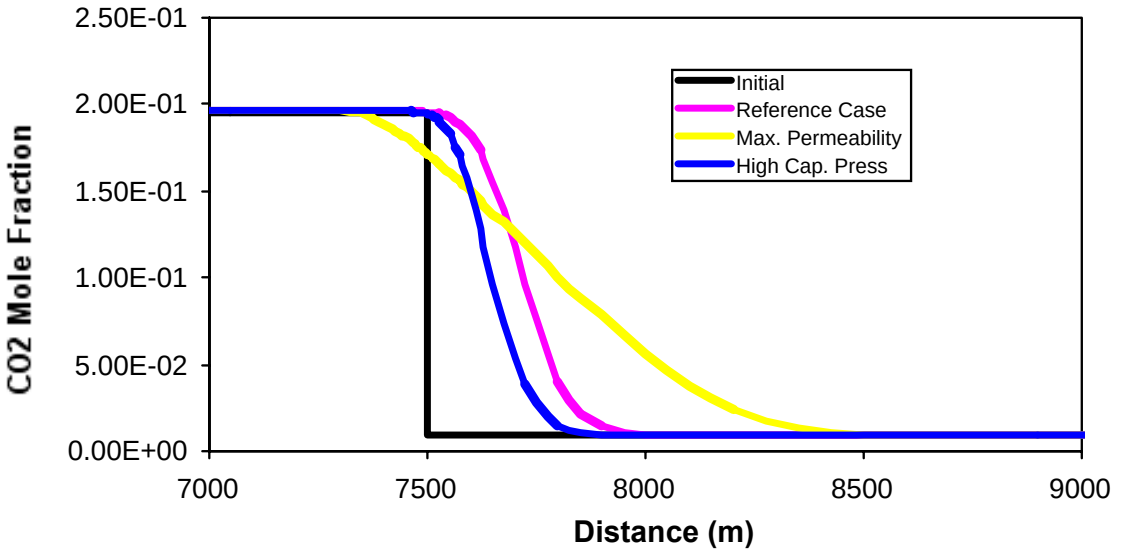

Figure 4.13: Comparison of concentration profiles for CO_2 5,000 years after the end of EOR operations. Initial CO_2 concentrations for the Intermediate Conceptual Model simulations are larger than the initial CO_2 concentrations used in the Early Conceptual Model simulations.

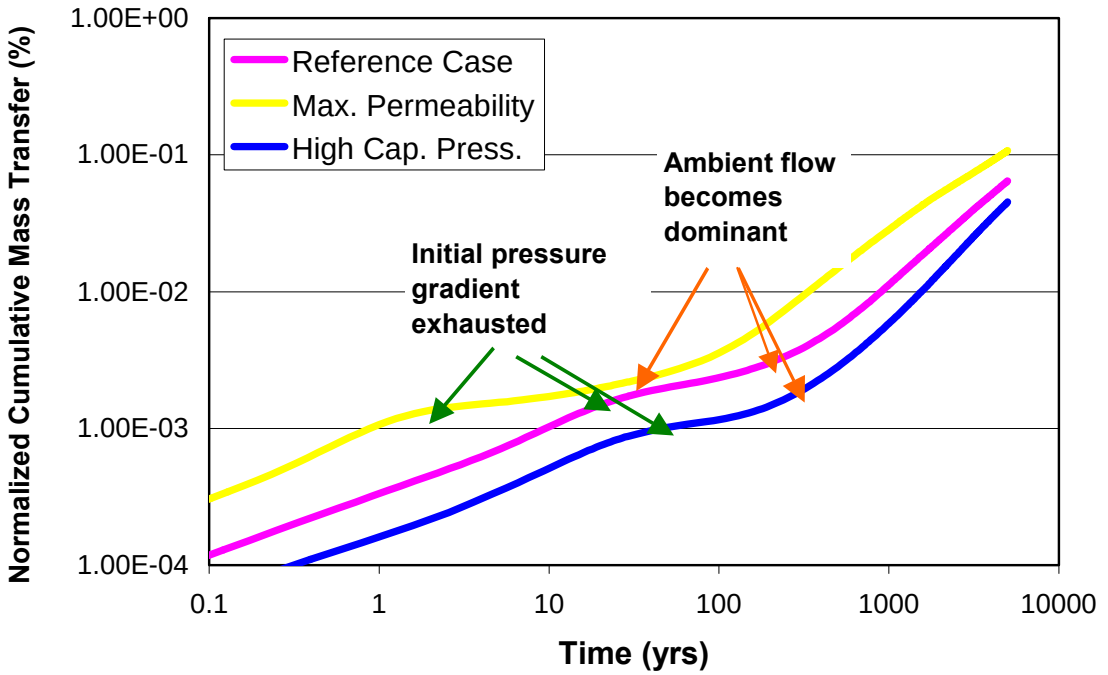

Figure 4.14: Comparison of cumulative mass transfer of CO_2 from the Weyburn reservoir as a function of time

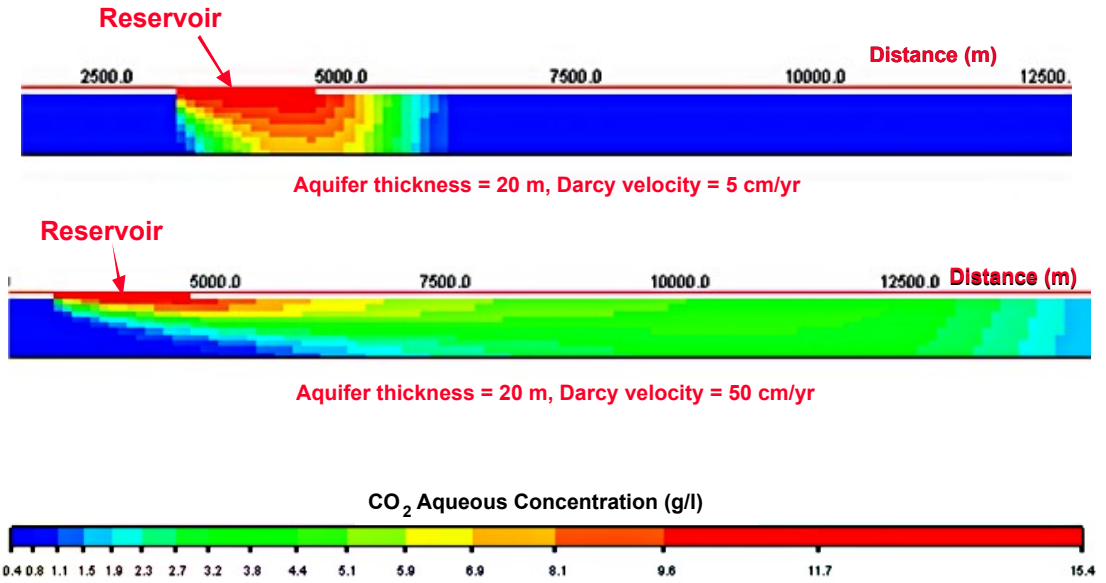

Figure 4.15: Migration of dissolved CO_2 along Frobisher aquifer

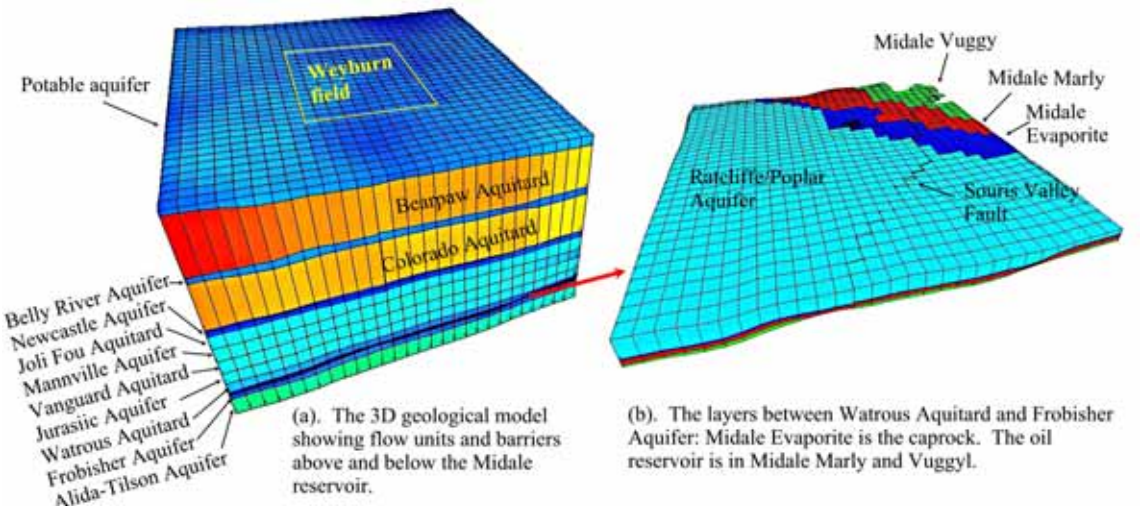

Figure 4.16: The geosphere components of the Final System Model

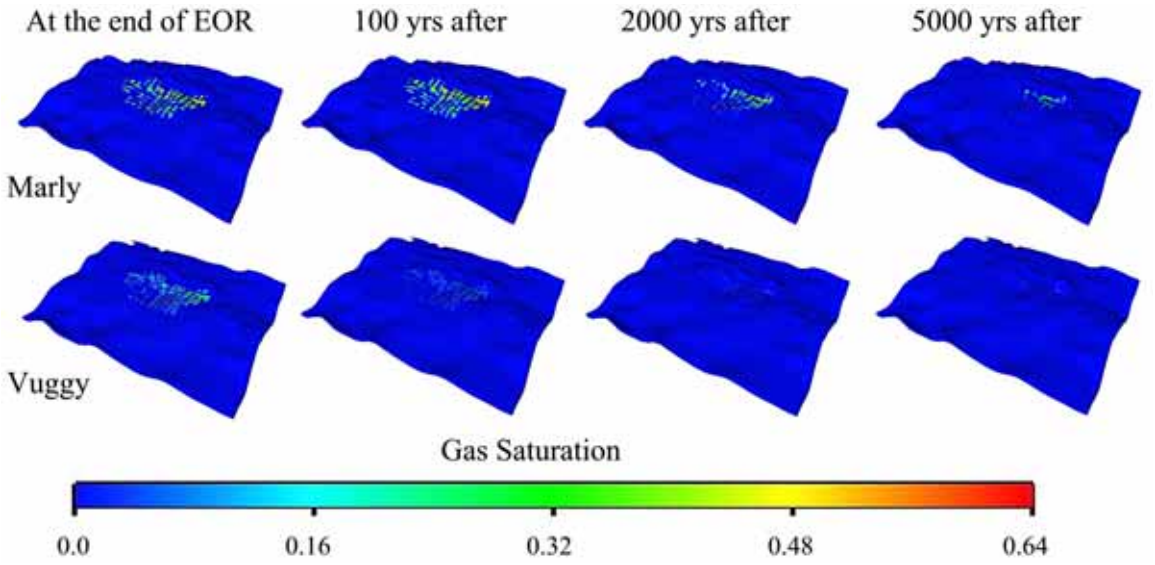

Figure 4.17: CO_2-rich gas phase movement in the Midale Marly and Vuggy layers at the end of EOR, and at 100-yrs, 2000-yrs, and 5000-yrs after the end of EOR.

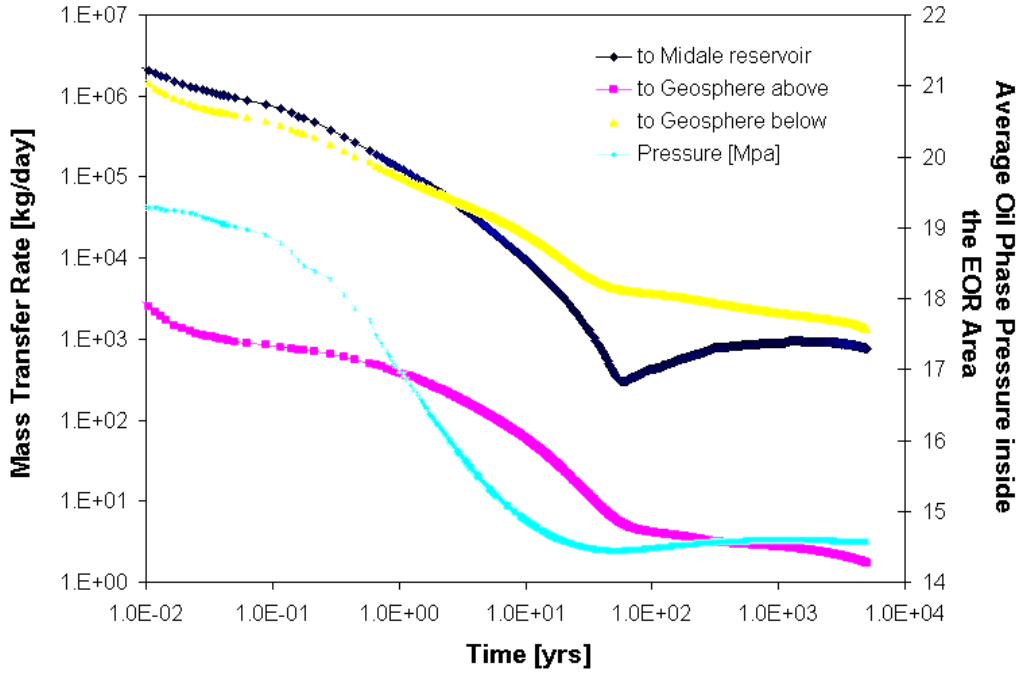

Figure 4.18: Time variation of CO_2 mass transfer rates into the geosphere, and average oil phase pressure inside the 75 patterns.

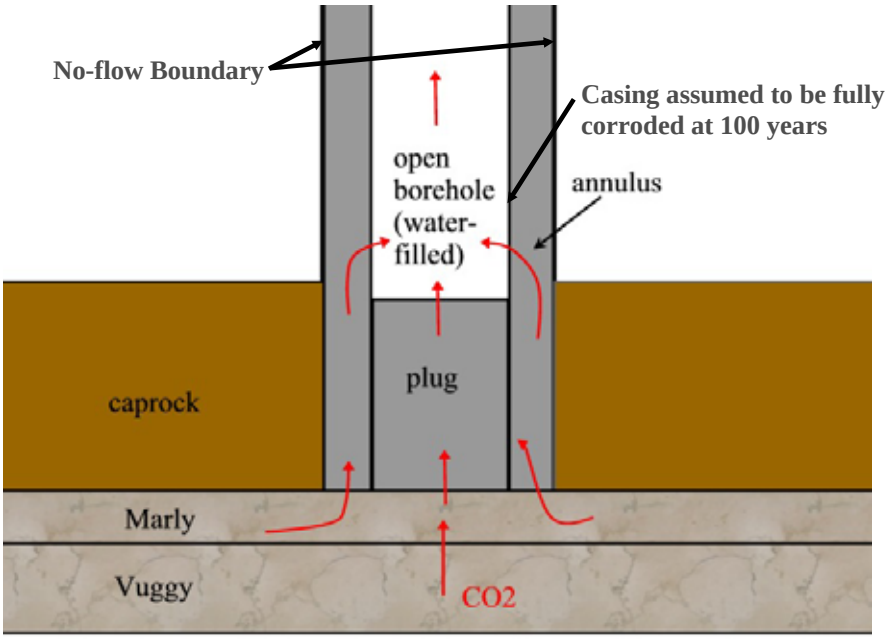

Figure 4.19: The "Unit Cell" model assessing leakage of CO_2 via abandoned wells.

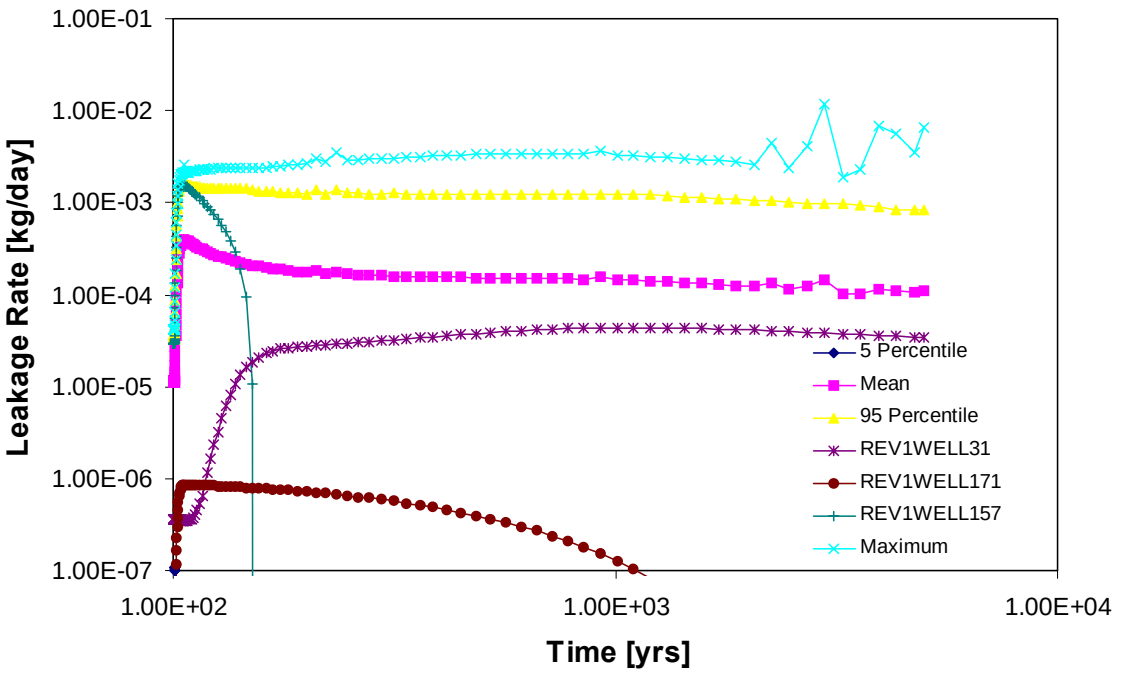

Figure 4.20: Stochastic results of CO_2 leakage rates as a function of time, predicted using the "Unit Cell" model with stochastic treatment.

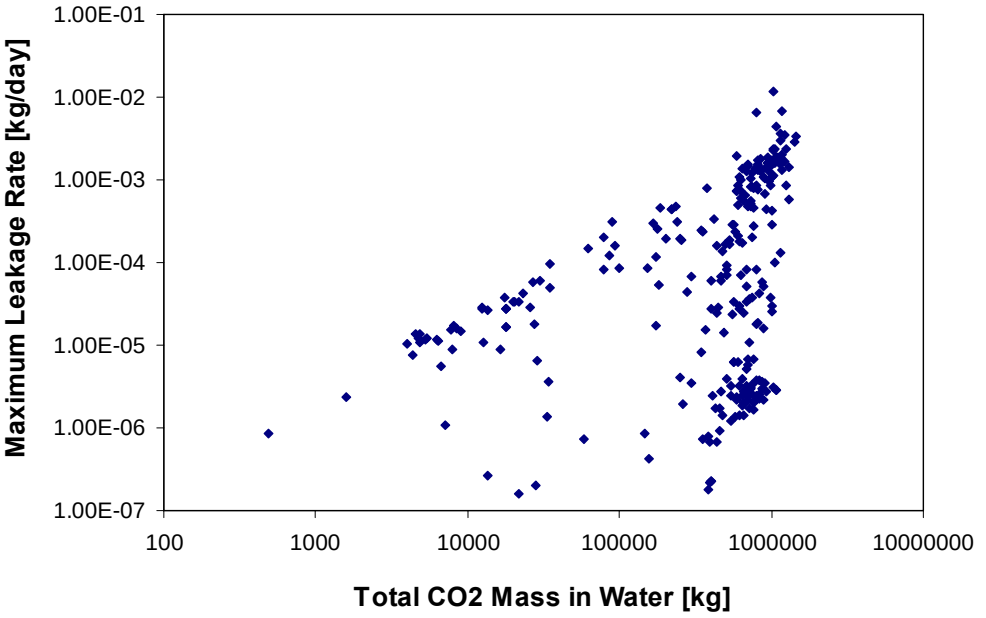

Figure 4.21: Scatter plot of the maximum CO_2 leakage rates and CO_2-in-water.

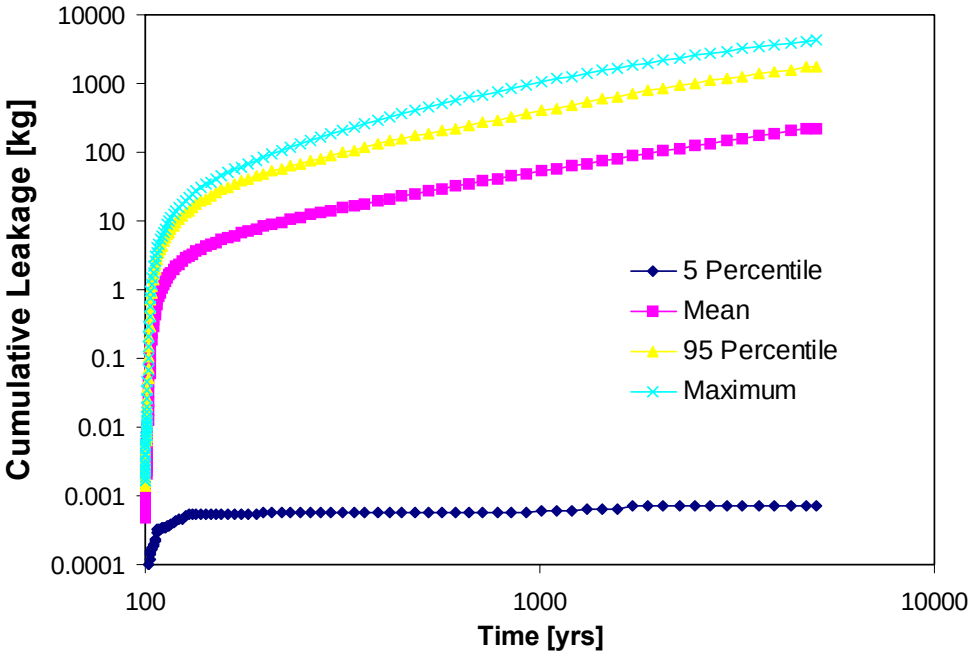

Figure 4.22: Stochastic results of cumulative leakages of CO_2 through abandoned wells.

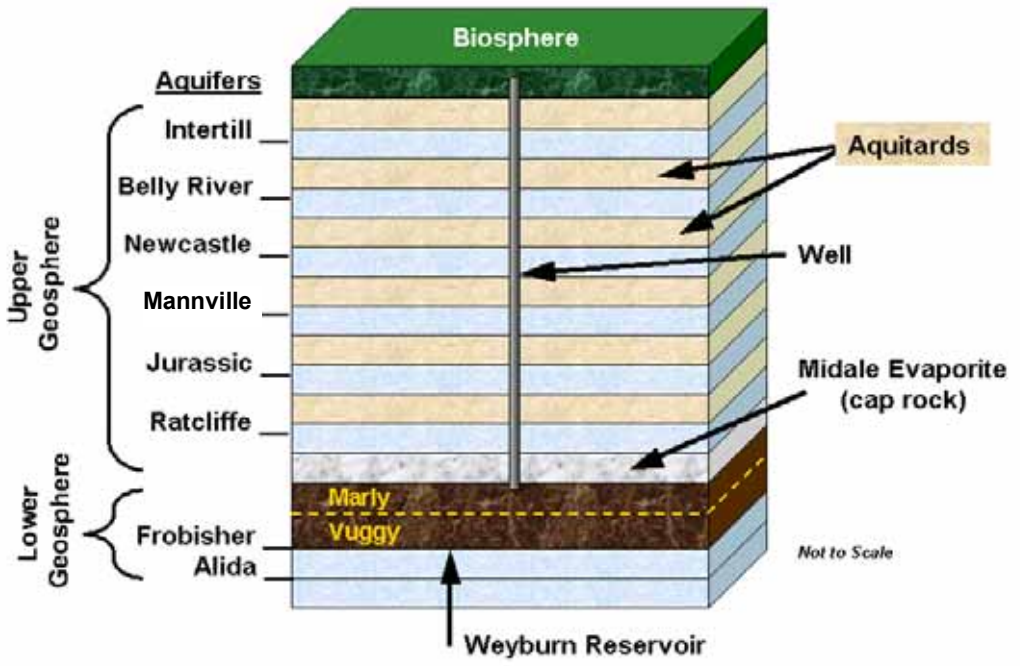

Figure 4.23: Schematic diagram showing the System domain and its components.

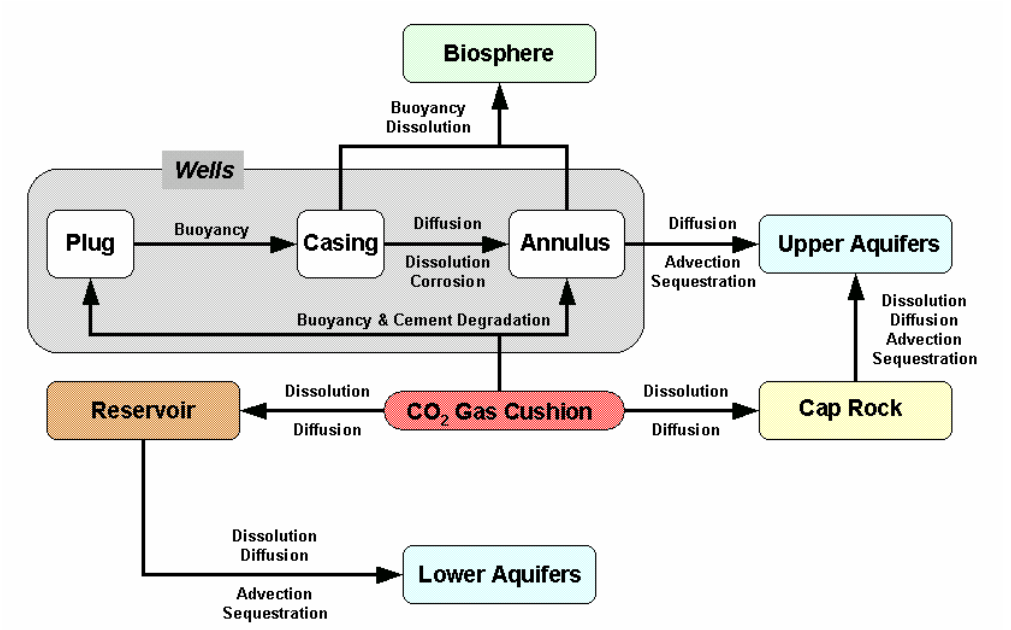

Figure 4.24: Flow diagram showing the interconnectivity of PCM domain components with the System processes.

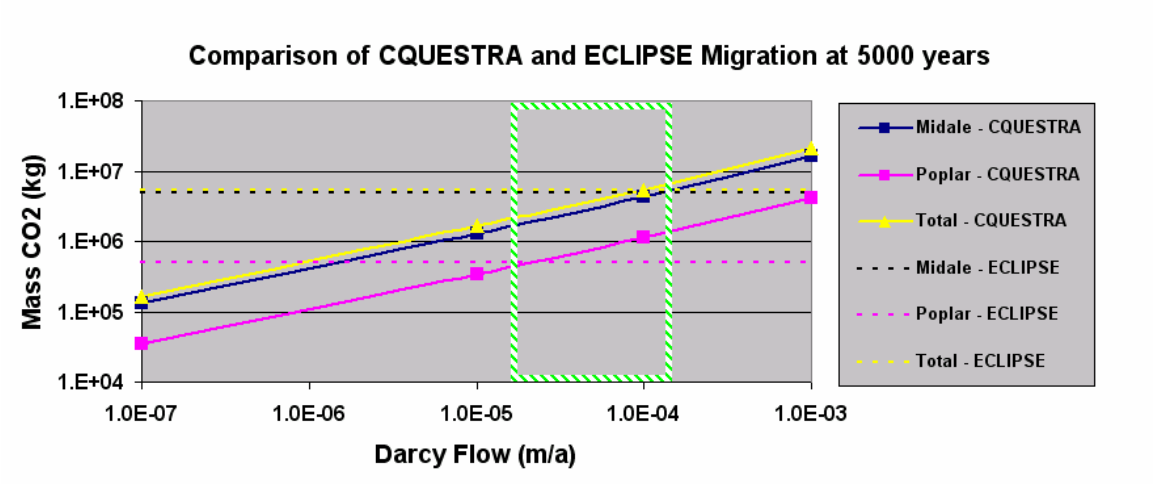

Figure 4.25: Prediction of cumulative CO_2 migration in Weyburn reservoir by CQ-1 at 5000 years after the end of EOR as a function of CQ-1 darcy flow rates. The green box shows the range of Darcy flows for which the best agreement between the two models is achieved.

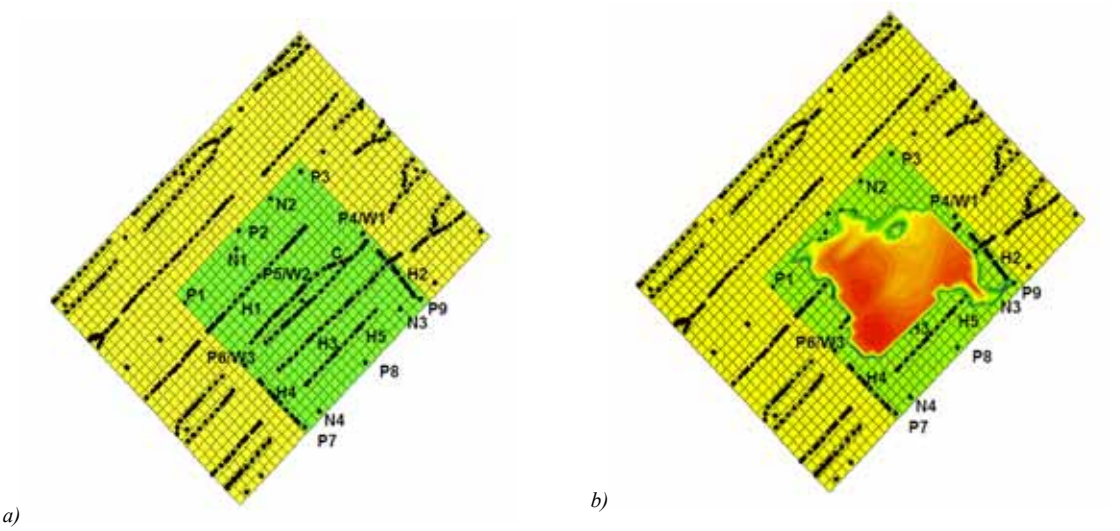

a) *b)*

Figure 4.26: Pattern 1 with a) buffer zone and well layout and b) overlay of CO_2 gas-phase inventory in the Marly M1 (top) layer at 600 years after the end of EOR.

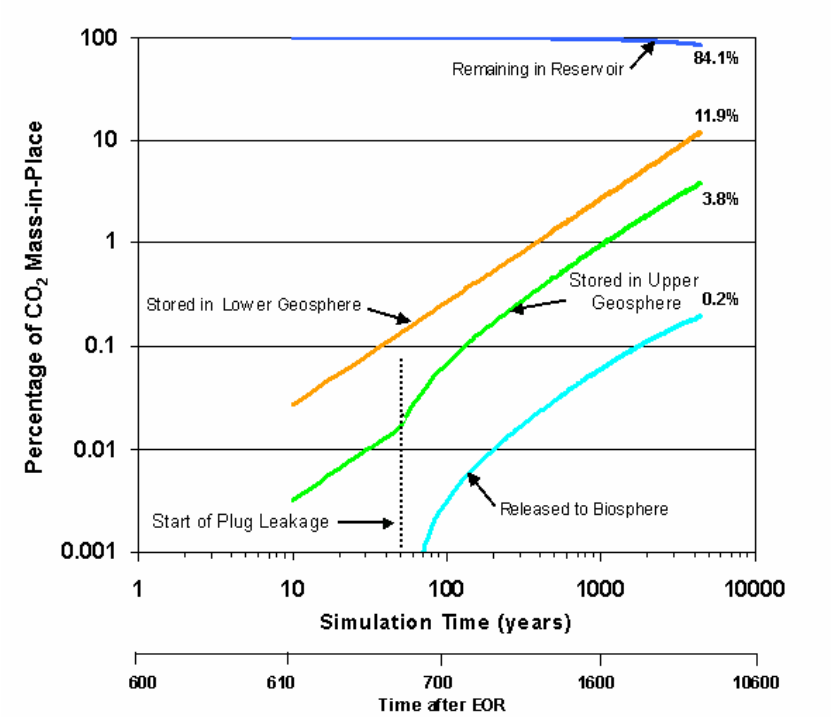

Figure 4.27: Results of the P1 case study deterministic simulation showing the percentage of the CO_2 MIP stored or released to components of the System domain over a 5000-year simulation period.

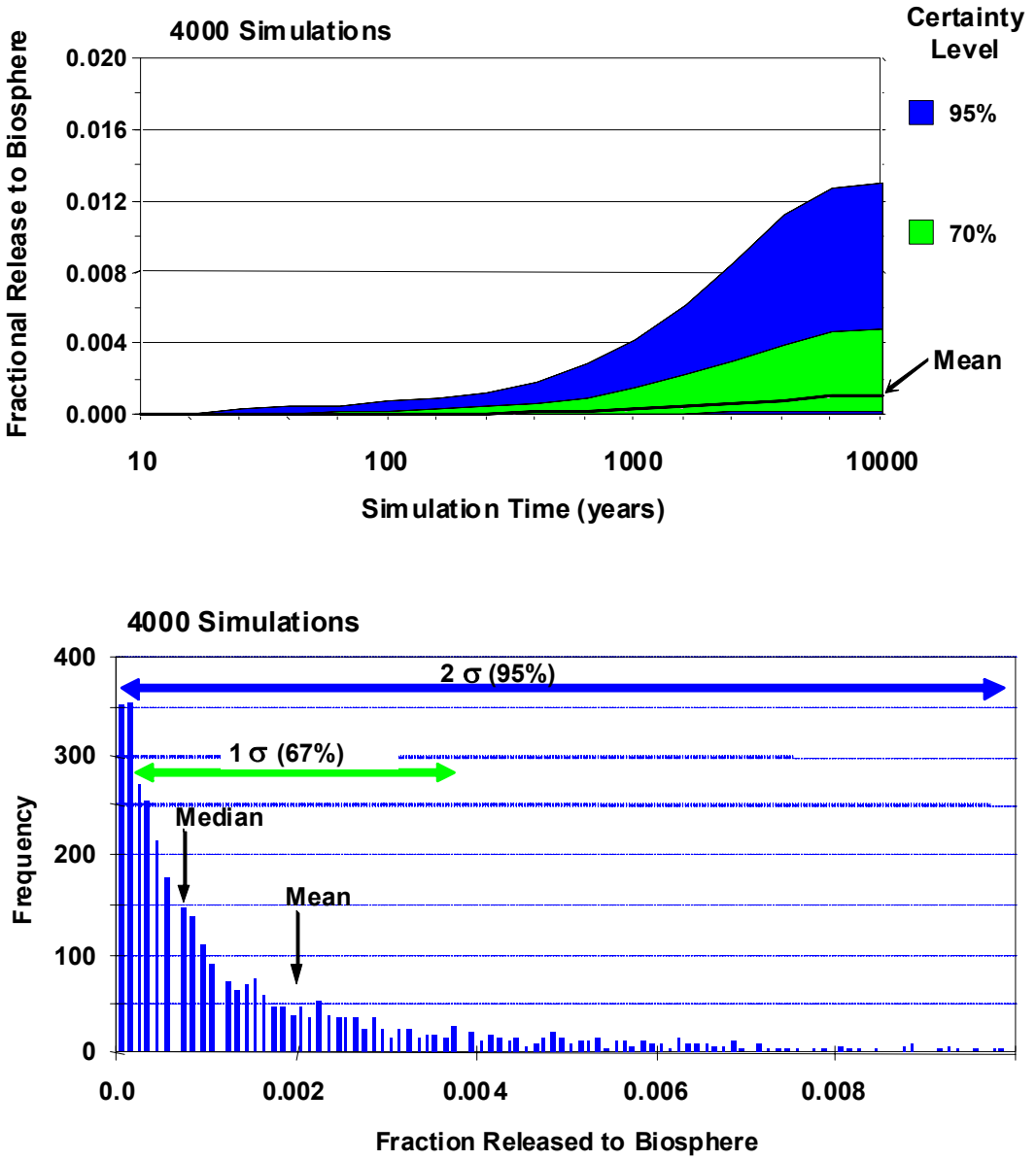

Figure 4.28: Trend plot showing the certainty levels and mean for the fractional releases to the biosphere as a function of simulation time.

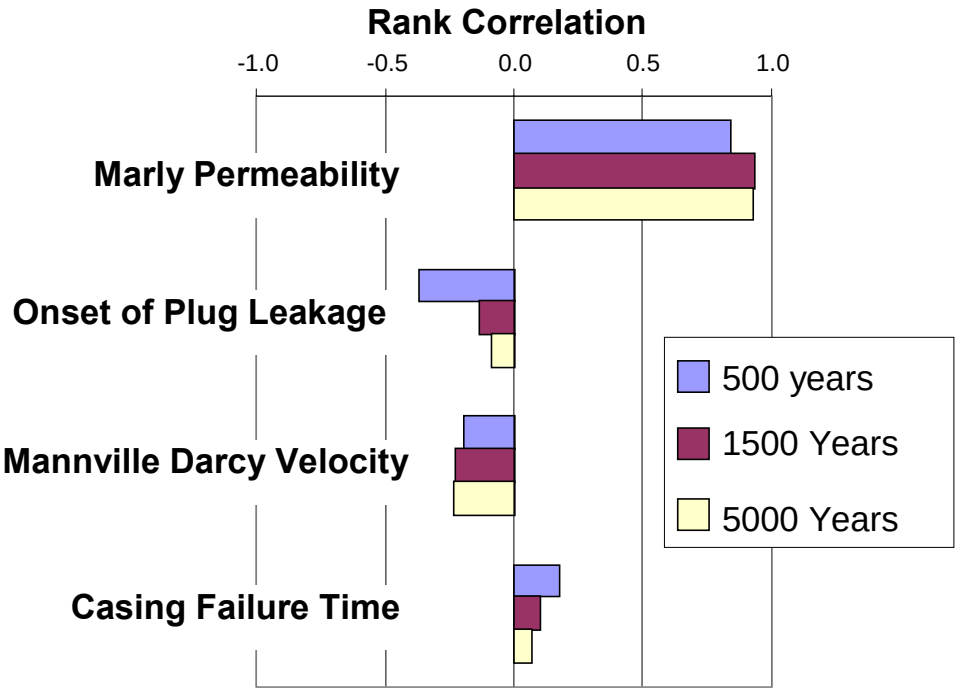

Figure 4.29: Simplified sensitivity plot showing the top four parameters influencing the fractional release to the biosphere at three different simulation times.

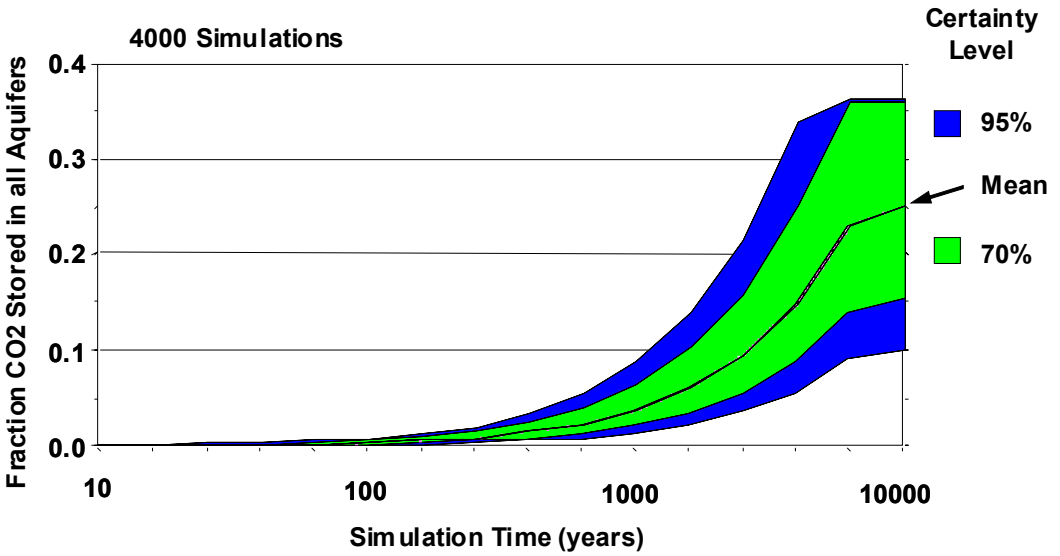

Figure 4.30: Trend chart showing the fraction of the total CO_2 inventory stored in all aquifers as a function of time.

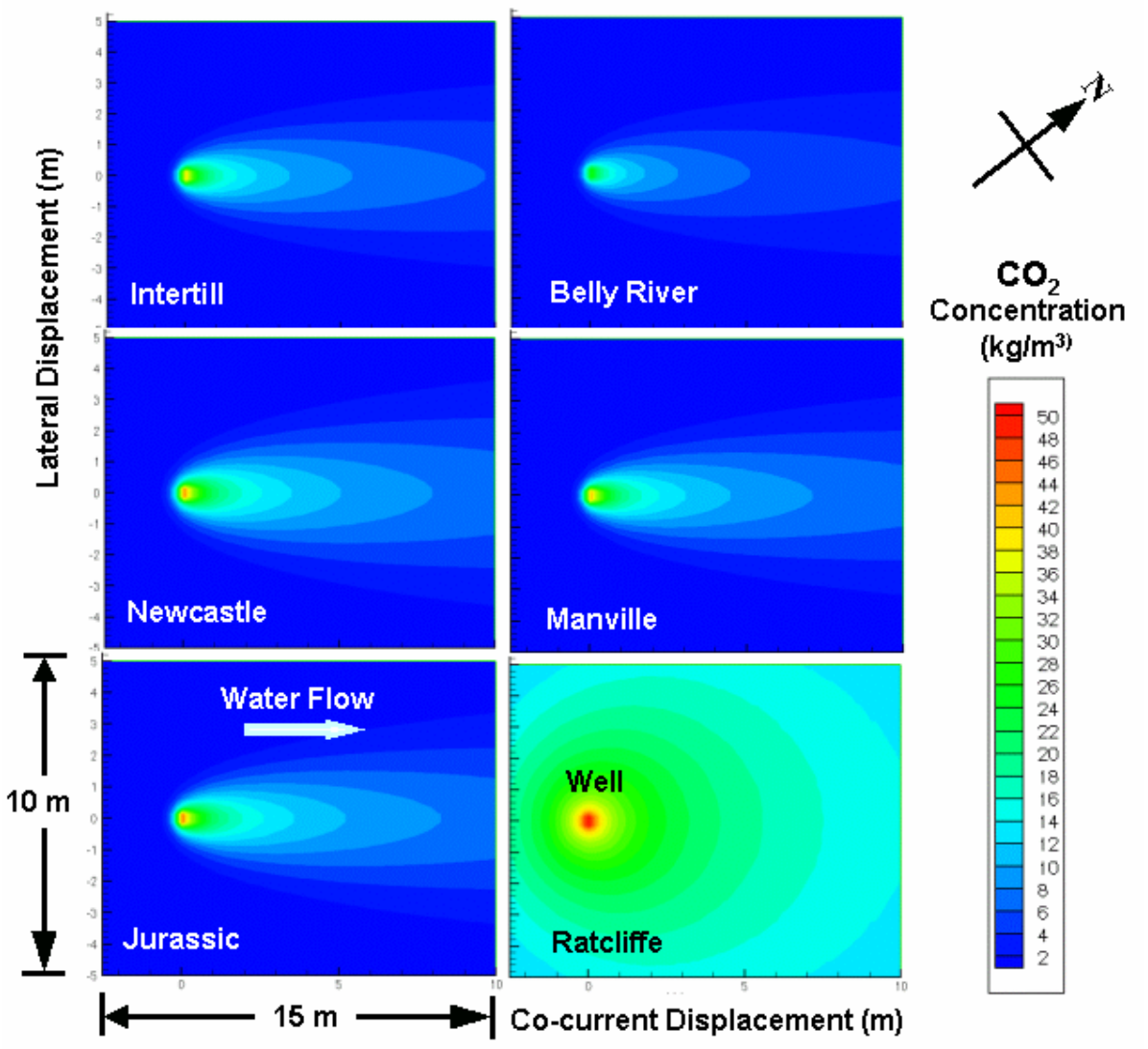

Figure 4.31: Dissolved CO_2 concentration gradient plots for upper geosphere aquifers at 100 years.

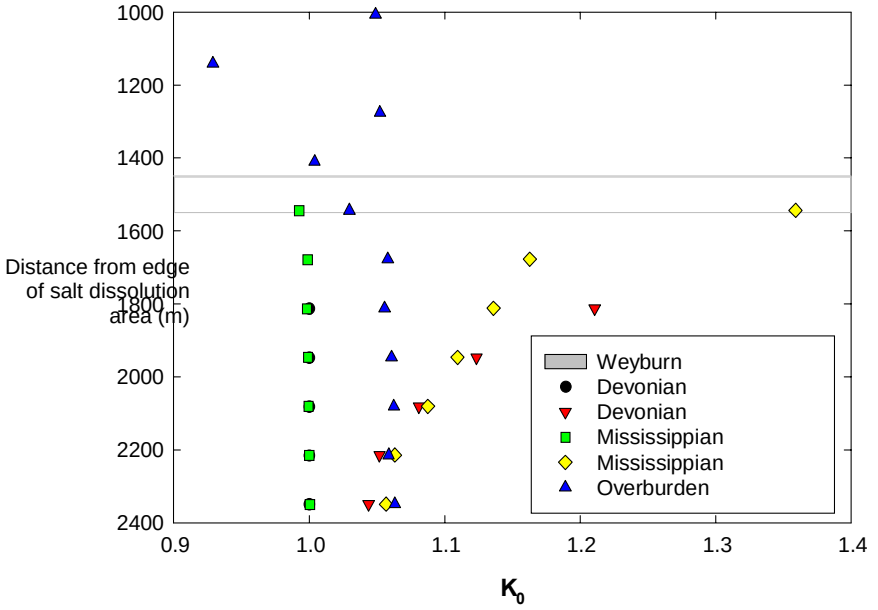

Figure 4.32: K_0 evolution during the depositional history of the basin

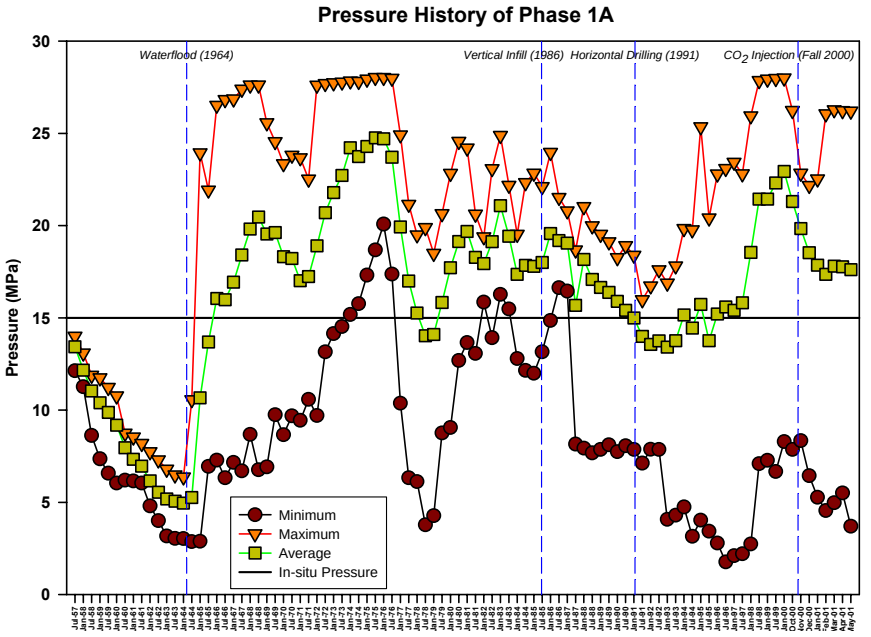

Figure 4.33: Pressure history of Phase 1A - maximum, minimum and average pressures.

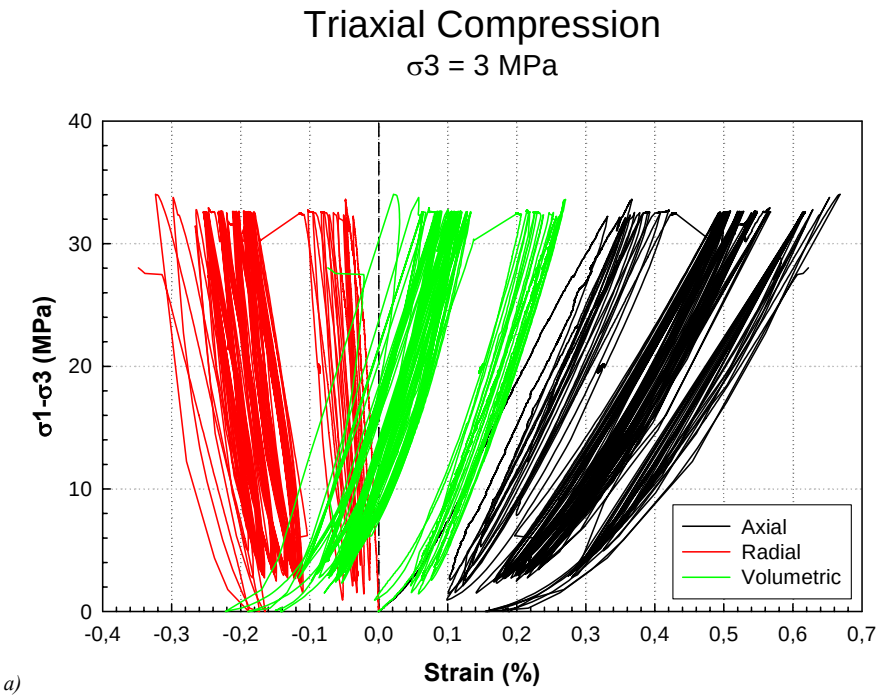

a)

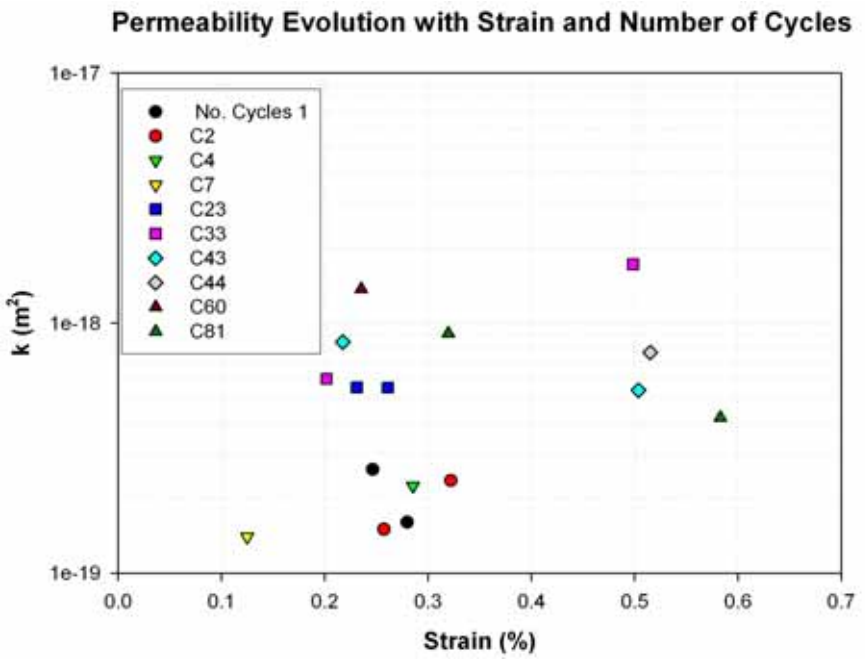

b)

Figure 4.34: a) Cyclic triaxial loading of a Midale Evaporite sample and b) permeability evolution during cycling loading

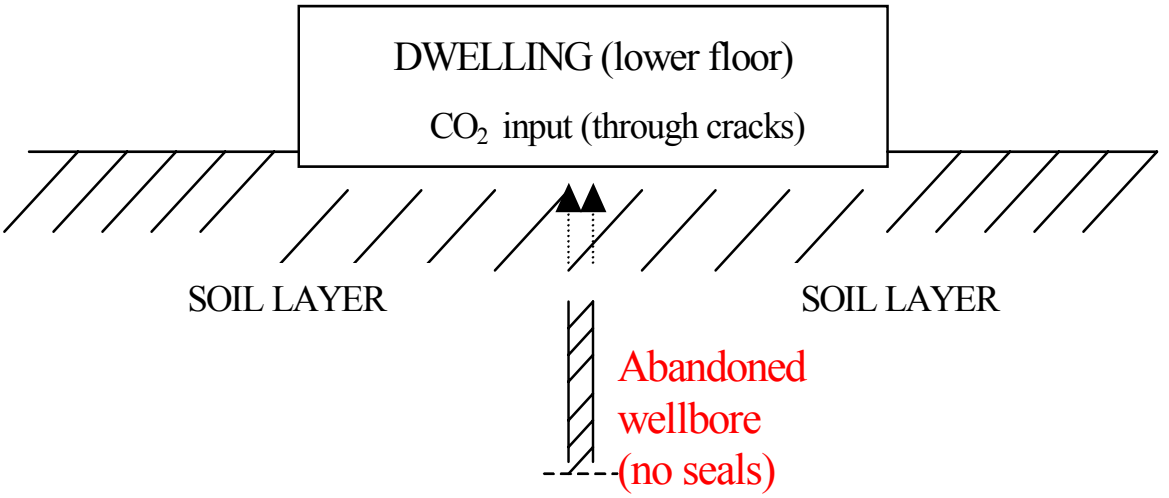

Figure 4.35: Schematic diagram of CO_2 leakage from a wellbore into a dwelling

GLOSSARY OF TECHNICAL TERMS

Anhydrite – A mineral consisting of anhydrous calcium sulphate, $CaSO_4$.

Aquifer – A rock unit that is sufficiently permeable to conduct subsurface fluids.

Aquitard – A rock unit that is relatively impermeable and which greatly retards the flow of subsurface fluids

Argillaceous – A rock containing abundant clay minerals.

Biosphere – As used in this study, the interval of rocks and sediment that contain aquifers having potable water. This interval includes glacial deposits at the surface to shale at the top of the Upper Cretaceous Bearpaw Formation.

Capture Cost – The cost for the gross tonnage of CO_2 physically captured, including accounting for the CO_2 generated through capture activities through penalty costs.

Carbon Dioxide (CO_2) Credit – A credit for reducing CO_2 emission to the atmosphere.

Conceptual Model – An abstraction of the geosphere/biosphere within the domain of the System Model, as the framework for running the long-term simulations.

Conformance Control – Directing injected or produced fluids to improve sweep efficiency within the reservoir.

Cost-benefit analysis – An evaluation of the financial cost and benefit (financial, societal, or environmental) of a large engineering project.

Deterministic risk assessment – A type of risk assessment that employs a single set of values for parameters in the model used to estimate negative impacts of the system under study.

Discounted Cash Flow – A calculation of the present value of a projected cash flow based on an assumed rate of interest.

Dolostone – A sedimentary carbonate rock composed mainly of dolomite, $CaMg(CO_3)_2$. Dolostones arise from the alteration of limestones.

DST – Drillstem test; a procedure to help determine the capacity, pressure, permeability, and/or extent of a reservoir.

EFWH – Equivalent freshwater head; the algebraic sum of the pressure head and elevation head.

Elevation head – The elevation of the interval of measurement of the pressure head with respect to an arbitrary datum.

Enhanced Oil Recovery (EOR) – The introduction of an artificial drive and displacement mechanism into a reservoir to produce oil unrecoverable by primary and secondary recovery methods.

Equation-of State (EOS) – Equations that relate pressure, volume, and temperature.

Evaporite – A sedimentary rock composed of minerals precipitated from saline fluids undergoing extensive evaporation.

Foams – A mobility control agent composed of agglomerations of gas bubbles separated from each other by thin liquid films.

Gelant – A polymer solution before it cross-links into a solid gel

Gel-Foams – A diverting or blocking agent formed of foamed gas bubbles separated by liquid lenses containing a polymer-gel solution.

Gels – A diverting or blocking agent made of a cross-linked polymer solution that behaves as an elastic solid rather than a liquid.

Geosphere – As used in this study, the portion of the rock column below the deepest aquifer containing potable water. The top of the geosphere is taken as equivalent to the top of the Upper Cretaceous Bearpaw Formation.

Grid Block – Element used to partition a region of interest in numerical simulation such that equations describing flow and energy between elements can be approximated using a finite-difference scheme.

HRAM – High resolution aeromagnetic geophysical survey; airborne surveys made with a magnetometer to measure the distribution of magnetism in the subsurface. High resolution surveys are generally conducted closer to the ground and with narrower line spacing than traditional aeromagnetic surveys.

Hydraulic head – The height of the free surface of a body of water above a given subsurface point.

Hydrostratigraphy – Organization of strata into units based on hydraulic characteristics of the rocks, such as the ability to conduct or restrict fluid movement.

Ionic Trapping – Occurs when carbon dioxide is stored in water in the form of charged ions and complexes such as bicarbonate ion (HCO_3^-), carbonate ion (CO_3^{--}), and various other complexes (*e.g.*, sodium carbonate species, $NaCO_3^-$).

Limestone – A sedimentary carbonate rock composed mainly of calcite ($CaCO_3$) and formed in a predominantly marine setting.

Lithostratigraphy – Organization of strata into units based on lithological characteristics of the rocks, such as mineralogy, grain-size, and structures.

LPNORM Analysis – A linear programming method that combines data from a variety of sources to obtain the normative (most likely) solution.

Mineral Trapping – Occurs when carbon dioxide is stored in the formation as a constituent of mineral phases (*e.g.*, CO_2 can be stored in calcite, becoming $CaCO_3$).

Mobility – The ratio of fluid relative permeability to fluid viscosity.

Net Present Value (NPV) – The difference between the discounted present value of benefits and the discounted present value of costs.

Performance assessment – Evaluation of the behaviour of a specified subsystem and comparison in terms of one or more performance standards.

Permeability – A measure of the ease with which a fluid can move through a porous medium.

Porosity – The ratio of pore volume to the bulk volume of a porous medium.

Pressure head – The height of a column of water, with density equivalent to that of fresh water, required to balance the average pore pressure exerted over an interval open to a saturated rock or soil body.

Primary Recovery – Recovery of oil without enhanced methods such as water or steam injection. The percentage of oil in the reservoir that is recovered by primary methods is usually very low.

Probabilistic risk assessment (PRA) – A type of risk assessment that takes into account the effects of uncertainty.

Probability density function (PDF) – A mathematical function of a random or uncertain parameter that expresses the likelihood that the parameter will take on particular values.

Profit – The income remaining after all business expenses are paid.

Rate of return – The profit that a regulated utility is given the opportunity to earn. The allowed rate of return is the percentage determined by the jurisdictional body based on standards that include the cost of capital in other sectors with comparable risk. The achieved rate of return is the actual result the utility obtained over any given period.

Revenue – The total amount of money received by a firm from sales of its products and/or services, gains from the sales or exchange of assets, interest and dividends earned on investments, and other increases in the owner's equity, except those arising from capital adjustments.

$$\text{Risk} = \Sigma\, p_i \times c_i$$

where p_i is the probability of occurrence of scenario or event i, which is associated with a deleterious consequence c_i. The summation extends over all significant scenarios or events to account for all possible futures. Risk assessment is then a quantified examination of the hazards associated with a practice wherein the possible scenarios or events and their probabilities of occurrence (p_i) are considered together with their potential consequences (c_i).

Risk and risk assessment – The term risk is commonly used in different ways and is understood in different ways by various segments of society. In technical terms, risk is the probability that an undesirable effect will occur relative to some endpoint. The total risk of a project is commonly given by the equation

Risk management – The activities used to identify and evaluate risk, followed by actions that make use of the information.

Royalty – With respect to oil and gas properties, a share of the production, which may or may not bear a share of the expenses of production, depending on the terms of the specific lease.

Safety assessment – Critical appraisal or evaluation of the behaviour of a specified system, with emphasis on potential impacts followed by comparison with appropriate standards, regulations, and guidelines that are concerned with human health and the environment.

Scanning Electron Microscope (SEM) – A method of visually examining solid samples by reflecting an electron beam from the surface.

Secondary Recovery – All methods of oil and natural gas extraction in which energy sources extrinsic to the reservoir other than pumps or pumping units are used.

Sensitivity analysis – Used with mathematical models to determine the important processes and parameters and, subsequently, to guide searches for crucial information and modified project designs that improve performance or safety.

Siliciclastic – A clastic (non-carbonate) sedimentary rock containing abundant quartz or other silicate minerals.

Solubility Trapping – Storage of carbon dioxide in the aqueous phase (water) as dissolved CO_2, typically referred to carbonic acid (H_2CO_3).

Stochastic simulation – The combination of using a linear estimator (the kriging estimator) to assign a best weighted linear estimate at unsampled locations and a random residual drawn through Monte Carlo simulation from the local conditional distribution (*i.e.* local uncertainty) at each location estimated.

Stratigraphy – The study of the character of rock strata, involving their distribution, form, age relations, fossil content, structure, mineral compositions, and geochemical and geophysical traits.

Supercritical – For CO_2, a phase neither gas nor liquid that exists at temperatures and pressures above the critical temperature of 31.1ºC and critical pressure of 7.38 MPa. CO_2 in the supercritical phase has a density between that of a gas and a liquid.

Surface lineaments – Discontinuously aligned linear escarpments, valleys, and smaller surface drainage depressions that vary in length and relief. Clusters of collinear individual lineaments similarly aligned define longer lineament zones.

System Model – A conceptual physical representation of the system that encompasses the reservoir, Geosphere, and biosphere and that includes artificial elements, such as wellbores and production history. The System Model for Weyburn includes an area extending approximately 10 km beyond the limits of the CO_2 flood.

System Model (System) – The physical system of the RA domain to be studied and the processes that govern the movement and migration of CO_2 within this domain.

Uncertainty – Incomplete understanding of a system and its behaviour.

Uncertainty analysis – Can be regarded as a special variant of sensitivity analysis used with mathematical models characterized by uncertain data or an incomplete understanding of system behaviour and evolution.

Unconformity – A substantial break or gap in the rock record such that a rock unit may be overlain by another not in stratigraphic succession.

Variability – A type of uncertainty that is inherent in a system and that (typically) cannot be reduced. For instance, the porosity of a geologic formation varies in an unpredictable manner from one location to the next.

Variogram – Characterizes the spatial continuity or roughness of a data set.

Viscous Fingering – Instability in displacement fronts due to an adverse mobility ratio between the displacing and the displaced fluids, which leads to reduced sweep efficiency.

WDF – Water driving force; he algebraic vector sum of the gradient of hydraulic head (*e.g.* gradient of equivalent freshwater head) and the force exerted on the same point by buoyancy due to a density contrast between the ambient formation water and water at the reference density used to calculate the hydraulic gradient.

X-Ray Diffraction (XRD) – A method of studying the atomic and molecular structure of crystalline substances by using X-rays; the characteristic patterns produced can be used to identify the material.

X-Ray Fluorescence (XRF) – A method of measuring the relative amounts of each element in a powered sample of minerals by measuring the x-ray fluorescence, which occurs when a sample is bombarded with X-rays.

IEA GHG Weyburn CO_2 Monitoring & Storage Project Summary Report 2000-2004

ptrc
Petroleum Technology Research Centre

The contents of this book represent the public summary of the IEA GHG Weyburn CO_2 Monitoring and Storage Project as presented at the 7th International Greenhouse Gas Control Technology Conference. The research results are the culmination of studies begun in 2000 and concluded in early 2004. Institutions and companies from Canada, the US, the UK, Italy, France, and Denmark were involved in making this practical study of CO_2 storage and enhanced oil recovery a success.

Sponsored by:

Natural Resources Canada
Ressources naturelles Canada

Saskatchewan Industry and Resources

European Commission

As well as 8 Industry Sponsors:

BP, ChevronTexaco, Dakota Gasification Co, Engineering Advancement Association of Japan, Nexen Canada, SaskPower, Total and TransAlta Utilities Corp.

ISBN 0-9736290-0-2